



TECHNISCHE  
UNIVERSITÄT  
WIEN

Vienna University of Technology

## DISSERTATION

# **From design and synthesis of novel organic semiconductors towards their applications in organic electronics**

ausgeführt zum Zwecke der Erlangung des akademischen Grades eines

Doktors der technischen Wissenschaften

unter der Leitung von

Univ.Prof. Dipl.-Ing. Dr.techn. Johannes Fröhlich

**Institut für Angewandte Synthesechemie**

**der Technischen Universität Wien**

von

Dipl. Ing. Johannes Binting, BSc

Matr.Nr.: 0425731

Hollitzergasse 2-6 / 55, A-1100 Wien

Vienna, May 2016



“Don’t ever let somebody tell you you can’t do something...

You’ve got a dream, you’ve gotta protect it. People can’t do something themselves, they wanna tell you you can’t do it.

You want something, go get it. Period.

— Will Smith, actor in “The pursuit of happiness”

“Never give in--never, never, never, never, in nothing great or small, large or petty, never give in except to convictions of honor and good sense. Never yield to force; never yield to the apparently overwhelming might of the enemy.”

— Winston Churchill

Dream the impossible,  
dare the unthinkable and  
aim for the unreachable!

— unknown



# Table of Contents

<b>Danksagung (Acknowledgement)</b>	1
<b>Abstract</b>	3
<b>Kurzfassung</b>	5
<b>Aims and Structure of the thesis</b>	7
<b>Collaborations</b>	9
<b>1. Brief Introduction</b>	11
1.1 Introduction and Motivation	13
1.2 Organic Semiconductors	14
1.2.1. Pentacenes	14
1.2.2. Heteroarenes	14
1.3 Organic field-effect transistors	15
1.4 Charge Transport	17
1.5 Molecular factors	17
1.6 Solution processing techniques	18
1.7 Self-assembled monolayer field-effect transistors for sensing applications	19
1.8 Conclusion	22
1.9 References	23
<b>2. Results and Discussion</b>	27
2.1 Overview of contributions	29
2.2 Context of Contributions	30
2.2.1. Design and synthesis of solution processable organic semiconductors	31
2.2.2. Development of a novel solution processing technique	31
2.2.3. Self-assembled monolayer field-effect transistors for sensing applications	31
2.2.4. Development and testing of an ultra-cheap, versatile USB-driven sensor platform	32
2.2.5. Design and Synthesis of novel OLED and PhOLED materials	32
2.3 Original Works	34
Manuscript #1	35

Manuscript #2	47
Manuscript #3	53
Manuscript #4	73
Manuscript #5	79
Manuscript #6	119
Manuscript #7	133
<b>3. Conclusion and Outlook</b>	149
<b>4. Statement of Contribution</b>	151
<b>5. Appendix</b>	153
Supporting Information - Manuscript #1	155
Supporting Information - Manuscript #3	177
Supporting Information - Manuscript #5	195
Supporting Information - Manuscript #6	241
Supporting Information - Manuscript #7	265
<b>6. Curriculum Vitae</b>	295

## Danksagung (Acknowledgement)

Zuallererst möchte ich mich bei meiner Familie, Marlene und Emma von ganzem Herzen für die unglaubliche Unterstützung, das große Verständnis und die vielen Entbehrungen bedanken. Ihr seid mein Licht und meine Stütze und habt mir die Durchführung und Verfassung dieser Dissertation erst ermöglicht.

Bei meinen Eltern möchte ich mich auf diesem Weg für die letzten 31 Jahre bedanken. Ihr wart immer für mich da und ohne eure permanente und großzügige Unterstützung wäre vieles nicht möglich gewesen.

Prof. Johannes Fröhlich danke ich die Unterstützung in den letzten Jahren sowie den mir zugestandenen Freiraum für meine Forschungsaktivitäten, die es mir ermöglicht haben viele eigene Ideen einzubringen und wertvolle Erfahrungen zu sammeln.

Dr. Hannes Mikula möchte ich für die außergewöhnliche Betreuung und Mentoring während meiner gesamten Dissertation danken sowie für die kritische Betrachtung und Evaluierung unzähliger Ideen.

Prof. Ioannis Kymissis danke ich für die einmalige Erfahrung in seiner tollen Gruppe gearbeitet haben zu dürfen sowie für den wertvollen Einblick in ein neues Forschungsgebiet. Besonderen Dank auch an die Mitglieder seiner Arbeitsgruppe: Dr. Shyuan Yang, MSc. Kostas Alexandrou, MSc. Chris Choi, MSc Amrita Masurkar, Dr. Fabio Carta sowie allen weiteren nicht genannten Mitgliedern von CLUE.

Dr. Christian Hametner möchte ich besonders für die unzähligen NMR Messungen und Ratschläge während der gesamten Arbeit danken.

Bei meinen Laborkollegen Dr. Phillip Fruhmann, DI Philipp Skrinjar, DI Julia Weber, DI Christoph Denk, Dr. Brigitte Holzer, Dr. Daniel Lumpi, DI Dennis Svatunek, DI Markus Schwarz, DI Stefan Lexmüller, Dr. Ernst Horkel, DI Paul Kautny sowie DI Florian Glöcklhofer möchte ich mich für die vielen spannenden, nervenaufreibenden und arbeitsintensiven aber auch humorvollen Stunden im Labor und abseits bedanken. Der gesamten FGHF für die letzten 5 Jahre und das tolle Arbeitsklima.

Ebenfalls bedanken möchte ich mich bei allen allgemeinen Mitarbeitern des IAS und der TU Wien, ganz im Besonderen Florian Untersteiner, Sabine Stiedry, Emiliya Hillebrand und Tanja Halbarth, für all die oft unsichtbaren Dinge, ohne die der reibungslose Ablauf an der TU Wien nicht möglich wäre.

Prof. Wolfgang Knoll danke ich für die tolle Zusammenarbeit, die Möglichkeit ein neues Forschungsgebiet kennenzulernen sowie für die zahlreichen interessanten und inspirierenden Gespräche.

Bei Prof. Peter Weinberger möchte ich mich für die Bewusstseinserschärfung bedanken wie wichtig der Blick über den Tellerrand ist.

Dr. Annette Foelske-Schmitz, Dr. Markus Sauer, Dr. Nathan Cernetic, Dr. Markus Holzweber, Dr. Ole Betghe, Prof. Helmuth Hoffmann, DI Roland Bittner, Dr. Berthold Stöger, Prof. Gernot Friedbacher, Dr. Theanne Schiros danke ich für die hervorragende Zusammenarbeit und die Unterstützung meiner Arbeit. Allen weiteren, namentlich nicht genannten Co-Autoren möchte ich selbstverständlich ebenfalls für die hervorragende Zusammenarbeit danken.

Bei der Austrian Marshall Plan Foundation möchte ich mich herzlich für die Zuerkennung des Marshall Plan Stipendiums bedanken sowie bei der Industriellenvereinigung und Wirtschaftskammer Kärnten ich für das zuerkannte Exzellenzstipendium. Besonderen Dank auch an den Österreichischen Ausstauschdienst für die großzügige Unterstützung im Rahmen des Marietta-Blau Stipendiums.





## Abstract

Organic electronics (OE) is a new technology based on organic semiconductors capable changing our everyday life within the next few years. In this context it is often being referred to as the transition of human kind from the silicon to the new carbon age.

The reason for the rise of OE is based on *the discovery and development of conductive polymers* and small molecules, for which Alan J. Heeger, Alan G. MacDiarmid and Hideki Shirakawa were awarded with the Nobel Prize in chemistry in 2000. Essentially, organic semiconductors (OSC) can conduct electricity and even surpass the performance of silicon based devices. Additionally, OE is based on a bottom-up approach, meaning that through rational design on a molecular level of the organic semiconducting material, novel properties are created, which are impossible to be replicated or imitated with silicon, expanding the world of electronics in ways unimaginable until now.

The main goal of this thesis was the design and synthesis of novel OSCs, for use as active materials in electronic devices such as organic field-effect transistors (OFETs), self-assembled monolayer field-effect transistors (SAMFETs), sensors, organic light emitting diodes (OLEDs) and phosphorescent light emitting diodes (PhOLEDs).

The focus for the development of novel OFET materials was to improve solution processability, charge carrier mobilities and environmental stability via incorporation of heteroatoms such as nitrogen and smart side chain engineering. In this context, novel printable alkylated indolo[3,2-*b*]carbazoles are discussed and their use as active materials in an OFET configuration is demonstrated exhibiting charge carrier mobility of up to  $10^{-2}\text{cm}^2/\text{Vs}$ . Furthermore, a novel low-cost pneumatic nozzle printing technique is presented capable of fabricating aligned crystalline thin films. This novel technique outperforms current solution processing techniques e.g. spin coating by a factor of 10 to 100, when comparing obtained charge carrier mobilities of different OSCs such as TIPS-pentacene and C8-BTBT. In addition, the great versatility of this technique was applied to fabricate an all-printed flexible OFET.

Improved PhOLED and OLED devices performances were obtained by implementation of novel indolo[3,2,1-*jk*]carbazole bearing compounds, realized via newly designed C-H activation methods.

One of the greatest potentials of organic electronics could be the realization of miniaturized, or even implanted, biosensors as low-cost point of care devices, capable of selectively detecting biomarkers or pathogens and creating an electronic read out for user friendly interaction. In this context two projects were designed to tackle different aspects and challenges related to this long term goal.

A novel ultra-cheap, versatile and robust USB-driven sensor platform is presented and used for detection of three different analytes ( $\text{H}_2\text{O}$  vapor, acetone,  $\text{NH}_3$ ) using PEDOT:PSS, functionalized graphene and DPP-CN respectively. The sensing mechanism is based on a chemiresistor configuration and allows for cheap and reliable sensing of various analytes by proper functionalization of the OSC.

Finally, a novel SAMFET using click chemistry for a facile approach towards sensing applications is demonstrated and benchmarked against conventional SAMFETs, which exhibited electron mobilities of  $\sim 2 \cdot 10^{-4}\text{cm}^2/\text{Vs}$ . These, CLICK-FETs present a facile and modular approach towards modifiable OSCs for use in sensing applications.



## Kurzfassung

Organische Elektronik (OE) ist eine neue, auf organischen Halbleitern basierende Technologie, die das Potential hat, unser Alltagsleben in den kommenden Jahren grundlegend zu verändern. In diesem Zusammenhang wird auch vom Übergang der Menschheit vom Silizium- ins Kohlenstoff- Zeitalter gesprochen. Ihren Ursprung nahm OE mit der *Entdeckung und Entwicklung leitfähiger Polymere* durch Alan J. Heeger, Alan G. MacDiarmid and Hideki Shirakawa, die dafür mit dem Nobelpreis für Chemie im Jahr 2000 ausgezeichnet wurden. Die Grundaussage ist, dass organische Halbleiter (OSC) Strom leiten und sogar die Leistung von siliziumbasierten Bauteilen übertreffen können. Zusätzlich basiert OE auf einem sogenannten *bottom-up* Aufbau. Dies bedeutet, dass durch rationales Design des Halbleiters auf molekularer Ebene neue Eigenschaften ermöglicht werden, die nicht durch siliziumbasierte Halbleiter imitiert oder nachgeahmt werden können. Dadurch wird die Welt der Elektronik in bisher nie geahnter Art und Weise verändert und erweitert.

Das Ziel dieser Dissertation war das Design und die Synthese neuer OSCs und deren Implementierung in organischen Bauteilen wie *organic field-effect transistors* (OFETs), *self-assembled monolayer field-effect transistors* (SAMFETs), Sensoren, *organic light emitting diodes* (OLEDs) and *phosphorescent light emitting diodes* (PhOLEDs).

Das Hauptaugenmerk bei der Entwicklung neuer OFET Materialien lag in der Lösungsverarbeitung, erhöhter Ladungsträgermobilität sowie Stabilität durch Einführung von Heteroatomen wie Stickstoff sowie durch Seitenkettenmodifikationen. In diesem Zusammenhang wurden neue druckfähige alkylierte Indolo[3,2-*b*]carbazol Verbindungen vorgestellt und deren Verwendung in OFETs mit einer Ladungsträgermobilität von bis zu  $10^{-2} \text{cm}^2/\text{Vs}$  demonstriert. Außerdem wurde eine neue günstige pneumatische Düsen-Drucktechnik vorgestellt, welche die Herstellung von orientierten kristallinen Dünnschichtfilmen ermöglicht. Diese neue Technik übertrifft bekannte Lösungsverarbeitungstechniken (wie z.B. *spin coating*) um einen Faktor von 10-100, wenn erhaltene Ladungsträgermobilitäten von bekannten OSCs wie TIPS-pentacene oder C8-BTBT verglichen werden. Aufgrund der Vielseitigkeit dieser Methode konnten zudem rein gedruckte und flexible OFETs hergestellt werden.

Verbesserte PhOLED und OLED Ergebnisse wurden durch gezielte Implementierung von neuartigen Indolo[3,2,1-*jk*]carbazol Verbindungen erzielt, welche mittels C-H Aktivierung synthetisiert wurden.

Eines der größten Potentiale von OE ist die Realisierung von miniaturisierten, oder sogar implantierbaren Biosensoren als kostengünstige patientennahe Geräte, welche in der Lage sind, Biomarker und Pathogene selektiv zu detektieren und in ein elektrisches Signal umzuwandeln, um auf diese Weise eine benutzerfreundliche Handhabung zu ermöglichen. In diesem Zusammenhang wurden zwei Projekte initiiert, um verschiedene Aspekte dieses Langzeitziels zu verwirklichen.

Eine neuartige kostengünstige, vielseitige und robuste USB-basierte Sensorplattform wird präsentiert, welche für die Detektion von drei verschiedenen Analyten ( $\text{H}_2\text{O}$  Dampf, Aceton,  $\text{NH}_3$ ) mittels PEDOT:PSS, funktionalisiertem Graphen und DPP-CN verwendet wurde. Das Messprinzip basiert auf einem chemischen Resistor und erlaubt eine billige und zuverlässige Detektion von verschiedenen Analyten durch geeignete Funktionalisierung des OSCs.

Abschließend, wird ein neuartiges Konzept für sogenannte CLICK-FETs - eine Weiterentwicklung von SAMFETs - basierend auf Click Chemie präsentiert und mit konventionell hergestellten SAMFETs, welche eine Elektronenmobilität von  $\sim 2 \cdot 10^{-4} \text{cm}^2/\text{Vs}$  aufweisen, verglichen. Diese CLICK-FETs stellen einen einfachen und modularen Zugang zu modifizierbaren OSCs dar und eignen sich somit für Anwendungen im Bereich der (Bio)Sensorik.



## Aims and Structure of the thesis

The main objective of this thesis was to develop novel organic semiconducting materials for use as active materials in electronic devices such as organic field-effect transistors (OFETs), self-assembled monolayer field-effect transistors (SAMFETs), (bio)sensors, organic light emitting diodes (OLEDs) and phosphorescent light emitting diodes (PhOLEDs). The nature of this research is located at the interface between organic synthesis, material science and device fabrication and is of a highly interdisciplinary character.

The applicant's thesis is composed of 7 publications (already published, submitted or manuscript drafts) and can be divided into 5 individual topics, touching nearly all aspects of organic electronics such as the design, synthesis and characterization of novel organic semiconductors and their implementation in electronic devices using various fabrication techniques (Figure A).



**Figure A.** Illustration of the 5 different projects and topics covered in the applicant's thesis together with the logos of the involved partner institutions; 12 o'clock position: Synthesis, Characterization and Printing Application of Alkylated Indolo[3,2-*b*]carbazoles (figure from Ref.<sup>1</sup>); 2 o'clock position: Pneumatic Nozzle Printing as a Versatile Approach to Crystal Growth Management and Patterning of Printed Organic Thin Film Transistors; 4 and 6 o'clock positions: Using click chemistry for a facile approach towards self-assembled monolayer field-effect transistors (SAMFETs): A new versatile approach for sensing applications (figure from Ref.<sup>2</sup>); 8 o'clock position: Design, Synthesis, Characterization for novel OLED and PhOLED materials (picture from Ref.<sup>3</sup>); 10 o'clock position: Ultra-cheap, versatile and robust USB-driven sensor platform (illustration from Ref.<sup>4</sup>).

This thesis is written as a cumulative work and consists of two parts:

- 1) a brief introduction to the overall topic of *organic electronics* and important aspects
- 2) the main part includes the Results and Discussion sections for materials applicable as printed OFETs, SAMFETs, CLICK-FETs, sensors, OLEDs and PhOLEDs.

Original works (manuscripts #1 to #7, already published, submitted or manuscript drafts) are included in the second part. Supporting Information of these manuscripts can be found in the Appendix of the thesis and contains experimental details and data. The applicant is first author of 4 (including 2 co-first authorships) and corresponding author of 3 of these publications. 4 manuscripts were written and composed predominantly by Johannes Bintinger. Contributions of the applicant to the other manuscripts were manifold and essential for successful completion of the respective research projects.



## Collaborations

The following collaborations were essential for a successful completion and the scientific outcome of this PhD thesis:

- Prof. Ioannis Kymissis, Department of Electrical Engineering, Columbia University, New York, NY 10027, USA
- Prof. Alex Jen and Prof. Hong Ma, Department of Materials Science and Engineering, Box 352120, University of Washington, Seattle, WA 98195-2120, Seattle, USA
- Prof. Wolfgang Knoll, AIT Austrian Institute of Technology, Donau City Strasse 1, 1220 Vienna, Austria
- Prof. Helmuth Hoffmann, Institute of Applied Synthetic Chemistry, Vienna University of Technology, Getreidemarkt 9, 1060 Vienna, Austria
- Dr. Annette Folske-Schmitz; Dr. Markus Sauer, Analytical Instrumentation Center, Vienna University of Technology, Getreidemarkt 9, 1060 Vienna, Austria
- Dr. Markus Holzweber, Institute of Chemical Technologies and Analytics, Vienna University of Technology, Getreidemarkt 9, 1060 Vienna, Austria
- Dr. Theanne Schiros, Center for Precision Assembly of Superstratic and Superatomic Solids, MRSEC, 530 W. 120th St., Columbia University, NY, USA and Fashion Institute of Technology, State University of New York, 227 W 27th St, NY 10001, USA
- Dr. Berthold Stöger, Institute of Chemical Technologies and Analytics, Vienna University of Technology, Getreidemarkt 9, 1060 Vienna, Austria





## 1. Brief Introduction



## 1.1 Introduction and Motivation

In our everyday life electronic devices are ubiquitous in various forms (displays), functions (smartphones) and numbers (computer chips). These devices are based on silicon semiconducting technology and have undoubtedly changed our contemporary society over the last 30 years. Their unparalleled success and increasing performance is based on a highly specialized, infrastructure intense industry that has managed to manufacture materials of an ever increasing quality nearly down to atomic scale. However, while this silicon electronics technology led to a manifold of products their potential applications are still limited by the inherent properties of silicon and the top-down device fabrication approach. Thus, a new technology is needed in order to create new features and possibilities.

Alan J. Heeger, Alan G. MacDiarmid and Hideki Shirakawa are considered to be the founding fathers of such a new technology called organic electronics (OE), as they were awarded with the Nobel prize in chemistry in 2000 "*for the discovery and development of conductive polymers*".

Organic electronics is a branch of electronics that uses organic (carbon based) semiconducting materials opposed to traditional silicon based electronics. This new technology is based on a bottom up approach (Figure 1), meaning that through rational design on a molecular level of the organic semiconducting material, novel properties are created which are impossible to replicate or imitate with silicon, expanding the world of electronics in ways unimaginable until now.<sup>5</sup>

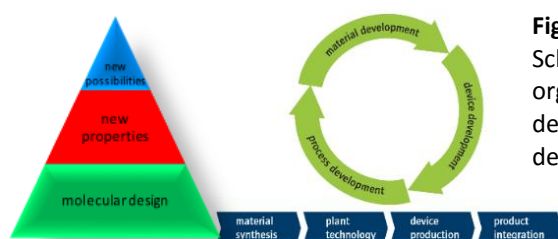
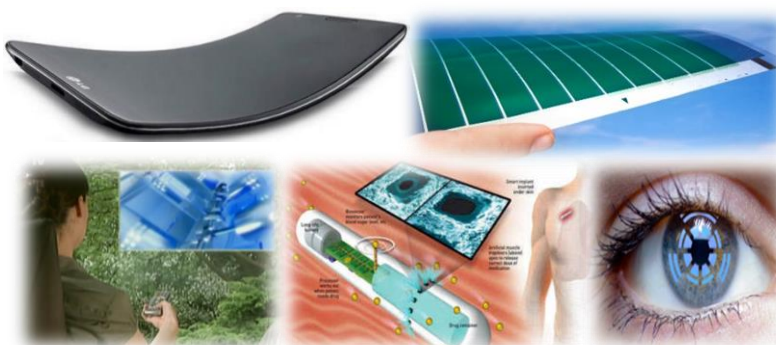


**Figure 1.** left: Illustration of the bottom up approach; right: Schematic illustration of the interdisciplinary character of organic electronics consisting of material synthesis (chemistry), device development (electrical engineering and process development (process engineering); Figure from Ref. <sup>6</sup>

One of the potential advantages of OE is the possibility to fabricate flexible, solution processed, light-weight electronic devices such as organic field-effect transistors (OFETs),<sup>6</sup> organic light emitting devices (OLEDs)<sup>7</sup>, organic photovoltaics (OPVs) as well as chemical and biological sensors<sup>8</sup>, with low manufacturing costs.<sup>9</sup> Whereas harbingers of OE such as ultrathin flexible displays in consumer electronics (LG Electronics Inc.; LG G Flex, Q1 2014) or organic solar cells (Heliatek Ltd.) have already entered the market, even more daring visions such as multifunctional windows<sup>10</sup>, implantable biosensors<sup>8,11</sup> or augmented reality in contact lenses<sup>12</sup> are within the scope of this technology (Figure 2). It goes without saying that the potential market is huge and is expected to reach several hundred billion dollars within the next 10 years. <sup>5,13</sup>

**Figure 2.** Visions of organic electronic products; top left: flexible smartphone display, Picture from LG Electronics<sup>10</sup>; top right: organic solar cell from Heliatek, Picture from Heliatek Ltd.<sup>11</sup>, bottom left: multifunctional window, picture from SAP-TV.com<sup>12</sup>; bottom middle: implantable biosensors, Picture from UCI<sup>13</sup>; bottom right: augmented reality contact lenses, Figure from Ref.<sup>14</sup>



## 1.2 Organic Semiconductors

The key to all OE applications and possibilities is the organic semiconductor (OSC) and its custom tailored properties. A semiconductor is defined as “*a nonmetallic solid that has electrical conductivity between that of a conductor and an insulator*”.<sup>14</sup> The OSCs can be classified into two categories: conjugated polymers and small molecules. Like small molecules, polymers can be deposited via solution processing techniques such as spin-coating, drop-casting, drop-coating and printing.<sup>15</sup> However, they usually exhibit a large polydispersity and are difficult to purify, making rational structure property investigations complicate.<sup>16</sup> Within this thesis the focus is set on the design, characterization and implementation of solution processable, air-stable conjugated small molecule OSCs.

In common, all OSCs share the feature of an extended  $\pi$ -conjugated system, allowing electrons to delocalize over the entire molecular backbone. This  $\pi$ -system is realized via the  $sp^2$  hybridization of carbon in a double bond or aromatic system, leaving a  $p_z$  orbital available for  $\pi$ -bonding, thus giving rise to charge carrier mobility.<sup>17</sup>

### 1.2.1. Pentacenes

(Figure 3) and its derivatives hold a special position amongst OSCs as devices based on these materials were the first to show charge carrier mobilities in the range of amorphous silicon.<sup>1,6,18</sup> Desirable physico-electronic properties of acenes scale with the degree of annelation due to predicted lower reorganization energy,<sup>19</sup> potential higher charge carrier mobility<sup>20</sup>, and smaller energy band gaps.<sup>21</sup> Unfortunately, this trend is inversely proportional to important properties like stability (under ambient operating conditions) and solubility (in common organic solvents). Because of elevated highest occupied molecular orbitals (HOMOs) and small band gaps, acenes exhibit irreversible degradation via cycloaddition reactions when exposed to air or water.<sup>18</sup> Additionally, poor solubility prevents handling and fabrication of these materials as solutions. This feature of solution processing is of great interest because it renders OE-technology compatible with established high-throughput printing techniques and can potentially lead to low-cost fabrication.<sup>17</sup> It is for those reasons that pentacene based devices have not yet been used commercially.

From these statements it is clear that the ideal OSC has to meet the following three key criteria:

1. High charge carrier mobility for fast electrical switching, low operating voltages and large on-off ratios.<sup>22–24</sup>
2. Environmental stability for integration into biomedical and flexible devices.<sup>25,26</sup>
3. Solution processability for enabling low cost and large scale production.<sup>6,27</sup>

While each of these requirements can be met individually, both, academia and industry, have yet failed to come up with a solution or a material that solves these issues all at once.

### 1.2.2. Heteroarenes

By incorporating heteroatoms, such as nitrogen (or sulfur, selenium) into the molecular backbone, lower HOMO levels are obtained, thus improving stability.<sup>25,28–30</sup> As an example the **indolo[3,2-*b*]carbazole (ICz)** scaffold was recently discussed within the OE community as it shows excellent mobilities combined with extraordinary stability over month (Figure 3).<sup>29–31</sup> Moreover, the NH moieties enable further functionalization and fine tuning of properties, e.g. enhancement of solubility through attachment of long alkyl side chains<sup>32</sup> or endowment of biological recognition capabilities for sensor applications.<sup>8</sup> Hence, the intrinsic properties of this structural scaffold represent high versatility and allow for a manifold of applications. However, so far the lack of a convenient synthetic methodology has hindered broad use of this substance class.<sup>32</sup> Examples for the chemical structures of popular small molecule p- and n-type OSCs are given in Figure 3.

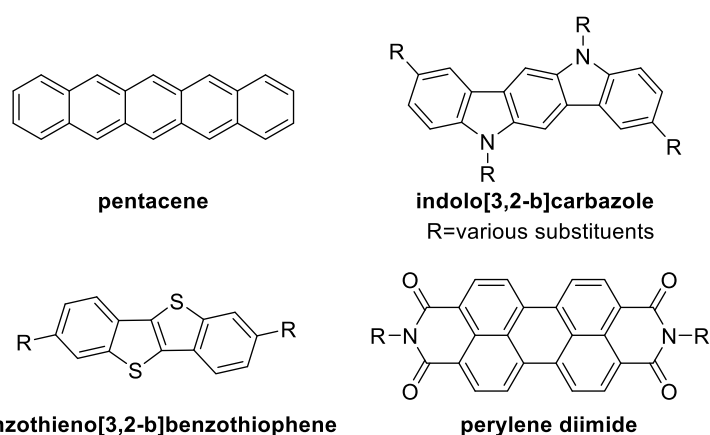


**Figure 3.** Molecular structures of pentacene, indolo[3,2-*b*]carbazole (ICz), benzothieno[3,2-*b*]benzothiophene and perylene diimide

Many of the highest-performing OSCs to date are based on **fused thiophenes** such as 2,7-dioctyl[1]benzothieno[3,2-*b*][1]benzothiophene<sup>33</sup> (C8-BTBT, Figure 3) and have attracted considerable attention in recent years.<sup>34</sup> They are superior to common acenes due to their inherent structural features, enabling enhanced stability combined with higher solubility, which is crucial for solution processing. The thiophene core structure contains six  $\pi$  electrons and is electronically similar to the benzene ring. However, fused thiophenes exhibit much higher stability owing to their lower lying HOMO energy levels and the absence of active Diels-Alder cyclization centers. Additionally, the sulfur atoms enable short intermolecular S-S interactions, which are beneficial for improved molecular packing arrangements.

Perylene-3,4,9,10-tetracarboxylic diimides (**perylene bisimides - PDIs**), belonging to the family of rylenes, are widely used as dyes and pigments in a broad range of applications owing to their outstanding chemical, thermal, and photochemical stability.<sup>35,36</sup> Besides fullerenes, these compounds are one of the few classes of materials that exhibit n-type charge transport behavior. N-type charge transport means that the majority of the charge carriers are electrons, as opposed to p-type materials in which case the majority of charge carriers are holes. It is crucial to have both n- and p-type materials available for realizing diodes and complementary circuits, structures offering high operating speeds and lower power consumption.<sup>37</sup> Their favorable electronic properties originate from the high electron affinity of the rylene core, and their strong  $\pi$ - $\pi$ -interactions which favor molecular self-assembly.<sup>35</sup>

### 1.3 Organic field-effect transistors

An organic field-effect transistor (OFET, Figure 4) is the heart of all electronic devices and basically an electrical switch. The standard OFET configuration, consists of three parts: (1) an insulator, (2) an organic semiconductor (OSC) and (3) three electrodes. The “source” and the “drain” electrodes are in direct contact with the semiconductor, while the third, the “gate”, is isolated from the OSC by the “insulator”.<sup>14</sup> The device can be seen as a plane capacitor. By applying a voltage between the gate and the source/drain electrodes, charges of opposite sign are induced at the semiconductor-dielectric interface. Because the charges in the semiconductor are mobile, current will flow in the channel when an additional voltage is applied between source and drain.<sup>38</sup> Other OFET geometries with differently arranged electrodes are possible<sup>39</sup>, but the general working principle of the transistor remains the same.

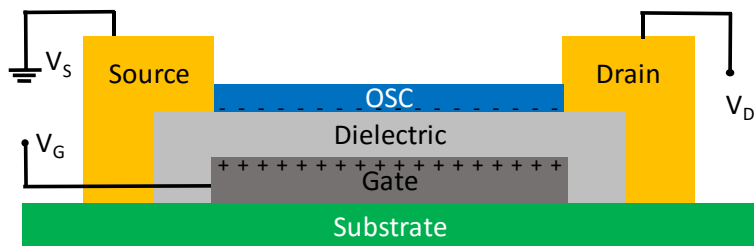


**Figure 4.** Schematic diagram of the main components of a bottom gate OFET, composed of a gate electrode, which is insulated by the dielectric (e.g. metal oxide), an OSC, the source and the drain electrodes. When a positive gate voltage is applied (+), charges of opposite signs (-) are introduced at the OSC/dielectric interface resulting in the formation of a conductive channel at the OSC/dielectric interface.

In this work, only bottom gate devices were fabricated and characterized. The advantage of this configuration is that the processing of the OSC is one of the last steps or even the final step, thus minimizing the potential of damaging or contaminating the organic thin film by other processing steps. Furthermore, bottom gate devices allow active tuning of the dielectric layer, leading to possibilities for optimizing the important OSC/dielectric interface.

As indicated in Figure 4, depending on the applied gate voltage and the used OSC, charges of opposite sign are induced at the OSC/dielectric interface and confined only to the first monolayers.<sup>40,41</sup> This is a fundamental concept that is being used when talking about self-assembled monolayer field-effect transistors (SAMFETs; section 1.7).

A schematic layout of a bottom gate OFET is composed of a gate electrode, which is insulated by the dielectric (e.g. metal oxide), an OSC and source and drain electrodes.

In contrast to traditional silicon FETs, OFETs operate in accumulation mode rather than in inversion.<sup>39</sup> However, many equations that describe silicon FETs are applicable to OFETs such as equation 1, which describes the drain current  $I_D$  in the saturation regime.

$$I_D = \frac{W}{2L} \mu_{sat} C_{ox} (V_{GS} - V_T)^2 \quad (1)$$

Where  $C_{ox}$  is the capacitance per unit area of the dielectric,  $W$  and  $L$  are OFET channel width and length, and  $V_{GS}$ , is the gate voltage,  $\mu$  is the field-effect mobility, and  $V_T$  is the threshold voltage. Fundamentally, mobility describes the relationships between the carrier velocity and the applied electric field in a given material, and is widely regarded as the most significant figure of merit to evaluate the performance of field effect transistors.<sup>39</sup> The effective mobility of an OFETs can be determined by measuring the drain-current ( $I_D$ ) vs. gate-voltage ( $V_{GS}$ ) characteristic in the saturation region according to equation 1. To eliminate the dependency on the ambiguity of the threshold voltage, the effective mobility is extracted by plotting the square-root  $I_D$  vs.  $V_{GS}$  and calculating the slope (Figure 5).

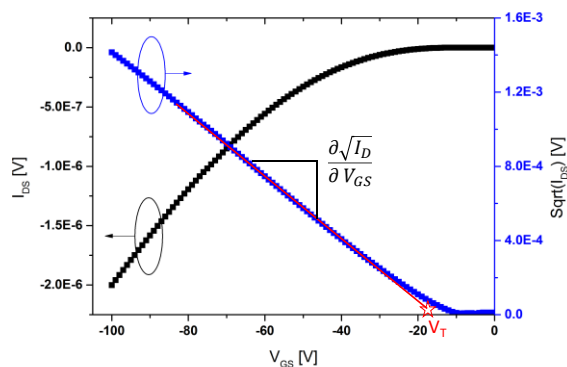


**Figure 5.** Exemplary transfer curve of an OFET containing a p-type OSC (in this case 2,8-Dihexyl indolo[3,2-*b*]carbazole as active layer). The characteristic parameters of a transistor, such as mobility,  $V_T$  or on/off-ratio can be extracted from this curve.

Typical mobility values of OSCs range from  $10^{-4}$  to  $10^1$   $\text{cm}^2/\text{Vs}$ , while mobilities as high as  $31$   $\text{cm}^2/\text{Vs}$  have been reported in case of single crystal OSCs.<sup>33</sup> The mobility determines the possible switching speed of the circuit and should be as high as possible.<sup>22–24</sup>

In summary, by varying the gate voltage, the amount of free charge carriers in the OSC is modulated. As the conductivity scales with the amount of free charge carriers, the current between source and drain can be modulated via the gate voltage.<sup>14,39,42</sup>

## 1.4 Charge Transport

In contrast to silicon, localized orbitals are responsible for charge transport in OSCs. Thus, a charge transport cannot be described with a band-like transport. It occurs via thermally activated hopping processes within the OSC along the plane of the substrate and is confined only to the first monolayer at the dielectric/semiconducting interface.<sup>40,41,43</sup> The hopping probability (electron-transfer rate) is described by the Marcus theory (equation 2) as

$$k_{ET} = \frac{4\pi^2}{h} \frac{1}{\sqrt{4\pi k_B T}} t^2 \exp\left(-\frac{\lambda}{4k_B T}\right) \quad (2)$$

where  $\lambda$  is the reorganization energy,  $t$  is the transfer integral,  $T$  is the temperature and  $h$  and  $k_B$  are the Planck and Boltzmann constants, respectively. The transfer integral  $t$  describes the degree of adjacent molecular orbital overlap and strongly depends on the  $\pi$ - $\pi$  distance and molecular packing arrangements. The reorganization energy  $\lambda$  describes the energy change associated with the geometry relaxation during the charge transfer. Hence, in order to achieve high charge carrier mobility, large transfer integrals and small reorganization energies are beneficial.<sup>9,44,45</sup> These factors highly depend on molecular factors as described below.

## 1.5 Molecular factors

Molecular packing motifs and film morphology have a huge influence on device performances, because high charge carrier mobilities are usually achieved in highly ordered systems, exhibiting dense molecular packing, extended  $\pi$ -conjugation and negligible defects.<sup>28,43,46</sup> A lot of these requirements are met in single crystal systems. In deed a lot of the highest reported mobilities are based on single crystal devices. Additionally, the orientation of the OSC on the dielectric surface plays a crucial role, as the induced charge carriers are confined only to the first few monolayers (Figure 6a).<sup>40,47–51</sup> The long axes of the molecules should stand perpendicular to the dielectric and parallel to each other, since charge transport occurs along the direction of intermolecular  $\pi$ - $\pi$  stacking (Figure 6b).<sup>52,53</sup>

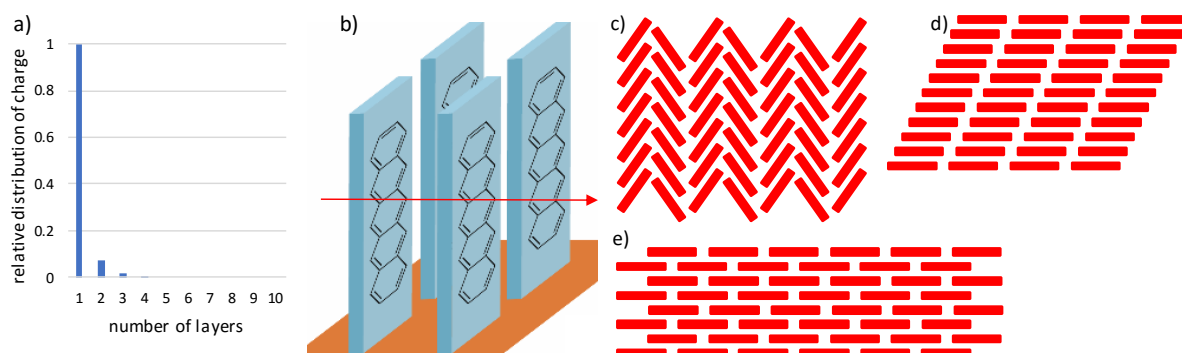


**Figure 6.** a) Relative distribution of charge in the first 10 monolayers in a pentacene OFET at  $V_G=25$  V indicating that the majority of the current flows in the first monolayer; redrawn data from Ref.<sup>42</sup>; b) Schematic illustration of an idealized molecular arrangement of the OSC on the dielectric surface (orange);  $\pi$ -stacking is indicated by parallel sheets; charge transport, indicated by the red arrow occurs perpendicular to the plane of the OSC; graphic adapted from Ref.<sup>54</sup>; c-e) Molecular packing arrangements in crystals: c) Herringbone packing motif with  $\pi$ - $\pi$  overlap between adjacent molecules; d) Lamellar arrangement with 1D  $\pi$ -stacking; e) Lamellar motif with 2D  $\pi$ -stacking; redrawn from Ref.<sup>44</sup>

The strongest form of intermolecular coupling arises from interactions between the  $\pi$ -electron clouds of aromatic molecules, which are maximized when molecules adopt a cofacial lamellar packing (Figure 6e). Theoretically, this arrangement is the most efficient mode, because it maximizes the transfer integrals. However, while some OSCs with cofacial lamellar packing exhibit excellent performances, the packing arrangement is not a prerequisite for high device performances.<sup>44</sup> For instance, even though pentacene shows a typical herringbone motif (Figure 6c) and TIPS-pentacene exhibits a 2D- $\pi$ -stacking (Figure 6e), pentacene still demonstrates higher mobilities.<sup>55</sup> Other kinds of packing motifs are illustrated in Figure 6.

## 1.6 Solution processing techniques

While a lot of OSCs were vacuum deposited in the past, solution processing is key for realizing low-cost devices and constitutes a major advantage of OE.<sup>15,56</sup> Thus, the main requirement for this technology is the solubility of the materials in common organic solvents. Additionally, the solution processed films should be crystalline, oriented and exhibit a desirable packing motif, as described in the previous section.<sup>33,57-60</sup> Many methods have been developed to generate aligned crystals of organic thin films such as dip coating,<sup>61</sup> zone casting,<sup>62</sup> doctor blade coating,<sup>63</sup> and solution shearing<sup>64</sup> (Figure 7). While these strategies can take advantage of super lateral crystallization and growth to extend crystal domains over large spatial extents, these techniques generally fail to simultaneously pattern the semiconductor while also controlling crystallization. Thus, the holy grail of printed electronics is to achieve solution processed, patterned and orientated crystalline thin films. In manuscript #2 a novel pneumatic nozzle printing technique is presented, which is attempting to tackle these requirements, by simultaneously enabling patterning and deposition of multiple materials.

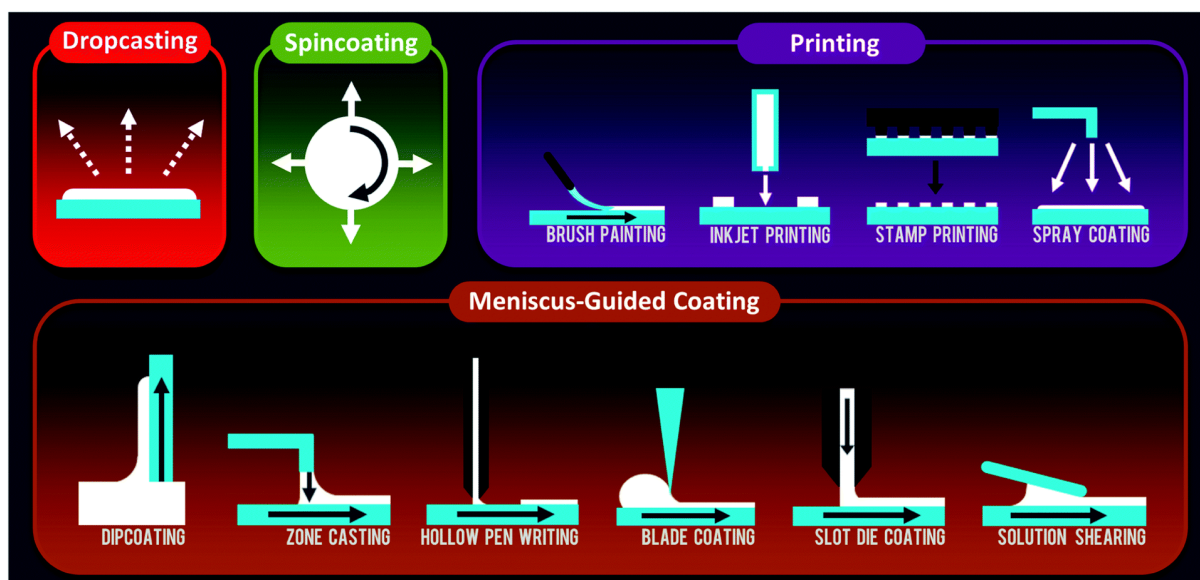


**Figure 7.** Schematic illustration of solution-based deposition techniques. Figure from Ref.<sup>15</sup>



## 1.7 Self-assembled monolayer field-effect transistors for sensing applications

Self-assembly is *the autonomous organization of components into patterns and structures*<sup>65</sup> and holds great potential for new applications in the field of organic electronics by enabling a rational bottom-up approach.<sup>51</sup> Self-assembled monolayers (SAMs) have been used amongst other things<sup>66</sup> as high-k nanodielectrics,<sup>67</sup> for interface engineering,<sup>68</sup> surface protection<sup>69</sup> and enhancing solar cell efficiencies.<sup>70</sup> One of the big advantages of SAMs is their solution processability thus providing a smart engineering approach for low cost device fabrication. SAM molecules typically consist of an anchor group, an alkyl-chain spacer and a functional head group. The anchor group is capable of attaching the SAM covalently to a metal oxide surface via dangling bonds, thus eliminating other surface reactions and ensuring the formation of only a single layer. Representative anchor groups are silanes, phosphonic acids or thiols which can bind to metal oxides (e.g. SiO<sub>2</sub>, Al<sub>2</sub>O<sub>3</sub>, HfO<sub>2</sub>) or gold (thiols), respectively.<sup>71-74</sup> It is noteworthy to mention that different anchor groups can account for different molecular tilt angles. Alkyl-phosphonic acid SAMs exhibit an inherent tilt angle of >30°, while monofunctional chlorosilanes demonstrate a tilt angle of only 10°. <sup>75</sup> The alkyl spacers ensure the upright orientation of the molecules and a dense packing as a result of van-der-Waals forces between the chains. Various functional head group can be used. The choice of a head group is of paramount importance, as their nature determines the overall surface chemistry and properties of the resulting SAM film.

The growth process of the SAM film passes through different stages, which are schematically depicted in Figure 8. The self-assembly process depends on various parameters such as the concentration of the self-assembling molecules, the solvent, the anchor group and its affinity to the substrate, the temperature and the immersion time.<sup>71,72</sup> However, a general process of self-assembly proceeds as follows. At first, molecules are physisorbed on the surface, followed by the chemisorption step, which establishes a chemical bond between the surface- and anchor group atoms. Subsequent molecules start to interact via van-der-Waals forces with these seed islands and thus begin to orient in an upward position, to form ever larger SAM islands. These islands grow bigger until a complete surface coverage is obtained and the molecules are densely packed in a monolayer.<sup>72,76</sup>

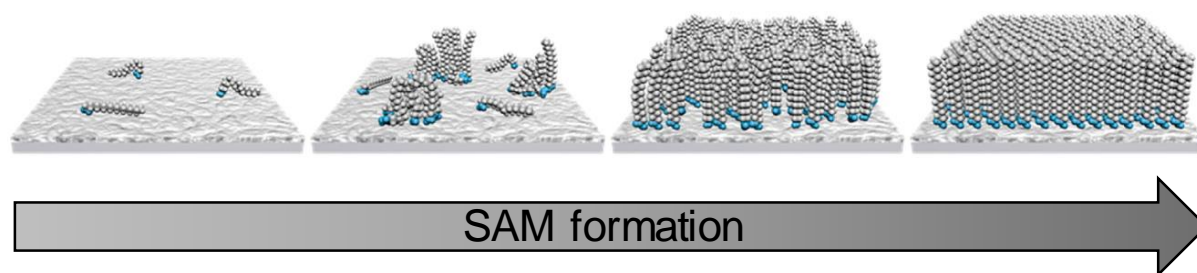


**Figure 8.** Schematic process of the formation of a self-assembled monolayer (SAM), from a few physisorbed molecules to more chemisorbed molecules on the surface to a densely packed monolayer. Graphic adapted with permission from Ref.<sup>76</sup> Copyright American Chemical Society 2012

As mentioned above, by varying the functional head groups a powerful tool for tuning surface chemistry is obtained leading to new properties and applications. For example, by employing fluorinated alkyl-chains as functional head groups super hydrophobic SAMs are created that are useful for corrosion prevention of surfaces.<sup>69,77</sup> In contrast, hydrophilic surfaces are created when using polar head groups such as OH-groups, which might find use in biomedical applications.<sup>78</sup>

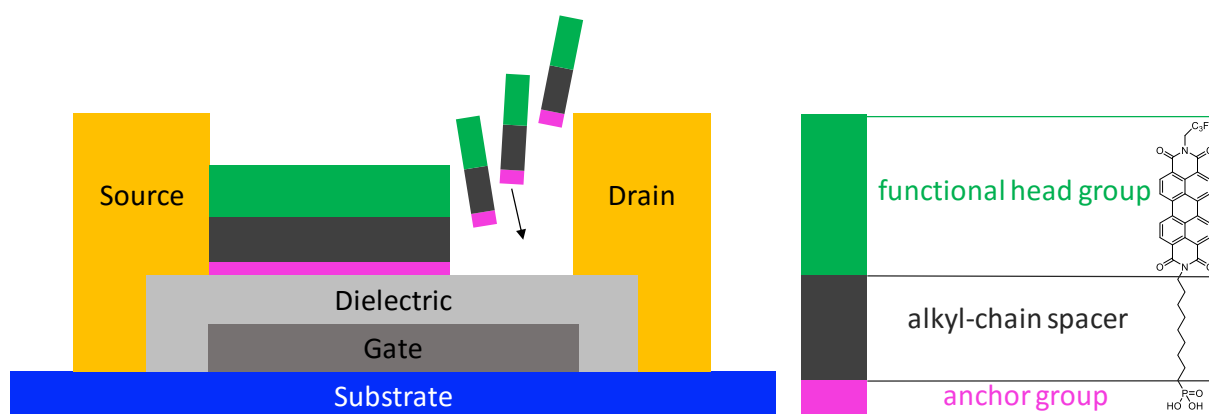


**Figure 9.** left: Schematic layout of a bottom gate SAMFET, in which the semiconductor film consists only of a single monolayer that self-assembles on the dielectric (metal oxide) and forms the active channel region of the transistor; right side: Schematic layout of self-assembling molecules composed of 3 building blocks: (1) the anchor group (pink), capable of covalently binding to the metal oxide surface (phosphonic acids, silanes, or thiols), (2) the alkyl-chain spacer (grey) providing an upright position of the molecule and additional van-der-Waals forces for self-assembling, and (3) the functional head group (green). These 3 building blocks are interchangeable depending on the desired properties. In this case an OSC (fluorinated perylene diimide) functional head group is shown.

However, SAMs are not limited to just modify surface properties. When an OSC is employed as the functional head group, a semiconducting monolayer is formed which can act as the active channel in a conventional OFET device (Figure 9). The result is called a self-assembled monolayer field-effect transistor (SAMFET). As stated before, the free charges in an OFET are predominantly confined to the first molecular layer of the OSC.<sup>40,41,79</sup> Hence, a SAMFET can be seen as an elegant way to fabricate functional electronic devices. Such an approach with an emphasis on synthesis of the required semiconducting SAMs is discussed in manuscript #3.

### ***SAMFETs for sensing applications***

One of the greatest potentials of organic electronics is the realization of miniaturized, or even implanted, biosensors as low-cost point-of-care devices, capable of label-free, selective detection of analytes (e.g. biomarkers, pathogens) while creating an electronic read out for user-friendly interaction. The basic working principle of these sensors is based on the aforementioned standard OFET configuration (Figure 4). An OFET-biosensor is an analytical device consisting of an OFET endowed with covalently attached biological recognition units to the OSC, whose specific interactions with analytes changes the electrical current flowing between source and drain.<sup>4</sup>

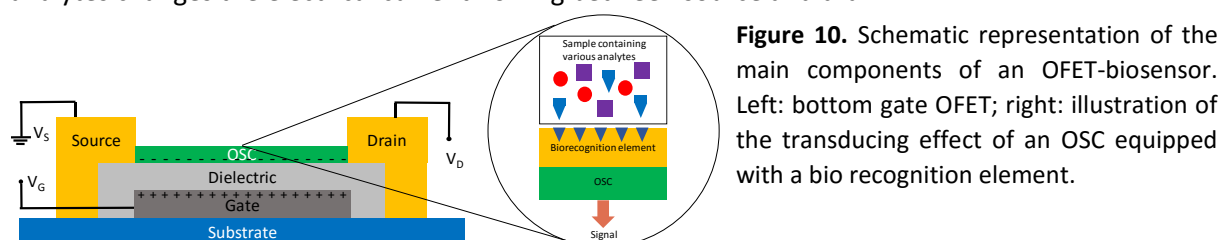


**Figure 10.** Schematic representation of the main components of an OFET-biosensor. Left: bottom gate OFET; right: illustration of the transducing effect of an OSC equipped with a bio recognition element.

It is important to acknowledge that in such a device, the OSC serves, as an active charge carrier transport layer and as a functional sensing surface (Figure 10). A huge advantage over other current sensing technologies (such as electrochemical or optical ones) is the capability of delivering a response that is label-free using a simple, inexpensive electronic read-out set-up that can easily be miniaturized by employing established printed circuit OE-technologies, ultimately enabling small point-of-care (POC) devices.<sup>8</sup>

The sensitivity of such a sensor is dependent on the thickness of the semiconductor,<sup>80</sup> thus the maximum sensitivity would be achieved in a device consisting of only one monolayer of the active material,<sup>81</sup> which is the case for SAMFETs (Figure 11).

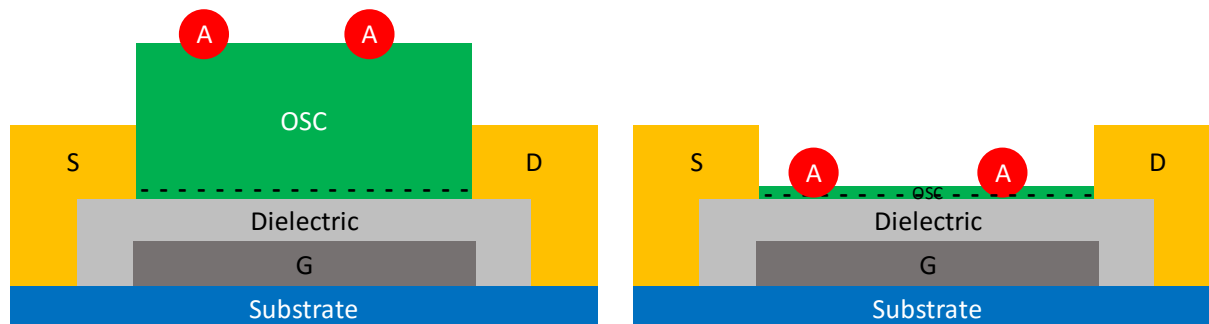


**Figure 11.** Schematic illustration of the operation principle of a SAMFET-sensor. On the left, analyte molecules which are absorbed on top of a thick semiconductor layer will only have a minor effect on the current modulation as this is limited by the thickness of the OSC. The electrostatic interactions (red circles) of the analyte will have a much bigger effect when the distance between analyte and the active channel is decreased (right side). Thus a SAMFET based biosensor could be a highly sensitive sensing platform.

However, current SAMFET materials<sup>2,51,82–84</sup> (Figure 12) require cumbersome synthesis and most importantly still lack the capability for further functionalization. The endowment of the OSC via functional groups with a biorecognition unit is essential for sensor selectivity.

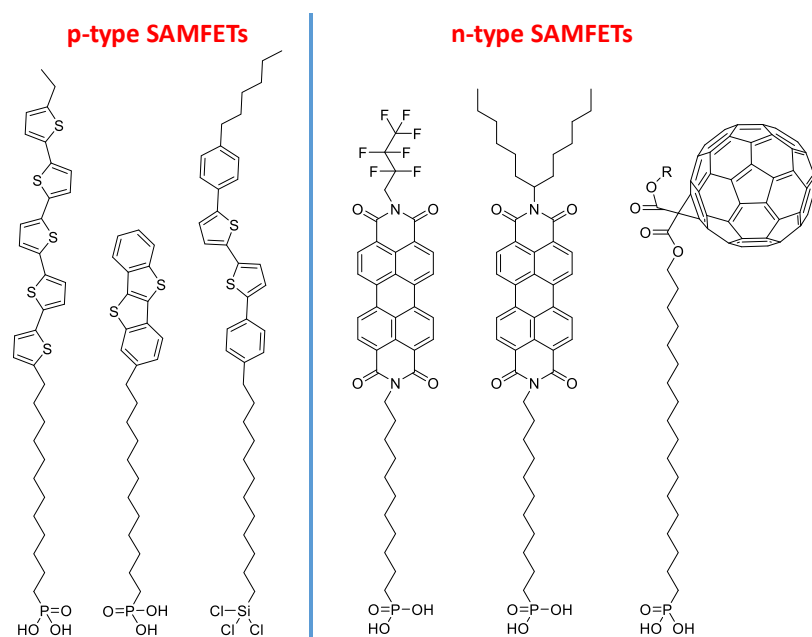


**Figure 12.** Molecular structures of currently used p- and n-type SAMFET materials. All materials are lacking possibilities for further functionalization and require cumbersome synthesis.

Using a novel approach towards these OFET based biosensors, the applicant is attempting to realize a novel building block like approach based on click chemistry to synthesize modifiable SAMFETs for the first time (Figure 13). This concept was used for the study described in manuscript #3.

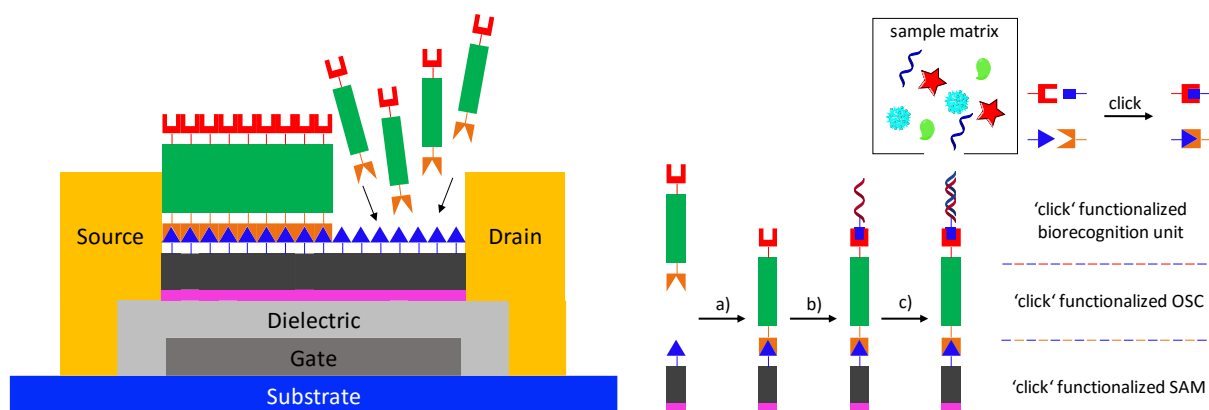


**Figure 13.** Schematic illustration showing the concept of a CLICK-FET device and the building block approach using click chemistry towards CLICK-FETs for sensing applications.

In contrast to conventional SAMFET devices (Figure 9), which are realized via a single self-assembly reaction of a pre-synthesized material, CLICK-FETs (Figure 13) use a truly, versatile and bottom-up approach as both the active OSC (shown as a green-colored rectangle) and the biorecognition unit (shown as a red-colored single helix) are realized stepwise using click chemistry directly on the substrate. Different click moieties ensure complete orthogonality of the method. Click chemistry or click ligations are types of nature inspired reactions, which lead to high yields, under moderate conditions and high efficiency. One of the most popular reactions within the click-chemistry concept is the azide alkyne cycloaddition using a copper catalyst at room temperature forming 1,2,3-triazoles.<sup>85</sup>

## 1.8 Conclusion

Organic electronics is a disruptive new area of research and development leading to technologies capable of changing our everyday life within the next few years, by enabling new applications and products based on organic semiconductors (OSC) such as implantable biosensors, large area low-cost photovoltaics or ultralight flexible displays. Rational bottom-up design and solution processability of these novel materials are key to the success of OE technology. The concepts and methods described in this chapter have given insight to the challenges of molecular engineering novel OSCs.

The aim of this thesis is the development of novel OSCs, their implementation and evaluation in various electronic devices such as sensors, OFETs, OLEDs and PhOLEDs.

## 1.9 References

- (1) Adachi Laboratory, Center for Futurer Laboratory, Kyushu University. Basic Structure of OFET [http://www.cstf.kyushu-u.ac.jp/~adachilab/research\\_b\\_e.html](http://www.cstf.kyushu-u.ac.jp/~adachilab/research_b_e.html) (accessed May 31, 2012).
- (2) Ringk, A.; Christian Roelofs, W. S.; Smits, E. C. P.; van der Marel, C.; Salzmann, I.; Neuhold, A.; Gelinck, G. H.; Resel, R.; de Leeuw, D. M.; Strohrriegl, P. *Org. Electron.* **2013**, *14* (5), 1297.
- (3) meharris. *OLED\_EarlyProduct*; 2020.
- (4) Graphic by Christine Daniloff, image via mit.edu.
- (5) Xi, Z.; Bäuerle, P.; Aida, T.; Skabara, P.; Kagan, C. San Francisco, CA, USA, 2012.
- (6) Mei, J.; Diao, Y.; Appleton, A. L.; Fang, L.; Bao, Z. *J. Am. Chem. Soc.* **2013**, *135* (18), 6724.
- (7) Tyan, Y.-S. *J. Photonics Energy* **2011**, *1* (1), 11009.
- (8) Torsi, L.; Magliulo, M.; Manoli, K.; Palazzo, G. *Chem. Soc. Rev.* **2013**.
- (9) Klauk, H. *Organic electronics II: more materials and applications*; Wiley-VCH: Weinheim, 2012.
- (10) Davidsson, H.; Perers, B.; Karlsson, B. *Sol. Energy* **2012**, *86* (3), 903.
- (11) Rivnay, J.; Owens, R. M.; Malliaras, G. G. *Chem. Mater.* **2013**.
- (12) Lingley, A. R.; Ali, M.; Liao, Y.; Mirjalili, R.; Klonner, M.; Sopanen, M.; Suihkonen, S.; Shen, T.; Otis, B. P.; Lipsanen, H.; Parviz, B. A. *J. Micromechanics Microengineering* **2011**, *21* (12), 125014.
- (13) Acatech. *Organische Elektronik in Deutschland: Bewertung und Empfehlungen Für Die Weiterentwicklung*; Gabler Wissenschaftsverlage, 2011.
- (14) Klauk, H. *Organic Electronics: Materials, Manufacturing, and Applications*; John Wiley & Sons, 2006.
- (15) Diao, Y.; Shaw, L.; Bao, Z.; Mannsfeld, S. C. B. *Energy Environ. Sci.* **2014**, *7* (7), 2145.
- (16) Facchetti, A. *Chem. Mater.* **2011**, *23* (3), 733.
- (17) Klauk, H. *Organic electronics. more materials and applications II II*; Wiley-VCH: Weinheim, 2012.
- (18) Anthony, J. E. *Angew. Chem. Int. Ed.* **2008**, *47* (3), 452.
- (19) Deng, W.-Q.; Goddard, W. A. *J Phys Chem B* **2004**, *108* (25), 8614.
- (20) Cheng, Y. C.; Silbey, R. J.; da Silva Filho, D. A.; Calbert, J. P.; Cornil, J.; Brédas, J. L. *J. Chem. Phys.* **2003**, *118* (8), 3764.
- (21) Brocks, G.; van den Brink, J.; Morpurgo, A. F. *Phys. Rev. Lett.* **2004**, *93* (14), 146405.
- (22) Kim, C. H.; Hlaing, H.; Carta, F.; Bonnassieux, Y.; Horowitz, G.; Kymissis, I. *ACS Appl. Mater. Interfaces* **2013**, *5* (9), 3716.
- (23) Mei, Y.; Loth, M. A.; Payne, M.; Zhang, W.; Smith, J.; Day, C. S.; Parkin, S. R.; Heeney, M.; McCulloch, I.; Anthopoulos, T. D.; Anthony, J. E.; Jurchescu, O. D. *Adv. Mater.* **2013**, *25* (31), 4352.
- (24) Yamashita, Y. *Sci. Technol. Adv. Mater.* **2009**, *10* (2), 24313.
- (25) Wu, Y.; Li, Y.; Gardner, S.; Ong, B. S. *J. Am. Chem. Soc.* **2005**, *127* (2), 614.
- (26) Jiang, H.; Zhao, H.; Zhang, K. K.; Chen, X.; Kloc, C.; Hu, W. *Adv. Mater.* **2011**, *23* (43), 5075.
- (27) Allard, S.; Forster, M.; Souharce, B.; Thiem, H.; Scherf, U. *Angew. Chem. Int. Ed.* **2008**, *47* (22), 4070.
- (28) Bunz, U. H. F. *Pure Appl. Chem.* **2010**, *82* (4), 953.
- (29) Park, K. S.; Salunkhe, S. M.; Lim, I.; Cho, C.-G.; Han, S.-H.; Sung, M. M. *Adv. Mater.* **2013**, *25* (24), 3351.
- (30) Boudreault, P.-L. T.; Wakim, S.; Tang, M. L.; Tao, Y.; Bao, Z.; Leclerc, M. *J. Mater. Chem.* **2009**, *19* (19), 2921.
- (31) Russell, F.; Harmody, D.; McCarthy, P. J.; Pomponi, S. A.; Wright, A. E. *J. Nat. Prod.* **2013**.
- (32) Boudreault, P.-L. T.; Virkar, A. A.; Bao, Z.; Leclerc, M. *Org. Electron.* **2010**, *11* (10), 1649.
- (33) Minemawari, H.; Yamada, T.; Matsui, H.; Tsutsumi, J.; Haas, S.; Chiba, R.; Kumai, R.; Hasegawa, T. *Nature* **2011**, *475* (7356), 364.
- (34) Cinar, M. E.; Ozturk, T. *Chem. Rev.* **2015**, *115* (9), 3036.
- (35) Würthner, F. *Chem. Commun.* **2004**, No. 14, 1564.
- (36) Chen, L.; Li, C.; Müllen, K. *J. Mater. Chem. C* **2014**, *2* (11), 1938.
- (37) Jones, B. A.; Facchetti, A.; Wasielewski, M. R.; Marks, T. J. *J. Am. Chem. Soc.* **2007**, *129* (49), 15259.
- (38) Donald, K. J. *J. Inorg. Organomet. Polym. Mater.* **2011**, *21* (2), 391.
- (39) Kymissis, I. *Organic Field Effect Transistors: Theory, Fabrication and Characterization*; Springer, 2008.
- (40) Dodabalapur, A.; Torsi, L.; Katz, H. E. *Science* **1995**, *268* (5208), 270.
- (41) Tanase, C.; Meijer, E. J.; Blom, P. W. M.; de Leeuw, D. M. *Org. Electron.* **2003**, *4* (1), 33.
- (42) *Organic field-effect transistors*; Optical science and engineering; CRC Press: Boca Raton, 2007.
- (43) Karl, N. *Synth. Met.* **2003**, *133–134*, 649.
- (44) Zhou, K.; Dong, H.; Zhang, H.; Hu, W. *Phys Chem Chem Phys* **2014**, *16* (41), 22448.

- (45) Brédas, J. L.; Calbert, J. P.; Filho, D. S.; A, D.; Cornil, J. *Proc. Natl. Acad. Sci.* **2002**, *99* (9), 5804.
- (46) Gershenson, M. E.; Podzorov, V. *Rev. Mod. Phys.* **2006**, *78* (3), 973.
- (47) Liu, S.-W.; Lee, C.-C.; Wen, J.-M.; Chen, C.-T. *Appl. Phys. Lett.* **2011**, *98* (2), 23306.
- (48) Dinelli, F.; Murgia, M.; Levy, P.; Cavallini, M.; Biscarini, F.; de Leeuw, D. *Phys. Rev. Lett.* **2004**, *92* (11).
- (49) Shehu, A.; Quiroga, S. D.; D'Angelo, P.; Albonetti, C.; Borgatti, F.; Murgia, M.; Scorzoni, A.; Stoliar, P.; Biscarini, F. *Phys. Rev. Lett.* **2010**, *104* (24).
- (50) Park, B.-N.; Seo, S.; Evans, P. G. J. *J. Phys. Appl. Phys.* **2007**, *40* (11), 3506.
- (51) Smits, E. C. P.; Mathijssen, S. G. J.; van Hal, P. A.; Setayesh, S.; Geuns, T. C. T.; Mutsaers, K. A. H. A.; Cantatore, E.; Wondergem, H. J.; Werzer, O.; Resel, R.; Kemerink, M.; Kirchmeyer, S.; Muzafarov, A. M.; Ponomarenko, S. A.; de Boer, B.; Blom, P. W. M.; de Leeuw, D. M. *Nature* **2008**, *455* (7215), 956.
- (52) Facchetti, A. *Mater. Today* **2007**, *10* (3), 28.
- (53) Coropceanu, V.; Cornil, J.; da Silva Filho, D. A.; Olivier, Y.; Silbey, R.; Brédas, J.-L. *Chem. Rev.* **2007**, *107* (4), 926.
- (54) Bao, Z. *Mater. Matters* **2007**.
- (55) Sheraw, C. d.; Jackson, T. n.; Eaton, D. I.; Anthony, J. e. *Adv. Mater.* **2003**, *15* (23), 2009.
- (56) Bao, Z. *Adv. Mater.* **2000**, *12* (3), 227.
- (57) Li, R.; Jiang, L.; Meng, Q.; Gao, J.; Li, H.; Tang, Q.; He, M.; Hu, W.; Liu, Y.; Zhu, D. *Adv. Mater.* **2009**, *21* (44), 4492.
- (58) Sele, C. W.; Kjellander, B. K. C.; Niesen, B.; Thornton, M. J.; van der Putten, J. B. P. H.; Myny, K.; Wondergem, H. J.; Moser, A.; Resel, R.; van Breemen, A. J. J. M.; van Aerle, N.; Heremans, P.; Anthony, J. E.; Gelinck, G. H. *Adv. Mater.* **2009**, *21* (48), 4926.
- (59) Dong, H.; Wang, C.; Hu, W. *Chem. Commun.* **2010**, *46* (29), 5211.
- (60) Wang, C.; Dong, H.; Hu, W.; Liu, Y.; Zhu, D. *Chem. Rev.* **2012**, *112* (4), 2208.
- (61) Liu, N.; Zhou, Y.; Ai, N.; Luo, C.; Peng, J.; Wang, J.; Pei, J.; Cao, Y. *Langmuir* **2011**, *27* (24), 14710.
- (62) James, D. T.; Frost, J. M.; Wade, J.; Nelson, J.; Kim, J.-S. *ACS Nano* **2013**, *7* (9), 7983.
- (63) Chang, Y.-H.; Tseng, S.-R.; Chen, C.-Y.; Meng, H.-F.; Chen, E.-C.; Horng, S.-F.; Hsu, C.-S. *Org. Electron.* **2009**, *10* (5), 741.
- (64) Diao, Y.; Tee, B. C.-K.; Giri, G.; Xu, J.; Kim, D. H.; Becerril, H. A.; Stoltenberg, R. M.; Lee, T. H.; Xue, G.; Mannsfeld, S. C. B.; Bao, Z. *Nat. Mater.* **2013**, *12* (7), 665.
- (65) Whitesides, G. M.; Grzybowski, B. *Science* **2002**, *295* (5564), 2418.
- (66) Halik, M.; Hirsch, A. *Adv. Mater.* **2011**, *23* (22–23), 2689.
- (67) Senanayak, S. P.; Sangwan, V. K.; McMorro, J. J.; Everaerts, K.; Chen, Z.; Facchetti, A.; Hersam, M. C.; Marks, T. J.; Narayan, K. S. *Adv. Electron. Mater.* **2015**, *1* (12), n/a.
- (68) Ito, Y.; Virkar, A. A.; Mannsfeld, S.; Oh, J. H.; Toney, M.; Locklin, J.; Bao, Z. *J. Am. Chem. Soc.* **2009**, *131* (26), 9396.
- (69) Kosian, M.; Smulders, M. M. J.; Zuilhof, H. *Langmuir* **2016**.
- (70) Wojciechowski, K.; Stranks, S. D.; Abate, A.; Sadoughi, G.; Sadhanala, A.; Kopidakis, N.; Rumbles, G.; Li, C.-Z.; Friend, R. H.; Jen, A. K.-Y.; Snaith, H. J. *ACS Nano* **2014**, *14*1121165501003.
- (71) Ulman, A. *Chem. Rev.* **1996**, *96* (4), 1533.
- (72) Carraro, C.; Yauw, O. W.; Sung, M. M.; Maboudian, R. *J. Phys. Chem. B* **1998**, *102* (23), 4441.
- (73) Schreiber, F. *Prog. Surf. Sci.* **2000**, *65* (5–8), 151.
- (74) Klauk, H.; Zschieschang, U.; Pflaum, J.; Halik, M. *Nature* **2007**, *445* (7129), 745.
- (75) Hutchins, D. O.; Acton, O.; Weidner, T.; Cernetic, N.; Baio, J. E.; Ting, G.; Castner, D. G.; Ma, H.; Jen, A. K.-Y. *Org. Electron.* **2012**, *13* (3), 464.
- (76) Lenz, T.; Schmaltz, T.; Novak, M.; Halik, M. *Langmuir* **2012**, *28* (39), 13900.
- (77) Portilla, L.; Halik, M. *ACS Appl. Mater. Interfaces* **2014**, *6* (8), 5977.
- (78) Chaki, N. K.; Vijayamohan, K. *Biosens. Bioelectron.* **2002**, *17* (1–2), 1.
- (79) Mottaghi, M.; Horowitz, G. *Org. Electron.* **2006**, *7* (6), 528.
- (80) Huang, J.; Sun, J.; Katz, H. E. *Adv. Mater.* **2008**, *20* (13), 2567.
- (81) Andringa, A.-M.; Spijkman, M.-J.; Smits, E. C. P.; Mathijssen, S. G. J.; Hal, P. A. van; Setayesh, S.; Willard, N. P.; Borshchev, O. V.; Ponomarenko, S. A.; Blom, P. W. M.; de Leeuw, D. M. *Org. Electron.* **2010**, *11* (5), 895.
- (82) Schmaltz, T.; Amin, A. Y.; Khassanov, A.; Meyer-Friedrichsen, T.; Steinrück, H.-G.; Magerl, A.; Segura, J. J.; Voitchovsky, K.; Stellacci, F.; Halik, M. *Adv. Mater.* **2013**, *25* (32), 4511.
- (83) Parry, A. V. S.; Lu, K.; Tate, D. J.; Urasinska-Wojcik, B.; Caras-Quintero, D.; Majewski, L. A.; Turner, M. L. *Adv. Funct. Mater.* **2014**, *24* (42), 6677.

- (84) Schmaltz, T.; Khassanov, A.; Steinrück, H.-G.; Magerl, A.; Hirsch, A.; Halik, M. *Nanoscale* **2014**, *6* (21), 13022.
- (85) Kolb, H. C.; Finn, M. G.; Sharpless, K. B. *Angew. Chem. Int. Ed.* **2001**, *40* (11), 2004.
- (86) Lumpi, D.; Holzer, B.; Bintliger, J.; Horkel, E.; Waid, S.; Wanzenböck, H. D.; Marchetti-Deschmann, M.; Hametner, C.; Bertagnolli, E.; Kymissis, I.; Fröhlich, J. *New J. Chem.* **2015**.
- (87) Kautny, P.; Lumpi, D.; Wang, Y.; Tissot, A.; Bintliger, J.; Horkel, E.; Stöger, B.; Hametner, C.; Hagemann, H.; Ma, D.; Fröhlich, J. *J. Mater. Chem. C* **2014**, *2* (11), 2069.
- (88) Dunlop, H. G.; Tucker, S. H. *J. Chem. Soc. Resumed* **1939**, 1945.
- (89) Henry, J. B.; Wharton, S. I.; Wood, E. R.; McNab, H.; Mount, A. R. *J Phys Chem A* **2011**, *115* (21), 5435.
- (90) Bintliger, J. Sterically tuned triarylaminines and oligothiophene derivatives as building blocks for novel organic electronic materials: synthesis and characterization, Vienna University of Technology, 2011.
- (91) Kautny, P.; Wu, Z.; Stöger, B.; Tissot, A.; Horkel, E.; Chen, J.; Ma, D.; Hagemann, H.; Fröhlich, J.; Lumpi, D. *Org. Electron.* **2015**, *17*, 216.
- (92) Kautny, P.; Wu, Z.; Eichelster, J.; Horkel, E.; Stöger, B.; Chen, J.; Ma, D.; Fröhlich, J.; Lumpi, D. *Org. Electron.* **2016**, *34*, 237.
- (93) Puntischer, H.; Kautny, P.; Stöger, B.; Tissot, A.; Hametner, C.; Hagemann, H. R.; Fröhlich, J.; Baumgartner, T.; Lumpi, D. *RSC Adv.* **2015**, *5* (114), 93797.
- (94) Lv, J.; Liu, Q.; Tang, J.; Perdih, F.; Kranjc, K. *Tetrahedron Lett.* **2012**, *53* (39), 5248.





## 2. Results and Discussion



## 2.1 Overview of contributions

- Manuscript #1

**J. Binting**\*, S. Yang, H. Mikula, P. Fruhmann, B. Holzer, B. Stöger, A. Svirikova, M. Marchetti-Deschmann, E. Horkel, C. Hametner, I. Kymissis, J. Fröhlich; Synthesis, Characterization and Printing Application of Alkylated Indolo[3,2-*b*]carbazoles, *manuscript draft*

- Manuscript #2

S. Yang\*, S. Park\*, **J. Binting**, Y. Bonnassieux, I. Kymissis; Pneumatic Nozzle Printing as a Versatile Approach to Crystal Growth Management and Patterning of Printed Organic Thin Film Transistors; *manuscript accepted SID conference 2016*

- Manuscript #3

**J. Binting**\*, N. Cernetic, R. Bittner, M. Sauer, A. Folske-Schmitz, M. Holzweber, T. Schiros, D. Nordlund, H. Ma, H. Hoffmann, J. Fröhlich, A. Jen, H. Mikula; Using click chemistry for a facile approach towards self-assembled monolayer field-effect transistors (SAMFETs): A new versatile approach for sensing applications, *manuscript draft*

- Manuscript #4

S. Yang\*, **J. Binting**\*, S. Park, S. Jain, K. Alexandrou, P. Fruhmann, K. Besar, H. Katz, I. Kymissis; Ultra-cheap, versatile and robust USB-driven sensor platform; *manuscript draft*

- Manuscript #5

**J. Binting**\*, H. Holzer\*, C. Choi, D. Lumpi, E. Horkel, B. Stöger, C. Hametner, M. Marchetti-Deschmann, F. Plasser, I. Kymissis, J. Fröhlich; Color Tuning of Oligothiophene Based Compounds – A Combined Experimental and Computational Approach, *manuscript draft*

- Manuscript #6

D. Lumpi\*, B. Holzer\*, **J. Binting**, E. Horkel, S. Waid, H. D. Wanzenböck, M. Marchetti-Deschmann, C. Hametner, E. Bertagnolli, I. Kymissis, J. Fröhlich; *New J. Chem.* 2015

Reproduced from Ref.<sup>86</sup> with permission from the Centre National de la Recherche Scientifique (CNRS) and The Royal Society of Chemistry.

- Manuscript #7

P. Kautny, D. Lumpi\*, Y. Wang, A. Tissot, **J. Binting**, E. Horkel, B. Stöger, C. Hametner, H. Hagemann, D. Ma, J. Fröhlich; *J. Mater. Chem. C*, 2014, 2 (11), 2069

Reproduced from Ref.<sup>87</sup> with permission from the Centre National de la Recherche Scientifique (CNRS) and The Royal Society of Chemistry.

## 2.2 Context of Contributions

In this chapter the context of the subsequently introduced manuscripts or paper drafts will be outlined. This chapter can be categorized into 5 main sections:

1. Design and synthesis of solution processable organic semiconductors
2. Development of a novel solution processing technique
3. Self-assembled monolayer field-effect transistors for sensing applications
4. Development and testing of an ultra-cheap, versatile USB-driven sensor platform
5. Design and Synthesis of novel OLED and PhOLED materials

The next paragraphs will briefly explain the focus of research in the individual topics, refer to theoretical fundamentals and reveal how these contribute to the main topic of this thesis. For detailed background information and respective references see Chapter 2.3.

### 2.2.1. Design and synthesis of solution processable organic semiconductors

In general, an OSC should exhibit solution processability combined with high charge carrier mobility, environmental stability, and versatility for functionalization. These properties are key to the success of organic electronics. Solution processing allows for low-cost large area fabrication of electronic devices. In contrast to conventional silicon semiconducting technology, printing technology is extremely cheap and has a very low thermal budget.

The aim of manuscript #1 was to rationally design such materials based on the indolo[3,2-*b*]carbazole scaffold and used a novel printing technique, described in manuscript #2, to test for its scope and limitations.

By incorporating heteroatoms, such as nitrogen into the molecular backbone, lower HOMO levels are obtained, thus improving environmental stability of the OSC, while at the same time opening up further opportunities for functionalization such as side-chain engineering. These side-chain modifications are crucial for enhancing solubility, which is a key requirement for solution processing.

Manuscript #1 demonstrates a multigram scale synthesis of solution processable OSCs and their printability using a novel pneumatic printing technique.

### 2.2.2. Development of a novel solution processing technique

As mentioned above, solution processing is a major advantage of organic electronics and allows for low-cost large area fabrication of electronic devices. The key requirement for solution processing is the solubility of the used OSC. However, the performance of the OSC strongly depends, besides intrinsic characteristics, on the deposition process, e.g. higher charge carrier mobility is generally achieved when larger crystals are aligned along the direction of charge transport. While many solution processing methods have been developed to generate aligned crystals of organic thin films such as dip coating, zone casting, doctor blade coating, and solution shearing, these techniques generally fail to simultaneously pattern the OSC while also controlling crystallization.

Our novel pneumatic nozzle-based printing technique, which is presented in manuscript #2, allows for patterning and depositing small-molecule OSCs, control the crystallization of the resulting organic thin-films and at the same time deposit additional patterned materials on nearly arbitrary substrates in order to make an all-printed OFET on flexible substrates.

### 2.2.3. Self-assembled monolayer field-effect transistors for sensing applications

One of the greatest potentials of organic electronics is the realization of miniaturized, or even implanted, biosensors as low-cost point-of-care devices, capable of label-free, selective detection of analytes (e.g. biomarkers, pathogens) while creating an electronic read out for user friendly interaction. The basic working principle of these sensors is based on a standard OFET configuration. An OFET-biosensor is an analytical device consisting of an OFET endowed with covalently attached biological recognition units to the OSC, whose specific interactions with analytes changes the electrical current flowing between source and drain. Since the sensitivity of such a sensor is dependent on the thickness of the semiconductor, or more precisely the distance between the analytes' electrostatic interactions and the charge carrying layer, the maximum sensitivity would be achieved in a device consisting of only one monolayer of the active material, because charges in OFETs are confined only

to one monolayer. Such devices called self-assembled monolayer field-effect transistors (SAMFETs) are the topic of manuscript #3. The applicant developed a novel building block like approach towards SAMFETs using click chemistry. The resulting devices, named CLICK-FETs, were extensively characterized and benchmarked against conventional SAMFET devices. The key advantage of the presented concept is its facile modular approach and the possibility of post-modification of OSC, thus allowing the endowment of bio recognitions units, which are prerequisites for enabling label-free selective and specific detection of biomarkers and pathogens.

#### 2.2.4. Development and testing of an ultra-cheap, versatile USB-driven sensor platform

While the topics and aims of manuscripts #1-3, were the development and synthesis of novel OSC, the goal pursued in manuscript #4 was to develop and optimize a suitable sensor platform for these materials.

The presented ultra-low cost sensor platform is based on a chemiresistor configuration and allows for cheap and reliable sensing of various analytes. By incorporating a direct USB-connection for power supply as well as automatically creating an electronic readout handling of this device is very simple, which is an important aspect when considering the development of so called point-of-care devices. The two electrode chemiresistor is realized with the simplest setup albeit allowing great sensitivity based on small perturbations occurring anywhere along the polymer chain rather than volumetric. The readily availability of all required components enabled the fabrication of these sensors for less than \$1 per piece. As a result, we refer to this platform as \$-Sensor (Dollar-Sensor). We have demonstrated the versatility of this sensor platform by fabricating sensors for three analytes (H<sub>2</sub>O vapor, acetone, NH<sub>3</sub>) using the same platform with targeted functionalization.

#### 2.2.5. Design and Synthesis of novel OLED and PhOLED materials

Manuscripts #5-7 focus on the design and synthesis of novel organic semiconductors and their implementation and evaluation in OLED and PhOLED devices.

In contrast to fluorescent OLEDs, PhOLEDs are using phosphorescent transition metal emitters that can harvest singlet and triplet excitons simultaneously, thus in theory 100 % internal quantum efficiency is achievable. Even though OLED and PhOLED based devices have entered the market there still is the need for new high performing materials in order to further enhance performance and lifetime stability.

In this context, the applicant's work towards a facile and easily scalable synthesis towards the indolo(3,2,1-*jk*)carbazole (ICz)scaffold should be noted. This substance class was first reported in 1934 by Dunlop and Tucker<sup>88</sup> using diazotization reaction and later in 2011 by Henry et al.<sup>89</sup> using an unpractical flash vacuum pyrolysis reaction. Already during his diploma thesis,<sup>90</sup> the applicant applied a novel C-H activation procedure the desired (ICz) via 2 steps in excellent yields on a multigram scale and extended this method towards a two-fold C-H activation during the work of his PhD.<sup>87</sup> The ICz moiety has since (2011) been mentioned in 50 patents and 13 publications and was used by other members of the Fröhlich research group for several publications.<sup>91-93</sup> In 2012 Lv et al.<sup>94</sup> reported on a similar one-fold C-H activation method using a different catalyst and obtaining lower yields.

The increasing interest, especially from industry, is due to the interesting properties of the ICz moiety. It exhibits a completely planarized structure, thermal stability and is not necessarily just an electron donor, but exhibits also electron accepting properties.

Manuscript #5 and #7 are investigating the unique properties of the ICz moiety in more detail.

## 2.3 Original Works

In the following section, all manuscripts (published, submitted, drafts) are included. Permissions for the reprint of already published articles were kindly given by the Centre National de la Recherche Scientifique (CNRS) and The Royal Society of Chemistry (manuscript #6 and #7). Supporting Information for manuscripts #1, #3, #5, #6 and #7 containing additional experimental details and data is included in the appendix of this thesis.



# Manuscript #1

**J. Bintinger\***, S. Yang, H. Mikula, P. Fruhmann, B. Holzer, B. Stöger, A. Svirkova, M. Marchetti-Deschmann, E. Horkel, C. Hametner, I. Kymissis, J. Fröhlich; Synthesis, Characterization and Printing Application of Alkylated Indolo[3,2-*b*]carbazoles, *manuscript draft*



# Synthesis, Characterization and Printing Application of Alkylated Indolo[3,2-*b*]carbazoles

J. Bintinger<sup>\*[a]</sup>, S. Yang<sup>[b]</sup>, H. Mikula<sup>[a]</sup>, P. Fruhmann<sup>[a,d]</sup>, B. Holzer<sup>[a]</sup>, B. Stöger<sup>[c]</sup>, A. Svirikova<sup>[c]</sup>, M. Marchetti-Deschmann<sup>[c]</sup>, E. Horkel<sup>[a]</sup>, C. Hametner<sup>[a]</sup>, I. Kymissis<sup>[b]</sup>, J. Fröhlich<sup>[a]</sup>

**Abstract:** The synthesis, characterization, and field-effect transistor (FET) properties of new alkylated indolo[3,2-*b*]carbazole (ICz) based materials are reported. Dialkyl substitution at the 2,8-positions of the ICz core structure do not affect strong N-H... $\pi$  interactions, thus favoring a herringbone packing motif. OFET devices fabricated by compounds of this substitution pattern displayed a charge carrier mobility of  $\sim 10^{-2}$  cm<sup>2</sup>Vs<sup>-1</sup>. These interactions are suppressed when introducing substituents at the 5,11-positions, resulting, in greatly enhanced solubility. A solution processable ICz derivative was finally used in a newly developed pneumatic printing setup to yield a crystalline film with aligned crystals along the printing direction.

## 1. Introduction

Since the discovery of high electrical conductivity in doped polyacetylene<sup>[1]</sup> organic electronic (OE) thin film devices have attracted enormous attention due to their ability to expand the world of electronics by enabling flexible, solution processed, light-weight devices with low manufacturing costs.<sup>[2]</sup> The properties and availability of custom tuned organic semiconductors (OSCs) are key to applications such as organic field-effect transistors (OFETs)<sup>[3]</sup>, organic light emitting diodes (OLEDs)<sup>[4]</sup>, organic photovoltaics (OPVs) and sensors.<sup>[5]</sup> In general, the OSC should exhibit a high charge carrier mobility, combined with environmental stability, solution processability and versatility for functionalization.<sup>[6]</sup> Since OE-technology is based on a bottom-up approach, these properties can, to some extent, be tuned and optimized by alterations on the molecular level of the OSC. However, while there are general guidelines to achieve these properties in materials and devices such as i) good molecular packing with maximized intermolecular interactions and  $\pi$ -stacking overlap; ii) large transfer integrals and iii) small reorganization energies, there is still a severe lack

of structure-property relationships for guiding rational molecular designs.<sup>[6]</sup> Additionally, the amount of parameters within the capabilities of molecular, interface and process engineering are sheer endless.

Since both industry and academia have yet failed to come up with a material to tackle all these problems, the quest for novel compounds is an ongoing process in material science.

Within this field the indolo[3,2-*b*]carbazole (ICz) scaffold has attracted a lot of interest owing to their favorable electronic and biological properties. ICz derivatives have shown great promise as OFETs<sup>[7,8]</sup>, gas-sensors<sup>[9]</sup>, OLEDs<sup>[10]</sup>, phosphorescent light emitting diodes (PHOLEDs)<sup>[11]</sup>, OPVs<sup>[12,13]</sup> and 2 photon absorbers.<sup>[14]</sup> Besides their remarkable electronic properties, ICz compounds also have a compelling biological significance as they are formed *in vivo* after consumption of vegetables belonging to the genus *Brassica*, such as cabbage, cauliflower, kohlrabi and Brussels sprouts.<sup>[15]</sup> Additionally, ICz derivatives have shown even stronger affinities towards the aryl hydrocarbon receptor (AHR) than TCDD (2,3,7,8-tetrachlorodibenzo-*p*-dioxin).<sup>[16]</sup>

ICz is a heterocyclic analogue of pentacene - one of the most used organic semiconductors<sup>[17]</sup> - and is considered to be a nitrogen-containing electron-rich heteroacene with a ladder-type structure. The nitrogen heteroatoms open up the possibility of functionalization and sensing capabilities, as well as lowering the HOMO energy levels, which renders them air-stable.<sup>[18,19]</sup> Additionally, ICz exhibit very strong N-H... $\pi$  interactions, which can enhance charge transport by improving intermolecular interactions and thus result in an improved molecular packing motive.<sup>[20]</sup> It was recently shown that rational side chain modifications along the long-side of the molecule can reduce

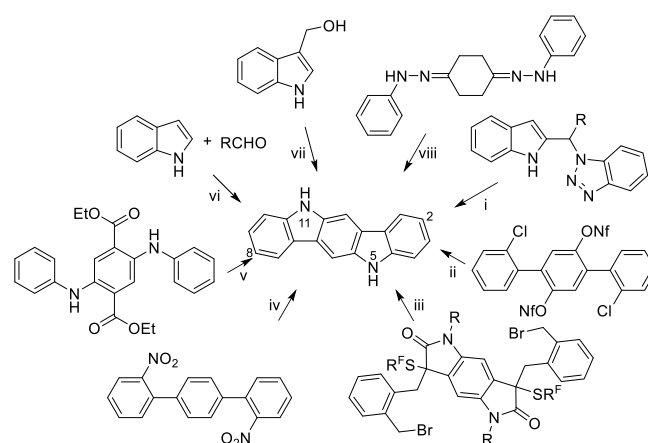


**Figure 1.** Synthetic strategies towards the indolo[3,2-*b*]carbazoles scaffold; (i) dimerization of 2-(benzotriazol-1-ylalkyl)indoles;<sup>[22]</sup> (ii) Pd-catalyzed double N-arylation;<sup>[23]</sup> (iii) a Sm(II)-mediated cascade approach;<sup>[24]</sup> (iv) double Cadogan ring closing reaction;<sup>[24]</sup> (v) Pd-mediated cyclization of an ester-substituted diphenyl phenylenediamine;<sup>[25]</sup> (vi) condensation of indoles with aliphatic aldehydes;<sup>[25]</sup> (vii) reactions of indole-3-carbinol, indole and 3-formylindole under acidic conditions;<sup>[26]</sup> and (viii) double Fischer cyclization.<sup>[27]</sup>

- [a] J. Bintinger, Dr. H. Mikula, Dr. E. Horkel, Dr. P. Fruhmann, Dr. B. Holzer, Dr. C. Hametner and Prof. J. Fröhlich  
Institute of Applied Synthetic Chemistry,  
Vienna University of Technology  
Getreidemarkt 9, 1060 Vienna (Austria)  
E-mail: johannes.bintinger@tuwien.ac.at
- [b] Dr. S. Yang, Prof. I. Kymissis  
Department of Electrical Engineering,  
Columbia University,  
500 W. 120th St., New York, NY 10027 (USA)
- [c] Dr. B. Stöger, A. Svirikova, Prof. M. Marchetti-Deschmann  
Institute of Chemical Technologies and Analytics,  
Vienna University of Technology,  
Getreidemarkt 9, 1060 Vienna (Austria)
- [d] Dr. P. Fruhmann  
CEST – Center for Electrochemical Surface Technology  
Viktor-Kaplan-Straße 2, 2700 Wiener Neustadt (Austria)

Supporting information for this article is given via a link at the end of the document

dynamic disorder by suppressing large-amplitude thermal motions.<sup>[21]</sup>

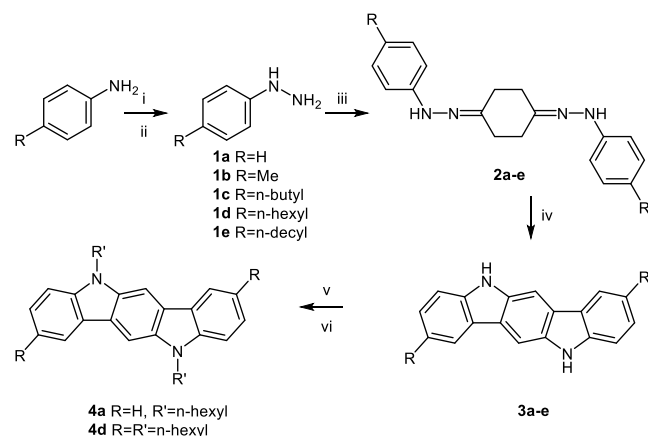
In this contribution, we report on the synthesis and characterization of novel alkyl-substituted ICz derivatives following these guidelines and demonstrate application in OFETs as well as their capability for solution processing.

## 2. Results and Discussion

### 2.1. Synthetic strategy and molecular design considerations

Various synthetic routes have been reported in literature towards the indolo[3,2-*b*]carbazole scaffold including (i) dimerization of 2-(benzotriazol-1-ylalkyl)indoles to various 6,12-disubstituted indolo[3,2-*b*]carbazoles under Lewis acidic conditions,<sup>[22]</sup> (ii) Pd-catalyzed double N-arylation of 2,5-bis(*o*-chloroaryl)hydroquinone intermediates,<sup>[23]</sup> (iii) a Sm(II)-mediated cascade approach towards dibenzoindolo[3,2-*b*]carbazoles,<sup>[24]</sup> (iv) double Cadogan ring closing reaction from 2,2'-dinitro-*p*-terphenyls,<sup>[25]</sup> (v) Pd-mediated cyclization of an ester-substituted diphenyl phenylenediamine,<sup>[26]</sup> (vi) condensation of indoles with aliphatic aldehydes,<sup>[26]</sup> (vii) reactions of indole-3-carbinol, indole and 3-formylindole under acidic conditions,<sup>[27]</sup> and (viii) double Fischer cyclization of bis-phenylhydrazones<sup>[28]</sup> (Figure 1).

However, these methods suffer either from low yields, undesirable substitution patterns and/or lead to the formation of side products, and thus to complex purification procedures. Furthermore, some approaches require long synthetic routes to obtain the precursor<sup>[25]</sup> (e.g. indole derivatives) or expensive catalysts.<sup>[18,23]</sup> To afford 2,8-dialkylated ICz derivatives we relied on a modified double Fischer indolization reaction<sup>[29]</sup> of bis-phenylhydrazones, which were readily available from the condensation of 1,4-cyclohexanedione with properly substituted phenylhydrazines (Scheme 1).



**Scheme 1.** Synthesis towards 2,8- and 2,5,8,11- substituted ICz using double Fischer cyclization of the bis-phenylhydrazone precursors **2a-e** as a key step; i) HCl, NaNO<sub>2</sub>, SnCl<sub>2</sub>·2H<sub>2</sub>O; ii) NaOH; iii) 1,4-cyclohexanedione; iv) AcOH:H<sub>2</sub>SO<sub>4</sub>=4:1; v) NaOH, benzyltriethylammonium chloride, 1-bromohexane; vi) NaH, 1-bromohexane.

In theory, 2,8-dialkyl substitution should allow for increased solubility, while retaining the good  $\pi$ -stacking as a result of the intact N-H... $\pi$  interactions. Additionally, the side chain modifications along the long-side of the molecule should reduce dynamic disorder by suppressing large-amplitude thermal motions and thus result in good charge transport properties.<sup>[21]</sup>

In a first step, readily available aniline precursors were converted to the corresponding hydrazines via diazotization in good to almost quantitative yields (81-98 %). The bis-hydrazones were then obtained in 84-98 % yield by condensation of hydrazines **1a-e** with 1,4-cyclohexanedione in anhydrous EtOH in the presence of catalytic amounts of AcOH. The hydrazones were used without further purification in the next step to afford the desired ICz derivatives **3a-e** via double Fischer cyclization. The yield of the reaction dropped dramatically with increased alkyl length (**1a** = 84 %, **1e** = 21 %). Purification of the highly insoluble compounds **3a-e** was achieved using multiple recrystallization from DMSO/EtOH and DMF/EtOH to afford the pure products as pale yellow solids. Finally, two different N-alkylation procedures were used to afford the target compounds: **4a** was obtained using basic conditions and benzyltriethylammonium chloride as a phase transfer catalyst along with 1-bromohexane, while **4d** (45 %) was deprotonated with NaH prior to alkylation with 1-bromohexane. It is noteworthy to mention that the solubility of the ICz derivative in CHCl<sub>3</sub> increased dramatically upon alkylation at the nitrogen positions from 0.2 mg/mL (**3a**) to 25 mg/mL (**4a**). This trend is in good agreement with previously published reports.<sup>[20,26]</sup>

### 2.2. Electrochemical and photophysical properties in comparison to computational results

Cyclic voltammetry (CV) of all compounds was performed in dry DMF (Figure 2). Since compounds **3a**, **3c-e** exhibit low solubility all measurements were carried out with saturated analyte solutions. Soluble **4a** and **4d** were measured as a 0.5 mM solution. The first oxidation potentials were used to determine the HOMO energy levels. Ferrocene served as an external standard for calibrating the potential and calculating the HOMO levels (-4.8 eV). Reversible oxidation indicating the formation of stable cation radicals could be observed for compounds **3c**, **3d**, **4a** and **4d**. For substances **3a** and **3e** only estimations

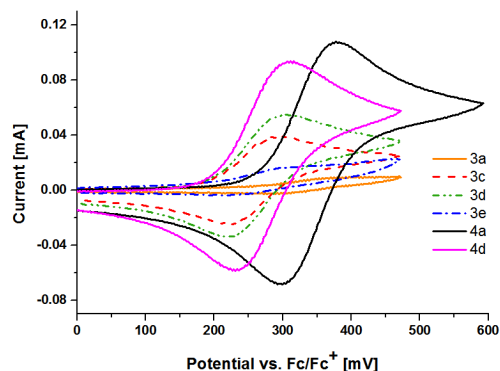


**Figure 2.** Cyclic voltammetry measurements of ICz **3a-e** and **4a,4d** in reference to ferrocene

concerning the oxidation peak can be given due to their insolubility. The HOMO energy levels determined from the cyclic voltammograms are in the order of  $5.01 \pm 0.03$  eV for all substances. The energy levels are summarized in table 1 together with the computational results.

We used quantum chemical calculations to investigate structure property relationships and verified the results via comparison to experimental data (Table 1). All computations were performed using the Gaussian 09 package, revision A.02<sup>[30]</sup>, and the Becke three parameters hybrid functional with Lee–Yang–Perdew correlation (B3LYP)<sup>[31,32]</sup> in combination with the 6-311+G\* basis set<sup>[33]</sup>. Geometry optimizations of the ground state ( $S_0$ ) for the calculation of HOMO/LUMO energy levels were conducted in gas phase allowing symmetry constraints. All obtained structures were verified as local minima by consecutive normal mode analysis. Both the computational and the crystal structure results indicate that the indolo[3,2-*b*]carbazole core unit is of planar structure with a transoid configuration of the side chains out of the plane. The HOMOs and LUMOs of the investigated compounds are predominantly localized on the indolo[3,2-*b*]carbazole core. Computational results show that the HOMOs of compounds **3d**, **4a** and **4d** are extended onto the adjacent carbon of the functionalized atoms (Figure 3). The calculated HOMO and LUMO energy levels (Table 1) are very close to 5.10 ( $\pm 0.1$ ) and -1.38 ( $\pm 0.04$ ) eV respectively. The HOMO-LUMO energy gap is around 3.72 ( $\pm 0.07$ ) eV.

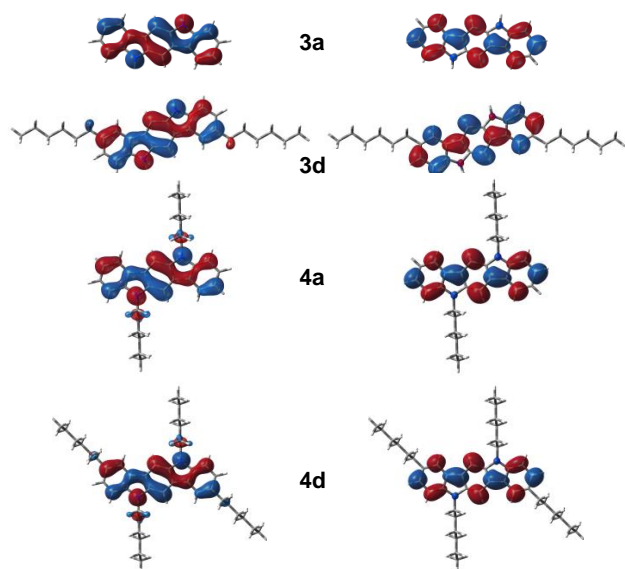


**Figure 4.** left: HOMO isosurface plots of compounds **3a,3d,4a,4d**; right: LUMO plots

While the experimental data for the HOMO levels are in good agreement with predicted values, the calculated LUMO levels are about 0.7 eV higher than the measured values.

**Table 1.** Experimental and calculated HOMO and LUMO energy levels.

substance	$E_{\text{HOMO}}^{\text{exp}}$ [eV]	$E_{\text{LUMO}}^{\text{exp}}$ [eV]	$E_g^{\text{exp}}$ [eV]	$E_{\text{HOMO}}^{\text{calc}}$ [eV]	$E_{\text{LUMO}}^{\text{calc}}$ [eV]	$E_g^{\text{calc}}$ [eV]
<b>3a</b>	-5.05	-2.08	2.97	-5.26	-1.45	3.81
<b>3c</b>	-4.99	-2.07	2.92	-5.12	-1.38	3.74
<b>3d</b>	-5.00	-2.08	2.92	-5.12	-1.37	3.75
<b>3e</b>	-4.98	-2.06	2.92	-5.11	-1.37	3.74
<b>4a</b>	-5.07	-2.19	2.88	-5.04	-1.38	3.66
<b>4d</b>	-5.00	-2.16	2.84	-4.92	-1.32	3.60

[exp] experimental data; HOMO-levels determined from solutions measured in dry DMF. All  $E_{\text{ox}}$  data are reported relative to ferrocene ( $\text{Fc}/\text{Fc}^+$ ,  $E_{\text{ox}} = 409$  mV). The scan rate in these experiments was 50 mV/s. LUMO levels were determined from the optical band gap and the HOMO energy level according to the following equation:  $E_{\text{LUMO}} = E_{\text{HOMO}} + E_g$ . [calc] calculated energy levels obtained from quantum chemical calculations using Becke three parameters hybrid functional with Lee–Yang–Perdew correlation (B3LYP) in combination with the 6-311+G\* Pople basis set.

UV-VIS absorption and fluorescence emission spectra were recorded in anhydrous DMF (1  $\mu\text{M}$ ). A representative comparison of the individual spectra for compound **3d** is shown in Figure 4. As previously reported, all ICz derivatives exhibit two strong absorptions in the wavelength regions of 260-300 nm and 300-350 nm, respectively, which are assigned to  $\pi-\pi^*$  transitions, while the very weak absorption beyond 400 nm is assigned to  $n-\pi^*$  interactions.<sup>[34]</sup> Compared with the conjugated system ICz (**3a**), the main absorption peaks of all other compounds experience a small bathochromic shift (Figure 5, Table 2) indicating a minor substitution effect on the electron delocalization of the molecules. The energy bandgap is estimated from the long-wavelength absorption edge, showing a relatively large energy band gap of  $\sim 2.92$  eV compared with other widely used organic semiconductors (e.g. pentacene  $\sim 2$  eV).

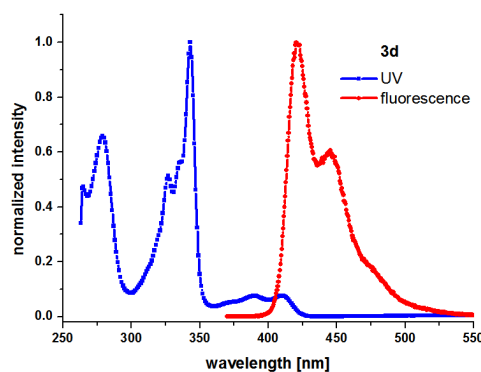


**Figure 5.** UV-VIS absorption and fluorescence emission spectra of **3d** ( $1 \times 10^{-5}$  M in DMF). Excitation wavelength is 343 nm

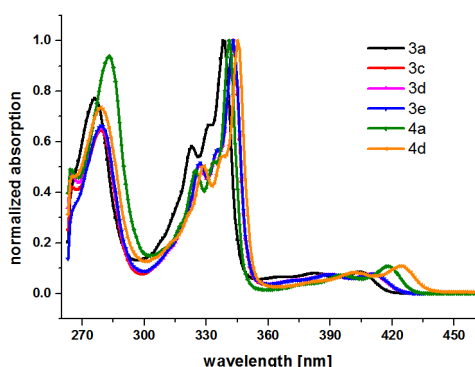


**Figure 6.** Normalized UV spectra of all investigated ICz ( $c = 1 \mu\text{M}$  in DMF)

In contrast to the small difference in the UV-VIS spectra, fluorescence emissions revealed a larger variation between the different compounds (Figure 6, Table 2). The influence of a symmetric alkyl substitution in positions 2 and 8 of ICz accounts for a 7 nm bathochromic shift within all substituted compounds compared to **3a**, while N-substitution at positions 5 and 11 corresponds to a 11 nm red shift. Since compound **4d** is comprised of substitutions in all four positions (2,5,8,11) the resulting fluorescence emission is an additive combination of these effects leading to an overall bathochromic shift of 18 nm (7 + 11 nm) relative to **3a**. This is attributed to the extension of the HOMO towards the C1 of the alkyl chain, as can be seen from the computational results shown in figure 3, as well as the lowering of the energy bandgap due to the slightly increased delocalized  $\pi$ -electron system (Table 1).

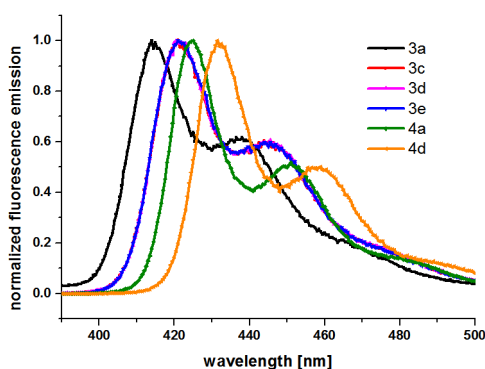


**Figure 7.** Normalized fluorescence emission spectra ( $c = 1 \mu\text{M}$  in DMF); excitation wavelength is 343 nm.

**Table 2.** UV-VIS and fluorescence data.

substance	Abs 1 max	Abs 2 max	Abs 3 max	Fluorescence max
<b>3a</b>	404	339	276	414
<b>3c</b>	411	343	279	421
<b>3d</b>	411	343	279	421
<b>3e</b>	411	343	279	421
<b>4a</b>	418	341	283	425
<b>4d</b>	425	345	279	432

**3c** was structurally characterized by single crystal diffraction (Figure 7). The compound crystallizes in the  $P2_1/c$  space group with the lattice parameters  $a = 20.541(7) \text{ \AA}$ ,  $b = 7.479(3) \text{ \AA}$ ,  $c = 6.523(2) \text{ \AA}$ , and  $\beta = 91.058(9)^\circ$ . The ICz moiety is virtually planar (largest distance of  $0.065 \text{ \AA}$  from the least squares plane defined by the non-H atoms). The molecules are connected via N-H... $\pi$  ( $2.585 \text{ \AA}$ ) and C-H... $\pi$  ( $2.893 \text{ \AA}$ , not shown) interactions to layers parallel to (001), which are delimited by the alkyl chains. Inside these layers, the molecules are arranged in a typical herring-bone packing (Figure 7).

As already described by Zhao et al.<sup>[20]</sup> substitution on the nitrogen atoms dramatically changes the observed packing mode by eliminating N-H... $\pi$  interactions, thus illustrating the power of molecular engineering.

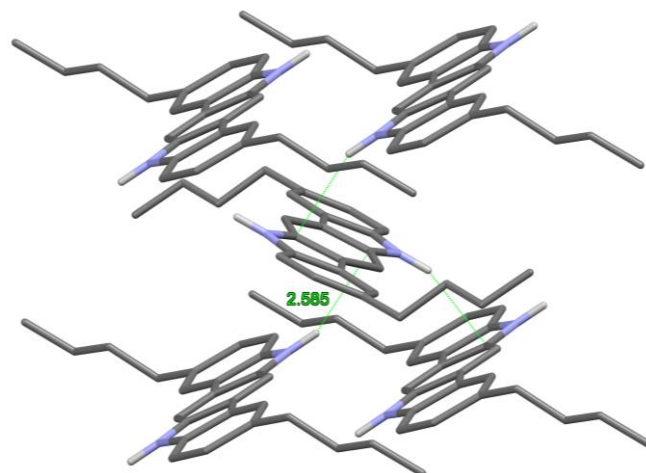


**Figure 8.** Molecular packing mode and N-H... $\pi$  interactions of **3c**; C, N and H atoms are drawn in grey blue and white colors respectively. H-atoms except N-H are omitted for clarity.

### 2.3. Field-effect transistor performance

In order to investigate the field-effect mobility of ICz derivatives top-contact, bottom-gate OFETs were fabricated on hexamethyldisilazan (HMDS)- modified Si/SiO<sub>2</sub> substrates. The mobility ( $\mu$ ) in the saturated region was calculated using equation 1.

$$I_D = \frac{W}{2L} \mu_{sat} C_{ox} (V_{GS} - V_T)^2 \quad (1)$$

$W$  and  $L$  are the channel width and length, respectively,  $C_{ox}$  is the unit dimensional dielectric capacitance of gate insulator,  $\mu$  is the field-effect mobility, and  $V_T$  is the threshold voltage. Fundamentally, mobility describes the relationships between the carrier velocity and the applied electric field in a given material, and is widely regarded as the most significant figure of merit to evaluate the performance of field effect transistors.<sup>[35]</sup> The effective mobility of our fabricated OFETs can be determined by measuring the drain-current vs. gate-voltage characteristic in the saturation region according to equation 1. To eliminate the dependency on the ambiguity of the threshold voltage, the effective mobility is extracted by plotting the square-root of drain-current ( $I_D$ ) vs. gate-voltage ( $V_G$ ) and calculating the slope. All ICz FET devices displayed p-type transistor behavior with well-defined linear and saturation regimes (Figure 8). The highest mobility of the devices using **3d** was  $\sim 10^{-2} \text{ cm}^2\text{Vs}^{-1}$ . In contrast, devices fabricated from **3a** and **4d** in the same way exhibited the highest mobility of  $\sim 10^{-3} \text{ cm}^2\text{Vs}^{-1}$ . The gate leakage for all devices was in the range of  $10^{-10} \text{ A}$ . Unfortunately, no field-effect behaviour was observed for other ICz compounds under investigation, either on bare-Si/SiO<sub>2</sub> or OTS-modified Si/SiO<sub>2</sub> substrates.

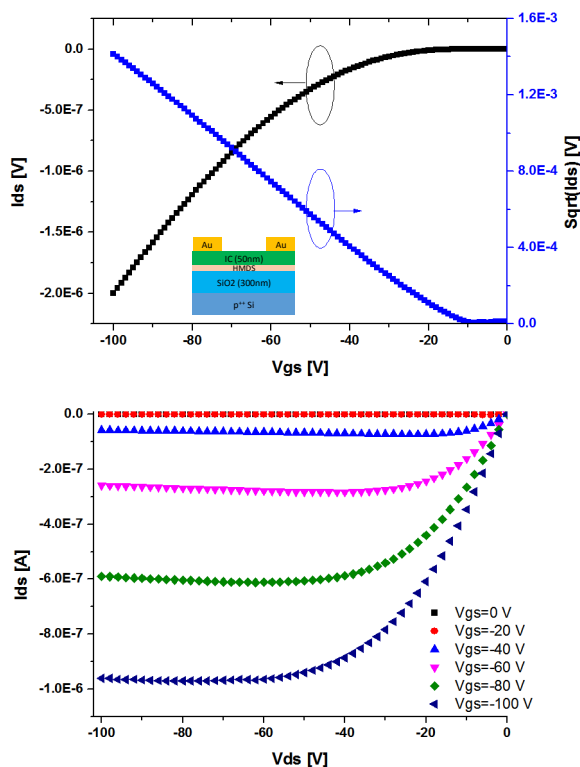


**Figure 10.** Transfer- and output characteristic of OFET devices based on **3d**. Top: transfer curve,  $V_{ds} = 100 \text{ V}$ ; bottom: output curve

## 2.4. Pneumatic printing results

Solution processability is key for realizing low-cost devices and constitutes a major advantage of OE.<sup>[36,37]</sup> Thus, the major requirement for this method is the solubility of the organic semiconductor in common organic solvents. Additionally, the mobility of the small organic molecule semiconductors is strongly depending on its crystal orientation and molecular packing.<sup>[6,38–41]</sup> The highest mobility is achieved when the direction of the current is aligned with the direction of molecular packing.<sup>[42–44]</sup> With our recently described pneumatic nozzle printing technique we have a powerful tool in hand to pattern and deposit soluble, small-molecule organic semiconductors and to control the crystallization of the OSC.

Since the solubility of compounds **4a** and **4d** exceeds more than  $25 \text{ mg/mL}$  in common organic solvents such as  $\text{CHCl}_3$ ,  $\text{CH}_2\text{Cl}_2$  and toluene, these compounds are well suited for printing. We tested **4a** in our pneumatic nozzle printing setup to fabricate ICz-based crystalline thin films (Figure 10). In contrast to **4a** (Figure 10), **4d** only yielded amorphous films with no crystalline domains.

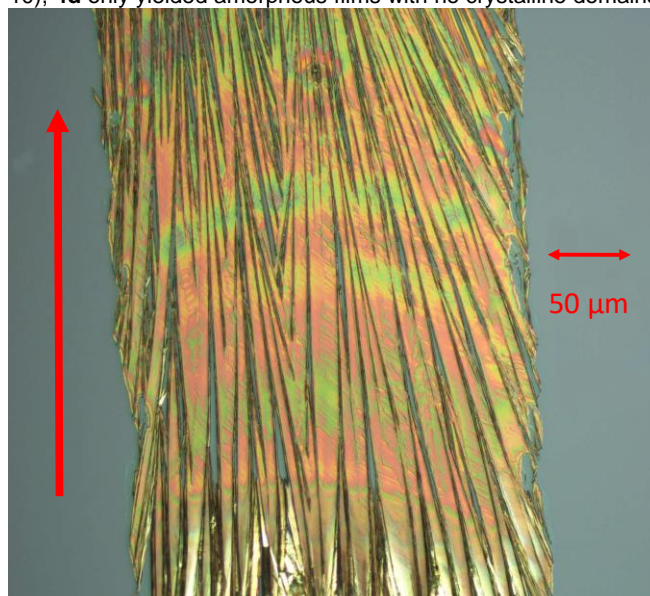


**Figure 9.** Microscopy image of the morphology of a pneumatic-printed thin film using compound **4a** ( $24 \text{ mg/mL}$  in toluene:  $\text{CHCl}_3$ ; printing speed  $0.4 \text{ mm/s}$ ); red upright arrow indicates the printing direction

Figure 9 shows aligned and continuous films of **4a** with crystalline domains with widths in the few of microns and lengths in the hundreds of microns range were formed. Preferential growth orientation along the direction of the moving nozzle can also be observed. At the given printing speed ( $0.4 \text{ mm/s}$ ), the evaporation rate at the meniscus matches the printing speed, thus yielding crystal growth along the direction of the moving meniscus. This produces aligned crystals with sufficient nucleation events to fill the entire film. In this ongoing research we now attempt to fabricate OFETs with this promising material.

### 3. Conclusions

In summary, multigram-scale pure 2,5,8,11 substituted ICz derivatives were synthesized and fully characterized using electrochemical and photophysical techniques. 2,8-substituted ICz are adopting a herringbone packing mode with strong N-H... $\pi$  interactions. OFET devices fabricated using **3d** displayed a charge carrier mobility of  $\sim 10^{-2}$  cm<sup>2</sup>Vs<sup>-1</sup>. While this substitution pattern is rendering the N-H... $\pi$  interactions intact, it does not increase the solubility of ICz derivatives. In contrast, 5,11-dialkyl substitution greatly enhances solubility by completely eliminating N-H... $\pi$  interactions, thus enabling solution processing using pneumatic printing. The significance of these interactions on the molecular packing and electrical properties is reflected in differences of OFET device performances.

### 4. Experimental Section

Substances purchased from commercial sources were used as received without further purification. Dimethylsulfoxide (DMSO) and N,N-dimethylformamide (DMF) were used in p.a. quality. Technical grade solvents were distilled prior to use. Anhydrous solvents were prepared by filtration through drying columns. Analytical TLC was performed on Merck silica gel 60 F<sub>254</sub> plates. Chromatographic separations at preparative scale were carried out on silica gel (Merck silica gel 60, 40 - 63  $\mu$ m). Nuclear magnetic resonance (NMR) spectra were obtained using a Bruker DPX-200 or Avance DRX-400 Fourier transform spectrometer operating at the following frequencies: DPX-200: 200.1 MHz (<sup>1</sup>H) and 50.3 MHz (<sup>13</sup>C); DRX-400: 400.1 MHz (<sup>1</sup>H) and 100.6 MHz (<sup>13</sup>C). The chemical shifts are reported in delta ( $\delta$ ) units, parts per million (ppm) downfield from tetramethylsilane using solvent residual signals for calibration. Coupling constants are reported in Hertz; multiplicity of signals is indicated by using following abbreviations: s = singlet, d = doublet, t = triplet, q = quartet. The multiplicity of <sup>13</sup>C signals was obtained by measuring JMOD spectra. High-resolution mass spectra (HRMS) were acquired as radical cations using either a SYNAPT HDMS instrument (Waters, Manchester, UK) equipped with a matrix-assisted laser desorption/ionization (MALDI) source or a Thermo Scientific LTQ Orbitrap XL hybrid FTMS (Fourier Transform Mass Spectrometer) equipped with Thermo Fischer Exactive Plus Orbitrap (LC-ESI+) and a Shimadzu IT-TOF Mass Spectrometer. Samples for MALDI-HRMS were applied at 1 mg/mL in THF on stainless steel using nitroanthracene (3 mg/mL in THF) as MALDI matrix. In case of solubility the sample was further diluted to approx. 50 pg/ $\mu$ L. In case of undissolved samples, the slurry was centrifuged and the supernatant and the residue was used for MALDI-qTOF-MS analysis. 1  $\mu$ L of the sample or residue/chloroform slurry was deposited on a stainless steel target and dried at room temperature. All MS spectra were recorded as accurate mass data with angiotensin II (m/z = 1046.542) as internal lock mass achieving a mass accuracy of 15 - 40 ppm (i.e.  $\Delta$ m/z = 0.01 - 0.04 amu).

UV/VIS absorption and fluorescence emission spectra were recorded in dry DMF solutions (1  $\mu$ M) with a Perkin Elmer Lambda 750 spectrometer and an Edinburgh FLS920, respectively. Cyclic voltammetry was performed using a three electrode configuration consisting of a Pt working electrode, a Pt counter electrode and an Ag/AgCl reference

electrode and a PGSTAT128N, ADC164, DAC164, External, D1048 potentiostat provided by Metrohm Autolab B. V. Measurements of **4a** and **4d** were carried in a 0.5 mM solution with Bu<sub>4</sub>NBF<sub>4</sub> (0.1 M) as the supporting electrolyte. Since all other compounds were less soluble, saturated analyte solutions with Bu<sub>4</sub>NBF<sub>4</sub> (0.1 M) as supporting electrolyte were used. The solutions were purged with nitrogen for 15 minutes prior to measurement. HOMO energy levels were calculated from the onset of oxidation. The onset potential was determined by the intersection of two tangents drawn at the background and the rising of oxidation peaks.

X-ray Structure Determination: A crystal of **3c** was grown by slow evaporation of a solution in DMF/ethanol 1:2. X-ray diffraction data were collected at  $T = 200$  K (phase transition below 200 K) in a dry stream of nitrogen on a Bruker Kappa APEX II diffractometer system using graphite-monochromatized Mo-K $\alpha$  radiation ( $\lambda = 0.71073$  Å) and fine sliced  $\varphi$ - and  $\omega$ -scans. Data were reduced to intensity values with SAINT and an absorption correction was applied with the multi-scan approach implemented in SADABS.<sup>[45]</sup> The structures were solved by charge flipping using SUPERFLIP<sup>[46]</sup> and refined against with JANA2006.<sup>[47]</sup> Non-hydrogen atoms were refined anisotropically. The H atoms were placed in calculated positions and thereafter refined as riding on the parent atoms. Molecular graphics were generated with the program MERCURY.<sup>[48]</sup>

Device fabrication: FET devices were fabricated with top-contact geometry. Thin films were deposited under vacuum on hexamethyldisilazane (HMDS)-treated SiO<sub>2</sub>/Si substrates. Gold electrodes were fabricated via shadow mask. ICz were deposited at an initial rate of 0.1 Ås<sup>-1</sup> with gradual increase to 0.4 Ås<sup>-1</sup> under a pressure of about 4.0x10<sup>-6</sup> Torr to a final thickness of 50 nm, as determined by a quartz crystal monitor. OFET characteristics were measured under ambient conditions. on a Keithley 2400 source measuring unit interfaced with Labview and a micromanipulator 6150 probe station.

#### General procedure for compounds 1a-e

A slightly modified procedure from Liu et al.<sup>[49]</sup> was used for the preparation of phenylhydrazines **1a-e**. All experiments were therefore based on the following approach: In a 1 l three-necked flask equipped with a mechanical stirrer, thermometer and dropping funnel concentrated HCl (0.65 mL/mmol starting material) was placed and cooled to 0-5 °C with an ice bath. The desired aniline (1.00 eq) was added quickly through the dropping funnel while rigorous stirring was maintained. To avoid agglomeration of the resulting white solid concentrated acetic acid (1.2 mL/mmol starting material) was added. An aqueous solution of sodium nitrite (~33 wt %, 1.10 eq) was then added dropwise over 30 min. The resulting dark blue solution was continued to stir for an additional 30 min. Then a suspension of tin chloride dihydrate (3.00 eq) in concentrated HCl (0.26 mL per mmol SnCl<sub>2</sub>·2 H<sub>2</sub>O) was added slowly and the resulting suspension was stirred at 0 °C for 3 h. The resulting yellow solid was filtered and washed with H<sub>2</sub>O, before being dissolved in 2N NaOH (0.65 mL/mmol starting material). The solid was again filtered, washed with H<sub>2</sub>O and lyophilized overnight. The product was obtained as yellow solid with yields in the range of 81 - 98 %. The materials were used in the next step without further purification.

#### 1a - phenylhydrazine

Sodium nitrite (3.19 g, 46.2 mmol, 1.00 eq), aniline (3.91 g, 42.00 mmol, 1.00 eq) and tin chloride dihydrate (28.43 g, 126.00 mmol, 3.00 eq) were used according to the general procedure to yield a yellow solid (4.04 g, 89 %).



<sup>1</sup>H NMR (400 MHz, CDCl<sub>3</sub>) δ = 7.33-7.26 (2 H, m), 6.91-6.84 (3 H, m), 3.62 (2 H, br s) ppm; NH not seen  
<sup>13</sup>C NMR (100 MHz, CDCl<sub>3</sub>) δ = 151.4, 129.3, 119.5, 112.2 ppm

#### **1b - p-tolylhydrazine**

Sodium nitrite (1.60 g, 23.25 mmol, 1.00 eq), 4-methylaniline (2.49 g, 23.25 mmol, 1.00 eq) and tin chloride dihydrate (15.74 g, 69.75 mmol, 3.00 eq) were used according to the general procedure to yield a yellow solid (2.30 g, 81 %).

<sup>1</sup>H NMR (200 MHz, DMSO-d<sub>6</sub>) δ = 6.91 (2 H, d, J = 8.3 Hz), 6.70 (2 H, d, J = 8.3 Hz), 6.42 (1 H, s), 3.83 (2 H, s), 2.16 (3 H, s) ppm  
<sup>13</sup>C NMR (50 MHz, DMSO-d<sub>6</sub>) δ = 150.5, 129.0, 125.3, 111.8, 20.2 ppm

#### **1c - (4-butylphenyl)hydrazine**

Sodium nitrite (8.03 g, 116.45 mmol, 1.10 eq), 4-butylaniline (15.80 g, 105.86 mmol, 1.00 eq) and tin chloride dihydrate (71.66 g, 317.58 mmol, 3.00 eq) were used according to the general procedure to yield an orange solid (15.11 g, 87 %).

<sup>1</sup>H NMR (400 MHz, DMSO-d<sub>6</sub>) δ = 6.91 (2 H, d, J = 8.4 Hz), 6.70 (2 H, d, J = 8.4 Hz), 6.44 (1 H, s), 3.85 (2 H, s), 2.43 (2 H, t, J = 7.6 Hz), 1.52-1.44 (2 H, m), 1.27 (2 H, sextet, J = 7.4 Hz), 0.88 (3 H, t, J = 7.4 Hz) ppm  
<sup>13</sup>C NMR (50 MHz, DMSO-d<sub>6</sub>) δ = 150.5, 130.6, 128.3, 111.8, 34.1, 33.7, 21.7, 13.8 ppm

#### **1d - (4-hexylphenyl)hydrazine**

Sodium nitrite (9.67 g, 140.10 mmol, 1.10 eq), 4-hexylaniline (22.58 g, 127.36 mmol, 1.00 eq) and tin chloride dihydrate (86.21 g, 382.08 mmol, 3.00 eq) were used according to the general procedure to yield a yellow solid (24.00 g, 98 %).

<sup>1</sup>H NMR (400 MHz, DMSO-d<sub>6</sub>) δ = 7.92 (3 H, br s), 7.00 (2 H, d, J = 8.5 Hz), 6.83 (2 H, d, J = 8.5 Hz), 2.45 (2 H, t, J = 7.6 Hz), 1.53-1.46 (2 H, m), 1.25 (6 H, m), 0.84 (3 H, t, J = 6.6 Hz) ppm

<sup>13</sup>C NMR (100 MHz, DMSO-d<sub>6</sub>) δ = 146.4, 133.4, 128.5, 113.5, 34.4, 31.2, 31.1, 28.2, 22.1, 13.9 ppm

#### **1e - (4-decylphenyl)hydrazine**

Sodium nitrite (3.25 g, 47.14 mmol, 1.10 eq), 4-decylaniline (10.00 g, 42.58 mmol, 1.00 eq) and tin chloride dihydrate (29.00 g, 128.55 mmol, 3.00 eq) were used according to the general procedure to yield a yellow solid (9.79 g, 92 %).

<sup>1</sup>H NMR (400 MHz, CDCl<sub>3</sub>) δ = 7.06 (2 H, d, J = 8.3 Hz), 6.76 (2 H, d, J = 8.2 Hz), 3.95 (2 H, br s), 2.52 (2 H, t, J = 7.7 Hz), 1.59-1.52 (2 H, m), 1.30-1.26 (14 H, m), 0.88 (3 H, t, J = 6.8 Hz) ppm

#### **General procedure for compounds 2a-e**

A slightly modified procedure from Shi et al.<sup>[50]</sup> was used to prepare cyclohexane-1,4-dione-diphenyl hydrazones **2a-e**.

To a solution of phenylhydrazines **1a-e** (2.20 eq) in absolute EtOH (0.93 mL/mmol) under argon atmosphere 1,4-cyclohexanedione (1.00 eq) was added. Catalytic amounts of acetic acid (0.27 mL) was added dropwise affording a yellow solid to precipitate immediately. The mixture was refluxed for 3 h, before being filtrated, washed carefully with EtOH and dried to give the desired compounds **2a-e** as yellow powders in 84-98 % yields. The materials were used in the next step without further purification.

#### **2a - cyclohexane-1,4-dione-diphenyl hydrazone**

Phenylhydrazine **1a** (23.27 g, 215.16 mmol, 2.20 eq), 1,4-cyclohexanedione (10.97 g, 10.07 mmol, 1.00 eq) were used according to the general procedure to yield a yellow solid (24.07 g, 84 %).

<sup>1</sup>H NMR (200 MHz, CDCl<sub>3</sub>) δ = 7.30-7.22 (4 H, m), 7.09-7.04 (4 H, m), 6.90-6.82 (2 H, m), 2.83-2.67 (4 H, m), 2.64-2.52 (4 H, m) ppm

<sup>13</sup>C NMR (50 MHz, DMSO-d<sub>6</sub>) δ = 146.8, 145.4, 129.2, 120.0, 113.0, 29.5, 24.9 ppm

#### **2b - 1,4-Cyclohexanedione, 1,4-bis[2-(4-methylphenyl)hydrazone]**

(4-Methylphenyl)hydrazine **1b** (4.09 g, 33.44 mmol, 2.20 eq), 1,4-cyclohexanedione (1.70 g, 15.20 mmol, 1.00 eq) were used according to the general procedure to yield a yellow solid (4.73 g, 97 %).

<sup>1</sup>H NMR (200 MHz, CDCl<sub>3</sub>) δ = 7.08-7.04 (4 H, m), 6.98-6.93 (4 H, m), 6.78 (2 H, br s), 2.84-2.66 (4 H, m), 2.60-2.49 (4 H, m), 2.27 (6 H, s) ppm

<sup>13</sup>C NMR (50 MHz, CDCl<sub>3</sub>) δ = 146.6, 143.4, 129.8, 129.4, 113.3, 29.6, 25.1, 20.7 ppm

#### **2c - 1,4-Cyclohexanedione, 1,4-bis[2-(4-butylphenyl)hydrazone]**

(4-Butylphenyl)hydrazine **1c** (14.82 g, 90.20 mmol, 2.20 eq), 1,4-cyclohexanedione (4.60 g, 41.00 mmol, 1.00 eq) were used according to the general procedure to yield a yellow solid (16.26 g, 98 %).

<sup>1</sup>H NMR (200 MHz, CDCl<sub>3</sub>) δ = 7.11-7.06 (4 H, m), 7.01-6.97 (4 H, m), 6.79 (2 H, s), 2.77 (4 H, t, J = 6.5 Hz), 2.59-2.48 (8 H, m), 1.66-1.51 (4 H, m), 1.45-1.27 (4 H, m), 0.93 (6 H, t, J = 7.2 Hz) ppm

<sup>13</sup>C NMR (50 MHz, CDCl<sub>3</sub>) δ = 146.5, 143.6, 134.6, 129.2, 113.2, 35.0, 34.0, 29.6, 25.0, 22.4, 14.1 ppm

#### **2d - 1,4-Cyclohexanedione, 1,4-bis[2-(4-hexylphenyl)hydrazone]**

(4-Hexylphenyl)hydrazine **1d** (4.26 g, 22.15 mmol, 2.20 eq), 1,4-cyclohexanedione (1.13 g, 10.07 mmol, 1.00 eq) were used according to the general procedure to yield a yellow solid (4.45 g, 96 %).

<sup>1</sup>H NMR (200 MHz, CDCl<sub>3</sub>) δ = 7.06 (4 H, d, J = 8.3 Hz), 6.97 (4 H, d, J = 8.3 Hz), 6.78 (2 H, s), 2.76 (4 H, t, J = 6.7 Hz), 2.52 (8 H, t, J = 7.5 Hz), 1.60-1.53 (4 H, m), 1.31-1.26 (12 H, m), 0.89-0.86 (6 H, m) ppm

<sup>13</sup>C NMR (50 MHz, CDCl<sub>3</sub>) δ = 146.3, 143.4, 134.6, 129.1, 113.1, 35.1, 31.8, 31.7, 29.5, 28.9, 24.9, 22.3, 14.1 ppm

#### **2e - 1,4-Cyclohexanedione, 1,4-bis[2-(4-decylphenyl)hydrazone]**

(4-Decylphenyl)hydrazine **1e** (10.65 g, 42.85 mmol, 2.20 eq), 1,4-cyclohexanedione (2.18 g, 19.48 mmol, 1.00 eq) were used according to the general procedure to yield a yellow solid (10.27 g, 92 %).

<sup>1</sup>H NMR (200 MHz, CDCl<sub>3</sub>) δ = 7.06 (4 H, d, J = 8.5 Hz), 6.96 (4 H, d, J = 8.5 Hz), 6.78 (2 H, s), 2.80-2.74 (4 H, m), 2.52 (8 H, t, J = 7.3 Hz), 1.56 (5 H, m), 1.26 (28 H, m), 0.91-0.84 (6 H, m) ppm

<sup>13</sup>C NMR (50 MHz, CDCl<sub>3</sub>) δ = 146.3, 143.4, 134.6, 129.1, 122.9, 113.1, 35.3, 32.0, 31.9, 29.8, 29.7, 29.5, 29.4, 25.1, 22.8, 14.3 ppm

#### **General procedure for compounds 3a-e**

A slightly modified procedure from Shi et al.<sup>[50]</sup> was used for the preparation of the indolo[3,2-*b*]carbazoles **3a-e**.

Phenylhydrazones **2a-e** were added portionwise to a mixture of acetic acid and H<sub>2</sub>SO<sub>4</sub> (4:1, 1.4 mL/mmol) with stirring at 5 °C. The mixture began to change color gradually from grey to green to dark purple. Thereafter, the mixture was gradually heated to 60 °C. Again a color change was observed from grey at around 20 °C to red between 30-40 °C to orange between 45-50 °C. At 60 °C a yellow solid precipitated. The mixture was kept at 70 °C for 12 h, before it was cooled down to room temperature. The precipitate was slowly filtered through a glass sinter funnel (Por 4) and washed carefully with water until neutral pH. The material was recrystallized from DMSO/EtOH (2 : 1) and dried to give the target compounds **3a-e** as beige to yellow solids in 21-84 % yields.

#### **3a - 5,11-dihydroindolo[3,2-*b*]carbazole**

**2a** (5.26 g, 18.00 mmol, 1.00 eq) was used according to the general procedure to yield a yellow solid (3.88 g, 84 %).

MS (MALDI-TOF): calcd for C<sub>18</sub>H<sub>12</sub>N<sub>2</sub>: 256.1000; found: 256.0773; difference: -0.0227 (-88 ppm)

<sup>1</sup>H NMR (600 MHz, DMSO-d<sub>6</sub>) δ = 11.02 (2 H, s), 8.19 (2 H, d, J = 7.4 Hz), 8.11 (2 H, s), 7.45 (2 H, d, J = 8.2 Hz), 7.37 (2 H, t, J = 7.0 Hz), 7.12 (2 H, t, J = 7.3 Hz) ppm

<sup>13</sup>C NMR (50 MHz, DMSO-*d*<sub>6</sub>) δ = 141.1, 135.1, 125.5, 122.6, 122.6, 120.2, 117.7, 110.5, 100.5 ppm

### 3b – 2,8-dimethyl-5,11-dihydroindolo[3,2-*b*]carbazole

**2b** (0.73 g, 2.29 mmol, 1.00 eq) was used according to the general procedure to yield a yellow solid (0.42 g, 65 %).

MS (MALDI-TOF): calcd for C<sub>20</sub>H<sub>16</sub>N<sub>2</sub>: 284.1313; found: 284.1159; difference: - 0.0154 (-55 ppm)

<sup>1</sup>H NMR (600 MHz, DMSO-*d*<sub>6</sub>) δ = 10.85 (2 H, s), 8.01 (2 H, s), 7.96 (2 H, s), 7.33 (2 H, d, J = 8.2 Hz), 7.18 (2 H, d, J = 8.1 Hz), 2.48 (6 H, s) ppm

<sup>13</sup>C NMR (151 MHz, DMSO-*d*<sub>6</sub>) δ = 139.4, 135.3, 126.8, 126.2, 122.8, 122.5, 120.1, 110.2, 100.3, 21.2 ppm

### 3c – 2,8-dibutyl-5,11-dihydroindolo[3,2-*b*]carbazole

**2c** (16.79 g, 41.50 mmol, 1.00 eq) was used according to the general procedure to yield a yellow solid (4.58 g, 30 %).

MS (MALDI-TOF): calcd for C<sub>26</sub>H<sub>28</sub>N<sub>2</sub>: 368.2252; found: 368.2246; difference: - 0.0007 (-2 ppm)

<sup>1</sup>H NMR (600 MHz, DMSO-*d*<sub>6</sub>) δ = 10.85 (2 H, s), 8.04 (2 H, s), 7.97 (2 H, s), 7.35 (2 H, d, J = 8.2 Hz), 7.20 (2 H, dd, J<sub>1</sub> = 8.2 Hz, J<sub>2</sub> = 1.5 Hz), 2.74 (4 H, t, J = 7.7 Hz), 1.67 (4 H, quintet, J = 7.5 Hz), 1.38 (4 H, quintet, J = 7.4 Hz), 0.94 (6 H, t, J = 7.2 Hz) ppm

<sup>13</sup>C NMR (151 MHz, DMSO-*d*<sub>6</sub>) δ = 139.5, 135.3, 131.5, 129.1, 122.7, 122.5, 119.4, 110.2, 100.3, 35.1, 34.2, 21.9, 13.9 ppm

### 3d – 2,8-dihexyl-5,11-dihydroindolo[3,2-*b*]carbazole

**2d** (7.37 g, 16.00 mmol, 1.00 eq) was used according to the general procedure to yield a yellow solid (2.11 g, 31 %).

MS (MALDI-TOF): calcd for C<sub>30</sub>H<sub>36</sub>N<sub>2</sub>: 424.2878; found: 424.2954; difference: - 0.0076 (-2 ppm)

<sup>1</sup>H NMR (400 MHz, DMSO-*d*<sub>6</sub>) δ = 10.85 (2 H, s), 8.04 (2 H, s), 7.98 (2 H, s), 7.35 (2 H, d, J = 8.2 Hz), 7.20 (2 H, dd, J<sub>1</sub> = 8.24 Hz, J<sub>2</sub> = 1.36 Hz), 2.75 (4 H, t, J = 7.6 Hz), 1.70-1.65 (4 H, m), 1.33-1.30 (12 H, m), 0.88 (6 H, t, J = 6.9 Hz) ppm

<sup>13</sup>C NMR (151 MHz, DMSO-*d*<sub>6</sub>) δ = 139.5, 135.3, 131.5, 126.1, 122.7, 122.5, 119.4, 110.2, 100.3, 35.4, 32.0, 31.3, 28.5, 22.2, 14.0 ppm

### 3e – 2,8-didecyl-5,11-dihydroindolo[3,2-*b*]carbazole

**2e** (16.10 g, 28.10 mmol, 1.00 eq) was used according to the general procedure to yield a beige solid (3.17 g, 21 %).

MS (MALDI-TOF): calcd for C<sub>38</sub>H<sub>52</sub>N<sub>2</sub>: 536.4131; found: 536.4434; difference: 0.0303 (51 ppm)

<sup>1</sup>H NMR (400 MHz, DMSO-*d*<sub>6</sub>) δ = 10.85 (2 H, s), 8.03 (2 H, s), 7.95 (2 H, s), 7.34 (2 H, d, J = 8.2 Hz), 7.19 (2 H, dd, J<sub>1</sub> = 8.2 Hz, J<sub>2</sub> = 1.6 Hz), 2.73 (4 H, t, J = 7.5 Hz), 1.72-1.60 (4 H, m), 1.39-1.16 (28 H, m), 0.84 (6 H, t, J = 6.9 Hz) ppm

### 4a – 5,11-dihexyl-5,11-dihydroindolo[3,2-*b*]carbazole

Compound **4a** was synthesized using a modified literature procedure.<sup>[7]</sup>

A freshly prepared 50 % aq. NaOH solution (4 mL) was added to a well-stirred mixture of **3a** (0.51 g, 2.00 mmol, 1.00 eq), benzyltriethylammonium chloride (0.12 g, 0.40 mmol, 0.20 eq), 1-bromohexane (1.32 g, 8.00 mmol, 4.00 eq), and DMSO (20 mL) in a 100 mL three-necked flask under argon atmosphere. The mixture was stirred at room temperature for 1 h and changed from grey to yellow after the addition of the base. The reaction was then heated to 65 °C for 3 h. Subsequently the mixture was cooled down to room temperature and poured into MeOH (200 mL) with stirring. The precipitated yellow solid was filtered off and purified by column chromatography on silica gel using hexane/DCM (3:1) as eluent yielding the product as yellow solid (0.40 g, 47 %).

MS (MALDI-TOF): calcd for C<sub>30</sub>H<sub>36</sub>N<sub>2</sub>: 424.2878; found: 424.2967; difference: 0.0088 (20 ppm)

<sup>1</sup>H NMR (400 MHz, CD<sub>2</sub>Cl<sub>2</sub>) δ = 8.21 (2 H, td, J<sub>1</sub> = 7.8 Hz, J<sub>2</sub> = 1.8 Hz), 8.06 (2 H, s), 7.50-7.43 (4 H, m), 7.22 (2 H, dt, J<sub>1</sub> = 7.4 Hz, J<sub>2</sub> = 1.4 Hz), 1.95 (4 H, q, J = 7.4 Hz), 1.52-1.27 (12 H, m), 0.88 (6 H, t, J = 7.1 Hz) ppm.

<sup>13</sup>C NMR (50 MHz, CD<sub>2</sub>Cl<sub>2</sub>) δ = 142.1, 136.4, 126.0, 123.1, 123.1, 120.5, 118.3, 108.8, 99.2, 43.7, 32.1, 29.2, 27.4, 23.0, 14.2 ppm.

### 4d – 2,5,8,11-tetrahexyl-5,11-dihydroindolo[3,2-*b*]carbazole

Under argon atmosphere **3d** (0.13 g, 0.30 mmol, 1.00 eq) was dissolved in absolute DMF (6 mL) and stirred at room temperature. Freshly washed sodium hydride (0.02 g, 0.9 mmol, 3.00 eq) was added quickly and the mixture was continued to stir for 30 min, before adding a solution of 1-bromohexane (0.12 g, 0.75 mmol, 2.50 eq) in absolute DMF (1 mL). After 2 h at room temperature the temperature was raised to 60 °C for 3 h. The resulting dark purple solution was reduced under high vacuum and extracted with H<sub>2</sub>O and DCM. Purification by column chromatography on silica gel using PE:EE=10:1 yielded a yellow solid (0.08 g, 45 %).

MS (MALDI-TOF): calcd for C<sub>42</sub>H<sub>60</sub>N<sub>2</sub>: 592.4757; found: 592.5146; difference: 0.0389 (66 ppm)

<sup>1</sup>H NMR (600 MHz, DMSO-*d*<sub>6</sub>) δ = 8.00 (4 H, s), 7.34-7.30 (4 H, m), 4.38 (4 H, m), 2.82 (4 H, t, J = 7.7 Hz), 1.93 (4 H, q, 7.5 Hz), 1.74 (4 H, q, J = 7.6 Hz), 1.48-1.29 (24 H, m), 0.92-0.87 (12 H, m) ppm.

<sup>13</sup>C NMR (151 MHz, DMSO-*d*<sub>6</sub>) δ = 140.5, 136.5, 133.0, 126.7, 123.1, 122.9, 119.8, 108.4, 98.9, 43.7, 36.4, 32.9, 32.3, 32.1, 29.5, 29.2, 27.5, 23.1, 23.0, 14.3, 14.2 ppm

## 5. Acknowledgements

JB is grateful to the Marietta Blau Grant of the OeAD.

**Keywords:** indolo(3,2-*b*)carbazole • pneumatic printing • organic electronics • OFET • computational chemistry

- [1] H. Shirakawa, E. J. Louis, A. G. MacDiarmid, C. K. Chiang, A. J. Heeger, *J. Chem. Soc. Chem. Commun.* **1977**, 578.
- [2] H. Klauk, *Organic Electronics II: More Materials and Applications*, Wiley-VCH, Weinheim, **2012**.
- [3] J. Mei, Y. Diao, A. L. Appleton, L. Fang, Z. Bao, *J. Am. Chem. Soc.* **2013**, *135*, 6724–6746.
- [4] Y.-S. Tyan, *J. Photonics Energy* **2011**, *1*, 011009–011009.
- [5] L. Torsi, M. Magliulo, K. Manoli, G. Palazzo, *Chem. Soc. Rev.* **2013**, *42*, 8612–8628.
- [6] H. Dong, X. Fu, J. Liu, Z. Wang, W. Hu, *Adv. Mater.* **2013**, *25*, 6158–6183.
- [7] Y. Wu, Y. Li, S. Gardner, B. S. Ong, *J. Am. Chem. Soc.* **2005**, *127*, 614–618.
- [8] Y. Li, Y. Wu, S. Gardner, B. S. Ong, *Adv. Mater.* **2005**, *17*, 849–853.
- [9] P.-L. T. Boudreault, S. Wakim, M. L. Tang, Y. Tao, Z. Bao, M. Leclerc, *J. Mater. Chem.* **2009**, *19*, 2921.
- [10] H. Shi, J. Dai, X. Wu, L. Shi, J. Yuan, L. Fang, Y. Miao, X. Du, H. Wang, C. Dong, *Org. Electron.* **2013**, *14*, 868–874.
- [11] H.-C. Ting, Y.-M. Chen, H.-W. You, W.-Y. Hung, S.-H. Lin, A. Chaskar, S.-H. Chou, Y. Chi, R.-H. Liu, K.-T. Wong, *J. Mater. Chem.* **2012**, *22*, 8399.
- [12] J. Tong, P. Guo, H. Zhang, J. Li, P. Zhang, C. Yang, D. Chen, Y. Xia, *Polym. Bull.* **2015**, 1–17.
- [13] J. Lu, F. Liang, N. Drolet, J. Ding, Y. Tao, R. Movileanu, *Chem. Commun.* **2008**, 5315.
- [14] G. Tian, N. Xiang, H. Zhou, Y. Li, B. Li, Q. Wang, J. Su, *Tetrahedron* **2016**, *72*, 298–303.
- [15] L. F. Bjeldanes, J. Y. Kim, K. R. Grose, J. C. Bartholomew, C. A. Bradfield, *Proc. Natl. Acad. Sci.* **1991**, *88*, 9543–9547.
- [16] Y.-D. Wei, H. Helleberg, U. Rannug, A. Rannug, *Chem. Biol. Interact.* **1998**, *110*, 39–55.
- [17] J. E. Anthony, *Angew. Chem. Int. Ed.* **2008**, *47*, 452–483.

- [18] M. T. Levick, I. Grace, S.-Y. Dai, N. Kasch, C. Murny, C. Lambert, M. L. Turner, D. J. Procter, *Org. Lett.* **2014**, DOI 10.1021/ol500841b.
- [19] K. S. Park, S. M. Salunkhe, I. Lim, C.-G. Cho, S.-H. Han, M. M. Sung, *Adv. Mater.* **2013**, *25*, 3351–3356.
- [20] H. Zhao, L. Jiang, H. Dong, H. Li, W. Hu, B. S. Ong, *ChemPhysChem* **2009**, *10*, 2345–2348.
- [21] S. Illig, A. S. Eggeman, A. Troisi, L. Jiang, C. Warwick, M. Nikolka, G. Schweicher, S. G. Yeates, Y. Henri Geerts, J. E. Anthony, et al., *Nat. Commun.* **2016**, *7*, 10736.
- [22] A. R. Katritzky, J. Li, C. V. Stevens, *J. Org. Chem.* **1995**, *60*, 3401–3404.
- [23] K. Kawaguchi, K. Nakano, K. Nozaki, *J. Org. Chem.* **2007**, *72*, 5119–5128.
- [24] M. T. Levick, I. Grace, S.-Y. Dai, N. Kasch, C. Murny, C. Lambert, M. L. Turner, D. J. Procter, *Org. Lett.* **2014**, *16*, 2292–2295.
- [25] N. Blouin, A. Michaud, S. Wakim, P.-L. T. Boudreault, M. Leclerc, B. Vercelli, S. Zecchin, G. Zotti, *Macromol. Chem. Phys.* **2006**, *207*, 166–174.
- [26] J. Tholander, J. Bergman, *Tetrahedron* **1999**, *55*, 12577–12594.
- [27] J. Bergman, *Tetrahedron* **1970**, *26*, 3353–3355.
- [28] B. Robinson, *J. Chem. Soc. Resumed* **1963**, 3097–3099.
- [29] L. N. Yudina, J. Bergman, *Tetrahedron* **2003**, *59*, 1265–1275.
- [30] M. J. Frisch, G. W. Trucks, H. B. Schlegel, G. E. Scuseria, M. A. Robb, J. R. Cheeseman, G. Scalmani, V. Barone, B. Mennucci, G. A. Petersson, et al., *Gaussian 09 Revis. A2* **2009**, Gaussian, Inc., Wallingford CT.
- [31] C. Lee, W. Yang, R. G. Parr, *Phys. Rev. B* **1988**, *37*, 785–789.
- [32] A. D. Becke, *J. Chem. Phys.* **1993**, *98*, 5648–5652.
- [33] R. Krishnan, J. S. Binkley, R. Seeger, J. A. Pople, *J. Chem. Phys.* **1980**, *72*, 650–654.
- [34] G. Zhao, H. Dong, H. Zhao, L. Jiang, X. Zhang, J. Tan, Q. Meng, W. Hu, *J. Mater. Chem.* **2012**, *22*, 4409–4417.
- [35] I. Kymissis, *Organic Field Effect Transistors: Theory, Fabrication and Characterization*, Springer, **2008**.
- [36] Z. Bao, *Adv. Mater.* **2000**, *12*, 227–230.
- [37] Y. Diao, L. Shaw, Z. Bao, S. C. B. Mannsfeld, *Energy Environ. Sci.* **2014**, *7*, 2145.
- [38] J. E. Anthony, *Chem. Rev.* **2006**, *106*, 5028–5048.
- [39] C. Wang, H. Dong, W. Hu, Y. Liu, D. Zhu, *Chem. Rev.* **2012**, *112*, 2208–2267.
- [40] G. Giri, S. Park, M. Vosgueritchian, M. M. Shulaker, Z. Bao, *Adv. Mater.* **2014**, *26*, 487–493.
- [41] G. Giri, E. Verploegen, S. C. B. Mannsfeld, S. Atahan-Evrenk, D. H. Kim, S. Y. Lee, H. A. Becerril, A. Aspuru-Guzik, M. F. Toney, Z. Bao, *Nature* **2011**, *480*, 504–508.
- [42] H. Minemawari, T. Yamada, H. Matsui, J. Tsutsumi, S. Haas, R. Chiba, R. Kumai, T. Hasegawa, *Nature* **2011**, *475*, 364–367.
- [43] R. Li, L. Jiang, Q. Meng, J. Gao, H. Li, Q. Tang, M. He, W. Hu, Y. Liu, D. Zhu, *Adv. Mater.* **2009**, *21*, 4492–4495.
- [44] C. W. Sele, B. K. C. Kjellander, B. Niesen, M. J. Thornton, J. B. P. H. van der Putten, K. Myny, H. J. Wondergem, A. Moser, R. Resel, A. J. J. M. van Breemen, et al., *Adv. Mater.* **2009**, *21*, 4926–4931.
- [45] Bruker computer programs: APEX2, SAINT and SADABS (Bruker AXS Inc., Madison, WI, 2015)
- [46] L. Palatinus, G. Chapuis, *J. Appl. Crystallogr.* **2007**, *40*, 786–790.
- [47] V. Petříček, M. Dušek, L. Palatinus, *Z. Für Krist. - Cryst. Mater.* **2014**, *229*, 345–352.
- [48] C. F. Macrae, P. R. Edgington, P. McCabe, E. Pidcock, G. P. Shields, R. Taylor, M. Towler, J. van de Streek, *J. Appl. Crystallogr.* **2006**, *39*, 453–457.
- [49] M. S. Liu, Y.-H. Niu, J.-W. Ka, H.-L. Yip, F. Huang, J. Luo, T.-D. Kim, A. K.-Y. Jen, *Macromolecules* **2008**, *41*, 9570–9580.
- [50] H. Shi, J. Yuan, X. Wu, X. Dong, L. Fang, Y. Miao, H. Wang, F. Cheng, *New J. Chem.* **2014**, *38*, 2368–2378.



# Manuscript #2

S. Yang\*, S. Park\*, **J. Binting**, Y. Bonnassieux, I. Kymissis; Pneumatic Nozzle Printing as a Versatile Approach to Crystal Growth Management and Patterning of Printed Organic Thin Film Transistors; *manuscript accepted SID conference 2016*



# Pneumatic Nozzle Printing as a Versatile Approach to Crystal Growth Management and Patterning of Printed Organic Thin Film Transistors

Shyuan Yang<sup>\*a</sup>, Steve Park<sup>\*a,d</sup>, Johannes Binting<sup>a,b</sup>, Yvan Bonnassieux<sup>a,c</sup>,  
Ioannis Kymissis<sup>†a</sup>

<sup>a</sup>Department of Electrical Engineering, Columbia University, New York, NY 10027, USA

<sup>b</sup>Institute of Applied Synthetic Chemistry, Vienna University of Technology, 1060 Vienna, Austria

<sup>c</sup>Laboratoire de Physique des Interfaces et des Couches Minces (LPICM), École Polytechnique, 91128 Palaiseau, France

<sup>d</sup>Department of Materials Science and Engineering, Korea Advanced Institute of Science and Technology, Daejeon, South Korea; (\* Equal Contribution, †johnkym@ee.columbia.edu)

## Abstract

We report a novel pneumatic nozzle-based printing technique that has the capability to deposit and control the crystallization and orientation of small molecule organic semiconductor (TIPS-pentacene) thin-films. By adjusting the writing speed to match the solvent evaporation rate at the meniscus, organic crystals were grown along the direction of nozzle movement, resulting in field-effect mobility as high as 0.8 cm<sup>2</sup>/Vs. Furthermore, we demonstrate the versatility of our technique by depositing electrodes and fabricating all-printed inverters on a flexible substrate with a gain as high as 15.9.

## Author Keywords

printing; crystal control; thin film; transistor; OFET

## 1. Introduction

Solution processable small molecule organic semiconductors are candidates as the active channel materials in organic field-effect transistors (OFET) and have recently been demonstrated to have high field-effect mobility in addition to the advantages of printability and low thermal budget.<sup>[1],[2]</sup> The mobility in small molecule organic semiconductors is strongly dependent on the crystallinity, crystal orientation, and molecular packing of the thin-film.<sup>[3],[4]</sup> The deposition process significantly influences thin-film characteristics, and higher mobility is generally achieved when larger crystals are aligned along the direction of charge transport. Many methods have been developed to generate aligned crystals of organic thin films such as dip coating,<sup>[5]</sup> zone casting,<sup>[6]</sup> brush painting,<sup>[7]</sup> doctor blade coating,<sup>[8]</sup> bar coating,<sup>[9]</sup> slot die coating,<sup>[10]</sup> hollow pen writing,<sup>[11]</sup> and solution shearing.<sup>[2]</sup> While these strategies can take advantage of superlateral crystallization and growth to

extend crystal domains over large spatial extents, these techniques generally fail to simultaneously pattern the semiconductor while also controlling crystallization. These techniques also often require blanket deposition, presenting obstacles to multi-material use by exposing unused areas of the substrate to unwanted reagents and not allowing patterning of other materials, such as conductors. For patterning of materials, various techniques such as ink jet printing,<sup>[12]</sup> aerosol-jet/spray printing,<sup>[13]</sup> screening printing,<sup>[14]</sup> and gravure printing,<sup>[15]</sup> have been proposed. However, these techniques generally have limitation in controlling the growth and alignment of organic crystals. Herein, we report a novel pneumatic nozzle-based printing approach to pattern and deposit soluble, small-molecule organic semiconductors, control the crystallization of organic thin-films, and deposit additional patterned materials on the same substrate in order to make an all-printed OFET.

## 2. Results and Discussion

Figure 1 illustrates the pneumatic printing set-up (1a) and process (1b).

1. Vacuum pressure is applied to the solution reservoir to retain the solution.
2. Instantaneous forward pressure is applied to contact the solution to the substrate surface; capillary force keeps the solution attached to the surface even after forward pressure is removed.
3. As the nozzle moves laterally, solution is continuously drawn out due to solvent evaporation at the meniscus, forming a thin film on the substrate. After printing, the nozzle is raised up to detach the solution from the substrate.

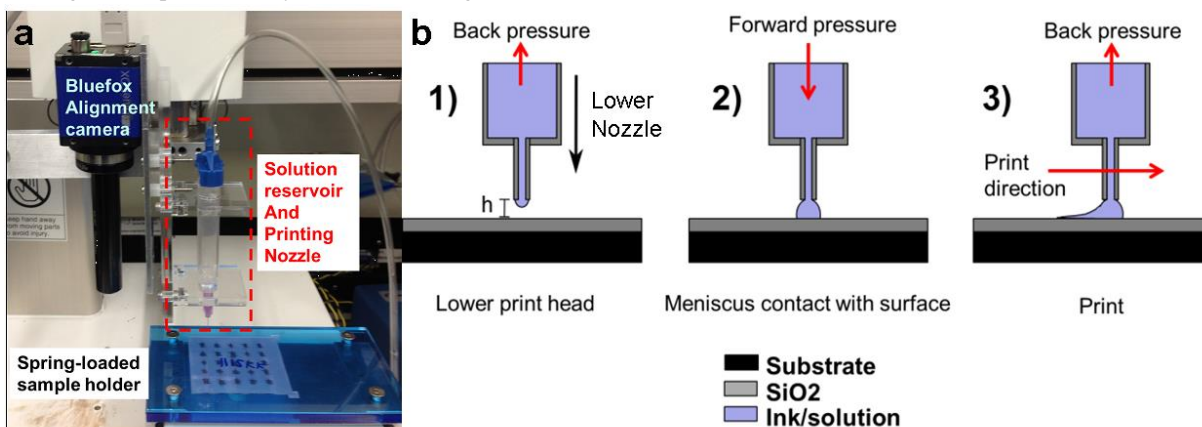
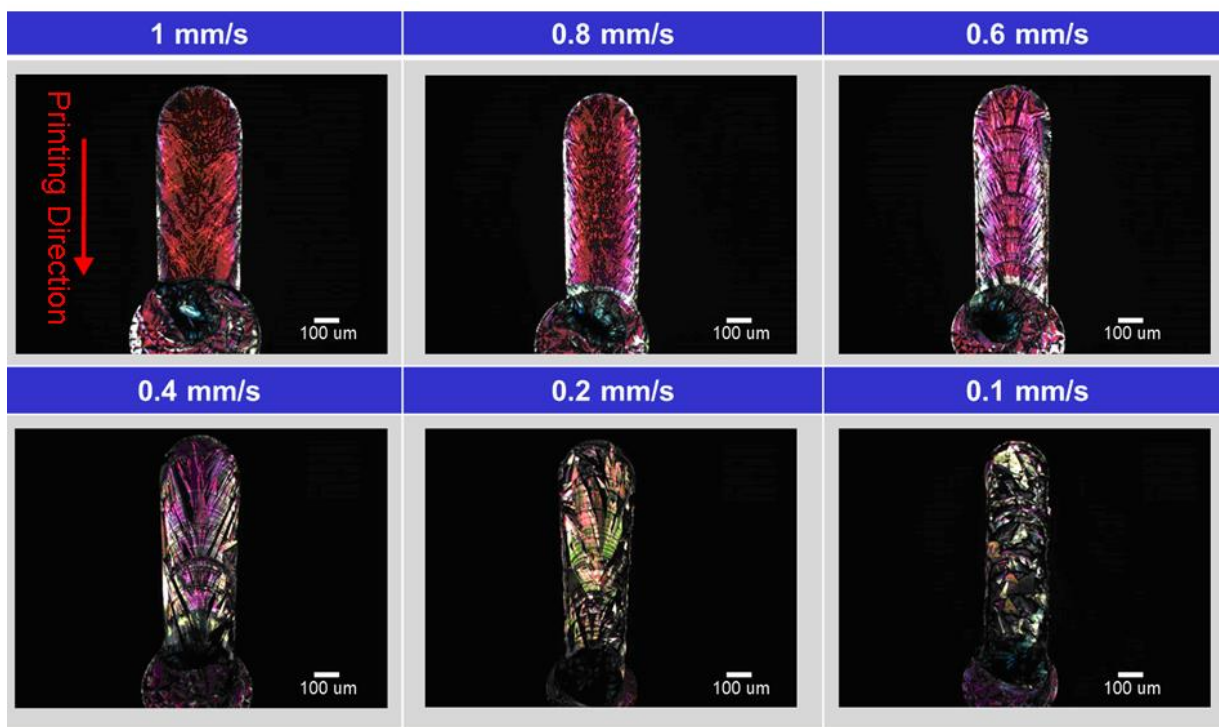


Figure 1. a) Pneumatic printing equipment with alignment camera, ink reservoir, and dispensing tip. b) Schematic of pneumatically controlled printing process.



**Figure 2.** Cross polarized microscopy images under various printing speeds showing different thin-film morphologies. Optimal morphology was delivered at intermediate draw speeds.

This technique continuously draws out the solution during printing rather than dispensing individual droplets, therefore, enabling both high utilization efficiency and a path to fine-tuning film morphology. To demonstrate such a capability, the orientation and size of crystals of a model small organic molecule, TIPS-pentacene (6,13-bis(triisopropylsilylethynyl)), were tuned by varying the printing speed under a fixed substrate temperature at 50°C. Figure 2 and 3 shows cross-polarized optical microscope images and AFM images of printed TIPS-pentacene under various printing speeds, from 1 mm/s to 0.1 mm/s. Under higher printing speeds (1 mm/s and 0.8 mm/s), amorphous film deposition was observed, evidenced by small crystalites oriented in random directions in the AFM image (1 mm/s). This was expected due to random nucleation of the drying film. Berre et al., for example, has previously shown that as a meniscus moves faster, the drawn film gets thinner and extends further away from the solution reservoir.<sup>[16]</sup> A thin-film of solution forms on the substrate and dries rapidly due to the high temperature gradient between the substrate and the air/liquid interface, resulting in a large number of nucleation sites and resulting randomly-oriented crystal growth. When the printing speed is significantly reduced (e.g. to less than 0.2 mm/s), large crystals were formed, but the film was discontinuous. The AFM image at 0.1 mm/s shows one of these large crystals, which did not have a preferential growth direction. This is due to a slow evaporation rate at the meniscus resulting from reduced air/liquid interface, which slows down the crystal growth rate while favoring crystal growth over nucleation. The previously formed crystals also seed the new crystal growth, allowing for the formation of a templated film with a better organized crystal structure. Fewer and slower growing crystals coupled with a slow supply of new solution leads to dewetting and attachment of the wet surface to the templated areas, leading to discontinuous films. At intermediate

printing speeds between 0.6 mm/s and 0.4 mm/s, aligned and continuous films of TIPS-pentacene crystalline domains with widths in the few of microns and lengths in the hundreds of microns were formed. As evident in the AFM images at 0.6 and 0.5 mm/s, the crystals have a preferential growth orientation along the direction of the moving nozzle. At these printing speeds, the evaporation rate at the meniscus matches the printing

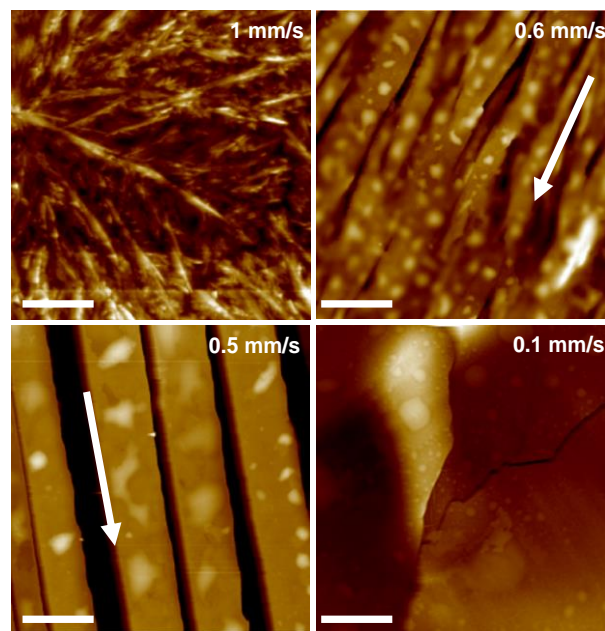


**Figure 3.** AFM images of TIPS-pentacene film at various speeds. The scale bar is 5 μm. The arrows indicate moving direction of the nozzle.



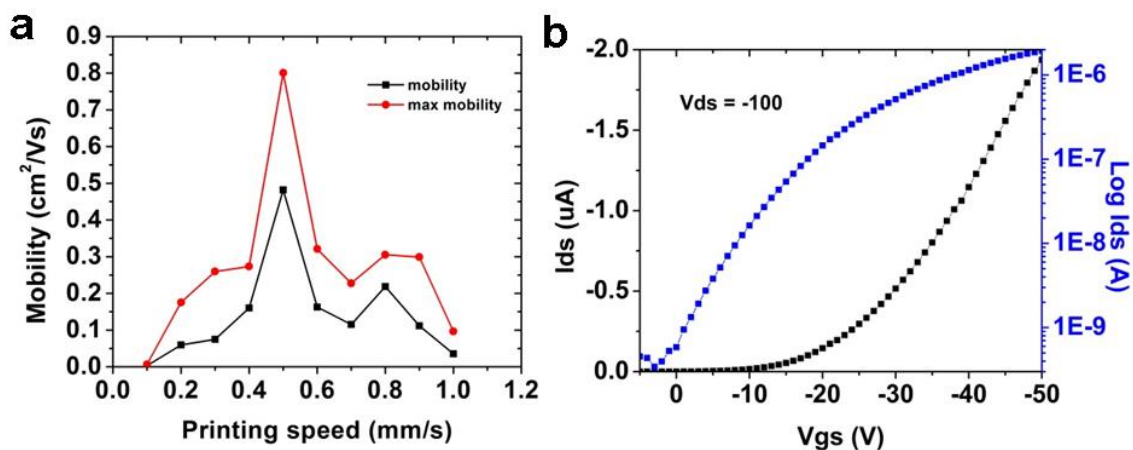


**Figure 4.** a) Average and maximum mobility versus printing speed. b) typical transfer characteristics under a printing speed of 0.5 mm/s

speed, yielding crystal growth along the direction of the moving meniscus. This produces aligned crystals with sufficient nucleation events to fill the entire film.

The average mobility versus printing speed is shown in Figure 4a. A maximum mobility of 0.8 cm<sup>2</sup>/Vs was achieved with 0.5 mm/s printing speed. Figure 4b shows a typical transfer characteristic under this printing condition. The difference in mobility can be attributed to the difference in the degree of crystallinity and continuity of the films. At faster speeds we obtained amorphous films, which due to their small grain sizes yield a higher density of grain boundaries, disordered organization, and lower mobility. The poor wet film organization seen under slow printing speeds, on the other hand, leads to discontinuities and voids in the film. At the optimal printing speed, the lower density of grain boundaries and formation of a continuous film results in higher mobilities. Furthermore, the crystals show better alignment along the printing direction, and since for TIPS-pentacene the direction of fast transport is also the direction of printing,<sup>[17]</sup> this likely further enhances the mobility.

Another advantage of this technique is the capability to print patterns using solutions of varying viscosities simply by adjusting the vacuum pressure level. Using the same general approach, we can print patterned silver lines on the substrate, and align the gate/source/drain/and patterned semiconductor area under active control. As a demonstration, we fabricated inverters on flexible PEN substrates with pneumatically printed silver ink as source, drain and gate electrodes and drop-casted

TIPS-pentacene as the channel. A blanket parylene-C gate was used between the printed metal layers and the gate dielectric. The fabricated devices are shown in Figure 5a and 5b. The transfer characteristic of 7 inverters is shown in Figure 5b. The devices were powered at 40V with a transition voltage of approximately 15 V. The maximum and average gain, were 15.9 and 10, respectively, with a standard deviation of 1.24 between these samples.

### 3. Conclusion

In summary, we have demonstrated a novel pneumatic printing technique for organic semiconductors and metal conductors that offers the following characteristics:

- A simple setup and process, with the ability to align and deposit solution-phase materials on nearly arbitrary substrates
- The ability to simultaneously pattern and deposit material at the resolutions required for large-area TFT circuit layout
- The ability to deposit multiple materials with a range of viscosities and solvents
- The ability to deposit multiple materials on the same substrate
- Control over crystal nucleation and growth

Optimum printing conditions resulted in high performance OFET devices (yielding a mobility of 0.8 cm<sup>2</sup>/Vs), and printed inverters were fabricated to demonstrate the feasibility of employing the pneumatic printing technique for multi-material printing process.

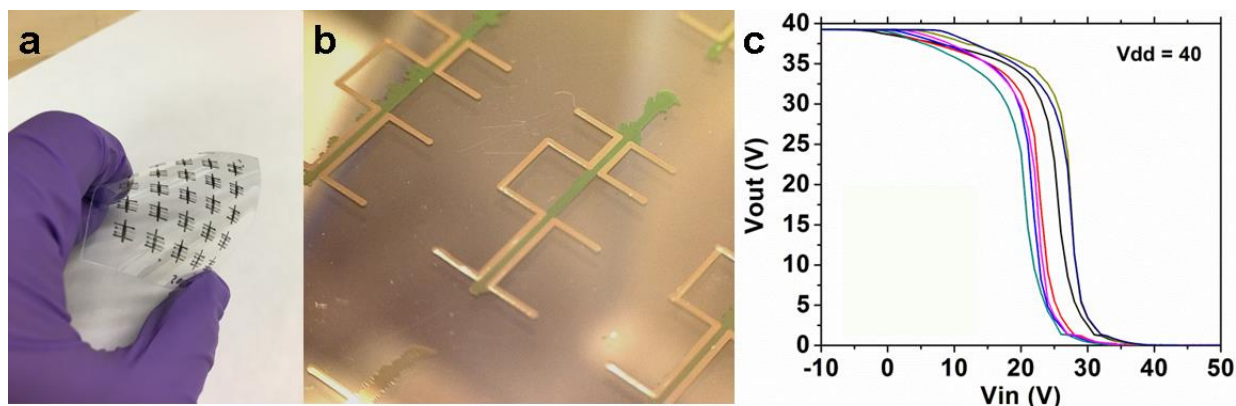


**Figure 5.** a) and b) Images of printed unipolar inverters on a flexible PEN substrate. c) Voltage transfer curve of 7 inverters.

## 4. Acknowledgements

This work was partially supported by the FlexTech Alliance and Columbia University's Research Initiatives for Science and Engineering program. YB further acknowledges support from the Alliance Program and JB is grateful to the Marietta Blau Grant of the OeAD.

## 5. References

- [1] H. Minemawari, T. Yamada, H. Matsui, J. Tsutsumi, S. Haas, R. Chiba, R. Kumai, and T. Hasegawa, "Inkjet printing of single-crystal films," *Nature*, vol. 475, no. 7356, pp. 364–367, Jul. 2011.
- [2] Y. Diao, B. C.-K. Tee, G. Giri, J. Xu, D. H. Kim, H. A. Becerril, R. M. Stoltenberg, T. H. Lee, G. Xue, S. C. B. Mannsfeld, and Z. Bao, "Solution coating of large-area organic semiconductor thin films with aligned single-crystalline domains," *Nat. Mater.*, vol. 12, no. 7, pp. 665–671, Jun. 2013.
- [3] C. Wang, H. Dong, W. Hu, Y. Liu, and D. Zhu, "Semiconducting  $\pi$ -Conjugated Systems in Field-Effect Transistors: A Material Odyssey of Organic Electronics," *Chem. Rev.*, vol. 112, no. 4, pp. 2208–2267, Apr. 2012.
- [4] H. Dong, C. Wang, and W. Hu, "High performance organic semiconductors for field-effect transistors," *Chem. Commun.*, vol. 46, no. 29, p. 5211, 2010.
- [5] N. Liu, Y. Zhou, N. Ai, C. Luo, J. Peng, J. Wang, J. Pei, and Y. Cao, "High-Performance, All-Solution-Processed Organic Nanowire Transistor Arrays with Inkjet-Printing Patterned Electrodes," *Langmuir*, vol. 27, no. 24, pp. 14710–14715, Dezember 2011.
- [6] D. T. James, J. M. Frost, J. Wade, J. Nelson, and J.-S. Kim, "Controlling Microstructure of Pentacene Derivatives by Solution Processing: Impact of Structural Anisotropy on Optoelectronic Properties," *ACS Nano*, vol. 7, no. 9, pp. 7983–7991, Sep. 2013.
- [7] Z. Qi, F. Zhang, C. Di, J. Wang, and D. Zhu, "All-brush-painted top-gate organic thin-film transistors," *J. Mater. Chem. C*, vol. 1, no. 18, pp. 3072–3077, Apr. 2013.
- [8] Y.-H. Chang, S.-R. Tseng, C.-Y. Chen, H.-F. Meng, E.-C. Chen, S.-F. Horng, and C.-S. Hsu, "Polymer solar cell by blade coating," *Org. Electron.*, vol. 10, no. 5, pp. 741–746, Aug. 2009.
- [9] D. Khim, H. Han, K.-J. Baeg, J. Kim, S.-W. Kwak, D.-Y. Kim, and Y.-Y. Noh, "Simple Bar-Coating Process for Large-Area, High-Performance Organic Field-Effect Transistors and Ambipolar Complementary Integrated Circuits," *Adv. Mater.*, vol. 25, no. 31, pp. 4302–4308, Aug. 2013.
- [10] J. Chang, C. Chi, J. Zhang, and J. Wu, "Controlled Growth of Large-Area High-Performance Small-Molecule Organic Single-Crystalline Transistors by Slot-Die Coating Using A Mixed Solvent System," *Adv. Mater.*, vol. 25, no. 44, pp. 6442–6447, Nov. 2013.
- [11] B. Kang, H. Min, U. Seo, J. Lee, N. Park, K. Cho, and H. S. Lee, "Directly Drawn Organic Transistors by Capillary Pen: A New Facile Patterning Method using Capillary Action for Soluble Organic Materials," *Adv. Mater.*, vol. 25, no. 30, pp. 4117–4122, Aug. 2013.
- [12] J. A. Lim, W. H. Lee, H. S. Lee, J. H. Lee, Y. D. Park, and K. Cho, "Self-Organization of Ink-jet-Printed Triisopropylsilylethynyl Pentacene via Evaporation-Induced Flows in a Drying Droplet," *Adv. Funct. Mater.*, vol. 18, no. 2, pp. 229–234, Jan. 2008.
- [13] J. H. Cho, J. Lee, Y. Xia, B. Kim, Y. He, M. J. Renn, T. P. Lodge, and C. Daniel Frisbie, "Printable ion-gel gate dielectrics for low-voltage polymer thin-film transistors on plastic," *Nat. Mater.*, vol. 7, no. 11, pp. 900–906, Nov. 2008.
- [14] S. C. Lim, S. H. Kim, Y. S. Yang, M. Y. Lee, S. Y. Nam, and J. B. Ko, "Organic Thin-Film Transistor Using High-Resolution Screen-Printed Electrodes," *Jpn. J. Appl. Phys.*, vol. 48, no. 8, p. 081503, Aug. 2009.
- [15] A. de la Fuente Vornbrock, D. Sung, H. Kang, R. Kitsomboonloha, and V. Subramanian, "Fully gravure and ink-jet printed high speed pBTTT organic thin film transistors," *Org. Electron.*, vol. 11, no. 12, pp. 2037–2044, Dezember 2010.
- [16] M. Le Berre, Y. Chen, and D. Baigl, "From Convective Assembly to Landau–Levich Deposition of Multilayered Phospholipid Films of Controlled Thickness," *Langmuir*, vol. 25, no. 5, pp. 2554–2557, März 2009.
- [17] G. Giri, E. Verploegen, S. C. B. Mannsfeld, S. Atahan-Evrenk, D. H. Kim, S. Y. Lee, H. A. Becerril, A. Aspuru-Guzik, M. F. Toney, and Z. Bao, "Tuning charge transport in solution-sheared organic semiconductors using lattice strain," *Nature*, vol. 480, no. 7378, pp. 504–508, Dezember 2011.

# Manuscript #3

**J. Bintinger\***, N. Cernetic, R. Bittner, M. Sauer, A. Folske-Schmitz, M. Holzweber, T. Schiros, D. Nordlund, D. Svatunek, H. Ma, H. Hoffmann, J. Fröhlich, A. Jen, H. Mikula; Using click chemistry for a facile approach towards self-assembled monolayer field-effect transistors (SAMFETs): A new versatile approach for sensing applications, *manuscript draft*



# Using click chemistry for a facile approach towards self-assembled monolayer field-effect transistors (SAMFETs): A new versatile approach for sensing applications

Johannes Bintinger<sup>[a,\*]</sup>, Nathan Cernetic<sup>[b]</sup>, Roland Bittner<sup>[a]</sup>, Markus Sauer<sup>[c]</sup>, Annette Folske-Schmitz<sup>[c]</sup>, Markus Holzweber<sup>[d]</sup>, Theanne Schiros<sup>[e,f]</sup>, Dennis Nordlund<sup>[g]</sup>, Dennis Svatunek<sup>[a]</sup>, Hong Ma<sup>[b]</sup>, Helmut Hoffmann<sup>[a]</sup>, Johannes Fröhlich<sup>[a]</sup>, Alex Jen<sup>[b]</sup>, Hannes Mikula<sup>[a]</sup>

[\*] Email: [johannes.bintinger@tuwien.ac.at](mailto:johannes.bintinger@tuwien.ac.at)

[a] Institute of Applied Synthetic Chemistry, Vienna University of Technology, Getreidemarkt 9/163, 1060 Vienna, Austria

[b] Department of Materials Science and Engineering, Box 352120, University of Washington, Seattle, WA 98195-2120, Seattle, USA

[c] Analytical Instrumentation Center, Vienna University of Technology, Getreidemarkt 9, 1060 Vienna, Austria

[d] Institute of Chemical Technologies and Analytics, Vienna University of Technology, Getreidemarkt 9, 1060 Vienna, Austria

[e] Fashion Institute of Technology, State University of New York, 227 W 27th St, NY 10001, USA

[f] Center for Precision Assembly of Superstratic and Superatomic Solids, MRSEC, 530 W. 120th St., Columbia University, NY, USA

[g] Stanford Synchrotron Radiation Lightsource, SLAC National Accelerator Laboratory, 2575 Sand Hill Road, Menlo Park, CA, USA

## 1. Introduction

Since a few years, organic electronic devices based on organic field-effect transistors (OFETs)<sup>1</sup>, organic light emitting devices (OLEDs)<sup>2</sup> and organic photovoltaics (OPVs)<sup>3</sup> are emerging into the market. However, one of the greatest potential of organic electronics could be the realization of miniaturized, or even implanted, biosensors as low-cost point of care devices, capable of selectively detecting biomarkers or pathogens and creating an electronic read out for user friendly interaction.<sup>4</sup> The basic working principle of these sensors is based on a standard OFET configuration (Figure 1), which consists of three parts – a dielectric, an organic semiconductor (OSC) and three electrodes. The “source” and the “drain” electrodes are in direct contact with the semiconductor, while the third, the “gate”, is isolated from the OSC by the “dielectric”.<sup>5</sup> By applying a voltage between the gate and the source/drain electrodes, charges of opposite sign are induced at the semiconductor-dielectric interface. Because the charges in the semiconductor are mobile, current will flow in the channel when an additional voltage is applied between source and drain.<sup>6</sup> An OFET-biosensor is an analytical device consisting of an OFET endowed with covalently attached biological recognition units to the OSC, whose specific interactions with analytes changes the electrical current flowing between source and drain.<sup>4</sup>

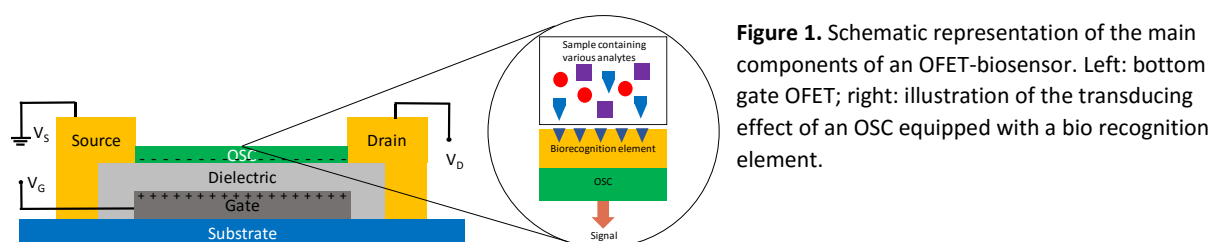


**Figure 1.** Schematic representation of the main components of an OFET-biosensor. Left: bottom gate OFET; right: illustration of the transducing effect of an OSC equipped with a bio recognition element.

It is important to acknowledge that in such a device, the OSC serves a dual function, as an active charge carrier transport layer and as a functional sensing surface (Figure 1). The advantages over any other current sensing technologies such as electrochemical or optical based (SPR) ones is the capability of delivering a response that is label-free using a simple, inexpensive electronic read-out set-up that can be easily miniaturized by employing established printed circuit OE-technologies, ultimately enabling small point-of-care (POC) devices.<sup>4</sup>

The sensitivity of such a sensor is dependent on the thickness of the semiconductor,<sup>7</sup> thus the maximum sensitivity would be achieved in a device consisting of only one monolayer of the active material.<sup>8</sup>

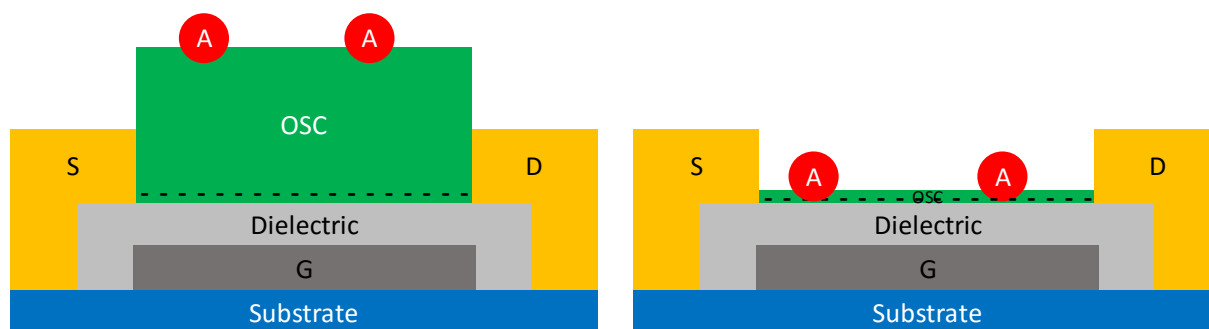


**Figure 2.** Schematic illustration of the operation principle of a SAMFET sensor. On the left, analyte molecules which are absorbed on top of a thick semiconductor layer will only have small effect on the current modulation as this is limited by the thickness of the OSC. However, the electrostatic interactions (red circles) of the analyte will have a much bigger effect when the distance between analyte and the active channel is decreased. Thus a SAMFET based biosensor could be a highly sensitive sensing platform.<sup>8</sup>

Such devices – self-assembled monolayer field-effect transistors (SAMFETs, Figure 4, left) - have recently been demonstrated and rely upon the 2D self-assembly of  $\pi$ -conjugated materials.<sup>9–13</sup> Self-assembly is *the autonomous organization of components into patterns and structures*<sup>14</sup> and holds great potential for the field of organic electronics by enabling a rational bottom-up approach.<sup>9</sup> Self-assembled monolayers (SAMs) have been used amongst other things<sup>15</sup> as high-k nanodielectrics,<sup>16</sup> for interface engineering,<sup>17</sup> surface protection<sup>18</sup> as well as enhancing solar cell efficiencies.<sup>19</sup> One of the big advantages of SAMs is their solution processability thus providing a smart engineering approach for low cost device fabrication.

Charge transport in SAMFETs is intrinsically confined to only one monolayer<sup>20,21</sup> and the concept is using rationally designed  $\pi$ -conjugated SAMs as the semiconductor of a transistor. However, current SAMFET materials<sup>9,10,22–24</sup> (Figure 2) require cumbersome synthesis and most importantly still lack the capability for further functionalization. The endowment of the OSC via functional groups with a biorecognition unit is essential for rendering the sensor selective.

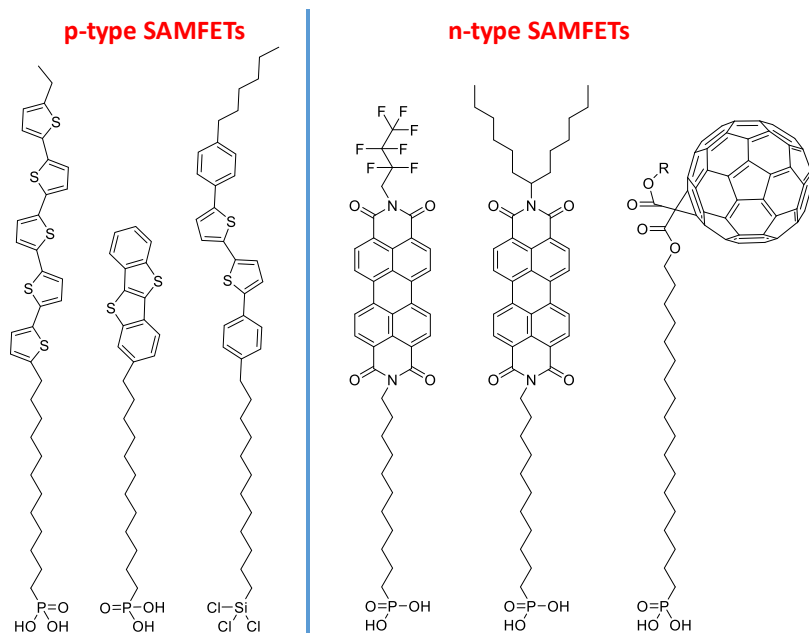


**Figure 3.** molecular structures of currently used p- and n-type SAMFET materials, lacking possibilities for further functionalization and requiring cumbersome synthesis.

We report on a novel building block like approach based on click chemistry for a facile and versatile route towards CLICK-FETs. These materials are designed to use click chemistry assisted self-assembly reactions to realize functional SAMFET materials.

## 2. Results and Discussion

### 2.1. Material Design and Synthesis

Figure 4 illustrates the layout and concept of both SAMFET and CLICK-FET devices. SAMFET devices are realized by a single self-assembly reaction of a pre-synthesized material. The choice of head group determines the properties and application of the final device. In contrast, CLICK-FETs use a truly, versatile and bottom up approach as both the active OSC (green rectangle) and the biorecognition unit are stepwise realized using click chemistry directly on the substrate. Different click groups ensure complete orthogonality of the method.

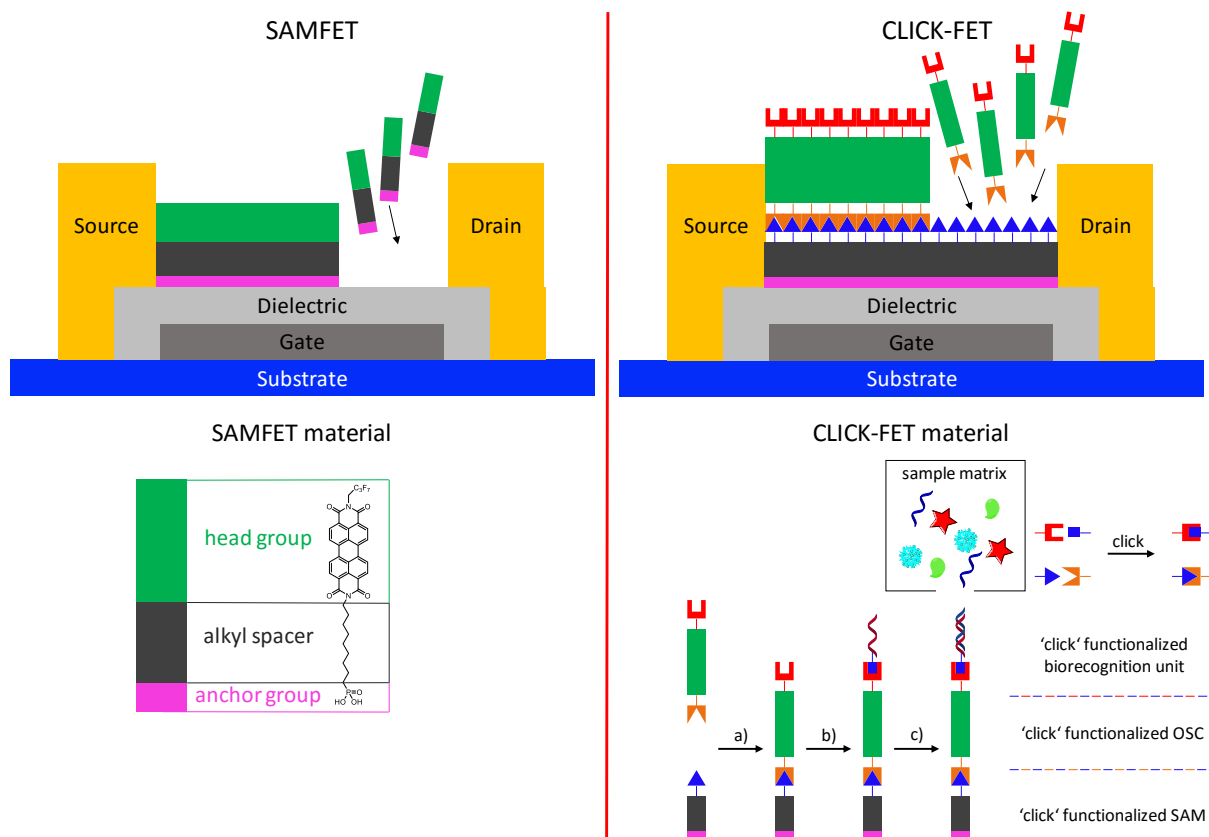
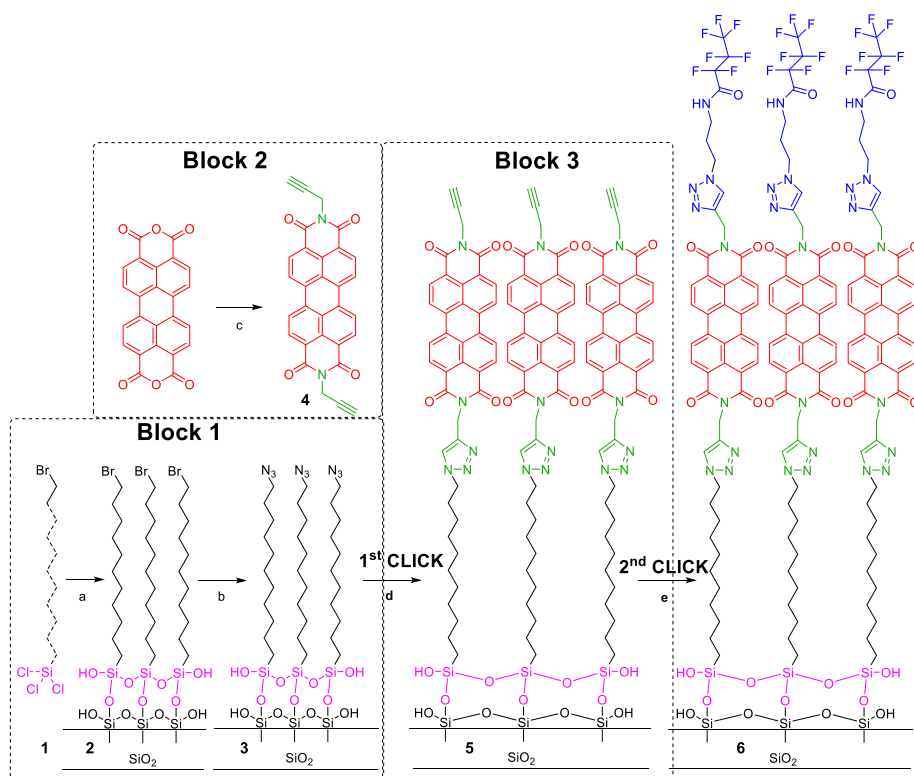


**Figure 4.** Schematic illustration of the layout and concept of a conventional SAMFET (left) our newly introduced CLICK-FET (right) device. The building block approach using click chemistry towards CLICK-FETs for sensing applications is depicted in the right bottom part of the graphic.

The importance of our modular approach and the possibility of post-functionalization is emphasized again in the bottom right corner of figure 4. Biorecognition units enable selective and specific sensing even in a sample matrix containing multiple other analytes.

For our proof of concept demonstration, we used our previously described azide-terminated monolayers<sup>25</sup> on silica to click a 2,9-dipropynyl-perylene diimide **4** semiconducting unit onto the surface (Scheme 1). The resulting alkyne group of **5** was then used in a second click reaction to further functionalize the SAM **6**, by introducing an easily detectable fluorine marker.

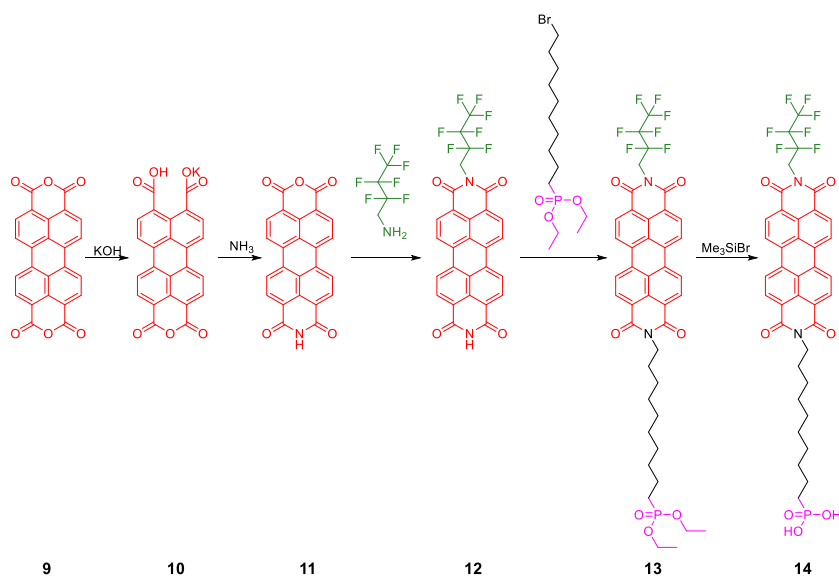




**Scheme 1.** Reaction scheme towards a CLICk-FET molecule. a) self-assembly of bromoundecyltrichlorosilane (1 mM in toluene) onto an activated SiO<sub>2</sub> surface; b) NaN<sub>3</sub>, DMF; c) propargylamine, dry DMF; d) 2,9-dipropynyl-perylene diimide, sodium ascorbate, copper sulphate, H<sub>2</sub>O; e) N-(3-azidopropyl)-2,2,3,3,4,4,4-heptafluorobutanamide (7), sodium ascorbate, copper sulphate, H<sub>2</sub>O

To the best of our knowledge this is the first report on a pre-functionalizable SAMFET material. The presented synthesis is very straight forward, modular and uses readily available starting materials. The obtained alkyne functionalized SAMFET is a key intermediate for a versatile sensing platform as it offers access towards a broad range of biological recognition units applying click-chemistry (Figure 4). Click-chemistry are types of nature inspired reactions, which generate target compounds in high yields, under moderate conditions and high efficiency. One of the most popular reactions within the click-chemistry concept is the azide alkyne cycloaddition using a copper catalyst at room temperature in order to join azide- and alkyne-bearing compounds together.<sup>26</sup>

In order to compare the obtained CLICk-FET results and benchmark it against a reference system we also synthesized an already established SAMFET material,<sup>23</sup> which is also based on a perylene diimide core (Scheme 2).



**Scheme 2.** Overview of the synthetic strategy towards the SAMFET molecule **6**. All molecules were synthesized according to slightly modified literature procedures from Langhals<sup>27</sup>- and Ringk et al.<sup>23</sup>

The use of readily available starting materials is a valuable aspect of the presented synthetic route and follows modified procedures from Langhals et al.<sup>27</sup> and Ringk et al.<sup>23</sup> In the first reaction step (Scheme 2) the perylene dianhydride is converted into the mono potassium salt **10**, before being transformed to the perylene anhydride imide **11**. This intermediate is needed for the non-symmetric substitution with heptafluoro butylamine (**12**) on one side and the SAM-anchoring group, dodecyl phosphonic acid ester, on the other side (**13**). In the last step the reactive phosphonic acid group is obtained **14**, which in turn covalently bonds onto the hafnium oxide dielectric of the SAMFET device (Figure 8).

## 2.2. Chemical characterization of the SAM films

To investigate each of the reaction steps of the CLICK-FET and SAMFET we used XPS, ToF-SIMS and IR measurements. The main contribution of XPS to the characterisation of SAMFET and subsequently CLICK-FET structures can be divided into two parts. First, we were able to follow the building process of CLICK-FETs and SAMFETs in several steps by performing XPS after intermediate processing steps. Figure 5a shows N 1s and F 1s regions of the SAMFET (**14**) and a n-Dodecylphosphonic (DDPA) reference SAM used in the production process. In the case of the SAMFET we observe increase in the intensities of F 1s and N 1s in contrast to the DDPA reference, which does not contain F or N (Figure 5a). N is found at ~400 eV, which has been observed for O=C-N bonds<sup>28</sup> similar to those in the perylene structures of the SAMFET. The F signal is observed around ~ 400 eV binding energy. This contribution is usually attributed to organic fluorine, mostly CF<sub>x</sub>. By also taking the results from C 1s detail scans (Figure 6b) into consideration we can therefore assume that F is present in the form of CF<sub>2</sub> and CF<sub>3</sub> bonds. While it is obvious that the F 1s signal is only visible in the CLICK-FET after the 2<sup>nd</sup> click (Scheme 1, Figure 5b), the N 1s signal is more difficult to interpret. Azides (**3**) show a very distinct peak structure,<sup>29</sup> which we are able to reproduce. After the first click we observe an increase in intensity in the N 1s signal at ~400 eV binding energy, characteristic for O=C-N bonding environments, while components observed for azides are strongly attenuated. The asymmetry of the N 1s signal when compared to the one from the SAMFET can be attributed to a small contribution from the N=N=N bonds in the triazole at ~402 eV, as described by Ciampi et al.<sup>30</sup> After the 2<sup>nd</sup> click (**5**) we also observe a fluorine signal. Like in the case of the SAMFET the F peak at 688–689 eV can be assigned to organic fluorine compounds. However, the amount of F is significantly lower than in the case of the SAMFET.

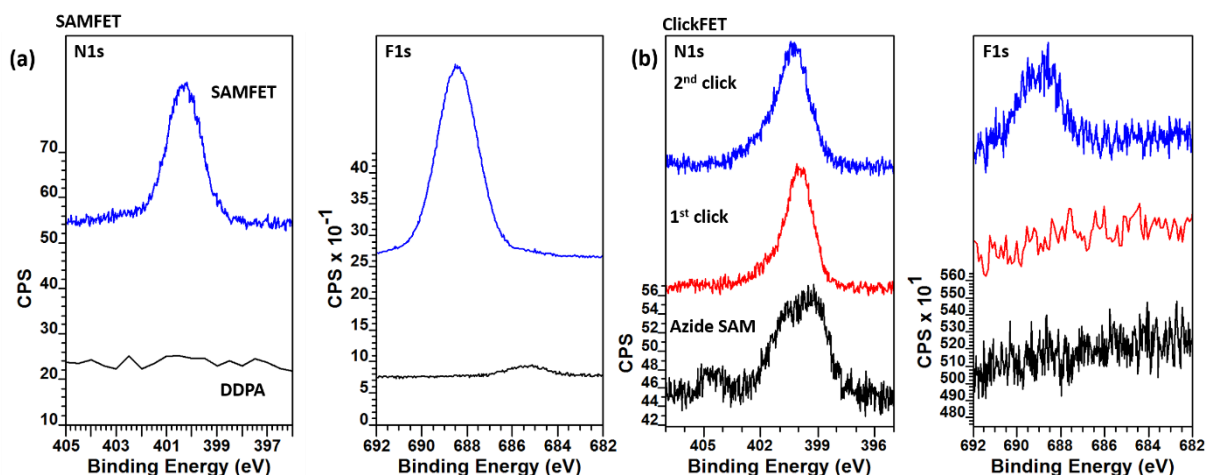


**Figure 5:** a) XPS detail spectra of a SAMFET (compound **14**) on  $\text{HfO}_2$ ; left: normalized N 1s and right: F 1s region; b) XPS detail spectra of a CLICK-FET on  $\text{SiO}_2$  showing the building process during intermediate production steps; left: normalized N 1s and right: F 1s region

Secondly, we focus on the arrangement of the molecules on the substrate surface. Using ARXPS we are able to determine if the SAMFET structures (**14**) are oriented perpendicular to the sample surface. Figure 6a shows analysis of ARXPS overview scans, clearly indicating that the F 1s signal is increased compared to the signal of C 1s at larger angles. As these larger angles (exit angle of the electron with respect to the surface normal of the sample) reflect higher surface sensitivity, we can therefore assume that F resides mostly on top of the molecules. Thus, we conclude that the molecules are predominantly arranged in an upright position on the substrate surface.

Figure 6b shows detail spectra of the C 1s region of a SAMFET structure. It is evident that the signals of the  $\text{CF}_x$  components are increased at large angles. While both  $\text{CF}_2$  and  $\text{CF}_3$  signals are enhanced it has been calculated that the  $\text{CF}_3$  component exhibits a larger increase in intensity when compared to  $\text{CF}_2$ , which strongly supports the assumption of the upright arrangement of most organic molecules. While the coverage of the CLICK-FET (**5**) is relatively low ( $F < 1$  at%), for SAMFETs we find a fluorine content of about 16 at%. In addition, it has to be noted this amount of fluorine could also be evidenced on different substrates like  $\text{TiO}_2$  which shows that the SAMFET production process is robust against any changes to the substrate material.

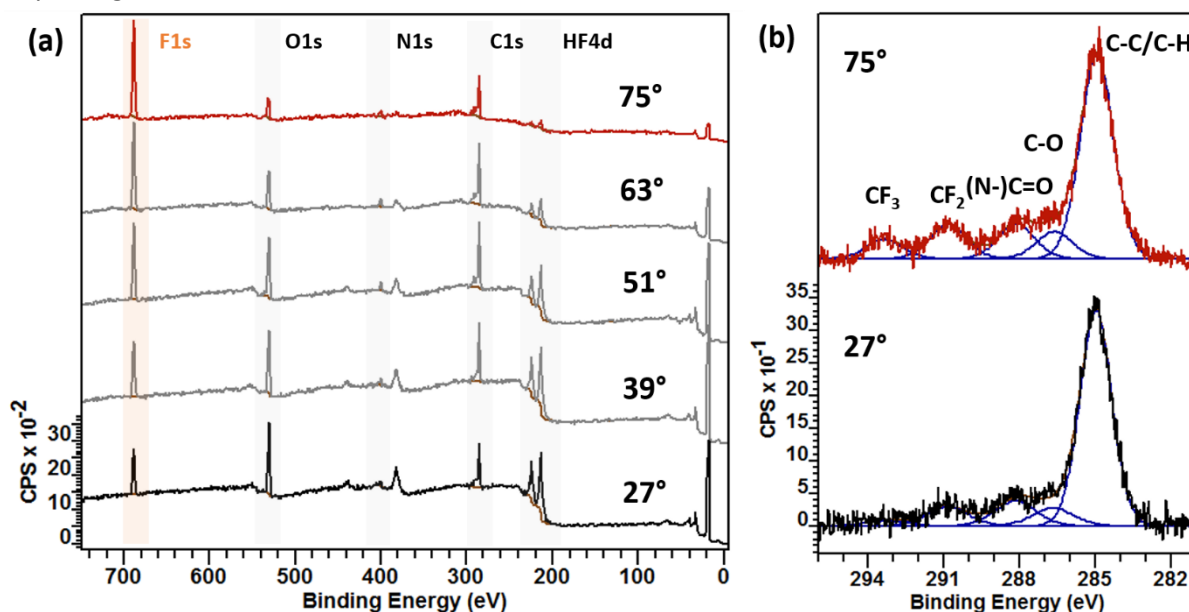


**Figure 6:** a) ARXPS overview spectra of a SAMFET (compound **14**) on  $\text{HfO}_2$ . All angles are measured from the surface normal of the sample. Larger angles correspond to increased surface sensitivity. The main quantification regions are highlighted with coloured backgrounds. b) ARXPS detail spectra of the C 1s region of a SAMFET on  $\text{HfO}_2$ . Line fits are depicted in blue with the corresponding bonding environments stated on top.

To produce high-quality SAM systems, process control of the chemical surface modification is mandatory. This can be achieved by time-of-flight secondary-ion-mass-spectrometry (ToF-SIMS).<sup>31</sup> ToF-SIMS is a highly sensitive surface characterization technique providing elemental and molecular surface chemical information. It has been shown that in well-ordered SAMs, the organic molecule is in an upright conformation thus having its functional group at the very surface.<sup>32</sup> For the present study, we anticipate the ToF-SIMS spectra to be very similar, as the tail is always terminated with a perylene diimide system containing a fluorine marker. Therefore, a univariate interpretation of the mass spectra is unreasonable and a multivariate approach has been chosen using principal component analysis (PCA, see Reference<sup>33</sup> and references therein). PCA is a multivariate statistical analysis method identifying the major directions of variation in a given data set. A data set is defined as a matrix where the rows contain samples and columns contains variables. In the case of ToF-SIMS data, samples are the mass spectra and the variables are the individual  $m/z$  ratios. The PCA is calculated from the covariance matrix of this original data set. PCA is an axis rotation that aligns a new set of axes, called principal components (PC) with the maximal directions of variance within a data set. PCA creates three new matrices containing the scores, the loadings and the residuals.<sup>33</sup> It thus aids in the interpretation of complex mass spectra (as is the case for ToF-SIMS spectra of organic surfaces) by revealing differences between (groups of) *samples* expressed as so called scores and relating them back to differences in the *variables* (called loadings) defining a sample.<sup>34</sup> The scores plot shows whether samples or a group of samples are different. The corresponding loadings-plot shows the difference in the mass spectra and fragmentation pattern of the samples (or the group of samples).<sup>33</sup> In principle, PCA provides the ability to identify key fragment peaks characterizing a given sample type, a survey of the point-to-point reproducibility across the sample set and a summary of the relationship between different sample sets.<sup>35–38</sup> It has been indicated by other authors that if a SAM is packed more regularly and well-ordered, more molecular secondary ions characteristic for the SAM are emitted by an impact of a primary ion.<sup>36,39</sup> Following this interpretation the good sample has a higher quality than the bad sample.

The results of a PCA using the peak list and the data preprocessing described above is shown in Figure 7.

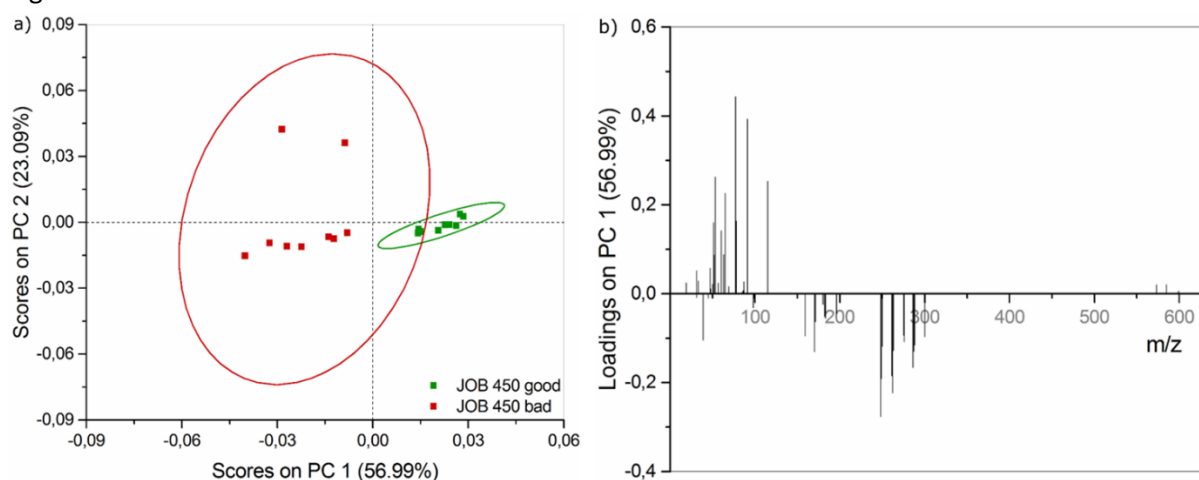


**Figure 7.** Scores and loadings plot for the SAMFET material **14** on a  $\text{HfO}_2$  substrate using ToF-SIMS.

It is clearly evident from the scores plot that the two sample systems are well separated on PC1 even though deviations in the mass spectra were not easily discernible by a univariate approach. It can be further seen, that the mean variation of the data points for the bad sample is large indicating a low

point to point reproducibility. In contrast the data points of the good sample show a minimal scattering. Hence, a higher layer quality for the good sample is obvious. The variables (i.e. mass fragments or m/z ratios) responsible for the separation seen in the scores plot are revealed by the loadings plot in Figure 7b and summarized in Table 1. Samples showing positive scores are described by positive loadings and vice versa. The positive scores are described by high mass fragments characteristic for the marker containing a perylene diimide ring system as well as low mass fragments originating from cleavage of the perylene diimide ring. Furthermore, F<sup>+</sup> (from the marker) and P<sup>+</sup> ions (from the phosphonic head group) are highlighted. The negative scores are represented by mass fragments attributable to the perylene diimide ring, fluorine marker and Hf-substrate.

m/z	Loadings	Assignment	m/z	Loadings	Assignment
18,998	+	F <sup>+</sup>	99,019	-	C <sub>3</sub> H <sub>3</sub> N <sub>2</sub> O <sub>2</sub> <sup>+</sup>
30,972	+	P <sup>+</sup>	115,052	+	C <sub>9</sub> H <sub>7</sub> <sup>+</sup>
30,998	-	CF <sup>+</sup>	159,007	-	C <sub>2</sub> H <sub>2</sub> F <sub>7</sub> <sup>+</sup>
33,013	+	CH <sub>2</sub> F <sup>+</sup>	170,000	-	C <sub>3</sub> HF <sub>7</sub> <sup>+</sup>
39,023	-	C <sub>3</sub> H <sub>3</sub> <sup>+</sup>	171,006	-	C <sub>3</sub> H <sub>2</sub> F <sub>7</sub> <sup>+</sup>
45,014	-	C <sub>2</sub> H <sub>2</sub> F <sup>+</sup>	179,932	-	Hf <sup>+</sup>
46,970	+	PO <sup>+</sup>	181,999	-	C <sub>4</sub> HF <sub>7</sub> <sup>+</sup>
47,975	+	POH <sup>+</sup>	183,001	-	C <sub>4</sub> F <sub>7</sub> H <sub>2</sub> <sup>+</sup>
49,996	+	CF <sub>2</sub> <sup>+</sup>	195,925	-	HfO <sup>+</sup>
51,004	+	CHF <sub>2</sub> <sup>+</sup>	248,022	-	C <sub>19</sub> H <sub>4</sub> O <sup>+</sup>
51,023	+	C <sub>4</sub> H <sub>3</sub> <sup>+</sup>	249,026	-	C <sub>19</sub> H <sub>5</sub> O <sup>+</sup>
52,031	+	C <sub>4</sub> H <sub>4</sub> <sup>+</sup>	250,054	-	C <sub>19</sub> H <sub>6</sub> O <sup>+</sup>
53,039	+	C <sub>4</sub> H <sub>5</sub> <sup>+</sup>	261,031	-	C <sub>20</sub> H <sub>5</sub> O <sup>+</sup>
57,012	+	C <sub>3</sub> H <sub>2</sub> F <sup>+</sup>	262,036	-	C <sub>20</sub> H <sub>6</sub> O <sup>+</sup>
60,045	+	C <sub>2</sub> H <sub>6</sub> NO <sup>+</sup>	263,044	-	C <sub>20</sub> H <sub>7</sub> O <sup>+</sup>
63,023	+	C <sub>5</sub> H <sub>3</sub> <sup>+</sup>	275,041	-	C <sub>21</sub> H <sub>7</sub> O <sup>+</sup>
65,039	+	C <sub>5</sub> H <sub>5</sub> <sup>+</sup>	276,045	-	C <sub>21</sub> H <sub>8</sub> O <sup>+</sup>
68,994	+	CF <sub>3</sub> <sup>+</sup>	286,025	-	C <sub>18</sub> H <sub>6</sub> O <sub>4</sub> <sup>+</sup>
77,038	+	C <sub>6</sub> H <sub>5</sub> <sup>+</sup>	287,025	-	C <sub>18</sub> H <sub>7</sub> O <sub>4</sub> <sup>+</sup>
78,045	+	C <sub>6</sub> H <sub>6</sub> <sup>+</sup>	288,045	-	C <sub>21</sub> H <sub>6</sub> NO <sup>+</sup>
85,004	+	C <sub>2</sub> HN <sub>2</sub> O <sub>2</sub> <sup>+</sup>	300,033	-	C <sub>19</sub> H <sub>8</sub> O <sub>4</sub> <sup>+</sup>
86,012	+	C <sub>2</sub> H <sub>2</sub> N <sub>2</sub> O <sub>2</sub> <sup>+</sup>	573,022	+	C <sub>28</sub> H <sub>12</sub> N <sub>2</sub> O <sub>4</sub> F <sub>7</sub> <sup>+</sup>
87,020	+	C <sub>2</sub> H <sub>3</sub> N <sub>2</sub> O <sub>2</sub> <sup>+</sup>	585,024	+	C <sub>29</sub> H <sub>12</sub> N <sub>2</sub> O <sub>4</sub> F <sub>7</sub> <sup>+</sup>
91,053	+	C <sub>7</sub> H <sub>7</sub> <sup>+</sup>	597,023	+	C <sub>30</sub> H <sub>12</sub> N <sub>2</sub> O <sub>4</sub> F <sub>7</sub> <sup>+</sup>
98,011	-	C <sub>3</sub> H <sub>2</sub> N <sub>2</sub> O <sub>2</sub> <sup>+</sup>	599,036	+	C <sub>30</sub> H <sub>14</sub> N <sub>2</sub> O <sub>4</sub> F <sub>7</sub> <sup>+</sup>

**Table 1:** Summary of the positive and negative loading peaks from the positive ion mode ToF-SIMS spectra of the compound **14** self-assembly.

Finally, transmission IR measurements (Figure 8) of both CLICK-FET and SAMFET samples were performed in order to proof the existence of a self-assembled monolayer on the dielectric.

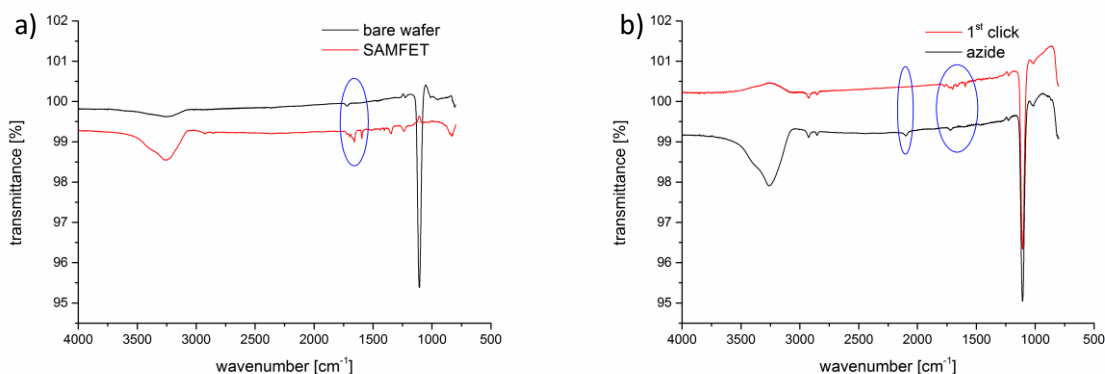


**Figure 8:** a) Transmission-IR measurements of compound **14** on a  $\text{Al}_2\text{O}_3$  bearing silicon wafer; b) Transmission-IR measurements of compound **5** formed after the first click reaction in reference to the starting azide SAM.

From figure 8a it is evident that a self-assembled monolayer of compound **14** was successfully formed. Characteristic IR peaks (C-H, C-F and C-C) are clearly visible (blue circles), which are in good agreement with theoretical predictions. Figure 8b illustrates the result of the first click reaction in comparison to the starting azide SAM. The disappearance of the distinct azide peak ( $\sim 2100 \text{ cm}^{-1}$ ) together with the appearance of similar peaks as seen for the SAMFET material ( $\sim 1600 \text{ cm}^{-1}$ ) is a clear evidence for the formation of a CLICK-FET SAM layer.

### 2.3. Computational considerations

Computational methods (DFT, B3LYP/6-31G(d,p), gas phase) were used to compare the introduced CLICK-FET structure with a previously reported SAMFET material<sup>23</sup> in regard to their geometry and electronic structure. In their lowest energy conformation both structures exhibit an out-of-plane orientation of the substituents on the perylene core (Figure 9).

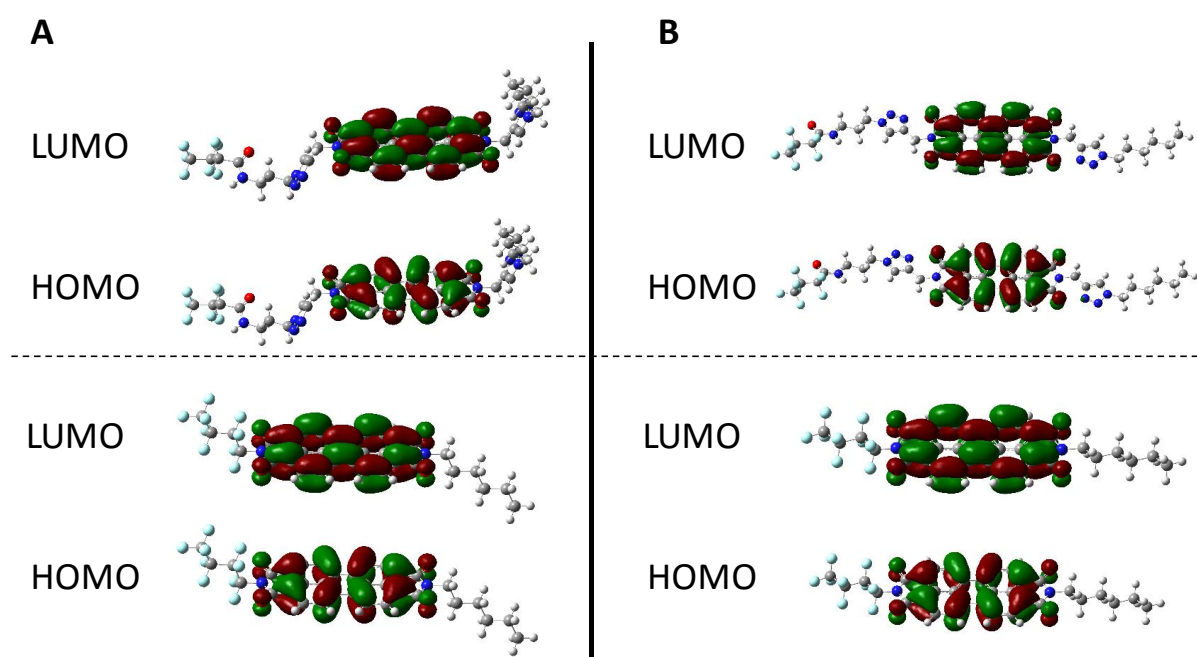


**Figure 9.** Illustration of HOMO/LUMO orbitals of CLICK-FET and SAMFFET materials; A: out of plane configurations of both CLICK-FET (top) and simplified SAMFET structures (bottom).

Both HOMO and LUMO orbitals are located exclusively on the central core and exhibit similar band gaps (2.53 eV). Neither the fluorinated, non-fluorinated nor the introduction of triazole units as a result of the click reaction does alter the shape or distribution of the HOMO/LUMO orbitals. Furthermore, when examining a flat structure, which is needed for efficient  $\pi$ - $\pi$ -stacking, both structures still exhibit a very similar band gap of 2.51 and 2.52 eV and HOMO/LUMO orbitals are still located on the perylene central core. These calculations suggest that CLICK-FETs are able to adapt a rather planarized overall geometry, which is beneficial for good molecular overlap and thus renders these materials suitable for use as active material in a CLICK-FET device.

## 2.4. Electrical Characterization

To benchmark CLICK-FET devices to a conventional SAMFET, bearing the same organic semiconductor unit (perylene diimide), we fabricated devices employing compound **14** as an active layer material. Compound **14** is a comparable SAMFET molecule to the system developed by Ringk et. al.<sup>23</sup> However, numerous attempts to replicate these results were unsuccessful and no working devices could be obtained due to the poor solubility of this material in DMF. It is assumed that the cause of failure was due to most of the compound being removed upon filtration with a 0.2  $\mu\text{m}$  PTFE filter resulting in a lower solution concentration. This most likely results in a monolayer with a packing density too low for charge carrier transport. It was found that a mixed solvent solution of DMSO:chlorobenzene (CB) allowed for the highest concentration of solution while minimizing the amount of material removed during filtration (see ESI).

With these optimized fabrication procedures, working SAMFET devices were fabricated and characterized. SAMFET devices were fabricated and characterized within a nitrogen filled glove without exposure to ambient condition. Electrical characterization was done immediately after device fabrication using an Agilent 4155B semiconductor parameter analyzer. Electron mobility of devices was determined from the slope of a linear fit of the saturated drain current ( $I_{ds}$ )<sup>1/2</sup> vs.  $V_{gs}$  while the threshold voltage ( $V_t$ ) was estimated as the intercept at the x-axis of the same linear fit. Mobility was then calculated using the standard MOSFET saturation equation. The average electron mobility for 14 transistors with channel width and length of 200  $\mu\text{m}$  and 100  $\mu\text{m}$  respectively was determined to be  $1.9\text{E-}4 \text{ cm}^2 \text{ V}^{-1} \text{ s}^{-1} \pm 0.4\text{E} \text{ cm}^2 \text{ V}^{-1} \text{ s}^{-1}$ . Threshold voltage ( $V_t$ ) was found to be  $45.5 \text{ V} \pm 5.1 \text{ V}$ . Representative transfer and output characteristics of SAMFET device based on compound **14** can be seen in figure 10.

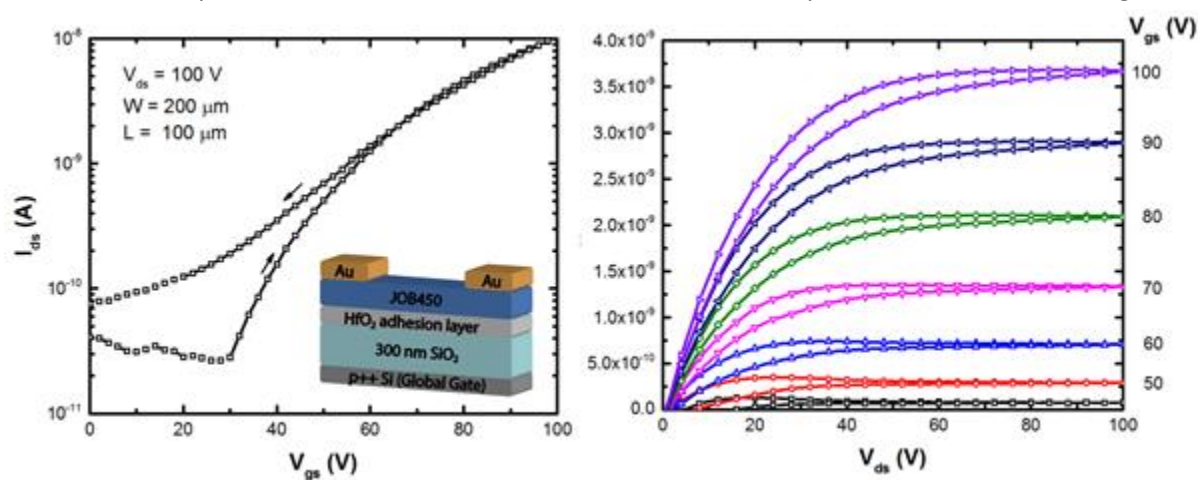


**Figure 10.** Representative transfer (left) and output (right) characteristic curves of SAMFET device using compound **14**. Device schematic shown as insert (left).

However, no electrically active CLICK-FET device could be produced so far. We hypothesize that the lack of solubility of 2,9-dipropynyl-perylene diimide prevents the formation of uniform SAM layers and results in packing densities too low for charge transport. Therefore, the development of soluble precursor materials for these CLICK-FETs is ongoing in our groups.

### 3. Conclusion

In summary, we have used a novel building block like approach based on click chemistry to synthesize functionalizable SAMFETs for the first time. The alkyne functional group of this CLICK-FET was in turn converted via a second click reaction to a fluorine bearing group. Comprehensive investigations of these films such as ARXPS, ToF-SIMS and IR confirm the surface chemistry and suggest an upright molecular orientation of the obtained films. Furthermore, a SAMFET based on compound **14** was successfully demonstrated and its fabrication process and optimization followed by ToF-SIMS investigations. The high sensitivity and readily availability of these measurements will allow for a faster implementation of beneficial optimization steps to improve SAM formation and device performance.

### 4. Acknowledgement

JB is grateful to the Marietta Blau Grant of the OeAD.

### 5. Experimental part:

#### **Materials and methods:**

The starting materials perylene-3,4,9,10-tetracarboxylic dianhydride **8**, potassium hydroxide, ammonia, 1,11-dibromoundecane, sodium hydride, triethyl phosphite, bromotrimethylsilane, propargylamine and solvents were purchased from Sigma-Aldrich. 11-Bromoundecyltrichlorosilane **1** was purchased from ABCR. Silicon wafers (p-doped, 10-20  $\Omega$  cm, 500-550  $\mu$ m, (100)-oriented, double sided polished) were purchased from MEMC Elect. Synthesis of 11-bromo-undecyl-phosphonic acid diethyl ester was synthesized following the procedure by Wang et al.<sup>40</sup>

Solvents used for precipitation and column chromatography were distilled once before use. Chromatographic separations at preparative scale were carried out on silica gel (Merck silica gel 60, 40 - 63  $\mu$ m). High-resolution mass spectra (HRMS) were acquired as radical cations using either a SYNAPT HDMS instrument (Waters, Manchester, UK) equipped with a matrix-assisted laser desorption/ionization (MALDI) source or a Thermo Scientific LTQ Orbitrap XL hybrid FTMS (Fourier Transform Mass Spectrometer) equipped with Thermo Fischer Exactive Plus Orbitrap (LC-ESI+) and a Shimadzu IT-TOF Mass Spectrometer. Samples for MALDI-HRMS were applied at 1 mg/mL in THF on stainless steel using nitroanthracene (3 mg/mL in THF) as MALDI matrix. In case of solubility the sample was further diluted to approx. 50 pg/ $\mu$ L. In case of undissolved samples, the slurry was centrifuged and the supernatant and the residue was used for MALDI-qTOF-MS analysis. 1  $\mu$ L of the sample or residue/chloroform slurry was deposited on a stainless steel target and dried at room temperature. All MS spectra were recorded as accurate mass data with angiotensin II ( $m/z = 1046.542$ ) as internal lock mass achieving a mass accuracy of 15 - 40 ppm (i.e.  $\Delta m/z = 0.01 - 0.04$  amu).

<sup>1</sup>H, <sup>13</sup>C, <sup>19</sup>F and <sup>31</sup>P NMR spectra were recorded on a Bruker Advance DRX-400 fourier transform spectrometer operating at the following frequencies: DRX-400: 400.1 MHz (<sup>1</sup>H), 100 MHz (<sup>13</sup>C), 376 MHz (<sup>19</sup>F), 242 MHz (<sup>31</sup>P). The chemical shifts are reported in delta ( $\delta$ ) units, parts per million (ppm) downfield from tetramethylsilane using solvent residual signals for calibration. Coupling constants are reported in Hertz; multiplicity of signals is indicated by using following abbreviations: s=singlet, d=doublet, t=triplet, q=quartet. Direct injection Mass spectroscopy was performed on a Thermo Scientific Ion Trap ITQ 1100 equipped with a DEP (Direct Exposure Probe).



### **CLICK-FET preparation**

Silicon wafers were cut to 18x25 mm pieces, sonicated for 10 minutes in toluene and wiped with a toluene wet tissue. The samples were then rinsed with toluene and remaining solvent was blown off with argon. Subsequently each side was treated 5 minutes in a UV/ozone cleaner (Boekel Industries, UVClean, low pressure mercury quartz lamp,  $\lambda_{\max}$  = 185 and 254 nm, intensity = 0.28 mW cm<sup>-2</sup>), respectively.

Freshly cleaned chips were immersed for one hour in a 1 mM solution of 11-bromoundecyltrichlorosilane (2.93  $\mu$ l) in toluene (10 ml). The samples were rinsed with toluene and blown dry with argon. Next the samples were treated with sodium azide saturated *N,N*-dimethylformamide (DMF) solution (10 ml), thoroughly rinsed with water, rinsed with acetone and blown dry with argon. Afterwards the samples were clicked for 15 h in a DMF solution (10ml) containing **4**, sodium ascorbate (25.5 mg, 12.8 mM), copper sulphate (0.82 mg, 0.5 mM) and water (200  $\mu$ l, 1.1M). They were then rinsed thoroughly with water and acetone and blown dry with argon. The same click procedure was applied for the second click.

### **SAMFET solution preparation**

0.1 mM of compound **6** in DMSO:CB (1:1 by vol) was fabricated in a dry box with anhydrous solvents and then heated/stirred at 60°C/600 rpm under nitrogen for 48 hours. Solutions were then filtered hot with a 0.2  $\mu$ m PTFE filter, and approximately 3-4 mL of solution were placed in 20 mL vials for assembly.

### **SAMFET substrate preparation and SAM assembly**

300 nm SiO<sub>2</sub> substrates were cleaned via sonication in acetone and IPA followed by a UV/O<sub>3</sub> treatment to further clean the surface. A HfO<sub>2</sub> adhesion layer was then fabricated as described previously.<sup>41</sup> Substrates were then immediately used and placed in the 20 mL vials with SAM solution and sealed. SAM assembly occurred over the course of 72 hr at 60°C in a dry nitrogen environment. After assembly, substrates were allowed to cool and then spin-rinsed at 3000 rpm with DMSO, CB, and hexanes in the dry box. Au electrodes (30 nm) were then deposited using a shadow mask via thermal evaporation.

### **XPS Experimental**

All photoelectron spectroscopy (PES) experiments have been performed on a SPECS X-ray photoelectron spectrometer which consists of a monochromatised Al-K $\alpha$  source (1486.6 eV) with variable spot size ( $\mu$ Focus 350) and a hemispherical wide-angle analyser with a delay-line detector (Phoibos WAL 150). Analysis area size and beam intensity have constantly been kept at 500  $\mu$ m and 88W respectively. Base pressure in the analysis area has been detected to be better than 8x10<sup>-10</sup> mbar, while a pressure rise to 4x10<sup>-9</sup> mbar has been registered during XPS measurements.

Angle-resolved XP spectra have been collected using five angle channels equally distributed around 51° tilt of the sample surface normal from the analyser axis with maximum angular resolution of 1°. All Overview/Survey scans have been carried out using a pass energy of 100 eV and an energy resolution of 500 meV, while 30 eV pass energy and 50 meV energy resolution have been used for detail/narrow scans. CASA XPS software has been utilised for data analysis. Transmission corrections (recorded as per the vendor's specifications) have been applied to all results. Furthermore, spectra have been energy corrected to show C 1s adventitious carbon peaks at 284.8 eV binding energy. Quantification has been carried out using standard Scofield parameters. Quantification errors lie between 10-20% of the values determined. Line fits have been employed to analyse detail spectra components. All peaks are represented by Voigtian line shapes. Assignment of the components was done according to literature procedures.<sup>42,43</sup> Similar accuracy can be reached by fitting as in the quantification process.

### **Time-of-Flight Secondary-Ion-Mass-Spectrometry (ToF-SIMS)**

All sample measurements were performed without further pre-treatment on a TOF.SIMS 5 instrument (ION-TOF GmbH, Münster, Germany) of the reflectron-type, equipped with a 25 keV bismuth liquid metal ion gun (LMIG) as primary ion source mounted at 45° with respect to the sample surface. The LMIG was operated at 0.5  $\mu$ A emission current in the so-called "high current bunched" mode (high mass resolution, low lateral resolution). Bi<sub>3</sub><sup>+</sup> was selected as primary ion by appropriate mass filter

settings. The primary ion current was directly determined using a Faraday cup located on a grounded sample holder. Operation conditions with these settings comprised a target current of approx. 0.15 pA (obtained by reducing the pulse width) for the selected primary ion. The total primary ion dose density was set to  $5 \times 10^{11}$  ions/cm<sup>2</sup> ensuring static conditions.<sup>31</sup> Scanning area for analysis was 100×100 μm<sup>2</sup> with a pixel resolution of 64×64. The vacuum in the analysis chamber was in the range of 10<sup>-9</sup> mbar during all measurements. ToF-SIMS spectra were acquired in positive ion mode with 9 spots per sample analyzed. The mass scale was internally calibrated using a number of well-defined and easily assignable secondary ions. C<sub>3</sub>H<sub>3</sub><sup>+</sup>, C<sub>5</sub>H<sub>5</sub><sup>+</sup>, C<sub>2</sub>H<sub>2</sub>F<sub>7</sub><sup>+</sup> and C<sub>19</sub>H<sub>4</sub>O<sup>+</sup> were used for the mass calibration. The error in calibration for all spectra was kept below 10 ppm.

#### **Principal Component Analysis (PCA)**

The peak list creation strategy to perform PCA was carried out by selecting 50 peaks unambiguously assignable to the SAM and the substrate in the mass range of m/z 0-600 for both, the good sample and the bad sample. As mentioned above, the error in calibration of the ToF-SIMS spectra was kept below 10 ppm to ensure minimum scattering in the peak position and to minimize errors in setting the integration limits. This ensures that the variance in the given data set is due to real sample differences. Integration limits in m/z regions with overlapping peaks were placed tightly around each peak to assure consistent and accurate measurements of all peak areas. PCA was performed using the software Solo+MIA 8.1.1 (Eigenvektor Research Inc., Manson, WA, USA). Each peak was normalized to the sum of the selected peak intensities to correct for variations in the total secondary ion yields between different spectra followed by Poisson scaling, and mean centering.

**Infrared Spectroscopy (IR)** spectra were measured using a Bruker Vertex 80 FT-IR spectrometer with either a DTGS (Fig. 2, Fig.3) or a narrow-band MCT (Fig. 4) detector. In case of the DTGS detector 16 scans and in case of the MCT detector 256 scans were recorded for sample and reference, respectively. The measurements were performed with a resolution of 4cm<sup>-1</sup> and under an angle of incidence of 40°. As reference a flat silicon wafer with native oxide layer was employed. Measurements of coated SiNW samples were then divided by a spectrum of the same uncoated sample. CO<sub>2</sub>, H<sub>2</sub>O and baseline correction was done using the software OPUS supplied by Bruker.

**Ellipsometric film thickness measurements** were carried out using a Sentech SE500adv. As light source a He-Ne laser (λ = 632.8 nm) was employed combined with a rotating analyzer. The film thickness was calculated using the commercial software, which is based on the McCrackin algorithm, out of the ellipsometric angles, namely phase shift and amplitude ratio. For each sample first the thickness of the native oxide layer was determined based on an isotropic three-phase model (Si: n=3.865, k=0.020; SiO<sub>2</sub>: n=1.465, k=0; air: n=1, k=0). These results were then used after coating to measure the thickness of the organic layer with the optical constant n=1.5 k=0 taken from literature. Each sample was measured on four different spots and the results were averaged. The variation of thicknesses across all samples was always below 1 Å.

#### **Synthesis**

Synthesis and precursor materials **11** and **12** of SAMFET material **13** were synthesized as described by Ringk et al with minor modifications to the reported protocol.<sup>23</sup> Precursors **9** and **10** were obtained following a procedure from Kaiser et al.<sup>27</sup> Reaction scheme towards compounds **7** and **8** are given in the supporting information (Scheme S1).

#### **2,9-dipropynyl-perylene diimide – 4**

Product was synthesized following a modified literature procedure.<sup>44</sup>

Under argon atmosphere perylene-3,4,9,10-tetracarboxylic dianhydride (392 mg, 1.0 mmol, 1.0 eq) and propargylamine (121 mg, 2.2 mmol, 2.2 eq) were combined in anhydrous DMF (5 mL). The mixture was stirred at 150 °C for 1 h in a microwave reactor. The precipitate was filtered out, rinsed with acetone and dried in a vacuum oven to yield the product as brown solid (340 mg, 79 %), which was used without any further purification.

#### N-(3-azidopropyl)-2,2,3,3,4,4,4-heptafluorobutanamide - **7**

To a solution of heptafluorobutanoic acid (2.14 g, 10 mmol) in anhydrous DCM was added 3-azidopropaneamine (0.90 g, 9 mmol) followed by DMAP (0.24 g, 2 mmol) and EDC·HCl (2.11 g, 11 mmol). The resulting solution was stirred under an Ar atmosphere at roomtemperature for 20 h, then washed with 1N HCl (2 x 100 mL) and saturated NaHCO<sub>3</sub> solution (2 x 150 mL). The organic layer was dried over Na<sub>2</sub>SO<sub>4</sub> and concentrated. The residue was purified by column chromatography (90 g SiO<sub>2</sub>, EtOAc in hexanes, 0-50%) to afford the desired product as a slightly yellowish (azide) oil (0.91 g, 34%). ESI-MS: calcd. for C<sub>7</sub>H<sub>7</sub>F<sub>7</sub>N<sub>4</sub>NaO<sup>+</sup> [M<sup>+</sup>Na<sup>+</sup>] 319.0, found 319.0

<sup>1</sup>H NMR (400 MHz, CDCl<sub>3</sub>): δ = 6.87 (1 H, br s), 3.48 (2 H, q, J=6.4 Hz), 3.42 (2 H, t, J=6.4 Hz), 1.85 (2 H, q, J= 6.5 Hz) ppm.

<sup>13</sup>C NMR (100 MHz, CDCl<sub>3</sub>): δ = 157.7 (t, J= 26.9 Hz), 117.4 (qt, J<sub>1</sub>= 287.7 Hz, J<sub>2</sub>= 33.45 Hz), 108.5 (tt, J<sub>1</sub>=266.7 Hz, J<sub>2</sub>= 31.6 Hz), 108.2 (m), 49.2, 38.1, 27.9 ppm.

#### 2,2,3,3,4,4,4-heptafluoro-N-(prop-2-yn-1-yl)butanamide - **8**

To a solution of heptafluorobutanoic acid (2.14 g, 10 mmol) in anhydrous DCM was added propargylamine (0.50 g, 9 mmol) followed by DMAP (0.24 g, 2 mmol) and EDC·HCl (2.11 g, 11 mmol). The resulting solution was stirred under an Ar atmosphere at roomtemperature for 20 h, then washed with 1N HCl (2 x 100 mL) and saturated NaHCO<sub>3</sub> solution (2 x 150 mL). The organic layer was dried over Na<sub>2</sub>SO<sub>4</sub> and concentrated. The residue was purified by column chromatography (90 g SiO<sub>2</sub>, EtOAc in hexanes, 0-50%) to afford the desired product as a colorless oil (1.75 g, 77%).

ESI-MS: calcd. for C<sub>7</sub>H<sub>4</sub>F<sub>7</sub>NNaO<sup>+</sup> [M<sup>+</sup>Na<sup>+</sup>] 274.0, found 274.1

<sup>1</sup>H NMR (400 MHz, CDCl<sub>3</sub>): δ = 6.72 (1 H, br s), 4.17 (2 H, dd, J<sub>1</sub>= 5.4 Hz, J<sub>2</sub>= 2.5 Hz), 2.33 (1 H, t, J= 2.6 Hz)

<sup>13</sup>C NMR (100 MHz, CDCl<sub>3</sub>): δ = 157.4 (t, J= 26.4 Hz), 117.5 (qt, J<sub>1</sub>= 287.5 Hz, J<sub>2</sub>= 33.5 Hz), 108.6 (tt, J<sub>1</sub>= 267.2 Hz, J<sub>2</sub>= 31.4 Hz), 108.4 (m), 77.1, 73.4, 30.1 ppm.

#### Monopotassium salt of perylene-3,4,9,10-tetracarboxylic dianhydride - **10**

Perylene-3,4,9,10-tetracarboxylic dianhydride (10.0 g, 25.5 mmol) and potassium hydroxide (34.4 g, 0.612 mol) were dissolved in 1 l distilled water and heated to 60 °C over a period of 2 h. The dark red solution exhibited green fluorescence upon dripping onto a filter paper. The solution was filtrated through a Sinternutsche (Por. 4), refluxed and neutralized with concentrated acetic acid. Upon neutralization (~pH=5) a distinct color change from dark red to brown was observed. The solution was filtrated again and washed thoroughly with water and methanol. The solvent was removed under reduced pressure yielding 10.2 g (89 %) of a red-brownish powder which was used in the next step without any further purification.

#### 3,4,9,10-Perylenetetracarboxylic-3,4-anhydride-9,10-imide - Monoimide - **11**

Diluted ammonia solution (3%, 177ml) was cooled to 0-5°C when **2** (5.61 g, 12.5 mmol, 1 eq) was added slowly. The mixture was refluxed for 2 h before potassium carbonate (10 g in 30 ml H<sub>2</sub>O, 25%) was added. The mixture was remained at reflux for another 2 h before cooled down to room temperature and filtrated using a Por. 4 Nutsche. The solid was washed repeatedly with 2 % K<sub>2</sub>CO<sub>3</sub> solution until the filtrate turned almost colorless. The following day the solid was refluxed for 2 h in potassium hydroxide (80 g) and 800 ml H<sub>2</sub>O. The dark red suspension was filtrated (Por. 4). The solid was redissolved in 10 % KOH and filtrated gain. The filtrate was acidified with a 2N HCl solution until pH 2. After filtration the brownish-red solid was refluxed in 10 % Et<sub>3</sub>N solution. After filtration the filtrate was acidified again with a 2N HCl solution until pH 2. Filtration yielded a red solid which was dried in vacuum at 130°C over night to yield (3.01 g, 61 %). It was used in the next step without any further purification.

#### N-(2,2,3,3,4,4,4-heptafluoro-butyl)-perylene-3,4,9,10-tetracarboxylic bisimide - **12**

Monoimide **3** (1.17 g, 3.00 mmol, 1.0 eq) and 2,2,3,3,4,4,4-heptafluoro-butylamine (0.63 ml, 4.00 mmol, 1.47 eq) was heated together with imidazole (17.77 g, 261.00 mmol, 87 eq) under argon in a sealed vessel at 150 °C. After 12 h the mixture was cooled to room temperature and poured into a mixture of HCl (60 mL, 2N) and EtOH (25 mL). The precipitate was filtered off, dried at 120 °C in vacuum for 12 h. 1.21 g (2.27 mmol, 89%) of a red solid was obtained, which was used without further purification.

<sup>1</sup>H NMR (400 MHz, CDCl<sub>3</sub>/TFA): δ = 8.89-8.83 (8 H, m), 5.10 (2H, t; 15.4 Hz) ppm.

<sup>13</sup>C NMR (150 MHz, CDCl<sub>3</sub>/TFA): δ = 166.3, 165.2, 136.9, 136.4, 133.9, 133.5, 131.2, 130.0, 127.2, 127.0, 125.3, 125.0, 124.7, 122.4, 122.3, 119.4, 39.5 (t, J<sub>CF</sub> = 23 Hz), CF<sub>3</sub>, CF<sub>2</sub> and CF not observed

#### N-(2,2,3,3,4,4,4-heptafluoro-butyl)-N'-(decyl-10-phosphonic acid diethyl ester) perylene-3,4,9,10-tetracarboxylic bisimide - **13**

Perylene bisimide **4** (859 mg, 1.50 mmol, 1.00 eq), sodium hydride (48 mg, 1.98 mmol, 1.32 eq) and 11-bromo-undecyl-phosphonic acid diethyl ester (598 mg, 1.67 mmol, 1.12 eq) were dissolved in anhydrous DMF (50 mL) and stirred at 85 °C for 12h. After additional 48 h the reaction mixture was cooled to room temperature, filtered and extracted with CH<sub>2</sub>Cl<sub>2</sub>. The solvent was evaporated and the crude product was purified by flash chromatography (solvent gradient DCM:MeOH = 10 : 0.4) yielding a red brownish solid (602 mg, 47 %) of **5**.

<sup>1</sup>H NMR (400 MHz, CDCl<sub>3</sub>): δ = 8.62-8.55 (4 H, m), 8.47-8.43 (4 H, m), 5.02 (2 H, t, J = 15.6 Hz), 4.17 (2 H, t, J = 7.7 Hz), 4.14-4.03 (4 H, m), 1.80-1.53 (8 H, m), 1.50-1.24 (16 H, m) ppm.

<sup>13</sup>C NMR (100 MHz, CDCl<sub>3</sub>): δ = 163.2, 163.0, 135.2, 134.0, 132.0, 131.3, 129.5, 129.2, 126.4, 126.2, 123.7, 123.5, 123.1, 122.3, 61.6, 61.5, 40.9, 38.5 (t, J<sub>CF</sub> = 23 Hz), 30.8-22.5 C2-C10 of the aliphatic chain, 16.7, 16.6 ppm.

<sup>19</sup>F NMR (376 MHz, CDCl<sub>3</sub>): δ = -80.4 (t, J = 8.7 Hz), -115.9 (m), -127.7 (d, 4.3 Hz) ppm.

<sup>31</sup>P NMR (242 MHz, CDCl<sub>3</sub>): δ = 32.6 ppm

#### N-(2,2,3,3,4,4,4-heptafluorobutyl)-N'-(undecyl-11-phosphonic acid) perylene-3,4,9,10-tetracarboxylic bisimide - **14**

Perylenebisimide **5** (272 mg, 0.32 mmol) was dissolved under argon in dry CH<sub>2</sub>Cl<sub>2</sub> (40 mL), cooled to 0 °C and bromotrimethylsilane (1 ml, 7.58 mmol) was added dropwise through a syringe. After addition of the silane, the reaction mixture was allowed to warm up to room temperature. After 48 h stirring, 5 ml water was added. After additional 2 h, the mixture was poured into a mixture of methanol and water (50 mL, 1:1). The resulting precipitate was collected by filtration. The red solid was dissolved in again in trifluoroacetic acid (TFA) yielding an intense orange solution, dropped into dioxane, and subsequently freeze dried to obtain a purple red solid (221 mg, 87 %), which was used without further purification.

<sup>1</sup>H NMR (400 MHz, CDCl<sub>3</sub>/TFA): δ = 8.90-8.80 (8 H, m), 5.11 (2 H, t, J<sub>HF</sub> = 15.3 Hz), 4.28 (2 H, t, J = 7.4 Hz), 2.05-1.92 (2 H, m), 1.82-1.75 (2 H, m), 1.74-1.63 (2 H, m), 1.52-1.24 (14 H, m) ppm.

<sup>19</sup>F NMR (376 MHz, CDCl<sub>3</sub>/TFA): δ = -80.8, -116.0, -128.0 ppm.

<sup>31</sup>P NMR (242 MHz, CDCl<sub>3</sub>/TFA): δ = 42.8 ppm.

MS (MALDI-TOF): calc. for C<sub>38</sub>H<sub>32</sub>F<sub>7</sub>N<sub>2</sub>O<sub>7</sub>P: 792.1835; found: 792.2867; difference: - 0.1032

## 6. References

- (1) Mei, J.; Diao, Y.; Appleton, A. L.; Fang, L.; Bao, Z. *J. Am. Chem. Soc.* **2013**, *135* (18), 6724.
- (2) Tyan, Y.-S. *J. Photonics Energy* **2011**, *1* (1), 11009.
- (3) Espinosa, N.; Hösel, M.; Jørgensen, M.; Krebs, F. C. *Energy Environ. Sci.* **2014**, *7* (3), 855.
- (4) Torsi, L.; Magliulo, M.; Manoli, K.; Palazzo, G. *Chem. Soc. Rev.* **2013**.

- (5) Klauk, H. *Organic Electronics: Materials, Manufacturing, and Applications*; John Wiley & Sons, 2006.
- (6) Donald, K. J. *J. Inorg. Organomet. Polym. Mater.* **2011**, *21* (2), 391.
- (7) Huang, J.; Sun, J.; Katz, H. E. *Adv. Mater.* **2008**, *20* (13), 2567.
- (8) Andringa, A.-M.; Spijkman, M.-J.; Smits, E. C. P.; Mathijssen, S. G. J.; Hal, P. A. van; Setayesh, S.; Willard, N. P.; Borshchev, O. V.; Ponomarenko, S. A.; Blom, P. W. M.; de Leeuw, D. M. *Org. Electron.* **2010**, *11* (5), 895.
- (9) Smits, E. C. P.; Mathijssen, S. G. J.; van Hal, P. A.; Setayesh, S.; Geuns, T. C. T.; Mutsaers, K. A. H. A.; Cantatore, E.; Wondergem, H. J.; Werzer, O.; Resel, R.; Kemerink, M.; Kirchmeyer, S.; Muzafarov, A. M.; Ponomarenko, S. A.; de Boer, B.; Blom, P. W. M.; de Leeuw, D. M. *Nature* **2008**, *455* (7215), 956.
- (10) Schmaltz, T.; Amin, A. Y.; Khassanov, A.; Meyer-Friedrichsen, T.; Steinrück, H.-G.; Magerl, A.; Segura, J. J.; Voitchovsky, K.; Stellacci, F.; Halik, M. *Adv. Mater.* **2013**, *25* (32), 4511.
- (11) Cernetic, N.; Weidner, T.; Baio, J. E.; Lu, H.; Ma, H.; Jen, A. K.-Y. *Adv. Funct. Mater.* **2015**, *25* (33), 5376.
- (12) Hutchins, D. O.; Acton, O.; Weidner, T.; Cernetic, N.; Baio, J. E.; Ting, G.; Castner, D. G.; Ma, H.; Jen, A. K.-Y. *Org. Electron.* **2012**, *13* (3), 464.
- (13) Ringk, A.; Li, X.; Gholamrezaie, F.; Smits, E. C. P.; Neuhold, A.; Moser, A.; Van der Marel, C.; Gelinck, G. H.; Resel, R.; de Leeuw, D. M.; Strohriegl, P. *Adv. Funct. Mater.* **2013**, *23* (16), 2016.
- (14) Whitesides, G. M.; Grzybowski, B. *Science* **2002**, *295* (5564), 2418.
- (15) Halik, M.; Hirsch, A. *Adv. Mater.* **2011**, *23* (22–23), 2689.
- (16) Senanayak, S. P.; Sangwan, V. K.; McMorrow, J. J.; Everaerts, K.; Chen, Z.; Facchetti, A.; Hersam, M. C.; Marks, T. J.; Narayan, K. S. *Adv. Electron. Mater.* **2015**, *1* (12), n/a.
- (17) Ito, Y.; Virkar, A. A.; Mannsfeld, S.; Oh, J. H.; Toney, M.; Locklin, J.; Bao, Z. *J. Am. Chem. Soc.* **2009**, *131* (26), 9396.
- (18) Kosian, M.; Smulders, M. M. J.; Zuilhof, H. *Langmuir* **2016**.
- (19) Wojciechowski, K.; Stranks, S. D.; Abate, A.; Sadoughi, G.; Sadhanala, A.; Kopidakis, N.; Rumbles, G.; Li, C.-Z.; Friend, R. H.; Jen, A. K.-Y.; Snaith, H. J. *ACS Nano* **2014**, 141121165501003.
- (20) Dodabalapur, A.; Torsi, L.; Katz, H. E. *Science* **1995**, *268* (5208), 270.
- (21) Tanase, C.; Meijer, E. J.; Blom, P. W. M.; de Leeuw, D. M. *Org. Electron.* **2003**, *4* (1), 33.
- (22) Parry, A. V. S.; Lu, K.; Tate, D. J.; Urasinska-Wojcik, B.; Caras-Quintero, D.; Majewski, L. A.; Turner, M. L. *Adv. Funct. Mater.* **2014**, *24* (42), 6677.
- (23) Ringk, A.; Christian Roelofs, W. S.; Smits, E. C. P.; van der Marel, C.; Salzmann, I.; Neuhold, A.; Gelinck, G. H.; Resel, R.; de Leeuw, D. M.; Strohriegl, P. *Org. Electron.* **2013**, *14* (5), 1297.
- (24) Schmaltz, T.; Khassanov, A.; Steinrück, H.-G.; Magerl, A.; Hirsch, A.; Halik, M. *Nanoscale* **2014**, *6* (21), 13022.
- (25) Lummerstorfer, T.; Hoffmann, H. J. *Phys. Chem. B* **2004**, *108* (13), 3963.
- (26) Kolb, H. C.; Finn, M. G.; Sharpless, K. B. *Angew. Chem. Int. Ed.* **2001**, *40* (11), 2004.
- (27) Kaiser, H.; Lindner, J.; Langhals, H. *Chem. Ber.* **1991**, *124* (3), 529.
- (28) Aluicio-Sarduy, E.; Singh, R.; Kan, Z.; Ye, T.; Baidak, A.; Calloni, A.; Berti, G.; Duò, L.; Iosifidis, A.; Beaupré, S.; Leclerc, M.; Butt, H.-J.; Floudas, G.; Keivanidis, P. E. *ACS Appl. Mater. Interfaces* **2015**, *7* (16), 8687.
- (29) Darlatt, E.; Traulsen, C. H.-H.; Poppenberg, J.; Richter, S.; Kühn, J.; Schalley, C. A.; Unger, W. E. S. J. *Electron Spectrosc. Relat. Phenom.* **2012**, *185* (3–4), 85.
- (30) Ciampi, S.; Luais, E.; James, M.; Choudhury, M. H.; Darwish, N. A.; Gooding, J. J. *Phys. Chem. Chem. Phys.* **2014**, *16* (17), 8003.
- (31) Benninghoven, A.; Rudenauer, F. G.; Werner, H. W. **1987**.
- (32) Poirier, G. E.; Pylant, E. D. *Science* **1996**, *272* (5265), 1145.
- (33) Graham, D. J.; Castner, D. G. *Biointerphases* **2012**, *7* (1), 49.
- (34) Muramoto, S.; Graham, D. J.; Wagner, M. S.; Lee, T. G.; Moon, D. W.; Castner, D. G. *J. Phys. Chem. C* **2011**, *115* (49), 24247.
- (35) Wagner, M. S.; Graham, D. J.; Ratner, B. D.; Castner, D. G. *Surf. Sci.* **2004**, *570* (1–2), 78.
- (36) Graham, D. J.; Ratner, B. D. *Langmuir* **2002**, *18* (15), 5861.

- (37) Biesinger, M. C.; Paepegaey, P.-Y.; McIntyre, N. S.; Harbottle, R. R.; Petersen, N. O. *Anal. Chem.* **2002**, *74* (22), 5711.
- (38) Wagner, M. S.; Castner, D. G. *Langmuir* **2001**, *17* (15), 4649.
- (39) Min, H.; Park, J.-W.; Shon, H. K.; Moon, D. W.; Lee, T. G. *Appl. Surf. Sci.* **2008**, *255* (4), 1025.
- (40) Wang, X.; Lieberman, M. *Langmuir* **2003**, *19* (18), 7346.
- (41) Acton, B. O.; Ting, G. G.; Shamberger, P. J.; Ohuchi, F. S.; Ma, H.; Jen, A. K.-Y. *ACS Appl. Mater. Interfaces* **2010**, *2* (2), 511.
- (42) NIST X-ray Photoelectron Spectroscopy Database NIST Standard Reference Database 20, Version 4.1 <http://srdata.nist.gov/xps/>.
- (43) *Handbook of X-ray photoelectron spectroscopy: a reference book of standard spectra for identification and interpretation of XPS data*; Moulder, J. F., Stickle, W. F., Sobol, P. E., Bomben, K. D., Chastain, J., King Jr., R. C., Physical Electronics, Incorporation, Eds.; Physical Electronics: Eden Prairie, Minn., 1995.
- (44) Koshkaryan, G.; Klivansky, L. M.; Cao, D.; Snauko, M.; Teat, S. J.; Struppe, J. O.; Liu, Y. *J. Am. Chem. Soc.* **2009**, *131* (6), 2078.

# Manuscript #4

S. Yang\*, **J. Binting\***, S. Park, S. Jain, K. Alexandrou, P. Fruhmann, K. Besar, H. Katz, I. Kymissis; Ultra-cheap, versatile and robust USB-driven sensor platform; *manuscript draft*





# Ultra-cheap, versatile and robust USB-driven sensor platform

S. Yang,<sup>a ‡</sup> J. Bintinger<sup>a,b ‡</sup>, S. Park<sup>a,c</sup>, S. Jain<sup>a</sup>, K. Alexandrou<sup>a</sup>, P. Fruhmann<sup>b,d</sup>, K. Besar<sup>e</sup>, H. Katz<sup>e</sup> and I. Kymissis<sup>a \*</sup>

Received 00th January 20xx,  
Accepted 00th January 20xx

DOI: 10.1039/x0xx00000x

www.rsc.org/

**An ultra-low cost sensor platform is developed, incorporating a chemresistor-based sensor that enables targeted sensing through surface functionalization. Humidity, ammonia and acetone sensing are demonstrated by PEDOT-PSS, DPP-CN and graphene surface modification respectively. The integrated USB connector and micro-controller allows install-free data collection on any devices with an USB port.**

Three of our five senses, namely touch, sight and hearing, have been commercialized in small powerful sensors and are ubiquitous in almost every electronic including laptops, tablets and cell phones. The remaining two, smell and taste, pose a greater challenge for commercializing due to their sensing mechanism. In this report, we demonstrate an ultra-low cost, versatile, sensitive and lightweight (gas) sensing platform which addresses these challenges. Miniature gas sensor devices for detection and analysis of various gases have recently attracted increasing interest due to their potential applications in various fields such as healthcare (exhaled breath analysis), work safety and industrial process managing.<sup>1</sup> A human being inhales between 11000 and 18000 liters of air every day. Thus, an effective and portable monitoring tool for gases would provide a useful tool to prevent or counteract respiratory diseases such as asthma, severe respiratory inflammations, and lung diseases.<sup>2</sup>

Herein, we report on a versatile USB-driven sensing platform employing a chemiresistor-based voltage divider design for use as humidity, ammonia and ketone sensor. Electrical based sensors with an integrated electronic (USB) readout have the potential for facile data collection, miniaturization, low power consumption, and low cost. It can also easily be integrated into other electronic circuits. By using different and perhaps more selective semiconducting materials the range of this platform can easily be extended to meet desired demands. One of the most common methods for chemo- and biosensing is the use of the conductometric transducing effects of conducting polymers.<sup>3</sup> A chemiresistor configuration offers several advantages compared with other sensing principles including fluorescence, surface plasmon resonance (SPR) or organic field-effect transistors (OFETs). A two electrode chemiresistor can be realized with the simplest setup albeit allowing great sensitivity based on small perturbations occurring anywhere along the polymer chain rather than volumetric. With such versatility and flexibility in sensing capability, the ultra-low cost sensor platform also has great potential in point-of-care diagnostic applications. Furthermore the simplicity of the setup provides the possibility of a straight forward integration into a larger sensor array as well as enabling the trend for miniaturization of analytical devices.<sup>3</sup> In addition to this easy scale

<sup>a</sup> Department of Electrical Engineering, Columbia University, New York, NY 10027, USA

\*E-mail: johnkym@ee.columbia.edu

<sup>b</sup> Institute of Applied Synthetic Chemistry, Vienna University of Technology, 1060 Vienna, Austria

<sup>c</sup> Department of Material Science and Engineering, Korea Advanced Institute of Science and Technology, 34141 Daejeon, South Korea

<sup>d</sup> Center for Electrochemical Surface Technology (CEST), 2700 Wiener Neustadt, Austria

<sup>e</sup> Department of Materials Science and Engineering, John Hopkins University, Baltimore, MD 21218-2608, USA

‡Both authors contributed equally

†Electronic Supplementary Information (ESI) available: [details of any supplementary information available should be included here]. See DOI: 10.1039/x0xx00000x

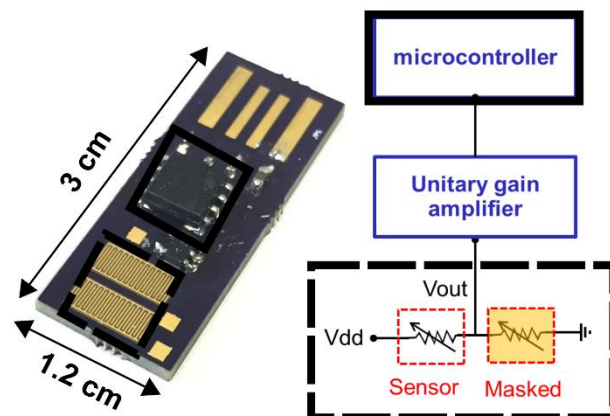
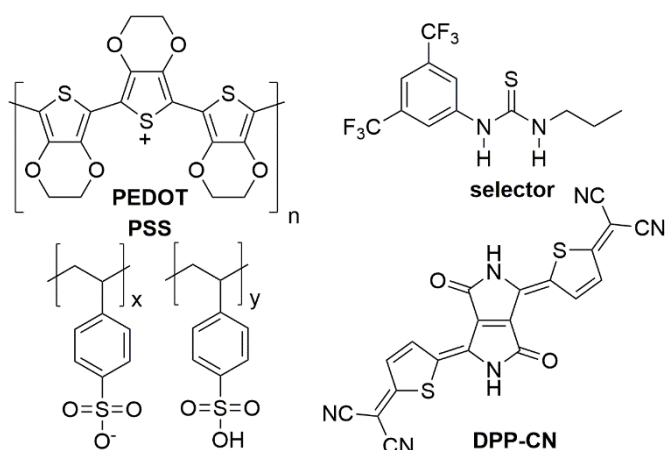


Figure 1: left: picture of the  $\zeta$ -Sensor with dimensions; right: schematic layout design



**Figure 2:** molecular structure of used materials; PEDOT:PSS, selector 1-(3,5-bis(trifluoromethyl)phenyl)-3-propylthiourea and DPP-CN

up, more sensing capabilities can be achieved via the incorporation of other sensing materials (Figure 2).

## Sensor platform design

We developed an ultra-low cost (<\$1) chemical sensor (\$-Sensor) that uses a direct USB connection and printable sensor materials to eliminate the need for a reader or user interface while delivering quality, digital readout of chemical species. We explored the minimalist approach to designing the sensor platform. The sensor incorporates only the bare essentials and nothing else. The dollar-sensor consists of four major components – a sensor, a unitary-gain amplifier, a micro controller and integrated USB connector as shown in Figure 1. The custom designed board is made by OSH PARK. The total bill of material (BOM) is around \$2 for small quantity (~30) and approaches less than \$1 for large quantity (>10k). The integrated USB connector allows further structural simplification and cost reduction. The dollar sensor platform can ultimately enable true ultra-low-cost, disposable sensor devices. The sensor portion of the device is a chemiresistor based voltage divider, consisting of two integrated electrodes. The interdigitated electrodes can be functionalized to form a chemiresistor, which eliminates the need for gate electrodes. Our sensor platform utilizes a voltage divider topology with two identical chemiresistors that are functionalized at the same time with the same material. This ensures natural impedance match and renders the device intrinsically insensitive to drift and degradation effects. One of the chemiresistors is exposed while the other one

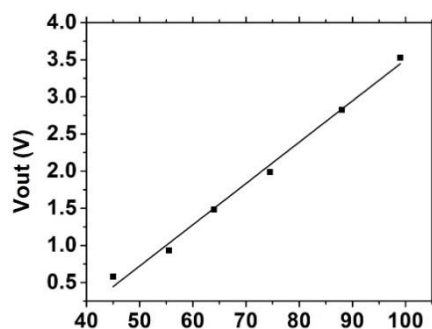


**Figure 3:** linear response curve of the \$-Sensor between voltage and humidity

remains encapsulated. The impedance of the exposed resistor will change during the exposure to the substance of interest, and the voltage will reflect the delta of the impedance. The voltage for the divider is supplied directly from the USB (5V). The resolution of the sensing is determined by the micro-controller (ATtiny85) ADC, and it is 10 bit in this case. The channel material can be easily varied, thus allowing to sense a broad range of other analytes. Within our work we focused on 3 different types of gas sensors capable of detecting water vapor (humidity), ketones (acetone) and ammonia by using different materials (Figure 2) and concepts.

## Functionalization and sensing principle

### Humidity

Conducting polymers have a long history as sensing material in organic electronic devices, since they exhibit an intrinsic affinity towards redox active species as well as to acidic or basic gases.<sup>3</sup> The use of PEDOT:PSS for humidity sensing is well established. The proposed sensing mechanism is that the adsorbed water molecules on the surface of the polymer are generating holes in the semiconducting layer because of their large dipole moments and thus enhance the carrier conductivity. The result is a decrease in resistance with increasing humidity.<sup>4,5</sup> We applied this concept and commercially available PEDOT:PSS (Heraeus) to the \$-Sensor and fabricated an ultra-cheap PEDOT:PSS based humidity sensor exhibiting linear response curve between humidity and Voltage shown in Figure 3.

The measurements were performed in an environmental chamber (CTS C-40/60) from Clima Temperature Systems. The climate chamber was set to a target value and the sensor was inserted. After an equilibration time of 3 minutes at the target value the experiment was started. The data acquisition for one data point was one minute each.

### Ketones (cyclohexanone)

Graphene and related 2D materials are considered top candidates for (bio)sensing applications, as they exhibit a number of crucial properties such as high charge carrier mobility, stability and versatility through functionalization.<sup>6-8</sup> Noncovalent functionalization of graphene ensures that the supreme electrical properties of the material remain largely intact.<sup>9</sup> We adapted the reported procedure from Frazier et al.<sup>10</sup> to produce CVD-graphene based chemiresistor to selectively detect acetone, which is an important biomarker for early diseases detection in exhaled breath (eg. Diabetes).<sup>11-14</sup>

In this approach selective sensing is achieved by noncovalent functionalization of graphene by a selector molecule. The selector molecule consists of two units: the bis(trifluoromethyl)aryl group which acts as an anchor group by promoting cofacial  $\pi$ - $\pi$ - interactions, while the thiourea component is known to bind ketones via hydrogen bonding.<sup>10,15,16</sup> This hydrogen bonding enhances the response by simply binding and thus concentrating the analyte to the graphene surface. Additionally, the formed hydrogen-bonded complex (selector plus ketone) enhances the collective dipole

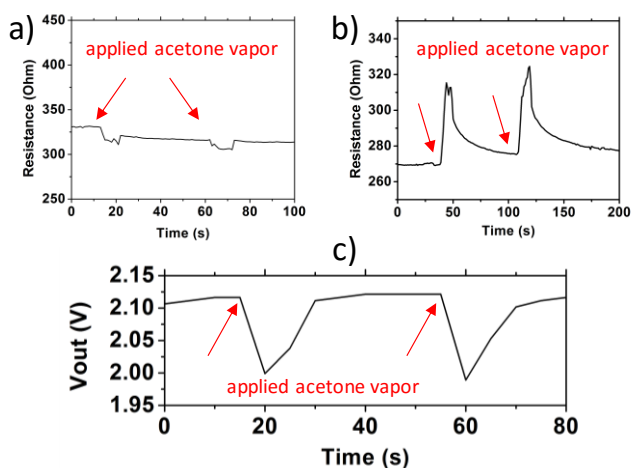


**Figure 4:** a): response curve of bare graphene-based chemiresistor to acetone vapor; b) reversible detection of acetone vapor using surface treated graphene on a single chemiresistor device; c) acetone vapor response of the  $\$$ -Sensor

and thus influences the charge carriers in graphene.<sup>10</sup> The acetone sensing experiments were performed on a Si-chip using an external measurement setup, because of graphene transfer difficulties. However, the recording was done using the same microcontroller and amplifier as on the  $\$$ -Sensor. The top of Figure 4 shows the reversible sensing of acetone using the  $\$$ -Sensor platform, while no signal was detected in the case of bare graphene (Figure 4, bottom).

#### Ammonia

We recently reported on printable OFETs using 2,2'-[2,5-dihexadecyl-3,6-dioxo-2,3,5,6-tetrahydropyrrole[3,4-c]pyrrole-1,4-diylidene)-5,2-diylidene] dimalononitrile (DPP-CN) as the active material for the selective detection of ammonia in the 0.5 ppm v/v range.<sup>2</sup> We now applied this material to our dollar sensor and obtained similar results.

DPP-CN was synthesized using a modified literature procedure in Prof. Katz's laboratory from JHU.<sup>17</sup> The n-type DPP-CN sensor showed large sensitivity to ammonia which manifested in an apparent resistance decrease upon exposure. The absorption of polar  $\text{NH}_3$

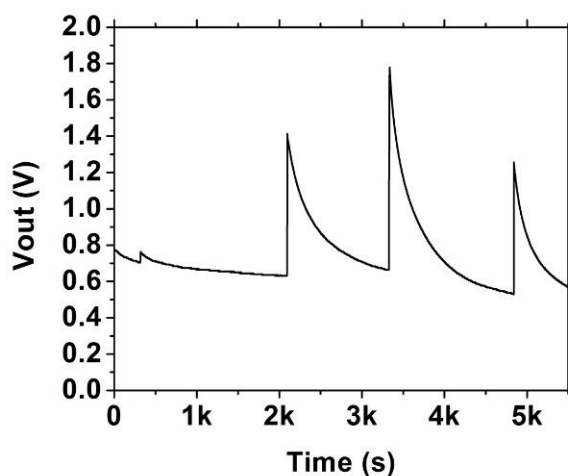


**Figure 5:**  $\$$ -Sensor response to ammonia

molecules by DPP-CN likely shifts the threshold voltage and alters the charge transport efficiency through charge-dipole interaction. This is similar to phenomena observed in other small molecule semiconductor based ammonia sensors.<sup>18-21</sup> Here, the decrease in resistance offsets the voltage divider ratio and results in increase  $V_{\text{out}}$  as shown in Figure 5.

## Conclusions

In summary, we have developed a versatile, ultra-low-cost sensing platform employing a chemiresistor-based sensor design that incorporates a direct USB-connection for power supply as well as automatically creating an electronic readout. We have demonstrated the versatility of our  $\$1$ -sensor by fabricating sensors for three analytes ( $\text{H}_2\text{O}$  vapour, acetone,  $\text{NH}_3$ ) using the same platform with targeted functionalization. By changing the channel material, one can broaden the range of detectable analytes and custom design the  $\$$ -sensor to specific needs.

## Acknowledgement

JB is grateful to the Marietta Blau Grant of the OeAD.

## Notes and references

The  $\$$ -Sensor was modified in the following way to allow for humidity-, ammonia-, and acetone sensing respectively. 5  $\mu\text{l}$  of a PEDOT:PSS solution (Heraeus) was applied manually on each of the electrode arrays using an Eppendorfer pipette. The  $\$$ -Sensor was then baked at 80  $^\circ\text{C}$  for 10 min on a hotplate under ambient conditions. Finally, the top electrode array was encapsulated by five layers of Kapton tape before any measurements were conducted. Ammonia sensing modifications were prepared similarly by using a 10 mg/ml solution of DPP-CN in chlorobenzene.

Acetone sensing was performed on a non-covalently modified CVD-graphene chemiresistor. The CVD-graphene process was done as described previously in our group.<sup>22</sup> Single layer CVD graphene grown on 20 $\mu\text{m}$  Cu foil was transferred on top of 300 nm thermally grown  $\text{SiO}_2$  on a p-doped Si substrate. A Poly(methyl methacrylate) (PMMA) support layer was spin coated on top of the graphene/Cu foil stack (3000 rpm, 45 s), followed by an annealing step at 145  $^\circ\text{C}$  for 2 min. Reactive ion etching (RIE) was then employed (50 W for 20 s) to remove unwanted graphene from the backside of the Cu foil that would prevent proper Cu etching. Polydimethylsiloxane (PDMS) stamps cured at 80  $^\circ\text{C}$  for 90 min were placed on top of the PMMA layer for extra support. PDMS stamps on top of PMMA/graphene/Cu foil stack enabled us to transfer graphene with fewer defects and low impurity doping. The Cu foil/graphene/PMMA/PDMS stack was inserted in ammonium persulfate (APS) copper etchant solution for 5 h, and after several baths in deionized (DI) water, it was left overnight to dry before being transferred on the wafer. Si/ $\text{SiO}_2$  substrates were cleaned using Piranha and annealed at 180  $^\circ\text{C}$  (hotplate) as the

PDMS/PMMA/graphene stack was placed carefully on top, promoting adhesion between graphene and the substrate. A chloroform bath was then used (5 h) to dissolve PMMA and leave a clean graphene surface on the Si/SiO<sub>2</sub> substrate. Finally, thermally evaporated Cr/Au (3 nm/45 nm) contacts (drain/source electrodes) were deposited using a shadowmask. Approximately 150 µl of a 1 mM solution of the selector in anhydrous THF was dropcasted on the channel. The chips were then dried in a vacuum oven at 40°C for 30 min before conducting sensing experiments. A small voltage of 100 mV was applied from a source measurement unit (Keithley 2400) and the source-drain current was monitored while exposition of the sensor to the gas.

Synthesis of 1-(3,5-bis(trifluoromethyl)phenyl)-3-propylthiourea was done according to literature<sup>10</sup>: Under argon atmosphere 3,5-Bis(trifluoromethyl)phenyl isothiocyanate (0.81 g, 3.00 mmol, 1.00 eq) was added dropwise to a stirred solution of propylamine (0.32 g, 5.45 mmol, 1.82 eq) in anhydrous dichloromethane (7 mL) at room temperature. The mixture was stirred overnight before the solvent was removed under reduced pressure. The crude product was washed multiple times with hexane and dried under reduced pressure to yield a white solid compound. Yield: 0.891 g (90%);

<sup>1</sup>H NMR (600 MHz, DMSO-d<sub>6</sub>): δ = 10.0 (1H, br s), 8.24 (3 H, m), 7.71 (1 H, s), 3.45 (2 H, br s), 1.58 (2 H, sextet, J = 7.3 Hz), 0.91 (3 H, t, J = 7.5 Hz) ppm; <sup>19</sup>F NMR (470 MHz, DMSO-d<sub>6</sub>) δ = -62.20 ppm; <sup>13</sup>C NMR (151 MHz, DMSO-d<sub>6</sub>) δ = 180.49, 141.99, 130.12 (q, J = 32.7 Hz), 123.26 (q, J = 272.7 Hz), 121.76, 115.87, 45.61, 21.50, 11.34 ppm

- 1 A. Bulbul and H. Kim, *Lab Chip*, 2015, **15**, 94–104.
- 2 K. Besar, S. Yang, X. Guo, W. Huang, A. M. Rule, P. N. Breyse, I. J. Kymissis and H. E. Katz, *Org. Electron.*, 2014, **15**, 3221–3230.
- 3 U. Lange and V. M. Mirsky, *Anal. Chim. Acta*, 2011, **687**, 105–113.
- 4 D. Nilsson, T. Kugler, P.-O. Svensson and M. Berggren, *Sens. Actuators B Chem.*, 2002, **86**, 193–197.
- 5 W. A. Daoud, J. H. Xin and Y. S. Szeto, *Sens. Actuators B Chem.*, 2005, **109**, 329–333.
- 6 J. F. Fennell, S. F. Liu, J. M. Azzarelli, J. G. Weis, S. Rochat, K. A. Mirica, J. B. Ravnsbæk and T. M. Swager, *Angew. Chem. Int. Ed.*, 2016, **55**, 1266–1281.
- 7 Q. He, S. Wu, Z. Yin and H. Zhang, *Chem. Sci.*, 2012, **3**, 1764–1772.
- 8 B. Zhan, C. Li, J. Yang, G. Jenkins, W. Huang and X. Dong, *Small*, 2014, **10**, 4042–4065.
- 9 V. Georgakilas, M. Otyepka, A. B. Bourlinos, V. Chandra, N. Kim, K. C. Kemp, P. Hobza, R. Zboril and K. S. Kim, *Chem. Rev.*, 2012, **112**, 6156–6214.
- 10 K. M. Frazier and T. M. Swager, *Anal. Chem.*, 2013, **85**, 7154–7158.
- 11 N. Marczin and M. Yacoub, Eds., *Disease markers in exhaled breath: basic mechanisms and clinical applications*, IOS Press, Amsterdam ; Washington, DC, 2002.
- 12 B. Buszewski, M. Kęsy, T. Ligor and A. Amann, *Biomed. Chromatogr.*, 2007, **21**, 553–566.
- 13 C. Turner, P. Španěl and D. Smith, *Physiol. Meas.*, 2006, **27**, 321–337.
- 14 Z. Wang and C. Wang, *J. Breath Res.*, 2013, **7**, 037109.
- 15 J. R. Cox, P. Müller and T. M. Swager, *J. Am. Chem. Soc.*, 2011, **133**, 12910–12913.
- 16 J. M. Schnorr, D. van der Zwaag, J. J. Walsh, Y. Weizmann and T. M. Swager, *Adv. Funct. Mater.*, 2013, **23**, 5285–5291.
- 17 H. Zhong, J. Smith, S. Rossbauer, A. J. P. White, T. D. Anthopoulos and M. Heeney, *Adv. Mater.*, 2012, **24**, 3205–3211.
- 18 J. W. Jeong, Y. D. Lee, Y. M. Kim, Y. W. Park, J. H. Choi, T. H. Park, C. D. Soo, S. M. Won, I. K. Han and B. K. Ju, *Sens. Actuators B Chem.*, 2010, **146**, 40–45.
- 19 J. Yu, X. Yu, L. Zhang and H. Zeng, *Sens. Actuators B Chem.*, 2012, **173**, 133–138.
- 20 S. Ji, H. Wang, T. Wang and D. Yan, *Adv. Mater.*, 2013, **25**, 1755–1760.
- 21 B. Lee, A. Wan, D. Mastrogiovanni, J. E. Anthony, E. Garfunkel and V. Podzorov, *Phys. Rev. B*, 2010, **82**, 085302.
- 22 K. Alexandrou, N. Petrone, J. Hone and I. Kymissis, *Appl. Phys. Lett.*, 2015, **106**, 113104.

# Manuscript #5

J. Bintliger\*, H. Holzer\*, C. Choi, Y. Kim, D. Lumpi, E. Horkel, B. Stöger, C. Hametner, M. Marchetti-Deschmann, F. Plasser, I. Kymissis, J. Fröhlich; Color Tuning of Oligothiophene Based Compounds – A Combined Experimental and Computational Approach, *manuscript draft*



# Color Tuning of Oligothiophene Based Compounds – A Combined Experimental and Computational Approach

Johannes Bintinger<sup>a\*†</sup>, Brigitte Holzer<sup>a\*</sup>, Daniel Lumpi<sup>a</sup>, Ernst Horkel<sup>a†</sup>, Chris Choi<sup>b</sup>,  
Youngwan Kim<sup>b</sup>, Berthold Stöger<sup>c</sup>, Christian Hametner<sup>a</sup>, Martina Marchetti-Deschmann<sup>c</sup>,  
Ioannis Kymissis<sup>b</sup>, Felix Plasser<sup>d</sup>, Johannes Fröhlich<sup>a</sup>

<sup>a</sup> Institute of Applied Synthetic Chemistry, Vienna University of Technology, 1060 Vienna, Austria

<sup>b</sup> Department of Electrical Engineering, Columbia University, New York, NY 10027, USA

<sup>c</sup> Institute of Chemical Technologies and Analytics, Vienna University of Technology,  
Getreidemarkt 9, 1060 Vienna, Austria

<sup>d</sup> Institute for Theoretical Chemistry, University of Vienna, Währinger Straße 17, 1090 Vienna, Austria

\* Both authors contributed equally

† Email: [johannes.bintinger@tuwien.ac.at](mailto:johannes.bintinger@tuwien.ac.at); [ernst.horkel@tuwien.ac.at](mailto:ernst.horkel@tuwien.ac.at)

## Abstract

We report on the synthesis of novel OLED compounds consisting of a symmetrical cap-linker-cap system. The individual building blocks allow for 5 possibilities of color tuning by means of altering both electronic and steric properties. Materials were characterized in regards to their fluorescence properties from both solution and exemplarily fabricated OLED devices. These results are in turn used to benchmark computational simulations in order to predict important material properties aiming towards a powerful tool to rationally guide future synthesis by means of quantum chemical calculations.

## 1. Introduction

Organic electronic (OE) thin film devices such as OLEDs[1] (organic light-emitting diodes), OFETs[2] (organic field-effect transistors), OPVs[3] (organic photovoltaics) have gained raising interest from academia and industry due to the variety of possible applications combined with an enormous commercial potential.[4] OE is an emerging technology based on a bottom up approach, meaning that through rational design on a molecular level of the organic semiconducting material (OSC), novel properties are created, which are impossible to replicate or imitate with silicon, expanding the world of electronics in ways unimaginable until now.[5]

The application of these novel materials in the field of display technology enables the construction of very-thin, flexible, energy-efficient, light-weight panels that are highly suitable for customer electronic displays.[6] Due to the huge potential of this technology intense efforts are made to overcome some of the deficits of these materials such as limited stability

and device lifetimes. However, the synthesis of novel organic materials is an expensive and time intense task, in which the desired outcome is often unknown until the materials are implemented and tested in real devices and applications. Thus, it would be a great benefit to obtain reliable information on the physical properties of interest of the materials prior to synthesis.[7] Based on such knowledge, the most promising candidates can be selected within a substance class under investigation. For OLED applications the availability of reliable and computationally efficient methods for the prediction of photoluminescent properties is of great importance. To assist a rational selection of the most promising structures to be synthesized, we recently developed a method based on time dependent density functional theory (TD-DFT) computations for predicting photoluminescent properties.[7] Of special interest was the calculation of the entire emission spectrum which is relevant for successful color tuning during the molecular design of novel OLED compounds. This was achieved by not only considering the vertical excitation energies obtained by the TD-DFT calculations but also including information upon vibrational broadening. While in that preliminary study only small model molecules were investigated, we now apply this method to real OLED materials and tested it for its scope and limitations.

Thiophenes have long been used in OE as they exhibit high charge carrier mobilities. Unfortunately, however thiophenes themselves are not suited for use in OLEDs, as they exhibit fluorescent self-quenching caused by strong  $\pi$ - $\pi$  stacking.[8] For this reason a common approach is to combine these thiophenes with modified triphenylamine (TPA) structures, which have excellent electron donor and hole transport properties.[9–13]

The materials under investigation combine these structural scaffolds consisting of thiophene based linker systems and triarylamine containing cap units (Figure 1), thus resulting in a material class incorporating good charge carrier transport as a result of the oligothiophene unit and enhanced luminescent properties by circumventing self-quenching.[14] Each individual building block can readily be synthesized or structurally modified to meet electronic and spectroscopic requirements.

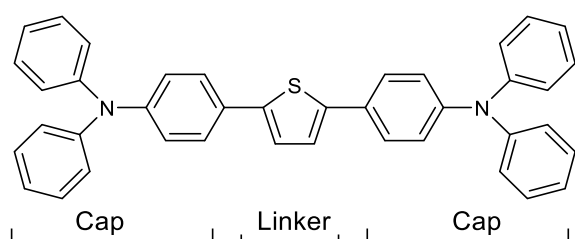


**Figure 1.** Schematic illustration of a cap-linker-cap system.

In this comprehensive study we report on 5 possibilities of color tuning by molecular design of novel OLED materials (electron donating/withdrawing groups, planarization and de-planarization, extension of the  $\pi$ -system). The experimentally obtained properties were in turn compared with the corresponding results of the computations. As the correlation



between experiment and simulation was very high, we feel confident to have a powerful tool in hand to rationally guide future synthesis by means of quantum chemical calculations.

## 2. Results and discussion

### 2.1. Molecular design

Useful for a tailor made compound that is designed according to customer requirements is a modular approach, which allows both economical synthesis and exhaustive tuning capabilities of various properties. The building blocks incorporated in the substances under investigations are thiophenes used as linkers and TPA units serving as caps. Combining these two subunits yields a cap-linker-cap system exhibiting good charge carrier transport originating from the oligothiophene units and tunable luminescent properties by selection of the appropriate cap unit.

Alteration of the molecular design of triphenylamine-based materials by introducing either electron-donating or -withdrawing substituents allows fine tuning of photophysical properties of a variety of fluorescent materials.[15] Also the application of planarized or deplanarized moieties strongly influences emission behavior. This study aims to give conclusive insight into structure/property relationships of triphenylamine-based substance classes both from an experimental as well as from a computational point of view. Therefore, in order to evaluate the electronic and steric effects of substituted triphenylamine-based materials the following strategies are applied altering the design of a cap-linker-cap system (Figure 2): (i) introduction of both electron-donating and -withdrawing substituents on the triphenylamine (TPA) cap, (ii) planarization and deplanarization of the TPA moiety by introduction of either indolocarbazole (ICz), phenylcarbazole (PCz) or ortho-methyl substituted TPA scaffolds, (iii) as well as elongation and planarization of the  $\pi$ -linker by applying bithiophene, terthiophene, quarterthiophene as well as thieno[3,2-*b*]thiophene or dithieno[3,2-*b*:2',3'-*d*]thiophene.

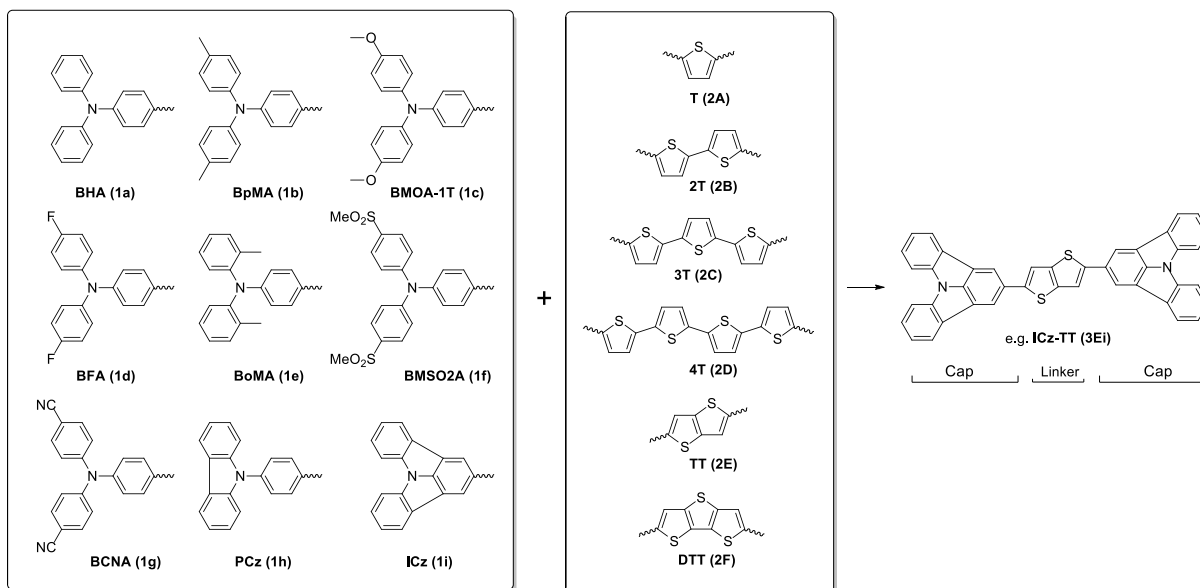


**Figure 2.** Molecular design of cap-linker-cap systems.

Rational permutation of a broad variety of caps and linkers yields a representative set of 31 compounds, which are thoroughly investigated regarding their relevant properties for their use in OE applications. Furthermore, the obtained experimental data are used as valuable references for benchmarking the computational method, ultimately leading towards a powerful tool for predicting structure property relationships.

## 2.2. Synthesis

The synthetic linkage of triphenylamines (TPA), indolocarbazole (ICz) as well as phenylcarbazole (PCz) scaffolds and thiophene-based linkers toward symmetrical bis(triaryl amines) was pursued by cross-coupling reactions based on a Suzuki cross-coupling reaction. A general Suzuki cross-coupling procedure developed in an earlier study tolerating a broad spectrum of functionalized TPA boronic acid esters[16] was applied for the synthesis of **3Ae**, **3Ba-e**, **3Bh**, **3Bi**, **3Ca-d**, **3Da-d**, **3Ea**, **3Ee**, **3Eh**, **3Ei**, **3Fa**, **3Fe**, **3Fh** and **3Fi** (Figure 3). The synthesis of 2,5-disubstituted thiophenes **3Aa-d** and **3Af-g** bearing various triphenylamines as well as PCz **1h** and ICz **1i** moieties have been previously described by our group.[17,18]

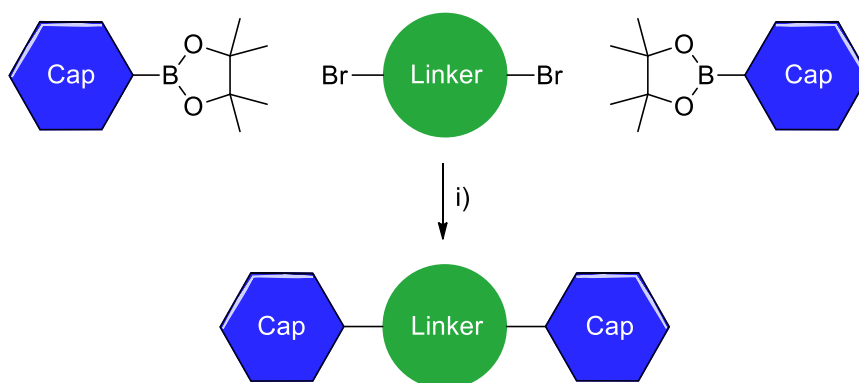
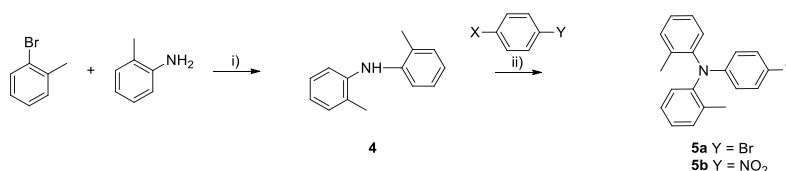


**Figure 3.** Synthetic pathway towards **3Ae**, **3Ba-e**, **3Bh**, **3Bi**, **3Ca-d**, **3Da-d**, **3Ea**, **3Ee**, **3Eh**, **3Ei**, **3Fa**, **3Fe**, **3Fh** and **3Fi**. Reaction conditions i): KOtBu, (IPr)Pd(allyl)Cl, isopropanol / water, reflux.

The obtained final compounds were all solid materials appearing yellow to red in color. Solubility strongly depends on linker length and planarization of the cap. In general, the higher the linker length and the greater the planarization of the compound the worse the solubility is. The characterization of **3Ae**, **3Ba-e**, **3Bh**, **3Bi**, **3Ca-d**, **3Da-d**, **3Ea**, **3Ee**, **3Eh**, **3Ei**, **3Fa**, **3Fe**, **3Fh** and **3Fi** was performed by  $^1\text{H}$  /  $^{13}\text{C}$ -NMR spectroscopy and MALDI-TOF MS analysis. All data are consistent with the proposed structural formulations.

Linker precursor like 2,5-dibrominated thiophene-, bi-, ter- and quaterthiophenes **2A-D** were synthesized according to literature[19–21], while fused thiophene derivatives **2E,F** were obtained by a procedure as described by Frey.[22] The synthesis of the required TPA boronic esters **1a-d,f,g** precursor for Suzuki cross-coupling was also described previously by our group.[16] All efforts to produce sterically hindered cap **1e** via the same classical methods (eg. Ullman-condensation, Buchwald-Hartwig amination) as applied before failed. For instance, typical Ullman conditions using 4-bromoaniline and 2-iodotoluene with either CuCl/phenanthroline or  $\text{CuSO}_4 \cdot 5\text{H}_2\text{O}/\text{K}_2\text{CO}_3$  yielded only trace amounts of the desired N-(4-bromophenyl)-bis(2-methylphenyl)benzeneamine. Hence an alternative synthetic protocol starting from 2-bromotoluene and 2-methylaniline was developed. Again Ullman and Buchwald-Hartwig based attempts failed we started investigating a route including a nucleophilic aromatic substitution step toward **5b** (Scheme 1, Table 1).



**Scheme 1.** Synthetic pathway toward **4** i): KOtBu, (IPr)Pd(allyl)Cl, reflux, and **5a-b** ii): nucleophilic aromatic substitution, details are given in table 1.

Entry	X	Y	reagent	product-Y
1	F	Br	Cs <sub>2</sub> CO <sub>3</sub> /K <sub>2</sub> CO <sub>3</sub>	-
2	F	Br	NaH	-
3	F	NO <sub>2</sub>	Cs <sub>2</sub> CO <sub>3</sub> /K <sub>2</sub> CO <sub>3</sub>	-
4	F	NO <sub>2</sub>	NaH	74%(isol.)

**Table1.** Synthetic attempts towards **5a** and **5b**.

Substrate/base combinations directly aiming for the target compound **5a** (entry 1, 2) were investigated. Since these attempts were not successful, more activated substrates were chosen as starting materials applying bases with different strength (entry 3, 4). Compound **5b** could be obtained in a multigram approach in 74% yield by nucleophilic aromatic substitution applying 4-fluoronitrobenzen and sodium hydride as base. However, it is noteworthy to mention that the use of DMF as solvent is mandatory, as parallel experiments with DMSO showed inferior results.

Having the nitro compound **5b** in hand the desired boronic ester derivative **1e** was obtained by following a straight forward route using reduction[23] applying SnCl<sub>2</sub>, diazotization and conversion of the obtained amide to the iodo species followed by Miyaura borylation.[24] The obtained final compounds were all solid materials appearing yellow to red in color. Solubility strongly depends on linker length and planarization of the cap. In general, the higher the linker length and the greater the planarization of the compound the worse the solubility is. The characterization of **3Ae**, **3Ba-e**, **3Bh**, **3Bi**, **3Ca-d**, **3Da-d**, **3Ea**, **3Ee**, **3Eh**, **3Ei**, **3Fa**, **3Fe**, **3Fh** and **3Fi** was performed by <sup>1</sup>H / <sup>13</sup>C-NMR spectroscopy and MALDI-TOF MS analysis. All data are consistent with the proposed structural formulations.

### 2.3. Molecular structures

Single crystals of compounds **3Ad** and **3Bd** were obtained by slow evaporation of solvent from saturated cyclohexane solutions. The crystal structures of **3Ad** and the cyclohexane solvate of **3Bd** were determined by single crystal diffraction (Figure 4). Table 2 summarizes the angles between the phenyl rings of the triphenylamine moieties linked to the aromatic thiophene cores and the thiophene linker of these compounds. In this table also a comparison of angles with those of compounds **3Aa**, **3Ba** and **3Bb** is given, for which structural characterizations have already been published.[7] The benzene/thiophene angles feature a large variance, ranging from a virtually coplanar benzene/thiophene pair in **3Aa** [1.21(8) °] to significantly the twisted pair in **3Ba** [26.13(7) °]. They may be very different in the same molecule [**3Aa**: 1.21(8) ° vs. 19.60(8) °] or identical in molecules located on twofold

rotation axes or centers of inversion [**3Ad**, **3Ba**]. The geometric parameters of **3Ba** were determined in two solvatomorphs (MeOH and CD<sub>2</sub>Cl<sub>2</sub>) with a total of four crystallographically independent molecules. The large variance of the benzene/thiophene angle in even this case demonstrates that packing effects are dominant.

The thiophene/thiophene twist angles in the bithiophene compounds feature an even more pronounced variance, ranging from perfectly coplanar in the **3Ba** molecules, which are symmetric by inversion, to 33.05(8) ° in **3Bb**.

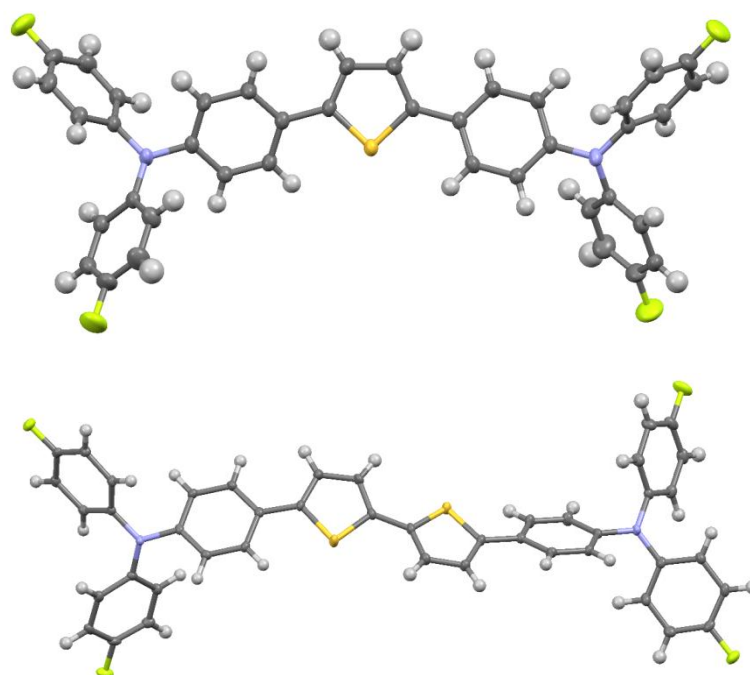


**Figure 4.** Molecular structures of **3Ad** (top) and **3Bd** (bottom). C, N, F and S atoms are represented by gray, blue, green and yellow ellipsoids drawn at the 50% probability levels. H atoms are represented by white spheres of arbitrary radius.

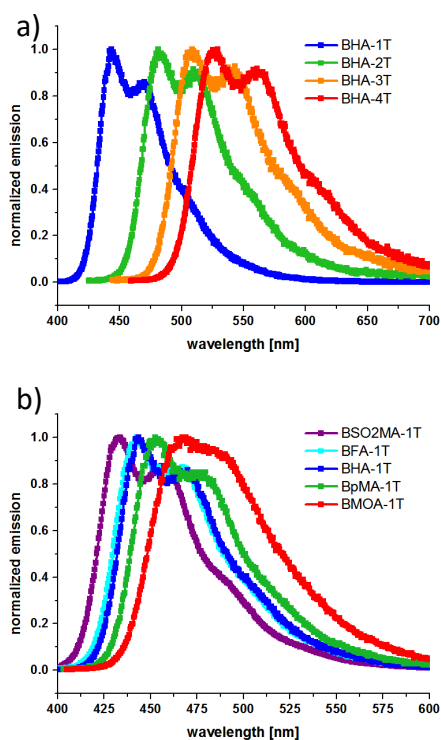
Crystal structure	Benzene / Thiophene	Benzene / Thiophene	Thiophene / Thiophene	Reference
<b>3Aa</b>	19.60(8)	1.21(8)	-	[7]
<b>3Ad</b>	16.43(6)	16.43(6) <sup>1</sup>	-	this work
<b>3Ba</b> ·MeOH	25.81(18)	25.81(18) <sup>2</sup>	0 <sup>2</sup>	[25]
<b>3Ba</b> MeOH	7.90(16)	7.90(16) <sup>2</sup>	0 <sup>2</sup>	[25]
<b>3Ba</b> ·CD <sub>2</sub> Cl <sub>2</sub>	14.64(7)	14.64(7) <sup>2</sup>	0 <sup>2</sup>	[26]
<b>3Ba</b> ·CD <sub>2</sub> Cl <sub>2</sub>	26.13(7)	26.13(7) <sup>2</sup>	0 <sup>2</sup>	[26]
<b>3Bb</b>	19.96(8)	6.76(8)	33.05(8)	[27]
<b>3Bd</b> ·cyclohexane	12.52(8)	24.34(8)	12.52(8)	this work

**Table 2.** Torsion angles between the least squares planes defined by the atoms in the central aromatic rings of the title compounds in °. The molecules in crystal structures with two independent molecules are listed in separated rows. <sup>1</sup>Molecule located on a twofold rotation axis; <sup>2</sup>Molecule located on a center of inversion

## 2.4. Photophysical properties

As a first step of photophysical characterization fluorescence spectra in solution were recorded. These data are in particular interesting for potential OLED application, as it has been demonstrated (e.g. for BMA-nT)[28] that photoluminescence spectra from solutions give a good first approximation for the electroluminescence spectra emitted by an OLED fabricated with this respective compound.

It's noteworthy to mention that all compounds show very little overlap between absorption and emission curves, indicating a very low self-absorption of the materials in the region of maximum emission intensity, which is beneficial for quantum efficiency (luminance properties).



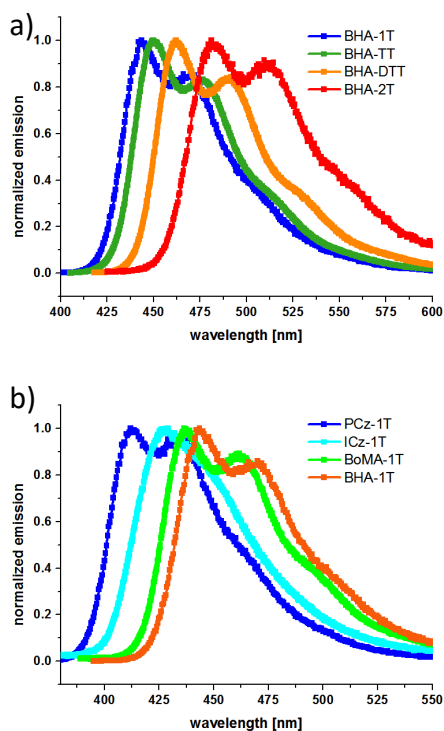
**Figure 5.** Overlay of fluorescence emission spectra of selected compounds recorded from 1  $\mu\text{M}$  THF solution. a) BHA-1-4T; b) BSO2MA-1T, BFA-1T, BHA-1T, BpMA-1T and BMOA-1T.

Figure 5a illustrates an overlay of the emission spectra for compounds BHA-1-4T and thus demonstrates the influence of the repetitive thiophene units. As expected two trends within oligomere series are confirmed by the experimental data; i) there is a correlation between the bathochromic shift and the conjugation length of the linker system; ii) the extend of the bathochromic shift decreases with the number of thiophene units.

Next the variation of the electronic properties of the cap is investigated, while keeping the linker constant (Figure 5b). Defining BHA-1T as a reference ( $\lambda_1=444$  nm) the influence of  $\pm M$  and  $\pm I$  substituents was analyzed. Consistently, electron withdrawing groups (SO2Me, F) exhibit a hypsochromic shift whereas electron donating (Me, OMe) groups induce a bathochromic shift. Since inductive effects are always weaker than mesomeric ones, this fact is also being reflected in the magnitude of the spectral shift in regard to the reference. Surprisingly, the fluorine substituent (having an  $-I$  effect) exhibits only a negligible impact on the emission maximum ( $\lambda_1=442$  nm) compared to the  $+I$  substituent (Me,  $\lambda_1=453$  nm).

To explore other means of color tuning, planarization and deplanarization of the linkers (Figure 6a) as well the caps (Figure 6b) was investigated. In comparison to figure 5a the effect of increasing the number of  $\pi$ -electron pairs within the linker unit from three (thiophene) to five (thienothiophene) only slightly increases the bathochromic shift (+6 nm). In contrast, the next analogue of the fused linker series, dithienothiophene which counts seven  $\pi$ -electron pairs, has an emission maximum shifted by +19 nm and +13 nm compared to BHA-1T and BHA-TT respectively.

Interestingly, the compound comprising the bithiophene linker which is bearing six  $\pi$ -electron pairs, is far more red shifted compared to BHA-1T than the one containing the diethienothiophene linker (+37 nm vs. +6 nm). This is remarkable since one would expect the reverse order as diethienothiophene exhibits an elongated  $\pi$ -electron system.



**Figure 6.** Overlay of fluorescence emission spectra of selected compounds recorded from 1  $\mu$ M THF solution. a) BHA-1T, BHA-TT, BHA-DTT and BHA-2T; b) PCz-1T, ICz-1T, BoMA-1T, and BHA-1T.

The results of planarized (ICz and Cz) and deplanarized (oMe) caps on the spectral properties of the same linker system are shown in figure 6b in comparison to the reference compound BHA-1T. A clear tendency amongst all investigated compounds bearing planarized PCz and fully planarized ICz for a hypsochromic shift compared to compounds with caps exhibiting a higher degree of freedom (BHA and BoMA) can be observed. The partially planarized cap systems PCz shows a larger blue shift than the corresponding fully planarized ICz bearing compound. The most red shifted spectra are observed for the BHA caps followed by the sterically demanding cap systems BoMA. UV and fluorescence spectra of all compounds are given in the supporting information.



compound	$\lambda_1$	$\lambda_2$	$\lambda_3$	$\lambda_{SS-PCM}$	$\lambda_{sim}$	$\lambda_{OLED}$	$\lambda_{SS-PCM} - \lambda_3$	$\lambda_1 - \lambda_{sim}$	$\lambda_{OLED} - \lambda_1$	
BHA-1T	<b>3Aa</b>	444	468	456	455	437	491	-1	7	47
BHA-2T	<b>3Ba</b>	481	510	496	498	494	536	3	-13	55
BHA-3T	<b>3Ca</b>	507	542	525	527	509	566	3	-2	59
BHA-4T	<b>3Da</b>	527	560	544	545	531	606	2	-4	79
BpMA-1T	<b>3Ab</b>	453	480	467	464	451	496	-2	2	43
BpMA-2T	<b>3Bb</b>	488	516	502	507	488	541	5	0	53
BpMA-3T	<b>3Cb</b>	514	545	530	534	517		5	-3	
BpMA-4T	<b>3Db</b>	529	564	547	551	551		5	-22	
BMOA-1T	<b>3Ac</b>	471	485	478	475	455		-3	16	
BMOA-2T	<b>3Bc</b>	499	522	511	516	491		5	8	
BMOA-3T	<b>3Cc</b>	521	551	536	542	534		6	-13	
BMOA-4T	<b>3Dc</b>	540	568	554	557	557		3	-17	
BFA-1T	<b>3Ad</b>	442	465	454	455	440	488	1	2	46
BFA-2T	<b>3Bd</b>	478	507	493	497	482		5	-4	
BFA-3T	<b>3Cd</b>	503	538	521	526	509		5	-6	
BFA-4T	<b>3Dd</b>	522	557	540	544	548		5	-26	
BCNA-1T	<b>3Ag</b>	434	456	445	338			-107		
BSO2MA-1T	<b>3Af</b>	434	456	445	441	442				
BoMA-1T	<b>3Ae</b>	437	462	450	447	423	483	-2	14	46
BoMA-TT	<b>3Ee</b>	446	472	459	457	465		-2	-19	
BoMA-2T	<b>3Be</b>	477	509	493	495	468		2	9	
BoMA-DTT	<b>3Fe</b>	457	489	473	468	459		-5	-2	
PCz-1T	<b>3Ah</b>	412	433	423	419	414	466	-3	-2	54
PCz-TT	<b>3Eh</b>	420	445	433	428	427		-4	-7	
PCz-2T	<b>3Bh</b>	450	479	465	464	461		0	-11	
PCz-DTT	<b>3Fh</b>	434	460	447	440	436		-7	-2	
ICz-1T	<b>3Ai</b>	427	-	427	415	408	549	-12	19	
ICz-TT	<b>3Ei</b>	429	444	437	425	408		-12	21	
ICz-2T	<b>3Bi</b>	458	486	472	466	466		-6	-8	
ICz-DTT	<b>3Fi</b>	436	461	449	439	429		-10	7	
BHA-TT	<b>3Ea</b>	450	477	464	463	464	500	0	-14	50
BHA-DTT	<b>3Fa</b>	463	491	477	473	465	541	-4	-2	78

**Table 3.** Photoluminescence data of all final compounds.  $\lambda_1$  = highest energy maximum of solution fluorescence;  $\lambda_2$  = lowest energy maximum of solution fluorescence;  $\lambda_3$  = mean of  $\lambda_1$  and  $\lambda_2$ ;  $\lambda_{SS-PCM}$  = calculated vertical emission;  $\lambda_{sim}$  = maximum of simulated spectrum;  $\lambda_1 - \lambda_{sim}$  refer to THF solutions;  $\lambda_{OLED}$  = maximum of OLED emission; all values in nm.

The building block like influence of individual cap and linker systems are depicted in table 4. This table is intended as a guideline for predicting certain trends, e.g. for the calculation of the emission of BMOA-4T table 4 reads +18 nm as a contribution from BMOA and additional +77 nm from the linker elongation to four thiophene units. When both increments are added to the reference emission of BHA-1T ( $\lambda_1=444$  nm), the result of 539 nm is in very good agreement with the experimentally obtained value of 540 nm. As only selected cap-linker combinations were synthesized and tested, one must be careful when applying these empirical increments to combinations outside the scope of this library. However, data of table 4 suggests that variation of cap and linker contribute independently to the observed emission shift based on the reference BHA-1T.

Caps		Linkers	
BMA	+ 6 ± 2 nm	2T	+ 34 ± 3 nm
BMOA	+ 18 ± 5 nm	3T	+ 59 ± 5 nm
BFA	- 4 ± 1 nm	4T	+ 77 ± 5 nm
BoMA	- 5 ± 1 nm	TT	+ 5 ± 3 nm
PCz	- 30 ± 1 nm	DTT	+16 ± 6 nm
ICz	- 22 ± 4 nm		

**Table 4.** Empirically obtained increments for the shift of the fluorescence maximum  $\lambda_1$  (from table 3) for various linkers and caps in respect to cap-reference BHA and linker reference T.

## 2.5. Theoretical calculations

In our previous study we developed a reliable procedure for the prediction of emission spectra of bis(aminophenyl)-substituted thiophene derivatives.[7] While the initial development was mainly based on simple model compounds, we also applied the complete procedure to one individual larger molecule in order to test the scope of the method. Inspired by the promising results, we are now expanding the predictive tools to a much broader set of real OLED compounds.

To get first insight on the molecular structures, ground state and first excited state geometries were optimized by means of density functional theory (DFT) and time-dependent (TD) DFT calculations using a combination of M06-2X functional[29] and the polarized double zeta SVP basis set.[30] This parametrization showed superior results[7] when compared to other functionals (e.g. B3LYP[31,32] and PBE0[33,34]). All ground and excited state minima were verified by normal mode analysis. In figure 7 the optimized geometries of both ground state ( $S_0$ ) and the first excited state ( $S_1$ ) of selected compounds BHA-3T, PCz-1T, ICz-1T and ICz-DTT are presented. Two observations are prominent when analyzing the molecular structures. An increasing curvature of the oligothiophene linkers in the 1-4T series is seen for  $S_0$  geometries while in contrast the molecules' central core (thiophene units and the two adjacent phenyl rings) is being completely planarized in  $S_1$ . This holds true also for

the other compounds, resulting in the case of ICz-derivatives in a completely planarized structure in  $S_1$ . For comprehensive illustration of additional compounds and their  $S_0$  and  $S_1$  geometries see supporting information.

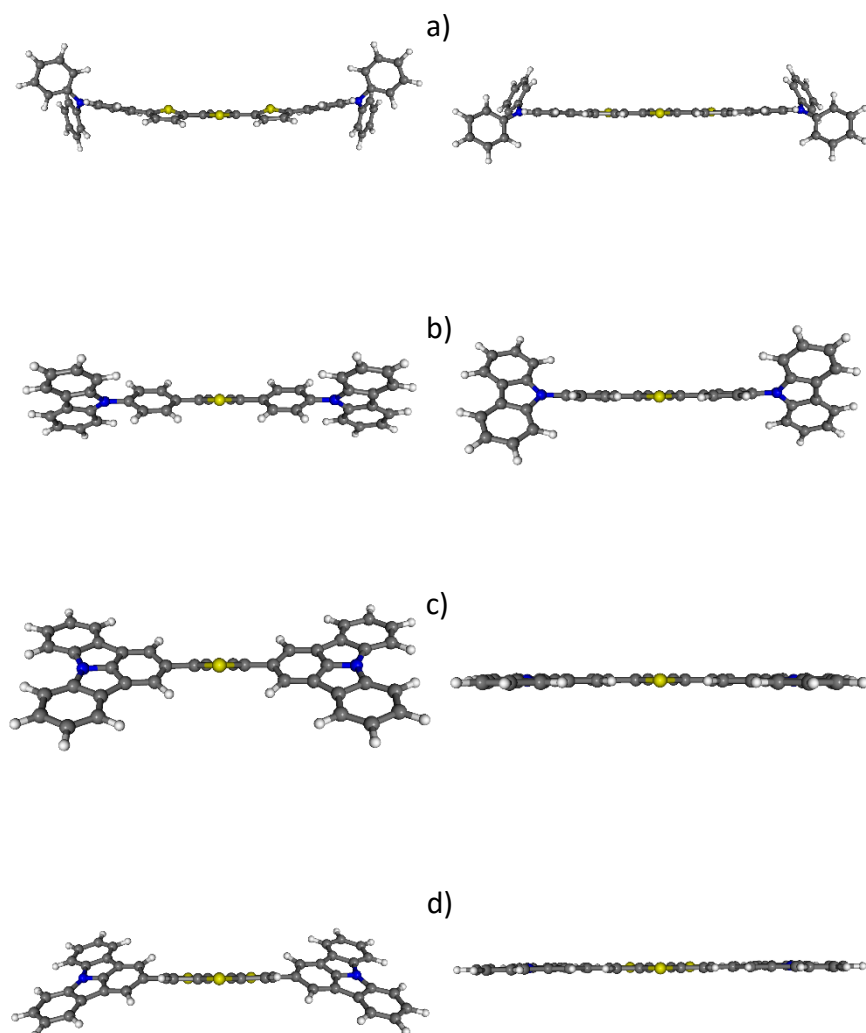


**Figure 7.** Optimized geometries of BHA-3T (a), PCz-1T (b), ICz-1T (c) and ICz-DTT (d) (M06-2X/SVP, LR-PCM/THF); left:  $S_0$ , right  $S_1$ .

Molecular orbital distributions of  $S_0$  for selected compounds BHA-1T, BMOA-1T, BMSO2A-1T, PCz-1T and ICz-1T are shown in figure 8. For all compounds, the HOMO is distributed over the entire molecule. The effect of the electron donating/withdrawing groups is clearly visible, resulting in a higher/lower electron density in the outer phenyl rings of the caps in BMOA-1T/BMSO2A-1T, respectively. In the case of the partially planarized PCz cap, an almost uniform distribution of the electron density is obtained. In contrast, ICz-1T does not exhibit this uniformity, as the electron density is decreased on the phenyl rings not directly connected to the thiophene linker.

Generally, the LUMOs are predominantly localized on the central core of the molecules (thiophene linker plus the adjacent phenyl rings). However, in the case of fully planarized ICz bearing compounds the LUMO is exclusively localized on the ICz moiety. This finding is in agreement with our previous studies on ICz containing compounds, where it was shown that ICz is not necessarily an electron donor, but also exhibits electron accepting properties.[35–37]

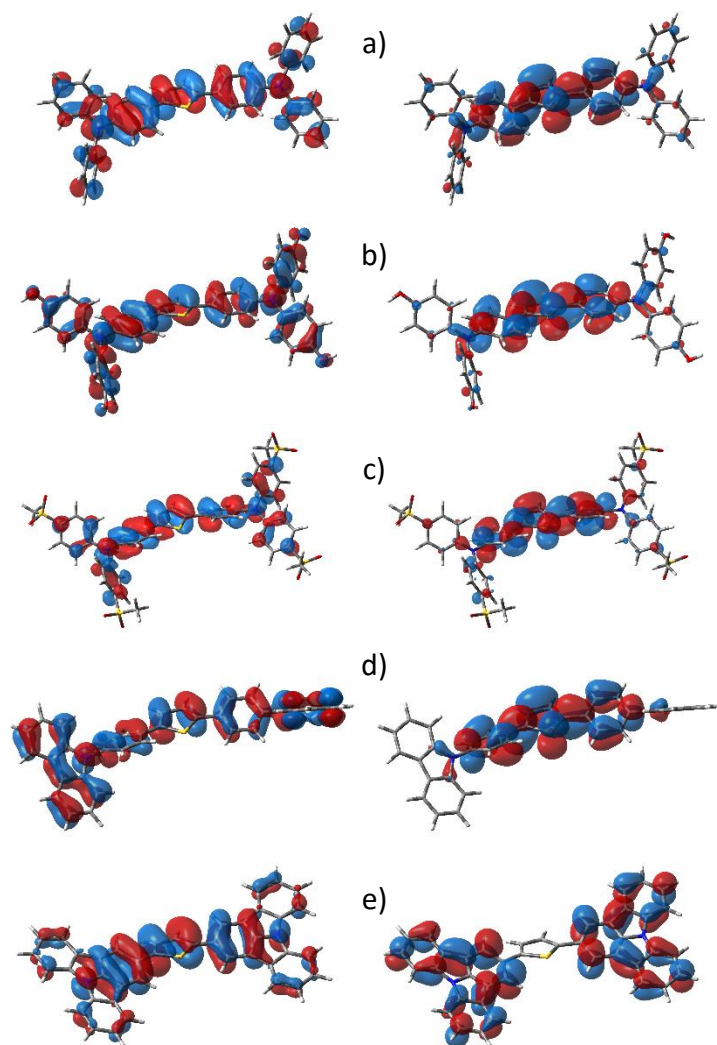


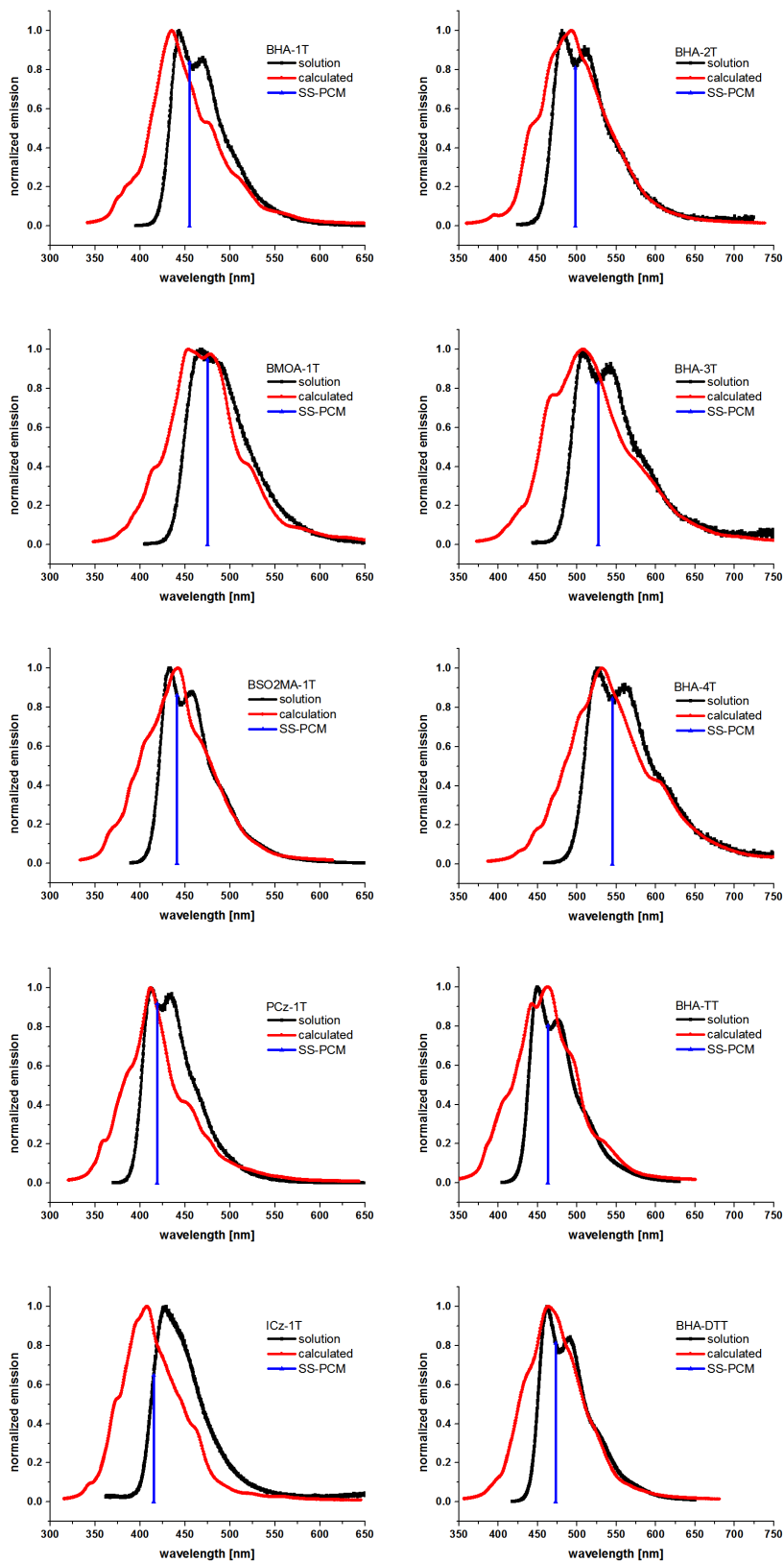
**Figure 8.** Molecular orbital plots for selected compounds BHA-1T (a), BMOA-1T (b), BMSO2A-1T (c), PCz-1T (d) and ICz-1T (e) (M06-2X/SVP, LR-PCM/THF); left: HOMO, right LUMO.

For additional HOMO/LUMO plots, the interested reader is referred to the supporting information.

To make computational results comparable with experimental data it is imperative to consider solvent effects, hence they were included through the polarizable continuum model (PCM)[38] in its linear response (LR-PCM)[39] and state specific (SS-PCM)[40] formulations, always considering the equilibrium time regime (eq) for the excited state. Within the method development we have shown that the SS-PCM model is clearly superior to the

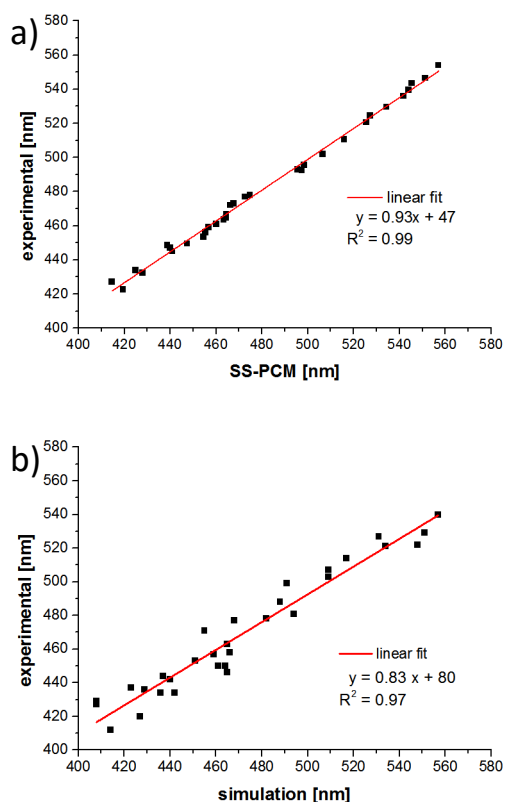
LR-PCM. As already observed[7], the computed vertical emissions using SS-PCM are always in between the two maxima of the recorded spectra in THF solutions (Table 3). These results being very promising, we intended to include the SS-PCM correction also in the spectra simulation. However, as Newton-X (version 1.2.4.) is somehow limited to the LR-PCM model, spectra were first simulated including the vibrational broadening with this model first using a Wigner distribution formalism, as described in Ref.[41] applying a phenomenological broadening of  $\delta = 0.1$  eV. Taking the output of the frequency computations of  $S_1$  as the source of the normal modes, this information is used to generate a set of non-equilibrium geometries with a selectable number of data points, in these particular cases 250. At each point the  $S_1 \rightarrow S_0$  excitation energy was calculated using the M06-2X/SVP parametrization at TDDFT level of theory applying LR-PCM solvent correction. It is noteworthy to mention that these are all independent single point energy calculations which can easily be distributed to a large number of compute nodes making this step very fast. After computation of all emission energies the data is combined to construct a vibrationally broadened spectrum, already having solvent effects at LR-PCM level included. However, as further improvement of the methodology, we now added the SS-PCM as a post processing correction consecutive to the spectrum simulation by NEWTON-X. In order to achieve this, a rather simple but nevertheless effective approach was chosen. We made the assumption that the energy difference between the LR-PCM and SS-PCM approach is constant for all the 250 geometries used for spectra simulation throughout the whole spectral range (which of course is a simplification of the model). Hence, the results of the single point calculations performed within the framework of NEWTON-X were in turn corrected by the difference between LR- and SS- results calculated for the vertical emission at the  $S_1$  equilibrium geometry. Finally, spectra are obtained which both include the more accurate SS-PCM correction as well as the vibrational broadening (Figure 9). To conclude, a robust procedure for the fluorescence spectra simulation of medium to large size oligothiophene derivatives is now available and is in turn benchmarked against experimental data, ultimately leading towards a powerful tool for predicting structure property relationships.

Figure 9 illustrates the comparison between computational results (both vertical emissions and simulated spectra) and experimentally obtained fluorescence spectra (for the complete set of data, the reader is referred to table 3, while all comparison graphs can be found in the supporting information). In left column the influence of the electronically and sterically altered cap systems is shown, while in the right column the effect of linker alteration is demonstrated. Generally spoken all results indicate a good agreement between experimental and computational data. As mentioned above the calculated vertical emissions (SS-PCM) are always located in between the two emission maxima, except for some ICz bearing compounds.



**Figure 9.** Selected examples for the comparison of experimental and computational results; solution refers to fluorescence measured in 1  $\mu\text{M}$  THF solution, calculated refers to the spectra simulation and SS-PCM refers to the vertical emission.

Also the spectral simulations match nicely with the experimental spectra, however while the red onset of the spectral simulation fits very well with the measurements, the blue part is somehow overestimated in the simulation. In figure 10 the correlation between experimental data and computational results and is analyzed for the entire data set. Each data point represents one compound; calculated values are plotted on the x-axis, while the experimental data are plotted on the y-axis. The resulting graphs show clear linear trends covering all compounds and their emission characteristics under investigation.



**Figure 10.** Correlation between experimental data and computational results a) SS-PCM refers to  $\lambda_{\text{SS-PCM}}$ ; experimental refers to  $\lambda_3$ ; b) simulated maximum refers  $\lambda_{\text{sim}}$ ; experimental maximum refers to  $\lambda_1$ .

As seen in the graphs the deviation between experimental and computational results is very small. Table 3 reads an average deviation of only  $\pm 4$  nm (maximum discrepancy -12 nm) when comparing the mean of the experimental emission maxima with results of SS-PCM calculations ( $\lambda_{\text{SS-PCM}} - \lambda_3$ ). The average deviation increases to  $\pm 9$  nm (maximum discrepancy -26 nm) when the maxima of the experimental emission are compared to the simulated maxima (Table 3,  $\lambda_1 - \lambda_{\text{sim}}$ ). These results strengthen our confidence in the power of this methodology to accurately predict emission spectral properties covering a large variety of different compounds, composed of miscellaneous structural motifs only by means of computational chemistry.

In order to obtain more application relevant data, emission spectra from OLEDs, fabricated using a selected subset of compounds, were recorded and compared to both experimental and simulated spectra. Some graphs are shown in figure 11, for additional graphs the reader is referred to the supporting information.

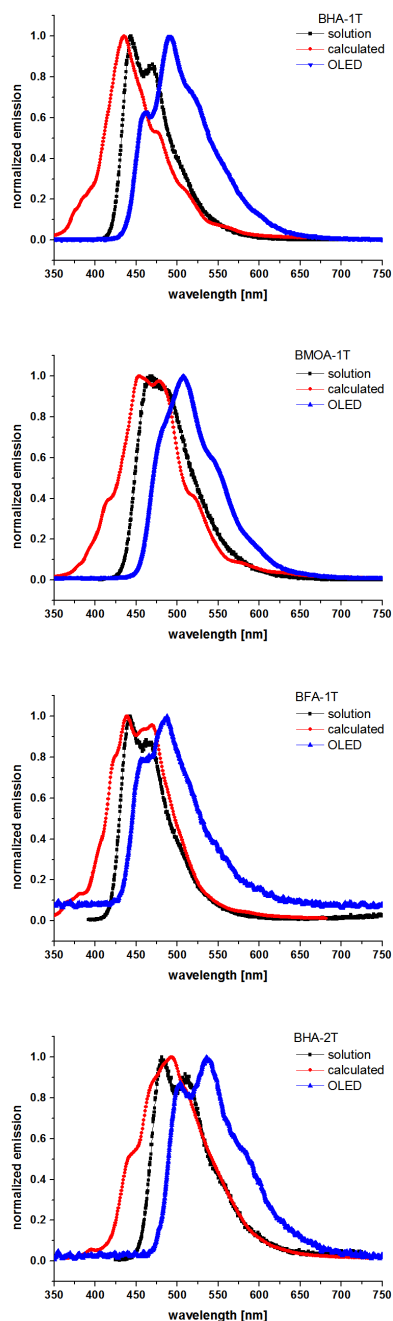


**Figure 11.** Selected examples for the comparison of experimental (solution and OLED) and simulated fluorescence spectra. Solution refers to fluorescence measured from 1  $\mu$ M THF solution.



The same influence of cap substitution and linker extension on the fluorescence spectra can be observed for the solid state spectra as it was already determined for the solution based spectra. This is illustrated graphically in figure 12a. However, the OLED spectra show a relatively constant red shift of about  $+55 \pm 12$  nm in respect to the solution based emissions. Figure 12b demonstrates the correlation between simulated and OLED spectra in comparison to the correlation between simulated and solution spectra. This is of great value for material design since the simulation can now be also used for the estimation of the OLED spectra when considering a constant shift has to be added to the simulation value.

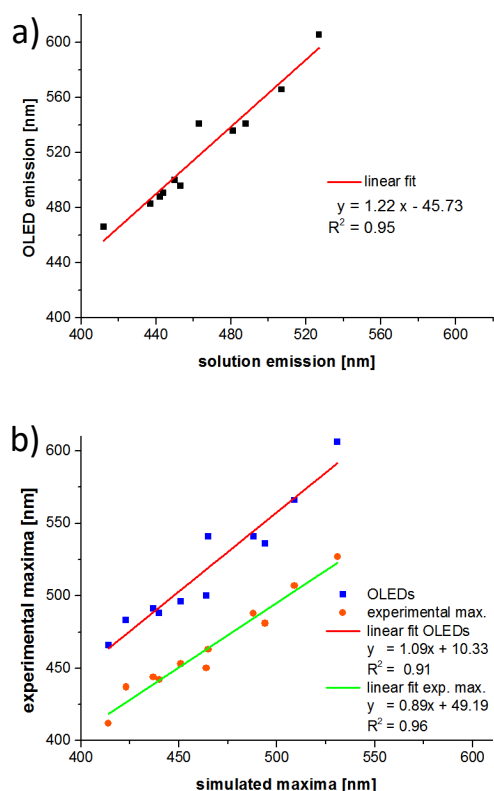


**Figure 12.** a) Correlation between OLED- and solution emissions ( $\lambda_{\text{OLED}}$  vs.  $\lambda_1$ ); b) correlation between simulated and OLED spectra in comparison to the correlation between simulated and solution spectra ( $\lambda_{\text{OLED}}$  vs.  $\lambda_{\text{Sim}}$  and  $\lambda_1$  vs.  $\lambda_{\text{Sim}}$ ).

### 3. Conclusion

In summary, 5 possibilities of color tuning for cap-linker-cap type OLED materials were investigated by means of a combined experimental and theoretical approach. The individual building blocks used for synthesis offer the possibility to alter both electronic (electron donating/withdrawing groups, extension of the pi-system) and steric (planarization and deplanarization) properties of the resulting compounds. Final materials were characterized regarding their photo physical properties in addition to the implementation of selected compounds into OLED devices. In parallel to experimental work, a recently presented computational method was further optimized in order to predict and simulate the entire emission spectra of organic compounds, meaning that not only the vertical emission is calculated, but additionally the vibrational broadening is considered. The obtained experimental data set was in turn used to benchmark these calculations. While the red onset of the spectral simulation fits very well with the measurements, the blue part is somehow overestimated in the calculation.

Overall good agreement was observed when comparing solution fluorescence spectra with the respective simulations. This consistency also holds true when comparing solid state OLED spectra with simulated solution spectra if a constant shift of ~ 55 nm is considered. We therefore feel confident to have a powerful tool in hand to rationally guide future synthesis by means of quantum chemical calculations in order to reduce synthetic efforts in the field of OLED research.

### 4. Acknowledgement

JB is grateful for the Marietta Blau Grant of the OeAD. Andreas Gaubitzer, Barbara Pokorny, Christian Aumayer are gratefully acknowledged for their synthetic help.

### 5. Materials and methods

#### 5.1. General information

Substances purchased from commercial sources were used as received without further purification.. 2-Methylaniline, 2-bromotoluene, 4-fluoronitrobenzene and pinacolborane were purchased from Apollo Scientific. Allyl[1,3-bis(2,6-diisopropylphenyl)imidazol-2-ylidene]chloropalladium(II) ((IPr)Pd(allyl)Cl, CAS 478980-03-9),[42] [1,1'-bis(diphenylphosphino)ferrocene]dichloro-palladium(II) (PdCl<sub>2</sub>(dppf), CAS 72287-26-4),[43] 2,5-dibromothiophene (CAS 3141-27-3),[20] 5,5'-dibromo-2,2'-bithiophene (CAS 4805-22-5),[19] 2,5-dibromothiopheno[3,2-*b*]thiophene,[44] 5,5'-dibromo-2,2':5',2''-terthiophene,[21] 2,6-dibromodithieno[3,2-*b*:2',3'-*d*]thiophene (CAS 67061-69-2)[45] and 5,5'''-dibromo-

2,2':5',2'':5'',2'''-quaterthiophene, *N,N*-Bis(4-fluorophenyl)-4-(4,4,5,5-tetramethyl-1,3,2-dioxaborolan-2-yl)benzene-amine,[15] 2-(4,4,5,5-tetramethyl-1,3,2-dioxaborolan-2-yl)indolo[3,2,1-*jk*]carbazole[18] and 9-[4-(4,4,5,5-tetramethyl-1,3,2-dioxaborolan-2-yl)phenyl]-9*H*-carbazole[46,47] were synthesized according to literature. 4,4'-(2,5-Thiophenediyl)bis[*N,N*-diphenylbenzenamine], 4,4'-(2,5-thiophenediyl)bis[*N,N*-bis(4-methylphenyl)benzenamine], 4,4'-(2,5-thiophenediyl)bis[*N,N*-bis(4-fluorophenyl)benzenamine], 4,4',4',4'''-[2,5-thiophenediylbis(4,1-phenylene)dinitrilo] tetrakis[benzonitrile] and 4,4'-(2,5-thiophenediyl)bis[*N,N*-bis[4-(methylsulfonyl)phenyl]benzenamine] were synthesized as described previously.[48] Anhydrous *N,N*-dimethylformamide was purchased from Aldrich Chemical Co. Anhydrous dioxane was prepared immediately prior to use by a PURESOLV-plant (it-innovative technology inc.). Isopropylalcohol (IPA), acetonitrile (ACN) and dimethylsulfoxide (DMSO) were used in p.a. quality. Technical grade solvents (dichloromethane (DCM)) were distilled prior to use. Anhydrous solvents were prepared by filtration through drying columns. Analytical TLC was performed on Merck silica gel 60 F254 plates. Chromatographic separations at preparative scale were carried out on silica gel (Merck silica gel 60, 40 - 63  $\mu\text{m}$ ). Nuclear magnetic resonance (NMR) spectra were obtained using a Bruker DPX-200 or Avance DRX-400 fourier transform spectrometer operating at the following frequencies: DPX-200: 200.1 MHz ( $^1\text{H}$ ) and 50.3 MHz ( $^{13}\text{C}$ ); DRX-400: 400.1 MHz ( $^1\text{H}$ ) and 100.6 MHz ( $^{13}\text{C}$ ). The chemical shifts are reported in delta ( $\delta$ ) units, parts per million (ppm) downfield from tetramethylsilane using solvent residual signals for calibration. Coupling constants are reported in Hertz; multiplicity of signals is indicated by using following abbreviations: s=singlet, d=doublet, t=triplet, q=quartet. The multiplicity of  $^{13}\text{C}$  signals was obtained by measuring JMOD spectra. UV-Vis absorption spectra and fluorescence emission spectra were recorded in THF solutions (1  $\mu\text{g}/\text{mL}$ ) with a Perkin Elmer Lambda 750 spectrometer and an Edinburgh FLS920, respectively. High-resolution mass spectra (HRMS) were acquired as radical cations using either a SYNAPT HDMS instrument (Waters, Manchester, UK) equipped with a matrix-assisted laser desorption/ionization (MALDI) source or a Thermo Scientific LTQ Orbitrap XL hybrid FTMS (Fourier Transform Mass Spectrometer) equipped with Thermo Fischer Exactive Plus Orbitrap (LC-ESI+) and a Shimadzu IT-TOF Mass Spectrometer. Samples for MALDI-HRMS were applied at 1  $\text{mg}/\text{mL}$  in THF on stainless steel using nitroanthracene (3  $\text{mg}/\text{mL}$  in THF) as MALDI matrix. In case of solubility the sample was further diluted to approx. 50  $\text{pg}/\mu\text{L}$ . In case of undissolved samples the slurry was centrifuged and the supernatant and the residue was used for MALDI-qTOF-MS analysis. 1  $\mu\text{L}$  of the sample or residue/chloroform slurry was deposited on a stainless steel target and dried at room temperature. The samples were measured by laser desorption/ionization (LDI) on a Synapt HDMS G2 (Waters, UK) using a 200Hz YAG laser in V-mode. All MS spectra were

recorded as accurate mass data with angiotensin II ( $m/z = 1046.542$ ) as internal lock mass achieving a mass accuracy of 15 - 40 ppm (i.e.  $\Delta m/z = 0.01 - 0.04$  amu).

X-ray Structure Determination. Crystals of **3Ad** (CCDC#1473931) and the cyclohexane solvate of **3Bd** (CCDC#1476440) were grown by slow evaporation of solutions in cyclohexane. X-ray diffraction data were collected at  $T = 180$  K (**3Ad**) and  $T = 100$  K (**3Bd**) in a dry stream of nitrogen Bruker Smart APEX (**3Ad**) and Kappa APEX II (**3Bd**) diffractometer systems using graphite-monochromatized Mo- $K\alpha$  radiation ( $\lambda = 0.71073$  Å) and fine sliced  $\phi$ - and  $\omega$ -scans. Data were reduced to intensity values with SAINT and an absorption correction was applied with the multi-scan approach implemented in SADABS.[47] The structures were solved by charge flipping implemented in SUPERFLIP[48] and refined against  $F$  with JANA2006.[49] Non-hydrogen atoms of the title molecules were refined anisotropically. The C atoms of the cyclohexane solvent molecule, which is disordered around a center of inversion, were refined with isotropic displacement parameters. The H atoms were placed in calculated positions and thereafter refined as riding on the parent atoms. Molecular graphics were generated with the program MERCURY.[50]

Bottom emitting OLEDs were fabricated via thermal evaporation onto clean glass pre-patterned indium tin oxide (ITO) cathodes under high vacuum ( $10E-6$  torr). 50 nm of the novel OLED compounds were evaporated directly onto the ITO-patterned glass at a rate of  $0.6$  Å/s to form the emissive layer where recombination of charge carriers produces luminescent photons. A 15 nm thick layer of Bathocuproine (BCP) was then deposited at a rate of  $0.3$  Å/s as a hole blocking layer. Following this, 35 nm of Tris (8-hydroxyquinolino) aluminum (AlQ<sub>3</sub>) was deposited at a rate of  $0.6$  Å/s as the electron transport layer. Finally, the cathode consisted of 1 nm LiF, evaporated at  $1$  Å/s, followed by Aluminum, evaporated at  $0.8$  Å/s. A schematic layout of the devices is given in the supporting information. The devices were powered using a Keithly 2400 source measurement unit, and the spectrum was recorded with a USB-4000 spectrometer.

## 5.2. Synthetic Details

General procedure for the synthesis of **3Ae**, **3Ah**, **3Ai**, **3Ba-e**, **3Bh**, **3Bi**, **3Ca-d**, **3Da-d**, **3Ea**, **3Ee**, **3Eh**, **3Ei**, **3Fa**, **3Fe**, **3Fh** and **3Fi** according to Marion.[49] Under an argon atmosphere, **2A-F** (1.0 eq.), boronic ester (3.0 eq.) and KOtBu (3.0 eq.) were suspended in a 3 : 1 mixture of IPA : H<sub>2</sub>O (degassed by bubbling with argon). A solution of (IPr)Pd(allyl)Cl (0.02 eq.) in degassed IPA was added and the reaction mixture was refluxed, monitoring the conversion by TLC. After completion, the reaction mixture was distributed between water and chloroform; the phases were separated and the aqueous layer was extracted with chloroform three times. The combined organic layer was dried over anhydrous sodium sulfate and the

solvent removed under reduced pressure to give the crude product. Purification was achieved by column chromatography.

#### 2.2.1. 4,4'-(2,5-Thiophenediyl)bis[N,N-bis(2-methylphenyl)benzenamine] (**3Ae**)

According to the general procedure **3Ae** was synthesized applying 2,5-dibromothiophene **2A** (242 mg, 1.0 mmol, 1.0 eq), **1c** (1198 mg, 3.0 mmol, 3.0 eq), KOtBu (337 mg, 3.0 mmol, 3.0 eq) and (IPr)Pd(allyl)Cl (11.4 mg, 20  $\mu$ mol; dissolved in 2 mL IPA). The reaction mixture was refluxed until complete conversion (1 h). After standard workup the crude product was loaded upon silica gel (3 g) and column chromatography (90 g silica gel) using light petroleum : DCM = 10 - 40% followed by crystallization from cyclohexane yielded **3Ae** as bright yellow solid (571 mg, 91%).  $R_f$  = 0.26 (light petroleum : DCM = 2 : 1).

$^1\text{H}$  NMR (400 MHz,  $\text{CD}_2\text{Cl}_2$ )  $\delta$  = 7.42 (4 H, d,  $J$  = 8.8 Hz), 7.23 (4 H, dd,  $J$  = 6.9, 1.61 Hz), 7.08 - 7.18 (10 H, m), 6.99 (4 H, d,  $J$  = 7.3 Hz), 6.63 (4 H, d,  $J$  = 8.8 Hz), 2.05 (12 H, s) ppm.

$^{13}\text{C}$  NMR (100 MHz,  $\text{CD}_2\text{Cl}_2$ )  $\delta$  = 148.5 (s), 146.2 (s), 142.9 (s), 135.4 (s), 132.3 (d), 129.4 (d), 128.0 (d), 127.5 (d), 126.9 (s), 126.5 (d), 125.6 (d), 123.1 (d), 120.2 (d), 19.2 (q) ppm.

MS (MALDI-TOF): calcd for  $\text{C}_{44}\text{H}_{38}\text{N}_2\text{S}$ : 626.2756; found: 626.2611.

#### 2.2.2. 9,9'-(2,5-Thiophenediyl)di-4,1-phenylene]bis-9H-carbazole (**3Ah**)

According to the general procedure **3Ah** was synthesized applying 2,5-dibromothiophene **2A** (480 mg, 2.0 mmol, 1.0 eq), **1h** (2216 mg, 6.0 mmol, 3.0 eq), KOtBu (670 mg, 6.0 mmol, 3.0 eq) and (IPr)Pd(allyl)Cl (23 mg, 20  $\mu$ mol; dissolved in 2 mL IPA) in a mixture of 15 mL IPA :  $\text{H}_2\text{O}$  (3 : 1). The reaction mixture was refluxed until complete conversion (2 h). After standard workup the crude product was loaded upon silica gel (8 g) and column chromatography (90 g silica gel) using light petroleum : DCM = 5 - 30% followed by crystallization from  $\text{CHCl}_3$  yielded **3Ah** as yellow solid (475 mg, 42%).

$^1\text{H}$  NMR (400 MHz,  $\text{CD}_2\text{Cl}_2$ ):  $\delta$  = 8.18 (4 H, d,  $J$  = 7.7 Hz), 7.93 (4 H, d,  $J$  = 8.4 Hz), 7.65 (4 H, d,  $J$  = 8.4 Hz), 7.53 - 7.42 (10 H, m), 7.35 (4 H, t) ppm.

$^{13}\text{C}$  NMR (100 MHz,  $\text{CD}_2\text{Cl}_2$ ):  $\delta$  = 143.6 (s), 141.3 (s), 137.5 (s), 133.7 (s), 128.0 (d), 127.5 (d), 126.6 (d), 125.4 (d), 124.0 (s), 120.8 (d), 120.6 (d), 110.4 (d) ppm.

MS (MALDI-TOF): calcd for  $\text{C}_{40}\text{H}_{26}\text{N}_2\text{S}$ : 566.1817; found: 566.1833.

#### 2.2.3. 2,2'-(2,5-Thiophenediyl)bis(indolo[3,2,1-jk]carbazole (**3Ai**)

According to the general procedure **3Ai** was synthesized applying 2,5-dibromothiophene **2A** (242 mg, 1.0 mmol, 1.0 eq), **1i** (1100 mg, 3.0 mmol, 3.0 eq), KOtBu (337 mg, 3.0 mmol, 3.0 eq) and (IPr)Pd(allyl)Cl (11 mg, 20  $\mu$ mol; dissolved in 2 mL IPA) in a mixture of 40 mL IPA :  $\text{H}_2\text{O}$  (3 : 1). The reaction mixture was refluxed until complete conversion (1 h). After standard workup the product was purified by crystallization from pyridine yielding **3Ai** as yellow solid (489 mg, 87%).

$^1\text{H}$  NMR (400 MHz,  $\text{CD}_2\text{Cl}_2$ )  $\delta$  = 8.44 (4 H, s), 8.23 (4 H, d,  $J$  = 7.9 Hz), 7.97 (4 H, d,  $J$  = 8.2 Hz), 7.62 (4 H, t,  $J$  = 7.6 Hz), 7.54 (2 H, s), 7.42 (4 H, t,  $J$  = 7.5 Hz) ppm.

$^{13}\text{C}$  NMR (100 MHz,  $\text{CD}_2\text{Cl}_2$ )  $\delta$  = 145.7, 139.8, 131.0, 130.4, 127.8, 124.5, 123.9, 122.6, 119.3, 118.3, 113.0 ppm.

MS (MALDI-TOF): calcd for  $\text{C}_{40}\text{H}_{22}\text{N}_2\text{S}$ : 562.1504; found: 562.1453.

#### 2.2.4. 4,4'-(2,2'-Bithiophene-5,5'-diyl)bis(*N,N*-diphenylbenzenamine) (**3Ba**)

According to the general procedure **3Ba** was synthesized applying **2B** (324 mg, 1.0 mmol, 1.0 eq), **1a** (1114 mg, 3.0 mmol, 3.0 eq), KOtBu (337 mg, 3.0 mmol, 3.0 eq) and (IPr)Pd(allyl)Cl (11 mg, 20  $\mu\text{mol}$ ; dissolved in 2 mL IPA) were suspended in a mixture of 15 mL degassed IPA /  $\text{H}_2\text{O}$  (3 : 1). The reaction mixture was refluxed until complete conversion (2 h). After standard workup the reaction mixture was loaded upon silica gel (7 g) and column chromatography (90 g silica gel) using light petroleum : DCM = 15 - 40% followed by crystallization from cyclohexane yielded **3Ba** as yellow crystals (555 mg, 85%).  $R_f$  = 0.19 (light petroleum : DCM = 5 : 1).

$^1\text{H}$  NMR (200 MHz,  $\text{CD}_2\text{Cl}_2$ )  $\delta$  = 7.48 (4 H, d,  $J$  = 8.6 Hz), 7.22 - 7.35 (8 H, m), 7.00 - 7.18 (20 H, m) ppm.

$^{13}\text{C}$  NMR (50 MHz,  $\text{CD}_2\text{Cl}_2$ )  $\delta$  = 148.0 (s), 148.0 (s), 143.4 (s), 136.4 (s), 129.9 (d), 128.4 (s), 126.8 (d), 125.2 (d), 124.9 (d), 124.0 (d), 123.8 (d), 123.5 (d) ppm.

MS (MALDI-TOF): calcd for  $\text{C}_{44}\text{H}_{32}\text{N}_2\text{S}_2$ : 648.1694; found: 648.1630.

#### 2.2.5. 4,4'-(2,2'-Bithiophene-5,5'-diyl)bis[*N,N*-bis(4-methylphenyl)benzenamine] (**3Bb**)

According to the general procedure **3Bb** was synthesized applying **2B** (324 mg, 1.0 mmol, 1.0 eq), **1b** (1198 mg, 3.0 mmol, 3.0 eq), KOtBu (337 mg, 3.0 mmol, 3.0 eq) and (IPr)Pd(allyl)Cl (11 mg, 20  $\mu\text{mol}$ ; dissolved in 2 mL IPA) were suspended in a mixture of 20 mL degassed IPA :  $\text{H}_2\text{O}$  (3 : 1). The reaction mixture was refluxed until complete conversion (1.5 h). After standard workup the crude product was loaded upon silica gel (6 g) and column chromatography (90 g silica gel) using cyclohexane : DCM = 8 - 16% followed by crystallization from cyclohexane yielded **3Bb** as light orange crystals (619 mg, 87%).

$^1\text{H}$  NMR (200 MHz,  $\text{CD}_2\text{Cl}_2$ )  $\delta$  = 7.43 (4 H,  $J$  = 8.8 Hz, d), 7.16 - 7.05 (12 H, m), 7.04 - 6.92 (12 H, m), 2.32 (12 H, s) ppm.

$^{13}\text{C}$  NMR (50 MHz,  $\text{CD}_2\text{Cl}_2$ )  $\delta$  = 148.5 (s), 145.5 (s), 143.5 (s), 136.1 (s), 133.7 (s), 130.5 (d), 127.4 (s), 126.7 (d), 125.4 (d), 124.8 (d), 123.2 (d), 122.6 (d), 21.1 (q) ppm.

MS (MALDI-TOF): calcd for  $\text{C}_{48}\text{H}_{40}\text{N}_2\text{S}_2$ : 708.2633; found: 708.2445.

#### 2.2.6. 4,4'-(2,2'-Bithiophene-5,5'-diyl)bis[N,N-bis(4-methoxyphenyl)benzenamine] (**3Bc**)

According to the general procedure **3Bc** was synthesized applying **2B** (324 mg, 1.0 mmol, 1.0 eq), **1c** (1294 mg, 3.0 mmol, 3.0 eq), KOtBu (337 mg, 3.0 mmol, 3.0 eq) and (IPr)Pd(allyl)Cl (11 mg, 20  $\mu$ mol; dissolved in 2 mL IPA) were suspended in a mixture of 16 mL degassed IPA : H<sub>2</sub>O (3 : 1). The reaction mixture was refluxed until complete conversion (1.5 h). After standard workup the crude product was loaded upon silica gel (6 g) and column chromatography (90 g silica gel) using light petroleum : diethyl ether = 5 - 100% followed by crystallization from cyclohexane yielded **3Bc** as yellow solid (646 mg, 84%).

<sup>1</sup>H NMR (200 MHz, CD<sub>2</sub>Cl<sub>2</sub>)  $\delta$  = 7.39 (4 H, d, J = 8.8 Hz), 7.13 - 7.01 (12 H, m), 6.94 - 6.80 (12 H, m), 3.79 (12 H, s) ppm.

<sup>13</sup>C NMR (50 MHz, CD<sub>2</sub>Cl<sub>2</sub>)  $\delta$  = 156.8 (s), 149.0 (s), 143.6 (s), 141.1 (s), 135.9 (s), 127.4 (d), 126.6 (d), 126.3 (s), 124.7 (d), 122.8 (d), 120.7 (d), 115.3 (d), 56.0 (q) ppm.

MS (MALDI-TOF): calcd for C<sub>48</sub>H<sub>40</sub>N<sub>2</sub>O<sub>4</sub>S<sub>2</sub>: 772.2429; found: 772.2386.

#### 2.2.7. 4,4'-(2,2'-Bithiophene-5,5'-diyl)-bis(N,N-bis[4-fluorophenyl]benzenamine) (**3Bd**)

According to the general procedure **3Bd** was synthesized applying **2B** (324 mg, 1.0 mmol, 1.0 eq), **1d** (1222 mg, 3.0 mmol, 3.0 eq), KOtBu (337 mg, 3.0 mmol, 3.0 eq) and (IPr)Pd(allyl)Cl (11 mg, 20  $\mu$ mol; dissolved in 2 mL IPA) were suspended in a mixture of 16 mL degassed IPA : H<sub>2</sub>O (3 : 1). The reaction mixture was refluxed until complete conversion (1.5 h). After standard workup the crude product was loaded upon silica gel (6 g) and column chromatography (90 g silica gel) using cyclohexane : DCM = 8 - 15% followed by crystallization from cyclohexane yielded **3Bd** as yellow solid (613 mg, 85%).

<sup>1</sup>H NMR (200 MHz, CD<sub>2</sub>Cl<sub>2</sub>)  $\delta$  = 7.46 (4 H, d, J = 8.8 Hz), 7.18 - 6.92 (24 H, m) ppm.

<sup>13</sup>C NMR (50 MHz, CD<sub>2</sub>Cl<sub>2</sub>)  $\delta$  = 159.7 (s, J<sub>CF</sub> = 242.3 Hz), 148.1 (s), 144.1 (s, J<sub>CF</sub> = 2.9 Hz), 143.3 (s), 136.4 (s), 128.1 (s), 127.0 (d, J<sub>CF</sub> = 7.8 Hz), 126.9 (d), 124.9 (d), 123.4 (d), 122.8 (d), 116.7 (d, J<sub>CF</sub> = 22.5 Hz) ppm.

MS (MALDI-TOF): calcd for C<sub>44</sub>H<sub>28</sub>F<sub>4</sub>N<sub>2</sub>S<sub>2</sub>: 724.1630; found: 724.1567.

#### 2.2.8. 4,4'-(2,2'-Bithiophene-5,5'-diyl)-bis(N,N-bis[2-methylphenyl]benzenamine) (**3Be**)

According to the general procedure **3Be** was synthesized applying **2B** (324 mg, 1.0 mmol, 1.0 eq), **1e** (1198 mg, 3.0 mmol, 3.0 eq), KOtBu (337 mg, 3.0 mmol, 3.0 eq) and (IPr)Pd(allyl)Cl (11 mg, 20  $\mu$ mol; dissolved in 2 mL IPA) were suspended in a mixture of 15 mL degassed IPA : H<sub>2</sub>O (3 : 1). The reaction mixture was refluxed until complete conversion (2 h). After standard workup the crude product was loaded upon silica gel (6.5 g) and column chromatography (90 g silica gel) using light petroleum : DCM = 10 - 40% followed by crystallization from cyclohexane yielded **3Be** as yellow solid (495 mg, 70%). R<sub>f</sub> = 0.38 (light petroleum : DCM = 3 : 1).

$^1\text{H}$  NMR (400 MHz,  $\text{CD}_2\text{Cl}_2$ )  $\delta$  = 7.41 (4 H, d,  $J$  = 8.77 Hz), 7.24 (4 H, dd,  $J$  = 7.0, 1.46 Hz), 7.07 - 7.19 (12 H, m), 7.00 (4 H, d,  $J$  = 7.0 Hz), 6.64 (4 H, d,  $J$  = 8.5 Hz), 2.06 (12 H, s) ppm.  
 $^{13}\text{C}$  NMR (100 MHz,  $\text{CD}_2\text{Cl}_2$ )  $\delta$  = 148.8, 146.1, 143.7, 136.0, 135.5, 132.3, 128.1, 127.6, 126.7, 126.4, 125.7, 124.7, 122.9, 120.1, 19.2 ppm.

MS (MALDI-TOF): calcd for  $\text{C}_{48}\text{H}_{40}\text{N}_2\text{S}_2$ : 708.2633; found: 708.2604.

#### 2.2.9. 9,9'-([2,2'-Bithiophene]-5,5'-diyldi-4,1-phenylene)bis-9H-carbazole (**3Bh**)

According to the general procedure **3Bh** was synthesized applying **2B** (648 mg, 2.0 mmol, 1.0 eq), **1h** (2216 mg, 6.0 mmol, 3.0 eq), KOtBu (673 mg, 6.0 mmol, 3.0 eq) and (IPr)Pd(allyl)Cl (23 mg, 40  $\mu\text{mol}$ ; dissolved in 2 mL IPA) were suspended in a mixture of 40 mL degassed IPA :  $\text{H}_2\text{O}$  (3 : 1). The reaction mixture was refluxed until complete conversion (2 h). After standard workup the crude product was purified by crystallization from pyridine yielding **3Bh** as yellow goldish solid (951 mg, 73%).

$^1\text{H}$  NMR (400 MHz,  $\text{CD}_2\text{Cl}_2$ )  $\delta$  = 8.17 (4 H, d,  $J$  = 7.6 Hz), 7.89 (4 H, d,  $J$  = 8.5 Hz), 7.64 (4 H, d,  $J$  = 8.5 Hz), 7.39 - 7.52 (10 H, m), 7.26 - 7.35 (6 H, m) ppm.

$^{13}\text{C}$  NMR (100 MHz,  $\text{CD}_2\text{Cl}_2/\text{CS}_2$ ):  $\delta$  = 142.3 (s), 140.5 (s), 137.0 (s), 136.9 (s), 132.9 (s), 127.3 (d), 126.9 (d), 126.0 (d), 124.9 (d), 124.5 (d), 123.4 (s), 120.2 (d), 120.1 (d), 109.8 (d) ppm.

MS (MALDI-TOF): calcd for  $\text{C}_{44}\text{H}_{28}\text{N}_2\text{S}_2$ : 648.1694; found: 648.1630.

#### 2.2.10. 2,2'-([2,2'-Bithiophene]-5,5'-diyldi)bisindolo[3,2,1-jk]carbazole (**3Bi**)

According to the general procedure **3Bi** was synthesized applying **2B** (324 mg, 1.0 mmol, 1.0 eq), **1i** (1100 mg, 3.0 mmol, 3.0 eq), KOtBu (337 mg, 3.0 mmol, 3.0 eq) and (IPr)Pd(allyl)Cl (11 mg, 20  $\mu\text{mol}$ ; dissolved in 2 mL IPA) were suspended in a mixture of 30 mL degassed IPA :  $\text{H}_2\text{O}$  (3 : 1). The reaction mixture was refluxed until complete conversion (2 h). After standard workup the product was purified by crystallization from pyridine yielding **3Bi** as yellow solid (403 mg, 62%).

MS (MALDI-TOF): calcd for  $\text{C}_{44}\text{H}_{24}\text{N}_2\text{S}_2$ : 644.1381; found: 644.1346.



#### 2.2.11. 4,4'-(2,2':5',2''-Terthiophene-5,5''-diyl)bis(N,N-diphenylbenzenamine) (**3Ca**)

According to the general procedure **3Ca** was synthesized applying **2C** (406 mg, 1.0 mmol, 1.0 eq), **1a** (1114 mg, 3.0 mmol, 3.0 eq), KOtBu (337 mg, 3.0 mmol, 3.0 eq) and (IPr)Pd(allyl)Cl (11 mg, 20  $\mu$ mol; dissolved in 2 mL IPA) were suspended in a mixture of 28 mL degassed IPA : H<sub>2</sub>O (3 : 1). The reaction mixture was refluxed until complete conversion (1.5 h). After standard workup the crude product was loaded upon silica gel (7 g) and column chromatography (90 g silica gel) using cyclohexane : DCM = 7 - 30% followed by crystallization from cyclohexane yielded **3Ca** as orange solid (573 mg, 78%).

<sup>1</sup>H NMR (200 MHz, CD<sub>2</sub>Cl<sub>2</sub>/CS<sub>2</sub>):  $\delta$  = 7.48 (4 H, d, J = 8.8 Hz), 7.34 - 7.22 (8 H, m), 7.19 - 7.00 (22 H, m) ppm.

<sup>13</sup>C NMR (50 MHz, CD<sub>2</sub>Cl<sub>2</sub>/CS<sub>2</sub>):  $\delta$  = 148.0 (s), 147.9 (s), 143.8 (s), 136.7 (s), 136.0 (s), 129.8 (d), 128.4 (s), 127.0 (d), 125.2 (d), 125.2 (d), 124.7 (d), 124.0 (d), 123.8 (d), 123.5 (d) ppm.

MS (MALDI-TOF): calcd for C<sub>48</sub>H<sub>34</sub>N<sub>2</sub>S<sub>3</sub>: 734.1884; found: 734.1750.

#### 2.2.12. 4,4'-(2,2':5',2''-Terthiophene-5,5''-diyl)bis[N,N-bis(4-methylphenyl)benzenamine] (**3Cb**)

According to the general procedure **3Cb** was synthesized applying **2C** (406 mg, 1.0 mmol, 1.0 eq), **1b** (1198 mg, 3.0 mmol, 3.0 eq), KOtBu (337 mg, 3.0 mmol, 3.0 eq) and (IPr)Pd(allyl)Cl (11 mg, 20  $\mu$ mol; dissolved in 2 mL IPA) were suspended in a mixture of 24 mL degassed IPA : H<sub>2</sub>O (3 : 1). The reaction mixture was refluxed until complete conversion (1.5 h). After standard workup the crude product was loaded upon silica gel (6 g) and column chromatography (90 g silica gel) using cyclohexane : DCM = 9 - 17% followed by crystallization from cyclohexane : benzene 9 : 1 yielded **3Cb** as orange solid (687 mg, 87%).

<sup>1</sup>H NMR (200 MHz, CD<sub>2</sub>Cl<sub>2</sub>):  $\delta$  = 7.43 (4 H, d, J = 8.6 Hz), 7.18 - 7.05 (14 H, m), 7.04 - 6.90 (12 H, m), 2.32 (12 H, s) ppm.

<sup>13</sup>C NMR (50 MHz, CD<sub>2</sub>Cl<sub>2</sub>):  $\delta$  = 148.5 (s), 145.4 (s), 143.9 (s), 136.6 (s), 135.6 (s), 133.7 (s), 130.5 (d), 127.3 (s), 126.7 (d), 125.5 (d), 125.1 (d), 124.5 (d), 123.2 (d), 122.6 (d), 21.1 (q) ppm.

MS (MALDI-TOF): calcd for C<sub>52</sub>H<sub>42</sub>N<sub>2</sub>S<sub>3</sub>: 790.2510; found: 790.260.

#### 2.2.13. 4,4'-(2,2':5',2''-Terthiophene-5,5''-diyl)bis[N,N-bis(4-methoxyphenyl)benzenamine] (**3Cc**)

According to the general procedure **3Cb** was synthesized applying **2C** (406 mg, 1.0 mmol, 1.0 eq), **1c** (1294 mg, 3.0 mmol, 3.0 eq), KOtBu (337 mg, 3.0 mmol, 3.0 eq) and (IPr)Pd(allyl)Cl (11 mg, 20  $\mu$ mol; dissolved in 2 mL IPA) were suspended in a mixture of 16 mL degassed IPA : H<sub>2</sub>O (3 : 1). The reaction mixture was refluxed until complete conversion (1.5 h). After standard workup the crude product was loaded upon silica gel (6 g) and column chromatography (90 g silica gel) using light petroleum : DCM = 16 - 100% followed by

crystallization from cyclohexane : benzene 9 : 1 yielded **3Cc** as orange solid (724 mg, 85%).  
<sup>1</sup>H NMR (200 MHz, CD<sub>2</sub>Cl<sub>2</sub>): δ = 7.40 (4 H, d, J = 8.8 Hz), 7.16 - 7.00 (14 H, m), 6.94 - 6.79 (12 H, m), 3.79 (12 H, s) ppm.

<sup>13</sup>C NMR (50 MHz, CD<sub>2</sub>Cl<sub>2</sub>): δ = 156.9 (s), 149.1 (s), 144.1 (s), 141.0 (s), 136.6 (s), 135.4 (s), 127.4 (d), 126.7 (d), 126.2 (s), 125.1 (d), 124.5 (d), 122.9 (d), 120.6 (d), 115.3 (d), 56.0 (q) ppm.

MS (MALDI-TOF): calcd for C<sub>52</sub>H<sub>42</sub>N<sub>2</sub>O<sub>4</sub>S<sub>3</sub>: 854.2307; found: 854.2266.

#### 2.2.14. 4,4'-(2,2':5',2''-Terthiophene-5,5''-diyl)bis[N,N-bis(4-fluorophenyl)benzenamine] (**3Cd**)

According to the general procedure **3Cd** was synthesized applying **2C** (406 mg, 1.0 mmol, 1.0 eq), **1d** (1222 mg, 3.0 mmol, 3.0 eq), KOtBu (337 mg, 3.0 mmol, 3.0 e) and (IPr)Pd(allyl)Cl (11 mg, 20 μmol; dissolved in 2 mL IPA) were suspended in a mixture of 20 mL degassed IPA : H<sub>2</sub>O (3 : 1). The reaction mixture was refluxed until complete conversion (1.5 h). After standard workup the crude product was loaded upon silica gel (6 g) and column chromatography (90 g silica gel) using cyclohexane : DCM = 8 - 20% followed by crystallization from cyclohexane : benzene 9 : 1 yielded **3Cd** as orange solid (704 mg, 82%).  
<sup>1</sup>H NMR (200 MHz, CD<sub>2</sub>Cl<sub>2</sub>): δ = 7.46 (4 H, d, J = 8.8 Hz), 7.18 - 6.92 (26 H, m) ppm.

<sup>13</sup>C NMR (100 MHz, CD<sub>2</sub>Cl<sub>2</sub>): δ = 159.7 (s, J<sub>CF</sub> = 242.3 Hz), 148.2 (s), 144.0 (s, J<sub>CF</sub> = 2.9 Hz), 143.6 (s), 136.6 (s), 135.9 (s), 128.0 (s), 127.0 (d, J<sub>CF</sub> = 8.1 Hz), 126.9 (d), 124.9 (d), 123.4 (d), 122.8 (d), 116.7 (d, J<sub>CF</sub> = 22.5 Hz) ppm.

MS (MALDI-TOF): calcd for C<sub>48</sub>H<sub>30</sub>F<sub>4</sub>N<sub>2</sub>S<sub>3</sub>: 806.1507; found: 806.1512.

#### 2.2.15. 4,4'-(Thieno[3,2-b]thiophene-2,5-diyl)bis[(N,N-diphenyl)benzenamine] (**3Ea**)

According to the general procedure **3Ea** was synthesized applying **2E** (596 mg, 2.0 mmol, 1.0 eq), **1a** (2228 mg, 6.0 mmol, 3.0 eq), KOtBu (673 mg, 6.0 mmol, 3.0 eq) and (IPr)Pd(allyl)Cl (23 mg, 40 μmol; dissolved in 2 mL IPA) were suspended in a mixture of 40 mL degassed IPA : H<sub>2</sub>O (3:1). The reaction mixture was refluxed until complete conversion (2 h). After standard workup the reaction mixture was loaded upon silica gel (7 g) and column chromatography using light petroleum : DCM = 5 - 50% followed by crystallization from n-hexane yielded **3Ea** as yellow crystals (1.091 g, 87%). R<sub>f</sub> = 0.38 (light petroleum:DCM=4 : 1).  
<sup>1</sup>H NMR (400 MHz, pyridine-d<sub>5</sub>,) δ = 7.71 – 7.68 (6 H, m), 7.37 – 7.33 (8 H, m), 7.10 - 7.21 (16 H, m) ppm.

<sup>13</sup>C NMR (100 MHz, pyridine-d<sub>5</sub>) δ = 148.4 (s), 148.3 (s), 146.3 (s), 139.9 (s), 130.4 (d), 129.6 (s), 127.4 (d), 125.5 (d), 124.5 (d), 124.3 (d), 116.0 (d) ppm.

MS (MALDI-TOF): calcd for C<sub>42</sub>H<sub>30</sub>N<sub>2</sub>S: 626.1850; found: 626.1699.

2.2.16. 4,4'-(2,5-Thieno[3,2-b]thiophenediyl)bis(N,N-bis[2-methylphenyl]benzenamine) (**3Ee**)

According to the general procedure **3Ee** was synthesized applying **2E** (298 mg, 1.0 mmol, 1.0 eq), **1e** (1198 mg, 3.0 mmol, 3.0 eq), KOtBu (337 mg, 3.0 mmol, 3.0 eq) and (IPr)Pd(allyl)Cl (11 mg, 20  $\mu$ mol; dissolved in 2 mL IPA) were suspended in a mixture of 20 mL degassed IPA : H<sub>2</sub>O (3 : 1). The reaction mixture was refluxed until complete conversion (2 h). After standard workup the crude product was loaded upon silica gel (6.3 g) and column chromatography using light petroleum : DCM = 5 - 18% followed by crystallization from cyclohexane yielded **3Ee** as yellow solid (360 mg, 53%).

R<sub>f</sub> = 0.33 (light petroleum : DCM = 5 : 1).

<sup>1</sup>H NMR (400 MHz, CD<sub>2</sub>Cl<sub>2</sub>)  $\delta$  = 7.43 (4 H, d, J = 8.8 Hz), 7.33 (2 H, brs), 7.24 (4 H, d, J = 8.2 Hz), 7.06 - 7.20 (8 H, m), 7.00 (4 H, d, J = 8.2 Hz), 6.65 (4 H, d, J = 8.8 Hz), 2.06 (12 H, s) ppm.

<sup>13</sup>C NMR (100 MHz, CD<sub>2</sub>Cl<sub>2</sub>)  $\delta$  = 148.9, 146.1, 139.0, 135.5, 132.3, 128.1, 127.6, 127.1, 126.8, 125.7, 120.1, 114.5, 19.2 ppm.

MS (MALDI-TOF): calcd for C<sub>46</sub>H<sub>38</sub>N<sub>2</sub>S<sub>2</sub>: 682.2476; found: 682.2272.

2.2.17. 9,9'-(Thieno[3,2-b]thiophene-2,5-diyl-di-4,1-phenylene)bis-9H-carbazole (**3Eh**)

According to the general procedure **3Eh** was synthesized applying **2E** (596 mg, 2.0 mmol, 1.0 eq), **1h** (2216 mg, 6.0 mmol, 3.0 eq), KOtBu (673 mg, 6.0 mmol, 3.0 eq) and (IPr)Pd(allyl)Cl (23 mg, 40  $\mu$ mol; dissolved in 2 mL IPA) were suspended in a mixture of 40 mL degassed IPA : H<sub>2</sub>O (3:1). The reaction mixture was refluxed until complete conversion (3 h). After standard workup the product was purified by crystallization from pyridine yielding **3Eh** as yellow goldish solid (745 mg, 60%). R<sub>f</sub> = 0.33 (light petroleum : DCM).

<sup>1</sup>H NMR (400 MHz, pyridine-d<sub>5</sub>)  $\delta$  = 8.33 (4 H, d, J = 7.9 Hz), 8.07 (4 H, d, J = 8.2 Hz), 7.98 (2 H, s), 7.64 (4 H, d, J = 8.5 Hz), 7.51 - 7.57 (8 H, m), 7.40 - 7.46 (4 H, m) ppm.

<sup>13</sup>C NMR (100 MHz, pyridine-d<sub>5</sub>)  $\delta$  = 146.3, 141.7, 141.2, 138.1, 134.8, 128.5, 128.3, 127.4, 124.8, 121.7, 121.5, 118.0, 111.1 ppm.

MS (MALDI-TOF): calcd for C<sub>42</sub>H<sub>26</sub>N<sub>2</sub>S<sub>2</sub>: 622.1537; found: 622.1442.

2.2.18. 2,2'-(2,5-Thieno(3,2-b)thiophenediyl)bisindolo[3,2,1-jk]carbazol (**3Ei**)

According to the general procedure **3Ei** was synthesized applying **2E** (298 mg, 1.0 mmol, 1.0 eq), **1i** (1100 mg, 3.0 mmol, 3.0 eq), KOtBu (337 mg, 3.0 mmol, 3.0 eq) and (IPr)Pd(allyl)Cl (11 mg, 20  $\mu$ mol; dissolved in 2 mL IPA) were suspended in a mixture of 40 mL degassed IPA : H<sub>2</sub>O (3:1). The reaction mixture was refluxed until complete conversion (2 h). After standard workup the product was purified by crystallization from pyridine yielding **3Ei** as yellow solid (293 mg, 47%). R<sub>f</sub> = 0.18 (light petroleum : DCM = 5 : 1).

MS (MALDI-TOF): calcd for C<sub>42</sub>H<sub>22</sub>N<sub>2</sub>S<sub>2</sub>: 618.1224; found: 618.1073.

2.2.19.4,4'-(Dithieno[3,2-b:2',3'-d]thiophene-2,6-diyl)bis(N,N-diphenylbenzenamine) (**3Fa**)

According to the general procedure **3Fa** was synthesized applying **2F** (354 mg, 1.0 mmol, 1.0 eq), **1a** (1114 mg, 3.0 mmol, 3.0 eq), KOtBu (337 mg, 3.0 mmol, 3.0 eq) and (IPr)Pd(allyl)Cl (11 mg, 20  $\mu$ mol; dissolved in 2 mL IPA) were suspended in a mixture of 15 mL degassed IPA : H<sub>2</sub>O (3 : 1). The reaction mixture was refluxed until complete conversion (2 h). After standard workup the reaction mixture was loaded upon silica gel (7 g) and column chromatography (90 g silica gel) using light petroleum : DCM = 15 - 40% followed by crystallization from cyclohexane yielded **3Fa** as yellow solid (560 mg, 82%).

<sup>1</sup>H NMR (400 MHz, CD<sub>2</sub>Cl<sub>2</sub>)  $\delta$  = 7.52 (4 H, d, J = 8.5 Hz), 7.45 (2 H, s), 7.31 – 7.27 (8 H, m), 7.12 (8 H, d, J = 7.9 Hz), 7.02 - 7.10 (8 H, m) ppm.

<sup>13</sup>C NMR (100 MHz, CD<sub>2</sub>Cl<sub>2</sub>)  $\delta$  = 148.3 (s), 147.9 (s), 145.4 (s), 142.2 (s), 130.1 (s), 129.9 (s), 128.8 (s), 126.9 (s), 125.3 (s), 123.9 (s), 116.1 (s) ppm.

MS (MALDI-TOF): calcd for C<sub>44</sub>H<sub>30</sub>N<sub>2</sub>S<sub>3</sub>: 682.1571; found: 682.1445.

2.2.20. 4,4'-(2,6-Dithieno[3,2-b]thiophenediyl)bis(N,N-bis[2-methylphenyl]benzenamine) (**3Fe**)

According to the general procedure **3Fe** was synthesized applying **2F** (354 mg, 1.0 mmol, 1.0 eq), **1e** (1198 mg, 3.0 mmol, 3.0 eq), KOtBu (337 mg, 3.0 mmol, 3.0 eq) and (IPr)Pd(allyl)Cl (11 mg, 20  $\mu$ mol; dissolved in 2 mL IPA) were suspended in a mixture of 40 mL degassed IPA : H<sub>2</sub>O (3 : 1). The reaction mixture was refluxed until complete conversion (2 h). After standard workup the crude product was loaded upon silica gel (6.5 g) and column chromatography (90g silica gel) using light petroleum : DCM = 8 - 30% followed by crystallization from cyclohexane yielded **3Fe** as yellow solid (679 mg, 92%). R<sub>f</sub> = 0.10 (light petroleum : DCM = 9 : 1).

<sup>1</sup>H NMR (200 MHz, CD<sub>2</sub>Cl<sub>2</sub>)  $\delta$  = 7.45 (4 H, d, J = 8.8 Hz), 7.37 (2 H, d, J = 6.7 Hz), 7.19 - 7.29 (4 H, m), 7.05 - 7.19 (8 H, m), 7.02 (2 H, d, J = 2.4 Hz), 6.96 - 7.00 (2 H, m), 6.65 (4 H, d, J = 8.8 Hz), 2.07 (12 H, s) ppm.

<sup>13</sup>C NMR (50 MHz, CD<sub>2</sub>Cl<sub>2</sub>)  $\delta$  = 149.0 (s), 146.0 (s), 145.7 (s), 142.0 (s), 135.5 (s), 132.3 (d), 129.7 (s), 128.1 (d), 127.6 (d), 126.8 (d), 125.7 (d), 120.1 (d), 115.5 (d), 19.2 (q) ppm.

MS (MALDI-TOF): calcd for C<sub>48</sub>H<sub>38</sub>N<sub>2</sub>S<sub>3</sub>: 738.2197; found: 738.2114.

2.2.21. 9,9'-(Dithieno[3,2-b:2',3'-d]thiophene-2,6-diyl-di-4,1-phenylene)bis-9H-carbazole (**3Fh**)

According to the general procedure **3Fh** was synthesized applying **2F** (708 mg, 2.0 mmol, 1.0 eq), **1e** (2216 mg, 6.0 mmol, 3.0 eq), KOtBu (673 mg, 6.0 mmol, 3.0 eq) and (IPr)Pd(allyl)Cl (23 mg, 40  $\mu$ mol; dissolved in 2 mL IPA) were suspended in a mixture of 40 mL degassed IPA : H<sub>2</sub>O (3 : 1). The reaction mixture was refluxed until complete conversion

(3 h). After standard workup the crude product was purified by crystallization from pyridine yielding **3Fh** as bright yellow solid (790 mg, 58%).

$^1\text{H}$  NMR (400 MHz,  $\text{CD}_2\text{Cl}_2$ )  $\delta$  = 8.13 - 8.21 (4 H, m), 7.93 (4 H, s), 7.71 (2 H, s), 7.68 (4 H, d,  $J$  = 8.4 Hz), 7.51 (4 H, d,  $J$  = 7.7 Hz), 7.45 (4 H, t,  $J$  = 7.3 Hz), 7.32 (4 H, t,  $J$  = 8.8 Hz) ppm.  
MS (MALDI-TOF): calcd for  $\text{C}_{44}\text{H}_{26}\text{N}_2\text{S}_3$ : 678.1258; found: 678.1226.

#### 2.2.22. 2,2'-(2,6-Dithieno(3,2-b)thiophenediyl)bisindolo[3,2,1-jk]carbazole (**3Fi**)

According to the general procedure **3Fi** was synthesized applying **2F** (354 mg, 1.0 mmol, 1.0 eq), **1i** (1100 mg, 3.0 mmol, 3.0 eq), KOtBu (337 mg, 3.0 mmol, 3.0 eq) and (IPr)Pd(allyl)Cl (11 mg, 20  $\mu\text{mol}$ ; dissolved in 2 mL IPA) were suspended in a mixture of 40 mL degassed IPA :  $\text{H}_2\text{O}$  (3 : 1). The reaction mixture was refluxed until complete conversion (2 h). After standard workup the product was purified by crystallization from pyridine (500 mL) yielding **3Fi** as dark yellow solid (360 mg, 53%).

MS (MALDI-TOF): calcd for  $\text{C}_{44}\text{H}_{22}\text{N}_2\text{S}_3$ : 674.0945; found: 674.1282.

#### 2.2.23. 4,4'-(2,2':5',2'':5'',2'''-Quaterthiophene-5,5'''-diyl)bis(N,N-diphenylbenzenamine) (**3Da**)

The synthesis of **3Da** was realized microwave assisted at 120°C applying **2D** (122 mg, 0.25 mmol, 1.0 eq), **1a** (278 mg, 0.75 mmol, 3.0 eq), KOtBu (84 mg, 0.25 mmol, 3.0 eq) and (IPr)Pd(allyl)Cl (2.9 mg, 2  $\mu\text{mol}$ ; dissolved in 1 mL IPA) in a mixture of 3 mL degassed IPA :  $\text{H}_2\text{O}$  (3 : 1) for 4 h. After standard workup the crude product was loaded upon silica gel (2.5 g) and column chromatography (45 g silica gel) using cyclohexane : DCM = 14 - 100% yielded **3Da** as orange solid (65 mg, 29%).

MS (MALDI-TOF): calcd for  $\text{C}_{52}\text{H}_{36}\text{N}_2\text{S}_4$ : 816.1761; found: 816.1741.

#### 2.2.24. 4,4'-(2,2':5',2'':5'',2'''-Quaterthiophene-5,5'''-diyl)bis[N,N-bis(4-methylphenyl)benzenamine] (**3Db**)

The synthesis of **3Db** was realized microwave assisted at 120°C applying **2D** (122 mg, 0.25 mmol, 1.0 eq), **1b** (300 mg, 0.75 mmol, 3.0 eq), KOtBu (84 mg, 0.25 mmol, 3.0 eq) and (IPr)Pd(allyl)Cl (2.9 mg, 2  $\mu\text{mol}$ ; dissolved in 1 mL IPA) in a mixture of 3 mL degassed IPA :  $\text{H}_2\text{O}$  (3 : 1) for 4 h. After standard workup the crude product was loaded upon silica gel (2.5 g) and column chromatography (45 g silica gel) using cyclohexane : DCM = 14 - 100% yielded **3Db** as orange solid (120 mg, 54%).

$^1\text{H}$  NMR (400 MHz,  $\text{CD}_2\text{Cl}_2$ ):  $\delta$  = 7.43 (4 H, d,  $J$  = 8.4 Hz), 7.14 (4 H, s), 7.11 - 7.09 (12 H, m), 7.01 - 6.96 (12 H, m), 2.32 (12 H, s) ppm.

$^{13}\text{C}$  NMR (100 MHz,  $\text{CD}_2\text{Cl}_2$ ):  $\delta$  = 148.6 (s), 145.4 (s), 144.1 (s), 137.0 (s), 136.1 (s), 135.5 (s), 133.8 (s), 130.5 (d), 127.2 (s), 126.7 (d), 125.5 (d), 125.3 (d), 124.9 (d), 124.6 (d), 123.2 (d), 122.5 (d), 21.1 (q) ppm.

MS (MALDI-TOF): calcd for  $\text{C}_{56}\text{H}_{44}\text{N}_2\text{S}_4$ : 872.2387; found: 872.2389.

2.2.25. 4,4'-(2,2':5',2'':5'',2''':5''''-Quaterthiophene-5,5''''-diyl)bis[N,N-bis(4-methoxyphenyl)benzenamine] (**3Dc**)

The synthesis of **3Dc** was realized microwave assisted at 120°C applying **2D** (122 mg, 0.25 mmol, 1.0 eq), **1c** (324 mg, 0.75 mmol, 3.0 eq), KOtBu (84 mg, 0.25 mmol, 3.0 eq) and (IPr)Pd(allyl)Cl (2.9 mg, 2 μmol; dissolved in 1 mL IPA) in a mixture of 3 mL degassed IPA : H<sub>2</sub>O (3 : 1) for 4 h. After standard workup the crude product was loaded upon silica gel (2.5 g) and column chromatography (45 g silica gel) using cyclohexane : DCM = 10 - 100% yielded **3Dc** as red solid (112 mg, 48%).

<sup>1</sup>H NMR (200 MHz, CD<sub>2</sub>Cl<sub>2</sub>): δ = 7.41 (4 H, d, J = 8.6 Hz), 7.19 - 7.00 (16 H, m), 6.95 - 6.80 (12 H, m), 3.79 (12 H, s) ppm.

<sup>13</sup>C NMR (100 MHz, CD<sub>2</sub>Cl<sub>2</sub>): δ = 156.8, 149.1, 144.3, 140.9, 137.0, 135.9, 135.2, 127.4, 126.6, 126.1, 125.2, 124.8, 124.4, 122.9, 120.5, 115.2, 56.0 ppm.

MS (MALDI-TOF): calcd for C<sub>56</sub>H<sub>44</sub>N<sub>2</sub>O<sub>4</sub>S<sub>4</sub>: 936.2184; found: 936.2422.

2.2.26. 4,4'-(2,2':5',2'':5'',2''':5''''-Quaterthiophene-5,5''''-diyl)bis[N,N-bis(4-fluorophenyl)benzenamine] (**3Dd**)

The synthesis of **3Dd** was realized microwave assisted at 120°C applying **2D** (122 mg, 0.25 mmol, 1.0 eq), **1d** (305 mg, 0.75 mmol, 3.0 eq), KOtBu (84 mg, 0.25 mmol, 3.0 eq) and (IPr)Pd(allyl)Cl (2.9 mg, 2 μmol; dissolved in 1 mL IPA) in a mixture of 3 mL degassed IPA : H<sub>2</sub>O (3 : 1) for 4 h. After standard workup the crude product was loaded upon silica gel (2.5 g) and column chromatography (45 g silica gel) using cyclohexane : DCM = 10 - 100% yielded **3Dd** as red solid (75 mg, 34%).

MS (MALDI-TOF): calcd for C<sub>52</sub>H<sub>32</sub>F<sub>4</sub>N<sub>2</sub>S<sub>4</sub>: 888.1384; found: 888.1388.

2.2.27. 2-Methyl-N-(2-methylphenyl)benzenamine (**4**)

A modified protocol of Ackermann was employed.[50] In a three-necked flask 2-bromotoluene (42.75 g, 250 mmol, 1 eq) and 2-methylaniline (32.15 g, 300 mmol, 1.2 eq) were well stirred in 500 mL of anhydrous toluene and under argon atmosphere, before KOtBu (36.47 g, 325 mmol, 1.3 eq) was quickly added in small portions. The reddish orange suspension was refluxed for 30 min before 40 (1.43 g, 2.5 mmol, 0.01 eq) was added quickly. The mixture was kept under reflux conditions until complete conversion (2 h). Et<sub>2</sub>O (100 mL) and brine (100 mL) were added to the cooled reaction mixture. The separated aqueous phase was extracted repeatedly with Et<sub>2</sub>O (3 x 50 mL). The combined organic layer were dried over Na<sub>2</sub>SO<sub>4</sub> and concentrated in vacuo. The remaining residue was purified by flash column chromatography on silica gel (light petroleum : ethyl acetate = 20:1; 350 g) to yield **4** as an orange liquid which solidified upon standing (37.11 g, 75 %). R<sub>f</sub> = 0.37 (light petroleum : ethyl acetate = 20 : 1).

$^1\text{H}$  NMR (200 MHz,  $\text{CDCl}_3$ )  $\delta$  = 7.30 - 7.17 (4 H, m), 7.09 – 6.95 (4 H, m), 5.23 (1 H, s.) 2.35 (6 H, s) ppm.

#### 2.2.28. 2-Methyl-N-(4-nitrophenyl)-N-benzeneamine (**5b**)

In a three-necked flask equipped with a mechanical stirrer **4** (19.73 g, 100 mmol, 1 eq) and NaH (7.20 g, 300 mmol, 3 eq) were stirred at 50 °C in 300 mL of anhydrous DMF for 30 min under argon atmosphere. Then 4-fluoronitrobenzene (21.17 g, 150 mmol, 1.5 eq) dissolved in 200 mL of DMF was added dropwise. The reaction was stirred at 50 °C until complete conversion (3 h) before DMF was removed in vacuo. DCM (300 mL) and  $\text{H}_2\text{O}$  (300 mL) were added to the reaction mixture. The separated aqueous phase was extracted repeatedly with DCM (3 x 50 mL). The combined organic layer was dried over  $\text{Na}_2\text{SO}_4$  and concentrated in vacuo yielding a brown liquid. The product was purified by flash chromatography (200 g, light petroleum :  $\text{Et}_2\text{O}$  = 20 : 1) followed by recrystallization from light petroleum, yielding **5b** as yellow solid (23.42 g, 74 %).  $R_f$  = 0.71 (light petroleum : ethyl acetate = 5 : 1).

$^1\text{H}$  NMR (200 MHz,  $\text{CDCl}_3$ )  $\delta$  = 7.99 (2 H, d,  $J$  = 9.2 Hz), 7.26 - 7.10 (6 H, m), 7.04 – 6.95 (2 H, m), 6.48 (2 H, d,  $J$  = 9.2 Hz) 2.06 (6 H, s) ppm.

$^{13}\text{C}$  NMR (50 MHz,  $\text{CDCl}_3$ ):  $\delta$  = 153.3 (s), 143.5 (s), 139.5 (s), 135.0 (s), 132.0 (d), 128.0 (d), 127.6 (d), 126.7 (d), 125.7 (d), 116.0 (d), 18.8 (q) ppm.

#### 2.2.29. N,N-Bis(2-methylphenyl)-1,4-diamine (**6**)

Synthesis of **6** followed a protocol by Chen.[23] To a solution of **5b** (22.92 g, 72 mmol, 1 eq) in 250 mL of EtOH,  $\text{SnCl}_2 \cdot 2\text{H}_2\text{O}$  (56.86 g, 252 mmol, 3.5 eq) was added quickly and then heated under reflux until complete conversion (6 h). Most of the ethanol was distilled off under reduced pressure, and the solution was alkalized by adding 40 wt% NaOH (50 mL) dropwisely under stirring and yellow solid precipitated. The resulting mixture was extracted with toluene and washed with water. The combined toluene extracts were dried over  $\text{Na}_2\text{SO}_4$  and the solvent was removed under reduced pressure. Orange yellowish solid product **6** was obtained (20.9 g, 99 %).  $R_f$  = 0.30 (light petroleum : ethyl acetate = 5 : 1).

$^1\text{H}$  NMR (200 MHz,  $\text{CD}_2\text{Cl}_2$ )  $\delta$  = 7.19 – 6.96 (6 H, m), 6.85 (2 H, dd,  $J$  = 7.6, 1.6 Hz), 6.61 – 6.52 (4 H, m), 3.52 (2 H, bs), 1.97 (6 H, s) ppm.

$^{13}\text{C}$  NMR (50 MHz,  $\text{CD}_2\text{Cl}_2$ ):  $\delta$  = 148.0 (s), 141.9 (s), 141.5 (s), 134.5 (s), 132.0 (d), 127.1 (d), 126.8 (d), 124.2 (d), 124.0 (d), 116.2 (d), 19.2 (q) ppm.

#### 2.2.30. N-(4-Iodophenyl)-bis(2-methylphenyl)benzeneamine (**7**)

A solution of **6** (14.42 g, 50 mmol, 1 eq) in ACN (80 mL), and  $\text{H}_2\text{O}$  (80 mL) was stirred in an ice bath while concentrated HCl (25 mL, 6 eq) was added dropwise over 5 min. To this mixture, still in an ice bath, was added a solution of  $\text{NaNO}_2$  (6.90 g, 100 mmol, 2 eq) in 80 mL of  $\text{H}_2\text{O}$  keeping the temperature between -5 to 0 °C. The reaction mixture turned from orange to green and was stirred at that temperature for 1 h. After that a solution of KI (41.50

g, 250 mmol, 5 eq) in 80 mL of H<sub>2</sub>O was added quickly. The red reaction mixture was then heated to reflux until no more purple or brown vapor was evolved. After complete conversion (2 h), ACN was removed in vacuo and the reaction was neutralized with 2N NaOH (200 mL). The black aqueous phase turned yellow and was extracted with CHCl<sub>3</sub> (3 x 100 mL). The combined organic layer was washed with a saturated solution of Na<sub>2</sub>S<sub>2</sub>O<sub>5</sub> and dried over Na<sub>2</sub>SO<sub>4</sub>. The solvent was removed in vacuo yielding black tar. The product was purified via flash chromatography (light petroleum) followed by crystallization from MeOH : ACN = 100 : 1 yielding **7** as slightly yellow solid (15.17 g, 76%).

<sup>1</sup>H NMR (400 MHz, CHCl<sub>3</sub>) δ = 7.43 (2 H, d, J = 9.2 Hz), 7.22 (2 H, d, J = 7.0 Hz), 7.16 - 7.07 (4 H, m), 6.97 (2 H, d, J = 8.8 Hz), 6.44 (2 H, d, J = 8.8 Hz), 2.03 (6 H, s) ppm.

<sup>13</sup>C NMR (100 MHz, CHCl<sub>3</sub>) δ = 148.3 (s), 145.3 (s), 137.6 (d), 134.6 (s), 131.7 (d), 127.4 (d), 127.0 (d), 125.1 (d), 121.5 (d), 82.0 (s), 18.9 (q) ppm.

#### 2.2.31. *2-Methyl-N-(2-methylphenyl)-N-[4-(4,4,5,5-tetramethyl-1,3,2-dioxaborolan-2-yl)phenyl] benzenamine (1e)*

Synthesis was done according to Murata.[24] **7** (6.15 g, 15.4 mmol, 1.0 eq) and PdCl<sub>2</sub>(dppf) (0.338 g, 0.46 mmol, 0.03 eq) were dissolved in anhydrous dioxane (60 mL). The mixture was heated to 80 °C under argon atmosphere. Pinacolborane (2.56 g, 20 mmol, 1.3 eq) and Et<sub>3</sub>N (4.68 g, 46 mmol, 3 eq) were added dropwise and the reaction was stirred until complete conversion (1 h). The solvent was removed under reduced pressure and the dark residue was purified by column chromatography (light petroleum : ethyl acetate = 100 : 3). Finally, the product was crystallized from ACN yielding **1e** as a white solid (3.97 g, 65 %).

<sup>1</sup>H NMR (400 MHz, CD<sub>2</sub>Cl<sub>2</sub>) δ = 7.55 (2 H, d, J = 8.5 Hz), 7.24 (2 H, dd, J = 7.3, 1.17 Hz), 7.17 - 7.10 (4 H, m), 6.99 (2 H, d, J = 7.3 Hz), 6.58 (2 H, d, J = 8.8 Hz), 2.05 (6 H, s), 1.31 (12 H, s) ppm.

<sup>13</sup>C NMR (100 MHz, CD<sub>2</sub>Cl<sub>2</sub>) δ = 151.5 (s), 145.9 (s), 136.2 (d), 135.7 (s), 132.2 (d), 128.4 (d), 127.6 (d), 125.8 (d), 118.4 (d), 83.9 (s), 25.2 (q), 19.2 (q) ppm.



## 6. References

- [1] N. Thejo Kalyani, S.J. Dhoble, Organic light emitting diodes: Energy saving lighting technology— A review, *Renew. Sustain. Energy Rev.* 16 (2012) 2696–2723. doi:10.1016/j.rser.2012.02.021.
- [2] C. Wang, H. Dong, W. Hu, Y. Liu, D. Zhu, Semiconducting  $\pi$ -Conjugated Systems in Field-Effect Transistors: A Material Odyssey of Organic Electronics, *Chem. Rev.* 112 (2012) 2208–2267. doi:10.1021/cr100380z.
- [3] T.M. Clarke, J.R. Durrant, Charge Photogeneration in Organic Solar Cells, *Chem. Rev.* 110 (2010) 6736–6767. doi:10.1021/cr900271s.
- [4] H. Klauk, *Organic Electronics: Materials, Manufacturing, and Applications*, John Wiley & Sons, 2006.
- [5] Z. Xi, P. Bäuerle, T. Aida, P. Skabara, C. Kagan, *Organic Electronics for a Better Tomorrow: Innovation, Accessibility, Sustainability*, in: San Francisco, CA, USA, 2012.
- [6] H. Klauk, *Organic electronics II: more materials and applications*, Wiley-VCH, Weinheim, 2012.
- [7] D. Lumpi, E. Horkel, F. Plasser, H. Lischka, J. Fröhlich, Synthesis, Spectroscopy, and Computational Analysis of Photoluminescent Bis(aminophenyl)-Substituted Thiophene Derivatives, *ChemPhysChem.* 14 (2013) 1016–1024. doi:10.1002/cphc.201201006.
- [8] Y. Shirota, Organic materials for electronic and optoelectronic devices, *J. Mater. Chem.* 10 (2000) 1–25. doi:10.1039/A908130E.
- [9] N. Metri, X. Sallenave, C. Plesse, L. Beouch, P.-H. Aubert, F. Goubard, C. Chevrot, G. Sini, Processable Star-Shaped Molecules with Triphenylamine Core as Hole-Transporting Materials: Experimental and Theoretical Approach, *J. Phys. Chem. C.* 116 (2012) 3765–3772. doi:10.1021/jp2098872.
- [10] J. Zhang, D. Deng, C. He, Y. He, M. Zhang, Z.-G. Zhang, Z. Zhang, Y. Li, Solution-Processable Star-Shaped Molecules with Triphenylamine Core and Dicyanovinyl Endgroups for Organic Solar Cells†, *Chem. Mater.* 23 (2011) 817–822. doi:10.1021/cm102077j.
- [11] Z. Ning, H. Tian, Triarylamine: a promising core unit for efficient photovoltaic materials, *Chem. Commun.* (2009) 5483. doi:10.1039/b908802d.
- [12] A. Iwan, D. Sek, D. Pocięcha, A. Sikora, M. Palewicz, H. Janeczek, New discotic-shaped azomethines with triphenylamine moieties: Thermal, structural behaviors and opto-electrical properties, *J. Mol. Struct.* 981 (2010) 120–129. doi:10.1016/j.molstruc.2010.07.039.
- [13] A. Iwan, D. Sek, Polymers with triphenylamine units: Photonic and electroactive materials, *Prog. Polym. Sci.* 36 (2011) 1277–1325. doi:10.1016/j.progpolymsci.2011.05.001.
- [14] D. Lumpi, B. Holzer, J. Bintinger, E. Horkel, S. Waid, H.D. Wanzenböck, M. Marchetti-Deschmann, C. Hametner, E. Bertagnolli, I. Kymissis, J. Fröhlich, Substituted triphenylamines as building blocks for star shaped organic electronic materials, *New J. Chem.* (2015). doi:10.1039/C4NJ01695E.
- [15] D. Lumpi, B. Holzer, J. Bintinger, E. Horkel, S. Waid, H.D. Wanzenböck, M. Marchetti-Deschmann, C. Hametner, E. Bertagnolli, I. Kymissis, J. Fröhlich, Substituted triphenylamines as building blocks for star shaped organic electronic materials, *New J Chem.* (2015). doi:10.1039/C4NJ01695E.
- [16] D. Lumpi, B. Holzer, J. Bintinger, E. Horkel, S. Waid, H.D. Wanzenböck, M. Marchetti-Deschmann, C. Hametner, E. Bertagnolli, I. Kymissis, J. Fröhlich, Substituted triphenylamines as building blocks for star shaped organic electronic materials, *New J Chem.* 39 (2015) 1840–1851. doi:10.1039/C4NJ01695E.
- [17] B. Holzer, M. Tromayer, M. Lunzer, D. Lumpi, E. Horkel, C. Hametner, A. Rosspeintner, E. Vauthey, R. Liska, J. Fröhlich, Initiators for Two-Photon Induced Polymerization Based on a Novel Cap-Linker-Cap System, *Manuscr. Prep.* (n.d.).
- [18] P. Kautny, D. Lumpi, Y. Wang, A. Tissot, J. Bintinger, E. Horkel, B. Stöger, C. Hametner, H. Hagemann, D. Ma, J. Fröhlich, Oxadiazole based bipolar host materials employing planarized triarylamine donors for RGB PHOLEDs with low efficiency roll-off, *J. Mater. Chem. C.* 2 (2014) 2069. doi:10.1039/c3tc32338b.

- [19] N.-X. Wang, Synthesis of 2-Bromo-2'-phenyl-5,5'-thiophene: Suzuki Reaction Versus Negishi Reaction, *Synth. Commun.* 33 (2003) 2119–2124. doi:10.1081/SCC-120021039.
- [20] J. Roncali, M. Giffard, P. Frère, M. Jubault, A. Gorgues, Extensively conjugated tetrathiafulvalene (TTF) $\pi$ -electron donors with oligothiophenes spacer groups, *J. Chem. Soc. Chem. Commun.* (1993) 689–691. doi:10.1039/C39930000689.
- [21] J. Nakayama, T. Konishi, S. Murabayashi, M. Hoshino, Preparation of a-Quater-, a-Sexi-, and a-Octithiophenes, *HETEROCYCLES*. 26 (1987) 1793. doi:10.3987/R-1987-07-1793.
- [22] J. Frey, A.D. Bond, A.B. Holmes, Improved synthesis of dithieno[3,2-b:2',3'-d]thiophene (DTT) and derivatives for cross coupling, *Chem. Commun.* (2002) 2424–2425. doi:10.1039/B207403F.
- [23] Y.-C. Chen, G.-S. Huang, C.-C. Hsiao, S.-A. Chen, High Triplet Energy Polymer as Host for Electrophosphorescence with High Efficiency, *J. Am. Chem. Soc.* 128 (2006) 8549–8558. doi:10.1021/ja060936t.
- [24] M. Murata, T. Oyama, S. Watanabe, Y. Masuda, Palladium-Catalyzed Borylation of Aryl Halides or Triflates with Dialkoxyborane: A Novel and Facile Synthetic Route to Arylboronates, *J. Org. Chem.* 65 (2000) 164–168. doi:10.1021/jo991337q.
- [25] T. Tao, H.-F. Qian, K. Zhang, J. Geng, W. Huang, Functionalized oligothiophene-based heterocyclic aromatic fluorescent compounds with various donor–acceptor spacers and adjustable electronic properties: a theoretical and experimental perspective, *Tetrahedron*. 69 (2013) 7290–7299. doi:10.1016/j.tet.2013.06.087.
- [26] K. Mereiter, R. Schuecker, W. Weissensteiner. Private Communication. CCDC#858840, (n.d.).
- [27] K. Mereiter, D. Lumpi. Private Communication. CCDC#858841, (n.d.).
- [28] T. Noda, H. Ogawa, N. Noma, Y. Shirota, A novel family of amorphous molecular materials containing an oligothiophene moiety as color-tunable emitting materials for organic electroluminescent devices, *Adv. Mater.* 9 (1997) 720–722. doi:10.1002/adma.19970090908.
- [29] Y. Zhao, D.G. Truhlar, The M06 suite of density functionals for main group thermochemistry, thermochemical kinetics, noncovalent interactions, excited states, and transition elements: two new functionals and systematic testing of four M06 functionals and 12 other functionals, *Theor. Chem. Acc.* 119 (2008) 525–525. doi:10.1007/s00214-007-0401-8.
- [30] A. Schafer, H. Horn, R. Ahlrichs, Fully Optimized Contracted Gaussian-Basis Sets for Atoms Li to Kr, *J. Chem. Phys.* 97 (1992) 2571–2577.
- [31] C. Lee, W. Yang, R.G. Parr, LYP functional, *Phys. Rev. B*. 37 (1988) 785–789.
- [32] A.D. Becke, Density-functional thermochemistry. III. The role of exact exchange, *J. Chem. Phys.* 98 (1993) 5648. doi:10.1063/1.464913.
- [33] C. Adamo, V. Barone, Toward reliable density functional methods without adjustable parameters: The PBE0 model, *J. Chem. Phys.* 110 (1999) 6158. doi:10.1063/1.478522.
- [34] J.P. Perdew, K. Burke, M. Ernzerhof, Generalized Gradient Approximation Made Simple, *Phys. Rev. Lett.* 77 (1996) 3865–3868. doi:10.1103/PhysRevLett.77.3865.
- [35] P. Kautny, D. Lumpi, Y. Wang, A. Tissot, J. Bintliger, E. Horkel, B. Stöger, C. Hametner, H. Hagemann, D. Ma, J. Fröhlich, Oxadiazole based bipolar host materials employing planarized triarylamine donors for RGB PHOLEDs with low efficiency roll-off, *J. Mater. Chem. C*. 2 (2014) 2069–2081. doi:10.1039/C3TC32338B.
- [36] P. Kautny, Z. Wu, J. Eichelter, E. Horkel, B. Stöger, J. Chen, D. Ma, J. Fröhlich, D. Lumpi, Indolo[3,2,1-jk]carbazole based planarized CBP derivatives as host materials for PhOLEDs with low efficiency roll-off, *Org. Electron.* 34 (2016) 237–245. doi:10.1016/j.orgel.2016.04.036.
- [37] H. Puntischer, P. Kautny, B. Stöger, A. Tissot, C. Hametner, H.R. Hagemann, J. Fröhlich, T. Baumgartner, D. Lumpi, Structure–property studies of P-triarylamine-substituted dithieno[3,2-b:2',3'-d]phospholes, *RSC Adv.* 5 (2015) 93797–93807. doi:10.1039/C5RA13651B.
- [38] M. Cossi, V. Barone, R. Cammi, J. Tomasi, Ab initio study of solvated molecules: a new implementation of the polarizable continuum model, *Chem. Phys. Lett.* 255 (1996) 327–335. doi:10.1016/0009-2614(96)00349-1.
- [39] M. Cossi, V. Barone, Time-dependent density functional theory for molecules in liquid solutions, *J. Chem. Phys.* 115 (2001) 4708–4717. doi:10.1063/1.1394921.

- [40] R. Improta, G. Scalmani, M.J. Frisch, V. Barone, Toward effective and reliable fluorescence energies in solution by a new state specific polarizable continuum model time dependent density functional theory approach, *J. Chem. Phys.* 127 (2007) 74504. doi:10.1063/1.2757168.
- [41] M. Barbatti, G. Granucci, M. Persico, M. Ruckebauer, M. Vazdar, M. Eckert-Maksić, H. Lischka, The on-the-fly surface-hopping program system Newton-X: Application to ab initio simulation of the nonadiabatic photodynamics of benchmark systems, *J. Photochem. Photobiol. Chem.* 190 (2007) 228–240. doi:10.1016/j.jphotochem.2006.12.008.
- [42] O. Navarro, S.P. Nolan, Large-Scale One-Pot Synthesis of N-Heterocyclic Carbene-Pd(allyl)Cl Complexes, *Synthesis*. (2006) 366–367. doi:10.1055/s-2005-918497.
- [43] T. Hayashi, M. Konishi, Y. Kobori, M. Kumada, T. Higuchi, K. Hirotsu, Dichloro[1,1'-bis(diphenylphosphino)ferrocene]palladium(II): an effective catalyst for cross-coupling of secondary and primary alkyl Grignard and alkylzinc reagents with organic halides, *J. Am. Chem. Soc.* 106 (1984) 158–163. doi:10.1021/ja00313a032.
- [44] P. Liu, Y. Wu, H. Pan, Y. Li, S. Gardner, B.S. Ong, S. Zhu, Novel High-Performance Liquid-Crystalline Organic Semiconductors for Thin-Film Transistors, *Chem. Mater.* 21 (2009) 2727–2732. doi:10.1021/cm900265q.
- [45] S.A. Odom, K. Lancaster, L. Beverina, K.M. Lefler, N.J. Thompson, V. Coropceanu, J.-L. Brédas, S.R. Marder, S. Barlow, Bis[bis-(4-alkoxyphenyl)amino] Derivatives of Dithienylethene, Bithiophene, Dithienothiophene and Dithienopyrrole: Palladium-Catalysed Synthesis and Highly Delocalised Radical Cations, *Chem. - Eur. J.* 13 (2007) 9637–9646. doi:10.1002/chem.200700668.
- [46] H. Xu, K. Yin, W. Huang, Highly Improved Electroluminescence from a Series of Novel EuIII Complexes with Functional Single-Coordinate Phosphine Oxide Ligands: Tuning the Intramolecular Energy Transfer, Morphology, and Carrier Injection Ability of the Complexes, *Chem. - Eur. J.* 13 (2007) 10281–10293. doi:10.1002/chem.200700678.
- [47] R. Anémian, D.C. Cupertino, P.R. Mackie, S.G. Yeates, Solution phase studies towards the synthesis of triarylamine oligomers using a germanium linker on a solid support, *Tetrahedron Lett.* 46 (2005) 6717–6721. doi:10.1016/j.tetlet.2005.07.150.
- [48] H. Brigitte, E. Horkel, A. Rosspeintner, D. Lumpi, in preparation, (n.d.).
- [49] N. Marion, O. Navarro, J. Mei, E.D. Stevens, N.M. Scott, S.P. Nolan, Modified (NHC)Pd(allyl)Cl (NHC = N-Heterocyclic Carbene) Complexes for Room-Temperature Suzuki–Miyaura and Buchwald–Hartwig Reactions, *J. Am. Chem. Soc.* 128 (2006) 4101–4111. doi:10.1021/ja057704z.
- [50] L. Ackermann, A. Althammer, P. Mayer, Palladium-Catalyzed Direct Arylation-Based Domino Synthesis of Annulated N-Heterocycles Using Alkenyl or (Hetero)Aryl 1,2-Dihalides, *Synthesis*. 2009 (2009) 3493–3503. doi:10.1055/s-0029-1216977.



# Manuscript #6

D. Lumpi\*, B. Holzer\*, **J. Binterger**, E. Horkel, S. Waid, H. D. Wanzenböck, M. Marchetti-Deschmann, C. Hametner, E. Bertagnolli, I. Kymissis, J. Fröhlich; *New J. Chem.* 2015

Reproduced from Ref.<sup>86</sup> with permission from the Centre National de la Recherche Scientifique (CNRS) and The Royal Society of Chemistry.





Cite this: DOI: 10.1039/c4nj01695e

## Substituted triphenylamines as building blocks for star shaped organic electronic materials†

Daniel Lumpi,<sup>‡</sup> Brigitte Holzer,<sup>‡</sup> Johannes Binting,<sup>ab</sup> Ernst Horkel,<sup>\*a</sup> Simon Waid,<sup>c</sup> Heinz D. Wanzenböck,<sup>c</sup> Martina Marchetti-Deschmann,<sup>d</sup> Christian Hametner,<sup>a</sup> Emmerich Bertagnoli,<sup>c</sup> Ioannis Kyriassis<sup>b</sup> and Johannes Fröhlich<sup>a</sup>

A versatile synthetic protocol toward a series of various substituted triphenylamine derivatives serving as building blocks for organic electronic materials was developed. Key steps during synthesis were either Ullmann condensations or nucleophilic aromatic substitutions giving rise to structural modification of triphenylamines and their electronic nature. In turn, these scaffolds were exemplarily attached to a dendritic tris(2-thienyl)benzene core affording star shaped organic semiconducting materials which were characterized regarding their photo-physical, electro-chemical and thermal properties. A strong influence of the substituent's nature on both photo-physical and morphological thin film characteristic of star shaped target compounds was observed. The applicability of these materials in organic electronic devices was demonstrated in an organic field effect transistor configuration yielding a hole mobility of nearly  $10^{-3} \text{ cm}^2 \text{ V}^{-1} \text{ s}^{-1}$ . The performance of the materials can be correlated to the substituents applied.

Received (in Montpellier, France)  
30th September 2014,  
Accepted 15th December 2014

DOI: 10.1039/c4nj01695e

www.rsc.org/njc

## Introduction

Organic electronic (OE) thin film devices have gained raising interest from academia and industry due to the variety of possible applications with enormous commercial potential.<sup>1</sup> This field covers the application of conducting and semi-conducting organic materials within electronic devices such as organic field effect transistors (OFETs),<sup>2</sup> organic light emitting devices (OLEDs)<sup>3</sup> and organic photovoltaics (OPVs).<sup>4,5</sup> The application of these materials in the field of organic electronics allows for solution processability, thus rendering OE-technology compatible with established high-throughput printing techniques and with the potential to realize thin, flexible and light-weight devices with low manufacturing costs.<sup>6</sup>

In general, a high charge carrier mobility is mandatory for the performance of different devices and strongly depends both

on the molecular structure and the morphology of the semiconducting material.<sup>2,7</sup> Therefore, a broadly applicable material with high charge carrier mobility independent of processing techniques is desirable.<sup>8,9</sup> The quest for novel compounds is an ongoing process in material science.

Poly- and oligothiophene based compounds have a long history in the field of OE.<sup>10</sup> While high hole mobilities (up to  $1.3 \text{ cm}^2 \text{ V}^{-1} \text{ s}^{-1}$ ) have been observed for thin films of poly-(3-hexylthiophene) (P3HT),<sup>11</sup> the material cannot be used in the light emitting layers of an OLED due to fluorescent self-quenching caused by strong  $\pi$ - $\pi$  stacking.<sup>12</sup> Another useful class of OE materials are modified triphenylamine (TPA) structures, which have excellent electron donor and hole transport properties.<sup>13-17</sup> The combination of these structural scaffolds results in a material class incorporating good charge carrier transport as a result of the oligothiophene unit and enhanced luminescent properties by circumventing self-quenching (e.g. **BMA-1T**, Fig. 1).<sup>18</sup> Moreover, star-shaped compounds are found to exhibit better solubility and film-forming properties than their linear counterparts.<sup>8,19,20</sup>

Combining TPA and thiophenes in  $C_3$  symmetric configurations leads to enhanced electronic and luminescent properties with the benefit of solution processability.<sup>21</sup> To realize  $C_3$  symmetry, one can think of two possible molecular designs. One possibility is to use the TPA moiety as a central node with thiophene moieties as dendrons.<sup>19,22,23</sup> Alternatively, a core (e.g. tris(2-thienyl)benzene) can be used to ensure  $C_3$  symmetry bearing TPA units as side arms.<sup>24</sup> Based on these two possible

<sup>a</sup> Institute of Applied Synthetic Chemistry, Vienna University of Technology, Getreidemarkt 9/163OC, A-1060 Vienna, Austria.

E-mail: ernst.horkel@tuwien.ac.at

<sup>b</sup> Department of Electrical Engineering, Columbia University, 520W 120th street, Suite 1300, 10027 New York, NY, USA

<sup>c</sup> Institute of Solid State Electronics, Vienna University of Technology, Floragasse 7, A-1040 Vienna, Austria

<sup>d</sup> Institute of Chemical Technologies and Analytics, Vienna University of Technology, Getreidemarkt 9/164IAC, A-1060 Vienna, Austria

† Electronic supplementary information (ESI) available: <sup>1</sup>H and <sup>13</sup>C NMR spectra of compounds **6c**, **6e-1**, **8c**, **8e-g**, **2**, **S2-3**, absorption and emission spectra of compounds **S1-3** and HOMO-LUMO plots of **S1-3**. See DOI: 10.1039/c4nj01695e

‡ Daniel Lumpi and Brigitte Holzer contributed equally to this article.

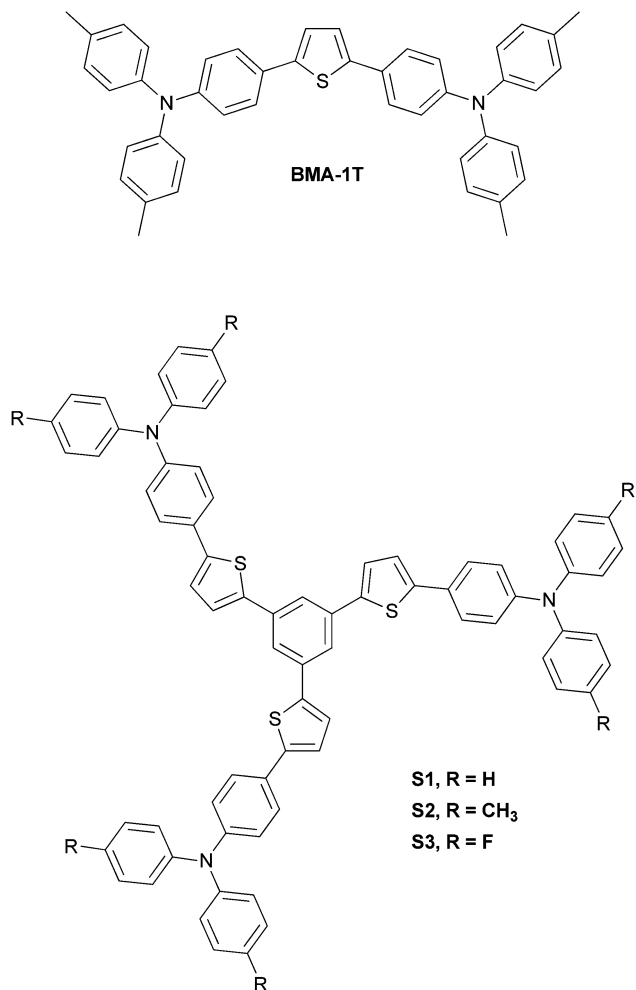


Fig. 1 Linear motifs (top) presented by Noda,<sup>18</sup> star shaped molecules described in this work (bottom).

structural connectivities, this paper focuses on the latter possibility, since substituent alteration on the three TPA moieties constituting the outer sphere of the molecule strongly influences glass- and film-forming behaviour<sup>8</sup> of the resulting materials, in turn affecting device performance.

Due to the widespread application of TPA-based compounds as building blocks in the field of organic electronics,<sup>25</sup> the synthetic protocol presented in this work is of considerable interest for the molecular design and potential modifications (e.g. in terms of photo-physical properties) toward a broad range of novel materials. Fine tuning of material properties can be realized by applying structurally and electronically diverse TPA motifs. However, due to the broad spectrum of substituents (electron donating or withdrawing) attached to the TPA, no general synthetic protocol is available. Access to TPAs bearing electron donating substituents is often described in literature, mainly applying Ullmann condensation.<sup>26</sup> On the other hand, this synthetic technique often fails when applied towards the synthesis of electron withdrawing groups. As a result of our investigations to overcome this drawback, we present a general protocol using nucleophilic aromatic substitution in order to

gain access to TPAs bearing electron withdrawing substituents. Reaction conditions for the consecutive transformation to the above-mentioned boronic acid esters also depend on the substituents' nature. While lithiation protocols can be applied for most TPAs under investigation, Miyaura borylation is required for TPAs bearing  $-M$  substituents (Scheme 2).

With these TPA boronic acid esters in hand, a set of three star shaped compounds **S1–3** was realized using a Suzuki reaction. This nontoxic procedure proved superior in yield to a previously reported procedure incorporating a Stille reaction for the same compound **S1**.<sup>24</sup>

Measurements of electro-chemical and optical properties (e.g. fluorescence spectra and quantum yields) of the star shaped compounds **S1–3** reveal the strong influence of the substituents' nature on the TPA moiety on the above-mentioned properties. The materials were characterized with respect to thermal stability, film-forming upon spin coating and semiconducting behaviour (charge carrier mobility in OFET configuration) to probe device applicability. Mobilities of almost  $10^{-3} \text{ cm}^2 \text{ V}^{-1} \text{ s}^{-1}$  and low threshold voltages of approx. 0 V were recorded using methyl-TPA substituted derivative **S2**.

## Experimental section

### Synthesis and characterization

Substances purchased from commercial sources were used as received. Anhydrous *N,N*-dimethylformamide (DMF), *n*-butyllithium solution (2.5 M in hexanes) and 1,3,5-tribromobenzene were purchased from Aldrich Chemical Co. Isopropyl pinacol borate<sup>27</sup> (CAS 61676-62-8), (IPr)Pd(allyl)Cl<sup>28</sup> (CAS 478980-03-9) were synthesized according to literature. Anhydrous tetrahydrofuran (THF), diethyl ether, toluene were prepared immediately prior to use by a PURESOLV-plant (*it-innovative technology inc.*). Technical grade solvents were distilled prior to use. Analytical TLC was performed on Merck silica gel 60 F254 plates. Chromatographic separations at preparative scale were carried out on silica gel (Merck silica gel 60, 40–63  $\mu\text{m}$ ), alox or RP-gel. Nuclear magnetic resonance (NMR) spectra were obtained using a Bruker DPX-200 or Avance DRX-400 Fourier transform spectrometer operating at the following frequencies: DPX-200: 200.1 MHz (<sup>1</sup>H) and 50.3 MHz (<sup>13</sup>C); DRX-400: 400.1 MHz (<sup>1</sup>H) and 100.6 MHz (<sup>13</sup>C). The chemical shifts are reported in delta ( $\delta$ ) units, parts per million (ppm) downfield from tetramethylsilane using solvent residual signals for calibration. Coupling constants are reported in Hertz; multiplicity of signals is indicated by using following abbreviations: s = singlet, d = doublet, t = triplet, q = quartet. The multiplicity of <sup>13</sup>C signals were obtained by measuring JMOD spectra. UV/VIS absorption and fluorescence emission spectra were recorded in THF solutions ( $1 \mu\text{g mL}^{-1}$ ) with a Perkin Elmer Lambda 750 spectrometer and an Edinburgh FLS920, respectively. Cyclic voltammetry was performed using a three electrode configuration consisting of a Pt working electrode, a Pt counter electrode and an Ag/AgCl reference electrode and a PGSTAT128N, ADC164, DAC164, external, DI048 potentiostat provided by Metrohm Autolab B. V. Measurements were carried



out in a 0.5 mM solution in anhydrous DCM (oxidation scan) with  $\text{Bu}_4\text{NBF}_4$  (0.1 M) as the supporting electrolyte. The solutions were purged with nitrogen for 15 minutes prior to measurement. HOMO energy levels were calculated from the onset of oxidation. The onset potential was determined by the intersection of two tangents drawn at the background and the rising of oxidation peaks. High-resolution mass spectra (HRMS) were acquired as radical cations using a SYNAPT HDMS instrument (Waters, Manchester, UK) equipped with a matrix-assisted laser desorption/ionization (MALDI) source (MALDI-HRMS). Samples were applied at  $1 \text{ mg mL}^{-1}$  in THF on stainless steel using nitroanthracene ( $3 \text{ mg mL}^{-1}$  in THF) as MALDI matrix. All MS spectra were recorded as accurate mass data with Angiotensin II ( $m/z$  1046.542) as internal lock mass achieving a mass accuracy of 15–40 ppm (*i.e.*  $\Delta m/z$  0.01–0.04 amu). GC-MS measurements were conducted on a GC-MS hyphenation from Thermo Finnigan: focus GC with a BGB5 column ( $l = 30 \text{ m}$ ,  $\varnothing = 0.25 \text{ mm}$ ,  $0.25 \mu\text{m}$  film); DSQ II Quadrupole ( $\text{EI}^+$  mode). The thermal behavior of substances **S1–3** was studied with differential scanning calorimetry (DSC) and thermogravimetric analysis (TGA) using a Netzsch simultaneous thermal analyzer (STA 449 F1 Jupiter). Powder samples with a mass of approx. 10 mg were lightly pressed into the bottom of open aluminum pans and heated at  $10 \text{ }^\circ\text{C min}^{-1}$  from  $25 \text{ }^\circ\text{C}$  to  $500 \text{ }^\circ\text{C}$  under  $\text{N}_2$  gas at a flow rate of  $40 \text{ mL min}^{-1}$ . The STA 449 type-K thermocouples were calibrated using indium, tin, bismuth and zinc metals.

Bottom-gate, top-contact OFETs were fabricated on ITO substrates with a 250 nm layer of vacuum deposited parylene-C which serves as a common gate electrode/gate dielectric structure. The substrates were ultrasonically cleaned with water, acetone and isopropanol followed by a 20 min treatment of UV/ozone. Compounds **S1–3** (25 nm) were vacuum deposited through a shadow mask ( $p = 10^{-7}$  Torr, rate  $0.1 \text{ \AA s}^{-1}$ ). The devices were completed by evaporation of gold source and drain electrodes (50 nm) on top. All characterizations were performed in ambient air. Current–voltage characteristics of the fabricated devices were recorded using a Keithley model 4200 semiconductor characterization system. Output and transfer characterization were recorded for at least four samples of the same channel width ( $W = 2000 \mu\text{m}$ ) and channel length ( $L = 100 \mu\text{m}$ ).

The spin-coated samples were prepared by the following procedure: the ITO substrates were ultrasonically cleaned with water, acetone and isopropanol followed by blow-drying with  $\text{N}_2$ . 400  $\mu\text{L}$  of a solution of the organic substance in chloroform ( $20 \text{ mg mL}^{-1}$ ) was prepared and filtered through a syringe filter (Teflon  $\varnothing$  25 mm,  $0.20 \mu\text{m}$ ). Consecutively 300  $\mu\text{L}$  of the prepared organic solution was spin-coated ( $2000 \text{ rpm s}^{-1}$ ; 30 s) directly on ITO.

The typical layer thickness was in the range of 30–50 nm as revealed from atomic force microscopy (AFM)-measurements. For AFM studies, a Multimode V scanner in conjunction with a Nanoscope V controller (Veeco Instruments) was used. Image processing and data analysis was performed using Gwyddion software version 2.40. Samples were measured in tapping mode using PPP-NCHR probes obtained from Nanoandmore in air.

Several scans were performed from different parts of the samples to check the uniformity of the surface. Final images were measured from a scanning area of  $10 \times 10 \mu\text{m}^2$  with a tip velocity in the range from 16 to  $18 \mu\text{m s}^{-1}$ . No image processing except flattening was done. Roughness values were calculated as root-mean-square (rms) values.

All computations were performed using the Gaussian 09 package, revision A.02.<sup>29</sup> For the calculation of HOMO/LUMO levels of compounds **S1–3**, ground state ( $S_0$ ) geometries were optimized in gas phase within  $C_3$  symmetry using the Becke three parameters hybrid functional with Lee–Yang–Perdew correlation (B3LYP)<sup>30,31</sup> in combination with Pople basis set 6-311+G\*.<sup>32</sup> To obtain vertical absorption and emission of model compounds **S<sub>m</sub>1–3**, ground state  $S_0$  and first excited singlet state  $S_1$  were optimized applying DFT and time-dependent (TD) DFT level of theory using M06-2X<sup>33,34</sup> functional in combination with the polarized double zeta SVP basis set.<sup>35</sup> This parameterization was shown to be superior in terms of accuracy for the calculation of vertical transitions.<sup>36</sup> Geometry optimizations were performed without symmetry constraints and solvent effects were included through the polarizable continuum model (PCM)<sup>37</sup> in its linear response (LR-PCM)<sup>38</sup> and state specific (SS-PCM)<sup>39</sup> formulations, always considering the equilibrium time regime (eq.) for the excited state.

#### General procedure for the synthesis of 6a–f

Synthesis was performed according to Goodbrand.<sup>26</sup> 4-Bromoaniline **4a** (1.0 eq.), substituted iodobenzene **5a–f** (2.2 eq.), KOH (7.8 eq.), CuCl (0.04 eq) and 1,10-phenanthroline monohydrate (0.04 eq.) were suspended in anhydrous toluene. After purging the apparatus with argon, the reaction mixture was refluxed on a Dean Stark trap for an appropriate time maintaining the argon atmosphere. Reaction progress was monitored by GC/MS. The reaction mixture was cooled to room temperature and water was added to solve the potassium hydroxide. Phases were separated and the hydrous phase was extracted with toluene three times. The combined organic layer was washed with brine, dried over anhydrous sodium sulfate and evaporated to dryness under reduced pressure. The obtained crude product was purified by Kugelrohr distillation and subsequent recrystallisation from methanol or acetonitrile.

**4-Bromo-N,N-bis(4-fluorophenyl)benzeneamine (6c)**. According to the general procedure; **4a** (7.04 g, 41 mmol), **5c** (20.0 g, 90 mmol), KOH (17.94 g, 320 mmol), CuCl (162 mg, 1.6 mmol) and phenanthroline monohydrate (325 mg, 1.6 mmol) were refluxed for 16 h using 250 mL anhydrous toluene. Kugelrohr distillation ( $130 \text{ }^\circ\text{C}$ ,  $3.8 \times 10^{-1}$  mbar) and recrystallization from methanol gave colourless crystals of **6c** (10.33 g, 70% of theory). TLC (silica gel, hexanes):  $r_f = 0.36$ .  $F_p = 56\text{--}58 \text{ }^\circ\text{C}$ .  $^1\text{H NMR}$  (200 MHz,  $\text{CD}_2\text{Cl}_2$ ):  $\delta = 7.38\text{--}7.25$  (m, 2H), 7.11–6.91 (m, 4H), 6.89–6.72 (m, 8H), 6.91–6.80 (m, 2H) ppm.  $^{13}\text{C NMR}$  (50 MHz,  $\text{CD}_2\text{Cl}_2$ ):  $\delta = 159.7$  (s,  $J_{\text{CF}} = 242.6$  Hz), 147.8 (s), 144.0 (s,  $J_{\text{CF}} = 2.8$  Hz), 132.7 (d), 126.9 (d,  $J_{\text{CF}} = 8.1$  Hz), 124.3 (d), 116.7 (d,  $J_{\text{CF}} = 22.6$  Hz), 114.7 (s) ppm. MS (EI):  $m/z$  359 ( $\text{M}^+$ , 100%), 279 (22), 184 (14).

**4-Bromo-*N,N*-bis[4-(trimethylsilyl)phenyl]benzeneamine (6e).** According to the general procedure; **4a** (7.82 g, 45.5 mmol), **5e** (27.62 g, 100 mmol), KOH (19.89 g, 355 mmol), CuCl (180 mg, 1.8 mmol) and phenanthroline monohydrate (360 mg, 1.8 mmol) were refluxed for 24 h using 250 mL anhydrous toluene. Kugelrohr distillation (130 °C,  $6.5 \times 10^{-2}$  mbar) and recrystallization from acetonitrile gave colourless crystals of **6e** (12.9 g, 60% of theory). TLC (silica gel, hexanes):  $r_f = 0.39$ .  $F_p = 143\text{--}145$  °C.  $^1\text{H}$  NMR (200 MHz,  $\text{CDCl}_3$ ):  $\delta = 7.42\text{--}7.27$  (m, 6H), 7.08–6.90 (m, 6H), 0.24 (s, 18H) ppm.  $^{13}\text{C}$  NMR (100 MHz,  $\text{CDCl}_3$ ):  $\delta = 147.9$  (s), 146.9 (s), 134.64 (s), 134.61 (d), 132.4 (d), 126.1 (d), 123.5 (d), 115.5 (s), 112.4 (s), –0.8 (q) ppm. MS (EI):  $m/z$  469 ( $\text{M}^+$ , 100%), 454 (61), 452 (58), 220 (65).

**4-Bromo-*N,N*-bis[4-(1,1-dimethylethyl)phenyl]benzeneamine (6f).** According to the general procedure; **4a** (3.7 g, 21.5 mmol), **5f** (12.3 g, 47.3 mmol), KOH (9.4 g, 168 mmol), CuCl (85 mg, 0.86 mmol) and phenanthroline monohydrate (170 mg, 0.86 mmol) were refluxed for 36 h using 130 mL anhydrous toluene. Kugelrohr distillation (160 °C,  $2.2 \times 10^{-1}$  mbar) and recrystallization from acetonitrile gave colourless crystals of **6f** (5.8 g, 61% of theory). TLC (silica gel, hexanes):  $r_f = 0.33$ .  $F_p = 165\text{--}168$  °C.  $^1\text{H}$  NMR (200 MHz,  $\text{CD}_2\text{Cl}_2$ ):  $\delta = 7.36\text{--}7.22$  (m, 6H), 7.07–6.95 (m, 4H), 6.95–6.82 (m, 2H), 1.32 (s, 18H) ppm.  $^{13}\text{C}$  NMR (50 MHz,  $\text{CD}_2\text{Cl}_2$ ):  $\delta = 148.1$  (s), 146.9 (s), 145.3 (s), 132.4 (d), 126.8 (d), 124.8 (d), 124.5 (d), 114.0 (s), 34.8 (s), 31.8 (q) ppm. MS (EI):  $m/z$  435 ( $\text{M}^+$ , 73%), 422 (96), 420 (100), 204 (35), 176 (47).

#### General procedure for the synthesis of **6g–6l** (nucleophilic substitution)

Synthesis was performed according to Davey<sup>40</sup> and Gorvin.<sup>40,41</sup> Under an argon atmosphere, 4-haloaniline **4a,b** (1 eq.), fluoro-benzene **8a–c** (2.2 eq.) and base (CsF or  $\text{KO}^t\text{Bu}$ , 2.0–2.2 eq.) were stirred in DMSO (stored over molecular sieve, 3 Å) at 120 °C overnight. The solvent was removed under reduced pressure and the remaining crude product dissolved in chloroform. After washing with water, the organic layer was dried over anhydrous sodium sulfate and evaporated to dryness under reduced pressure. Further purification was achieved by column chromatography or recrystallization.

**4-Bromo-*N,N*-bis(4-nitrophenyl)benzeneamine (6g).** Under an argon atmosphere, 4-bromoaniline (6.88 g, 40 mmol) and CsF (12.15 g, 80 mmol) were suspended in 100 mL of dry DMSO. To the stirred suspension **7a** (12.42 g, 88 mmol) was added drop wise and the reaction was heated to 110 °C for 40 h. After cooling to r.t., the reaction mixture was poured on 800 mL of water. The formed brown precipitate was filtered over a glass sinter funnel and crystallized from pyridine to give **6g** (9.00 g, 54% of theory) as yellow crystals. TLC (silica gel, hexanes/ethyl acetate = 9/1):  $r_f = 0.76$ .  $F_p = 312\text{--}315$  °C.  $^1\text{H}$  NMR (400 MHz,  $\text{CDCl}_3$ ):  $\delta = 8.19\text{--}8.10$  (m, 4H), 7.57–7.49 (m, 2H), 7.17–7.09 (m, 4H), 7.07–7.00 (m, 2H) ppm.  $^{13}\text{C}$  NMR (100 MHz,  $\text{CDCl}_3$ ):  $\delta = 151.7$  (s), 144.2 (s), 143.3 (s), 133.9 (d), 128.7 (d), 125.9 (d), 122.8 (d), 120.5 (s) ppm. MS (EI):  $m/z$  413 ( $\text{M}^+$ , 100%), 323 (20), 321 (20), 241 (96).

**4-Bromo-*N,N*-bis[4-(methylsulfonyl)phenyl]benzeneamine (6h).** Under an argon atmosphere, 4-bromoaniline (86 mg, 0.5 mmol),

**7b** (192 mg, 1.1 mmol) and  $\text{KO}^t\text{Bu}$  (118 mg, 1.05 eq.) were stirred in 2 mL of dry DMSO at 120 °C for 12 h. After cooling to r.t., the solvent was removed under reduced pressure. The residue was taken up with chloroform and filtered over a pad of celite. The solvent was removed under reduced pressure and the crude product purified by column chromatography (40 g silica gel, hexanes/ethyl acetate gradient 20 → 50%) to give **6h** as light brown powder (184 mg, 77% of theory). TLC (silica gel, hexanes/ethyl acetate = 1/1):  $r_f = 0.20$ .  $F_p = 240$  °C.  $^1\text{H}$  NMR (200 MHz,  $\text{CDCl}_3$ ):  $\delta = 7.86\text{--}7.73$  (m, 4H), 7.55–7.44 (m, 2H), 7.22–7.11 (m, 4H), 7.06–6.96 (m, 2H), 3.05 (s, 6H) ppm.  $^{13}\text{C}$  NMR (50 MHz,  $\text{CDCl}_3$ ):  $\delta = 151.0$  (s), 144.5 (s), 134.8 (s), 133.6 (d), 129.4 (d), 128.4 (d), 123.2 (d), 119.7 (s), 44.8 (q) ppm.

**4,4'-[[4-Bromophenyl]imino]bisbenzotrile (6i).** Under an argon atmosphere, 4-bromoaniline (8.1 g, 47 mmol) and CsF (14.3 g, 94 mmol) were suspended in 120 mL of dry DMSO. A solution of **7c** (12.5 g, 103 mmol) in 50 mL of dry DMSO was added drop wise and the reaction mixture was heated to 110 °C for 50 h. After cooling to r.t., the reaction mixture was poured on 800 mL of water and extracted three times with 200 mL chloroform. The combined organic layer was washed with brine, dried over anhydrous sodium sulfate and the solvent was removed under reduced pressure. The crude product was crystallized from ethanol to give **6i** (4.05 g, 23% of theory) as light brown solid. TLC (silica gel, hexanes/ethyl acetate = 4/1):  $r_f = 0.41$ .  $F_p = 261\text{--}262$  °C.  $^1\text{H}$  NMR (200 MHz,  $\text{CDCl}_3$ ):  $\delta = 7.58\text{--}7.42$  (m, 6H), 7.14–7.03 (m, 4H), 7.03–6.93 (m, 2H) ppm.  $^{13}\text{C}$  NMR (50 MHz,  $\text{CDCl}_3$ ):  $\delta = 149.9$  (s), 144.3 (s), 133.8 (d), 133.6 (d), 128.3 (d), 123.3 (d), 119.7 (s), 118.9 (s), 106.5 (s) ppm. MS (EI):  $m/z$  373 ( $\text{M}^+$ , 100%), 293 (29), 192 (38), 147 (80).

**4-Iodo-*N,N*-bis(4-nitrophenyl)benzeneamine (6j).** Under an argon atmosphere, 4-iodoaniline (5.6 g, 26 mmol) and  $\text{KO}^t\text{Bu}$  (6.1 g, 54 mmol) were suspended in 150 mL of dry DMSO. To the stirred suspension **7a** (8.00 g, 57 mmol) was added drop wise and the reaction was heated to 120 °C for 40 h. After cooling to r.t., the solvent was removed under reduced pressure. The residue was taken up with chloroform and filtered over a pad of celite. The solvent was removed under reduced pressure and the crude product crystallized from pyridine to give **6j** (6.96 g, 58% of theory) as orange solid. TLC (silica gel, hexanes/ethyl acetate = 9/1):  $r_f = 0.26$ .  $F_p = 295\text{--}297$  °C.  $^1\text{H}$  NMR (400 MHz,  $\text{CDCl}_3$ ):  $\delta = 8.19\text{--}8.10$  (m, 4H), 7.76–7.68 (m, 2H), 7.17–7.09 (m, 4H), 6.94–6.87 (m, 2H) ppm.  $^{13}\text{C}$  NMR (100 MHz,  $\text{CDCl}_3$ ):  $\delta = 151.6$  (s), 144.9 (s), 143.4 (s), 139.8 (d), 128.8 (d), 125.9 (d), 122.9 (d), 91.4 (s) ppm. MS (EI):  $m/z$  461 ( $\text{M}^+$ , 100%), 369 (11), 241 (83).

**4-Iodo-*N,N*-bis[4-(methylsulfonyl)phenyl]benzeneamine (6k).** Under an argon atmosphere, 4-iodoaniline (4.38 g, 20 mmol), **7b** (7.6 g, 44 mmol) and  $\text{KO}^t\text{Bu}$  (4.94 g, 44 mmol) were stirred in 150 mL of dry DMSO at 120 °C for 18 h. After cooling to r.t., the solvent was removed under reduced pressure. The residue was taken up with 100 mL of chloroform and washed with 50 mL of water. After drying over anhydrous sodium sulfate, the solvent was removed under reduced pressure and the crude product was purified by recrystallization from acetic acid/water ( $v/v = 15/1$ ) to give **6k** as a brown solid (6.74 g, 64% of theory).

TLC (silica gel, hexanes/ethyl acetate = 1/1):  $r_f$  = 0.19.  $F_p$  = 232–235 °C.  $^1\text{H}$  NMR (200 MHz,  $\text{CDCl}_3$ ):  $\delta$  = 7.83–7.73 (m, 4H), 7.70–7.62 (m, 2H), 7.23–7.11 (m, 4H), 6.92–6.83 (m, 2H), 3.04 (s, 6H) ppm.  $^{13}\text{C}$  NMR (50 MHz,  $\text{CDCl}_3$ ):  $\delta$  = 151.0 (s), 145.2 (s), 139.5 (d), 134.8 (s), 129.4 (d), 128.5 (d), 123.3 (d), 90.5 (s), 44.8 (q) ppm.

**4,4'-[(4-Iodophenyl)imino]bisbenzotrile (6l).** Under an argon atmosphere, 4-iodoaniline (4.48 g, 20.5 mmol) and CsF (6.52 g, 43 mmol) were suspended in 40 mL of dry DMSO. A solution of **7c** (5.45 g, 45 mmol) in 20 mL of dry DMSO was added drop wise and the reaction mixture was heated to 140 °C for 18 h. After cooling to r.t., the solvent was removed under reduced pressure. The residue was taken up with chloroform and filtered over a pad of celite. The solvent was removed under reduced pressure and the crude product purified by column chromatography (90 g silica gel, dry loading on 10 g silica, hexanes/ethyl acetate gradient 5 → 20%) to give **6l** (2.10 g, 24% of theory) as light yellow solid. TLC (silica gel, hexanes/ethyl acetate = 4/1):  $r_f$  = 0.42.  $F_p$  = 228–230 °C.  $^1\text{H}$  NMR (200 MHz,  $\text{CDCl}_3$ ):  $\delta$  = 7.73–7.61 (m, 2H), 7.59–7.45 (m, 4H), 7.15–7.02 (m, 4H), 6.92–6.81 (m, 2H) ppm.  $^{13}\text{C}$  NMR (50 MHz,  $\text{CDCl}_3$ ):  $\delta$  = 149.9 (s), 145.0 (s), 139.5 (d), 133.8 (d), 128.5 (d), 123.4 (d), 118.9 (s), 106.5 (s), 90.5 (s) ppm. MS (EI):  $m/z$  421 ( $M^+$ , 100%), 294 (12), 192 (12).

#### General procedure for the synthesis of 8a–f

Synthesis was performed according to Anemian:<sup>42</sup> all operations were performed under argon atmosphere. Triphenylamine (**6a–f**) (1.0 eq.) was dissolved in anhydrous THF. The solution was cooled to –80 °C and a solution of *n*-butyllithium (2.5 M in hexanes) (1.2 eq.) was added *via* a syringe, keeping the temperature below –75 °C. The reaction mixture was stirred at –80 °C for appropriate time before isopropyl pinacol borate (1.2 eq.) was added drop-wise at the same temperature. After slowly warming to room temperature (approx. 2 h), stirring was continued overnight. The solvent was distilled off under reduced pressure and the residue was distributed between water and chloroform. The phases were separated and the aqueous phase was extracted twice with chloroform. The combined organic layer was washed with brine and dried over sodium sulfate. The solvent was removed under reduced pressure to give the crude product, which was further purified by recrystallization or Kugelrohr distillation.

***N,N*-Bis(4-fluorophenyl)-4-(4,4,5,5-tetramethyl-1,3,2-dioxaborolan-2-yl)benzeneamine (8c).** According to the general procedure; **6c** (4.8 g, 13.3 mmol) was lithiated with *n*-BuLi (6.4 mL, 16 mmol) in 50 mL anhydrous THF for 2 h before isopropyl pinacol borate (3.0 g, 16 mmol) was added. After general workup the crude product was purified by Kugelrohr distillation (130 °C,  $8.0 \times 10^{-2}$  mbar) to give **8c** as white crystalline powder (4.9 g, 91% of theory). TLC (silica gel, hexanes/ethyl acetate = 8/1):  $r_f$  = 0.67.  $F_p$  = 92–95 °C.  $^1\text{H}$  NMR (200 MHz,  $\text{CD}_2\text{Cl}_2$ ):  $\delta$  = 7.65–7.53 (m, 2H), 7.16–6.84 (m, 10H), 1.31 (s, 12H) ppm.  $^{13}\text{C}$  NMR (50 MHz,  $\text{CD}_2\text{Cl}_2$ ):  $\delta$  = 159.8 (s,  $J_{\text{CF}}$  = 242.8 Hz), 151.2 (s), 143.9 (s,  $J_{\text{CF}}$  = 3.2 Hz), 136.3 (d), 127.5 (d,  $J_{\text{CF}}$  = 8.2 Hz), 120.7 (d), 116.7 (d,  $J_{\text{CF}}$  = 22.6 Hz), 84.1 (s), 25.2 (q) ppm (C–B not detected). MS (EI):  $m/z$  407 ( $M^+$ , 100%), 349 (10), 307 (18).

***N,N*-Bis[4-(trimethylsilyl)phenyl]-4-(4,4,5,5-tetramethyl-1,3,2-dioxaborolan-2-yl)benzeneamine (8e).** According to the general

procedure; **6e** (7.03 g, 15 mmol) was lithiated with *n*-BuLi (7.2 mL, 18 mmol) in 75 mL of anhydrous THF for 2 h before isopropyl pinacol borate (3.35 g, 18 mmol) was added. After general workup the crude product was purified by recrystallization from acetonitrile to give **8e** as white crystalline powder (6.60 g, 85% of theory). TLC (silica gel, hexanes/ethyl acetate = 8/1):  $r_f$  = 0.72.  $F_p$  = 206–209 °C.  $^1\text{H}$  NMR (200 MHz,  $\text{CDCl}_3$ ):  $\delta$  = 7.73–7.64 (m, 2H), 7.44–7.34 (m, 4H), 7.13–7.02 (m, 6H), 1.34 (s, 12H), 0.26 (s, 18H) ppm.  $^{13}\text{C}$  NMR (50 MHz,  $\text{CDCl}_3$ ):  $\delta$  = 150.4 (s), 147.9 (s), 136.1 (d), 134.7 (s), 134.5 (d), 124.0 (d), 122.8 (d), 83.8 (s), 25.1 (q), –0.8 (q) ppm (C–B not detected). MS (EI):  $m/z$  515 ( $M^+$ , 100%), 500 (22), 400 (11), 243 (11).

***N,N*-Bis[4-(1,1-dimethylethyl)phenyl]-4-(4,4,5,5-tetramethyl-1,3,2-dioxaborolan-2-yl)benzeneamine (8f).** According to the general procedure; **6f** (10.91 g, 25 mmol) was lithiated with *n*-BuLi (12 mL, 30 mmol) in 150 mL of anhydrous THF for 2 h before isopropyl pinacol borate (5.58 g, 30 mmol) was added. After general workup the crude product was triturated with methanol to give **8f** as white crystalline powder (9.05 g, 79% of theory). TLC (silica gel, hexanes/ethyl acetate = 8/1):  $r_f$  = 0.71.  $F_p$  = 212–214 °C.  $^1\text{H}$  NMR (200 MHz,  $\text{CDCl}_3$ ):  $\delta$  = 7.64–7.53 (m, 2H), 7.37–7.26 (m, 4H), 7.10–7.00 (m, 4H), 7.00–6.91 (m, 2H), 1.37–1.29 (m, 30H) ppm.  $^{13}\text{C}$  NMR (50 MHz,  $\text{CDCl}_3$ ):  $\delta$  = 151.5 (s), 147.2 (s), 145.2 (s), 136.2 (d), 126.8 (d), 125.4 (d), 120.9 (d), 84.0 (s), 34.8 (s), 31.8 (q), 25.3 (q) ppm (C–B not detected). MS (EI):  $m/z$  483 ( $M^+$ , 16%), 468 (18), 368 (12), 168 (11), 57 (100).

***N,N*-Bis(4-nitrophenyl)-4-(4,4,5,5-tetramethyl-1,3,2-dioxaborolan-2-yl)benzeneamine (8g).** Synthesis was performed according to Murata.<sup>43</sup> In a 100 mL round-bottom flask, **6j** (2.08 g, 4.5 mmol, 1.0 eq.) and  $\text{PdCl}_2(\text{dppf})$  (98.8 mg, 0.135 mmol, 0.03 eq.) were suspended in 20 mL of dry dioxane. After flushing the apparatus with argon, triethylamine (1.37 g, 13.5 mmol, 3.0 eq.) and pinacolborane (749 mg, 5.85 mmol, 1.3 eq.) were added drop wise. After stirring for 15 h at room temperature the solvent was removed under reduced pressure. The crude product was purified by column chromatography (100 g basic alumina, dry loading on 6 g neutral alumina, hexanes/DCM gradient 25 → 100%) to give **8g** as orange powder (390 mg, 19% of theory). TLC (silica gel, hexanes/ethyl acetate = 8/1):  $r_f$  = 0.52.  $F_p$  = 175–178 °C.  $^1\text{H}$  NMR (200 MHz,  $\text{CDCl}_3$ ):  $\delta$  = 8.18–8.06 (m, 4H), 7.89–7.77 (m, 2H), 7.20–7.07 (m, 6H), 1.33 (s, 12H) ppm.  $^{13}\text{C}$  NMR (50 MHz,  $\text{CDCl}_3$ ):  $\delta$  = 151.9 (s), 147.6 (s), 143.2 (s), 137.1 (d), 126.0 (d), 125.7 (d), 123.0 (d), 84.3 (s), 25.1 (q) ppm (C–B not detected). MS (EI):  $m/z$  461 ( $M^+$ , 100%), 361 (21), 268 (17).

#### General procedure for the Suzuki coupling towards 2, S1–3

The synthesis was performed according to Marion.<sup>44</sup> Under an argon atmosphere, (hetero)aromatic halide (1.0 eq.), boronic ester (3.0–4.5 eq.) and  $\text{KO}^t\text{Bu}$  (3.0–4.5 eq.) were suspended in a sufficient amount of solvent (IPA/ $\text{H}_2\text{O}$  = 3/1; degassed by bubbling with argon). A solution of (IPr)Pd(allyl)Cl (0.02–0.05 eq.) in degassed IPA was added and the reaction mixture was refluxed for an appropriate time, monitoring the conversion by TLC. After completion, the reaction mixture was distributed between water and chloroform; the phases were separated and the aqueous

layer was extracted with chloroform three times. The combined organic layer was dried over anhydrous sodium sulfate and the solvent removed under reduced pressure to give the crude product. Purification was achieved by column chromatography.

**2,2',2''-(1,3,5-Benzenetriyl)tristhiophene (2).** According to the general procedure; 1,3,5-tribromobenzene (0.787 g, 2.5 mmol), 2-thiopheneboronic acid pinacol ester (2.364 g, 11.25 mmol) and KO<sup>t</sup>Bu (1.262 g, 11.25 mmol) were suspended in 50 mL solvent. (IPr)Pd(allyl)Cl (71.4 mg, 125 μmol; dissolved in 1 mL IPA) was added before refluxing for 1 h. After general workup the crude product was purified by column chromatography (90 g silica gel, hexanes/DCM 0 → 3%) to give **2** as white powder (0.697 g, 86% of theory). TLC (silica gel, hexanes/ethyl acetate = 20/1):  $r_f$  = 0.35. <sup>1</sup>H NMR (200 MHz, CDCl<sub>3</sub>): δ = 7.74 (s, 3H), 7.40 (dd,  $J$  = 1.1, 3.6 Hz, 3H), 7.33 (dd,  $J$  = 1.1, 5.1 Hz, 3H), 7.11 (dd,  $J$  = 3.6, 5.1 Hz, 3H) ppm. <sup>13</sup>C-NMR (50 MHz, CDCl<sub>3</sub>): δ = 143.7 (s), 135.9 (s), 128.3 (d), 125.6 (d), 124.1 (d), 122.9 (d) ppm.

**4,4',4''-(1,3,5-Benzenetriyltri-5,2-thiophenediyl)tris[*N,N*-diphenylbenzenamine] (S1).** According to the general Suzuki procedure; compound **3** (280.1 mg, 0.5 mmol), boronic acid pinacol ester **6a** (835.0 mg, 2.25 mmol) and KO<sup>t</sup>Bu (252.5 mg, 2.25 mmol) were suspended in 12 mL solvent. (IPr)Pd(allyl)Cl (14.3 mg, 25 μmol; dissolved in 1 mL IPA) was added before refluxing for 2 h. After general workup the crude product was purified by column chromatography (90 g silica gel, hexanes/DCM = 6/1); after removing the solvent under reduced pressure, the residue was dissolved in 40 mL of boiling 2-butanone. The product was precipitated by adding 50 mL of 2-propanol to give **S1** as yellow powder (512.8 mg, 97% of theory). TLC (silica gel, cyclohexane/DCM = 3/1):  $r_f$  = 0.30. <sup>1</sup>H NMR and <sup>13</sup>C NMR data according to literature.<sup>21</sup> MS (MALDI-TOF): calcd for C<sub>72</sub>H<sub>51</sub>N<sub>3</sub>S<sub>3</sub>: 1053.3245; found: 1053.3020.

**4,4',4''-(1,3,5-Benzenetriyltri-5,2-thiophenediyl)tris[*N,N*-bis-(4-methylphenyl)benzenamine] (S2).** According to the general Suzuki procedure; compound **3** (280.1 mg, 0.5 mmol), boronic acid pinacol ester **6b** (898.5 mg, 2.25 mmol) and KO<sup>t</sup>Bu (252.5 mg, 2.25 mmol) were suspended in 12 mL solvent. (IPr)Pd(allyl)Cl (14.3 mg, 25 μmol; dissolved in 1 mL IPA) was added before refluxing for 2 h. After general workup the crude product was purified by column chromatography (90 g silica gel, hexanes/DCM 25 → 27%) to give **S2** as yellow powder (473.3 mg, 83% of theory). TLC (silica gel, cyclohexane/DCM = 3/1):  $r_f$  = 0.30. <sup>1</sup>H NMR (200 MHz, CD<sub>2</sub>Cl<sub>2</sub>): δ = 7.74 (s, 3H), 7.53–7.44 (m, 6H), 7.40 (d,  $J$  = 3.78 Hz, 3H), 7.23 (d,  $J$  = 3.80 Hz, 3H), 7.15–7.05 (m, 12H), 7.05–6.94 (m, 18H), 2.32 (s, 18H) ppm. <sup>13</sup>C NMR (50 MHz, CD<sub>2</sub>Cl<sub>2</sub>): δ = 148.5 (s), 145.5 (s), 144.9 (s), 141.8 (s), 136.2 (s), 133.7 (s), 130.50 (d), 127.5 (s), 126.8 (d), 125.45 (d), 125.39 (d), 123.4 (d), 122.6 (d), 121.7 (d), 20.1 (s) ppm. MS (MALDI-TOF): calcd for C<sub>78</sub>H<sub>63</sub>N<sub>3</sub>S<sub>3</sub>: 1137.4184; found: 1137.4006.

**4,4',4''-(1,3,5-Benzenetriyltri-5,2-thiophenediyl)tris[*N,N*-bis-(4-fluorophenyl)benzenamine] (S3).** According to the general procedure; compound **3** (280.6 mg, 0.5 mmol), boronic acid pinacol ester **6c** (916.3 mg, 2.25 mmol) and KO<sup>t</sup>Bu (252.5 mg, 2.25 mmol) were suspended in 12 mL solvent. (IPr)Pd(allyl)Cl (14.3 mg, 25 μmol; dissolved in 1 mL IPA) was added before refluxing for 2 h. After general workup the crude product was

purified by column chromatography (90 g silica gel, hexanes/DCM 25 → 30%) to give **S3** as yellow powder (323.3 mg, 56% of theory). TLC (silica gel, hexanes/DCM = 5/1):  $r_f$  = 0.32. <sup>1</sup>H NMR (200 MHz, CD<sub>2</sub>Cl<sub>2</sub>): δ = 7.72 (s, 3H), 7.56–7.45 (m, 6H), 7.39 (d,  $J$  = 3.76 Hz, 3H), 7.24 (d,  $J$  = 3.78 Hz, 3H), 7.14–6.92 (m, 30H) ppm. <sup>13</sup>C NMR (50 MHz, CD<sub>2</sub>Cl<sub>2</sub>): δ = 159.7 (s,  $J_{CF}$  = 242.5 Hz), 148.2 (s), 144.6 (s), 144.1 (s,  $J_{CF}$  = 3.0 Hz), 142.1 (s), 136.1 (s), 128.2 (s), 126.98 (d), 126.97 (d,  $J_{CF}$  = 8.1 Hz), 125.4 (d), 123.7 (d), 122.8 (d), 121.8 (d), 116.7 (d,  $J_{CF}$  = 22.7 Hz) ppm. MS (MALDI-TOF): calcd for C<sub>72</sub>H<sub>45</sub>F<sub>6</sub>N<sub>3</sub>S<sub>3</sub>: 1161.2680; found: 1161.3152.

## Results and discussion

### Synthesis

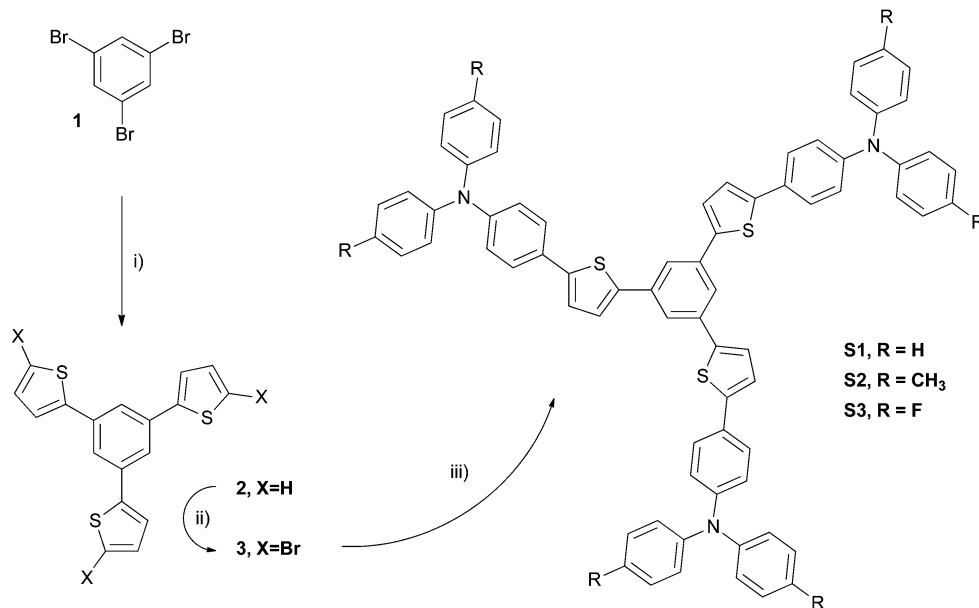
The synthetic linkage of TPA structures **8** bearing either electron withdrawing (–I, –M-effect) or donating (+I, +M) substituents with **3** is realized *via* Suzuki cross-coupling reactions.<sup>45,46</sup> Therefore, a general cross-coupling procedure was developed tolerating a broad spectrum of functionalized TPA boronic acid esters (Scheme 1).

Stille cross-coupling reactions are commonly applied in literature,<sup>47</sup> however they require toxic stannyl intermediates. In order to avoid these undesirable precursors, highly stable pinacol boronic acid esters are used in Suzuki cross-coupling reactions ensuring high conversion, selectivity, and tolerance of functional groups representing a more convenient synthetic approach.<sup>48</sup> Herein we report the synthetic pathway towards diversely substituted triphenylamine structures (R = –H, –Me, –OMe, –TMS, –*t*Bu, –F, –NO<sub>2</sub>, –CN, –SO<sub>2</sub>Me), functionalization towards boronic acid esters and subsequent cross-coupling with brominated tris(2-thienyl)benzene **3** *via* Suzuki reaction.

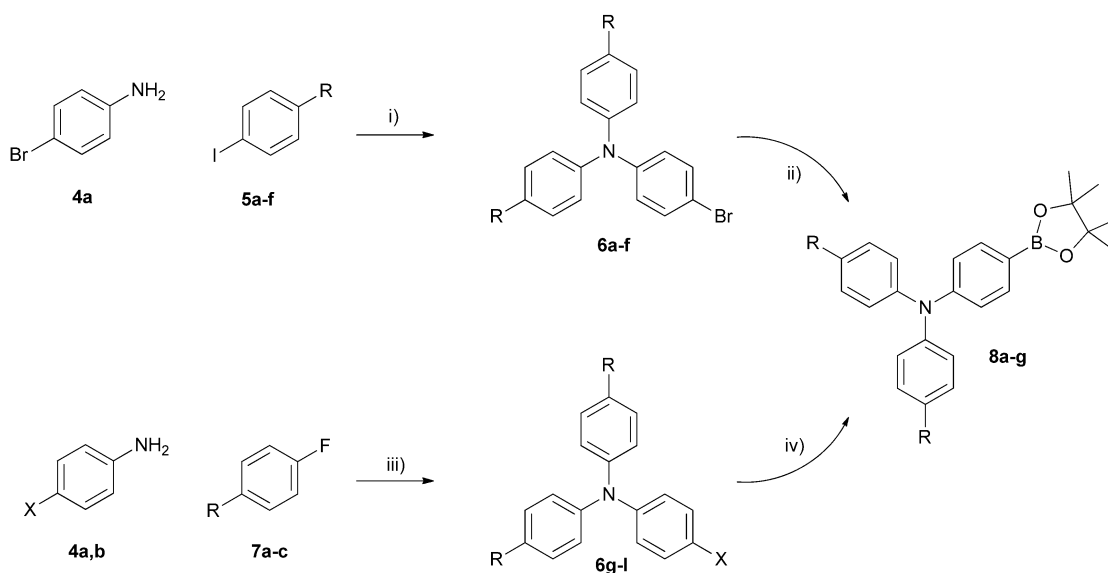
In order to synthesize the desired TPA building blocks two synthetic pathways towards halide species **6a–l** were developed depending on the nature of substituent R (Scheme 2).

The conversion of suitably substituted iodobenzenes **5a–f** and 4-bromoaniline **4a** to the corresponding bromo substituted triphenylamines **6a–f** was realized in good to excellent yields *via* Ullmann condensation applying copper(i)chloride and 1,10-phenanthroline as catalytic system.<sup>26</sup> When applying the same strategy on substrates bearing –M substituents relatively low conversions have been observed. Consequently, nucleophilic aromatic substitution of properly substituted fluorobenzenes **7a–c** with anilines **4a,b** was chosen as an alternative synthetic approach leading to bromo (**6g–i**) and iodo (**6j–l**) substituted triphenylamine derivatives in good yields (Table 1).

The synthesis of the boronic acid pinacolates **8a–f** was achieved *via* metal halogen exchange using *n*-butyllithium and further conversion with isopropyl pinacol borate in good yields (Table 1). Again, substrates bearing –M substituent turned out to be troublesome, since neither bromo **6g–i** nor iodo derivatives **6k,l** showed proper conversion. Nevertheless, starting from iodo derivative **6j** the synthesis of boronic acid esters **8g** could be achieved (despite the rather low yields of 18%) when switching to the palladium catalyzed Miyaura borylation using pinacol borane as boron source (Scheme 2).



**Scheme 1** Synthetic pathway towards **S1–3**. Reaction conditions: (i) thiophene-2-boronic acid pinacol ester,  $\text{KO}^t\text{Bu}$ ,  $(\text{IPr})\text{Pd}(\text{allyl})\text{Cl}$ , isopropanol/water, reflux; (ii) NBS, chloroform/glacial acetic acid, r.t.; (iii) **8a–c**,  $\text{KO}^t\text{Bu}$ ,  $(\text{IPr})\text{Pd}(\text{allyl})\text{Cl}$ , isopropanol/water, reflux.



**Scheme 2** Synthesis of intermediates **6** and boronic acid esters **8**. Reaction conditions: (i)  $\text{KOH}$ ,  $\text{CuCl}$ , phenanthroline in toluene, reflux; (ii)  $n\text{-BuLi}$ ,  $-78\text{ }^\circ\text{C}$  in THF, then isopropyl pinacol borate; (iii)  $\text{CsF}$  or  $\text{KO}^t\text{Bu}$  in DMSO,  $\Delta T$ ; (iv) pinacolborane, triethylamine,  $\text{PdCl}_2(\text{dppf})$  in dioxane, r.t. For a definition of R and X please refer to Table 1.

**Table 1** Experimental data for compounds **6a–l** and boronic acid esters **8a–f**

Ullmann condensation		Nucleophilic aromatic substitution		Synthesis of boronic esters					
R	Yield (%)	X	R	Yield (%)	R	Yield (%)			
<b>6a</b>	H	74	<b>6g</b>	Br	$\text{NO}_2$	54	<b>8a</b>	H	77
<b>6b</b>	Me	89	<b>6h</b>	Br	$\text{SO}_2\text{Me}$	77	<b>8b</b>	Me	74
<b>6c</b>	F	70	<b>6i</b>	Br	CN	23	<b>8c</b>	F	91
<b>6d</b>	OMe	86	<b>6j</b>	I	$\text{NO}_2$	58	<b>8d</b>	OMe	76
<b>6e</b>	TMS	60	<b>6k</b>	I	$\text{SO}_2\text{Me}$	64	<b>8e</b>	TMS	85
<b>6f</b>	<i>t</i> Bu	61	<b>6l</b>	I	CN	24	<b>8f</b>	<i>t</i> Bu	79

For the consecutive Suzuki cross-coupling reaction, palladium NHC-complex  $(\text{IPr})\text{Pd}(\text{allyl})\text{Cl}$  showed superior efficiency over tetrakis(triphenyl)palladium(0) in terms of reactivity and selectivity. Additionally, high conversion and high tolerance of TPA boronic acid esters **8a–f** bearing either electron donating (e.g.  $-\text{Me}$ ) or electron withdrawing substituents (e.g.  $-\text{F}$ ) were observed using isopropanol–water as solvent and  $\text{K}^t\text{OBu}$  as base.

Applying these reaction conditions, compounds **2** and **S1–3** were obtained. The synthesis of **2** was achieved in good yield of 86% *via* cross-coupling of thiophene-2-boronic acid pinacol

Table 2 Photophysical characterization of compounds **S1–3** and computational data for compounds **S<sub>m</sub>1–3**

Comp.	$\lambda_{\max}$ ( $\epsilon_{\max}$ ) <sup>a</sup> (nm)	$\lambda_{\max}$ <sup>b</sup> (nm)	$\lambda_{\text{em}}$ ( $\phi_f$ ) <sup>c</sup> (nm)	$\lambda_{\text{em}}$ <sup>d</sup> (nm)	$\lambda_{\text{em}}$ <sup>e</sup> (nm)	Comp.	$\lambda_{\max}$ <sup>f</sup> (nm)	$\lambda_{\text{em}}$ <sup>g</sup> (nm)	$\lambda_{\text{em}}$ <sup>h</sup> (nm)
<b>S1</b>	302 (61.2), 387 (112.9)	474	461 (62)	471	486	<b>S<sub>m</sub>1</b>	344	450	445
<b>S2</b>	304 (61.7), 394 (104.2)	482	474 (71)	477	498	<b>S<sub>m</sub>2</b>	349	454	459
<b>S3</b>	297 (51.0), 384 (104.7)	472	459 (62)	466	482	<b>S<sub>m</sub>3</b>	343	449	445

<sup>a</sup> Measured in THF solution,  $\epsilon_{\max} \times 10^{-3}$  in  $\text{M}^{-1} \text{cm}^{-1}$  in parentheses. <sup>b</sup> Absorption of solid samples. <sup>c</sup> Measured in a THF solution;  $\phi_f$  fluorescence quantum yield. <sup>d</sup> Film samples. <sup>e</sup> Solid samples. <sup>f</sup> Calculated absorption of model compounds **S<sub>m</sub>1–3**. <sup>g</sup> Calculated emission (LR-PCM) of model compounds **S<sub>m</sub>1–3**. <sup>h</sup> Calculated emission (SS-PCM) of model compounds **S<sub>m</sub>1–3**.

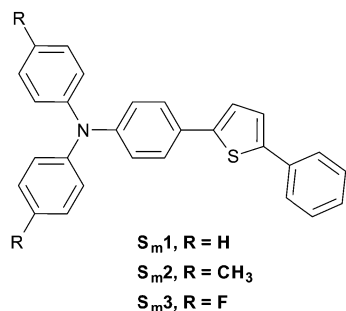
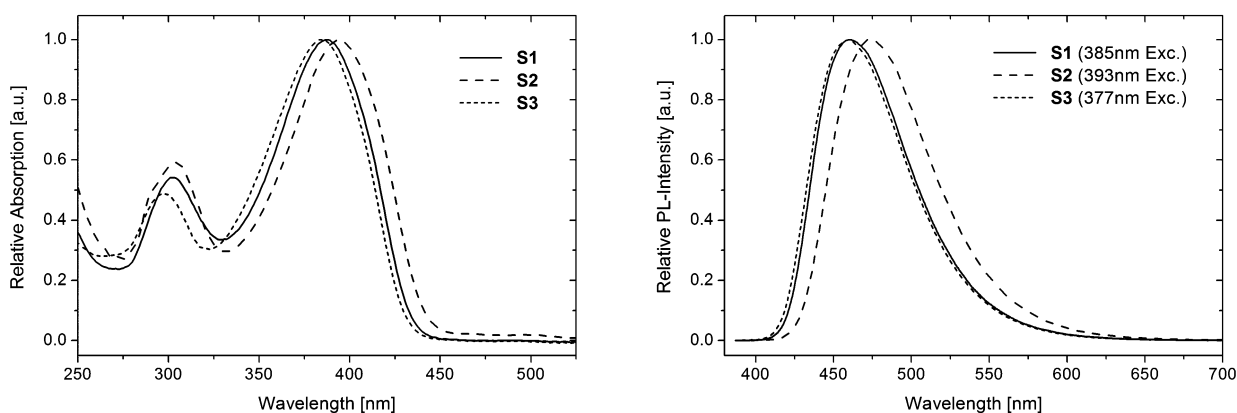
ester and 1,3,5-tribromobenzene **1** according to the above protocol. Consecutive bromination with NBS in chloroform/glacial acetic acid gave the tribromo derivative **3**, the precursor for the final Suzuki coupling with boronic acid esters **8a–c**. Star-shaped compounds **S1–3** bearing either electron donating or withdrawing substituents were obtained in satisfactory to excellent yields (Table 3). These solid materials appear yellow in color and are soluble in common organic solvents. The characterization of **S1–3** was performed by  $^1\text{H}/^{13}\text{C}$ -NMR spectroscopy and HR-MS analysis. The data are consistent with the proposed structural formulations.

Photo-physical properties of **S1–3** were determined by UV-VIS and fluorescence spectrometry in THF solution, for amorphous films and in the solid state (Table 2 and Fig. 3). Two absorption maxima were located in relatively narrow ranges of 297–304 and 384–394 nm for substances **S1–3** when measured in THF solution. While the former is assigned to the

$n-\pi^*$  transition of the triphenylamine moiety, the longer wavelength absorption originates from the  $\pi-\pi^*$  transitions of the electron-donating triphenylamine moiety to the electron-accepting thiophene moiety.<sup>49</sup> A clear trend can be observed, as the electron withdrawing fluoro derivative **S3** shows the absorption maximum with the highest energy, whereas the electron donating methyl derivative **S2** has the absorption maximum at the longest wavelength; the absorption maximum of the electron neutral **S1** lies in between.

These findings are supported by quantum chemical calculations of model substances **S<sub>m</sub>1–3** (Fig. 2). In order to mimic  $C_3$  symmetric substances **S1–3**, suitable model substances were chosen, comprising one dendritic arm and the benzene core. This approach ensures a realistic representation of **S1–3** while keeping the computational costs at a reasonable level. Absorption and emission wavelengths in THF of **S<sub>m</sub>1–3** were estimated by applying density functional (DFT) and time dependent density functional (TDDFT) level of theory according to a protocol presented recently.<sup>36</sup> The calculated absorption and emission wavelengths of **S<sub>m</sub>1–3** are in agreement with experimental data of **S1–3** showing the lowest shift in emission for fluoro-substituted **S3/S<sub>m</sub>3** and highest emission shifts for methyl-substituted compounds **S2/S<sub>m</sub>2** (Table 2).

Again this behavior can be correlated to the increased electron density on the aromatic ring (Fig. 3) in the case of **S2** ( $\lambda_{\text{em}} = 474 \text{ nm}$ ) causing a significant bathochromic shift and a decreased electron density in the case of **S3** ( $\lambda_{\text{em}} = 459 \text{ nm}$ ) causing a hypsochromic shift in reference to **S1** ( $\lambda_{\text{em}} = 461 \text{ nm}$ ) (Table 2). Stokes shifts for all compounds **S1–3** are comparable and range from 0.51–0.53 eV. Quantum yields in solution are

Fig. 2 Model substances **S<sub>m</sub>1–3**.Fig. 3 Absorption (left) and emission (right) spectra of **S1–3** in THF solution.

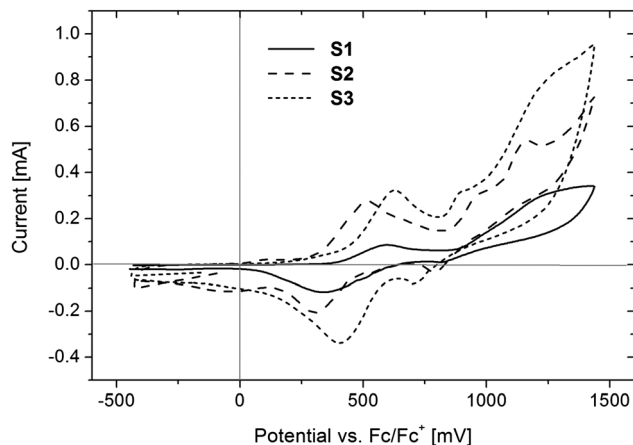


Fig. 4 Cyclic voltammograms of **S1–3** in DCM.

shifted to higher values correlating with enhanced electron density (Table 2). The values of **S1** and **S3** are identical ( $\phi_f = 0.62$ ), whereas

Table 3 Experimental data, physical characterization and computational data of compounds **S1–3**

Comp.	Yield (%)	$T_g^a$ (°C)	$T_d^b$ (°C)	Band gap <sup>c</sup> (nm, eV)	HOMO/LUMO <sup>d</sup> (eV)	HOMO/LUMO <sup>e</sup> (eV)
<b>S1</b>	97	128	541	387, 3.20	−5.19/−1.99	−5.17/−1.76
<b>S2</b>	83	135	528	394, 3.14	−5.24/−2.10	−5.01/−1.66
<b>S3</b>	50	121	538	384, 3.23	−5.21/−1.98	−5.36/−1.91

<sup>a</sup> Obtained from DSC measurements. <sup>b</sup> Thermal decomposition temperature determined from 5% mass loss. <sup>c</sup> Bandgaps were determined from the onsets of the absorption in THF solution. <sup>d</sup> HOMO-levels determined from solutions measured in DCM. All  $E_{ox}$  data are reported relative to ferrocene ( $Fc/Fc^+$ ,  $E_{ox} = 446$  mV). The concentration of the compounds used in this experiment was  $1 \text{ mg } \mu\text{L}^{-1}$  and the scan rate was  $50 \text{ mV s}^{-1}$ . LUMO levels were determined from the optical band gap and the HOMO energy level according to the following equation:  $E_{LUMO} = E_{HOMO} + E_{bandgap}$ . <sup>e</sup> Calculated HOMO/LUMO levels (B3LYP/6-311+G(d)).

the quantum yield is considerably higher ( $\phi_f = 0.71$ ) for the methyl substituted derivative **S2**.

Emission spectra of solid samples **S1–3** are in the narrow range of 482–498 nm, whereas spin coated samples are in the range of 466–477 nm (for spectra please refer to the ESI†).

Electro-chemical characteristics of the star-shaped molecules **S1–3** were investigated by cyclic voltammetric methods (Fig. 4). The first oxidation potentials were used to determine the HOMO energy levels. Ferrocene served as an external standard for calibrating the potential and calculating the HOMO levels (−4.8 eV). All compounds **S1–3** undergo reversible oxidation indicating the formation of stable cation radicals. Only small variations of HOMO levels (−5.19 eV to −5.24 eV) were observed. The LUMO levels were determined from the optical bandgap and the HOMO energy level obtained from CV measurements and vary in the range from −1.98 to −2.10 eV. Calculated HOMO/LUMO levels are in good accordance with the experimental data for compounds **S1** and **S3**, whereas the deviation is somewhat higher for substance **S2**. The pertinent data are listed in Table 3.

Thermal properties were investigated by DSC and TGA measurements. Glass-forming properties and thermal stability of the compounds were examined by simultaneous thermal analysis (STA). The glass transition temperature ( $T_g$ ) was estimated from DSC curves (Fig. 5). The determined  $T_g$  values are in the range from 121 to 135 °C, the methyl substituted **S2** showing the highest value while fluoro substituted **S3** exhibits the lowest  $T_g$ . All materials exhibit high thermal stability as evidenced by decomposition temperatures corresponding to 5% mass loss between 528 and 541 °C (Table 3 and Fig. 5). This high thermal stability allows for fabrication of homogeneous and stable amorphous thin films by vacuum deposition.

The semiconducting properties of the materials under investigation were tested by using a top-contact OFET architecture as shown in Fig. 6. A hole mobility up to  $7.7 \times 10^{-4} \text{ cm}^2 \text{ V}^{-1} \text{ s}^{-1}$

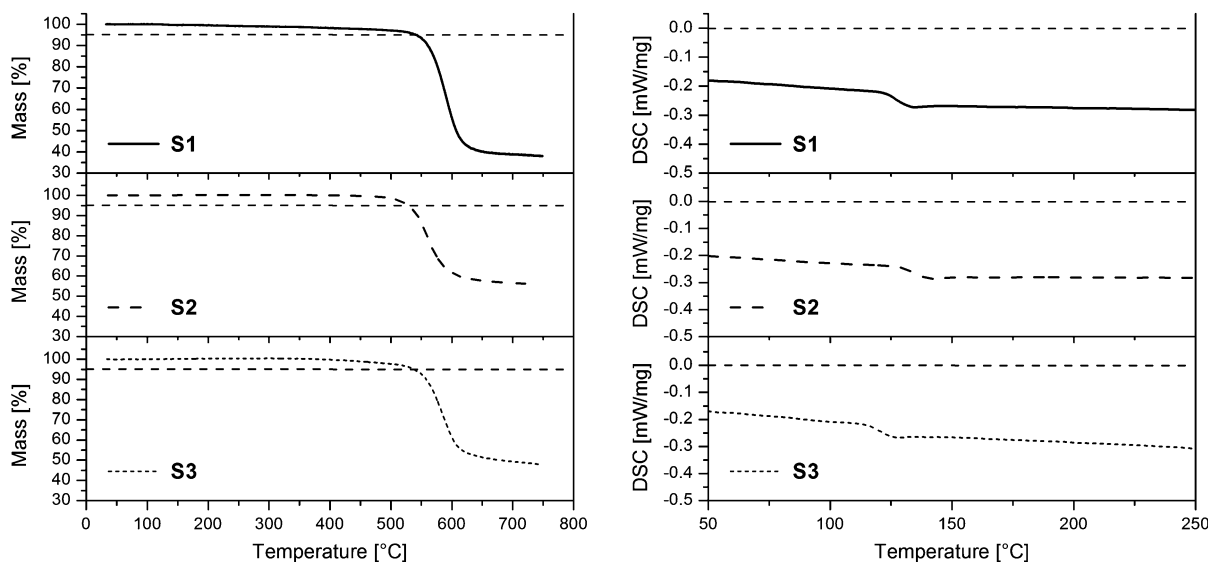


Fig. 5 TGA (left) and DSC (right) measurements of **S1–3**.

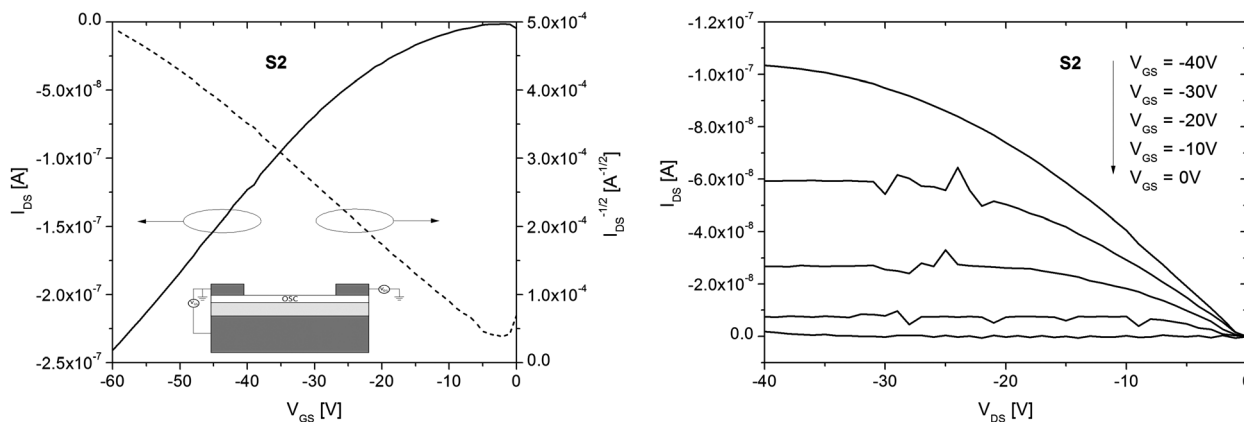


Fig. 6 Output characteristics (left) and corresponding transfer curve (right) of **S2**.

and average threshold voltages of approx. 0 V which can be attributed to a low background charge density in the material were recorded using **S2** as semiconducting layer (Fig. 6), while no working OFET device could be fabricated using **S1** or **S3**. As the performance of an OFET highly depends on the quality of the interface between dielectric and organic semiconductor, these results might be correlated to the tendency of **S2** to form nearly defect free films, which was observed in spin coating experiments.

All compounds **S1–3** readily form stable glasses. Spin coated thin films of **S1–3** were produced on ITO substrates using chloroform as solvent. Their surface morphology and thickness were further investigated by atomic force microscopy (AFM, Fig. 7). In principle, all films showed very little average

thickness (30–50 nm) and low roughness of the surface (root mean square = 0.63, 0.32 and 0.34 nm for **S1**, **S2** and **S3** respectively). However, when examining the surface of **S1** sub- $\mu\text{m}$  sized pinholes were observed. Potential reasons for pinholes are trapped air, solvent gas-bubble formation or contaminations on the substrate or in the organic solution. Since numerous spin coating samples were prepared applying the same procedure yielding reproducible results, the origin of these defects is unlikely to come from the fabrication process. Therefore, the formation of these pinholes is probably substance specific and might be attributed to higher propensity to crystallization of **S1** compared to **S2** and **S3**. Thus, in contrast to **S1**, solution-processed films of **S2** and **S3** can readily be prepared.

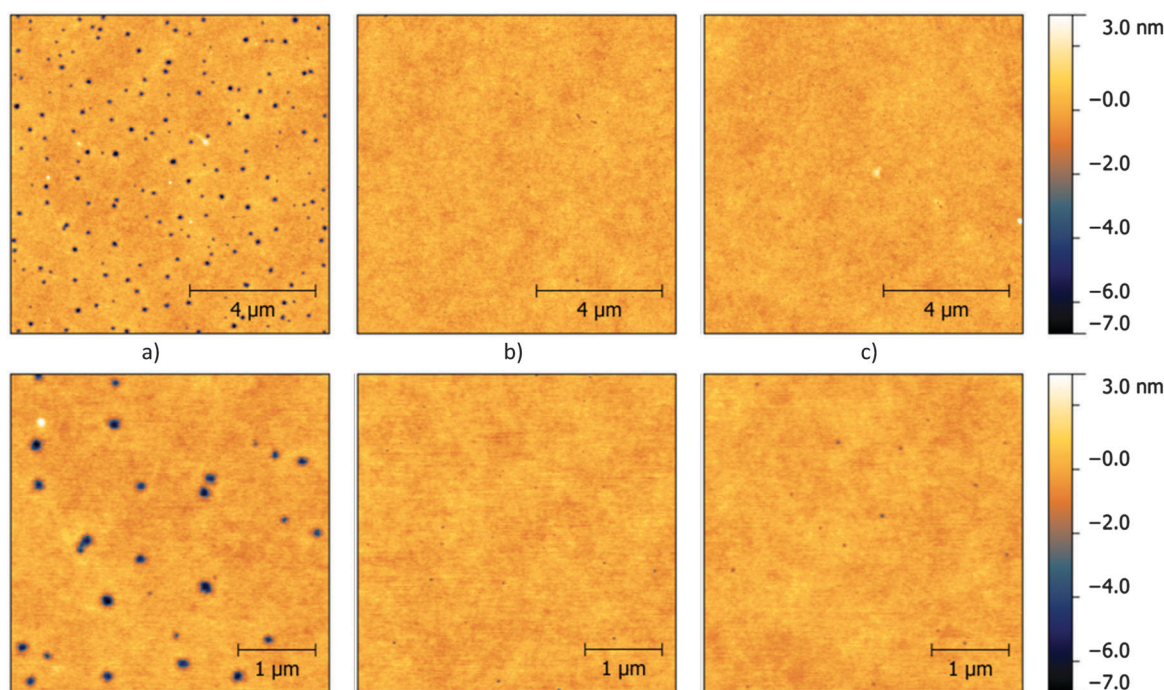


Fig. 7 Topography AFM images of **S1–3** (a–c).



## Conclusion

This contribution outlines an optimized synthetic pathway towards a broad spectrum of *p*-substituted triphenylamines, suitable as building blocks for organic semiconducting materials.

We employed these triphenylamine moieties in  $C_3$  symmetric dendritic tris(2-thienyl)benzene structures and elucidated the influence of the molecular design on photo-physical properties. The electronic characteristics of the substituents show a strong influence on the fluorescence spectra thus enabling color tuning. These star shaped materials exhibit good solubility and thermal stability allowing for both solution processing and physical vapor deposition, respectively. The novel materials were tested as semiconductors in organic field effect transistor devices, exhibiting hole mobilities of almost  $10^{-3} \text{ cm}^2 \text{ V}^{-1} \text{ s}^{-1}$ .

Spin coating experiments showed a strong correlation between the nature of the substituents and the morphology of the resulting thin film; similar results were observed for transistor performance. The structural versatility and capability of our molecular design will contribute to the further development of functional organic materials.

## Acknowledgements

J. Binteringer gratefully acknowledges funding from the Marshall Plan Foundation. The authors thank Dr K. Föttinger for supporting the photophysical characterization, D. Bomze, A. Aster, M. Lunzer and K. Kandra for contributing to the synthetic experiments. M. Eberl is acknowledged for assisting in cyclic voltammetric measurements and K. Fohringer and P. Kautny for STA measurements.

## References

- 1 S. R. Forrest, *Nature*, 2004, **428**, 911.
- 2 J. Mei, Y. Diao, A. L. Appleton, L. Fang and Z. Bao, *J. Am. Chem. Soc.*, 2013, **135**, 6724.
- 3 Y.-S. Tyan, *J. Photonics Energy*, 2011, **1**, 011009.
- 4 M. C. Scharber and N. S. Sariciftci, *Prog. Polym. Sci.*, 2013, **38**, 1929.
- 5 B. Kippelen and J.-L. Brédas, *Energy Environ. Sci.*, 2009, **2**, 251.
- 6 H. Klauk, *Organic electronics II: more materials and applications*, Wiley-VCH, Weinheim, 2012.
- 7 Y. Yamashita, *Sci. Technol. Adv. Mater.*, 2009, **10**, 024313.
- 8 Y. Shirota and H. Kageyama, *Chem. Rev.*, 2007, **107**, 953.
- 9 J. Kwon, M. K. Kim, J.-P. Hong, W. Lee, S. Lee and J.-I. Hong, *Bull. Korean Chem. Soc.*, 2013, **34**, 1355.
- 10 F. Geiger, M. Stoldt, H. Schweizer, P. Bäuerle and E. Umbach, *Adv. Mater.*, 1993, **5**, 922.
- 11 S. H. Kim, K. Hong, K. H. Lee and C. D. Frisbie, *ACS Appl. Mater. Interfaces*, 2013, **5**, 6580.
- 12 Y. Shirota, *J. Mater. Chem.*, 2000, **10**, 1.
- 13 N. Metri, X. Sallenave, C. Plesse, L. Beouch, P.-H. Aubert, F. Goubard, C. Chevrot and G. Sini, *J. Phys. Chem. C*, 2012, **116**, 3765.
- 14 J. Zhang, D. Deng, C. He, Y. He, M. Zhang, Z.-G. Zhang, Z. Zhang and Y. Li, *Chem. Mater.*, 2011, **23**, 817.
- 15 Z. Ning and H. Tian, *Chem. Commun.*, 2009, 5483.
- 16 A. Iwan, D. Sek, D. Pocięcha, A. Sikora, M. Palewicz and H. Janeczek, *J. Mol. Struct.*, 2010, **981**, 120.
- 17 A. Iwan and D. Sek, *Prog. Polym. Sci.*, 2011, **36**, 1277.
- 18 T. Noda, H. Ogawa, N. Noma and Y. Shirota, *Adv. Mater.*, 1997, **9**, 720.
- 19 J. Roncali, P. Leriche and A. Cravino, *Adv. Mater.*, 2007, **19**, 2045.
- 20 C. He, Q. He, Y. Yi, G. Wu, F. Bai, Z. Shuai and Y. Li, *J. Mater. Chem.*, 2008, **18**, 4085.
- 21 A. Cravino, S. Roquet, P. Leriche, O. Alévêque, P. Frère and J. Roncali, *Chem. Commun.*, 2006, 1416.
- 22 T.-T. Bui, L. Beouch, X. Sallenave and F. Goubard, *Tetrahedron Lett.*, 2013, **54**, 4277.
- 23 N. Metri, X. Sallenave, L. Beouch, C. Plesse, F. Goubard and C. Chevrot, *Tetrahedron Lett.*, 2010, **51**, 6673.
- 24 K. R. Justin Thomas, J. T. Lin, Y.-T. Tao and C.-W. Ko, *Chem. Mater.*, 2002, **14**, 1354.
- 25 A. Iwan, H. Janeczek, B. Kaczmarczyk, B. Jarzabek, M. Sobota and P. Rannou, *Spectrochim. Acta, Part A*, 2010, **75**, 891.
- 26 H. B. Goodbrand and N.-X. Hu, *J. Org. Chem.*, 1999, **64**, 670.
- 27 M. W. Andersen, B. Hildebrandt, G. Köster and R. W. Hoffmann, *Chem. Ber.*, 1989, **122**, 1777.
- 28 O. Navarro and S. P. Nolan, *Synthesis*, 2006, 366.
- 29 J. Frisch, G. W. Trucks, H. B. Schlegel, G. E. Scuseria, M. A. Robb, J. R. Cheeseman, G. Scalmani, V. Barone, B. Mennucci, G. A. Petersson, H. Nakatsuji, M. Caricato, X. Li, H. P. Hratchian, A. F. Izmaylov, J. Bloino, G. Zheng, J. L. Sonnenberg, M. Hada, M. Ehara, K. Toyota, R. Fukuda, J. Hasegawa, M. Ishida, T. Nakajima and Y. Honda, *Gaussian 09, Revision A.02*, Gaussian, Inc., Wallingford, CT, 2009.
- 30 C. Lee, W. Yang and R. G. Parr, *Phys. Rev. B: Condens. Matter Mater. Phys.*, 1988, **37**, 785.
- 31 A. D. Becke, *J. Chem. Phys.*, 1993, **98**, 5648.
- 32 R. Krishnan, J. S. Binkley, R. Seeger and J. A. Pople, *J. Chem. Phys.*, 1980, **72**, 650.
- 33 Y. Zhao and D. G. Truhlar, *Theor. Chem. Acc.*, 2007, **120**, 215.
- 34 Y. Zhao and D. G. Truhlar, *Theor. Chem. Acc.*, 2008, **119**, 525.
- 35 A. Schäfer, H. Horn and R. Ahlrichs, *J. Chem. Phys.*, 1992, **97**, 2571.
- 36 D. Lumpi, E. Horkel, F. Plasser, H. Lischka and J. Fröhlich, *ChemPhysChem*, 2013, **14**, 1016.
- 37 M. Cossi, V. Barone, R. Cammi and J. Tomasi, *Chem. Phys. Lett.*, 1996, **255**, 327.
- 38 M. Cossi and V. Barone, *J. Chem. Phys.*, 2001, **115**, 4708.
- 39 R. Improta, G. Scalmani, M. J. Frisch and V. Barone, *J. Chem. Phys.*, 2007, **127**, 074504.
- 40 M. H. Davey, V. Y. Lee, L.-M. Wu, C. R. Moylan, W. Volksen, A. Knoesen, R. D. Miller and T. J. Marks, *Chem. Mater.*, 2000, **12**, 1679.
- 41 J. H. Gorvin, *J. Chem. Soc., Perkin Trans. 1*, 1988, 1331.

- 42 R. Anemian, D. C. Cupertino, P. R. Mackie and S. G. Yeates, *Tetrahedron Lett.*, 2005, **46**, 6717.
- 43 M. Murata, T. Oyama, S. Watanabe and Y. Masuda, *J. Org. Chem.*, 2000, **65**, 164.
- 44 N. Marion, O. Navarro, J. Mei, E. D. Stevens, N. M. Scott and S. P. Nolan, *J. Am. Chem. Soc.*, 2006, **128**, 4101.
- 45 A. Leliège, J. Grolleau, M. Allain, P. Blanchard, D. Demeter, T. Rousseau and J. Roncali, *Chem. – Eur. J.*, 2013, **19**, 9948.
- 46 J. K. Choi, K. Cho and T.-H. Yoon, *Synth. Met.*, 2010, **160**, 1938.
- 47 R. A. Rossi, *J. Organomet. Chem.*, 2014, **751**, 201.
- 48 R. Martin and S. L. Buchwald, *Acc. Chem. Res.*, 2008, **41**, 1461.
- 49 Z. Ge, T. Hayakawa, S. Ando, M. Ueda, T. Akiike, H. Miyamoto, T. Kajita and M. Kakimoto, *Adv. Funct. Mater.*, 2008, **18**, 584.

# Manuscript #7

P. Kautny, D. Lumpi\*, Y. Wang, A. Tissot, **J. Binting**, E. Horkel, B. Stöger, C. Hametner, H. Hagemann, D. Ma, J. Fröhlich; *J. Mater. Chem. C*, 2014, 2 (11), 2069

Reproduced from Ref.<sup>87</sup> with permission from the Centre National de la Recherche Scientifique (CNRS) and The Royal Society of Chemistry.



# Oxadiazole based bipolar host materials employing planarized triarylamine donors for RGB PHOLEDs with low efficiency roll-off†

Cite this: *J. Mater. Chem. C*, 2014, 2, 2069

Paul Kautny,<sup>a</sup> Daniel Lumpi,<sup>\*a</sup> Yanping Wang,<sup>b</sup> Antoine Tissot,<sup>c</sup> Johannes Bintinger,<sup>a</sup> Ernst Horkel,<sup>a</sup> Berthold Stöger,<sup>d</sup> Christian Hametner,<sup>a</sup> Hans Hagemann,<sup>c</sup> Dongge Ma<sup>b</sup> and Johannes Fröhlich<sup>a</sup>

A series of 6 novel triarylamine-containing oxadiazole compounds (*o*-PCzPOXD, *o*-ICzPOXD, *o*-TPATOXD, *o*-PCzTOXD, *o*-ICzTOXD, *o*-CzTOXD) have been designed, synthesized and characterized concerning applications as host materials in PHOLED devices. To further improve the *ortho*-linkage concept, the impact of incorporating planarized electron-donating triarylamine (TAA) structures on intramolecular charge transfer was examined. The effect was evaluated for two series of electron-accepting oxadiazole scaffolds, realizing *ortho*-linkage on the benzene (POXD) and the thiophene (TOXD) cores. Thermal analysis shows increased glass-transition temperatures for planarized structures indicating an improved morphological stability. A higher degree of planarization also results in significantly increased singlet and triplet energy values, revealing the impact on the intramolecular charge transfer. Employing the developed materials, red (*o*-TPATOXD: CE<sub>max</sub>: 28.8 cd A<sup>-1</sup>, EQE<sub>max</sub>: 16.9%), green (*o*-PCzPOXD: CE<sub>max</sub>: 62.9 cd A<sup>-1</sup>, EQE<sub>max</sub>: 17.1%) and blue (*o*-PCzPOXD: CE<sub>max</sub>: 29.8 cd A<sup>-1</sup>, EQE<sub>max</sub>: 13.4%) devices were achieved showing remarkably low efficiency roll-off for planarized donors. Hence, this is the first report of efficient blue devices for this specific class of host materials. It is proposed that the results correlate with an increasing *ortho*-linkage effect and decreasing donor strength of the TAA moiety by planarization and, thus, tackling one of the major challenges in PHOLED research: improving both triplet energy and compound stability.

Received 26th November 2013  
Accepted 4th January 2014

DOI: 10.1039/c3tc32338b

www.rsc.org/MaterialsC

## Introduction

Organic Light Emitting Diodes (OLEDs) and their application in display technology represent the most advanced technology among the rapidly growing field of organic electronics.<sup>1–7</sup> Since the groundbreaking work of Forrest *et al.* from 1998 (ref. 8 and 9) great efforts have been made in developing Phosphorescent Organic Light Emitting Diodes (PHOLEDs) typically employing heavy transition metal complexes.<sup>10,11</sup> In contrast to fluorescent OLEDs phosphorescent emitters are capable of

harvesting triplet and singlet excitons simultaneously and, thus, can theoretically achieve 100% internal quantum efficiency.<sup>12,13</sup>

However, high concentration of triplet excitons leads to triplet-triplet annihilation at high current rates resulting in efficiency roll-off.<sup>14</sup> Thus, phosphorescent emitters are generally widely dispersed in an organic host material. Efficient host materials have to fulfill some basic requirements:<sup>7</sup> (i) higher triplet energy ( $E_t$ ) value than that of the dopant to effectively confine triplet excitons on the phosphorescent emitter; (ii) suitable HOMO/LUMO levels to facilitate charge injection; and (iii) morphological stability for durable and long lasting devices.

Bipolar host materials have received great attention in recent years, due to their balanced charge transport properties resulting in broad charge recombination zones. However, combining donor and acceptor subunits in one molecule ultimately lowers the  $E_t$  as a result of the intramolecular charge transfer.<sup>7</sup> Therefore, the molecular design of bipolar host materials focuses on the interruption of the conjugated  $\pi$ -system in order to reduce donor-acceptor interactions and thus to retain high  $E_t$  values. Among the most efficient ways to separate the molecular subunits is the introduction of specific linkage modes.<sup>7</sup> Particularly, *ortho*-linkage of donor and

<sup>a</sup>Institute of Applied Synthetic Chemistry, Vienna University of Technology, Getreidemarkt 9/163, A-1060 Vienna, Austria. E-mail: daniel.lumpi@tuwien.ac.at

<sup>b</sup>State Key Laboratory of Polymer Physics and Chemistry, Changchun Institute of Applied Chemistry, Chinese Academy of Sciences, Changchun, 130022, China

<sup>c</sup>Département de Chimie Physique, Université de Genève, 30, quai E. Ansermet, 1211 Geneva 4, Switzerland

<sup>d</sup>Institute of Chemical Technologies and Analytics, Vienna University of Technology, Getreidemarkt 9/164, A-1060 Vienna, Austria

† Electronic supplementary information (ESI) available: NMR spectra, TGA/DSC analyses, cyclic voltammetry, phosphorescence as well as electroluminescence spectra, DFT calculations and crystallographic information. CCDC 955416–955418. For ESI and crystallographic data in CIF or other electronic format see DOI: 10.1039/c3tc32338b

acceptor subunits, inducing twisted molecular conformations, proved to be a highly efficient strategy to achieve large triplet bandgap materials.<sup>15</sup>

In this contribution we reveal the enhancement of the effect of *ortho*-linkage by applying increasingly planarized triarylamine donors (from *N,N*-diphenylbenzenamine (TPA) to 9-phenyl-9*H*-carbazole (PCz) and indolo[3,2,1-*jk*]carbazole (ICz)) to an established phenyl-oxadiazole-phenyl (POXD) acceptor. The corresponding triphenylamine compound (**o**-TPAPOXD) has been previously demonstrated to be highly efficient as the host in red and green PHOLED devices.<sup>16,17</sup> Utilizing the planarized arylamines we were able to increase singlet as well as triplet energies resulting in higher efficiencies and significantly reduced efficiency roll-off in non-optimized red, green and blue PHOLED devices. We propose that these findings correlate with an increasing *ortho*-linkage effect due to steric impact and decreasing donor strength of the triarylamine moiety by planarization as a result of the contribution of the nitrogen lone-pair to the aromaticity of the formed pyrrole subunit(s). To prove the developed concept, TPA, PCz, ICz as well as carbazole (Cz) donors were also applied to a new thiophene-oxadiazole-thiophene (TOXD) acceptor moiety confirming the trends.

By employing the developed materials red (**o**-TPATOXD:  $CE_{\max}$ : 28.7 cd A<sup>-1</sup>,  $EQE_{\max}$ : 16.9%), green (**o**-PCzPOXD:  $CE_{\max}$ : 62.9 cd A<sup>-1</sup>,  $EQE_{\max}$ : 17.1%) and blue (**o**-PCzPOXD:  $CE_{\max}$ : 29.8 cd A<sup>-1</sup>,  $EQE_{\max}$ : 13.4%) devices have been obtained.

Hence, we report on an efficient approach to gain control of intramolecular charge transfer, significantly affecting singlet as well as triplet energies, by the planarization of electron donating triarylamine moieties. As a result, novel host materials have been designed, synthesized and characterized exhibiting remarkably low efficiency roll-off, which is of technological relevance for both single doped devices and multi-color based white PHOLEDs.

## Results and discussion

### Synthesis

The synthesis of target host materials and precursors primarily relies on organo-lithium assisted and transition-metal catalyzed (Ullman condensation, Suzuki cross-coupling) reactions. The first part describes the synthetic pathways towards planarized triarylamine (TAA) structures phenylcarbazole and indolocarbazole particularly focusing on C–H activation as an efficient approach to acquire the desired planarization. In the second part the realization of the *ortho*-linkage on the benzene (**5a–c**) core and subsequently the thiophene core (**8a–d**), achieved *via* a Halogen Dance (HD) reaction, is outlined.

Boronic esters of triphenylamine (**3a**) and phenylcarbazole (**3b**) were obtained in analogy to the literature.<sup>18–20</sup> The synthesis of indolocarbazole boronic ester (**3c**) is based on a recently developed methodology utilizing C–H activation.<sup>21</sup> Compared to previously reported procedures this synthetic approach towards indolo[3,2,1-*jk*]carbazole **2** (Scheme 1) is shorter (less steps), more efficient and does not rely on the application of special equipment (*e.g.* vacuum flash pyrolysis).<sup>22,23</sup> Although good yields of 83% (15 mol% Pd(OAc)<sub>2</sub> catalyst) were accomplished

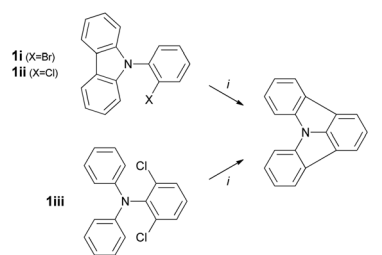
the reduction of catalyst loads drastically decreased the reaction conversion. The use of 5 mol% Pd(OAc)<sub>2</sub> even limits the product formation to trace amounts.<sup>21</sup> Hence, we report on an improved procedure at significantly reduced catalyst amounts (2 mol%) towards indolo[3,2,1-*jk*]carbazole employing Pd(PPh<sub>3</sub>)<sub>4</sub> and K<sub>2</sub>CO<sub>3</sub> (71% yield). In fact, the application of a (NHC)Pd(allyl)Cl<sup>24,25</sup> catalyst (2 mol%) further improves the yields to 94% (Scheme 1 and Table 1). Moreover, the substrate scope could be broadened to chlorine derivatives (no conversion for Pd(PPh<sub>3</sub>)<sub>4</sub>, Table 1).

Particularly, the demonstrated two-fold C–H activation of chlorine derivatives allows for a convenient and selective synthesis of a variety of novel target structures, broadening the scope of accessible indolo[3,2,1-*jk*]carbazole moieties.

Selective bromination (NBS, 54%)<sup>23</sup> of **2** and organo-lithium assisted transformation (*n*-BuLi, isopropyl pinacol borate, 69%) yielded the indolocarbazole pinacol boronic ester **3c**. The crystal structure (see the ESI† for details) discloses the desired planarity of this TAA type structure. **3c** (ref. 26) crystallizes with one crystallographically unique molecule in the asymmetric unit located on a general position. The aromatic system is close to flat: the N atom is located 0.1573(5) Å from the least square (LS) plane defined by the C atoms of the benzene rings.

The dibrominated POXD (benzene-oxadiazole-benzene structure) precursor **4** was synthesized according to the literature.<sup>27</sup> The conversion towards target compounds **5a–c** was accomplished utilizing TAA boronic esters **3a–c** applying a standard Suzuki protocol (Scheme 2).<sup>28</sup> Good to excellent yields of 85% and 93% were achieved for **5a** and **5b**, respectively; the lower yield of **5c** (39%) is attributed to a lower solubility affecting both reaction conversion and work-up.

In contrast to the POXD series the dibrominated TOXD (thiophene-oxadiazole-thiophene structure), precursor **7i**, is unavailable in the literature. The *ortho*-substitution pattern is realized by applying a double-sided halogen dance (HD)<sup>29–31</sup>

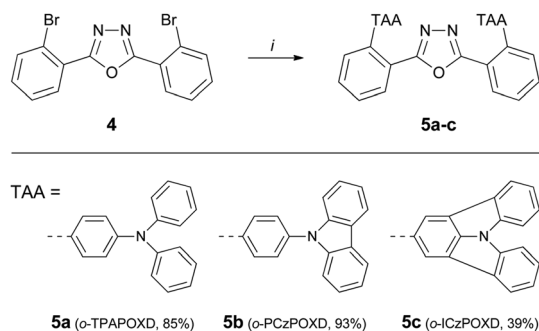


Scheme 1 Synthetic pathways towards indolo[3,2,1-*jk*]carbazole **2**: (i) (NHC)Pd(allyl)Cl (2 mol%), K<sub>2</sub>CO<sub>3</sub> (2.0 eq.), DMA (0.2 M), 130 °C, 1–2 h.

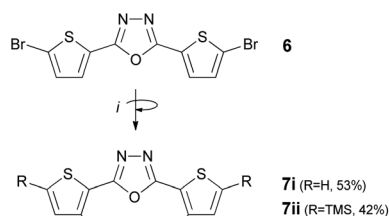
Table 1 Results of the C–H activation of substrates 1i–iii

Substrate	Pd(PPh <sub>3</sub> ) <sub>4</sub>	(NHC)Pd(allyl)Cl
<b>1i</b>	71% <sup>a</sup>	94% <sup>a</sup>
<b>1ii</b>	n.c. <sup>b</sup>	94% <sup>a</sup>
<b>1iii</b>	n.c. <sup>b</sup>	80% <sup>a</sup>

<sup>a</sup> Isolated yields. <sup>b</sup> No conversion (GC-MS).



**Scheme 2** Synthesis of POXD based host materials **5a–c**: (i) boronic acid ester **3a–c** (2.5 eq.),  $\text{K}_2\text{CO}_3$  (5.0 eq., 2 M aq.),  $\text{Pd}(\text{PPh}_3)_4$  (5 mol%), THF (~0.5 M), reflux.

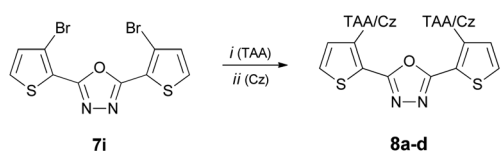


**Scheme 3** Halogen dance reaction towards *ortho*-substitution patterns (**7i,ii**): (i) THF,  $-25\text{ }^\circ\text{C}$ , LDA (2.4 eq.), 30 min stirring prior to addition of electrophiles (MeOH and TMS-Br).

methodology (Scheme 3) starting from **6** (synthesized according to the literature). Due to coordinating and activating effects of the oxadiazole moiety<sup>32</sup> the lithium diisopropylamide (LDA) induced metallation selectively takes place in the respective *ortho*-positions. Subsequently, a rearrangement of the bromine atoms (“halogen dance”), resulting in the thermodynamically most stable organo-lithium intermediate, yields the desired *ortho*-substitution pattern.

As a consequence, this approach enables direct introduction of substituents R in the 5-positions by addition of suitable electrophiles (R), which has been demonstrated utilizing TMS-Br to yield the silylated compound **7ii**. Hence, specific alterations of material properties *e.g.* solubility (for *e.g.* solution processing) can be achieved; however, reaction conditions were not further optimized in this study.

The triarylamine and carbazole cap structures are attached to the TOXD core *via* Suzuki cross-coupling reaction<sup>33–35</sup> and Ullmann condensation,<sup>36–38</sup> respectively (Scheme 4).



**Scheme 4** Synthesis of TOXD based host materials **8a–d**: (i) Suzuki cross-coupling: boronic acid ester **3a–c** (3.0 eq.),  $\text{KO}^t\text{Bu}$  (3.0 eq.),  $(\text{NHC})\text{Pd}(\text{allyl})\text{Cl}$  (2 mol%),  ${}^i\text{PrOH-H}_2\text{O}$  (3 : 1, 5 mM), rf; (ii) Ullmann condensation: carbazole (3.0 eq.),  $\text{K}_2\text{CO}_3$  (3.0 eq.) and  $\text{CuSO}_4 \cdot 5\text{H}_2\text{O}$  (6.4 mol%),  $230\text{ }^\circ\text{C}$ .

The Suzuki reaction utilizing TAA precursors **3a–c** was shown to proceed with good to moderate yields using  $\text{Pd}(\text{PPh}_3)_4$ . However, improved yields and more reliable results could be obtained by applying  $(\text{NHC})\text{Pd}(\text{allyl})\text{Cl}$ ,<sup>24</sup> (55–74%) which generally turned out to be a highly efficient catalyst for thiophene–benzene cross-coupling. Attempts of Buchwald–Hartwig reactions in order to introduce the carbazole did not give satisfactory results, which led to a solvent-free Ullmann procedure<sup>20</sup> using  $\text{CuSO}_4 \cdot 5\text{H}_2\text{O}$  as the catalyst.

### Thermal properties

The thermal stability of the target host materials was investigated by TGA. High decomposition temperatures ( $T_d$  – determined from 5% mass loss) between  $392\text{ }^\circ\text{C}$  and  $426\text{ }^\circ\text{C}$  were observed for all materials. Glass transition temperatures ( $T_g$ ) were analyzed by DSC. While *o*-TPAPOXD exhibits glass transition at  $94\text{ }^\circ\text{C}$ <sup>16</sup> the values for *o*-PCzPOXD ( $125\text{ }^\circ\text{C}$ ) and *o*-ICzPOXD ( $152\text{ }^\circ\text{C}$ ) are significantly higher indicating improved morphological stability of thin films in PHOLED devices. Within the TOXD series *o*-PCzTOXD also features higher glass transition at  $135\text{ }^\circ\text{C}$  compared to *o*-TPATOXD ( $101\text{ }^\circ\text{C}$ ) or *o*-CzTOXD ( $106\text{ }^\circ\text{C}$ ) while no glass transition was detected for *o*-ICzTOXD. In general, the incorporation of the thiophene linker (TOXD derivatives) resulted in slightly higher glass transition temperatures in relation to the corresponding POXD compounds. Higher  $T_g$  values for PCz and ICz compounds compared to that of the TPA structure are attributed to an increased rigidity of the TAA moieties. All observed values are distinctly higher compared to that of CBP ( $62\text{ }^\circ\text{C}$  (ref. 7)).

### Photo-physical properties

Fig. 1 (left) displays the UV/VIS absorption and photoluminescence (PL) spectra of *o*-PCzPOXD and *o*-ICzPOXD as well as “reference compound” *o*-TPAPOXD. Spectra of the TOXD series are depicted in Fig. 1 (right). The optical bandgaps (opt. BG), determined from absorption onsets, are summarized in Table 2.

The absorption bands of *o*-TPAPOXD and *o*-TPATOXD at 305 nm are assigned to triphenylamine centered  $n-\pi^*$  transition.<sup>39</sup> All carbazole containing compounds exhibit sharp absorption peaks around 290 nm, which are attributed to the  $n-\pi^*$  transition of the carbazole moiety.<sup>40</sup> Indolocarbazole containing *o*-ICzTOXD and *o*-ICzPOXD features a related  $n-\pi^*$  transition below 300 nm. Longer wavelength absorption bands result from  $\pi-\pi^*$  charge transfer transitions from electron-donating arylamines to electron-accepting oxadiazole.<sup>41</sup> Strikingly, the absorbance of charge transfer transition is significantly lower for *o*-PCzPOXD and *o*-ICzPOXD compared to that of *o*-PCzTOXD and *o*-ICzTOXD, indicating that the partial disruption of the conjugated  $\pi$ -system by *ortho*-linkage is more effectively realized on the benzene spacer.

For the TOXD series also a significant blue shift of the absorption onset from *o*-TPATOXD ( $\sim 450\text{ nm}$ ) to *o*-PCzTOXD and *o*-ICzTOXD (both located at  $\sim 400\text{ nm}$ ) has been observed, indicating increased optical bandgaps as a result of planarized TAA donors.

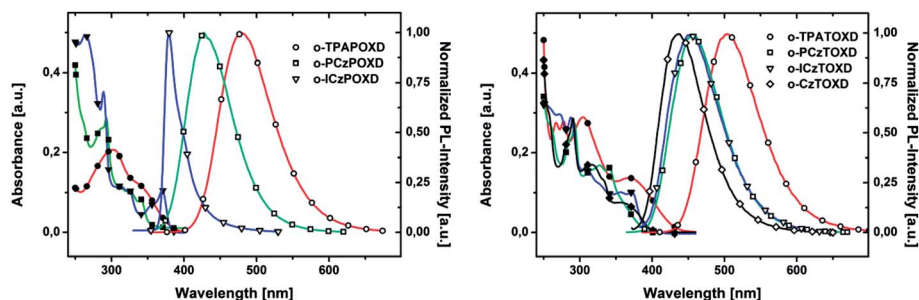


Fig. 1 Absorption (full symbols) and PL (hollow symbols) characteristics of host materials **5a–c** (POXD series, left) and **8a–d** (TOXD series, right); recorded in a 5  $\mu\text{M}$  solution in DCM at r.t.

Photoluminescence (PL) spectroscopy revealed a fluorescence emission maximum of **o**-TPAPOXD located at 479 nm. A significant blue shift of the emission maxima is observed for both **o**-PCzPOXD (428 nm) and **o**-ICzPOXD (379 nm). These results impressively demonstrate the impact of planarizing TAA donors by shifting the singlet emission by up to 100 nm ( $\Delta E = 0.68$  eV). Similar trends were observed for the TOXD series (**o**-TPATOXD (502 nm), **o**-PCzTOXD (456 nm) and **o**-ICzTOXD (452 nm)). We propose that these findings correlate with an increasing *ortho*-linkage effect (more twisted conformation) and decreasing donor strength of the TAA moiety (ICz < PCz < TPA) by planarization. The alteration in donor strength is attributed to the fact that the lone pair of the nitrogen increasingly contributes to the aromaticity (PCz and ICz). **o**-CzTOXD shows an emission maximum at 436 nm; the deep blue emission characteristic is due to the less extended conjugated  $\pi$ -system compared to the TAA structures. Clearly, all POXD compounds exhibit blue shifted emission with respect to the thiophene analogs (TOXD) indicating a more effective donor–acceptor separation for the benzene spacer.

Phosphorescence spectroscopy (77 K) revealed that planarization also impacts triplet emission, although the effect is less pronounced compared to singlet emission. The  $E_t$  values, deduced from the highest vibronic sub-band of the phosphorescence spectra, of **o**-TPAPOXD, **o**-PCzPOXD and **o**-ICzPOXD were determined to be 2.49 eV (2.46 eV (ref. 16)), 2.62 eV and

2.83 eV, respectively. Compared to the POXD series the  $E_t$  values of the TOXD materials **o**-TPATOXD (2.21 eV), **o**-PCzTOXD (2.29 eV), **o**-ICzTOXD (2.37 eV) and **o**-CzTOXD (2.39 eV) are shifted to lower energies.

Although the  $E_t$  values significantly increase as a consequence of planarization for both series, host materials of the TOXD series are restricted to low energy emitters. In contrast, the triplet energies of the POXD series are suitable for the construction of green devices.<sup>16,17</sup>  $E_t$  values >2.60 eV for the PCz and ICz donor structures potentially broaden the scope even to blue phosphorescent emitters (e.g. FIrPic). Particularly the unexpectedly high  $E_t$  value (2.83 eV) for **o**-ICzPOXD reveals the effect of incorporating indolo[3,2,1-*j*]*k*carbazole structures; a possible explanation for these findings is given by DFT calculations (see below).

Additionally, lifetimes for the excited singlet and triplet states were determined. Most striking are the significantly longer triplet lifetimes ( $\tau$ ) found in the POXD series (**o**-TPAPOXD (~790 ms), **o**-PCzPOXD (~335 ms), **o**-ICzPOXD (~349 ms)) compared to those of the TOXD compounds; triplet lifetimes for the TOXD structures range from 8.2 to 12.3 ms. The sulfur atoms in the TOXD compounds are subject to stronger spin–orbit coupling which leads to somewhat relaxed selection rules for transitions between singlet and triplet states (i.e. shorter lifetimes of the triplet). Further details on photo-physical properties are given in the ESI.†

Table 2 Physical data of synthesized materials

	$T_g/T_c/T_m/T_d^a$ [°C]	opt. BG <sup>b,c</sup> [eV]	$\lambda_{\text{PL,max}}^c$ [nm]	HOMO/LUMO [eV]		$E_t$ (eV)	
				Exp. <sup>d</sup>	Cal. <sup>e</sup>	Exp. <sup>f</sup>	Cal. <sup>g</sup>
<b>o</b> -TPAPOXD	94/—/270/432 (ref. 16)	3.24	479	−5.25/−2.41 (ref. 16)	−5.14/−1.77	2.49	2.63
<b>o</b> -PCzPOXD	125/n.o. <sup>h</sup> /252/395	3.51	428	−5.64/−2.50	−5.55/−2.04	2.62	2.83
<b>o</b> -ICzPOXD	152/231/308/404	3.26	379	−5.73/−2.50 <sup>i</sup>	−5.70/−1.84	2.83	2.88
<b>o</b> -TPATOXD	101/n.o. <sup>h</sup> /184/414	2.88	502	−5.30/−2.57	−5.19/−2.11	2.21	2.21
<b>o</b> -PCzTOXD	135/n.o. <sup>h</sup> /261/426	3.19	456	−5.66/−2.68	−5.57/−2.37	2.29	2.30
<b>o</b> -ICzTOXD	n.o. <sup>h</sup> /302/341/402	3.19	452	−5.68/−2.56	−5.70/−2.03	2.37	2.36
<b>o</b> -CzTOXD	106/n.o. <sup>h</sup> /211/392	3.11	436	−5.69/−2.66	−5.65/−2.39	2.39	2.33

<sup>a</sup> Determined from TGA/DSC analysis;  $T_c$ : crystallization temperature. <sup>b</sup> Estimated from the absorption onset. <sup>c</sup> Measurement in DCM (5  $\mu\text{M}$ ) at r.t. <sup>d</sup> Calculated from onsets of oxidation and reduction peaks. <sup>e</sup> Calculated applying the density functional theory level (B3LYP/6-311 + G\*). <sup>f</sup> Estimated from the highest energy vibronic transition in toluene at 77 K. <sup>g</sup> Calculated applying the time-dependent density functional theory level (B3LYP/6-311 + G\*). <sup>h</sup> Not observed. <sup>i</sup> Calculated from HOMO level and absorption onset.



## Electro-chemical properties

Electro-chemical properties (Table 2) of target materials were investigated by cyclic voltammetry (CV). Predominately determined by electron-rich triarylaminines, the HOMO energy levels span a narrow range of  $-5.73$  eV to  $-5.64$  eV with the exception of *o*-TPAPOXD and *o*-TPATOXD at  $-5.25$  eV (ref. 16) and  $-5.30$  eV, respectively. Thus, the incorporation of planarized TAA donors significantly lowers the HOMO energy levels. While *o*-TPATOXD shows reversible oxidation, all carbazole and indolocarbazole containing materials exhibit irreversible oxidation waves due to the instability of the formed cations.<sup>23,42,43</sup> Quasi-reversible reductions were observed during cathodic scans; however, no significant reduction process was observed for *o*-ICzPOXD. The LUMO energy levels of the compounds are located between  $-2.68$  eV and  $-2.41$  eV. These values indicate no significant injection barrier for charge carriers from adjacent charge transporting layers.

## Theoretical calculations

To investigate the geometrical and electronic properties of the target compounds at the molecular level studies applying density functional theory (DFT) and time-dependent DFT (TDDFT) calculations were conducted (for additional details see the Experimental section). According to DFT calculations, absolute HOMO/LUMO values are in the range of  $5.14$ – $5.70$  eV/ $1.77$ – $2.39$  eV, which correlates with the experimental data; LUMO levels show a systematic shift of  $\sim 0.5$  eV.

The contour plots for **5a** and **8a**, comparing the POXD with the corresponding TOXD compounds, are depicted in Fig. 2. As expected, HOMO levels are mainly located at one of the TAA

structures and the LUMOs at the oxadiazole containing cores (POXD and TOXD). This separation, particularly crucial for high triplet energies, was found to be more efficiently realized for the POXD series (benzene linker) for all substance pairs, which is in agreement with photo-physical data (Table 2). Inspecting the TPA (Fig. 2 (left)) and PCz (Fig. 3 (left)) scaffolds a similar trend is observed: a reduced HOMO/LUMO overlap is indicated for the more rigidified PCz *versus* the TPA structures. The comparison of the average tilting angles of the of POXD and the TOXD benzene to the TAA benzene core supports the aforementioned assumptions:  $54.6^\circ$  ( $56.2^\circ/53.0^\circ$ ) *o*-TPAPOXD  $<$   $58.7^\circ$  ( $62.2^\circ/55.2^\circ$ ) *o*-PCzPOXD  $<$   $59.7^\circ$  ( $61.9^\circ/57.5^\circ$ ) *o*-ICzPOXD and  $50.2^\circ$  ( $52.0^\circ/48.3^\circ$ ) *o*-TPATOXD  $<$   $54.3^\circ$  ( $57.8^\circ/50.8^\circ$ ) *o*-PCzTOXD  $<$   $54.9^\circ$  ( $57.0^\circ/52.8^\circ$ ) *o*-ICzTOXD (the exact tilting angle values for each side of the asymmetric molecules are given in brackets).

A remarkable result of the calculation was acquired for *o*-ICzPOXD (Fig. 3 (right)). While the HOMO is positioned at the TAA (ICz) scaffold (as expected), the LUMO is not located on the POXD core but on the opposing ICz moiety. Potentially, this fact is an explanation for the aforementioned unexpectedly high triplet energy observed as a result of the enhanced spatial separation and modified acceptor properties. This finding outlines the significant deviation in donor strength for the applied TAA structures and the effect on material properties. In contrast, the LUMO in the *o*-ICzTOXD remains located at the TOXD core (as observed for all other molecules), which corresponds to the detected triplet and singlet energy value relationships, thus, supporting the hypothesis for the LUMO located on the ICz core in *o*-ICzPOXD.

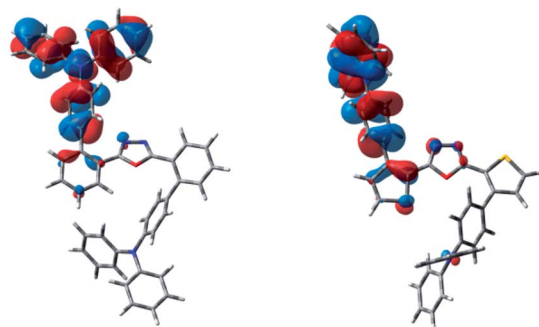
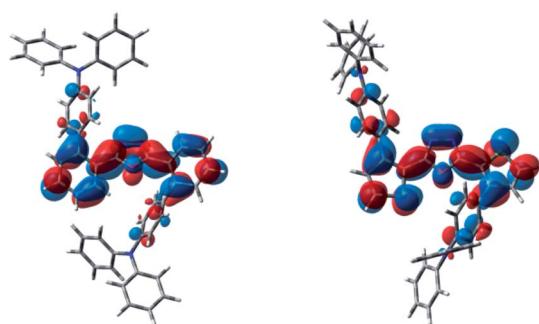


Fig. 2 HOMO (bottom) and LUMO (top) of *o*-TPAPOXD **5a** (left) and *o*-TPATOXD **8a** (right).

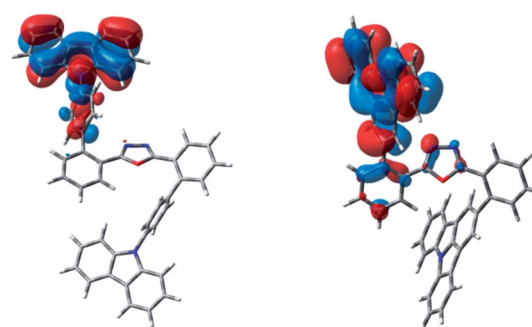
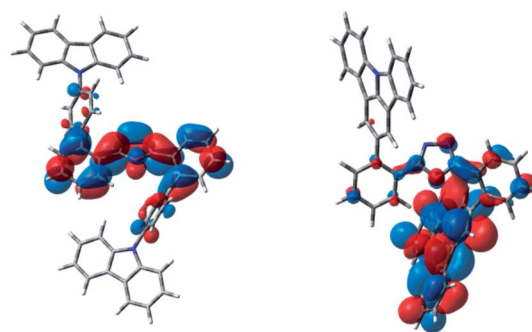


Fig. 3 HOMO (bottom) and LUMO (top) of *o*-PCzPOXD **5b** (left) and *o*-ICzPOXD **5c** (right).

## Crystallography

***o*-PCzPOXD (5b)**<sup>44</sup> (Fig. 4 (left)) crystallizes with one crystallographically unique molecule in the asymmetric unit. The molecules are pseudo-symmetric by twofold rotation around an axis passing through the O atom of the oxadiazole ring. The PCz donor units are located on the side of the O atom of the oxadiazole ring. Due to steric interaction of these groups, the core benzenes (POXD) are strongly inclined to each other (angle between the LS planes: 60.95(3)°) and to the central oxadiazole ring (32.45(8)° and 33.64(8)°). The carbazole moieties are moderately inclined with respect to the core benzenes (15.58(9)° and 16.25(9)°). On the other hand the PCz-benzene rings are distinctly inclined to the POXD benzenes (53.49(6)° and 54.12(6)°) and carbazoles (56.38(5)° and 57.68(5)°).

***o*-PCzTOXD (8b)**<sup>45</sup> (Fig. 4 (right)) crystallizes with two crystallographically different molecules ( $Z' = 2$ ) located in general positions. Both molecules are geometrically virtually equivalent. One thiophene ring is in *trans*- and one in *cis*-conformation with respect to the central oxadiazole ring. Thus, both PCz moieties face opposite directions. This is in contrast to the crystal structures of ***o*-PCzPOXD** and the solvates of the thiadiazole analog of ***o*-PCzTOXD** (as reported in earlier studies), in which the thiadiazole and thiophene rings are all in *trans*- and, therefore, the PCz units in *cis*-conformation.<sup>46</sup> The thiophene and oxadiazole rings in *cis*-conformation are practically planar with tilt angles of 3.17(10)° and 3.53(10)°. In contrast, the thiophenes in the *trans*-conformation feature distinct inclination to the oxadiazole ring (12.03(11)° and 11.44(11)°). While the carbazole connected *via* the PCz-benzene to the *cis*-located thiophene is nearly coplanar with the latter (3.17(8)°, 2.33(8)°), the *trans*-located thiophene is strongly inclined to the corresponding carbazole (76.91(9)°, 76.86(9)°). The PCz-benzenes on the other hand are, as in ***o*-PCzPOXD**, always strongly inclined to the neighboring aromatic moieties (tilt angles to thiophene: 45.82(10)–47.93(10)°; to carbazoles: 44.59(8)–61.06(8)°).

## Charge transport properties

In order to study the influence of the four investigated arylamine-donors on charge transport properties within the TOXD series, hole-only devices (HODs; structure: ITO/MoO<sub>3</sub>,

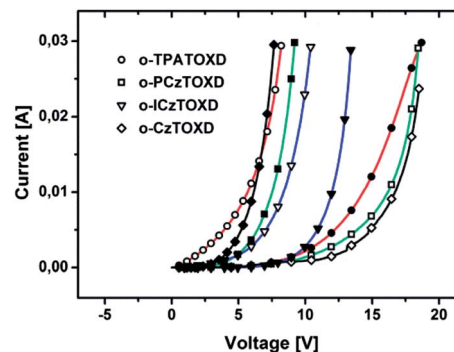


Fig. 5 Current–voltage ( $I$ – $V$ ) curves of hole- (hollow symbols) and electron-only (full symbols) devices.

(8 nm)/host (80 nm)/MoO<sub>3</sub> (8 nm)/Al) and electron-only devices (EODs; structure: Al/Li<sub>2</sub>CO<sub>3</sub> (1 nm)/Be:Li<sub>2</sub>CO<sub>3</sub> (30 nm)/host (80 nm)/Be:Li<sub>2</sub>CO<sub>3</sub> (30 nm)/Li<sub>2</sub>CO<sub>3</sub> (1 nm)/Al) were fabricated. It is noted that the HOMO levels of ***o*-CzTOXD**, ***o*-PCzTOXD** and ***o*-ICzTOXD** are nearly 0.4 eV lower compared to those of ***o*-TPATOXD**. This fact may hamper hole injection into the HODs; however, this displays the actual situation in the PHOLED devices. Current–voltage curves are shown in Fig. 5.

***o*-TPATOXD** exhibits good hole transport properties due to the presence of the triphenylamine moiety; significantly lower current density was observed in the EOD. In contrast carbazole based ***o*-CzTOXD** and ***o*-PCzTOXD** feature better electron

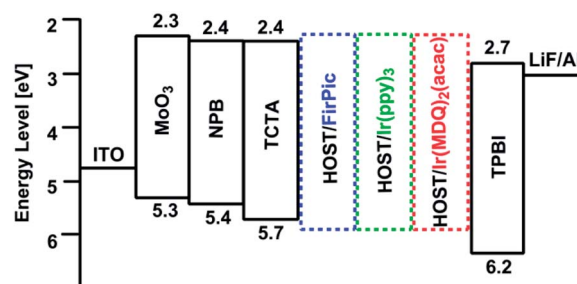


Fig. 6 Schematic energy level diagram of the device architecture employed in this work.

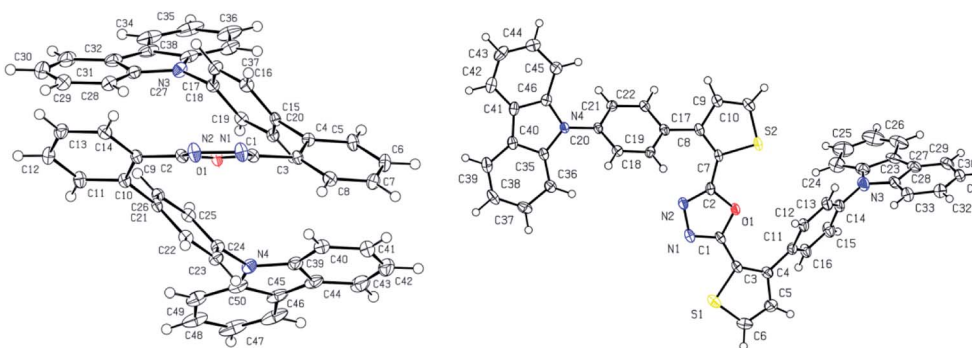


Fig. 4 Molecular structures of ***o*-PCzPOXD** (left) and ***o*-PCzTOXD** (right) – C, N, O and S atoms are represented by white, blue, red and yellow ellipsoids drawn at 50% probability levels, and H atoms by spheres of arbitrary radius. For ***o*-PCzTOXD** only one out of two unique molecules is shown.

transport properties. While *o*-PCzTOXD exhibits similarly low hole current density compared to *o*-CzTOXD, the current density in the EOD applying *o*-PCzTOXD is lower and therefore charge transport in *o*-PCzTOXD is more balanced than that in *o*-CzTOXD. For *o*-ICzTOXD the HOD shows higher current density than the EOD. Furthermore, carrier properties in *o*-ICzTOXD are more balanced compared to the other host materials. Thus, the incorporation of the indolocarbazole moiety resulted in the most bipolar character of *o*-ICzTOXD among this series of materials. The same trends were found for the POXD series with the exception of the EOD of *o*-ICzPOXD featuring hardly any electron transport. This finding can be explained by the

significantly altered orbital distribution of *o*-ICzPOXD as discussed in the theoretical part.

### Electroluminescent properties

To evaluate the applicability of the POXD series as universal host materials for RGB PHOLED devices with a standard architecture of ITO/MoO<sub>3</sub> (8 nm)/NPB (50 nm)/TCTA (5 nm)/EML (10 nm)/TPBI (25 nm)/LiF (1 nm)/Al, in which the EMLs consist of coevaporated hosts *o*-TPAPOXD (I), *o*-PCzPOXD (II) or *o*-ICzPOXD (III) and guests Ir(MDQ)<sub>2</sub>(acac) (R), Ir(ppy)<sub>3</sub> (G) or FIrPic (B), were fabricated. NPB is used as a hole transporting

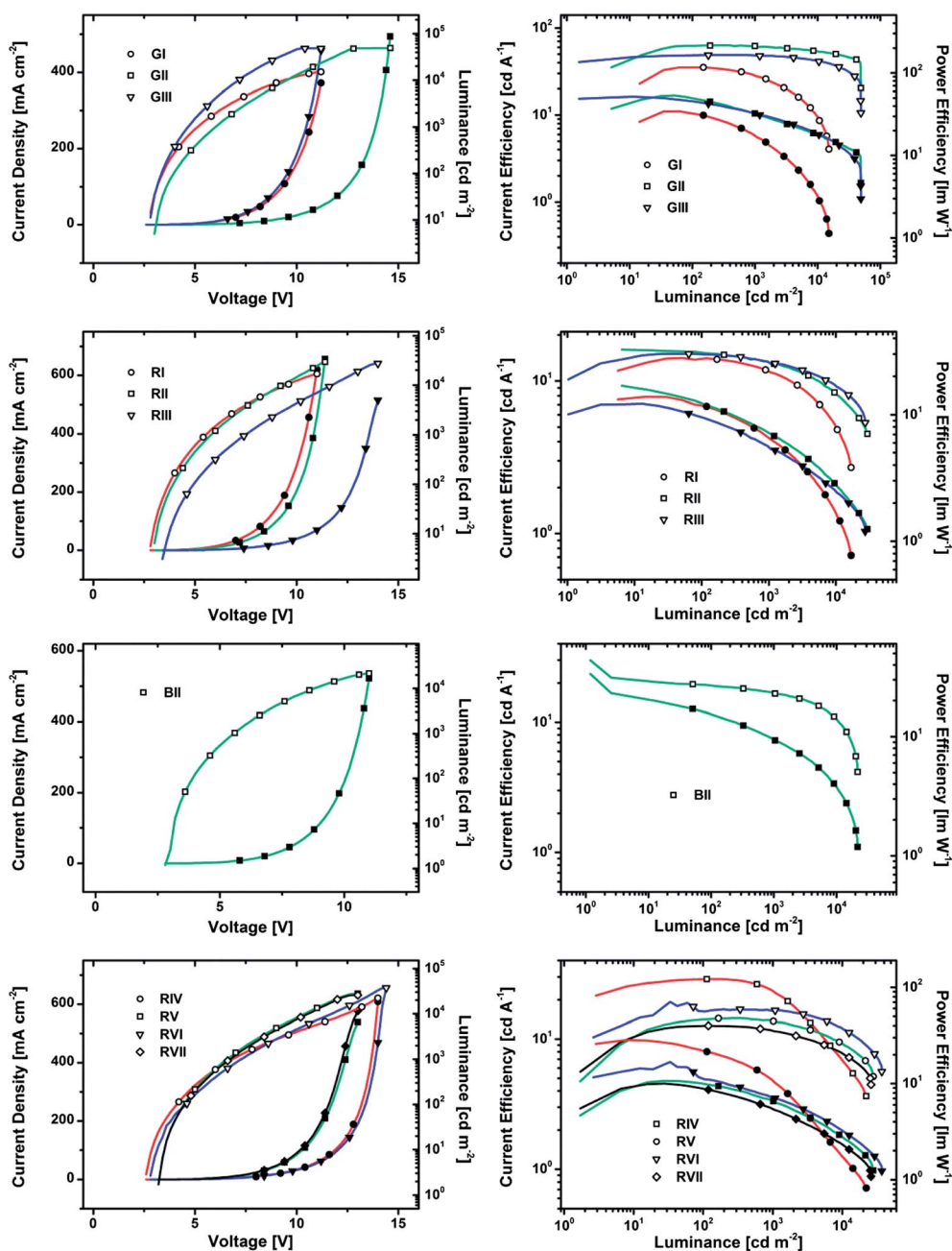


Fig. 7 Current density–voltage–luminance (full symbols: current density; hollow symbols: luminance) and current efficiency–luminance–power efficiency (full symbols: power efficiency; hollow symbols: current efficiency) curves of all devices investigated in this work.

layer while TPBI is applied as an electron transporting and hole blocking layer due to its low lying HOMO level.<sup>47–50</sup> Additionally a thin TCTA layer is inserted between the hole transporting and emitting layers in order to confine triplet excitons more effectively in the EML as a result of a larger triplet energy of TCTA compared to that of NPB.<sup>48</sup> The standard device architecture including HOMO and LUMO levels of all employed materials is depicted in Fig. 6.

Current density–voltage–luminance and current efficiency–luminance–power efficiency curves for all devices are depicted in Fig. 7 and the electroluminescent properties of all fabricated PHOLED devices are summarized in Table 3. Among green devices the best efficiency was achieved for device GII (host material: **o-PCzPOXD**), giving a maximum current efficiency (CE) of 62.9 cd A<sup>-1</sup>, a maximum power efficiency (PE) of 53.5 lm W<sup>-1</sup> and a maximum external quantum efficiency (EQE) of 17.1%, while lower values were obtained for GI and GIII with CE<sub>max</sub> of 35.1 cd A<sup>-1</sup> and 48.8 cd A<sup>-1</sup>, PE<sub>max</sub> of 34.4 lm W<sup>-1</sup> and 51.6 lm W<sup>-1</sup> and EQE<sub>max</sub> of 10.3% and 13.8%, respectively. We emphasize that significantly higher efficiencies were obtained by applying **o-PCzPOXD** and **o-ICzPOXD** in our standard device configuration compared to **o-TPAPOXD**. In fact, using **o-TPAPOXD** Tao *et al.*<sup>17</sup> reported highly efficient green PHOLED devices reaching an EQE<sub>max</sub> of 22.0% (vs. EQE<sub>max</sub> of 10.3%) after optimization of the device architecture, thus revealing the potential of the newly developed materials within this paper. Notably, at an illumination relevant brightness of 1000 cd m<sup>-2</sup> devices GII and GIII retained high CE of 61.2 cd A<sup>-1</sup> and 48.1 cd A<sup>-1</sup>. These values correspond to remarkably low efficiency roll-offs of 2.7 and 1.5%. Even at a brightness of 5000 cd m<sup>-2</sup> GII showed a CE of 56.8 cd A<sup>-1</sup> (9.7% roll-off), while GIII displayed a CE of 44.8 cd A<sup>-1</sup> (8.2% roll-off). In contrast a significantly higher overall efficiency roll-off of 55.3% for device GI, featuring CE of 28.2 cd A<sup>-1</sup> and 15.7 cd A<sup>-1</sup> at brightness of 1000 cd m<sup>-2</sup> and 5000 cd m<sup>-2</sup>, was observed. This efficiency roll-off is attributed to the dominant hole transport properties of **o-TPAPOXD**, due to the TPA donor unit (more balanced charge transport for the planarized donor structures; see the section Charge transport properties). The unbalanced charge transport properties lead to accumulation of holes at the interface of the emissive and TPBI layer and a narrow exciton recombination

zone. Since triplet–triplet annihilation (TTA) is strongly dependent on the triplet exciton concentration the thickness of the recombination zone is of crucial importance and a major factor for efficiency roll-off in PHOLED devices at high current densities.<sup>51</sup> Thus, the incorporation of planarized arylamine donors significantly decreases the efficiency roll-off as a result of more balanced charge transport properties resulting in broader recombination zones.

Red devices RI, RII and RIII showed similar performance exhibiting CE<sub>max</sub> of 14.0 cd A<sup>-1</sup>, 16.1 cd A<sup>-1</sup> and 15.0 cd A<sup>-1</sup>, PE<sub>max</sub> of 13.7 lm W<sup>-1</sup>, 16.8 lm W<sup>-1</sup> and 12.2 lm W<sup>-1</sup> and EQE<sub>max</sub> of 8.3%, 11.2% and 10.1%. In analogy to the green devices lower efficiency roll-off was observed for devices RII and RIII (incorporating planarized host materials) compared to RI.

Furthermore, blue device BII, utilizing **o-PCzPOXD** as the host, was fabricated displaying a CE<sub>max</sub> of 29.8 cd A<sup>-1</sup>, a PE<sub>max</sub> of 33.5 lm W<sup>-1</sup> and an EQE<sub>max</sub> of 13.4%. Thus, it was demonstrated that **o-PCzPOXD** is applicable as a universal host material in efficient red, green and blue PHOLED devices. However, low device performance has been observed for blue devices applying **o-ICzPOXD**. For these devices also the recorded emission could not be assigned to the FIrPic emitter only. Systematic investigation is necessary to understand these findings.

As a result of the lower triplet energies of the TOXD materials compared to those of the POXD series, **o-TPATOXD** (IV), **o-PCzTOXD** (V), **o-ICzTOXD** (VI) and **o-CzTOXD** (VII) were examined in red (R) devices only. Identical device architecture as for the POXD series was applied. Among this series of devices RIV exhibited the highest CE<sub>max</sub> of 28.8 cd A<sup>-1</sup>, PE<sub>max</sub> of 28.4 lm W<sup>-1</sup> and EQE<sub>max</sub> of 16.9%, while RV, RVI, and RVII displayed CE<sub>max</sub> of 14.4, 19.2 and 12.6 cd A<sup>-1</sup>, PE<sub>max</sub> of 10.6, 16.7 and 10.0 lm W<sup>-1</sup> and EQE<sub>max</sub> of 11.2%, 13.2% and 9.4%, respectively, displaying similar device performance as the corresponding POXD compounds. The same tendency for decreased efficiency roll-off observed for the POXD series was found for devices RIV–VII. While the CE of device RIV drops to 10.5 cd A<sup>-1</sup> at a brightness of 5000 cd m<sup>-2</sup>, corresponding to an efficiency roll-off of 64%, current efficiencies for devices RV, RVI and RVII (incorporating planarized donors) decreased only by 24% to 27%.

Table 3 Electroluminescent properties of devices GI–III, BII and RI–VII

	V <sub>on</sub> [V]	L <sub>max</sub> [cd m <sup>-2</sup> ]	CE <sup>a</sup> [cd A <sup>-1</sup> ]	PE <sup>a</sup> [lm W <sup>-1</sup> ]	EQE <sup>a</sup> [%]
GI	2.8	15 049	35.0/28.2/15.7/35.1	32.3/17.1/6.3/34.4	10.3/8.1/4.7/10.3
GII	3.0	49 386	62.3/61.2/56.8/62.9	48.9/31.1/21.5/53.5	17.0/16.4/15.5/17.1
GIII	2.6	48 768	48.4/48.1/44.8/48.8	44.9/32.1/22.4/51.6	13.7/13.6/12.7/13.8
BII	2.8	21 710	18.9/16.7/13.4/29.8	15.3/9.4/5.6/33.5	8.5/7.5/6.1/13.4
RI	2.8	16 838	13.9/11.5/7.4/14.0	11.7/6.4/2.9/13.7	8.2/6.6/4.1/8.3
RII	3.0	29 615	15.3/13.2/10.1/16.1	12.4/7.2/4.0/16.8	10.6/9.1/6.7/11.2
RIII	3.0	27 517	14.9/12.9/10.8/15.0	9.4/5.3/3.3/12.2	9.1/6.9/5.3/10.1
RIV	2.6	22 160	28.7/22.6/10.5/28.8	21.4/10.1/3.0/28.4	16.8/13.2/6.0/16.9
RV	3.2	27 768	14.2/13.7/10.9/14.4	9.7/6.5/3.7/10.6	11.1/9.5/7.3/11.2
RVI	2.8	36 975	16.2/16.5/14.2/19.2	11.0/7.0/4.3/16.7	11.3/11.4/9.6/13.2
RVII	3.0	25 837	12.6/11.4/9.2/12.6	8.6/5.3/3.1/10.0	9.3/7.2/5.8/9.4

<sup>a</sup> Measured at a brightness of 100 cd m<sup>-2</sup>/1000 cd m<sup>-2</sup>/5000 cd m<sup>-2</sup>/max.

## Conclusion

In this study, the impact of planarizing TAA donors in bipolar host materials on the *ortho*-linkage effect was investigated in detail. Hence, oxadiazole based structures **5a–c** and **8a–d** have been designed, synthesized and examined regarding thermal, photo-physical and electro-chemical properties.

The straight-forward synthesis of target compounds relies on efficient cross-coupling and organolithium based procedures. In particular, the developed C–H activation protocol allows for a convenient and selective access to potential target scaffolds, clearly broadening the scope of accessible indolo[3,2,1-*jk*]-carbazole moieties.

For increasingly planarized TAA donor structures the following conclusions can be drawn: (i) improved morphological stability; (ii) elevated singlet and triplet energy values, which are attributed to an enhanced *ortho*-linkage effect and reduced donor strength of the planarized structures; and (iii) significantly reduced efficiency roll-off for all devices. Hence, the concept of planarization addresses major challenges in PHOLED research: improving both triplet energy and compound stability. In fact, triplet energies >2.60 eV enable the construction of efficient blue (FIrPic) PHOLEDs, which has not been reported for this specific substance class to date.

Improved PHOLED performance in standard device configurations compared to that of non-planarized reference compound **o**-TPAPOXD (EQE<sub>max</sub> of 22.0% reported for optimized architecture)<sup>17</sup> reveals the great potential of the developed compounds as highly efficient host materials.

## Experimental section

### General information

All reagents and solvents were purchased from commercial suppliers and used without further purification. Anhydrous solvents were prepared by filtration through drying columns; dry DMF was obtained from Acros. Column chromatography was performed on silica 60 (Merck, 40–63 μm). NMR spectra were recorded on a Bruker Avance DRX-400 spectrometer or a Bruker Avance 200 spectrometer. High resolution mass spectra (HRMS) were obtained from a Thermo Scientific LTQ Orbitrap XL hybrid FTMS (Fourier transform mass spectrometer) and Thermo Scientific MALDI LTQ Orbitrap interface;  $\alpha$ -cyano-4-hydroxycinnamic acid was used as the matrix. Thermogravimetric (TG) and differential scanning calorimetry (DSC) measurements were carried out at a heating rate of 5 K min<sup>-1</sup> in a flowing argon atmosphere (25 ml min<sup>-1</sup>). For the TG measurements, a Netsch TG 209 F9 Tarsus system, working with open aluminium oxide crucibles, was used. For the DSC measurements, a Netsch DSC 200 F3 Maia, working with aluminium pans with pierced lids, was employed. UV/VIS absorption and fluorescence emission spectra were recorded in DCM solutions (5 μM) with a Perkin Elmer Lambda 750 spectrometer and an Edinburgh FLS920, respectively. Time resolved experiments were performed using a Quantel Brilliant tripled Nd-YAG laser (355 nm, 20 Hz repetition rate, pulse width: ~5 ns). Spectra were measured using a SPEX

270 monochromator equipped with both photomultiplier and CCD. This set-up is controlled using a home-built Labview-based program which allows using different instruments such as photon counting devices, oscilloscopes, and additional mechanical shutters. For the measurement of the triplet emission, a mechanical shutter was triggered by the pulsed laser. A pretrigger period of 0.5 ms was followed by a 1 ms aperture and a rest time of 300–500 ms allowed obtaining the measurements shown in the ESI.† The slit of the monochromator was also opened further (up to 0.5 mm) to measure the triplet emission. Triplet energy ( $E_T$ ) values were determined from the highest energy vibronic subband (first significant peak/shoulder) of the time-resolved low-temperature phosphorescence spectra. Cyclic voltammetry was performed using a three electrode configuration consisting of a Pt working electrode, a Pt counter electrode and an Ag/AgCl reference electrode and a PGSTAT128N, ADC164, DAC164, External, DI048 potentiostat provided by Metrohm Autolab B. V. Measurements were carried out in a 0.5 mM solution in anhydrous DCM (oxidation scan) and THF or DMF (reduction scan) with Bu<sub>4</sub>NBF<sub>4</sub> (0.1 M) as the supporting electrolyte. The solutions were purged with nitrogen for 15 minutes prior to measurement. HOMO and LUMO energy levels were calculated from the onset of oxidation and reduction, respectively. The onset potential was determined by the intersection of two tangents drawn at the background and the rising of oxidation or reduction peaks.

### Synthetic details

*N,N*-Diphenyl-4-(4,4,5,5-tetramethyl-1,3,2-dioxaborolan-2-yl)benzenamine (**3a**),<sup>18,19</sup> 9-[4-(4,4,5,5-tetramethyl-1,3,2-dioxaborolan-2-yl)phenyl]-9*H*-carbazole (**3b**),<sup>19,20</sup> 2,5-bis(5-bromo-2-thienyl)-1,3,4-oxadiazole (**4**),<sup>52</sup> and 2,5-bis(2-bromophenyl)-1,3,4-oxadiazole (**6**)<sup>27</sup> were prepared according to published procedures.

**9-(2-Chlorophenyl)-9*H*-carbazole (1ii).** **1ii** was synthesized following procedures in the literature.<sup>20</sup> Carbazole (2.51 g, 15.0 mmol, 1.00 eq.), 1-bromo-2-chlorobenzene (3.45 g, 18.0 mmol, 1.20 eq.), K<sub>2</sub>CO<sub>3</sub> (2.07 g, 15.0 mmol, 1.00 eq.) and CuSO<sub>4</sub>·5H<sub>2</sub>O (0.19 g, 0.75 mmol, 0.05 eq.) were added to a 250 ml three-necked round-bottomed flask. The mixture was heated with a heating jacket to 230 °C for 72 h. After cooling to r.t. H<sub>2</sub>O (100 ml) was added and the mixture was extracted with toluene. The brown suspension was filtered and the remaining solvent removed *in vacuo*. Purification by crystallization from EtOH yielded **1ii** as a white solid (1.93 g, 6.9 mmol, 46%). <sup>1</sup>H NMR (400 MHz, CDCl<sub>3</sub>):  $\delta$  = 8.21 (d,  $J$  = 7.7 Hz, 2H), 7.73–7.71 (m, 1H), 7.56–7.44 (m, 5H), 7.35 (t,  $J$  = 7.5 Hz, 2H), 7.15 (d,  $J$  = 8.1 Hz, 2H) ppm. <sup>13</sup>C NMR (100 MHz, CDCl<sub>3</sub>):  $\delta$  = 140.8 (s), 135.0 (s), 133.7 (s), 131.0 (d), 130.8 (d), 129.8 (d), 128.1 (d), 125.9 (d), 123.3 (s), 120.3 (d), 120.0 (d), 109.9 (d) ppm. Calculated:  $m/z$ : 277.07 [M]<sup>+</sup>. Found: MS (EI):  $m/z$ : 277.03 [M]<sup>+</sup>.

**2,6-Dichloro-*N,N*-diphenylbenzenamine (1iii).** Diphenylamine (1.02 g, 6.0 mmol, 1.00 eq.) was dissolved in dry DMF (18 ml). The solution was purged with argon, subsequently heated to 50 °C and NaH (0.43 g, 18.0 mmol, 3.00 eq.) was added quickly. The suspension was stirred for 5 min at 50 °C before 1,3-dichloro-2-fluorobenzene (1.49, 9.0 mmol, 1.50 eq.) was

added. Due to incomplete conversion (TLC) after stirring overnight additional NaH (0.14 g, 6.0 mmol 1.00 eq.) was added. After full conversion (TLC – 24 h) the reaction mixture was poured on H<sub>2</sub>O, extracted with DCM repeatedly and the combined organic layers were dried over Na<sub>2</sub>SO<sub>4</sub> and concentrated under reduced pressure. Column chromatography (PE) yielded **1iii** (0.79 g, 2.5 mmol, 42%) as a white solid. <sup>1</sup>H NMR (400 MHz, CD<sub>2</sub>Cl<sub>2</sub>): δ = 7.46 (d, *J* = 8.1 Hz, 2H), 7.29–7.22 (m, 5H), 6.99–7.96 (m, 6H) ppm. <sup>13</sup>C NMR (100 MHz, CD<sub>2</sub>Cl<sub>2</sub>): δ = 145.7 (s), 140.7 (s), 137.6 (s), 130.2 (d), 129.6 (d), 129.3 (d), 122.6 (d), 121.0 (d) ppm. Calculated: *m/z*: 313.04 [M]<sup>+</sup>. Found: MS (EI): *m/z*: 313.01 [M]<sup>+</sup>.

**Indolo[3,2,1-*jk*]carbazole (2).** **1i/1ii/1iii** (1.0 eq.), (NHC)Pd(allyl)Cl<sup>24,25</sup> (2 mol%) and K<sub>2</sub>CO<sub>3</sub> (2.00 eq.) were dissolved in degassed *N,N*-dimethylacetamide (DMA, 0.2 M) under an argon atmosphere and heated to 130 °C until complete conversion (GCMS). The reaction mixture was poured on water and extracted with Et<sub>2</sub>O. The combined organic layers were dried over anhydrous Na<sub>2</sub>SO<sub>4</sub> and the solvent was removed under reduced pressure. Purification was accomplished by column chromatography (PE). Starting from **1i** (9.66 g, 30.0 mmol), (NHC)Pd(allyl)Cl (0.34 g, 0.60 mmol) and K<sub>2</sub>CO<sub>3</sub> (8.29 g, 60.0 mmol) **2** was obtained as a white powder (6.78 g, 28.1 mmol, 94%). Starting from **1ii** (3.70 g, 13.3 mmol), (NHC)Pd(allyl)Cl (0.15 g, 0.27 mmol) and K<sub>2</sub>CO<sub>3</sub> (3.67 g, 26.6 mmol) **2** was obtained as a white powder (3.02 g, 12.5 mmol, 94%). Starting from **1iii** (0.47 g, 1.5 mmol), (NHC)Pd(allyl)Cl (0.02 g, 0.03 mmol) and K<sub>2</sub>CO<sub>3</sub> (0.43 g, 3.1 mmol) **2** was obtained as a white powder (0.29 g, 1.2 mmol, 80%). <sup>1</sup>H NMR (400 MHz, CD<sub>2</sub>Cl<sub>2</sub>): δ = 8.16 (d, *J* = 7.8 Hz, 2H), 8.06 (d, *J* = 7.4 Hz, 2H), 7.92 (d, *J* = 8.1 Hz, 2H), 7.62–7.55 (m, 3H), 7.38 (t, *J* = 7.7 Hz, 2H) ppm. <sup>13</sup>C NMR (100 MHz, CD<sub>2</sub>Cl<sub>2</sub>): δ = 144.2 (s), 139.2 (s), 130.5 (s), 127.3 (d), 123.6 (d), 123.4 (d), 122.3 (d), 119.9 (d), 118.9 (s), 112.7 (d) ppm. Calculated: *m/z*: 241.09 [M]<sup>+</sup>. Found: MS (EI): *m/z*: 241.11 [M]<sup>+</sup>.

**2-Bromoindolo[3,2,1-*jk*]carbazole.** **2** (14.26 g, 59.1 mmol, 1.0 eq.) was dissolved in AcOH–CHCl<sub>3</sub> = 1 : 1 (300 ml) and heated to 55 °C. NBS (10.51 g, 59.1 mmol, 1.0 eq.) was added in small portions over a period of 1 h to the grey suspension. Since GC-MS analysis indicated incomplete conversion, more NBS (1.05 g, 5.9 mmol, 0.10 eq.) was added. After complete conversion the reaction mixture was poured on an aqueous NaOH solution (1000 ml, 6 M, 2 eq.) and extracted with DCM. The organic layer was dried over Na<sub>2</sub>SO<sub>4</sub> and the solvent was removed *in vacuo*. Crystallization from ACN yielded 2-bromoindolo[3,2,1-*jk*]carbazole as a beige powder (10.30 g, 32.2 mmol, 54%). Physical data are in accordance with the literature.<sup>23</sup>

**2-(4,4,5,5-Tetramethyl-1,3,2-dioxaborolan-2-yl)indolo[3,2,1-*jk*]carbazole (3c).** The synthesis of **3c** was accomplished analogously to published procedures.<sup>19,23</sup> To a solution of 2-bromoindolo[3,2,1-*jk*]carbazole (10.25 g, 32.0 mmol, 1.00 eq.) in anhydrous THF (100 ml) under an argon atmosphere *n*-BuLi (14.1 ml, 2.5 M in hexanes, 35.2 mmol, 1.10 eq.) was added dropwise at –78 °C. Subsequently the reaction mixture was stirred at –80 °C for 1 h before Pinbop® (7.14 g, 38.4 mmol, 1.20 eq.) was added and the reaction mixture was allowed to warm to

room temperature slowly. After stirring overnight the solvent was removed under reduced pressure and the residue was partitioned between aqueous HCl (1 N) and DCM. The aqueous phase was extracted with DCM, and the combined organic layers were dried over anhydrous Na<sub>2</sub>SO<sub>4</sub> and concentrated *in vacuo*. **3c** (8.10 g, 22.1 mmol, 69%) was isolated as a white solid after crystallization from acetonitrile. <sup>1</sup>H NMR (400 MHz, CDCl<sub>3</sub>): δ = 8.58 (s, 2H), 8.14 (d, *J* = 7.7 Hz, 2H), 7.90 (d, *J* = 8.0 Hz, 2H), 7.56 (dd, *J* = 8.0, 7.6 Hz, 2H), 7.37 (dd, *J* = 7.7, 7.6 Hz, 2H), 1.46 (s, 12H) ppm. <sup>13</sup>C NMR (100 MHz, CDCl<sub>3</sub>): δ = 145.9 (s), 138.9 (s), 130.0 (s), 126.7 (d), 126.3 (d), 123.2 (d), 122.0 (d), 118.2 (s), 112.2 (d), 83.8 (s), 25.0 (s) ppm (C–B not detected). Calculated: *m/z*: 367.17381 [M]<sup>+</sup>, 368.18164 [M + H]<sup>+</sup>. Found: MS (MALDI): *m/z*: 367.17526 [M]<sup>+</sup>, 368.17856 [M + H]<sup>+</sup>.

**General procedure for the Suzuki cross-coupling towards 5a–c.** The reactions towards **5a–c** were performed under an argon atmosphere. **4** (1.00 eq.) and boronic acid ester **3a–c** (2.50 eq.) were dissolved in degassed THF (~0.5 M). Subsequently degassed 2 M aqueous K<sub>2</sub>CO<sub>3</sub> (5.00 eq.) and Pd(PPh<sub>3</sub>)<sub>4</sub> (5 mol%) were added. The reaction mixture was heated to reflux until full conversion of the dibromide (4–20 h, TLC). Afterwards the solution was poured on water and repeatedly extracted with DCM. The combined organic layers were dried over anhydrous Na<sub>2</sub>SO<sub>4</sub> and concentrated under reduced pressure. The crude products were purified by column chromatography.

**2',2''-(1,3,4-Oxadiazole-2,5-diyl)bis[*N,N*-diphenyl[1,1'-biphenyl]-4-amine] (5a).** Starting from **4** (0.27 g, 0.70 mmol), **3a** (0.65 g, 1.75 mmol), 1.75 ml aqueous K<sub>2</sub>CO<sub>3</sub> solution and Pd(PPh<sub>3</sub>)<sub>4</sub> (40 mg, 35 μmol) **5a** (0.42 g, 0.59 mmol, 85%) was isolated after column chromatography (DCM) as a white solid. Physical data are in accordance with the literature.<sup>16</sup>

**9,9'-(1,3,4-Oxadiazole-2,5-diyl)di(1,1'-biphenyl)-2',4-diyl)bis[9*H*-carbazole] (5b).** Starting from **4** (0.19 g, 0.50 mmol), **3b** (0.46 g, 1.25 mmol), 1.25 ml aqueous K<sub>2</sub>CO<sub>3</sub> solution (2.5 mmol) and Pd(PPh<sub>3</sub>)<sub>4</sub> (29 mg, 25 μmol) **5b** (0.33 g, 93%) was isolated after column chromatography (DCM) as a white solid. <sup>1</sup>H NMR (400 MHz, CD<sub>2</sub>Cl<sub>2</sub>): δ = 8.14 (d, *J* = 7.7 Hz, 4H), 7.96 (d, *J* = 7.8 Hz, 2H), 7.69 (ddd, *J* = 7.6, 7.5, 1.1 Hz, 2H), 7.56–7.49 (m, 8H), 7.40–7.21 (m, 16H) ppm. <sup>13</sup>C NMR (100 MHz, CD<sub>2</sub>Cl<sub>2</sub>): δ = 165.6 (s), 141.6 (s), 141.3 (s), 140.1 (s), 137.4 (s), 132.1 (d), 131.7 (d), 131.0 (d), 130.6 (d), 128.7 (d), 127.2 (d), 126.6 (d), 123.9 (s), 123.3 (s), 120.8 (d), 120.5 (d), 110.1 (d) ppm. Calculated: *m/z*: 704.25706 [M]<sup>+</sup>, 705.26489 [M + H]<sup>+</sup>, 727.24683 [M + Na]<sup>+</sup>. Found: MS (MALDI): *m/z*: 704.25807 [M]<sup>+</sup>, 705.26586 [M + H]<sup>+</sup>, 727.24966 [M + Na]<sup>+</sup>.

**2,2'-(1,3,4-Oxadiazole-2,5-diyl)di-2,1-phenylene)bis[indolo[3,2,1-*jk*]carbazole] (5c).** Starting from **4** (0.76 g, 2.0 mmol), **3c** (1.84 g, 5.0 mmol), 5 ml aqueous K<sub>2</sub>CO<sub>3</sub> solution (10 mmol) and Pd(PPh<sub>3</sub>)<sub>4</sub> (0.12 g, 0.1 mmol) **5c** (0.55 g, 0.8 mmol, 39%) was isolated after column chromatography (DCM) as a white solid. <sup>1</sup>H NMR (400 MHz, CD<sub>2</sub>Cl<sub>2</sub>): δ = 8.09 (d, *J* = 7.8 Hz, 4H), 7.98 (d, *J* = 8.1 Hz, 4H), 7.91 (s, 4H), 7.61 (dd, *J* = 7.7, 7.7 Hz, 4H), 7.50–7.30 (m, 10H), 7.01 (dd, *J* = 7.7, 7.7 Hz, 2H) ppm. <sup>13</sup>C NMR (100 MHz, CD<sub>2</sub>Cl<sub>2</sub>): δ = 165.0 (s), 144.0 (s), 143.9 (s), 139.7 (s), 136.8 (s), 132.6 (d), 131.3 (d), 130.4 (s), 129.8 (d), 127.7 (d), 127.6 (d), 123.8 (d), 123.7 (s), 122.4 (d), 121.2 (d), 118.5 (s), 112.9 (d) ppm. Calculated: *m/z*: 700.22576 [M]<sup>+</sup>, 701.23359 [M + H]<sup>+</sup>, 723.21553

$[M + Na]^+$ . Found: MS (MALDI):  $m/z$ : 700.22461  $[M]^+$ , 701.23624  $[M + H]^+$ , 723.21879  $[M + Na]^+$ .

**General procedure for double-sided halogen dance reactions.** A protocol described in the literature<sup>53</sup> was adopted for the double-sided halogen dance reaction. Freshly prepared LDA was used. To a solution of diisopropylamine (2.40 eq.) in anhydrous THF (0.75 M), *n*-BuLi (2.40 eq., 2.5 M in hexanes) was slowly added at 0–5 °C and the solution was stirred for 30 min. Subsequently, the LDA solution was added dropwise to dibromide **6** (1.00 eq.) dissolved in anhydrous THF (25 mM) at –25 °C *via* a syringe. The temperature was maintained at –25 °C for 30 min before the reaction was quenched with an electrophile and warmed to room temperature. For work up the THF was removed under reduced pressure, the remaining oil was dissolved in DCM and washed with water. The aqueous phase was extracted with DCM, the combined organic layers were dried over anhydrous Na<sub>2</sub>SO<sub>4</sub> and the solvent was removed *in vacuo*. Purification was accomplished by column chromatography.

**2,5-Bis(3-bromo-2-thienyl)-1,3,4-oxadiazole (7i).** Starting from DIPA (0.18 g, 1.8 mmol), *n*-BuLi (0.72 ml, 1.8 mmol), **6** (0.29 g, 0.75 mmol) and MeOH (0.25 ml) **7i** (0.16 g, 0.40 mmol, 53%) was yielded after column chromatography (light petrol : Et<sub>2</sub>O = 60 : 40) as a white solid. <sup>1</sup>H NMR (400 MHz, CDCl<sub>3</sub>): δ = 7.52 (d, *J* = 5.3 Hz, 2H), 7.16 (d, *J* = 5.3 Hz, 2H) ppm. <sup>13</sup>C NMR (100 MHz, CDCl<sub>3</sub>): δ = 159.2 (s), 132.8 (d), 130.2 (d), 120.9 (s), 114.0 (s) ppm. Calculated:  $m/z$ : 390.82046  $[M + H]^+$ , 412.80240  $[M + Na]^+$ . Found: MS (MALDI):  $m/z$ : 390.82188  $[M + H]^+$ , 412.80376  $[M + Na]^+$ .

**2,5-Bis(3-bromo-5-trimethylsilyl-2-thienyl)-1,3,4-oxadiazole (7ii).** Starting from DIPA (0.18 g, 1.80 mmol), *n*-BuLi (0.72 ml, 1.80 mmol), **6** (0.29 g, 0.75 mmol) and TMSBr (0.35 g, 2.25 mmol, 3.00 eq.) **7ii** (0.17 mg, 0.31 mmol, 42%) was yielded after column chromatography (light petrol : Et<sub>2</sub>O = 95 : 5) as a colorless oil that solidified after an extended period of time at –30 °C. <sup>1</sup>H NMR (400 MHz, CDCl<sub>3</sub>): δ = 7.22 (s, 2H), 0.37 (s, 18H) ppm. <sup>13</sup>C NMR (100 MHz, CDCl<sub>3</sub>): δ = 159.2 (s), 147.0 (s), 138.6 (d), 125.0 (s), 114.6 (s), –0.5 (q) ppm. Calculated:  $m/z$ : 534.89951  $[M + H]^+$ , 556.88145  $[M + Na]^+$ . Found: MS (MALDI):  $m/z$ : 534.90132  $[M + H]^+$ , 556.88296  $[M + Na]^+$ .

**General procedure for the Suzuki cross-coupling reaction of 7i and boronic acid esters 3a–c.** Target compounds **8a–c** were synthesized by a Suzuki cross-coupling procedure according to a published protocol.<sup>24</sup> Dibromide **7i** (1.00 eq.), boronic acid esters **3a–c** (3.00 eq.), KO<sup>t</sup>Bu (3.00 eq.) and (NHC)Pd(allyl)Cl<sup>24,25</sup> (2 mol%) were suspended in <sup>1</sup>PrOH–H<sub>2</sub>O (3/1, 5 mM) under an argon atmosphere. The mixture was heated to reflux until full conversion (4–20 h, TLC), poured on H<sub>2</sub>O and repeatedly extracted with DCM. The combined organic layers were dried over anhydrous Na<sub>2</sub>SO<sub>4</sub> and the solvent removed *in vacuo*.

**4,4'-(1,3,4-Oxadiazole-2,5-diyldi-2,3-thiophenediyl)bis[*N,N*-diphenylbenzenamine] (8a).** Starting from **7i** (1.76 g, 4.5 mmol), **3a** (5.01 g, 13.5 mmol), KO<sup>t</sup>Bu (1.51 g, 13.5 mmol) and (NHC)Pd(allyl)Cl (51 mg, 90 μmol) **8a** (1.97 g, 2.7 mmol, 61%) was isolated after column chromatography (light petrol : DCM = 35 : 65 → 0 : 100) as a yellow solid. <sup>1</sup>H NMR (400 MHz, CD<sub>2</sub>Cl<sub>2</sub>): δ = 7.56 (d, *J* = 5.1 Hz, 2H), 7.31–7.24 (m, 12H), 7.19 (d, *J* = 5.1 Hz, 2H), 7.12–7.03 (m, 12H), 6.98 (d, *J* = 8.5 Hz, 4H) ppm. <sup>13</sup>C NMR

(100 MHz, CD<sub>2</sub>Cl<sub>2</sub>): δ = 160.9 (s), 148.4 (s), 148.0 (s), 145.4 (s), 131.8 (d), 130.6 (d), 129.9 (d), 129.6 (d), 128.8 (s), 125.4 (d), 123.9 (d), 122.9 (d), 118.9 (s) ppm. Calculated:  $m/z$ : 720.20120  $[M]^+$ , 721.20903  $[M + H]^+$ , 743.19097  $[M + Na]^+$ . Found: MS (MALDI):  $m/z$ : 720.20177  $[M]^+$ , 721.20580  $[M + H]^+$ , 743.19167  $[M + Na]^+$ .

**9,9'-(1,3,4-Oxadiazole-2,5-diyldi-2,3-thiophenediyl-4,1-phenylene)bis[9*H*-carbazole] (8b).** Starting from **7i** (78 mg, 0.20 mmol), **3b** (222 mg, 0.60 mmol), KO<sup>t</sup>Bu (67 mg, 0.60 mmol) and (NHC)Pd(allyl)Cl (2.3 mg, 4 μmol) **8b** (78 mg, 0.11 mmol, 55%) was isolated after column chromatography (light petrol : DCM = 80 : 20) as a white solid. <sup>1</sup>H NMR (400 MHz, CD<sub>2</sub>Cl<sub>2</sub>): δ = 8.16 (d, *J* = 7.7 Hz, 4H), 7.74 (d, *J* = 8.4 Hz, 4H), 7.64–7.62 (m, 6H), 7.49 (d, *J* = 8.1 Hz, 4H), 7.40 (ddd, *J* = 8.2, 7.3, 1.2 Hz, 4H), 7.32–7.28 (m, 6H) ppm. <sup>13</sup>C NMR (100 MHz, CD<sub>2</sub>Cl<sub>2</sub>): δ = 160.8 (s), 144.9 (s), 141.2 (s), 138.1 (s), 134.4 (s), 131.9 (d), 131.3 (d), 130.1 (d), 127.1 (d), 126.5 (d), 124.0 (s), 120.8 (d), 120.6 (d), 120.1 (s), 110.4 (d) ppm. Calculated:  $m/z$ : 716.16990  $[M]^+$ , 717.17773  $[M + H]^+$ , 739.15967  $[M + Na]^+$ . Found: MS (MALDI):  $m/z$ : 716.17188  $[M]^+$ , 717.17841  $[M + H]^+$ , 739.16278  $[M + Na]^+$ .

**2,2'-(1,3,4-Oxadiazole-2,5-diyldi-2,3-thiophenediyl)bis[indolo-[3,2,1-*jk*]carbazole] (8c).** Starting from **7i** (118 mg, 0.30 mmol), **3c** (330 mg, 0.90 mmol), KO<sup>t</sup>Bu (101 mg, 0.90 mmol) and (NHC)Pd(allyl)Cl (3.4 mg, 6 μmol) **8c** (158 mg, 0.22 mmol, 74%) was isolated after column chromatography (DCM) as a white solid. <sup>1</sup>H NMR (400 MHz, d<sub>6</sub>-DMSO): δ = 8.03–8.00 (m, 8H), 7.93–7.87 (m, 6H), 7.57 (dd, *J* = 7.7, 7.7 Hz, 4H), 7.38–7.34 (m, 6H) ppm. <sup>13</sup>C NMR (100 MHz, d<sub>6</sub>-DMSO): δ = 159.9, 146.1, 142.5, 138.1, 132.5, 130.4, 129.2, 129.0, 127.1, 123.2, 121.9, 120.9, 117.8, 117.1, 112.7 ppm. Calculated:  $m/z$ : 712.13860  $[M]^+$ , 713.14643  $[M + H]^+$ , 735.12837  $[M + Na]^+$ . Found: MS (MALDI):  $m/z$ : 712.13611  $[M]^+$ , 713.14685  $[M + H]^+$ , 735.129520  $[M + Na]^+$ .

**9,9'-(1,3,4-Oxadiazole-2,5-diyldi-2,3-thiophenediyl)bis[9*H*-carbazole] (8d).** **7i** (2.16 g, 5.5 mmol, 1.0 eq.), carbazole (2.76 g, 16.5 mmol, 3.0 eq.), K<sub>2</sub>CO<sub>3</sub> (2.28 g, 16.5 mmol, 3.0 eq.) and CuSO<sub>4</sub>·5H<sub>2</sub>O (88 mg, 0.35 mmol, 6.4 mol%) were mixed in a sealed reaction vial and heated to 230 °C. After cooling the reaction mixture was dissolved in CHCl<sub>3</sub>, washed with water and the aqueous phase was extracted with CHCl<sub>3</sub>. The combined organic layers were dried over anhydrous Na<sub>2</sub>SO<sub>4</sub> and concentrated under reduced pressure. **8d** (0.81 g, 1.4 mmol, 26%) was isolated after column chromatography (light petrol : DCM = 85 : 15 → 78 : 22) as a white solid. <sup>1</sup>H NMR (400 MHz, CD<sub>2</sub>Cl<sub>2</sub>): δ = 8.13 (d, *J* = 7.7 Hz, 4H), 7.67 (d, *J* = 5.3 Hz, 2H), 7.36–7.23 (m, 10H), 7.04 (d, *J* = 7.9 Hz, 4H) ppm. <sup>13</sup>C NMR (100 MHz, CD<sub>2</sub>Cl<sub>2</sub>): δ = 158.6 (s), 141.2 (s), 137.2 (s), 130.7 (d), 128.7 (d), 128.6 (d), 124.1 (s), 120.9 (d), 120.9 (d), 119.9 (s), 110.5 (d) ppm. Calculated:  $m/z$ : 564.10730  $[M]^+$ , 565.11513  $[M + H]^+$ , 587.09707  $[M + Na]^+$ . Found: MS (MALDI):  $m/z$ : 564.10961  $[M]^+$ , 565.11649  $[M + H]^+$ , 587.09908  $[M + Na]^+$ .

## Computational details

All computations were performed using the Gaussian 09 package, revision A.02.<sup>54</sup> Density functional theory (DFT) and time-dependent (TD) DFT calculations were performed using the Becke three parameters hybrid functional with Lee–Yang–Perdew correlation (B3LYP),<sup>55,56</sup> in combination with Pople

basis sets (6-31 G\*, 6-311 + G\*).<sup>57</sup> Geometry optimization was performed in the gas phase and without symmetry constraints. For the calculation of HOMO/LUMO levels, ground state ( $S_0$ ) geometries were optimized applying the 6-311 + G\* basis set. The determination of triplet energy ( $E_T$ ) was achieved by the calculation of the  $T_1$  excitation energy applying the TDDFT level and the 6-311 + G\* basis to a  $S_0$  geometry optimized at the DFT level using the 6-31 G\* basis set.

### Single crystal diffraction

Single crystals were obtained by recrystallization from hot solvents (**3c** – acetonitrile, **5b** – toluene, **8b** – toluene). Crystals of **3c**, **o-PCzPOXD (5b)** and **o-PCzTOXD (8b)** suitable for single-crystal diffraction were selected under a polarizing microscope, embedded in perfluorinated oil and attached to Kapton® micro-mounts. Intensity data were collected on a Bruker KAPPA APEX II diffractometer equipped with a CCD detector using MoK $\alpha$  radiation ( $\lambda = 0.71072 \text{ \AA}$ ). Data were reduced with Saint-Plus<sup>58</sup> and an absorption correction was applied using the multi-scan approach implemented in SADABS.<sup>58</sup> All non-H atoms were located in the electron-density maps obtained by charge-flipping implemented in Superflip.<sup>59</sup> The structures were refined against  $F$  values using Jana2006.<sup>60</sup> H atoms were placed at computed positions and refined as riding on the parent C atoms. All non-H atoms were refined with anisotropic displacement parameters.

### Device fabrication and measurement

The devices were fabricated on cleaned glass substrates pre-coated by 180 nm thick indium-tin-oxide (ITO) with a sheet resistance of 10  $\Omega$  per square. Prior to deposition, the surface of ITO was treated by oxygen plasma for 2 min, following a decrease in an ultrasonic solvent bath. All layers were deposited by thermal evaporation in a high vacuum system (pressure < 10<sup>-4</sup> Pa) without breaking the vacuum. The device structures are described in the text. For the case of doping, the deposition rates of both host and guest were measured by a quartz crystal oscillator, and monitored by a frequency counter and calibrated by a Dektak 6M profiler (Veeco). The aluminum (Al) electrodes were deposited on the organic films through shadow masks. The overlap between ITO and Al electrode was 4 mm  $\times$  4 mm as the active emissive area of the devices.

The current–voltage–brightness characteristics were measured by using a Keithley source measurement unit (Keithley 2400 and Keithley 2000) with a calibrated silicon photodiode. The electroluminescence (EL) spectra were measured by a Spectrascan PR650 spectrophotometer. All the measurements were carried out in ambient atmosphere at room temperature.

## Acknowledgements

This work was supported in part by the Swiss National Science Foundation. The authors thank F.-A. Miannay and B. Lang (University of Geneva) for help with the picosecond lifetime measurements. The X-ray centre of the Vienna University of Technology is acknowledged for providing access to the

single-crystal diffractometer. G. Fafilek is acknowledged for support regarding the CV measurements, B. Holzer for collaboration during the synthetic experiments, K. Föttinger assisting the photo-physical analysis and J. Chen for fruitful discussions.

## References

- 1 C. W. Tang and S. A. VanSlyke, *Appl. Phys. Lett.*, 1987, **51**, 913–915.
- 2 S. R. Forrest, *Nature*, 2004, **428**, 911–918.
- 3 Y. Sun, N. C. Giebink, H. Kanno, B. Ma, M. E. Thompson and S. R. Forrest, *Nature*, 2006, **440**, 908–912.
- 4 S. Reineke, F. Lindner, G. Schwartz, N. Seidler, K. Walzer, B. Luessem and K. Leo, *Nature*, 2009, **459**, 234–238.
- 5 M. C. Gather, A. Koehnen and K. Meerholz, *Adv. Mater.*, 2011, **23**, 233–248.
- 6 L. Xiao, Z. Chen, B. Qu, J. Luo, S. Kong, Q. Gong and J. Kido, *Adv. Mater.*, 2011, **23**, 926–952.
- 7 Y. Tao, C. Yang and J. Qin, *Chem. Soc. Rev.*, 2011, **40**, 2943–2970.
- 8 M. A. Baldo, D. F. O'Brien, Y. You, A. Shoustikov, S. Sibley, M. E. Thompson and S. R. Forrest, *Nature*, 1998, **395**, 151–154.
- 9 M. A. Baldo, S. Lamansky, P. E. Burrows, M. E. Thompson and S. R. Forrest, *Appl. Phys. Lett.*, 1999, **75**, 4–6.
- 10 P.-T. Chou and Y. Chi, *Chem. – Eur. J.*, 2007, **13**, 380–395.
- 11 Y. Chi and P.-T. Chou, *Chem. Soc. Rev.*, 2010, **39**, 638–655.
- 12 M. A. Baldo, D. F. O'Brien, M. E. Thompson and S. R. Forrest, *Phys. Rev. B: Condens. Matter Mater. Phys.*, 1999, **60**, 14422–14428.
- 13 C. Adachi, M. A. Baldo, M. E. Thompson and S. R. Forrest, *J. Appl. Phys.*, 2001, **90**, 5048–5051.
- 14 M. A. Baldo, C. Adachi and S. R. Forrest, *Phys. Rev. B: Condens. Matter Mater. Phys.*, 2000, **62**, 10967–10977.
- 15 Y. Tao, Q. Wang, C. Yang, Q. Wang, Z. Zhang, T. Zou, J. Qin and D. Ma, *Angew. Chem., Int. Ed.*, 2008, **47**, 8104–8107.
- 16 Y. Tao, Q. Wang, Y. Shang, C. Yang, L. Ao, J. Qin, D. Ma and Z. Shuai, *Chem. Commun.*, 2009, 77–79.
- 17 Y. Tao, Q. Wang, C. Yang, J. Qin and D. Ma, *ACS Appl. Mater. Interfaces*, 2010, **2**, 2813–2818.
- 18 H. B. Goodbrand and N.-X. Hu, *J. Org. Chem.*, 1999, **64**, 670–674.
- 19 R. Anemian, D. C. Cupertino, P. R. Mackie and S. G. Yeates, *Tetrahedron Lett.*, 2005, **46**, 6717–6721.
- 20 H. Xu, K. Yin and W. Huang, *Chem. – Eur. J.*, 2007, **13**, 10281–10293.
- 21 J. Lv, Q. Liu, J. Tang, F. Perdih and K. Kranjc, *Tetrahedron Lett.*, 2012, **53**, 5248–5252.
- 22 H. G. Dunlop and S. H. Tucker, *J. Chem. Soc.*, 1939, 1945–1956.
- 23 S. I. Wharton, J. B. Henry, H. McNab and A. R. Mount, *Chem. – Eur. J.*, 2009, **15**, 5482–5490.
- 24 N. Marion, O. Navarro, J. Mei, E. D. Stevens, N. M. Scott and S. P. Nolan, *J. Am. Chem. Soc.*, 2006, **128**, 4101–4111.
- 25 O. Navarro and S. P. Nolan, *Synthesis*, 2006, 366–367.



- 26 (**3c**):  $C_{24}H_{22}BNO_2$ ,  $M_r = 367.3$ , trigonal,  $R\bar{3}$ ,  $a = b = 30.3853(6)$  Å,  $c = 10.5350(2)$  Å,  $V = 8423.5(3)$  Å<sup>3</sup>,  $Z = 18$ ,  $\mu = 0.081$  mm<sup>-1</sup>,  $T = 100$  K, 124 955 measured, 11 591 independent and 9475 observed [ $I > 3\sigma(I)$ ] reflections, 253 parameters,  $wR$  (all data) = 0.060,  $R[I > 3\sigma(I)] = 0.041$ .†
- 27 X. Zheng, Z. Li, Y. Wang, W. Chen, Q. Huang, C. Liu and G. Song, *J. Fluorine Chem.*, 2003, **123**, 163–169.
- 28 S. Zrig, G. Koeckelberghs, T. Verbiest, B. Andrioletti, E. Rose, A. Persoons, I. Asselberghs and K. Clays, *J. Org. Chem.*, 2007, **72**, 5855–5858.
- 29 J. Froehlich, *Prog. Heterocycl. Chem.*, 1994, **6**, 1–35.
- 30 M. Schnuerch, M. Spina, A. F. Khan, M. D. Mihovilovic and P. Stanetty, *Chem. Soc. Rev.*, 2007, **36**, 1046–1057.
- 31 d. S. M. V. Nora, *Curr. Org. Chem.*, 2007, **11**, 637–646.
- 32 A. E. Lozano, M. L. Jimeno, J. de Abajo and J. G. de la Campa, *Macromolecules*, 1994, **27**, 7164–7170.
- 33 N. Miyaura, K. Yamada and A. Suzuki, *Tetrahedron Lett.*, 1979, 3437–3440.
- 34 N. Miyaura and A. Suzuki, *J. Chem. Soc., Chem. Commun.*, 1979, 866–867.
- 35 N. Miyaura and A. Suzuki, *Chem. Rev.*, 1995, **95**, 2457–2483; and references cited therein.
- 36 F. Ullmann, *Ber. Dtsch. Chem. Ges.*, 1903, **36**, 2382–2384.
- 37 F. Ullmann, *Ber. Dtsch. Chem. Ges.*, 1904, **37**, 853–854.
- 38 S. V. Ley and A. W. Thomas, *Angew. Chem., Int. Ed.*, 2003, **42**, 5400–5449; and references cited therein.
- 39 Z. Ge, T. Hayakawa, S. Ando, M. Ueda, T. Akiike, H. Miyamoto, T. Kajita and M.-a. Kakimoto, *Adv. Funct. Mater.*, 2008, **18**, 584–590.
- 40 Z. Ge, T. Hayakawa, S. Ando, M. Ueda, T. Akiike, H. Miyamoto, T. Kajita and M.-a. Kakimoto, *Org. Lett.*, 2008, **10**, 421–424.
- 41 Y. Tao, Q. Wang, C. Yang, C. Zhong, K. Zhang, J. Qin and D. Ma, *Adv. Funct. Mater.*, 2010, **20**, 304–311.
- 42 J. F. Ambrose and R. F. Nelson, *J. Electrochem. Soc.*, 1968, **115**, 1159–1164.
- 43 J. F. Ambrose, L. L. Carpenter and R. F. Nelson, *J. Electrochem. Soc.*, 1975, **122**, 876–894.
- 44 (**5b**):  $C_{50}H_{32}N_4O$ ,  $M_r = 704.8$ , orthorhombic,  $Pna2_1$ ,  $a = 17.9874(4)$  Å,  $b = 9.2989(8)$  Å,  $c = 21.5822(9)$  Å,  $V = 3609.9(4)$  Å<sup>3</sup>,  $Z = 4$ ,  $\mu = 0.078$  mm<sup>-1</sup>,  $T = 100$  K, 146 762 measured, 3589 independent and 10 547 observed [ $I > 3\sigma(I)$ ] reflections, 496 parameters,  $wR$  (all data) = 0.044,  $R[I > 3\sigma(I)] = 0.040$ .†
- 45 (**8b**):  $C_{46}H_{28}N_4OS_2$ ,  $M_r = 716.9$ , orthorhombic,  $Pna2_1$ ,  $a = 16.6992(7)$  Å,  $b = 8.3716(3)$  Å,  $c = 49.404(2)$  Å,  $V = 6906.7(5)$  Å<sup>3</sup>,  $Z = 8$ ,  $\mu = 0.199$  mm<sup>-1</sup>,  $T = 100$  K, 124 623 measured, 15 888 independent and 12 302 observed [ $I > 3\sigma(I)$ ] reflections, 955 parameters,  $wR$  (all data) = 0.036,  $R[I > 3\sigma(I)] = 0.036$ .†
- 46 B. Stoeger, P. Kautny, D. Lumpi, E. Zobetz and J. Froehlich, *Acta Crystallogr., Sect. B: Struct. Sci.*, 2012, **68**, 667–676.
- 47 M. Ikai, S. Tokito, Y. Sakamoto, T. Suzuki and Y. Taga, *Appl. Phys. Lett.*, 2001, **79**, 156–158.
- 48 D.-H. Lee, Y.-P. Liu, K.-H. Lee, H. Chae and S. M. Cho, *Org. Electron.*, 2010, **11**, 427–433.
- 49 M. E. Kondakova, T. D. Pawlik, R. H. Young, D. J. Giesen, D. Y. Kondakov, C. T. Brown, J. C. Deaton, J. R. Lenhard and K. P. Klubek, *J. Appl. Phys.*, 2008, **104**, 094501.
- 50 S. H. Kim, J. Jang, K. S. Yook, J. Y. Lee, M.-S. Gong, S. Ryu, G.-k. Chang and H. J. Chang, *J. Appl. Phys.*, 2008, **103**, 054502.
- 51 Q. Fu, J. Chen, H. Zhang, C. Shi and D. Ma, *Opt. Express*, 2013, **21**, 11078–11085.
- 52 L. G. Liu, Y. F. Xu, X. H. Qian and Q. C. Huang, *Chin. Chem. Lett.*, 2004, **15**, 7–10.
- 53 J. Froehlich, C. Hametner and W. Kalt, *Monatsh. Chem.*, 1996, **127**, 325–330.
- 54 M. J. Frisch, G. W. Trucks, H. B. Schlegel, G. E. Scuseria, M. A. Robb, J. R. Cheeseman, G. Scalmani, V. Barone, B. Mennucci, G. A. Petersson, H. Nakatsuji, M. Caricato, X. Li, H. P. Hratchian, A. F. Izmaylov, J. Bloino, G. Zheng, J. L. Sonnenberg, M. Hada, M. Ehara, K. Toyota, R. Fukuda, J. Hasegawa, M. Ishida, T. Nakajima, Y. Honda, O. Kitao, H. Nakai, T. Vreven, J. A. Montgomery, Jr, J. E. Peralta, F. Ogliaro, M. Bearpark, J. J. Heyd, E. Brothers, K. N. Kudin, V. N. Staroverov, R. Kobayashi, J. Normand, K. Raghavachari, A. Rendell, J. C. Burant, S. S. Iyengar, J. Tomasi, M. Cossi, N. Rega, N. J. Millam, M. Klene, J. E. Knox, J. B. Cross, V. Bakken, C. Adamo, J. Jaramillo, R. Gomperts, R. E. Stratmann, O. Yazyev, A. J. Austin, R. Cammi, C. Pomelli, J. W. Ochterski, R. L. Martin, K. Morokuma, V. G. Zakrzewski, G. A. Voth, P. Salvador, J. J. Dannenberg, S. Dapprich, A. D. Daniels, Oe. Farkas, J. B. Foresman, J. V. Ortiz, J. Cioslowski and D. J. Fox, *Gaussian 09, Revision A.2*, Gaussian, Inc., Wallingford, CT, 2009.
- 55 C. Lee, W. Yang and R. G. Parr, *Phys. Rev. B: Condens. Matter*, 1988, **37**, 785–789.
- 56 A. D. Becke, *J. Chem. Phys.*, 1993, **98**, 5648–5652.
- 57 R. Krishnan, J. S. Binkley, R. Seeger and J. A. Pople, *J. Chem. Phys.*, 1980, **72**, 650–654.
- 58 *Saint and SADABS*, Bruker Analytical X-ray Instruments, Inc., Madison, WI, USA, 2008.
- 59 L. Palatinus and G. Chapuis, *J. Appl. Crystallogr.*, 2007, **40**, 786–790.
- 60 V. Petříček, M. Dušek and L. Palatinus, *Jana2006: The crystallographic computing system*, Institute of Physics, Praha, Czech Republic, 2006.



### 3. Conclusion and Outlook

In summary, novel organic semiconductors (OSC) have been developed and implemented into various electronic devices such as OFETs, SAMFETs, sensors, OLEDs and PhOLEDs and tested for their properties within an interdisciplinary PhD thesis.

Novel printable alkylated indolo[3,2-*b*]carbazoles were presented (manuscript #1) and their use as active materials in an OFET configuration demonstrated a charge carrier mobility of up to  $10^{-2}\text{cm}^2/\text{Vs}$ . Furthermore, one derivative was successfully used as solution processable OSC using a novel pneumatic nozzle printing technique (manuscript #2) and exhibited aligned crystalline domains in the hundreds of micrometer range.

The scope and limitations of this novel printing technique was further tested and yielded an all-printed OFET on a flexible substrate. To the best of our knowledge this is the first report of achieving an all printed OFET on a flexible substrate in which all parts of the device were fabricated (printed) using the same tool. We also demonstrated that devices fabricated using this novel method outperform current solution processing techniques such as spin coating by a factor of 10 to 100, when comparing measured charge carrier mobilities. The great versatility of this technique and low-cost will enable other researchers to apply this technique for further purposes.

Other newly designed OSC, partially composed of the indolo[3,2,1-*jk*]carbazole scaffold, also demonstrate great potential for use in OLED and PhOLED devices. (manuscripts #5-7).

Novel self-assembled monolayer field-effect transistors (SMAFETs) using click chemistry for a facile approach towards sensing applications were demonstrated and benchmarked against conventional SAMFETs (manuscript #3). SAMFET devices exhibited electron mobility of  $\sim 2 \cdot 10^{-4}\text{cm}^2/\text{Vs}$ . These CLICK-FETs represent a valuable tool for surface modifications.

A novel ultra-cheap, versatile and robust USB-driven sensor platform was demonstrated. (manuscript #4). The presented ultra-low cost sensor platform is based on a chemiresistor configuration and allows for cheap and reliable sensing of various analytes by proper functionalization of the OSC. In a successful demonstration, three analytes ( $\text{H}_2\text{O}$  vapor, acetone,  $\text{NH}_3$ ) were detected using the same platform of this  $\text{S}$ -sensor with targeted functionalization of the OSC. The know-how from these projects will benefit future design and sensing concepts.



## 4. Statement of Contribution

### **Manuscript #1**

The research subject of Manuscript #1 was initiated and designed by the applicant (J. Bintinger). All synthetic work, fluorescent measurements and the composition of the manuscript was performed by the applicant. OFET measurements and printing experiments were conducted by the applicant and S. Yang. B. Holzer conducted the CV and A. Svirikova the MALDI-TOF measurements. The acquisition of crystallographic data was performed by B. Stöger. DFT calculations were carried out by E. Horkel. All authors contributed to the manuscript discussion and correction.

### **Manuscript #2**

The research subject of Manuscript #2 was initiated and designed by S. Yang and I. Kymissis. The applicant (J. Bintinger) contributed in optimizing the printing parameters, testing several hundred OFET transistors as well as performing cross polarized microscopy images. The manuscript was written by S. Yang, S. Park and J. Bintinger. All authors contributed to the manuscript discussion and correction.

### **Manuscript #3**

The research subject of Manuscript #3 was initiated and designed by the applicant (J. Bintinger). All synthetic work, initial XPS measurements and the composition of the manuscript was performed by the applicant. SAMFET measurements were conducted by N. Cernetic. R. Bittner synthesized the functionalized azide SAMs precursors and performed IR measurements. M. Sauer and A. Folske-Schmitz conducted angle resolved XPS measurements. M. Holzweber performed ToF-SIMS experiments. T. Schiros and D. Nordlund conducted NEXAFS measurements. DFT calculations were carried out by D. Svatunek. All authors contributed to the manuscript discussion and correction.

### **Manuscript #4**

The research subject of Manuscript #4 was initiated and designed by S. Yang, the applicant (J. Bintinger) under the supervision of I. Kymissis. The applicant (J. Bintinger) fabricated CVD-graphene chemiresistors, synthesized the required selector molecule and conducted acetone gas sensing measurements. S. Yang and S. Jian designed the  $\text{S}$ -Sensor. K. Alexandrou contributed in the fabrication of the graphene devices. P. Fruhmann conducted humidity sensing experiments. K. Besar performed some ammonia gas sensing experiments. The manuscript was equally written and composed by S. Yang and J. Bintinger.

### **Manuscript #5**

The research subject of Manuscript #5 was initiated and designed by the applicant (J. Binting), B. Holzer and D. Lumpi. Synthetic work and photophysical characterization was equally shared between the applicant and B. Holzer. OLED fabrication was performed by C. Choi, Y. Kim and the applicant. DFT calculations were carried out by F. Plasser and E. Horkel. The acquisition of crystallographic data was performed by B. Stöger. M. Marchetti-Deschmann performed MALDI-TOF measurements. The manuscript was composed and written by the applicant, B. Holzer and E. Horkel. All authors contributed to the manuscript discussion and correction.

### **Manuscript #6**

The research subject of Manuscript #6 was initiated and designed by D. Lumpi and B. Holzer. Synthetic work and photophysical characterization was performed by B. Holzer and D. Lumpi. OFET fabrication and characterization was performed by the applicant (J. Binting). DFT calculations were carried out by E. Horkel. M. Marchetti-Deschmann performed MALDI-TOF measurements. AFM measurements were done by S. Waid. The manuscript was composed and written by B. Holzer, the applicant and E. Horkel. All authors contributed to the manuscript discussion and correction.

### **Manuscript #7**

The research subject of Manuscript #7 was initiated and designed by P. Kautny and D. Lumpi. The applicant developed the synthesis for the indolo[3,2,1-jk]carbazole key component. PhOLEDs were fabricated and tested by Y. Wang. DFT calculations were carried out by E. Horkel. The acquisition of crystallographic data was performed by B. Stöger. The manuscript was composed and written by P. Kautny and D. Lumpi. All authors contributed to the manuscript discussion and correction.

## 5. Appendix





# Manuscript #1

Supporting Information

**J. Bintinger\***, S. Yang, H. Mikula, P. Fruhmann, B. Holzer, B. Stöger, A. Svirkova, M. Marchetti-Deschmann, E. Horkel, C. Hametner, I. Kymissis, J. Fröhlich; Synthesis, Characterization and Printing Application of Alkylated Indolo[3,2-*b*]carbazoles, *manuscript draft*



# **Synthesis, Characterization and Printing Application of Alkylated Indolo[3,2-b]carbazoles**

J. Bintinger\*<sup>[a]</sup>, S. Yang<sup>[b]</sup>, H. Mikula<sup>[a]</sup>, E. Horkel<sup>[a]</sup>, P. Fruhmann<sup>[a,d]</sup>, B. Holzer<sup>[a]</sup>, B. Stöger<sup>[c]</sup>, A. Svirikova<sup>[c]</sup>, M. Marchetti-Deschmann<sup>[c]</sup>, C. Hametner<sup>[a]</sup>, I. Kymissis<sup>[b]</sup>, J. Fröhlich<sup>[a]</sup>

## **Electronic Supplementary Information**

### **Content**

**A) NMR Spectra**

**B) Photoluminescence data**

## A) NMR Spectra

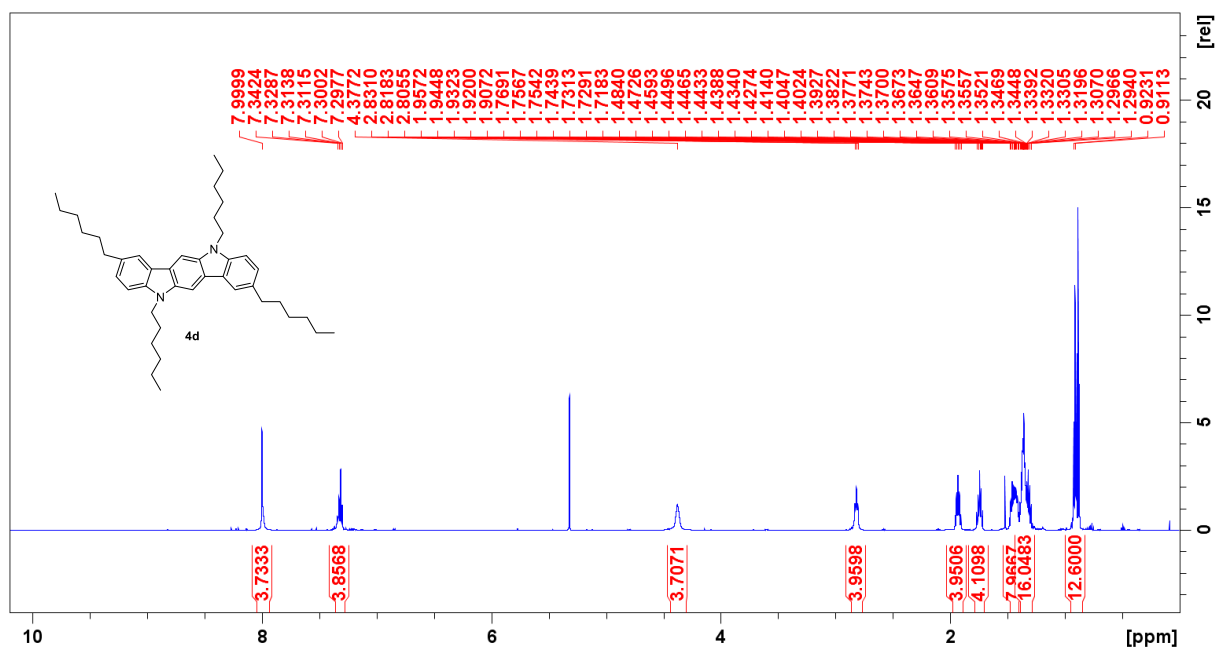


Figure S1. Proton NMR spectrum of compound 4d.

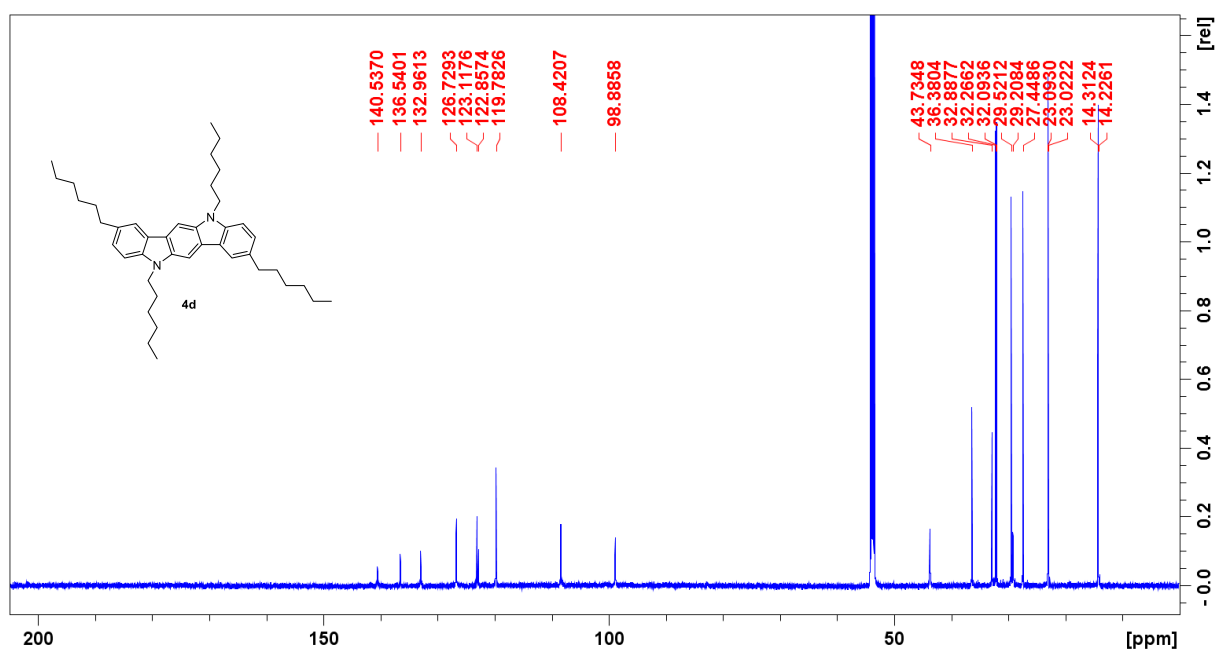


Figure S2. Carbon NMR spectrum of compound 4d.

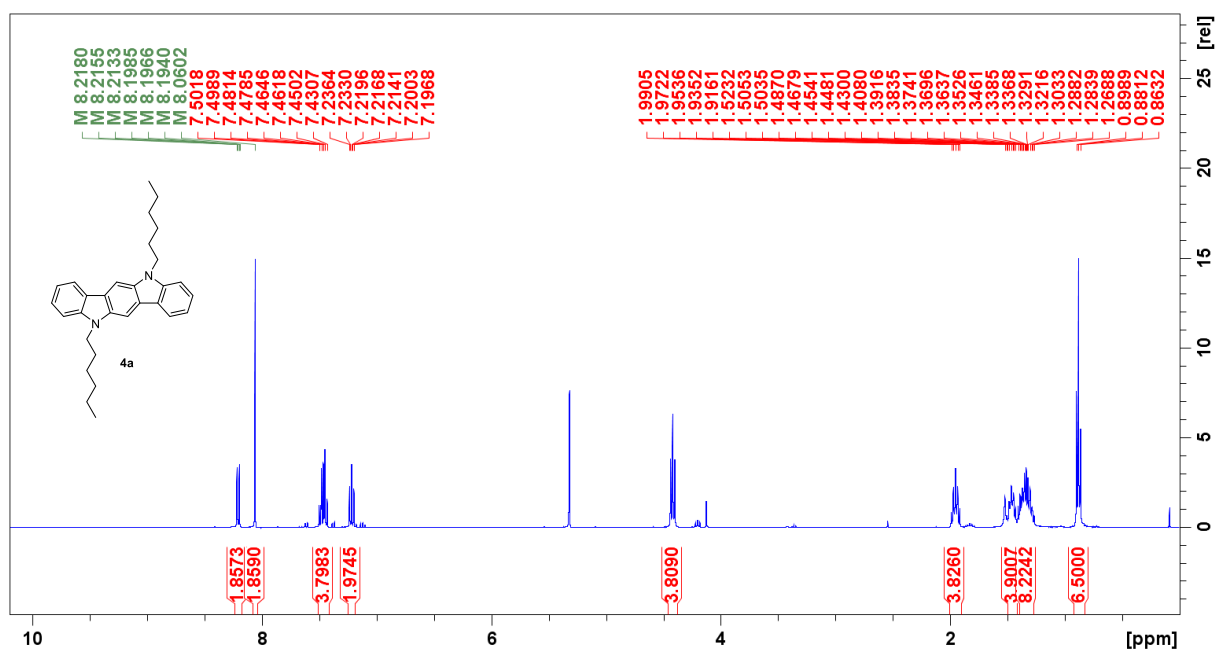


Figure S3. Proton NMR spectrum of compound 4a.

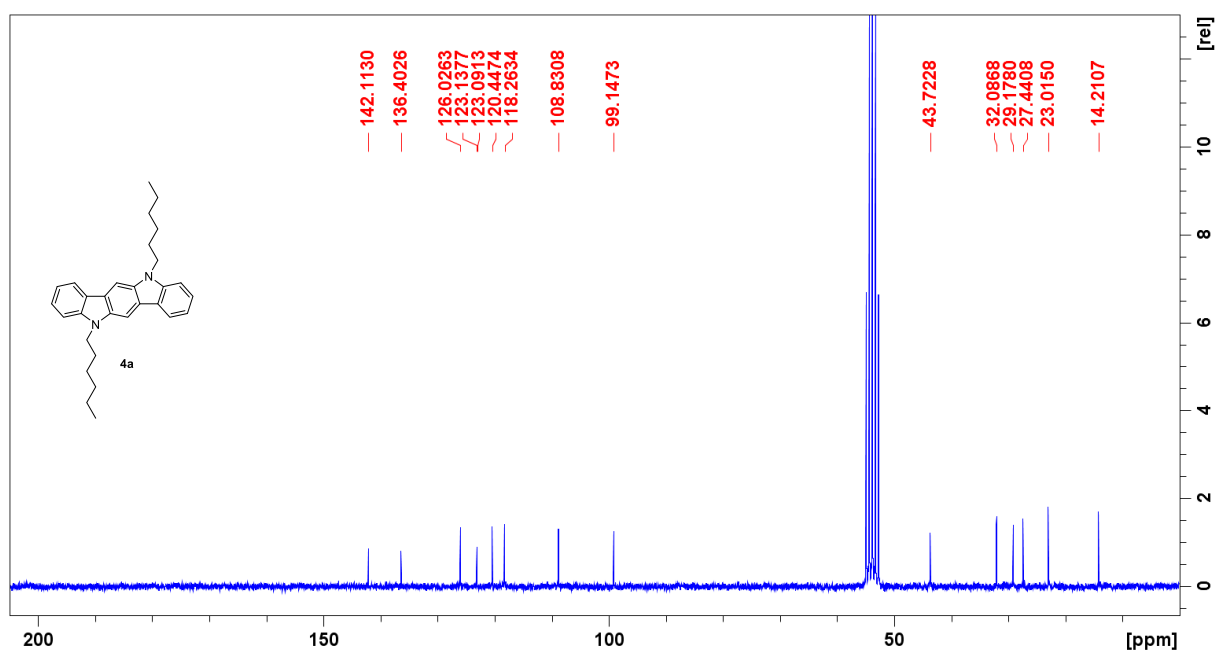
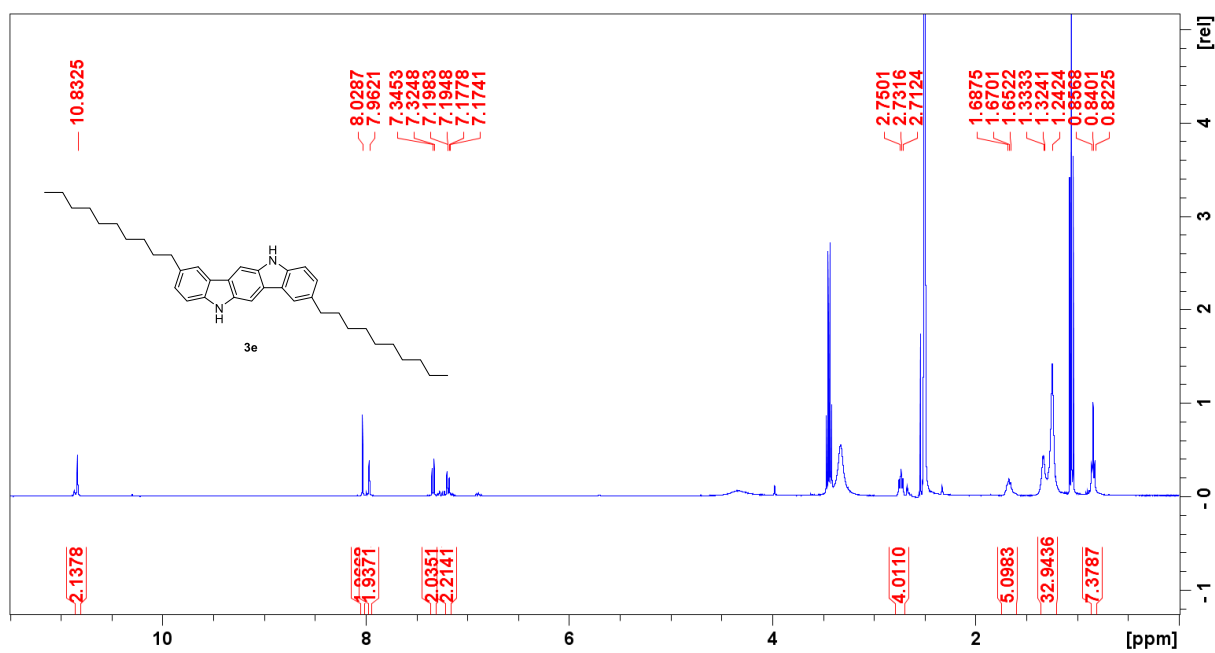


Figure S4. Carbon NMR spectrum of compound 4a.



**Figure S5.** Proton NMR spectrum of compound **3e**. Compound too insoluble for carbon spectra.

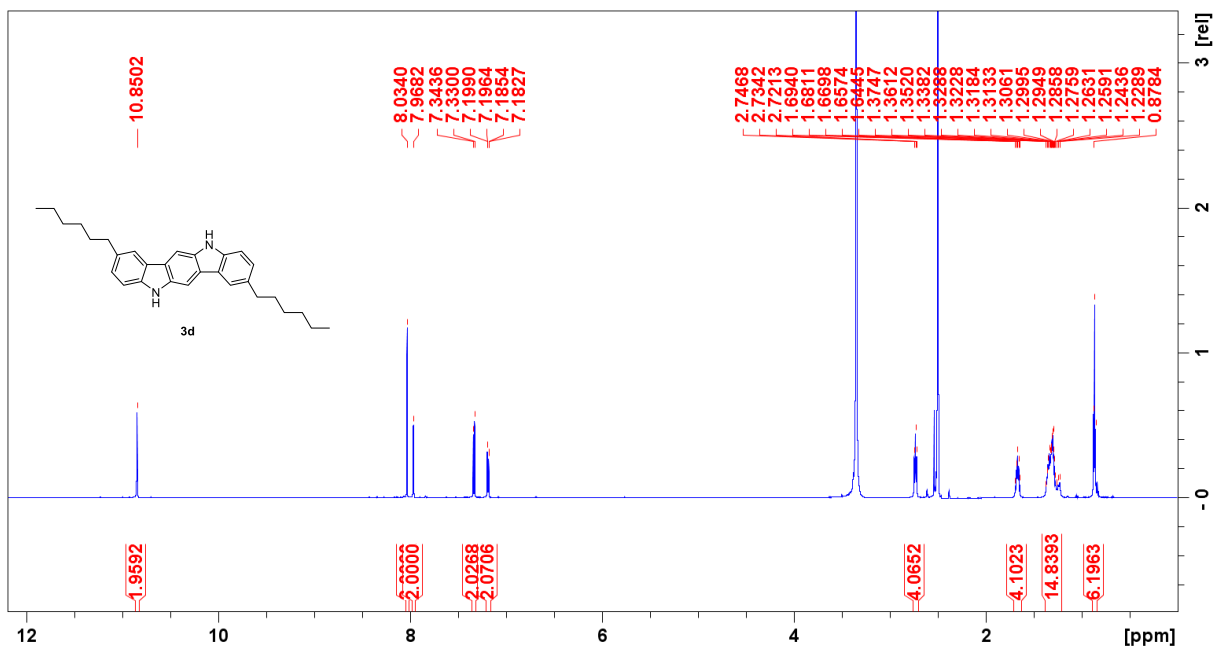


Figure S6. Proton NMR spectrum of compound 3d.

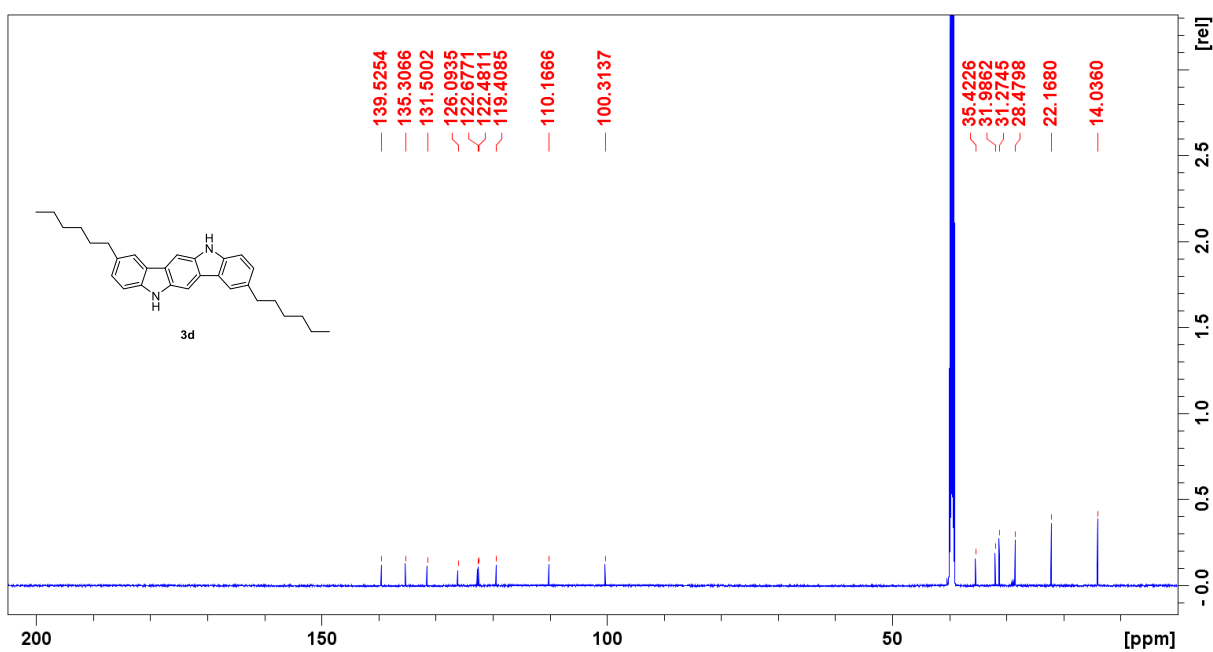


Figure S7. Carbon NMR spectrum of compound 3d.

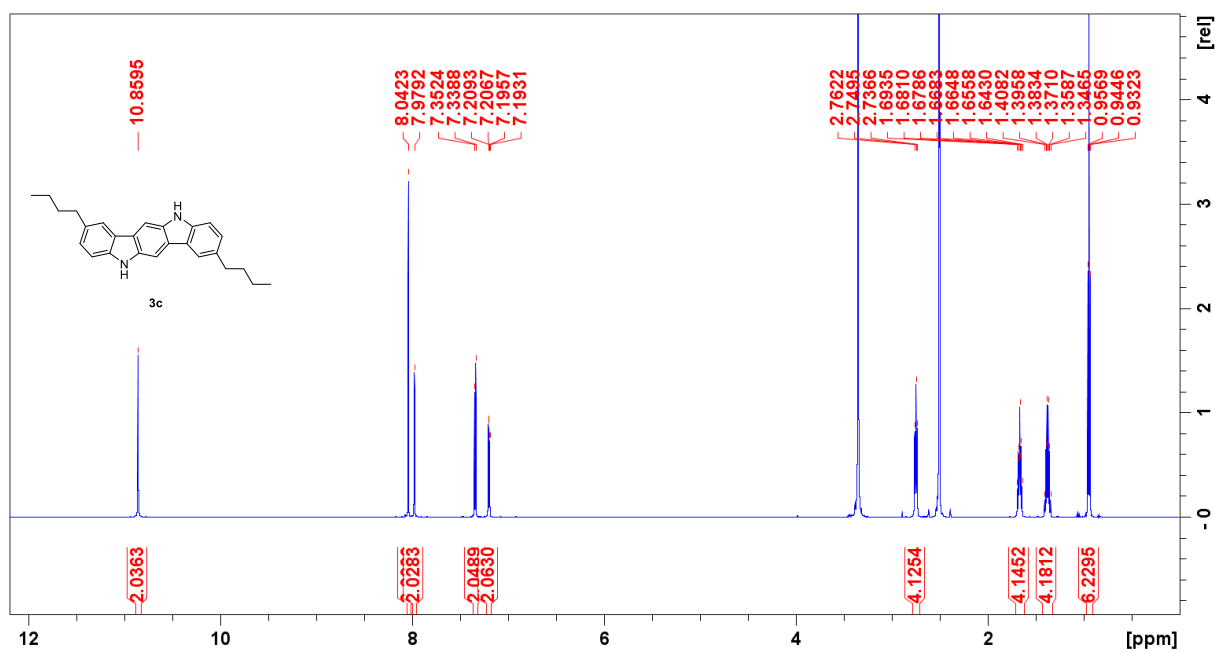


Figure S8. Proton NMR spectrum of compound 3c.

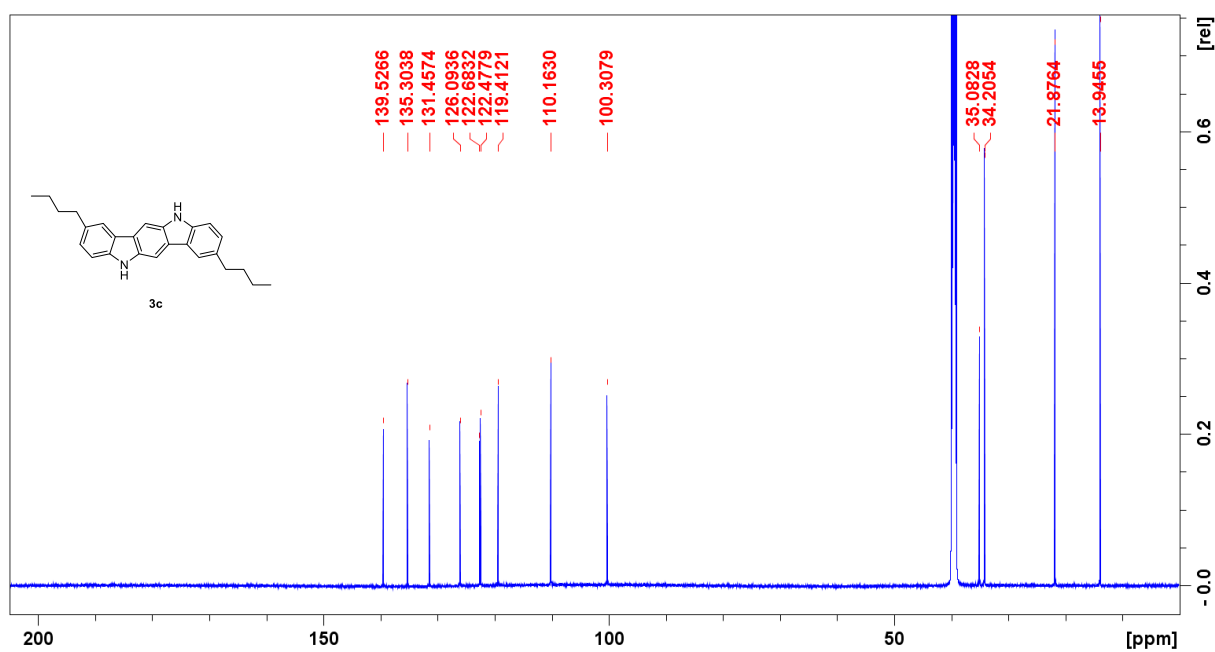


Figure S9. Carbon NMR spectrum of compound 3c.



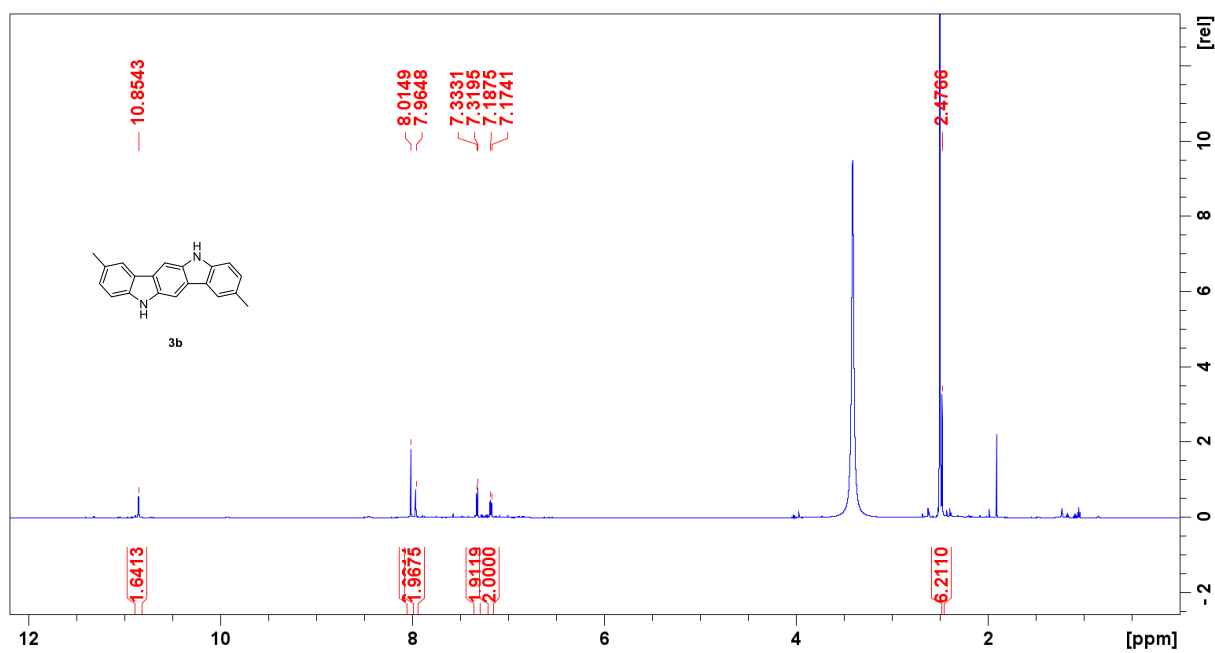


Figure S10. Proton NMR spectrum of compound 3b.

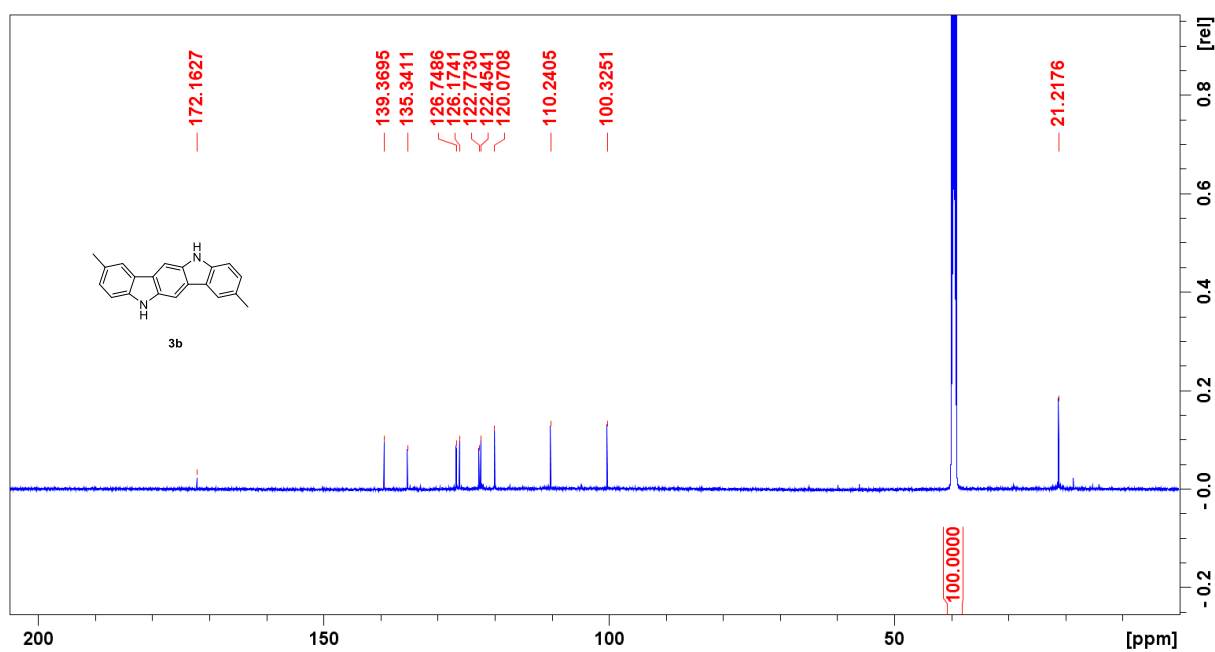


Figure S11. Carbon NMR spectrum of compound 3b.

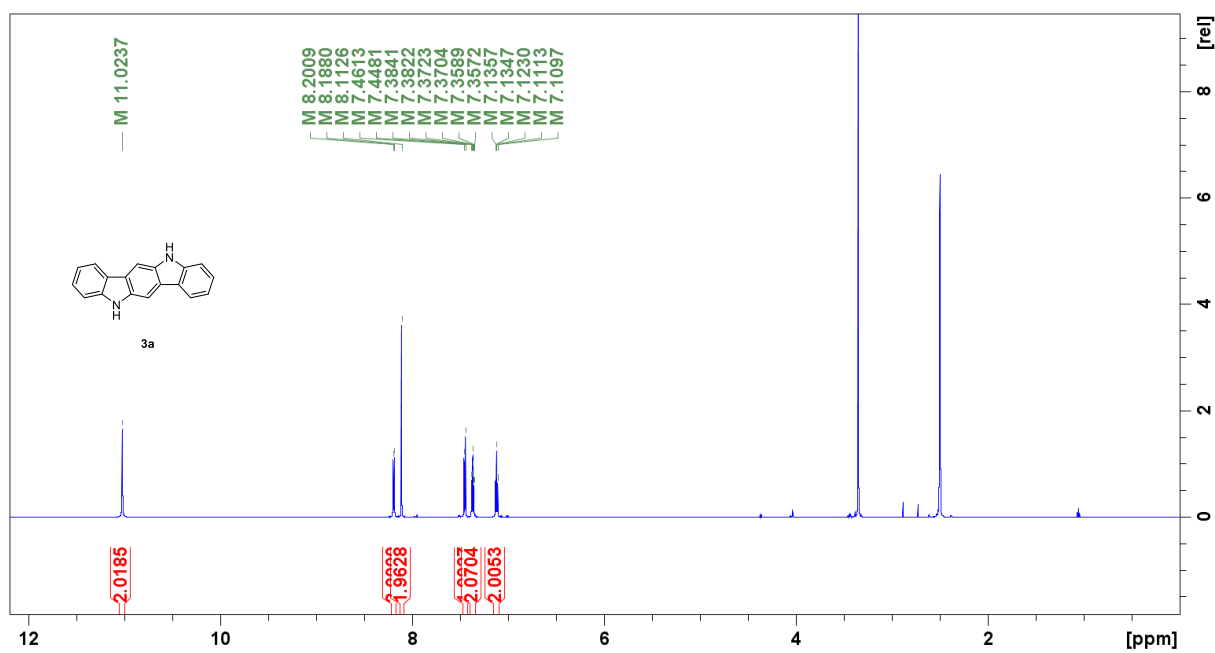


Figure S12. Proton NMR spectrum of compound 3a.

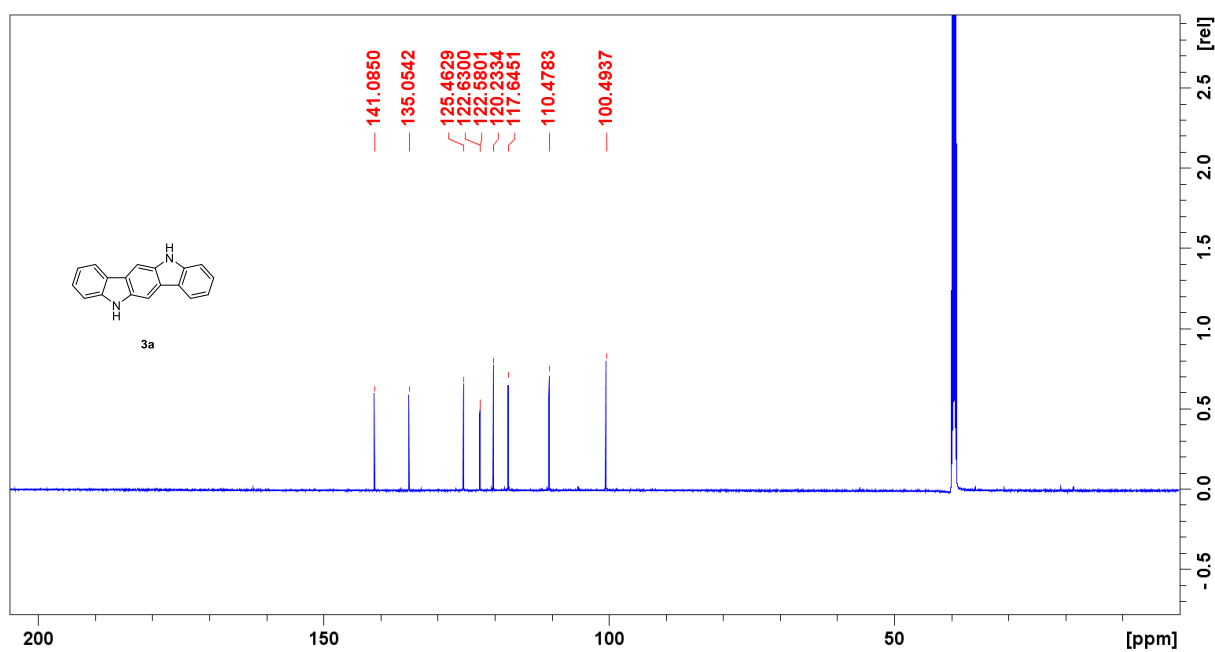


Figure S13. Carbon NMR spectrum of compound 3a.

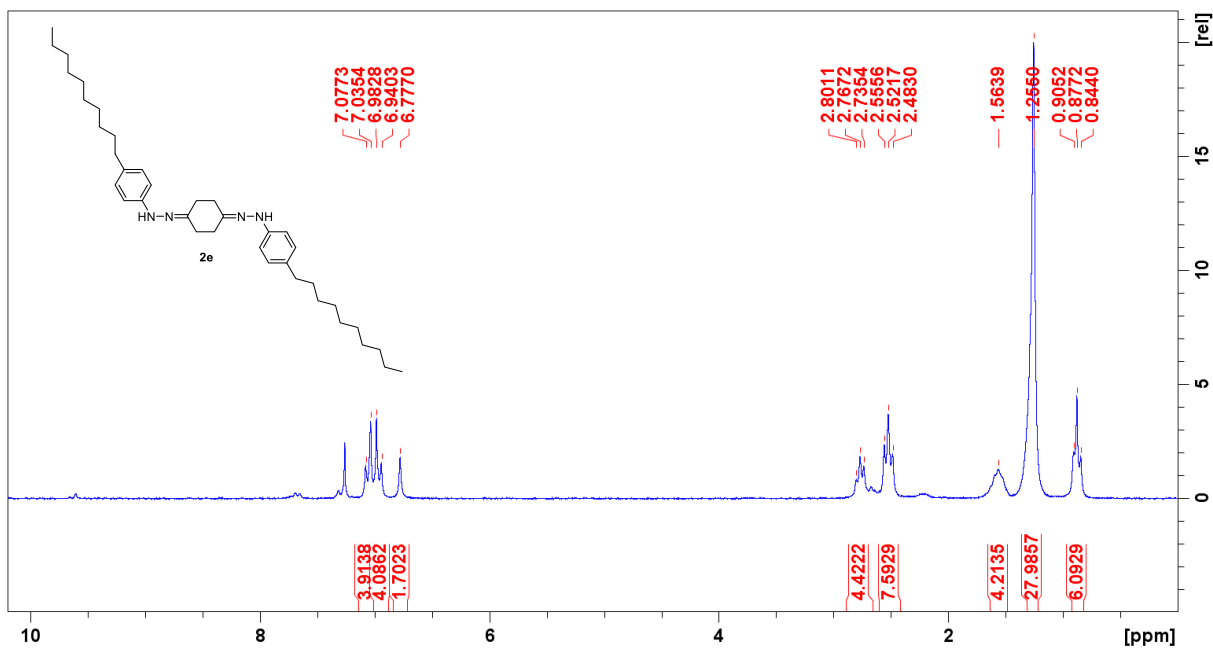


Figure S14. Proton NMR spectrum of compound 2e.

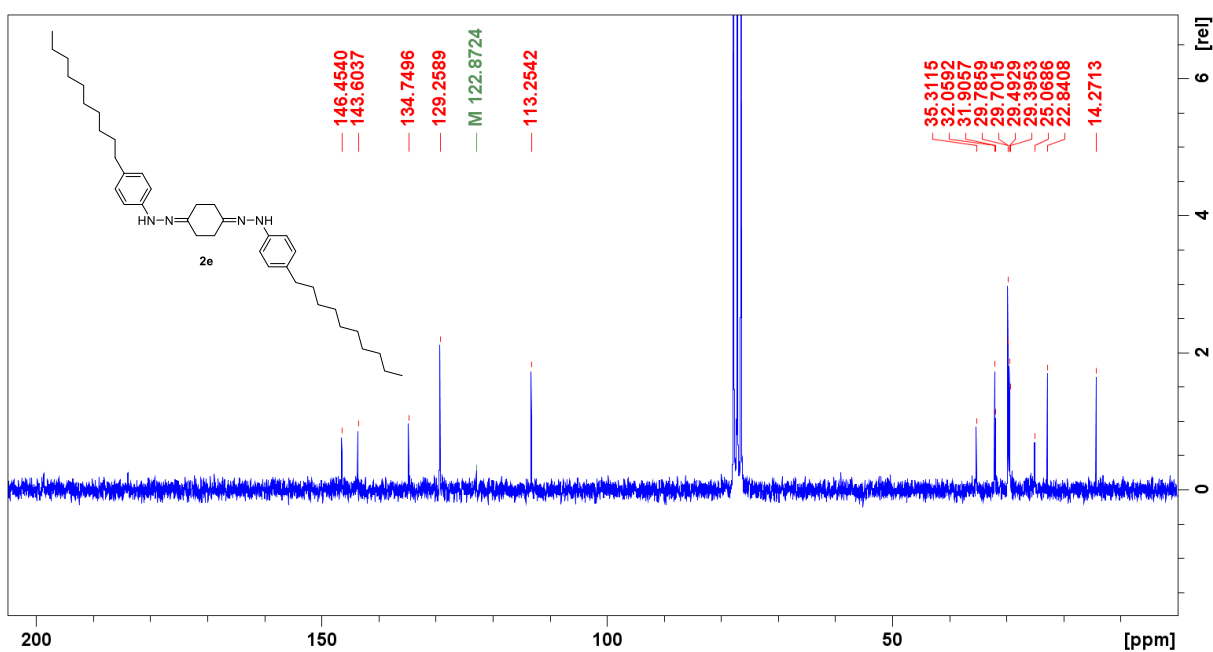


Figure S15. Carbon NMR spectrum of compound 2e.

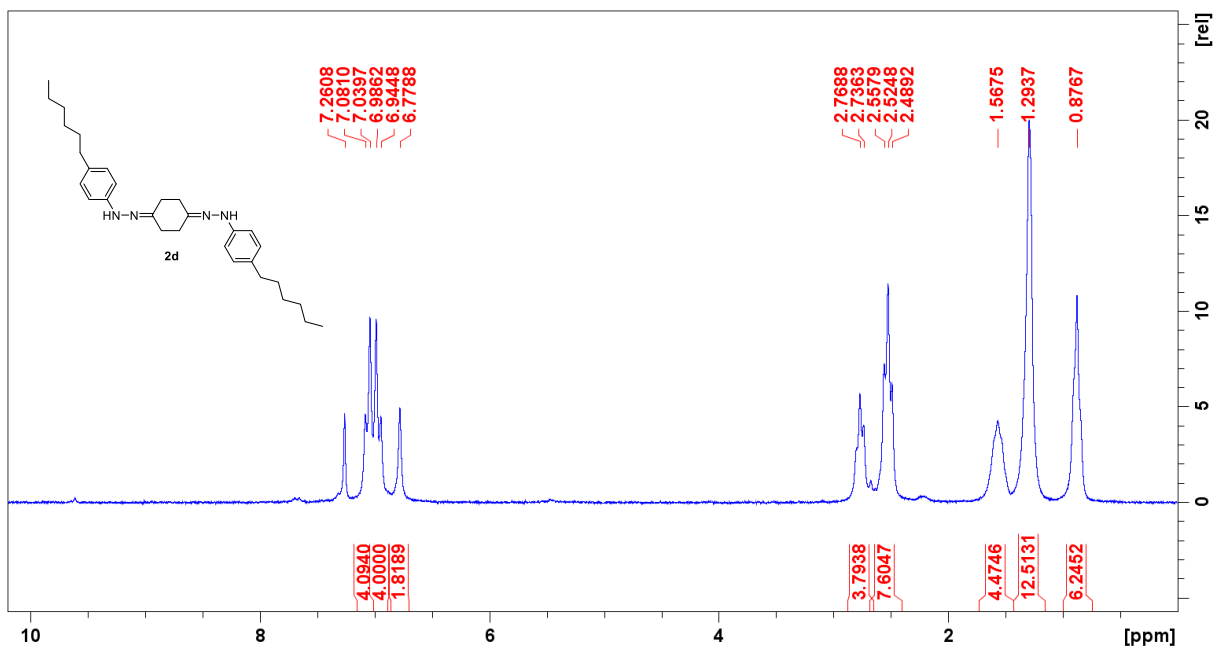


Figure S16. Proton NMR spectrum of compound 2d.

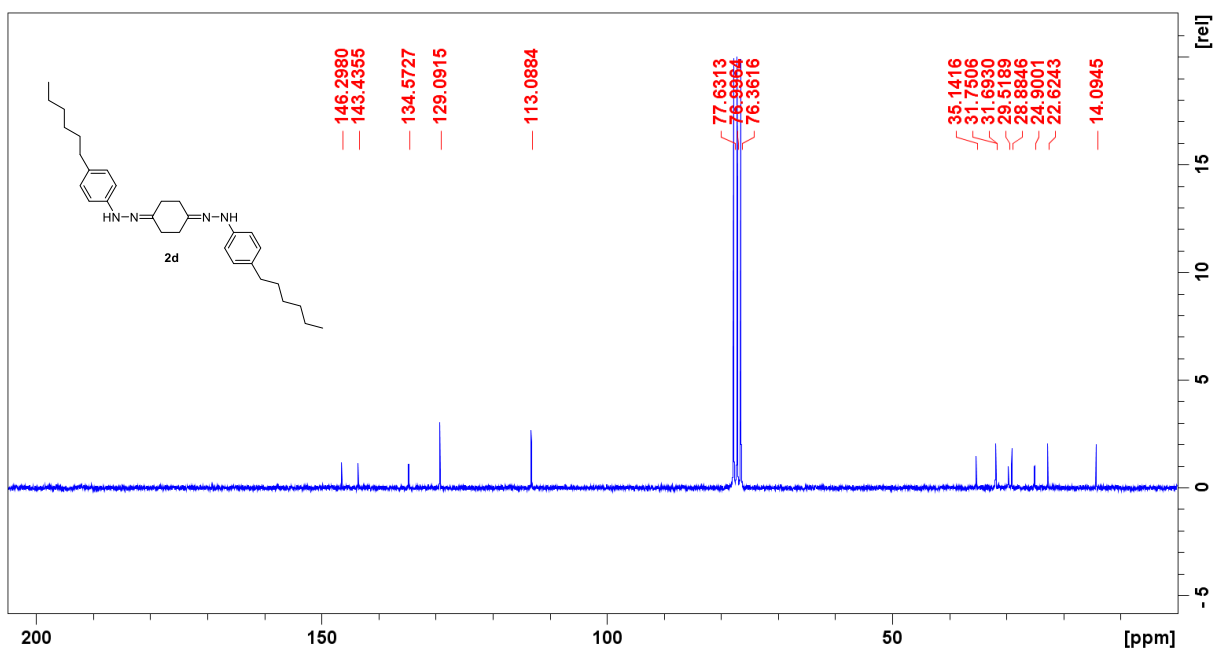


Figure S17. Carbon NMR spectrum of compound 2d.

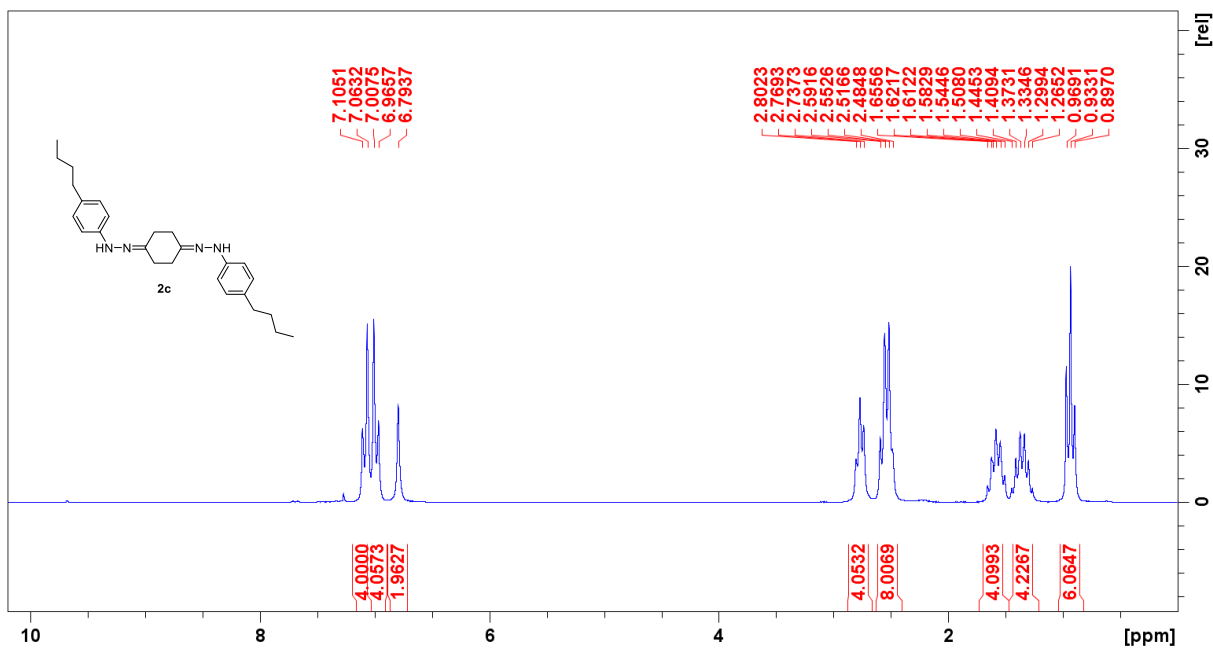


Figure S18. Proton NMR spectrum of compound **2c**.

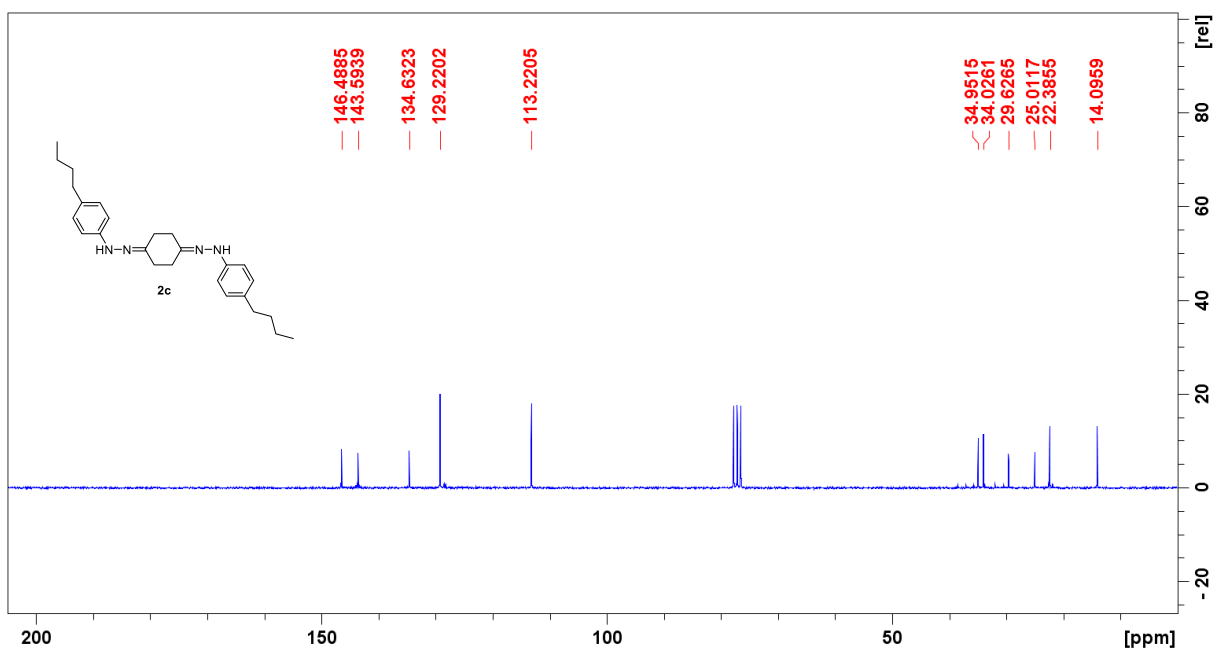


Figure S19. Carbon NMR spectrum of compound **2c**.

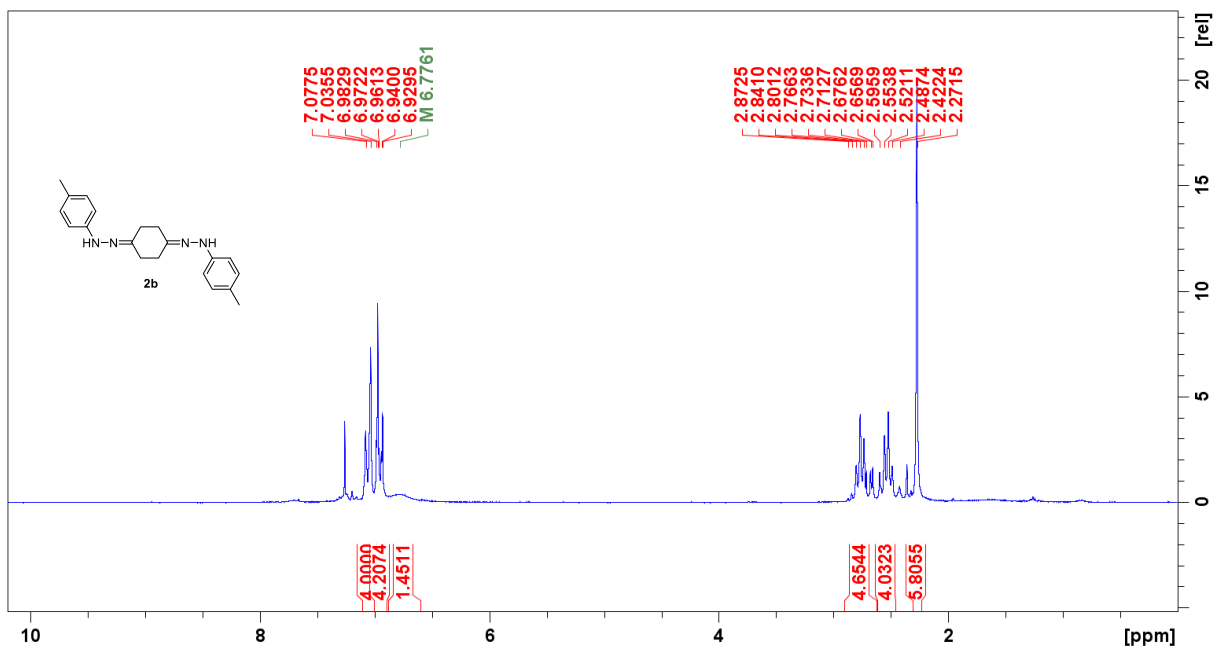


Figure S20. Proton NMR spectrum of compound 2b.

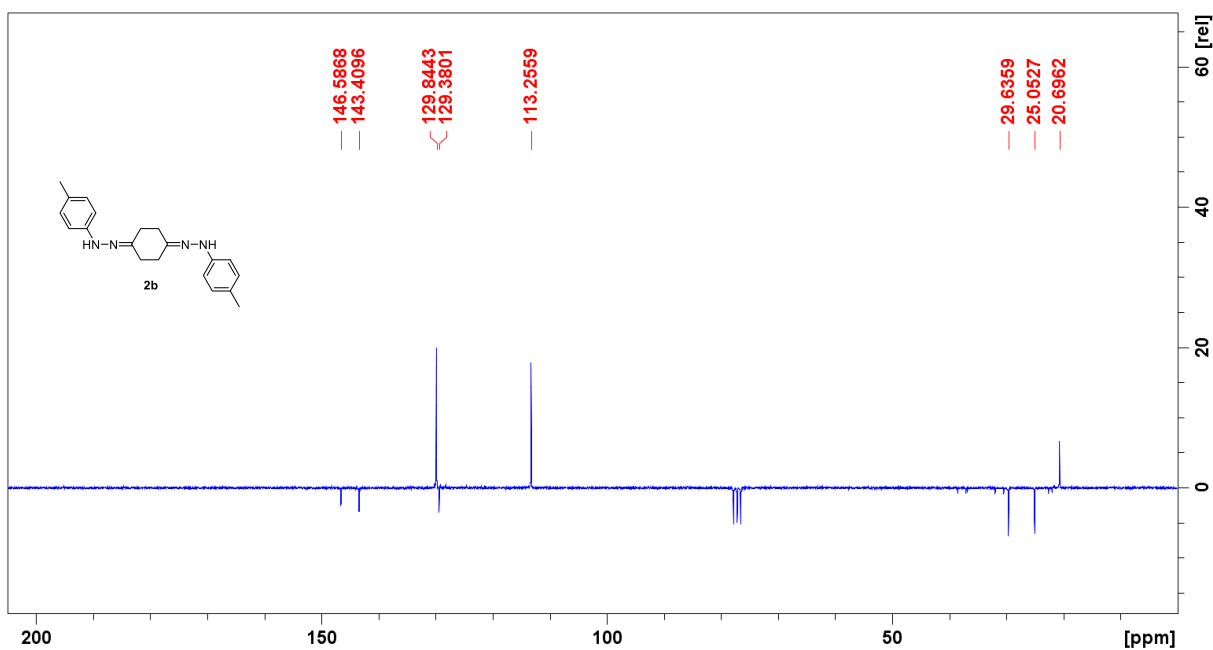


Figure S21. Carbon NMR spectrum of compound 2b.

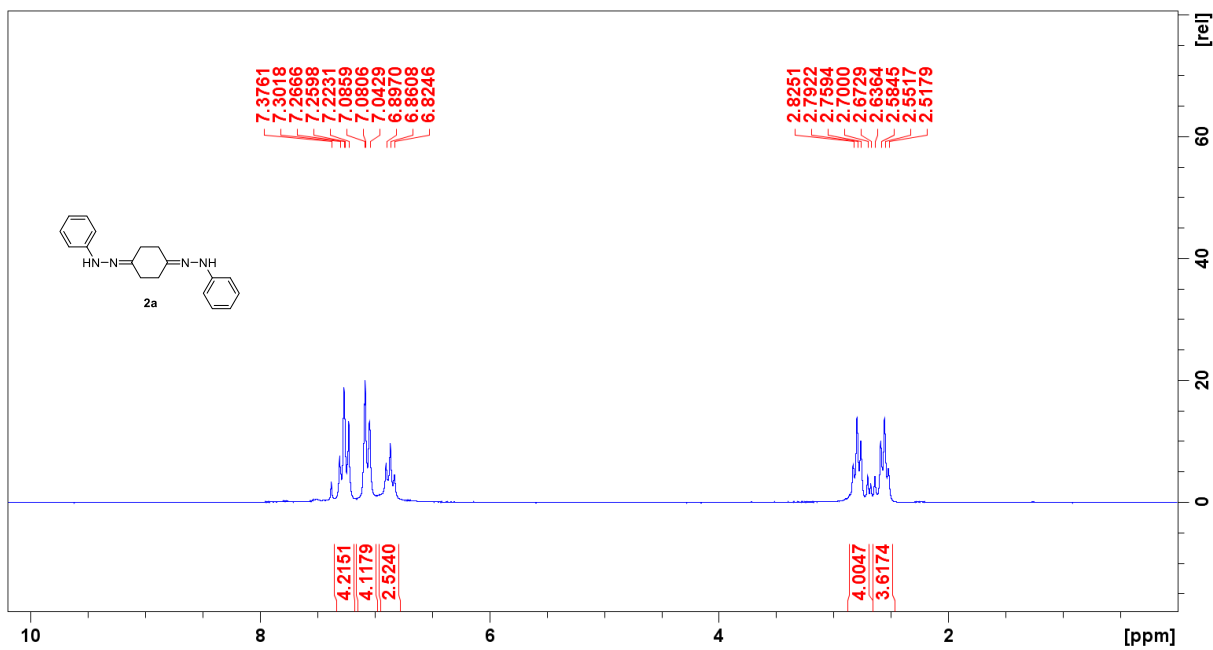


Figure S22. Proton NMR spectrum of compound 2a.

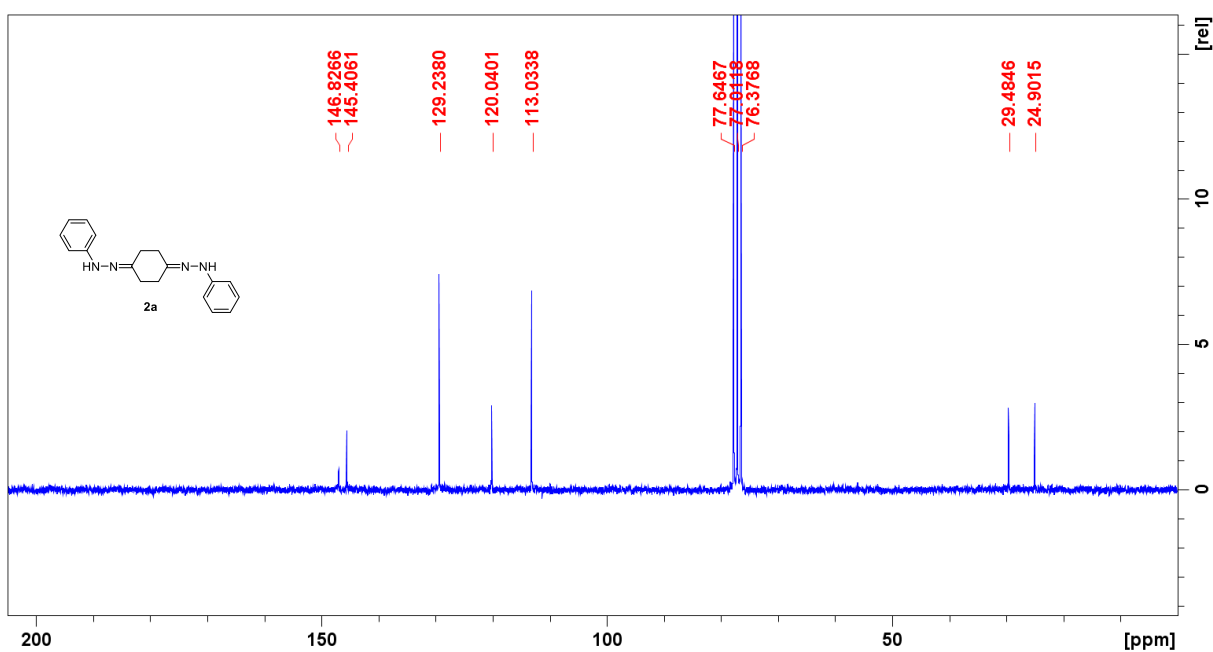


Figure S23. Carbon NMR spectrum of compound 2a.

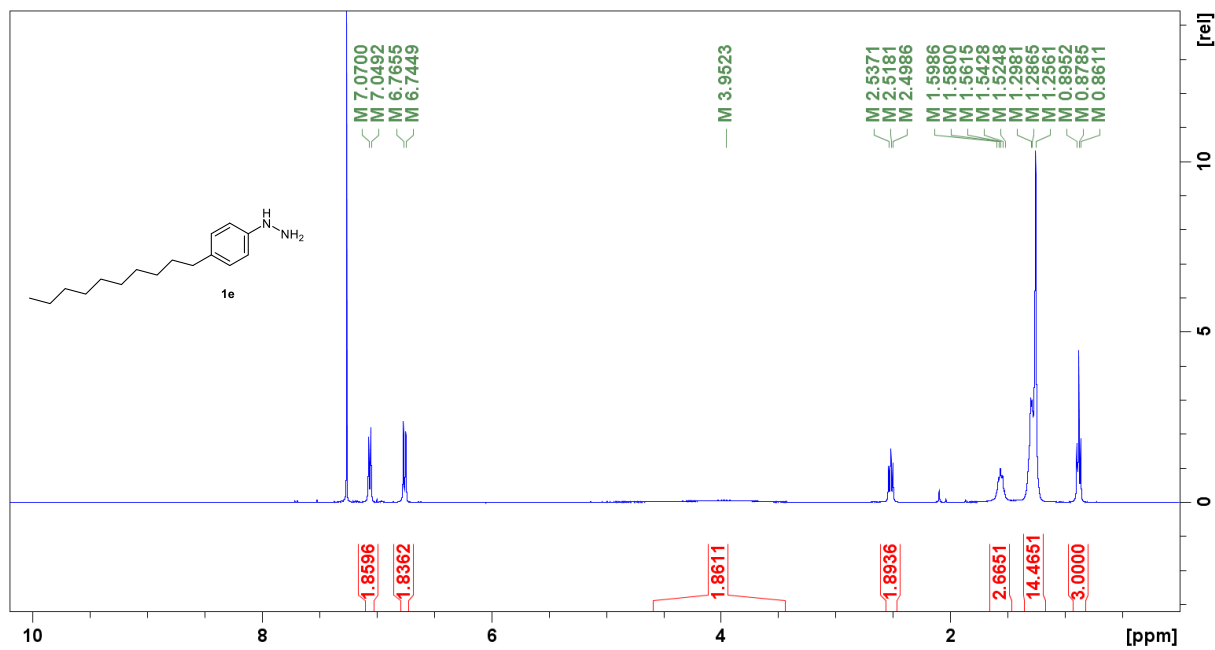


Figure S24. Proton NMR spectrum of compound **1e**.



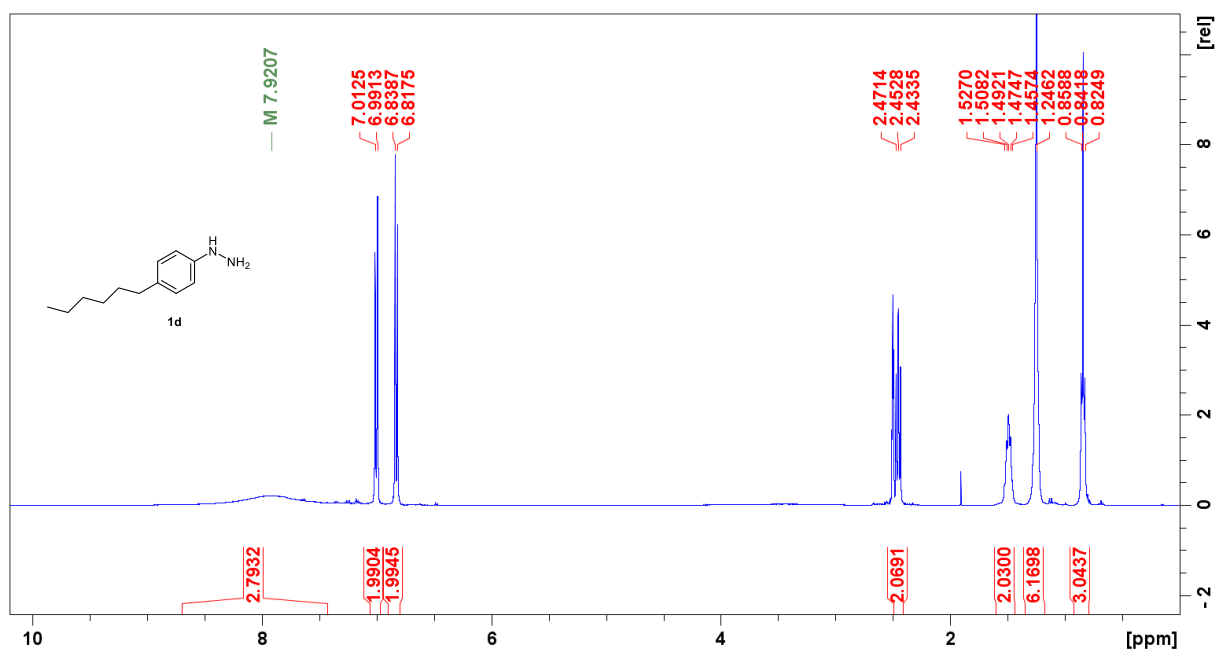


Figure S25. Proton NMR spectrum of compound 1d.

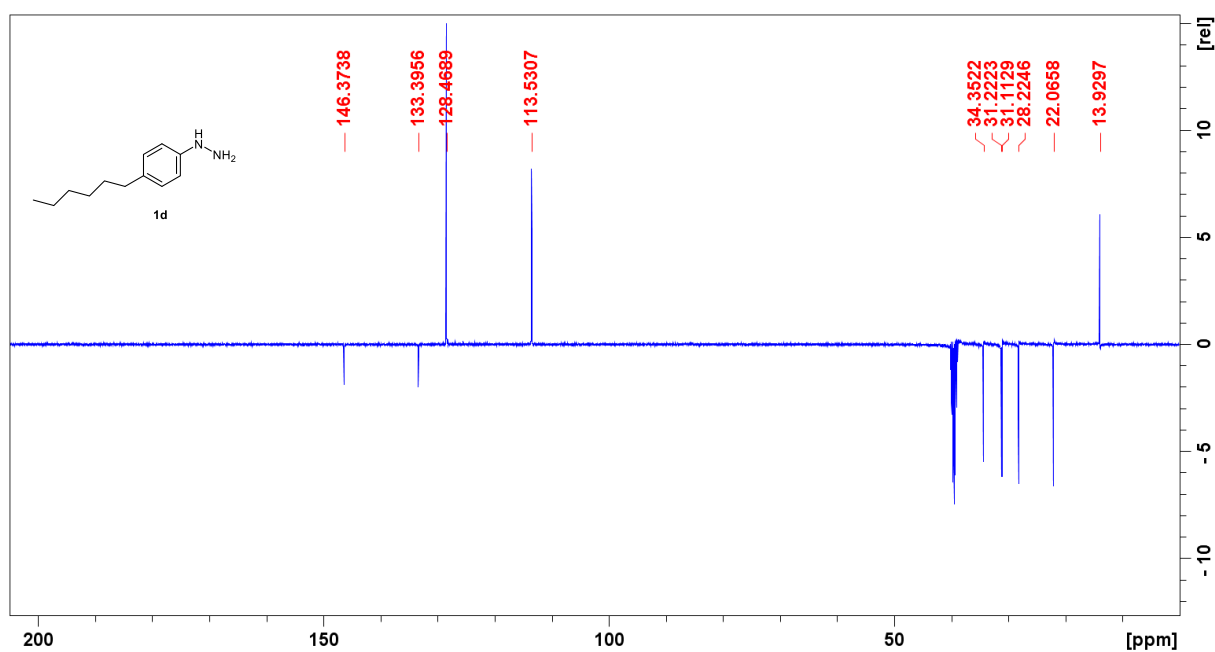


Figure S26. Carbon NMR spectrum of compound 1d.

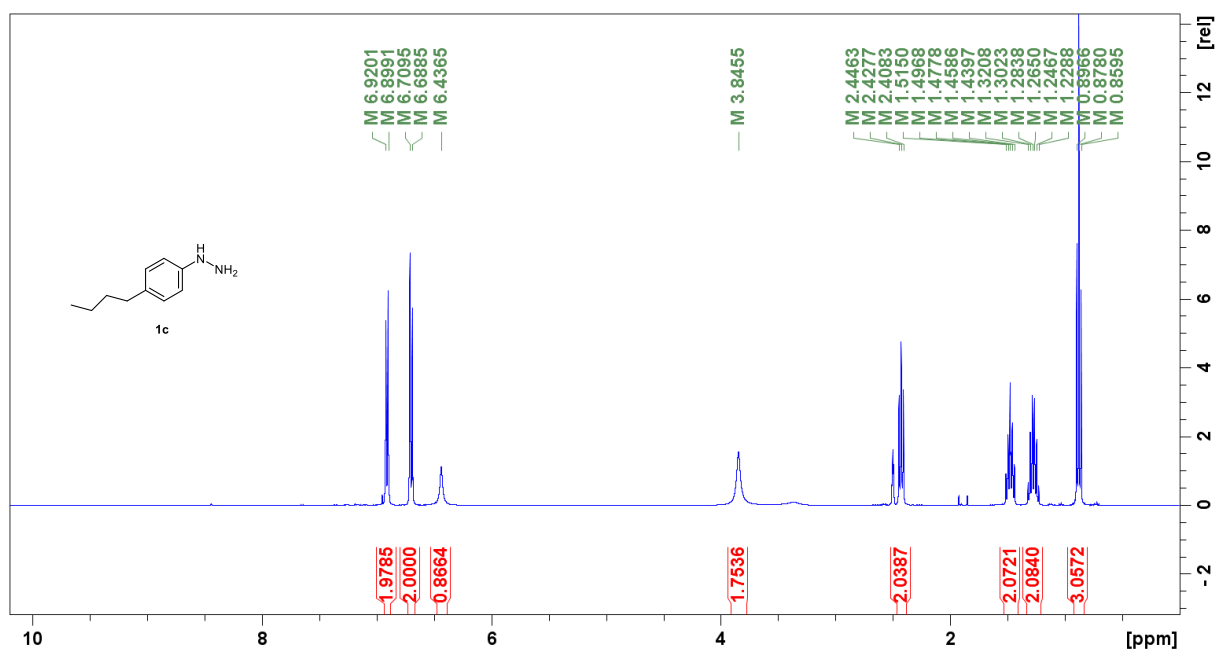


Figure S27. Proton NMR spectrum of compound **1c**.

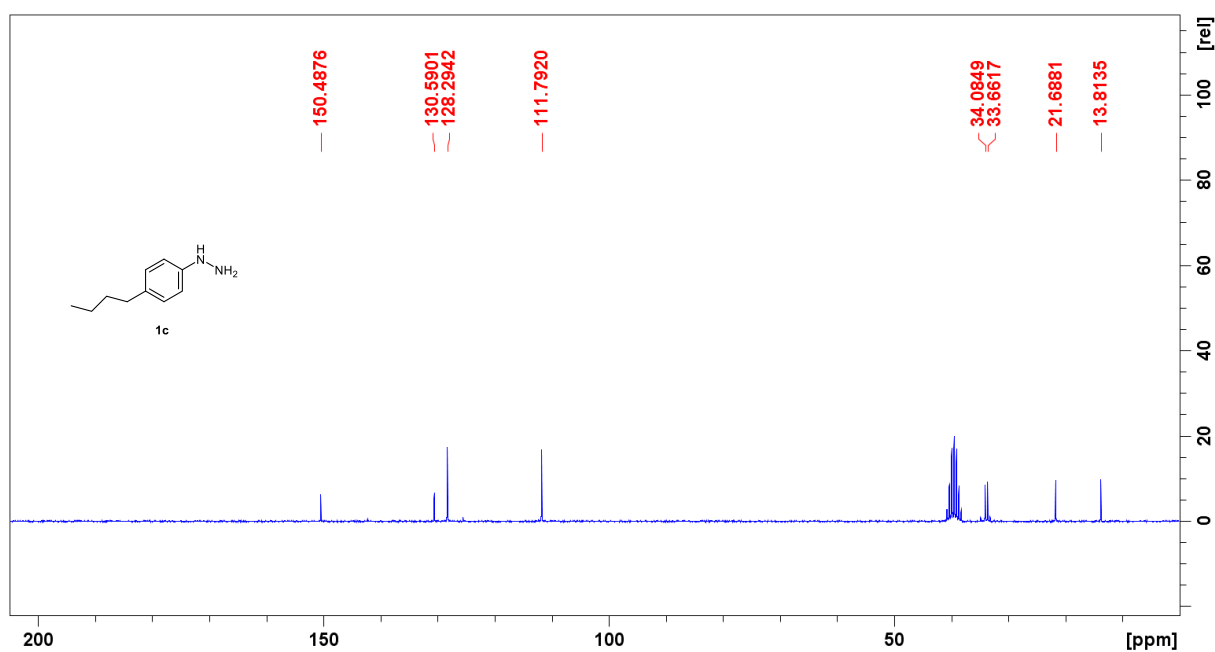


Figure S28. Carbon NMR spectrum of compound **1c**.

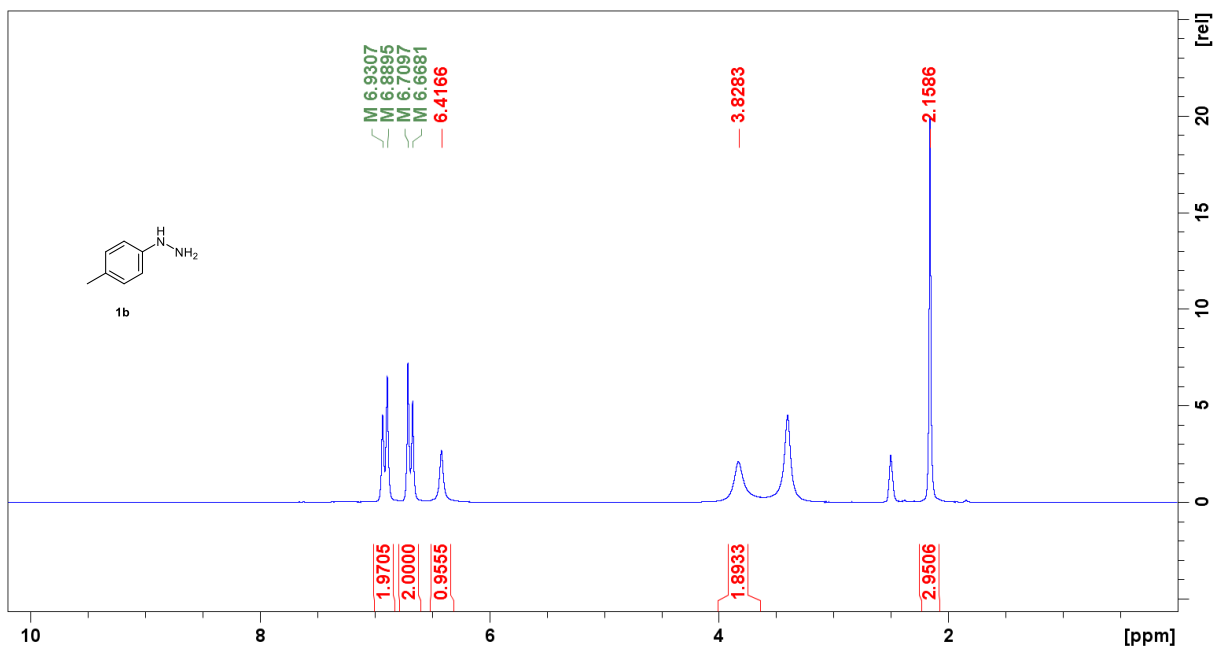


Figure S29. Proton NMR spectrum of compound **1b**.

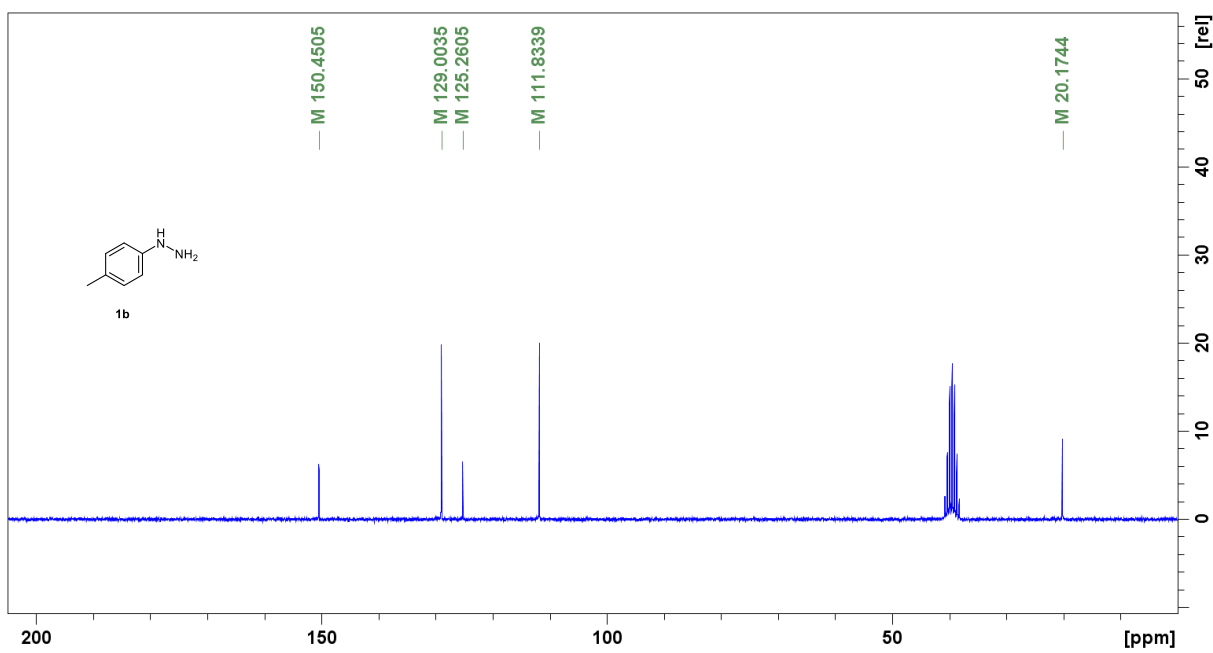


Figure S30. Carbon NMR spectrum of compound **1b**.

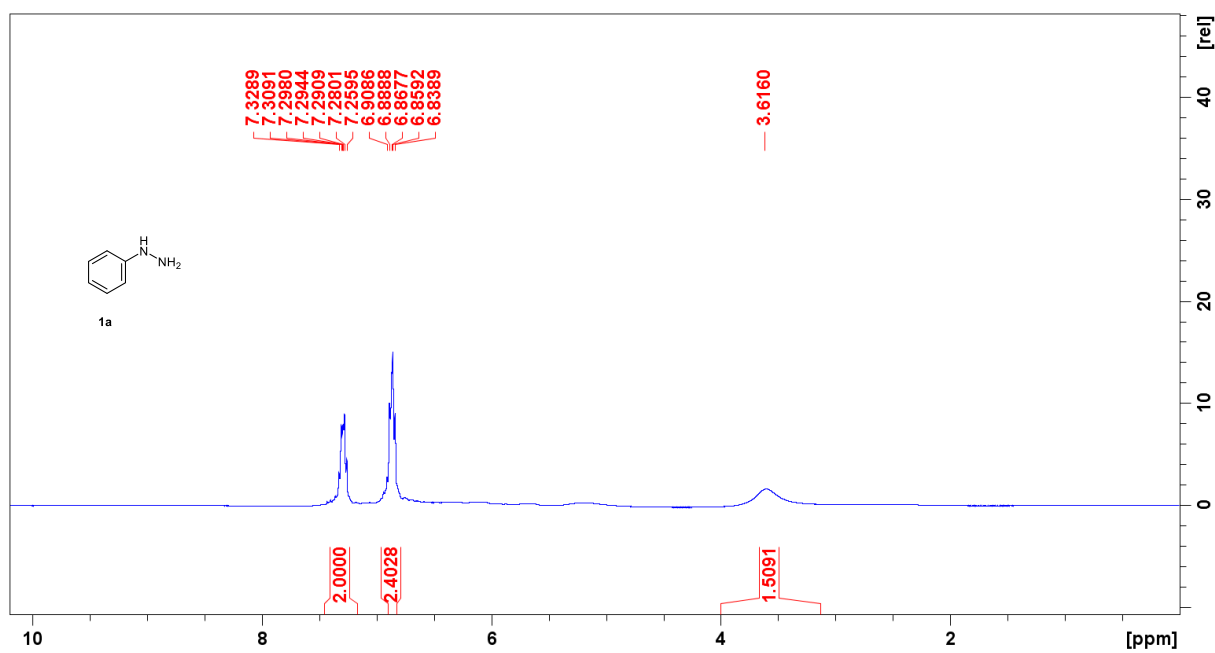


Figure S31. Proton NMR spectrum of compound 1a.

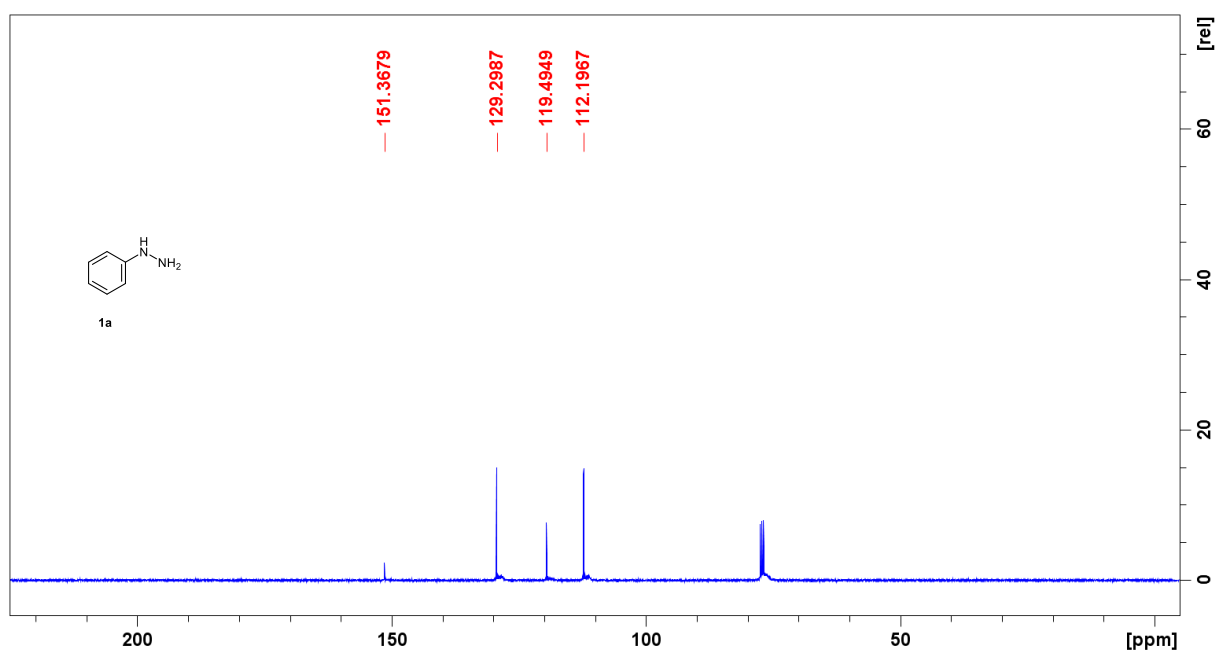
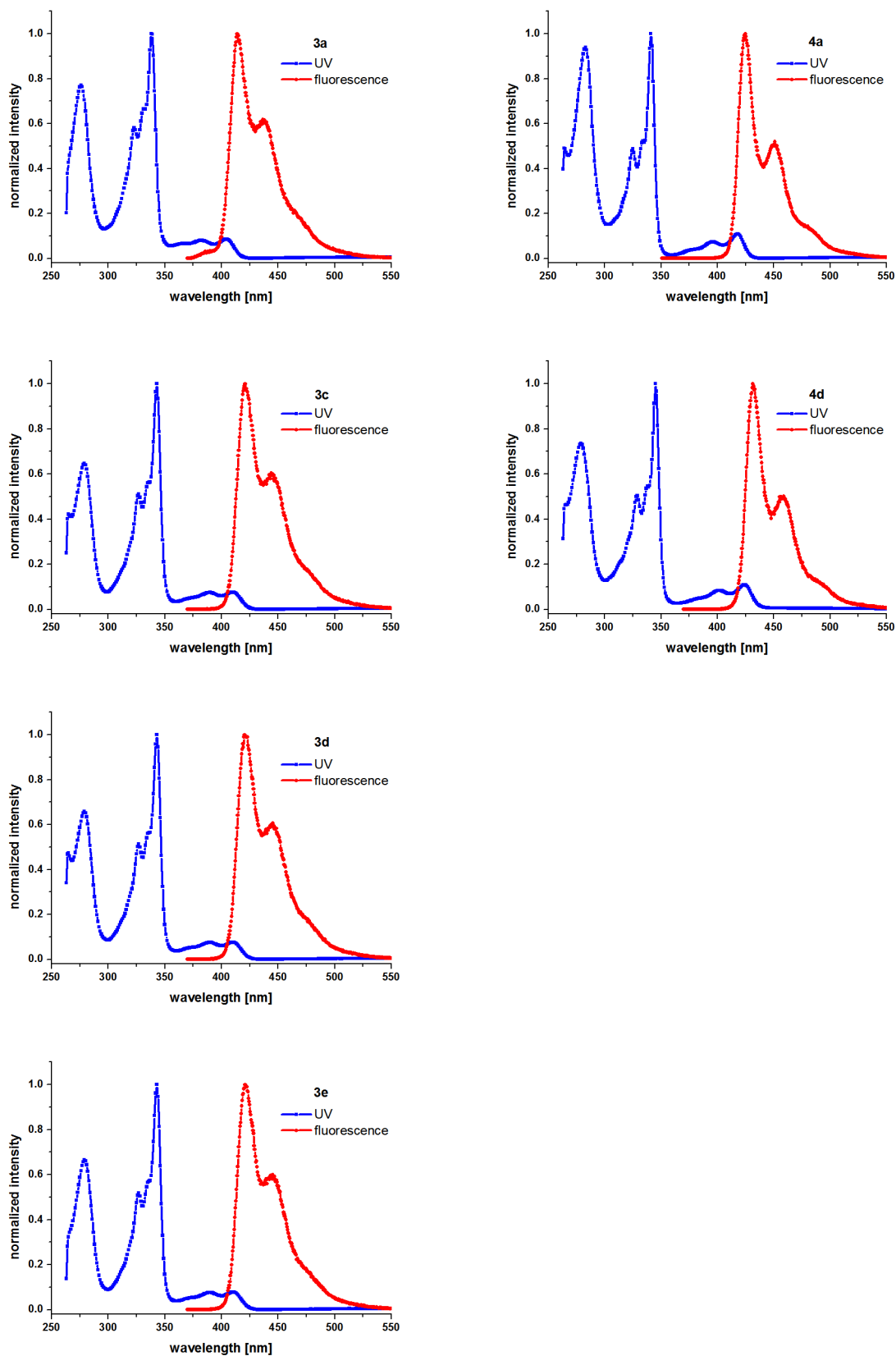


Figure S32. Carbon NMR spectrum of compound 1a.



**Figure S33.** UV-VIS absorption and fluorescence emission spectra of compounds **3a,3c-e, 4a** and **4d** ( $1 \times 10^{-5}$  M in DMF). Excitation wavelength is 343 nm



# Manuscript #3

Supporting Information

**J. Bintinger\***, N. Cernetic, R. Bittner, M. Sauer, A. Folske-Schmitz, M. Holzweber, T. Schiros, D. Nordlund, D. Svatunek, H. Ma, H. Hoffmann, J. Fröhlich, A. Jen, H. Mikula; Using click chemistry for a facile approach towards self-assembled monolayer field-effect transistors (SAMFETs): A new versatile approach for sensing applications, *manuscript draft*





# Using click chemistry for a facile approach towards self-assembled monolayer field-effect transistors (SAMFETs): A new versatile approach for sensing applications

Johannes Bintinger<sup>[a\*]</sup>, Nathan Cernetic<sup>[b]</sup>, Roland Bittner<sup>[a]</sup>, Markus Sauer<sup>[c]</sup>, Annette Folske-Schmitz<sup>[c]</sup>, Markus Holzweber<sup>[d]</sup>, Theanne Schiros<sup>[e,f]</sup>, Dennis Nordlund<sup>[g]</sup>, Dennis Svatunek<sup>[a]</sup>, Hong Ma<sup>[b]</sup>, Helmuth Hoffmann<sup>[a]</sup>, Johannes Fröhlich<sup>[a]</sup>, Alex Jen<sup>[b]</sup>, Hannes Mikula<sup>[a]</sup>

[\*] Email: [johannes.bintinger@tuwien.ac.at](mailto:johannes.bintinger@tuwien.ac.at)

<sup>[a]</sup> Institute of Applied Synthetic Chemistry, Vienna University of Technology, Getreidemarkt 9/163, 1060 Vienna, Austria

<sup>[b]</sup> Department of Materials Science and Engineering, Box 352120, University of Washington, Seattle, WA 98195-2120, Seattle, USA

<sup>[c]</sup> Analytical Instrumentation Center, Vienna University of Technology, Getreidemarkt 9, 1060 Vienna, Austria

<sup>[d]</sup> Institute of Chemical Technologies and Analytics, Vienna University of Technology, Getreidemarkt 9, 1060 Vienna, Austria

<sup>[e]</sup> Fashion Institute of Technology, State University of New York, 227 W 27th St, NY 10001, USA

<sup>[f]</sup> Center for Precision Assembly of Superstratic and Superatomic Solids, MRSEC, 530 W. 120th St., Columbia University, NY, USA

<sup>[g]</sup> Stanford Synchrotron Radiation Lightsource, SLAC National Accelerator Laboratory, 2575 Sand Hill Road, Menlo Park, CA, USA

## Electronic Supplementary Information

### Content

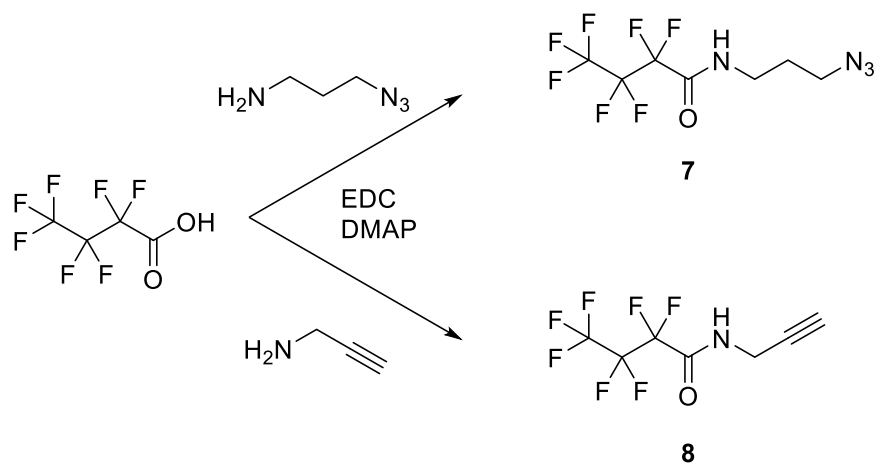
**A) Synthesis of compounds 7 and 8**

**B) NMR Spectra**

**C) Computational part**

**D) Solubility issues of SAMFET compound 14**

## A) Synthesis of compounds 7 and 8



**Scheme S1:** Synthesis towards compounds **7** and **8**. Synthesis is described in the experimental part.





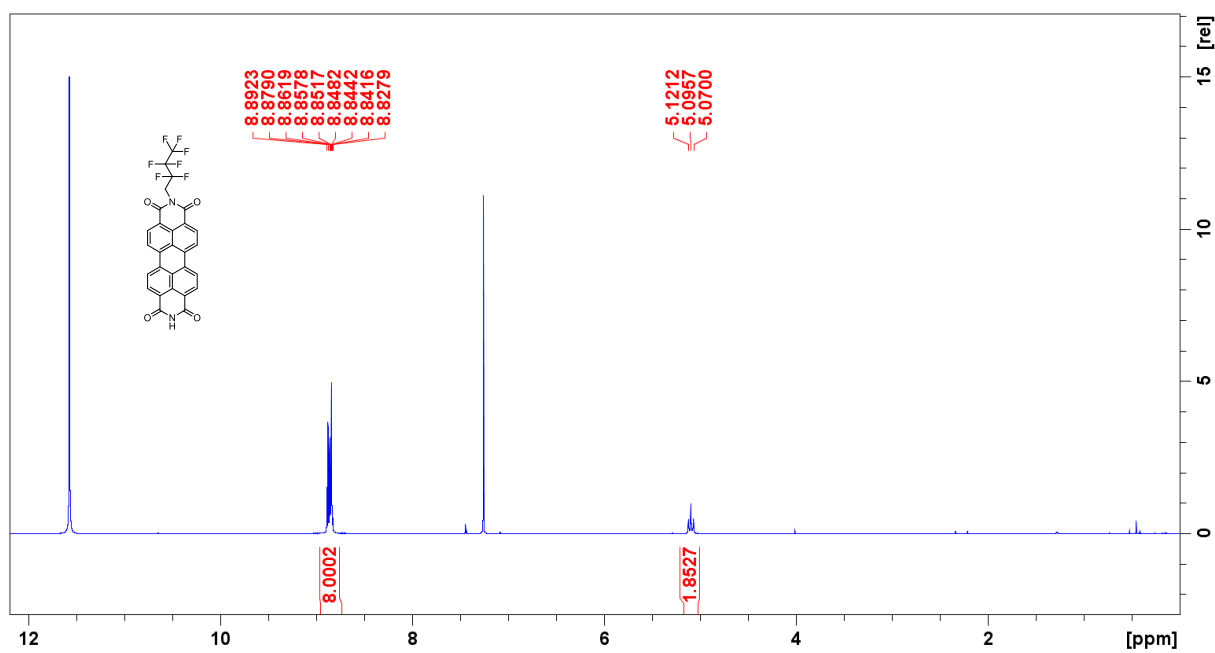


**Figure S5.** Proton NMR spectrum of compound 12.

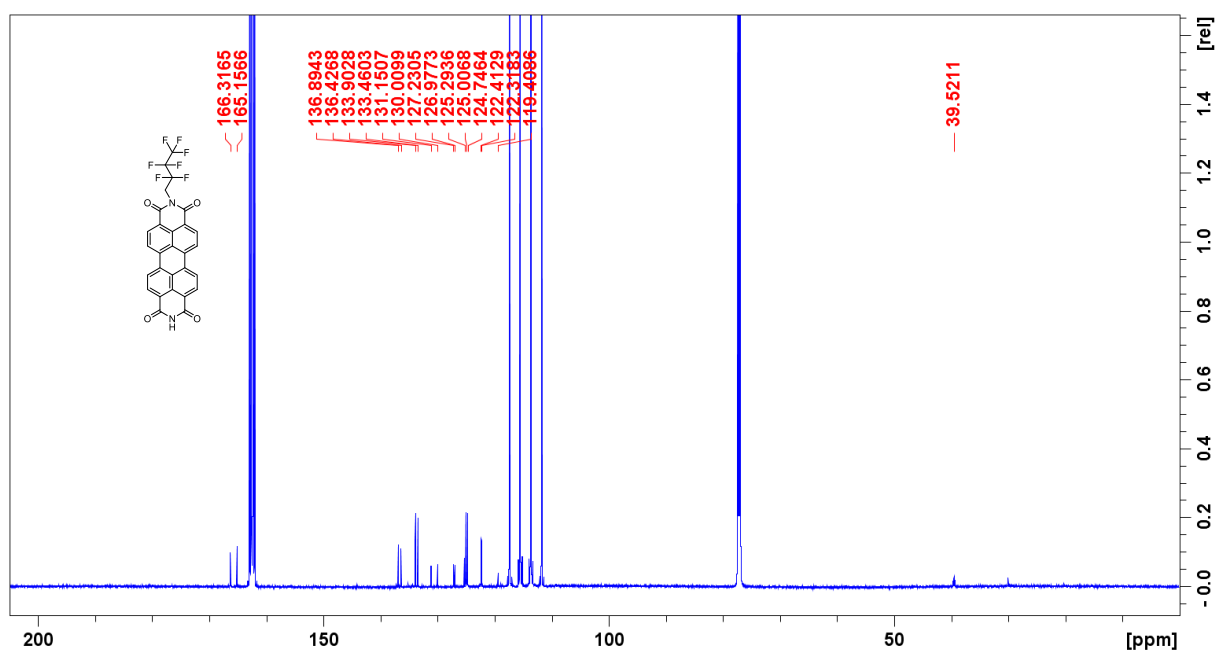


**Figure S6.** Carbon NMR spectrum of compound 12.

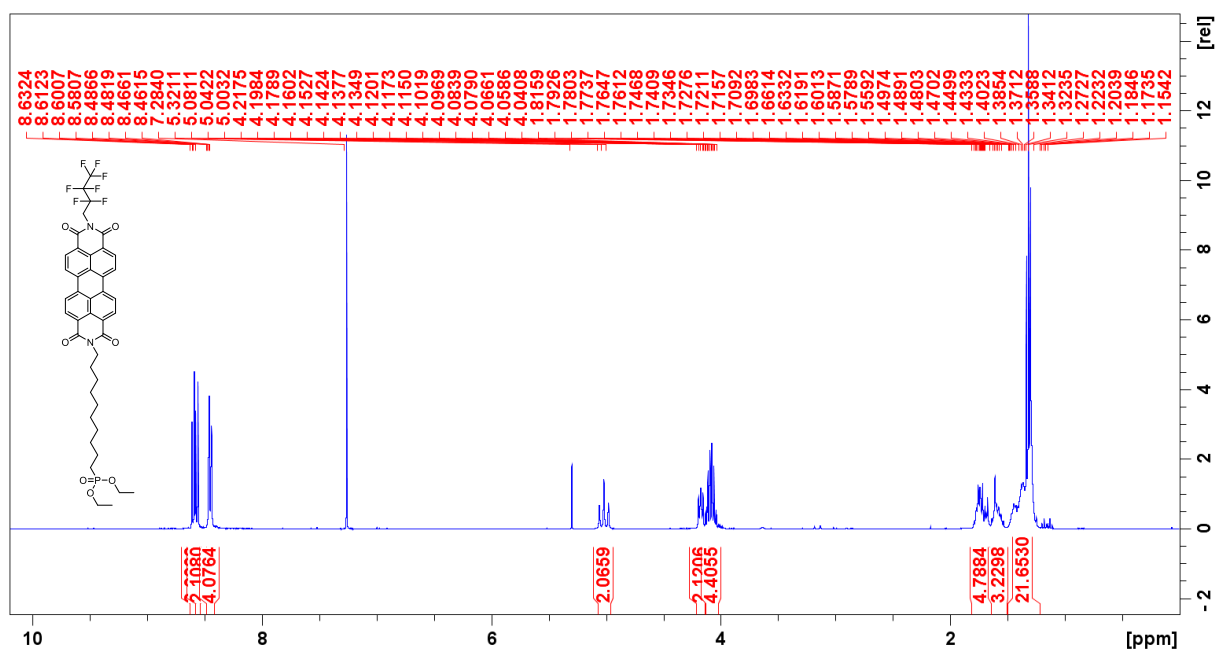


Figure S7. Proton NMR spectrum of compound 13.

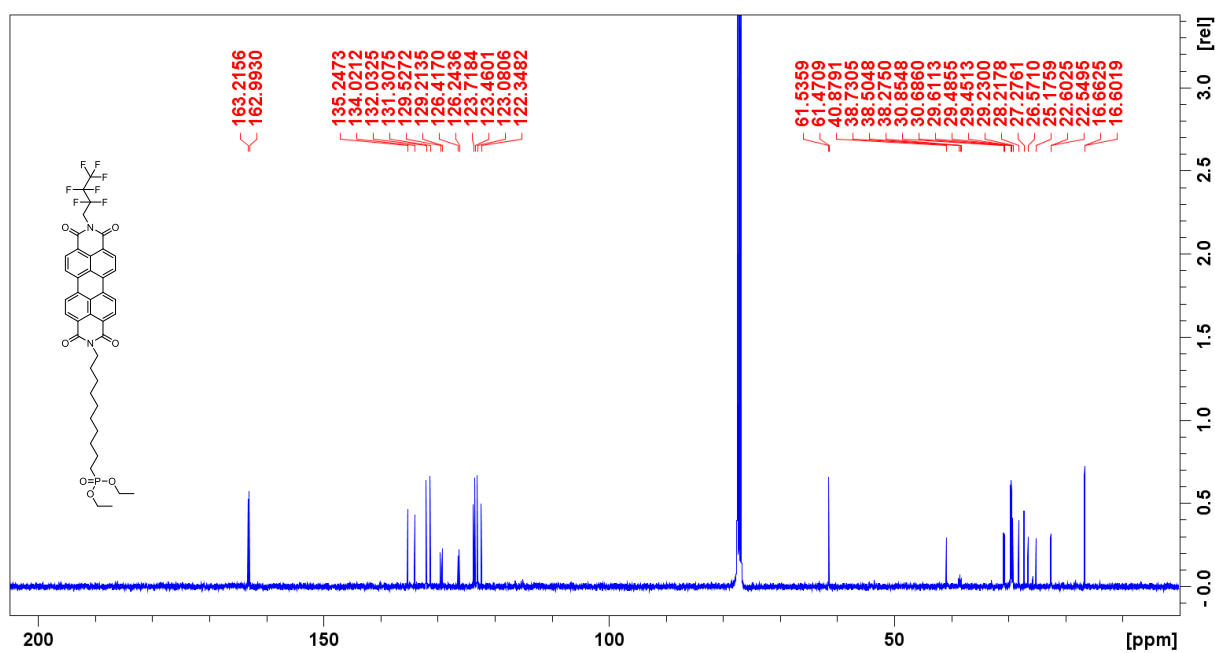
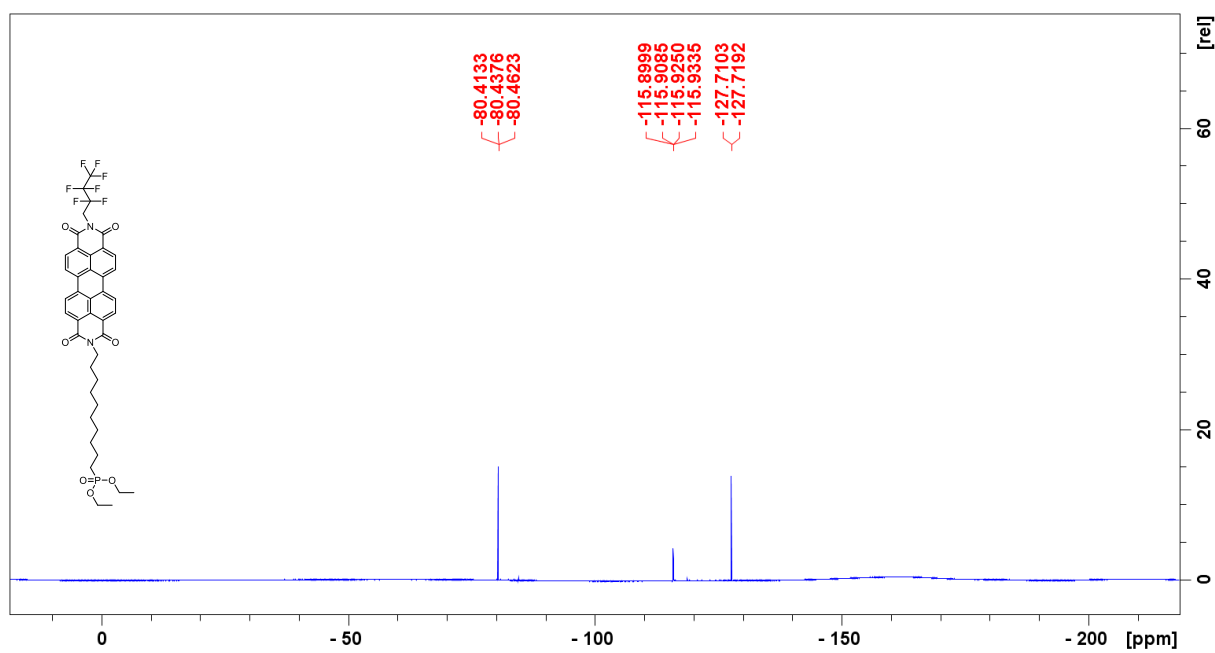
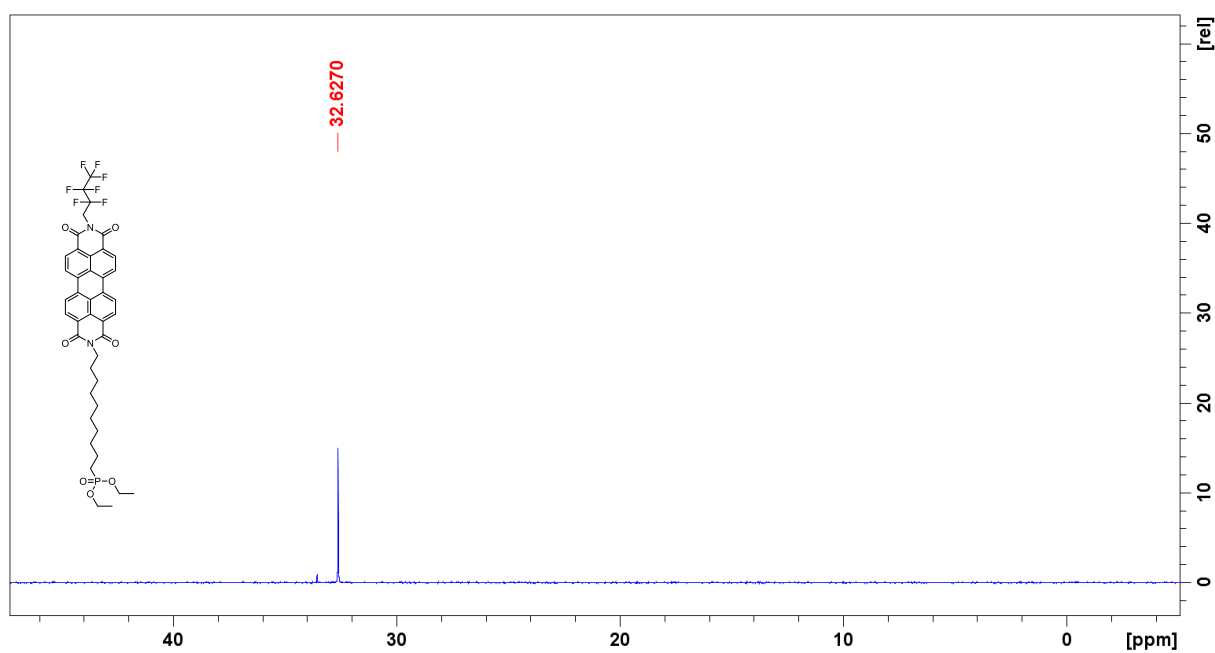


Figure S8. Carbon NMR spectrum of compound 13.



**Figure S9.** Fluorine NMR spectrum of compound 13.



**Figure S10.** Phosphorus NMR spectrum of compound 13.

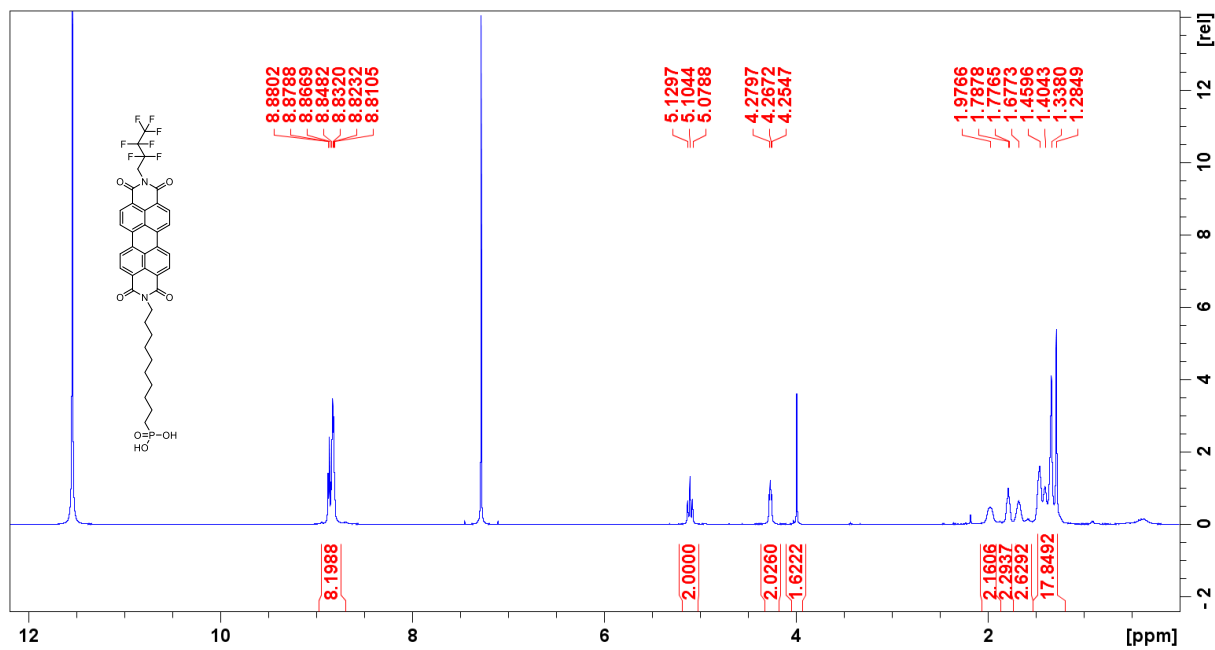


Figure S11. Proton NMR spectrum of compound 14.

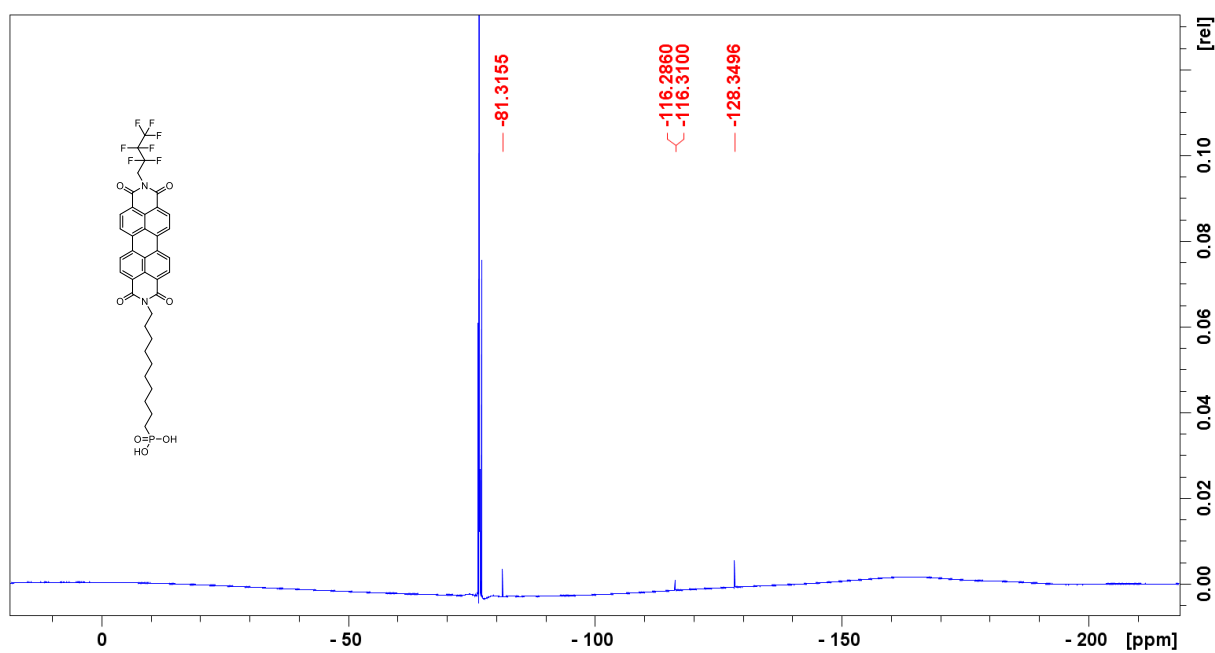
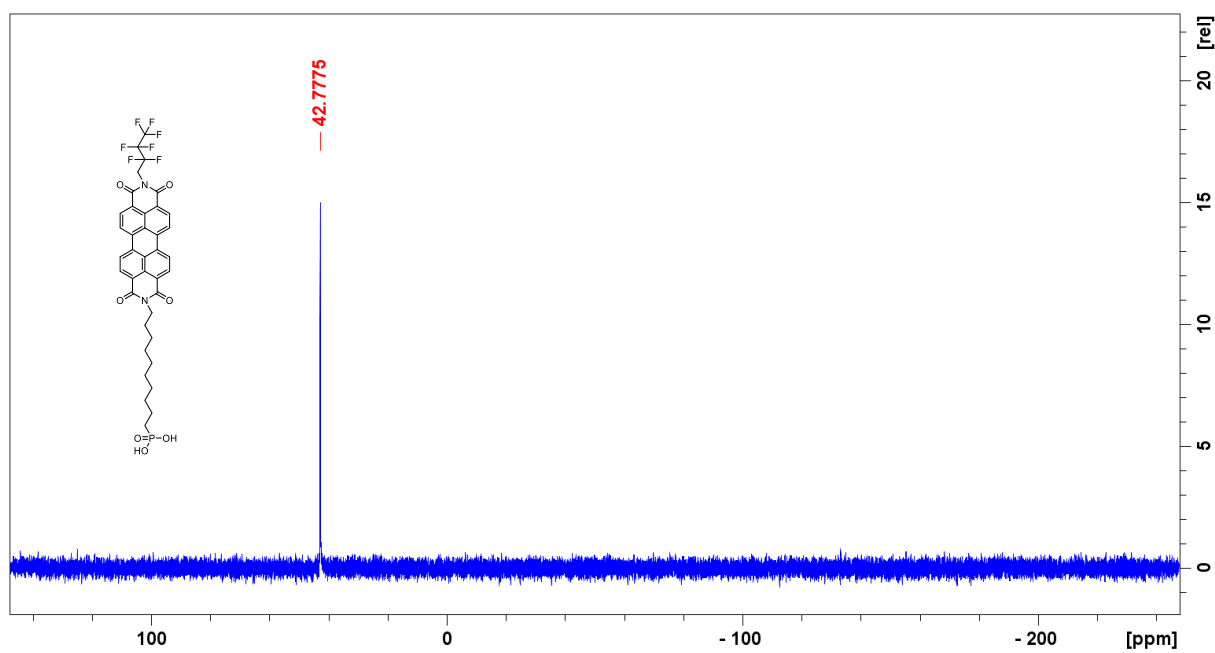


Figure S12. Fluorine NMR spectrum of compound 14.





**Figure S13.** Phosphorus NMR spectrum of compound 14.

## C)Computational part

DFT calculations were performed using Gaussian 09 Rev.D.011 at the Vienna Scientific Cluster 3. Gaussview5 was used for data analysis. Calculations were performed using the B3LYP method with the 6-31G(d,p) basis set as implemented in Gaussian 09.

Cartesian coordinates of calculated structures

SAMFET bend

C	13.8335650	5.4334610	-2.7607850
C	14.3682400	4.1144490	-2.1952370
C	13.2694900	3.0724760	-1.9526520
C	13.7983520	1.7506170	-1.3824640
C	12.6958090	0.7145670	-1.1337650
C	13.2529490	-0.5916910	-0.5564520
N	12.2226930	-1.5966920	-0.3183320
N	12.0076910	-2.5749390	-1.2319020
N	11.0182460	-3.3053450	-0.7978990
C	10.5796280	-2.8065300	0.3965080
C	11.3495680	-1.7043620	0.7114550
C	9.4700730	-3.4599120	1.1631570
C	-0.2033610	-0.6755440	-1.2852860
C	1.0299050	-1.3214180	-1.1507610
C	2.0734890	-0.7717420	-0.4032560
C	1.8646540	0.4894770	0.2405830
C	0.6044580	1.1466130	0.0906240
C	-0.4246590	0.5470090	-0.6751140
C	2.8844400	1.1108670	1.0291740
C	2.6154480	2.3510390	1.6117900
C	6.4285810	0.2981340	2.1340910
C	0.3775890	2.4018120	0.7046540
C	3.3734870	-1.4430400	-0.2566390
C	3.6560570	-2.6649940	-0.8703150
C	4.8915930	-3.3023520	-0.7157200
C	5.8831550	-2.7300100	0.0617970
C	5.6447940	-1.4901690	0.7018460
C	4.3872220	-0.8295900	0.5457150
C	6.6591420	-0.9114620	1.5023920
C	1.3822910	2.9914070	1.4521290
C	5.2030990	0.9550020	1.9810970
C	4.1742560	0.4256780	1.1993870
C	-1.7420060	1.2077580	-0.8249160
C	-0.9193800	3.1059960	0.5531630
O	-2.6565600	0.7081040	-1.4737310
N	-1.9125750	2.4399110	-0.1891230
C	7.1792220	-3.4364410	0.2164620
C	7.9672470	-1.5866940	1.6762560
O	8.8560560	-1.1192830	2.3816690
O	7.3922440	-4.5235980	-0.2979400

O	-1.1239920	4.2079240	1.0389120
C	-3.2309340	3.0985000	-0.3405050
N	8.1562560	-2.7931470	0.9985790
C	-4.3054580	2.4995790	0.5164680
C	-5.0058940	1.3178830	0.3738470
N	-5.8506440	1.2985650	1.4334730
N	-5.6971220	2.4124640	2.1909970
N	-4.7617940	3.1332750	1.6383190
C	-8.2355790	0.6631970	1.1469130
C	-9.3196330	-0.3301840	1.5867430
N	-10.6181280	-0.0549900	0.9841220
C	-10.9622380	-0.5842640	-0.2122140
C	-12.3649470	-0.1601180	-0.7212330
O	-10.2827430	-1.3445880	-0.8808230
C	-13.3484960	-1.3542010	-0.7840970
C	-14.8364710	-0.9785760	-1.0073010
F	-12.9758030	-2.1756370	-1.7853610
F	-13.2696440	-2.0229070	0.3978110
F	-15.5396650	-2.0920550	-1.2487350
F	-15.3422340	-0.3800980	0.0785890
F	-14.9576820	-0.1539470	-2.0567520
F	-12.9145570	0.7941040	0.1012290
F	-12.2423480	0.3719930	-1.9574260
C	-6.8802710	0.3290500	1.7816920
H	13.1109270	5.8936740	-2.0774160
H	13.3267330	5.2769010	-3.7197100
H	15.1164990	3.6972640	-2.8826380
H	14.8975440	4.3077250	-1.2523330
H	12.5191800	3.4897660	-1.2660900
H	12.7409690	2.8755510	-2.8959080
H	14.5443450	1.3305980	-2.0715360
H	14.3313720	1.9497450	-0.4416870
H	11.9476620	1.1251730	-0.4435410
H	12.1707420	0.4871960	-2.0691100
H	13.9627960	-1.0498200	-1.2493810
H	13.7737880	-0.4084380	0.3893000
H	11.3247600	-1.0272810	1.5495090
H	9.6947260	-3.4686020	2.2310000
H	9.3409080	-4.4779270	0.8004340
H	-1.0037750	-1.1188690	-1.8672520
H	1.1581890	-2.2758070	-1.6461980
H	3.3708330	2.8493150	2.2066860
H	7.2158570	0.7229060	2.7469450
H	2.9107260	-3.1504370	-1.4880680
H	5.0938150	-4.2520910	-1.1983440
H	1.1907850	3.9554610	1.9101730
H	5.0669370	1.8987130	2.4946760
H	-3.0905600	4.1379860	-0.0498720
H	-3.5004720	3.0367630	-1.3960890
H	-4.9443940	0.5305120	-0.3596140
H	-8.1505880	0.6373780	0.0555420
H	-8.5171590	1.6823930	1.4333280
H	-9.4418040	-0.3140470	2.6748190
H	-9.0418600	-1.3464020	1.2928780
H	-11.2419140	0.6133740	1.4114150
H	-6.5331360	-0.6603870	1.4687740

H	-6.9508730	0.3343270	2.8728960
H	14.6405630	6.1544630	-2.9255070

SAMFET flat

C	-14.2128591	1.1743061	0.6300271
C	-13.1387440	0.1113610	0.3807440
C	-11.7180489	0.6868881	0.3372870
C	-10.6354858	-0.3711100	0.0930420
C	-9.2198817	0.2253970	0.0419400
C	-8.2068276	-0.8969051	-0.1888670
C	1.5681481	2.6997402	-0.1061720
C	0.1773380	2.5645832	-0.1346590
C	-0.4442960	1.3131361	-0.1174740
C	0.3760330	0.1412260	-0.0721390
C	1.7973491	0.2893910	-0.0438150
C	2.3789482	1.5776731	-0.0597740
C	-0.1862740	-1.1745121	-0.0548680
C	0.6807551	-2.2689522	-0.0097890
C	-3.6630763	-2.7112002	-0.1020240
C	2.6354312	-0.8483051	0.0005540
C	-1.9055891	1.1601691	-0.1436990
C	-2.7735662	2.2537932	-0.1855270
C	-4.1632883	2.0969032	-0.2092810
C	-4.7279204	0.8325701	-0.1913760
C	-3.8877633	-0.3029000	-0.1510540
C	-2.4668472	-0.1551230	-0.1261300
C	-4.4726723	-1.5887061	-0.1392470
C	2.0697912	-2.1127622	0.0169360
C	-2.2710552	-2.5773242	-0.0737780
C	-1.6476011	-1.3270621	-0.0845260
C	3.8461613	1.7463061	-0.0267160
C	4.1162093	-0.7282521	0.0267030
O	4.3792813	2.8488182	-0.0352040
C	-6.2129795	0.7071101	-0.2173660
C	-5.9450804	-1.7523541	-0.1647270
N	-6.7430555	-0.5913810	-0.1853110
O	-6.4651125	-2.8613662	-0.1671480
O	-6.9143605	1.7082031	-0.2685250
O	4.8317434	-1.7143571	0.0633760
C	9.7692307	-0.4708830	0.1194810
C	8.5543346	0.4915760	0.0900240
C	7.1487885	-0.1850310	0.0746140
C	6.0833724	0.9071021	0.0253720
F	7.1322495	-0.9904321	-1.0185811
F	7.0838796	-0.9361381	1.2040011
F	8.6463877	1.2878211	1.1879831
F	8.6843216	1.2648501	-1.0206311
F	10.8925629	0.2635720	0.1463910
F	9.7903727	-1.2451751	-0.9709921
F	9.7384757	-1.2462831	1.2090811
N	4.6415154	0.5800700	0.0132720
H	-14.0501841	1.6847011	1.5860681
H	-14.2044671	1.9380002	-0.1559250
H	-13.3483180	-0.4066620	-0.5650580
H	-13.1945380	-0.6564830	1.1644671
H	-11.5087049	1.2084281	1.2819871

H	-11.6609909	1.4532151	-0.4486850
H	-10.8481338	-0.8965721	-0.8490581
H	-10.6891138	-1.1339451	0.8832601
H	-9.0082237	0.7495871	0.9784291
H	-9.1622307	0.9760011	-0.7484031
H	-8.4175226	-1.3981461	-1.1402911
H	-8.3435266	-1.6665341	0.5764680
H	2.0347642	3.6785673	-0.1188700
H	-0.4190520	3.4677963	-0.1702610
H	0.2844250	-3.2767153	0.0054110
H	-4.1312613	-3.6893023	-0.0941120
H	-2.3780492	3.2620003	-0.2004380
H	-4.8222784	2.9572012	-0.2414490
H	2.7276322	-2.9740582	0.0504530
H	-1.6757711	-3.4816533	-0.0430660
H	6.2677745	1.5593291	0.8818331
H	6.2942425	1.5096881	-0.8605841
H	-15.2145622	0.7333071	0.6545480

#### CLICK-FET bend

C	-14.2128591	1.1743061	0.6300271
C	-13.1387440	0.1113610	0.3807440
C	-11.7180489	0.6868881	0.3372870
C	-10.6354858	-0.3711100	0.0930420
C	-9.2198817	0.2253970	0.0419400
C	-8.2068276	-0.8969051	-0.1888670
C	1.5681481	2.6997402	-0.1061720
C	0.1773380	2.5645832	-0.1346590
C	-0.4442960	1.3131361	-0.1174740
C	0.3760330	0.1412260	-0.0721390
C	1.7973491	0.2893910	-0.0438150
C	2.3789482	1.5776731	-0.0597740
C	-0.1862740	-1.1745121	-0.0548680
C	0.6807551	-2.2689522	-0.0097890
C	-3.6630763	-2.7112002	-0.1020240
C	2.6354312	-0.8483051	0.0005540
C	-1.9055891	1.1601691	-0.1436990
C	-2.7735662	2.2537932	-0.1855270
C	-4.1632883	2.0969032	-0.2092810
C	-4.7279204	0.8325701	-0.1913760
C	-3.8877633	-0.3029000	-0.1510540
C	-2.4668472	-0.1551230	-0.1261300
C	-4.4726723	-1.5887061	-0.1392470
C	2.0697912	-2.1127622	0.0169360
C	-2.2710552	-2.5773242	-0.0737780
C	-1.6476011	-1.3270621	-0.0845260
C	3.8461613	1.7463061	-0.0267160
C	4.1162093	-0.7282521	0.0267030
O	4.3792813	2.8488182	-0.0352040
C	-6.2129795	0.7071101	-0.2173660
C	-5.9450804	-1.7523541	-0.1647270
N	-6.7430555	-0.5913810	-0.1853110
O	-6.4651125	-2.8613662	-0.1671480
O	-6.9143605	1.7082031	-0.2685250
O	4.8317434	-1.7143571	0.0633760
C	9.7692307	-0.4708830	0.1194810

C	8.5543346	0.4915760	0.0900240
C	7.1487885	-0.1850310	0.0746140
C	6.0833724	0.9071021	0.0253720
F	7.1322495	-0.9904321	-1.0185811
F	7.0838796	-0.9361381	1.2040011
F	8.6463877	1.2878211	1.1879831
F	8.6843216	1.2648501	-1.0206311
F	10.8925629	0.2635720	0.1463910
F	9.7903727	-1.2451751	-0.9709921
F	9.7384757	-1.2462831	1.2090811
N	4.6415154	0.5800700	0.0132720
H	-14.0501841	1.6847011	1.5860681
H	-14.2044671	1.9380002	-0.1559250
H	-13.3483180	-0.4066620	-0.5650580
H	-13.1945380	-0.6564830	1.1644671
H	-11.5087049	1.2084281	1.2819871
H	-11.6609909	1.4532151	-0.4486850
H	-10.8481338	-0.8965721	-0.8490581
H	-10.6891138	-1.1339451	0.8832601
H	-9.0082237	0.7495871	0.9784291
H	-9.1622307	0.9760011	-0.7484031
H	-8.4175226	-1.3981461	-1.1402911
H	-8.3435266	-1.6665341	0.5764680
H	2.0347642	3.6785673	-0.1188700
H	-0.4190520	3.4677963	-0.1702610
H	0.2844250	-3.2767153	0.0054110
H	-4.1312613	-3.6893023	-0.0941120
H	-2.3780492	3.2620003	-0.2004380
H	-4.8222784	2.9572012	-0.2414490
H	2.7276322	-2.9740582	0.0504530
H	-1.6757711	-3.4816533	-0.0430660
H	6.2677745	1.5593291	0.8818331
H	6.2942425	1.5096881	-0.8605841
H	-15.2145622	0.7333071	0.6545480

#### CLICK-FET flat

C	-14.2128591	1.1743061	0.6300271
C	-13.1387440	0.11113610	0.3807440
C	-11.7180489	0.6868881	0.3372870
C	-10.6354858	-0.37111100	0.0930420
C	-9.2198817	0.2253970	0.0419400
C	-8.2068276	-0.8969051	-0.1888670
C	1.5681481	2.6997402	-0.1061720
C	0.1773380	2.5645832	-0.1346590
C	-0.4442960	1.3131361	-0.1174740
C	0.3760330	0.1412260	-0.0721390
C	1.7973491	0.2893910	-0.0438150
C	2.3789482	1.5776731	-0.0597740
C	-0.1862740	-1.1745121	-0.0548680
C	0.6807551	-2.2689522	-0.0097890
C	-3.6630763	-2.7112002	-0.1020240
C	2.6354312	-0.8483051	0.0005540
C	-1.9055891	1.1601691	-0.1436990
C	-2.7735662	2.2537932	-0.1855270
C	-4.1632883	2.0969032	-0.2092810
C	-4.7279204	0.8325701	-0.1913760

C	-3.8877633	-0.3029000	-0.1510540
C	-2.4668472	-0.1551230	-0.1261300
C	-4.4726723	-1.5887061	-0.1392470
C	2.0697912	-2.1127622	0.0169360
C	-2.2710552	-2.5773242	-0.0737780
C	-1.6476011	-1.3270621	-0.0845260
C	3.8461613	1.7463061	-0.0267160
C	4.1162093	-0.7282521	0.0267030
O	4.3792813	2.8488182	-0.0352040
C	-6.2129795	0.7071101	-0.2173660
C	-5.9450804	-1.7523541	-0.1647270
N	-6.7430555	-0.5913810	-0.1853110
O	-6.4651125	-2.8613662	-0.1671480
O	-6.9143605	1.7082031	-0.2685250
O	4.8317434	-1.7143571	0.0633760
C	9.7692307	-0.4708830	0.1194810
C	8.5543346	0.4915760	0.0900240
C	7.1487885	-0.1850310	0.0746140
C	6.0833724	0.9071021	0.0253720
F	7.1322495	-0.9904321	-1.0185811
F	7.0838796	-0.9361381	1.2040011
F	8.6463877	1.2878211	1.1879831
F	8.6843216	1.2648501	-1.0206311
F	10.8925629	0.2635720	0.1463910
F	9.7903727	-1.2451751	-0.9709921
F	9.7384757	-1.2462831	1.2090811
N	4.6415154	0.5800700	0.0132720
H	-14.0501841	1.6847011	1.5860681
H	-14.2044671	1.9380002	-0.1559250
H	-13.3483180	-0.4066620	-0.5650580
H	-13.1945380	-0.6564830	1.1644671
H	-11.5087049	1.2084281	1.2819871
H	-11.6609909	1.4532151	-0.4486850
H	-10.8481338	-0.8965721	-0.8490581
H	-10.6891138	-1.1339451	0.8832601
H	-9.0082237	0.7495871	0.9784291
H	-9.1622307	0.9760011	-0.7484031
H	-8.4175226	-1.3981461	-1.1402911
H	-8.3435266	-1.6665341	0.5764680
H	2.0347642	3.6785673	-0.1188700
H	-0.4190520	3.4677963	-0.1702610
H	0.2844250	-3.2767153	0.0054110
H	-4.1312613	-3.6893023	-0.0941120
H	-2.3780492	3.2620003	-0.2004380
H	-4.8222784	2.9572012	-0.2414490
H	2.7276322	-2.9740582	0.0504530
H	-1.6757711	-3.4816533	-0.0430660
H	6.2677745	1.5593291	0.8818331
H	6.2942425	1.5096881	-0.8605841
H	-15.2145622	0.7333071	0.6545480

## D) Solubility issues of SAMFET compound 14

Sonicated 2 h, not filtered

THF      DMSO      CB

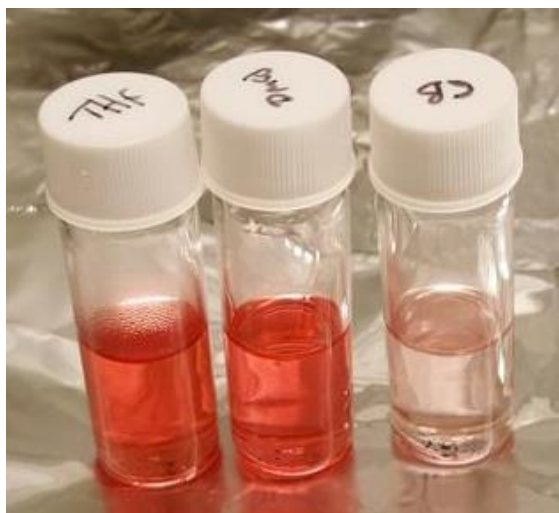


Figure S14. 0.1 mM solutions of compound 14 in various solvents.

**DMSO:CB (1:1 by vol)**  
Not Filtered    Filtered



**DMSO:TCE (1:1 by vol)**  
Not Filtered    Filtered



**THF**  
Not Filtered    Filtered



**DMSO**  
Not Filtered    Filtered



Figure S15. Comparison of filtered and unfiltered 0.1 mM solutions of compound 14 in various solvents.

- (1) M. J. Frisch, G.; Trucks, W.; Schlegel, H. B.; Scuseria, G. E.; Robb, M. A.; Cheeseman, J. R.; Scalmani, G.; Barone, V.; Mennucci, B.; Petersson, G. A.; Nakatsuji, H.; Caricato, M.; Li, X.; Hratchian, H. P.; Izmaylov, A. F.; Bloino, J.; Zheng, G.; Sonnenberg, J. L. *Gaussian 09, Revision D. 01; Gaussian*; 2009.



# Manuscript #5

Supporting Information

**J. Bintinger\***, H. Holzer\*, C. Choi, Y. Kim, D. Lumpi, E. Horkel, B. Stöger, C. Hametner, M. Marchetti-Deschmann, F. Plasser, I. Kymissis, J. Fröhlich; Color Tuning of Oligothiophene Based Compounds – A Combined Experimental and Computational Approach, *manuscript draft*



# Color Tuning of Oligothiophene Based Compounds – A Combined Experimental and Computational Approach

Johannes Bintinger<sup>a\*‡</sup>, Brigitte Holzer<sup>a\*</sup>, Daniel Lumpi<sup>a</sup>, Ernst Horkel<sup>a‡</sup>, Chris Choi<sup>b</sup>, Youngwan Kim<sup>b</sup>, Berthold Stöger<sup>c</sup>, Christian Hametner<sup>a</sup>, Martina Marchetti-Deschmann<sup>c</sup>, Ioannis Kymissis<sup>b</sup>, Felix Plasser<sup>d</sup>, Johannes Fröhlich<sup>a</sup>

<sup>a</sup> Institute of Applied Synthetic Chemistry, Vienna University of Technology, 1060 Vienna, Austria

<sup>b</sup> Department of Electrical Engineering, Columbia University, New York, NY 10027, USA

<sup>c</sup> Institute of Chemical Technologies and Analytics, Vienna University of Technology, Getreidemarkt 9, 1060 Vienna, Austria

<sup>d</sup> Institute for Theoretical Chemistry, University of Vienna, Währinger Straße 17, 1090 Vienna, Austria

\* Both authors contributed equally

‡ Email: [johannes.bintinger@tuwien.ac.at](mailto:johannes.bintinger@tuwien.ac.at); [ernst.horkel@tuwien.ac.at](mailto:ernst.horkel@tuwien.ac.at)

## Electronic Supplementary Information

### Content

**A) NMR Spectra**

**B) Photoluminescence Spectra**

**C) OLED Spectra**

**D) computational part**

# A) NMR Spectra

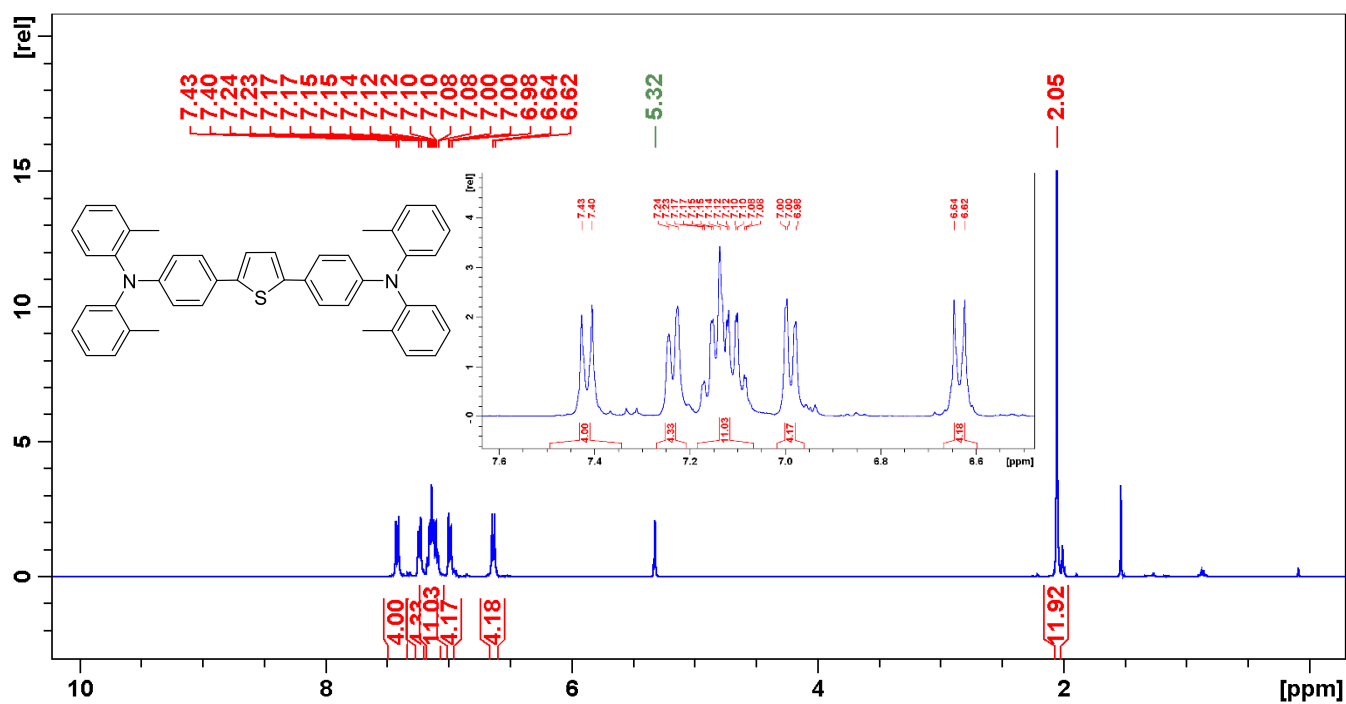


Figure S1. Proton NMR spectrum of compound 3Ae.

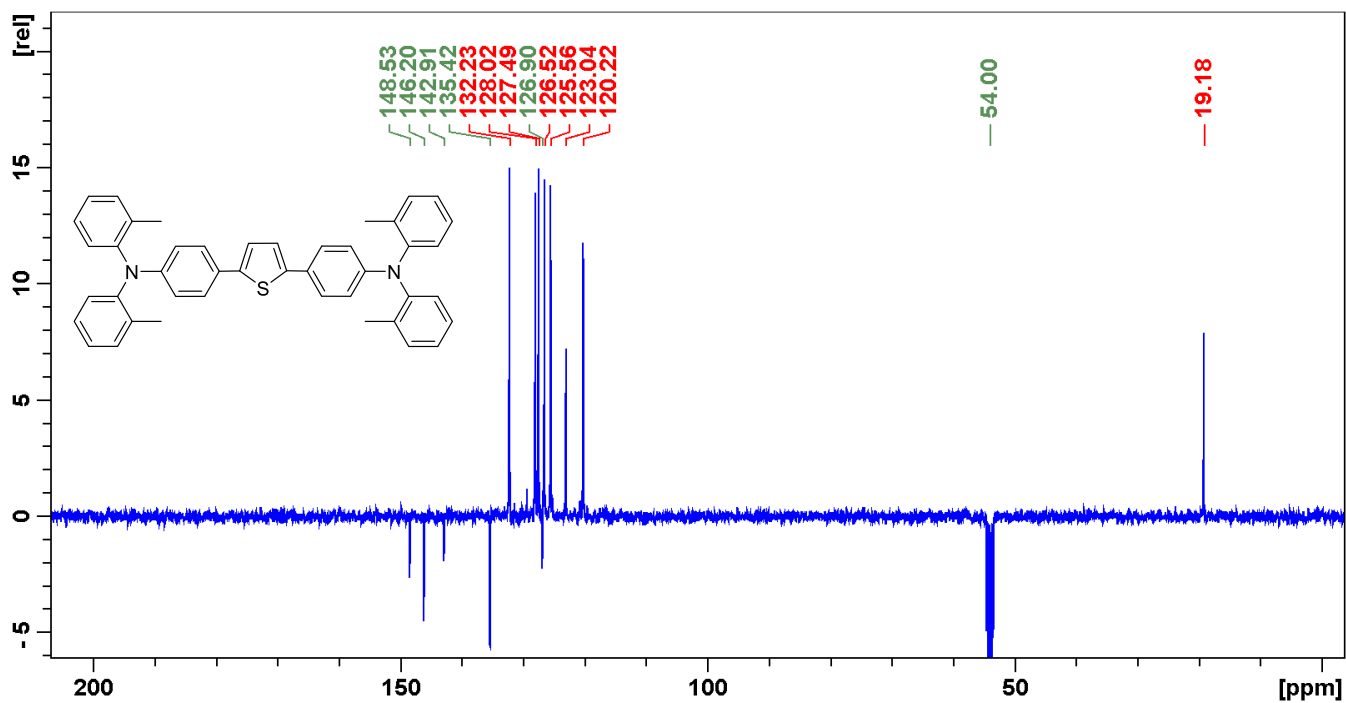


Figure S2. Carbon NMR spectrum of compound 3Ae.

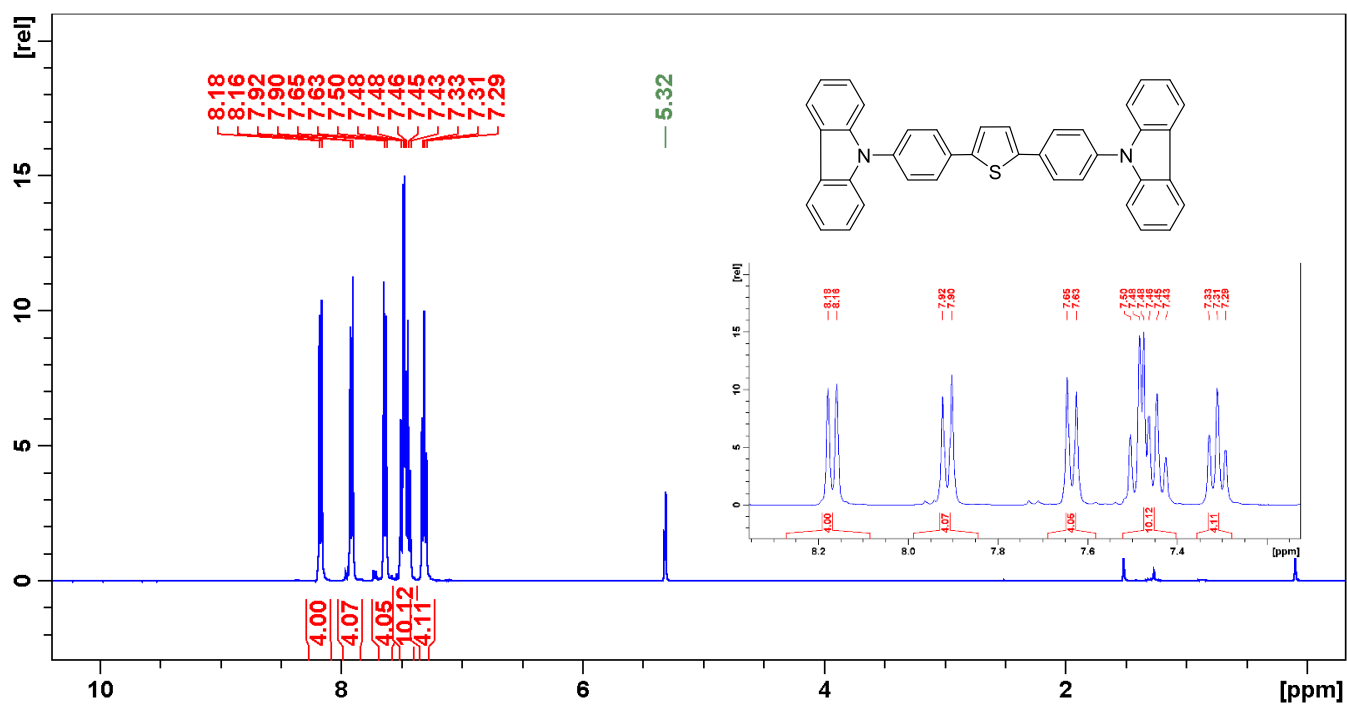


Figure S3. Proton NMR spectrum of compound 3Ah.

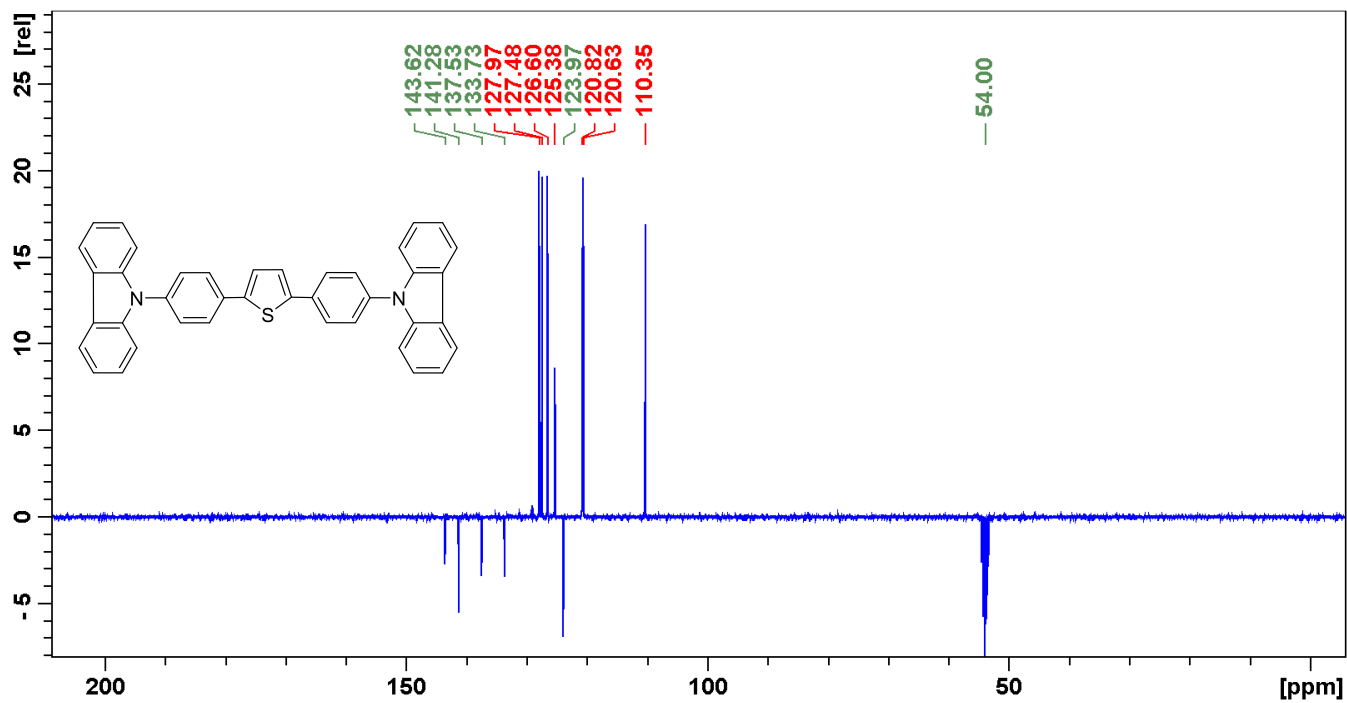


Figure S4. Carbon NMR spectrum of compound 3Ah.

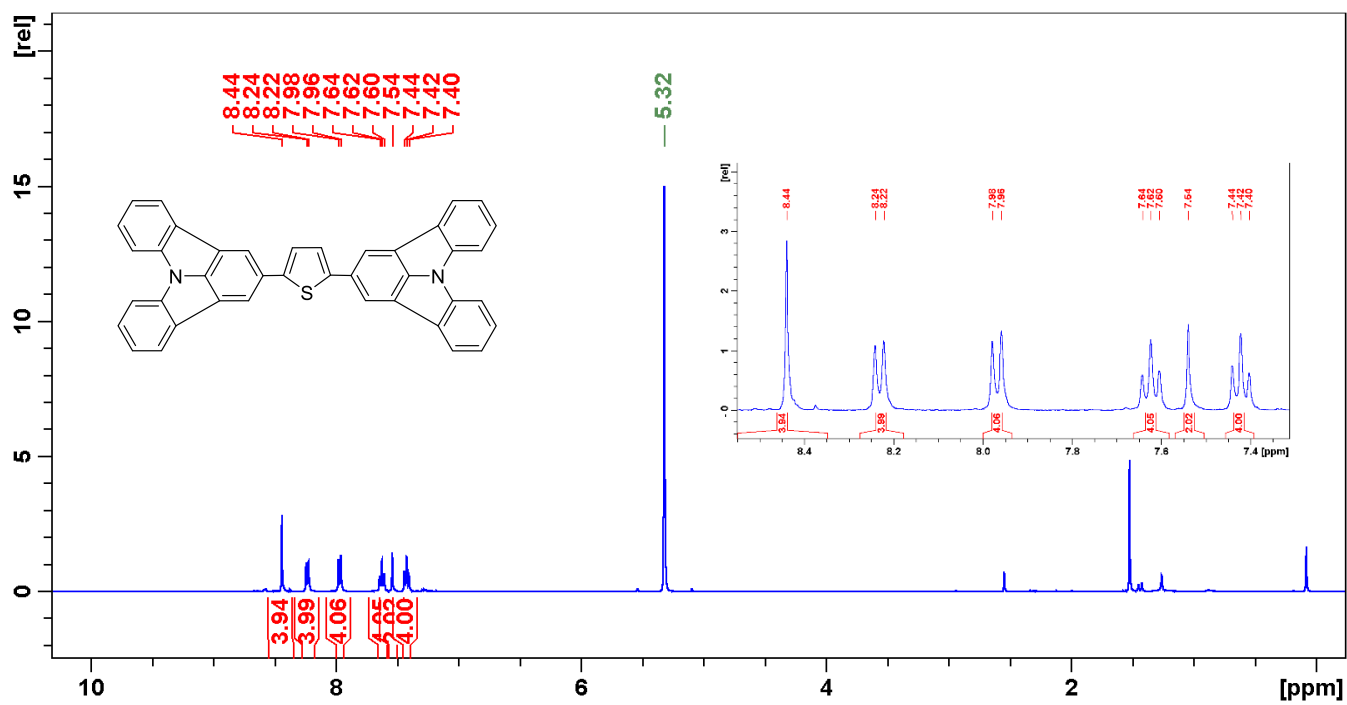


Figure S5. Proton NMR spectrum of compound 3Ai.

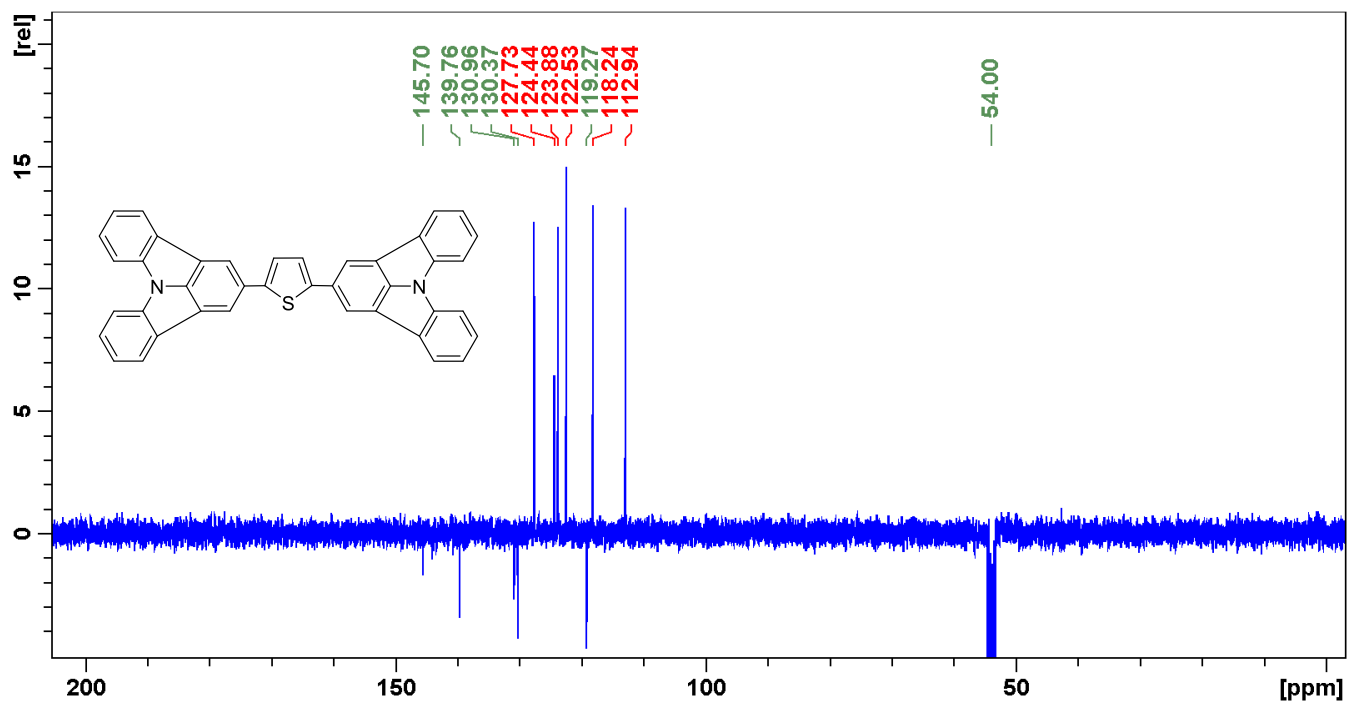


Figure S6. Carbon NMR spectrum of compound 3Ai.

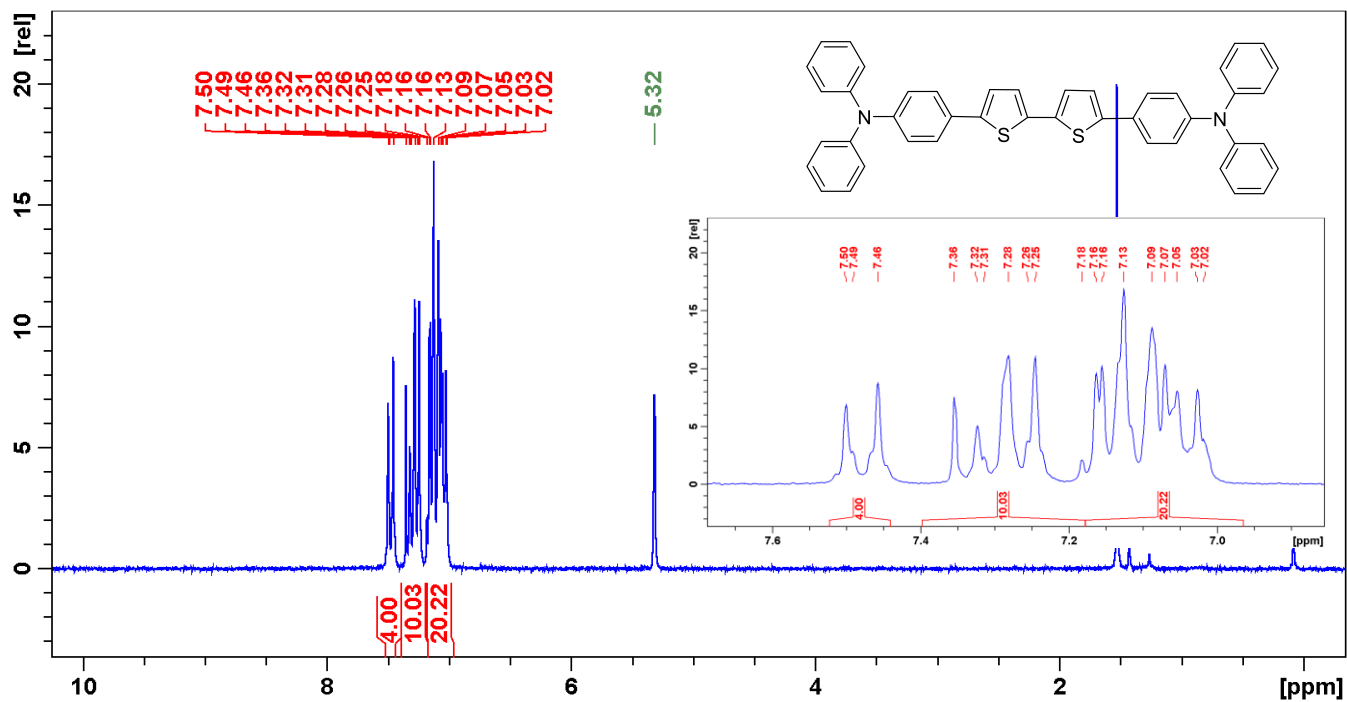


Figure S7. Proton NMR spectrum of compound 3Ba.

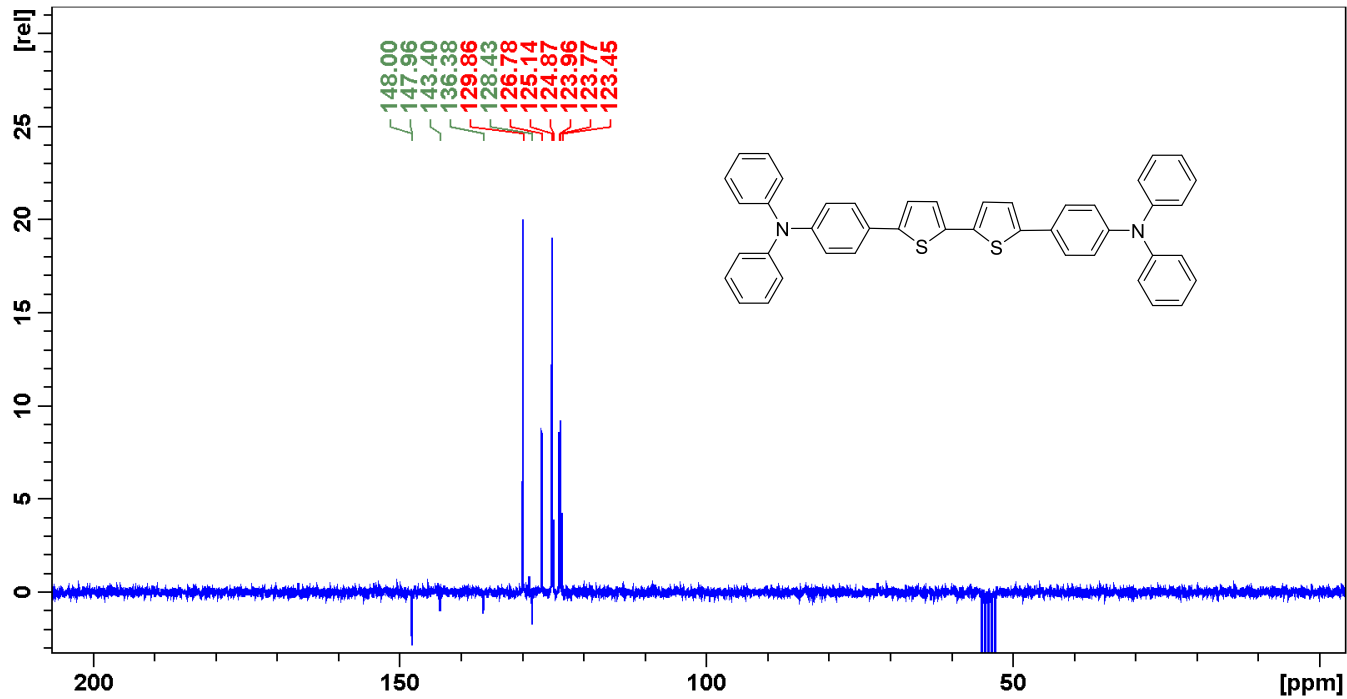


Figure S8. Carbon NMR spectrum of compound 3Ba.

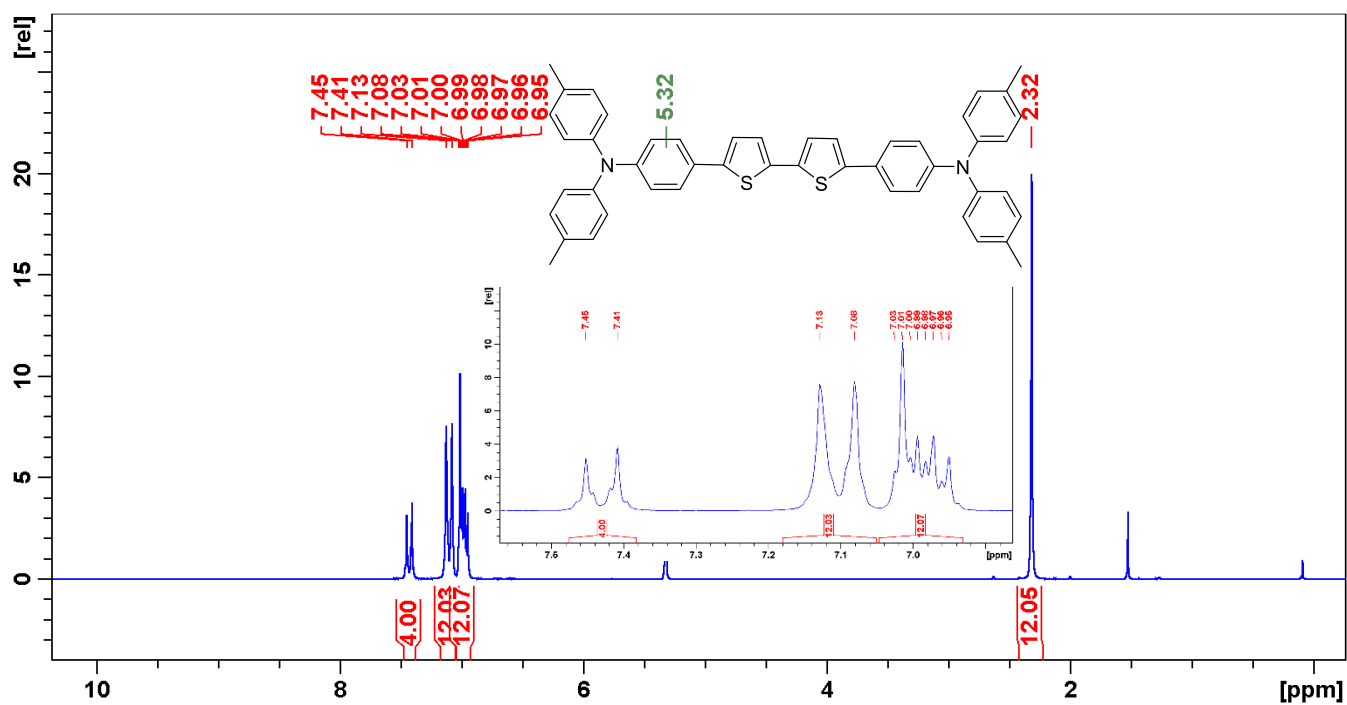


Figure S9. Proton NMR spectrum of compound 3Bb.

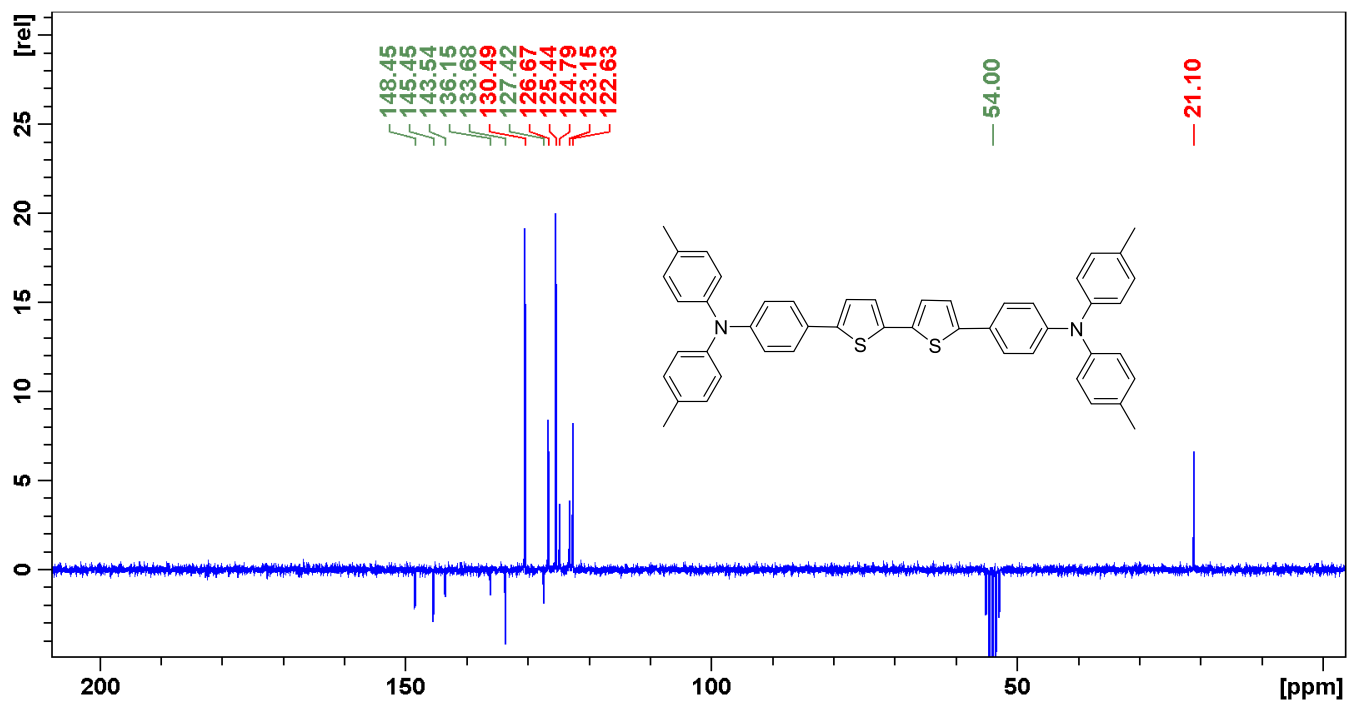


Figure S10. Carbon NMR spectrum of compound 3Bb.



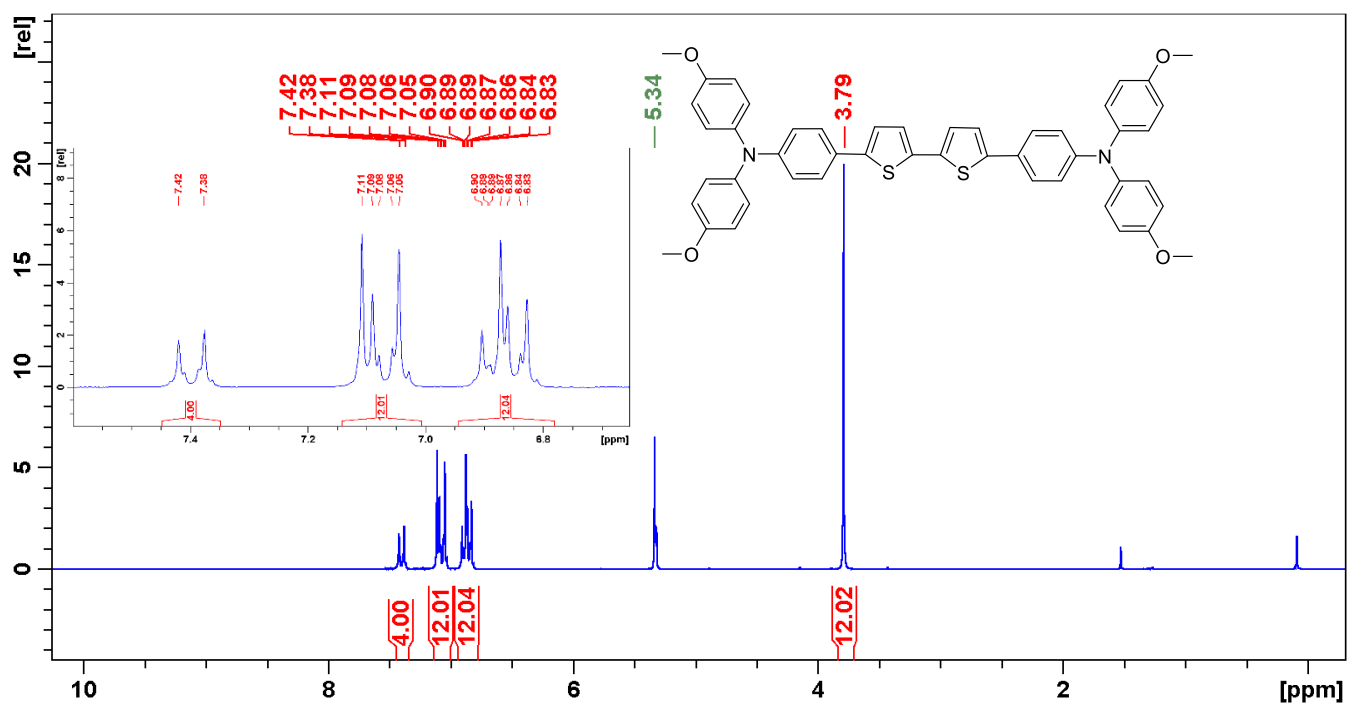


Figure S11. Proton NMR spectrum of compound 3Bc.

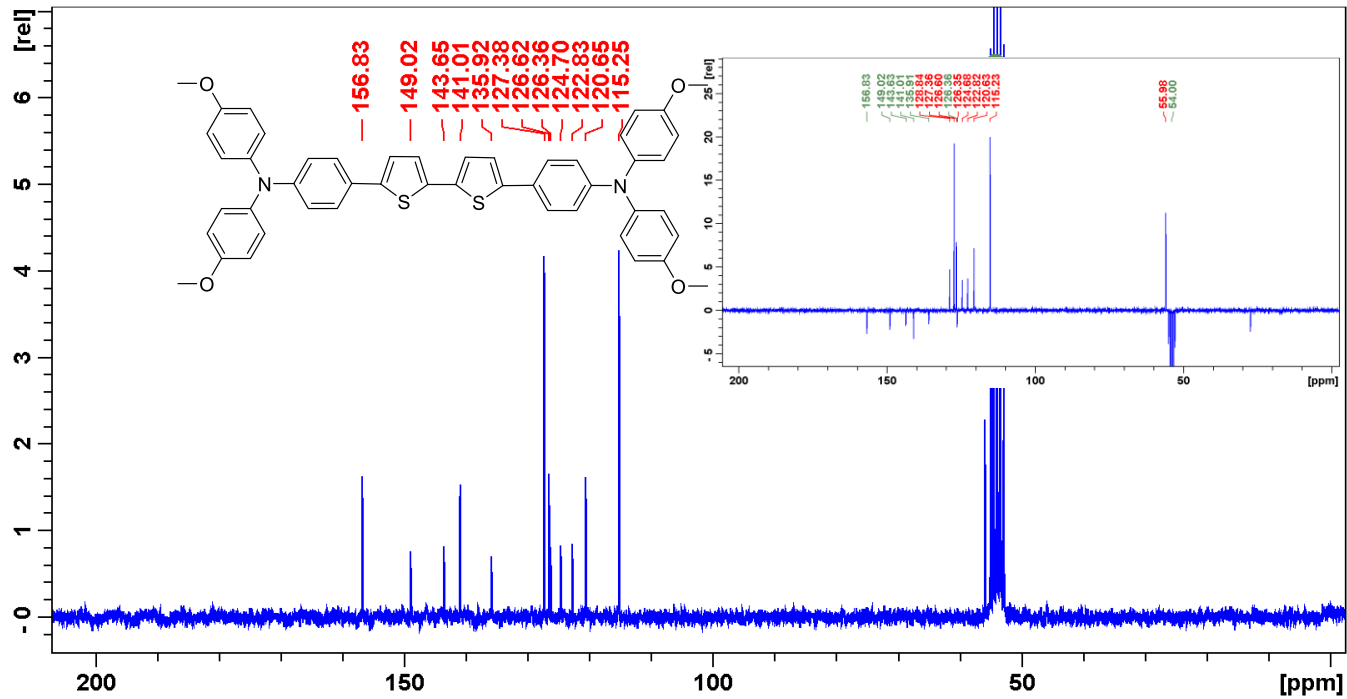


Figure S12. Carbon NMR spectrum of compound 3Bc.

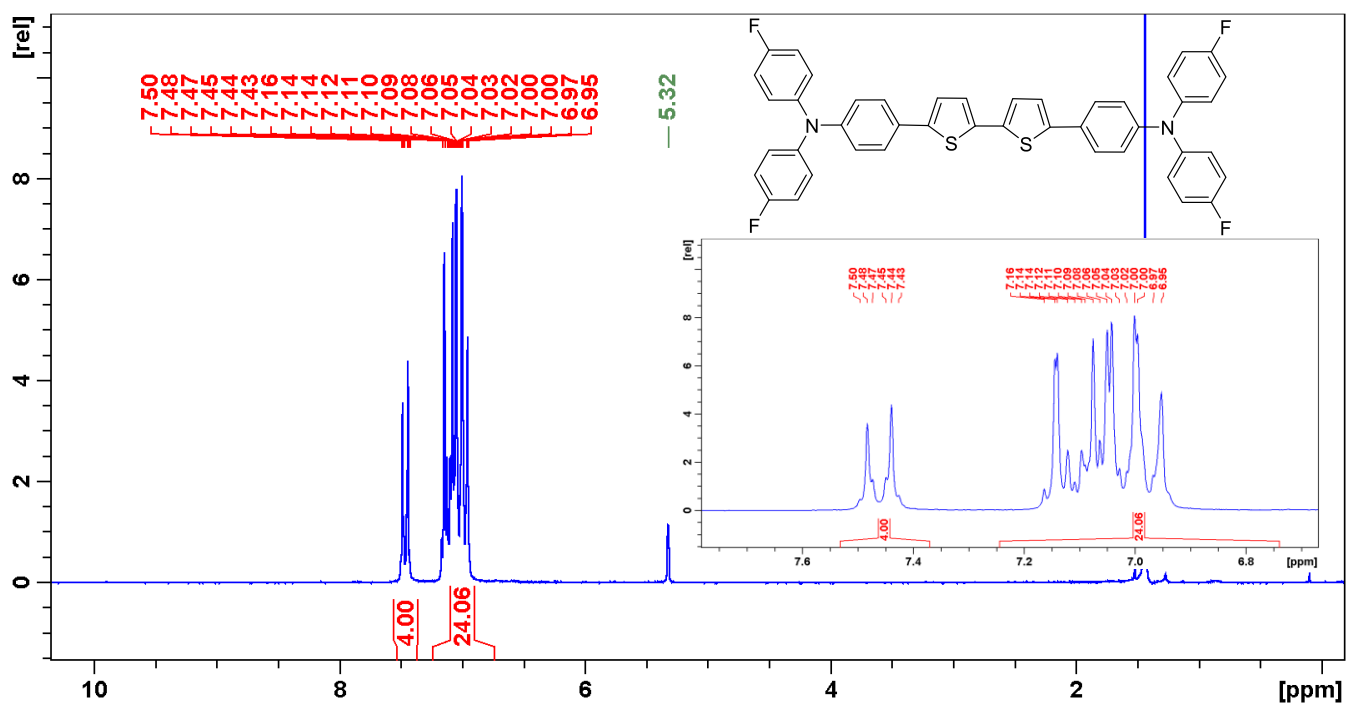


Figure S13. Proton NMR spectrum of compound 3Bd.

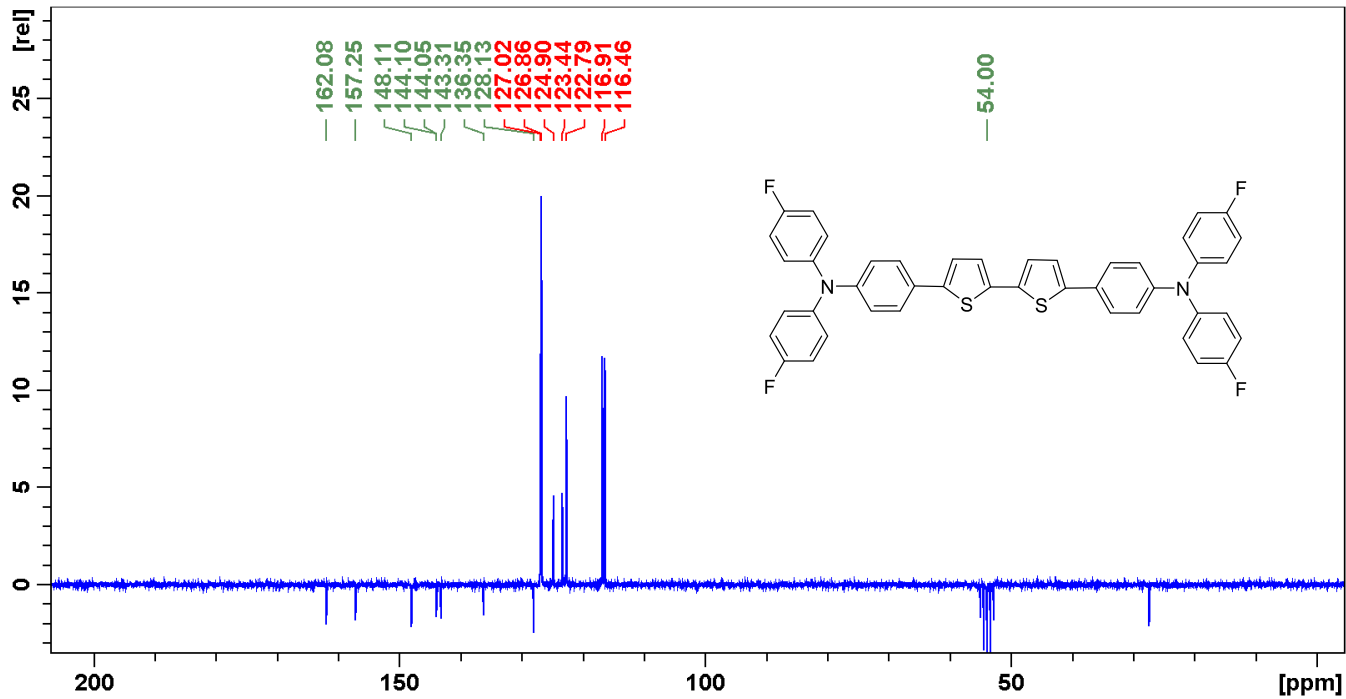


Figure S14. Carbon NMR spectrum of compound 3Bd.

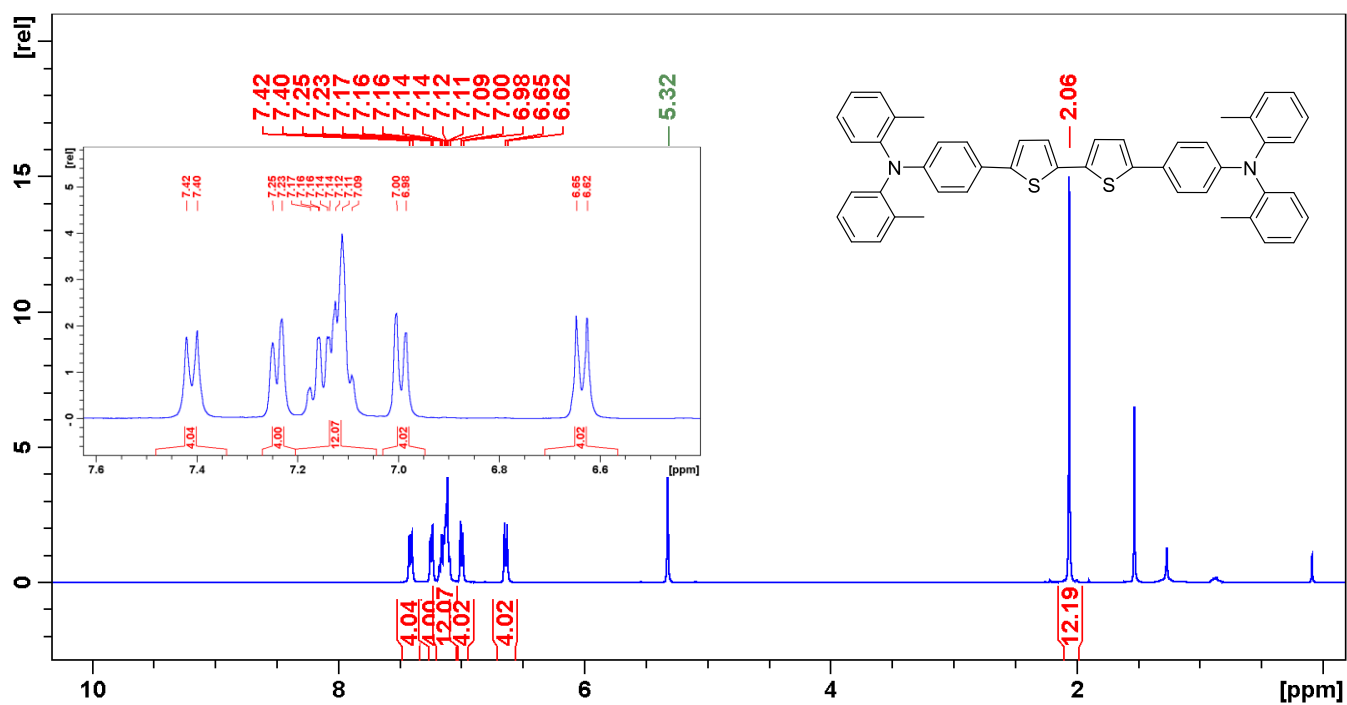


Figure S15. Proton NMR spectrum of compound 3Be.

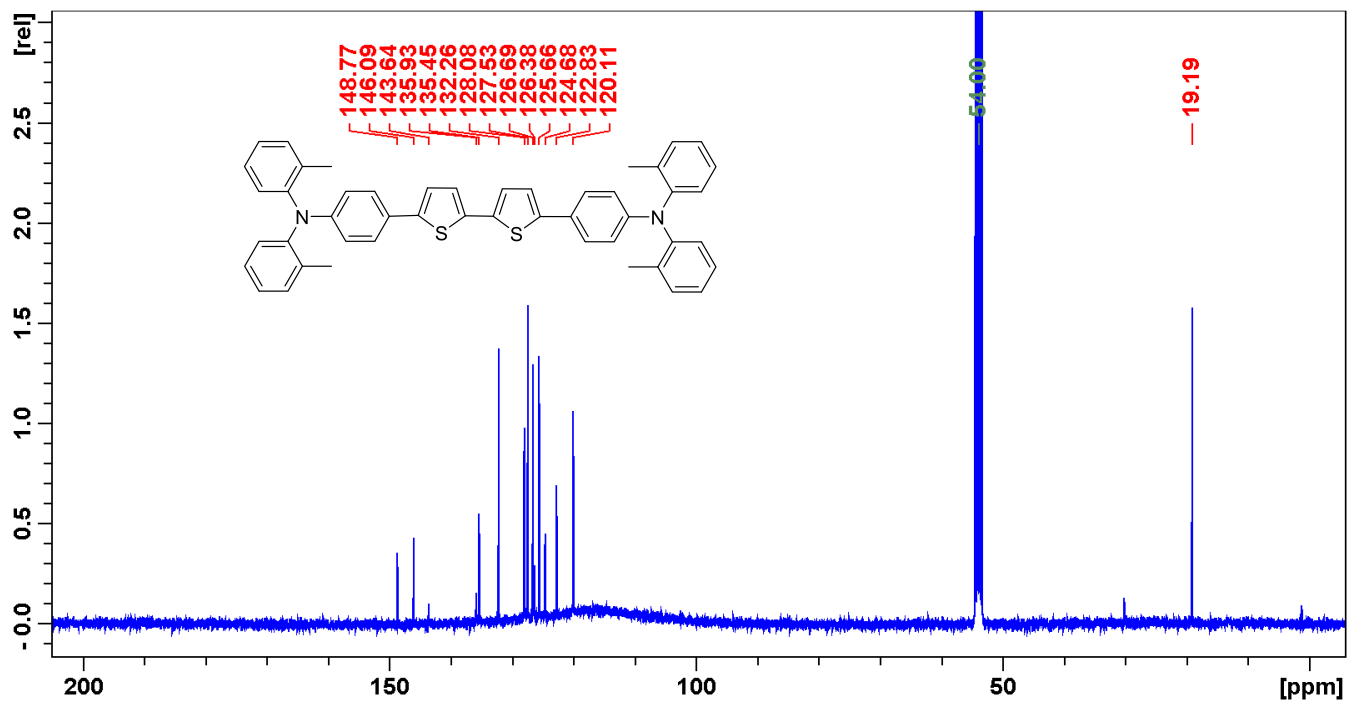


Figure S16. Carbon NMR spectrum of compound 3Be.

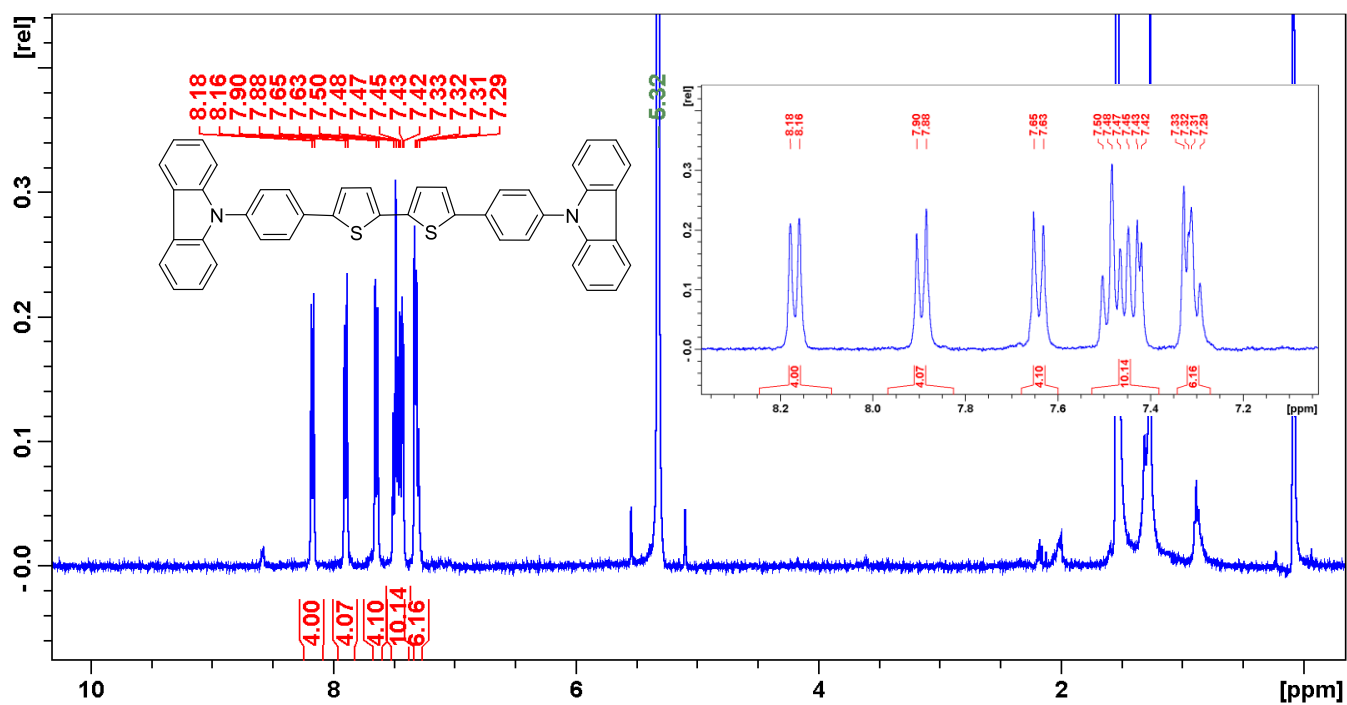


Figure S17. Proton NMR spectrum of compound 3Bh.

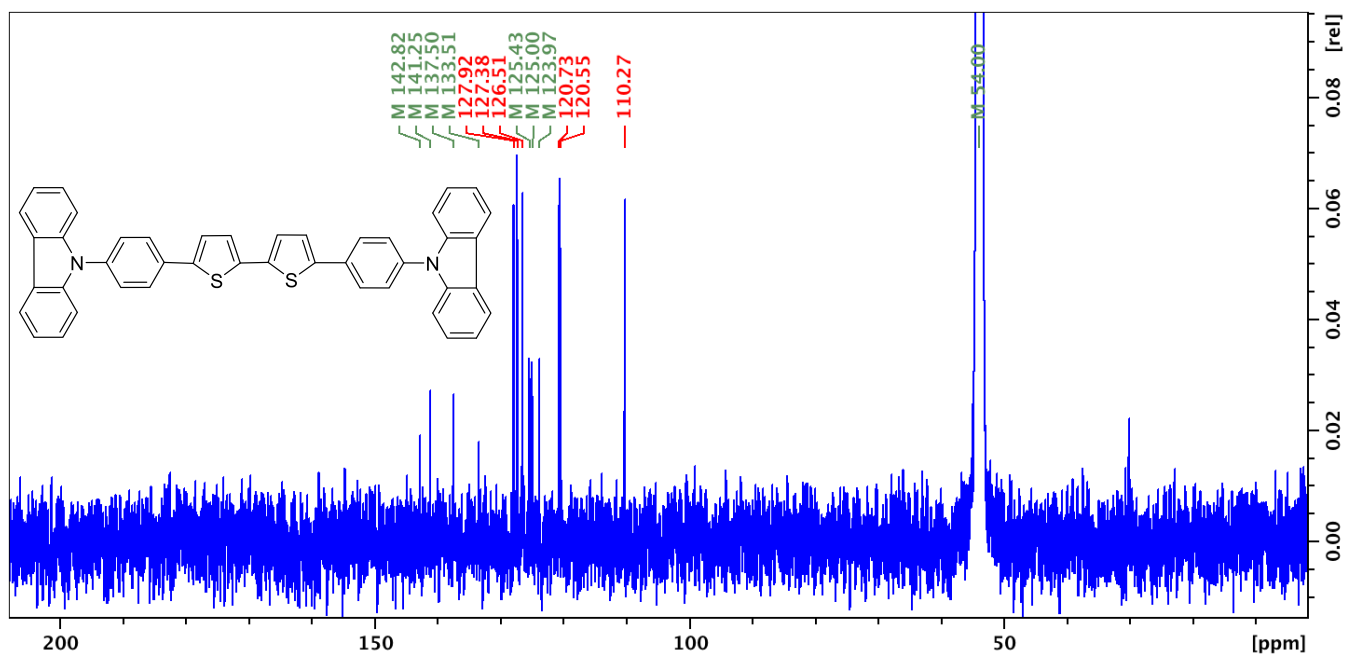


Figure S18. Carbon NMR spectrum of compound 3Bh.

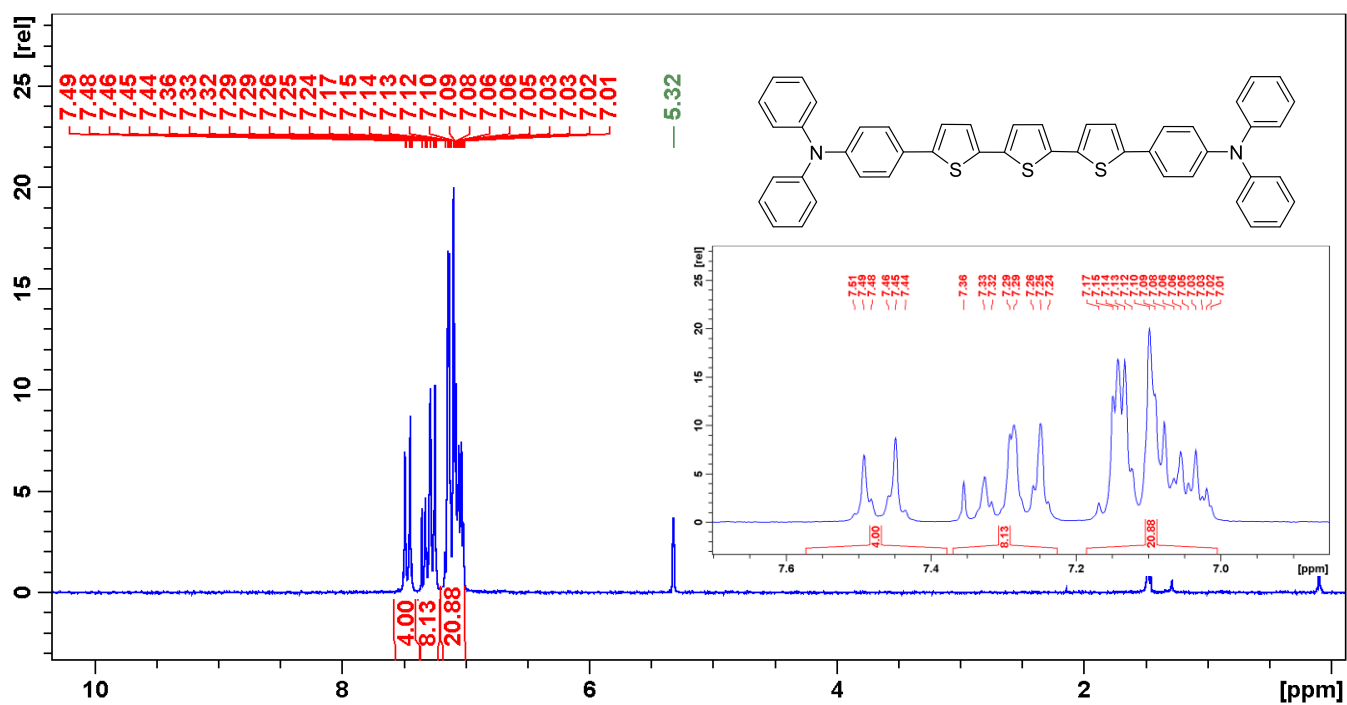


Figure S19. Proton NMR spectrum of compound 3Ca.

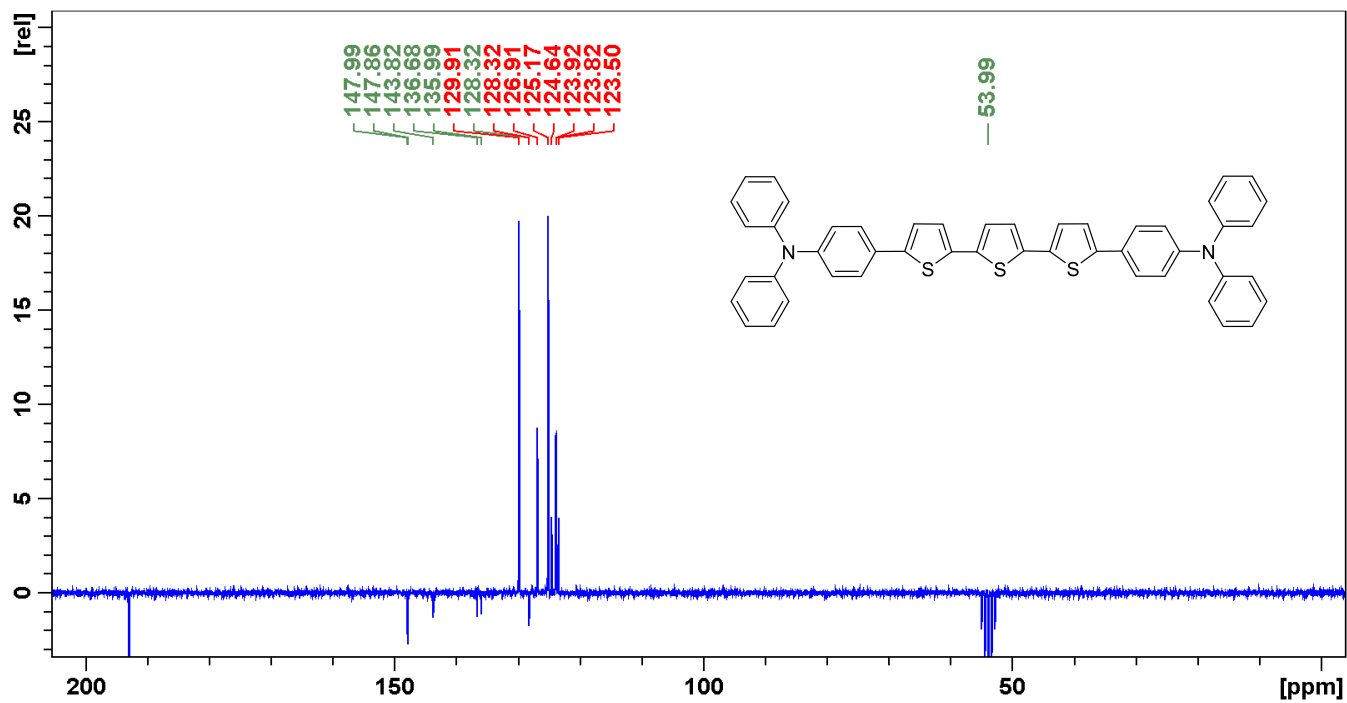


Figure S20. Carbon NMR spectrum of compound 3Ca.

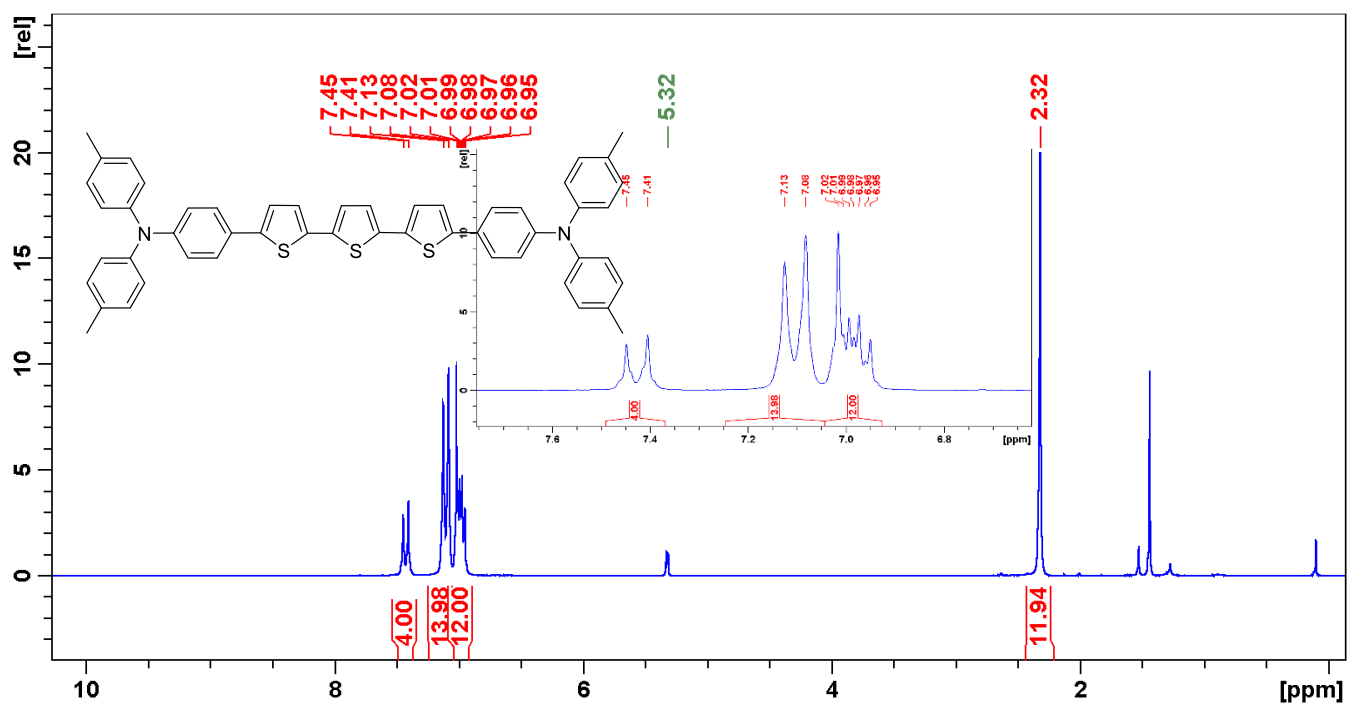


Figure S21. Proton NMR spectrum of compound 3Cb.

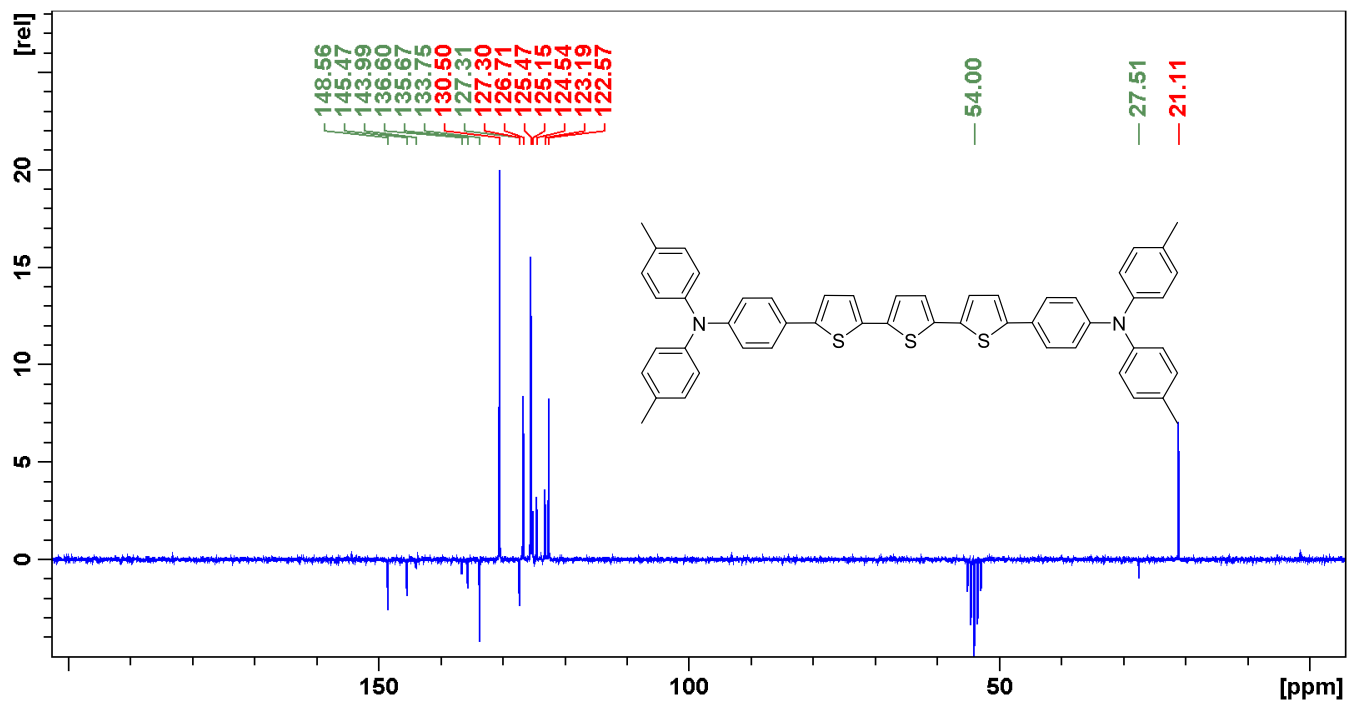


Figure S22. Carbon NMR spectrum of compound 3Cb.

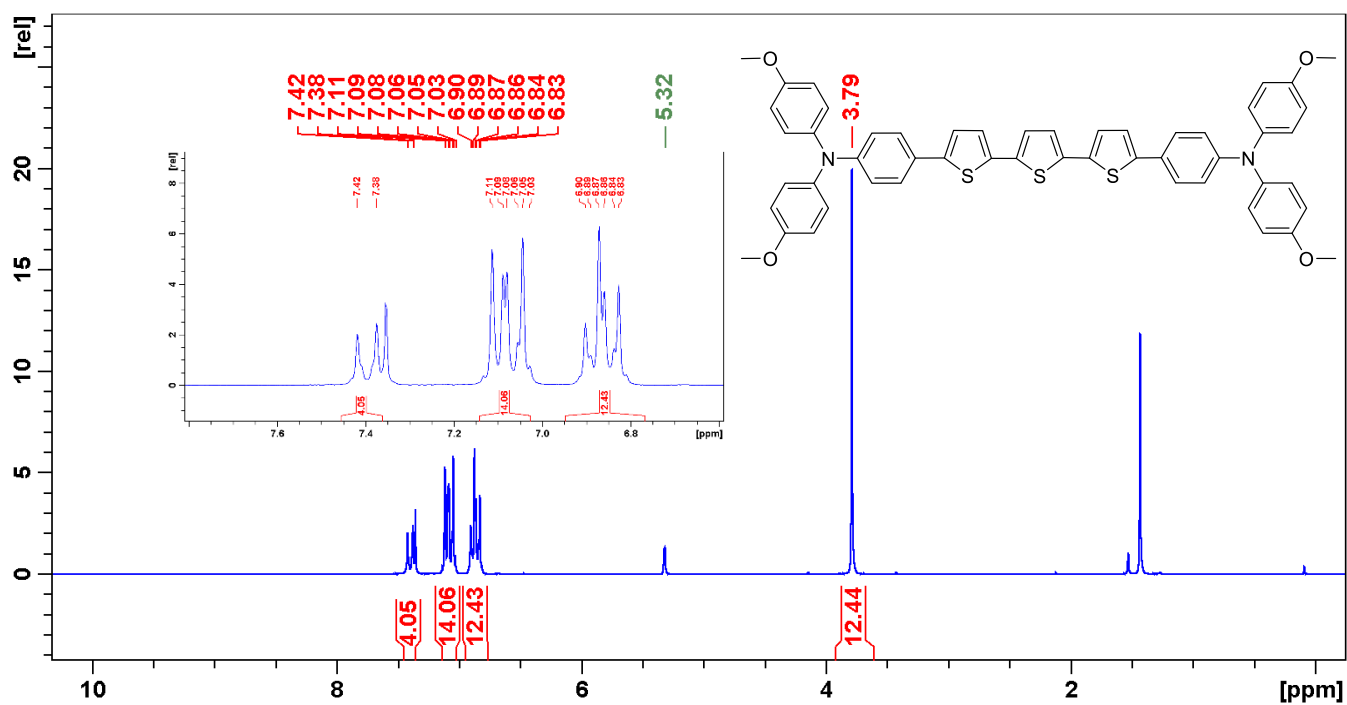


Figure S23. Proton NMR spectrum of compound 3Cc.

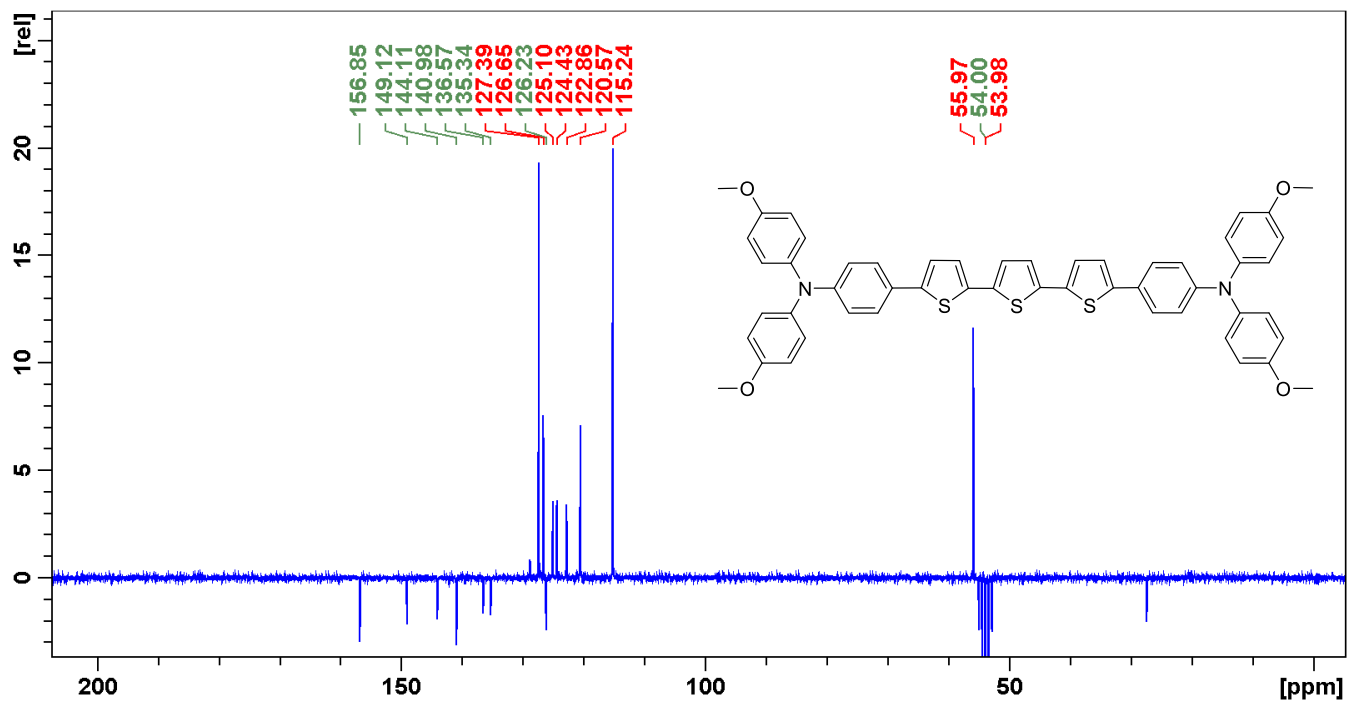


Figure S24. Carbon NMR spectrum of compound 3Cc.

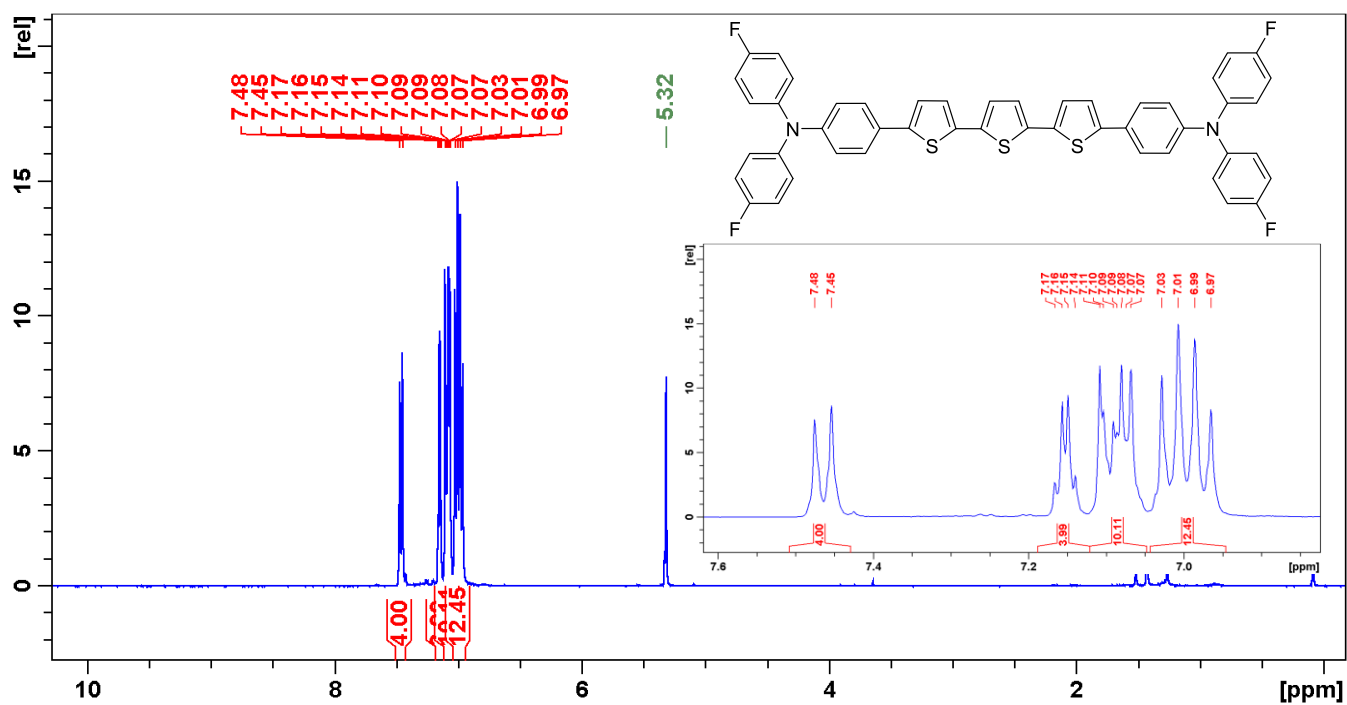


Figure S25. Proton NMR spectrum of compound 3Cd.

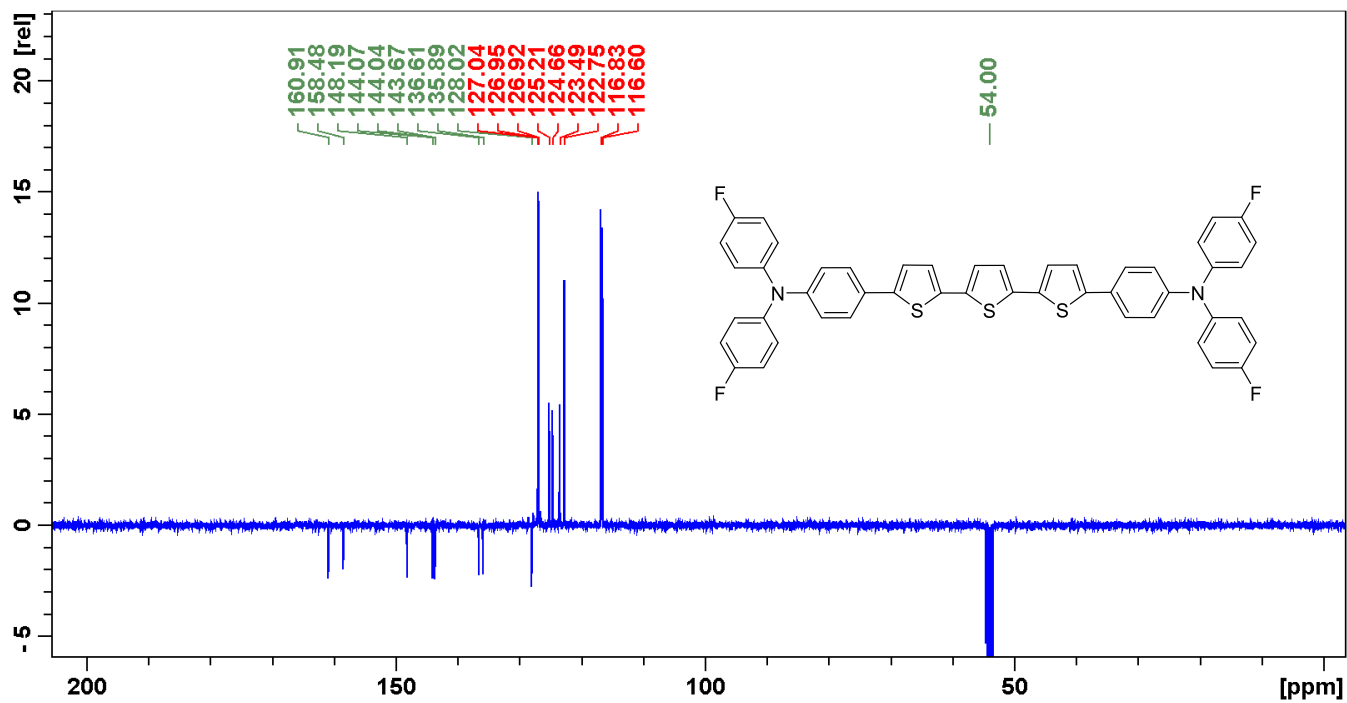


Figure S26. Carbon NMR spectrum of compound 3Cd.



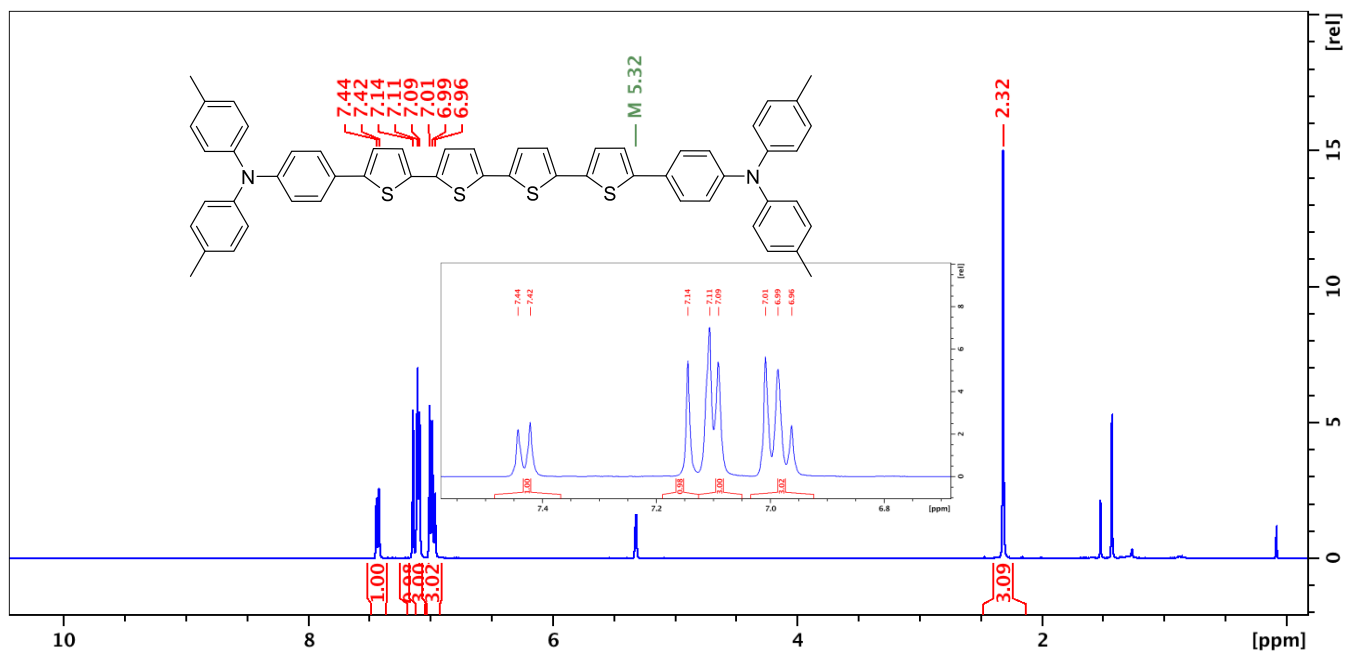


Figure S27. Proton NMR spectrum of compound 3Db.

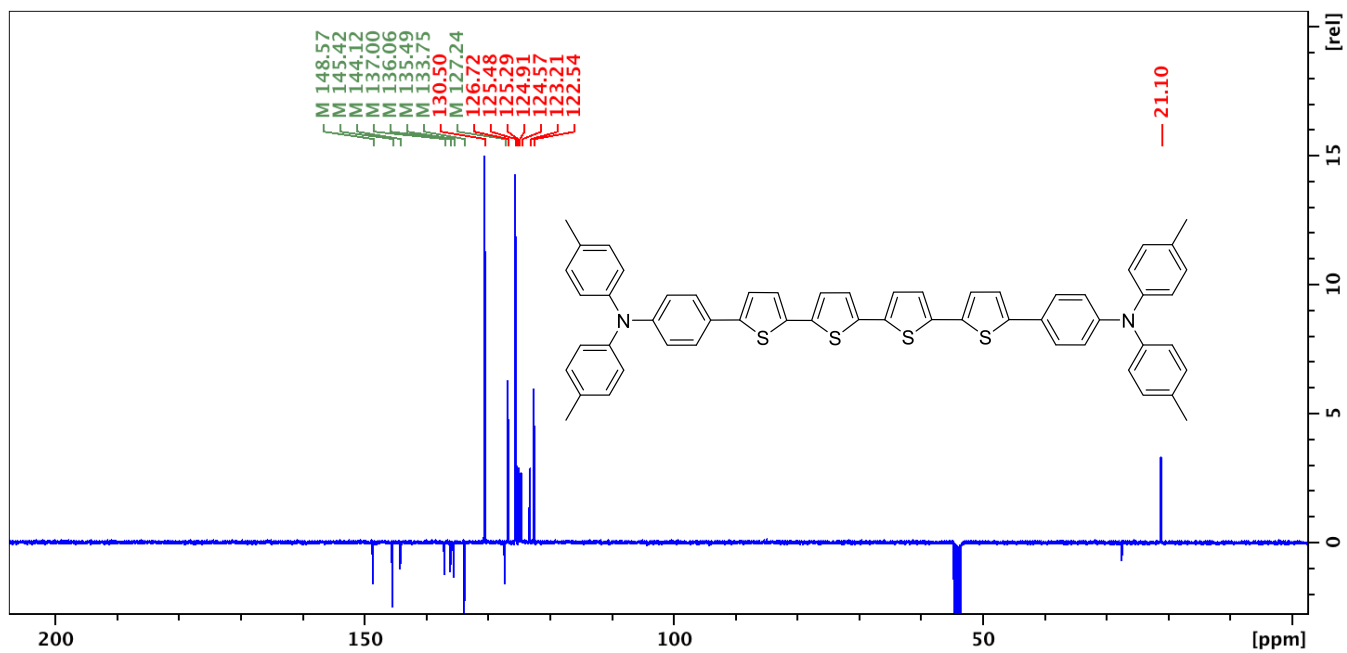


Figure S28. Carbon NMR spectrum of compound 3Db.

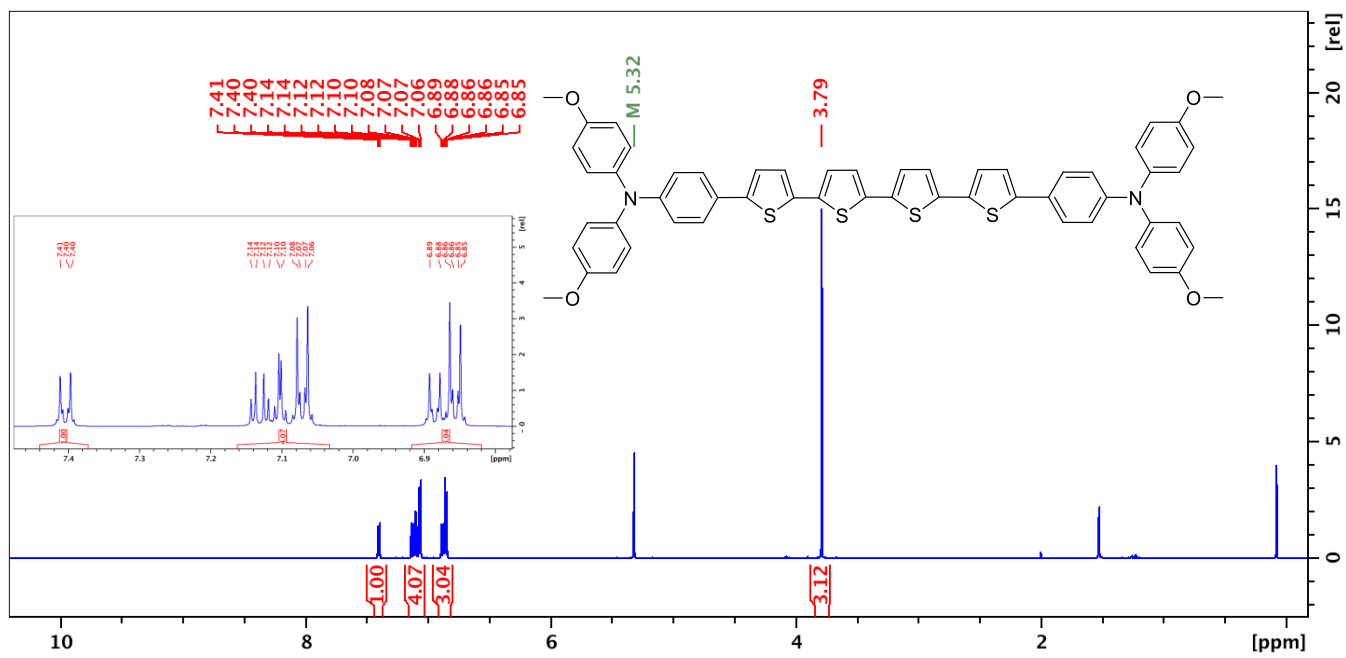


Figure S29. Proton NMR spectrum of compound **3Dc**.

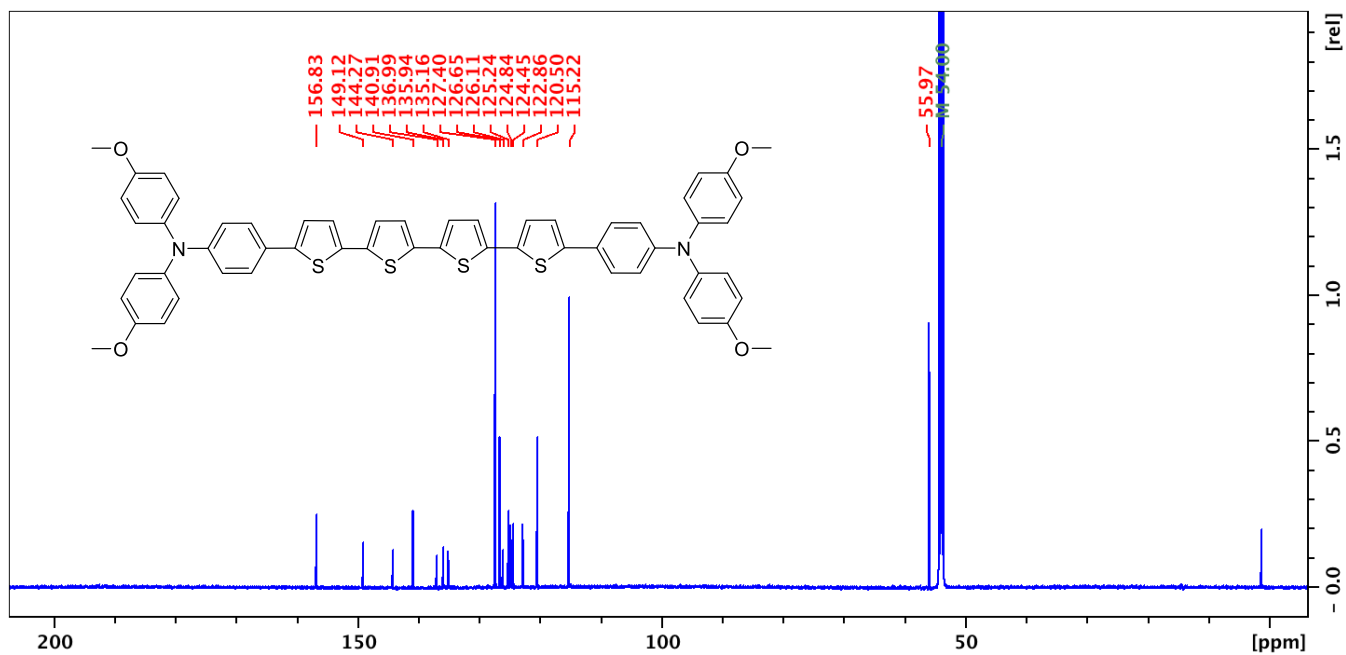


Figure S30. Carbon NMR spectrum of compound **3Dc**.

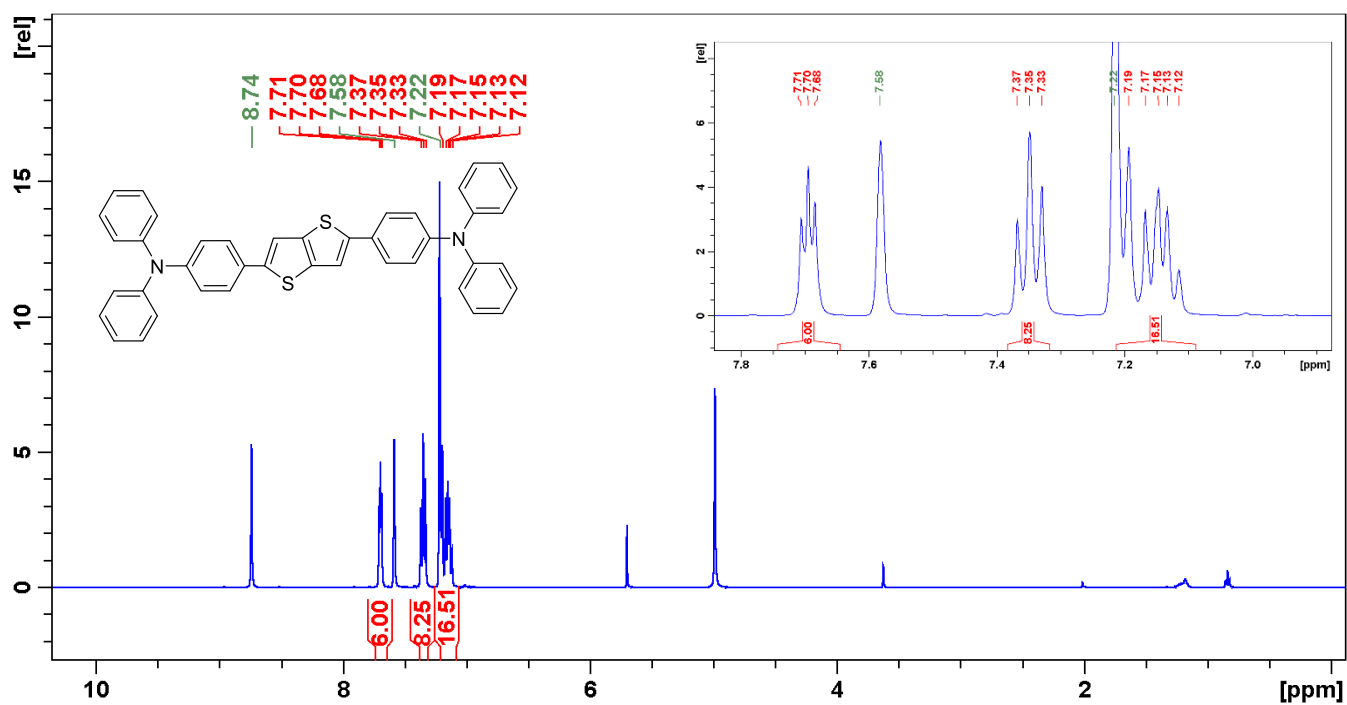


Figure S31. Proton NMR spectrum of compound 3Ea.

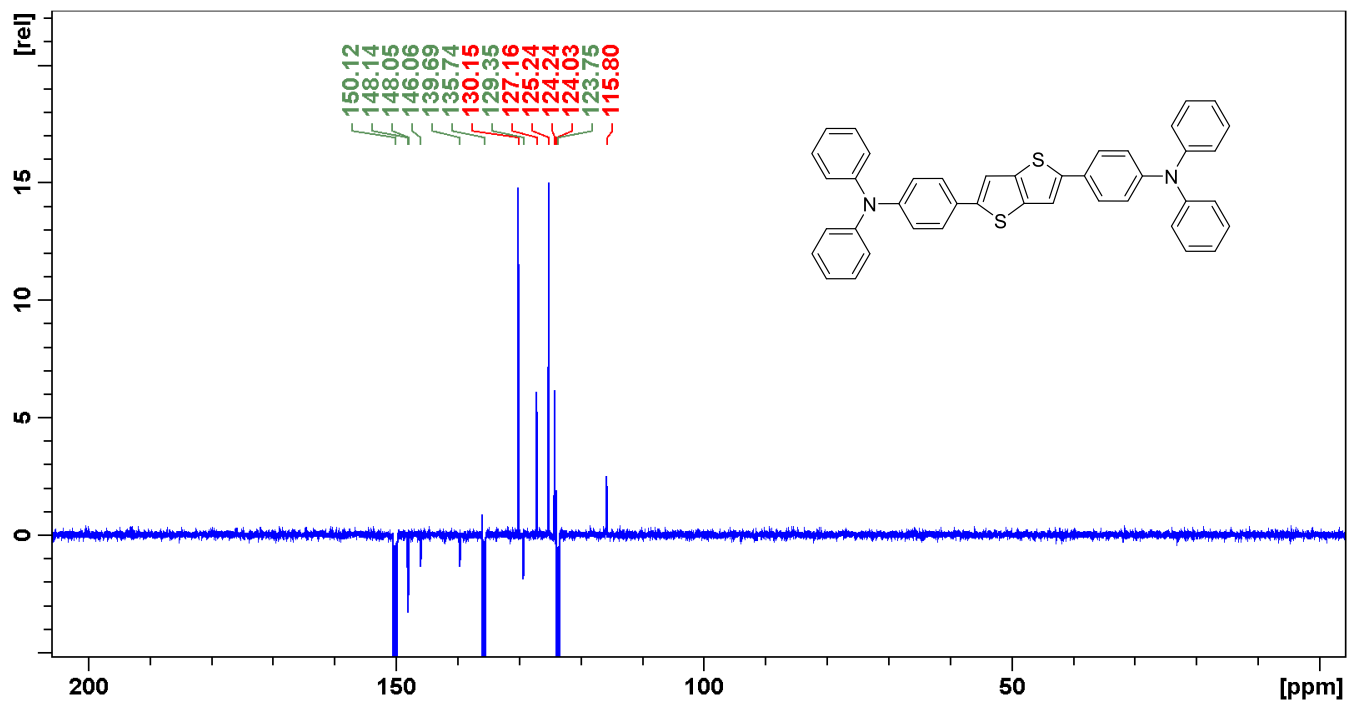


Figure S32. Carbon NMR spectrum of compound 3Ea.

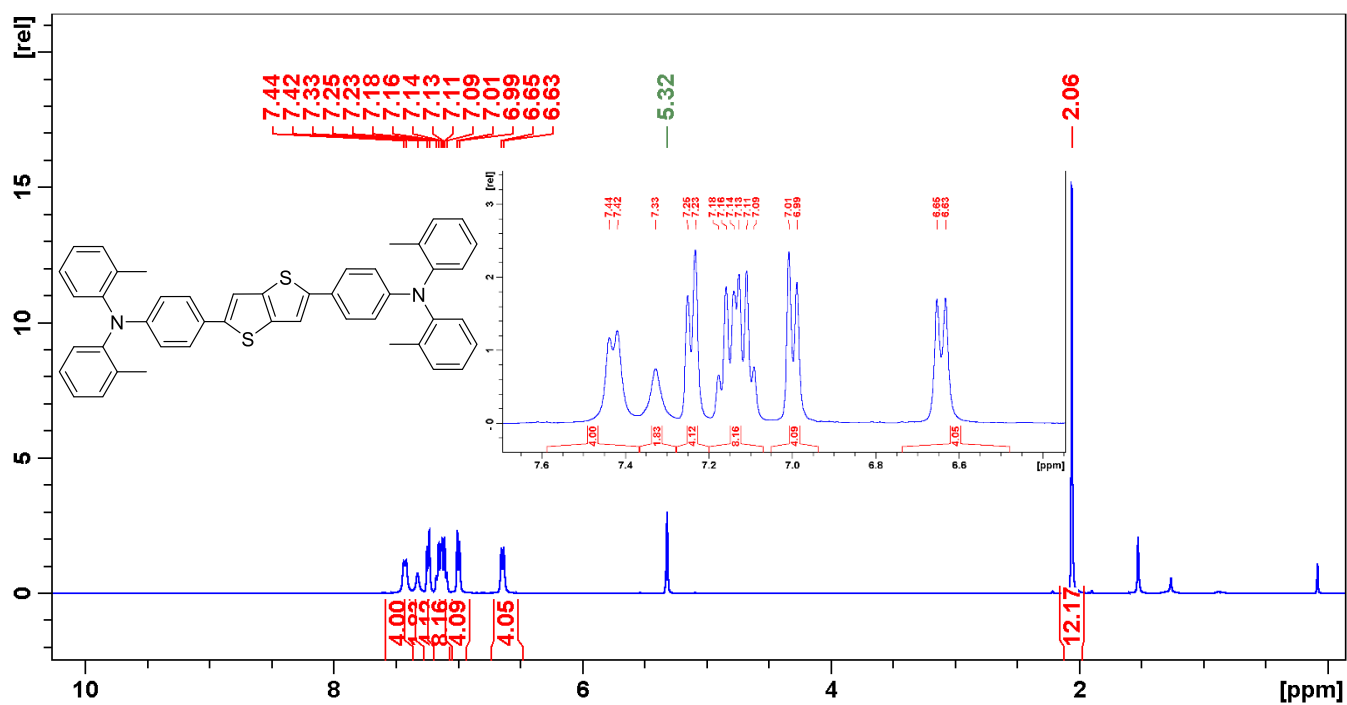


Figure S33. Proton NMR spectrum of compound 3Ee.

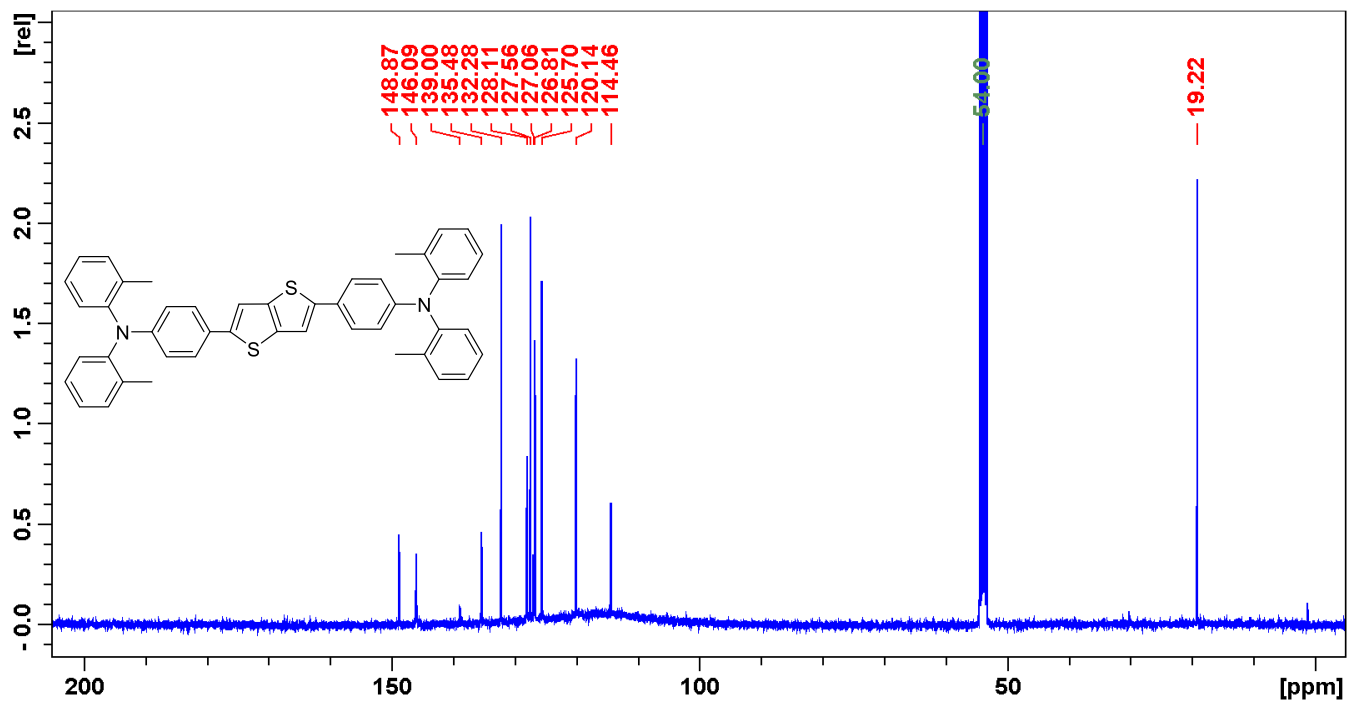


Figure S34. Carbon NMR spectrum of compound 3Ee.

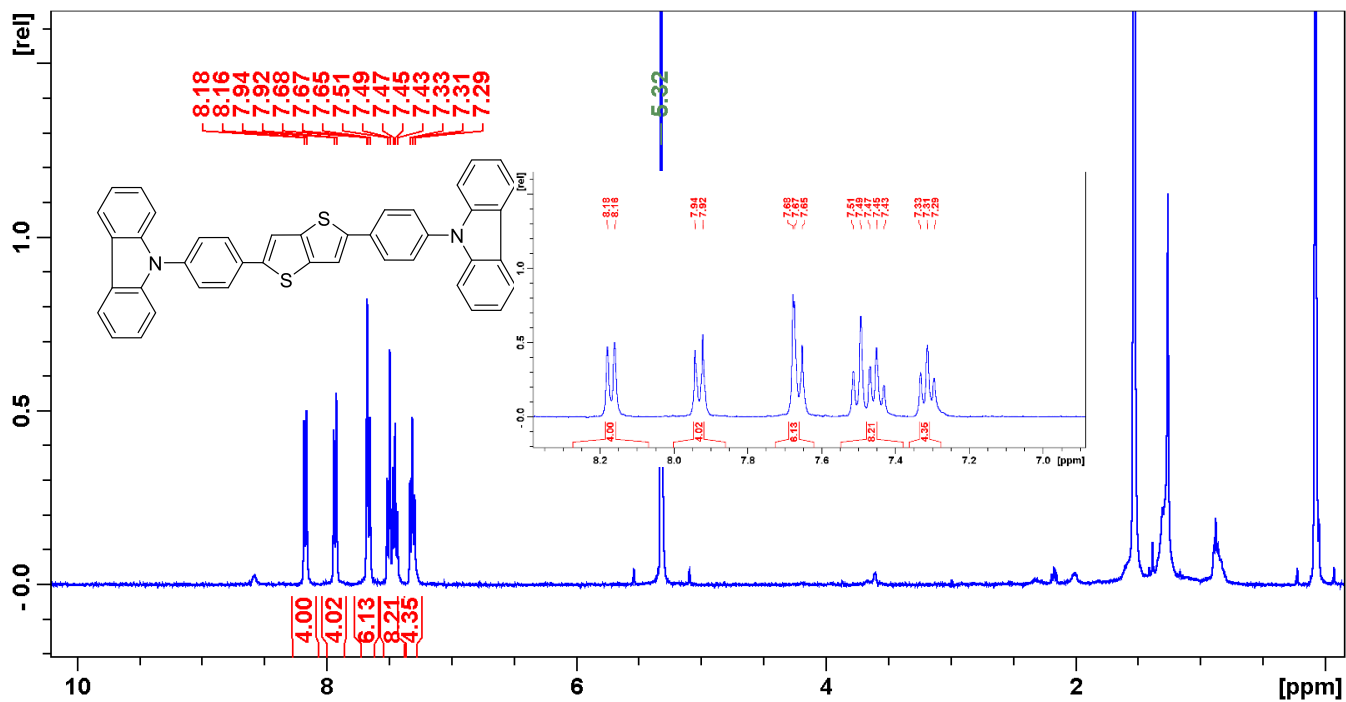


Figure S35. Proton NMR spectrum of compound 3Eh.

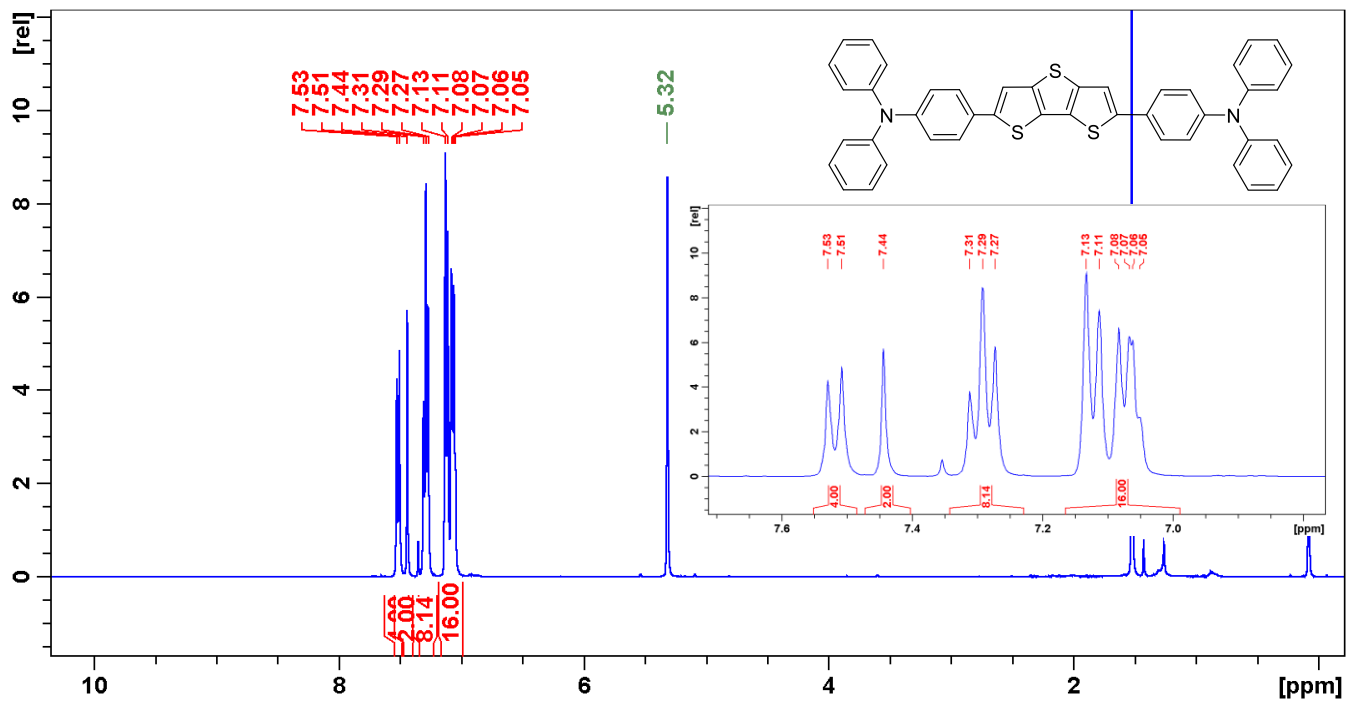


Figure S36. Proton NMR spectrum of compound 3Fa.

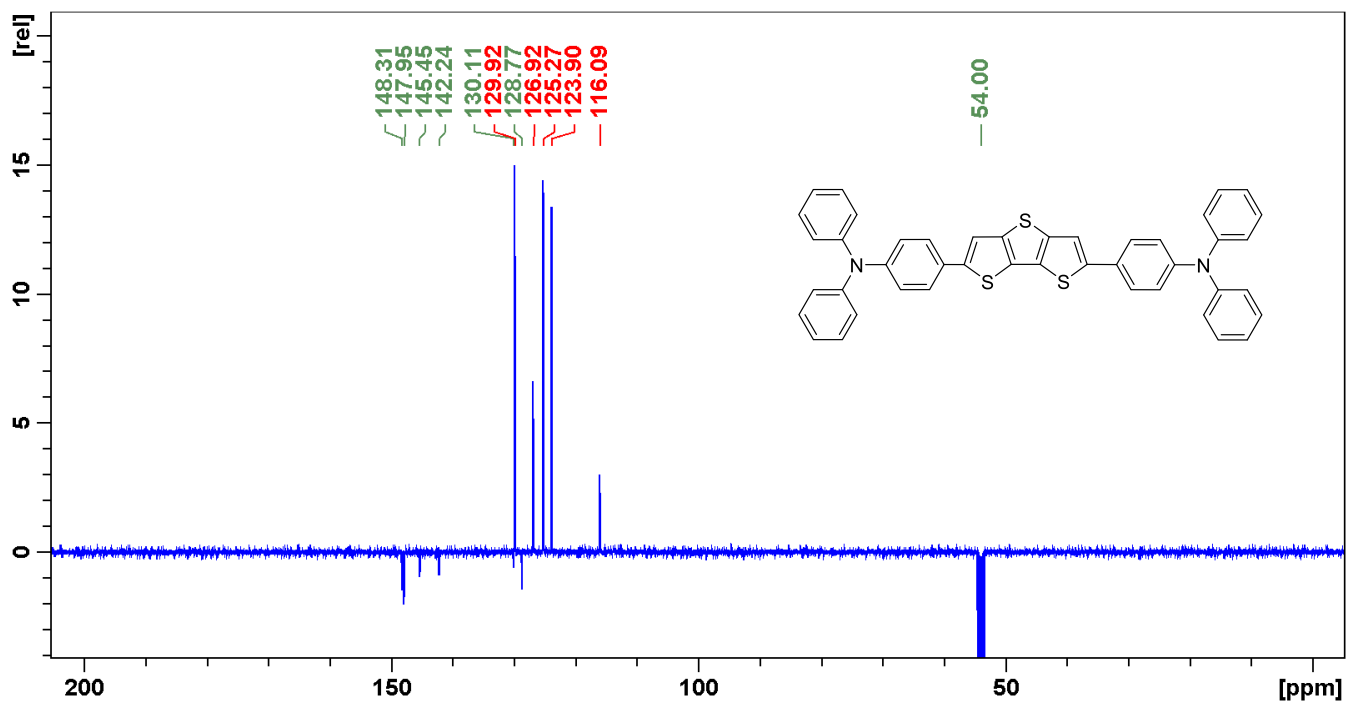


Figure S37. Carbon NMR spectrum of compound 3Fa.

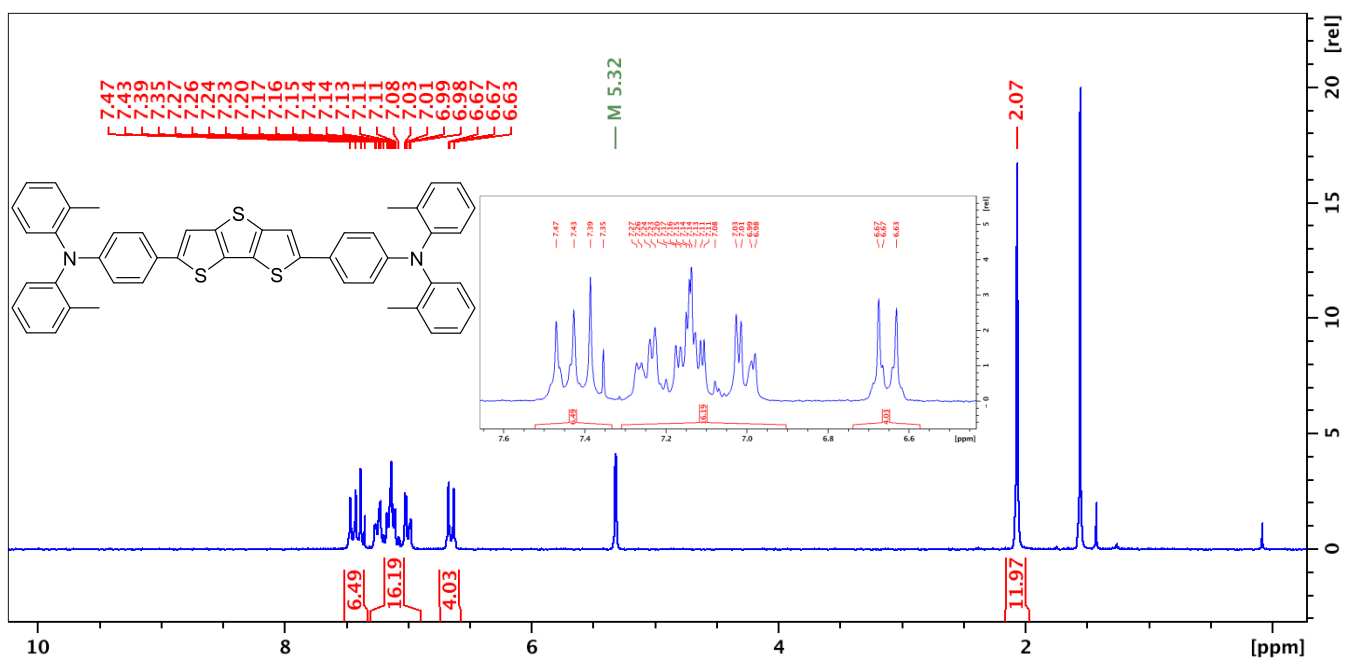


Figure S38. Proton NMR spectrum of compound 3Fe.

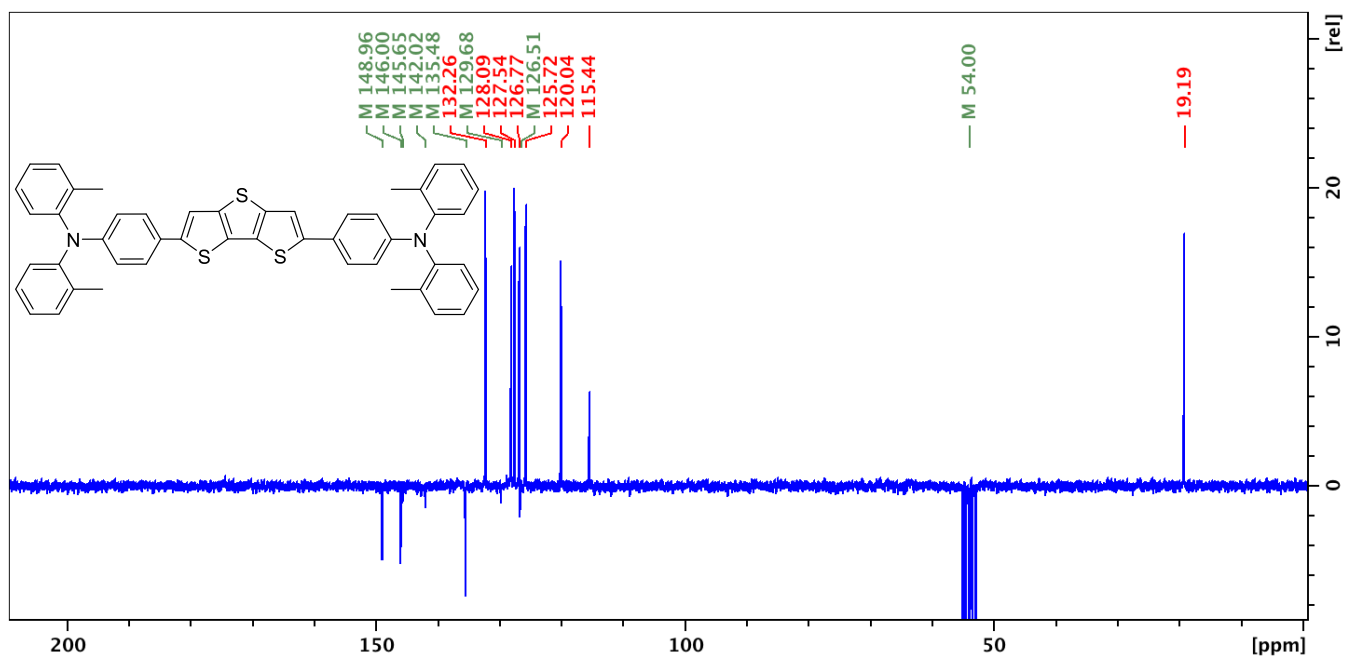


Figure S39. Carbon NMR spectrum of compound 3Fe.

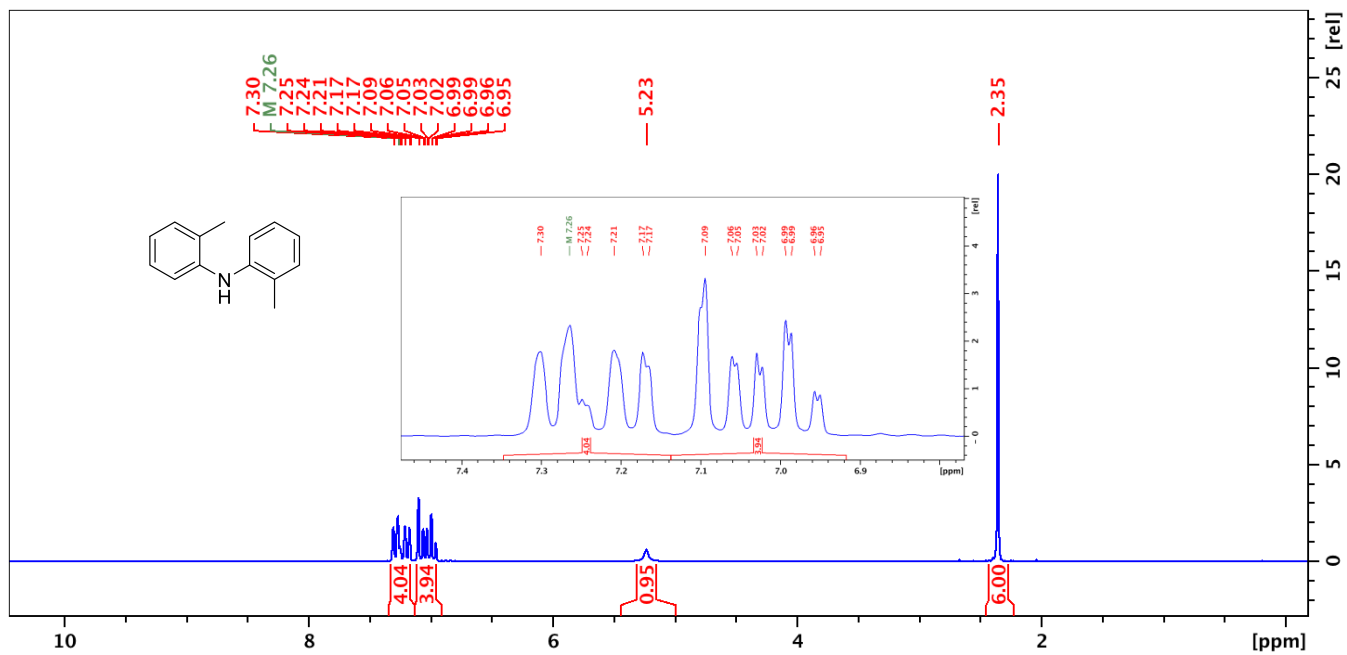


Figure S40. Proton NMR spectrum of compound 4.

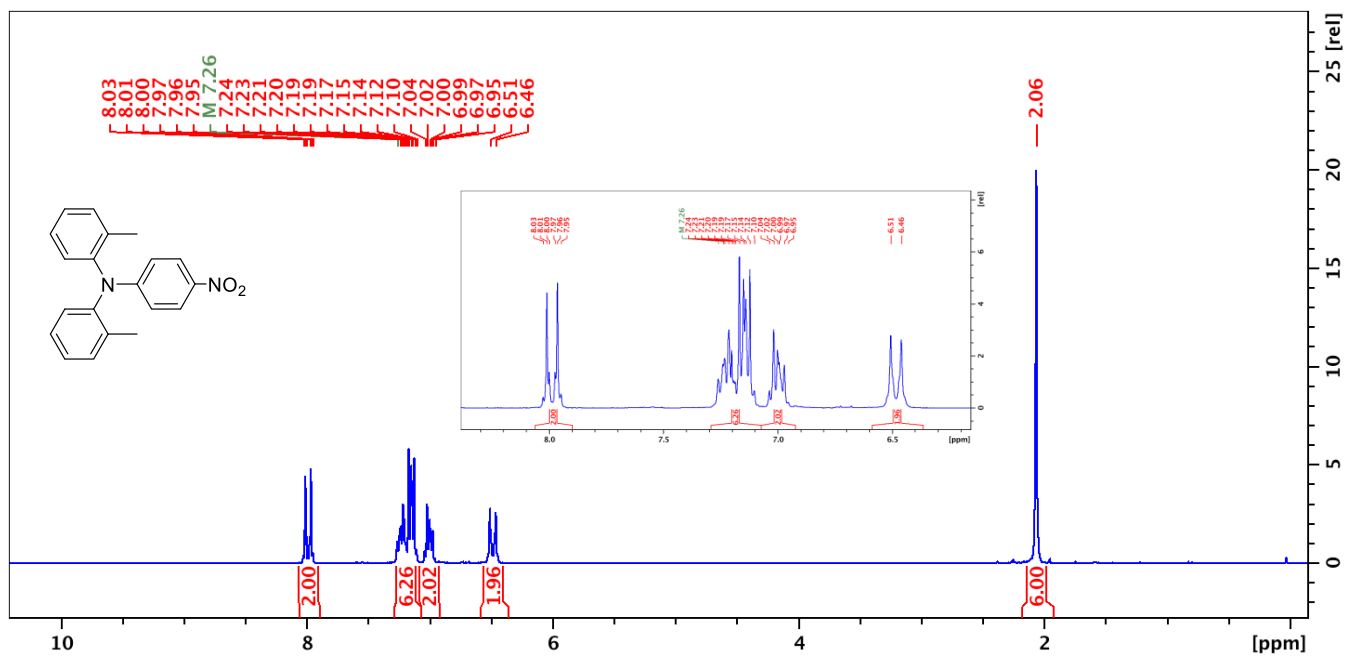


Figure S41. Proton NMR spectrum of compound **5b**.

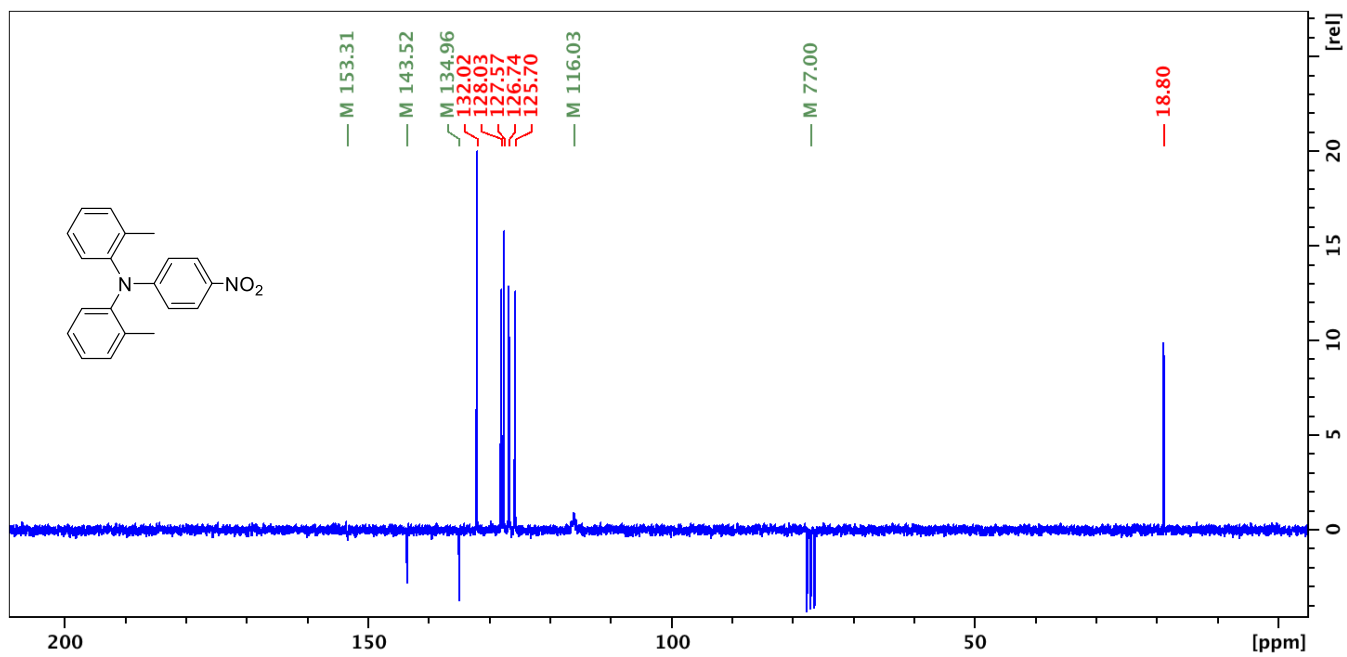


Figure S42. Carbon NMR spectrum of compound **5b**.



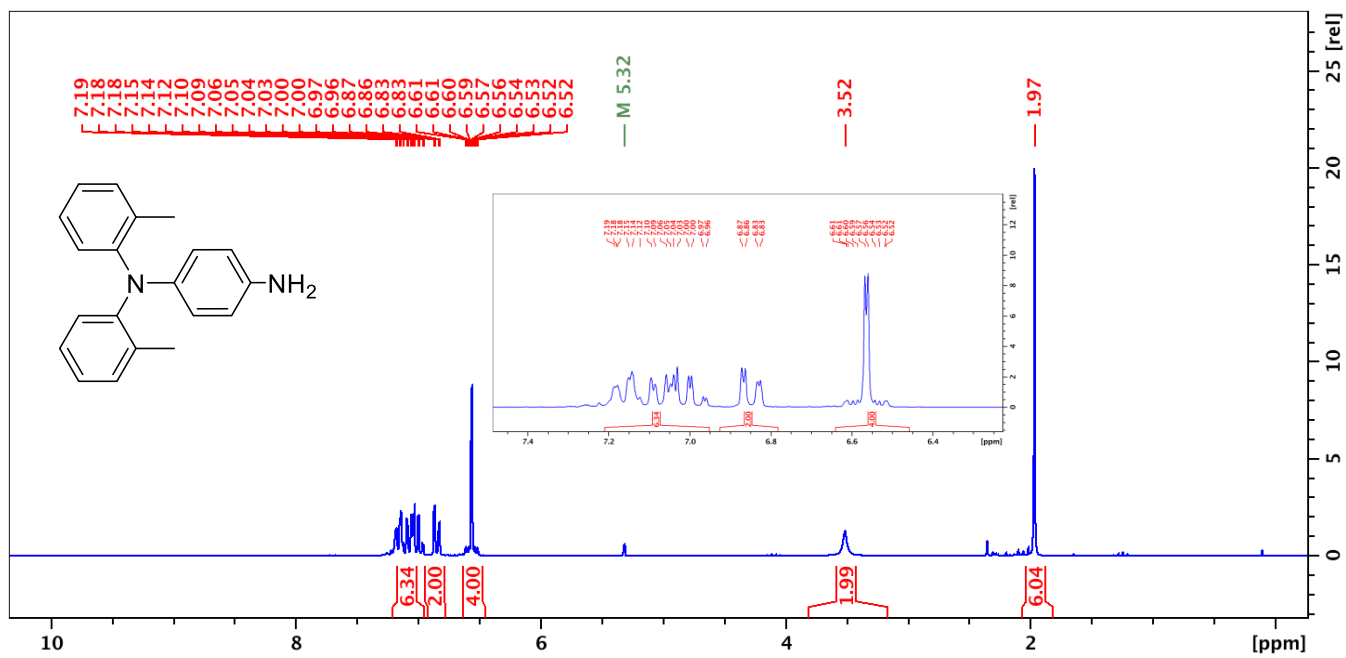


Figure S43. Proton NMR spectrum of compound 6.

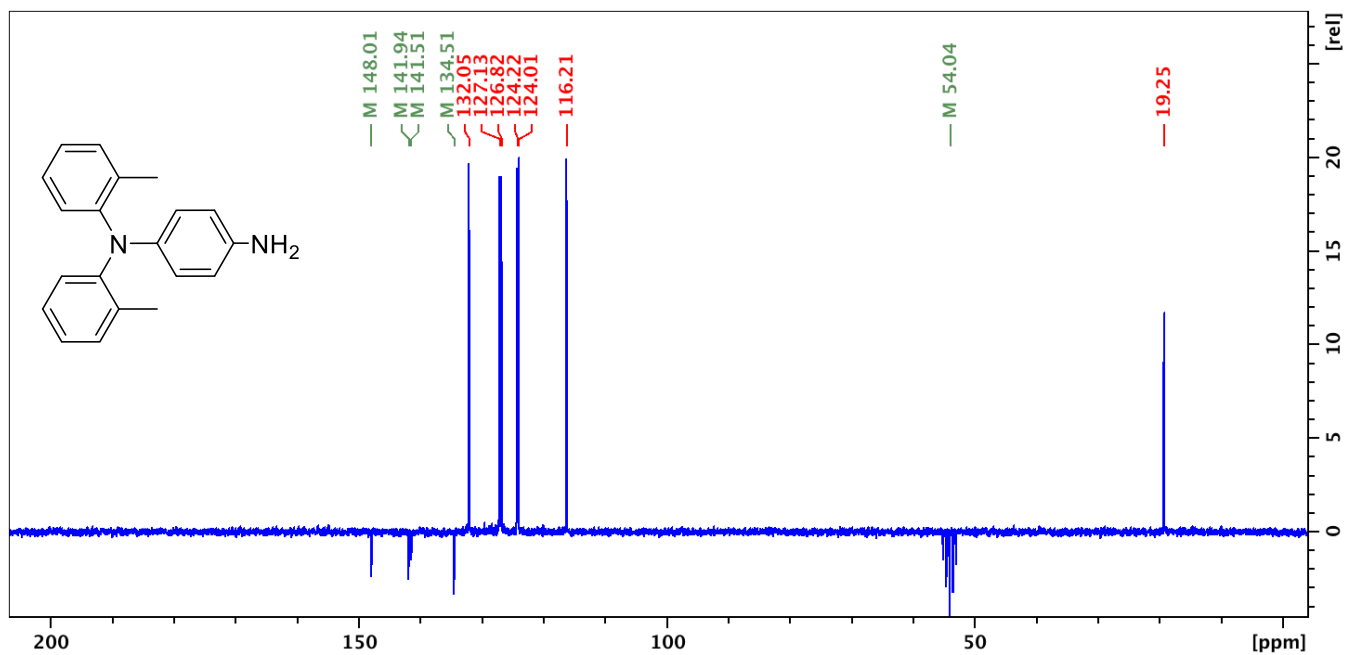


Figure S44. Carbon NMR spectrum of compound 6.

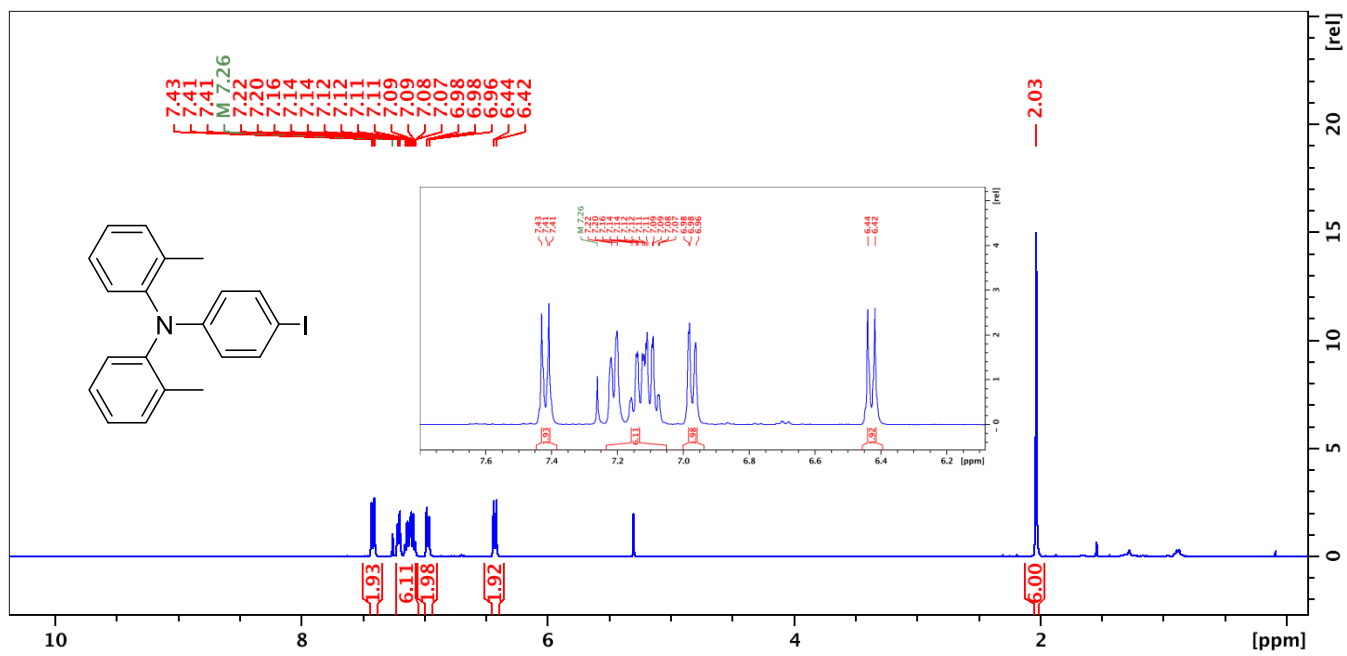


Figure S45. Proton NMR spectrum of compound 7.

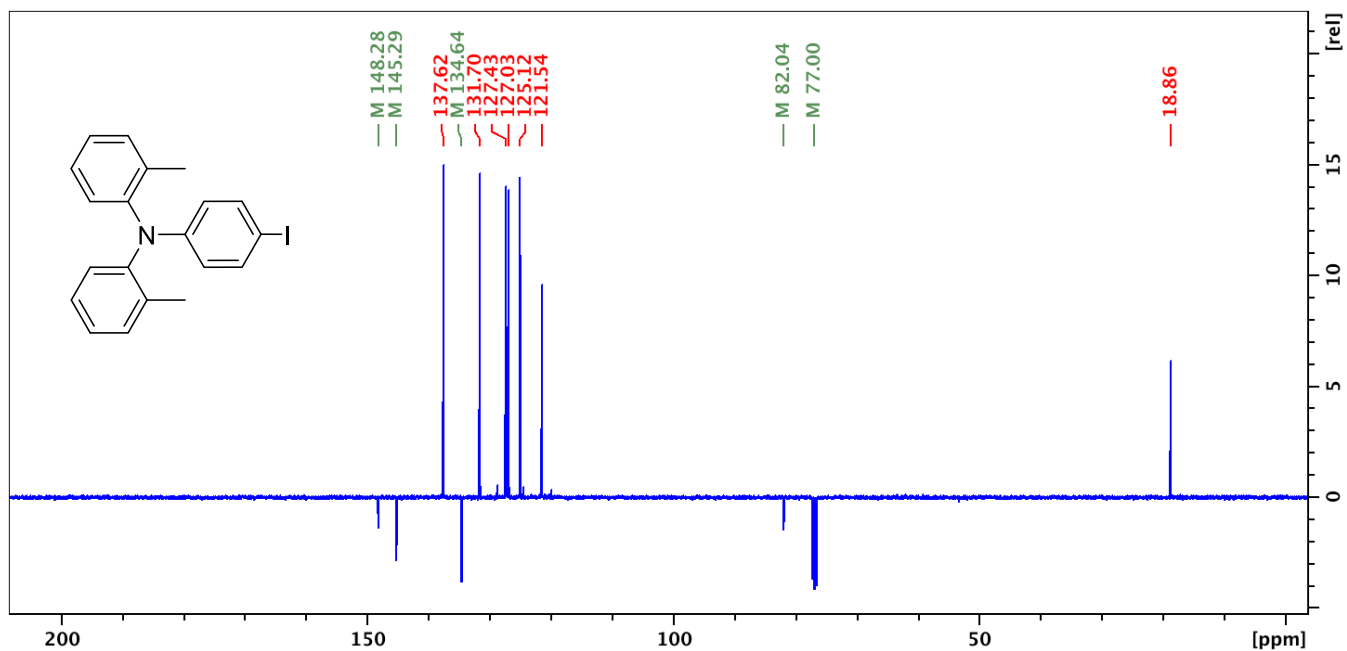


Figure S46. Carbon NMR spectrum of compound 7.

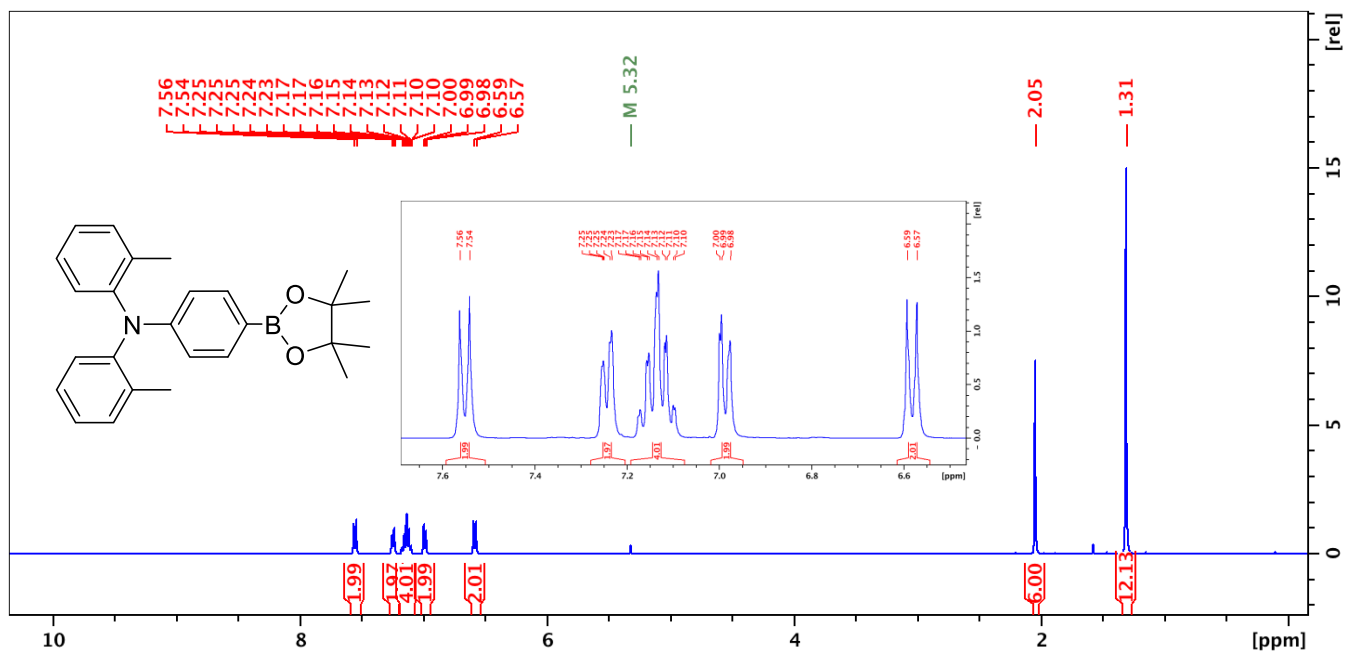


Figure S47. Proton NMR spectrum of compound **1e**.

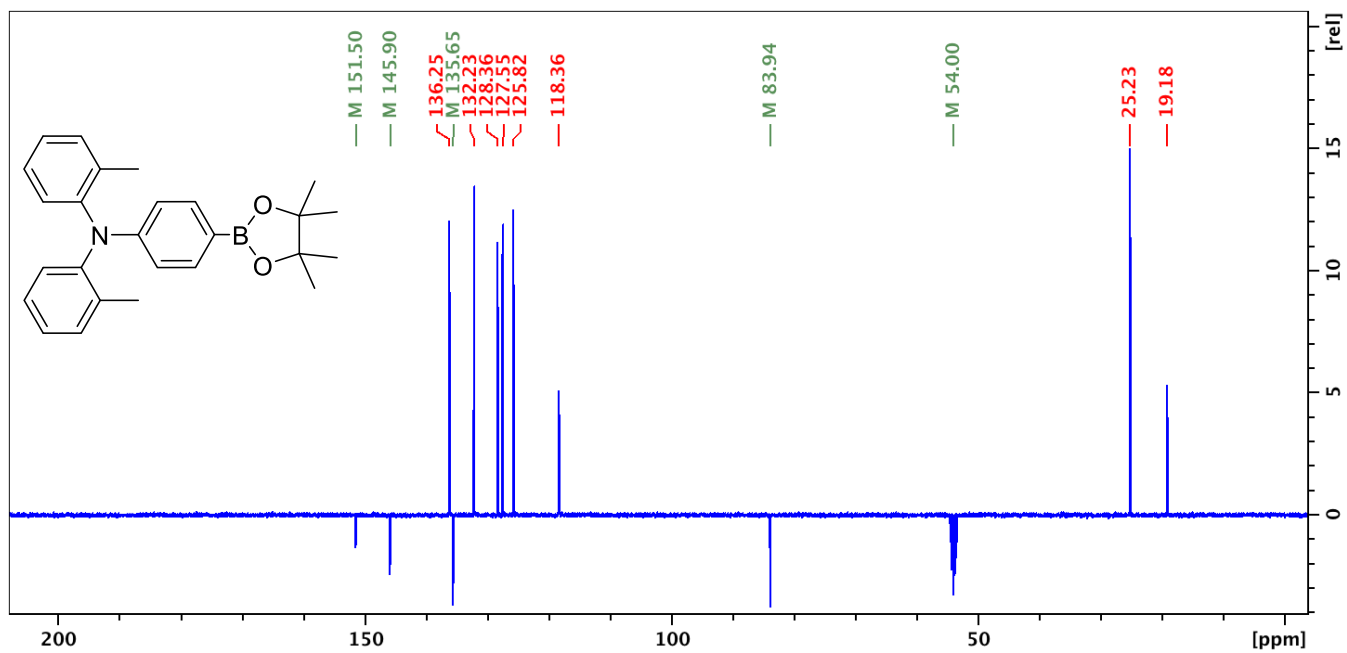
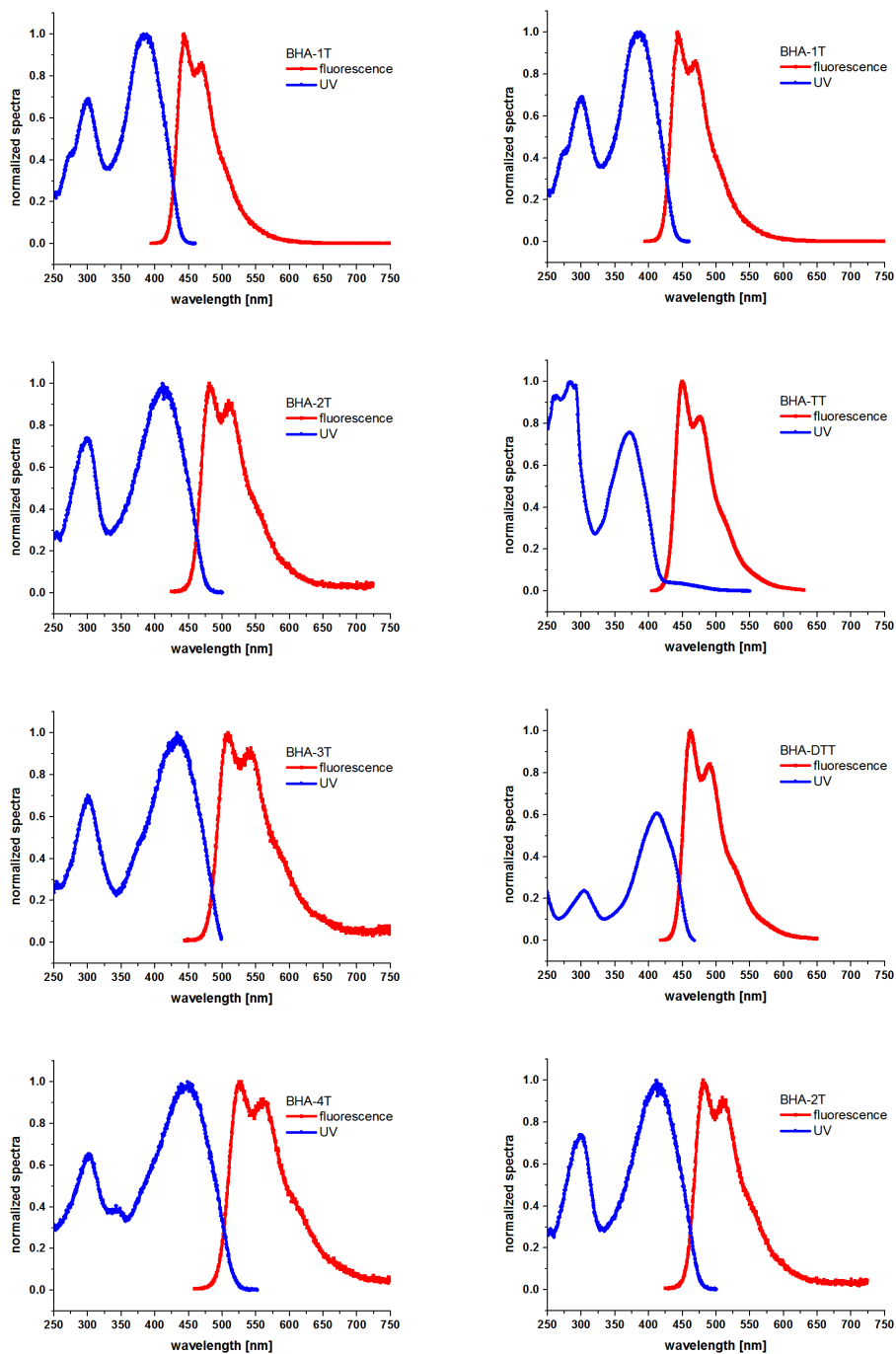
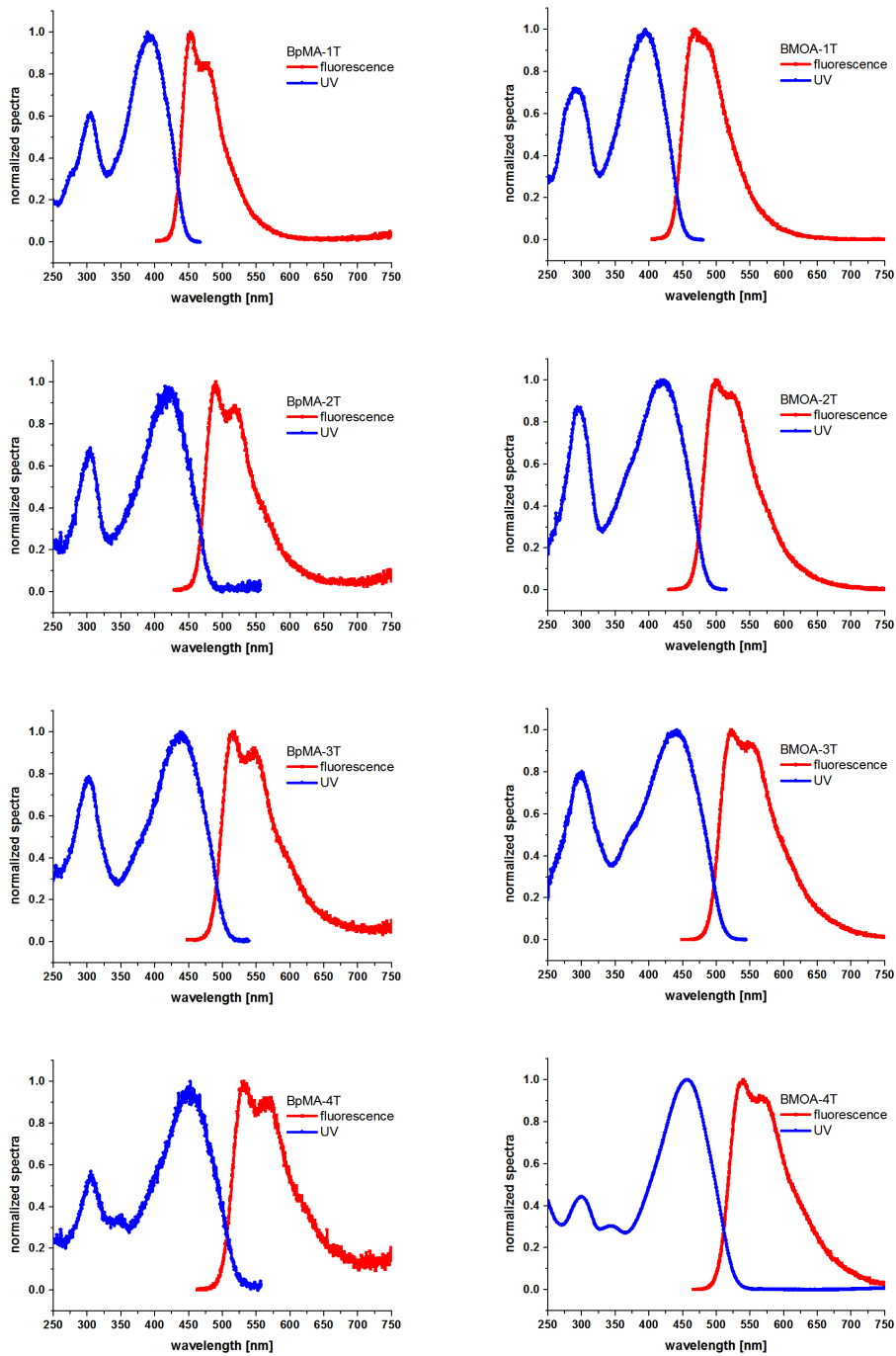


Figure S48. Carbon NMR spectrum of compound **1e**.

## B) Photophysical properties



**Figure S49.** Absorption and emission spectra of BHA-1-4T, BHA-TT, and BHA-DDT recorded from 1  $\mu$ M THF solution.



**Figure S50.** Absorption and emission spectra of BpMA-1-4T and BMOA-1-4T recorded from 1  $\mu$ M THF solution.

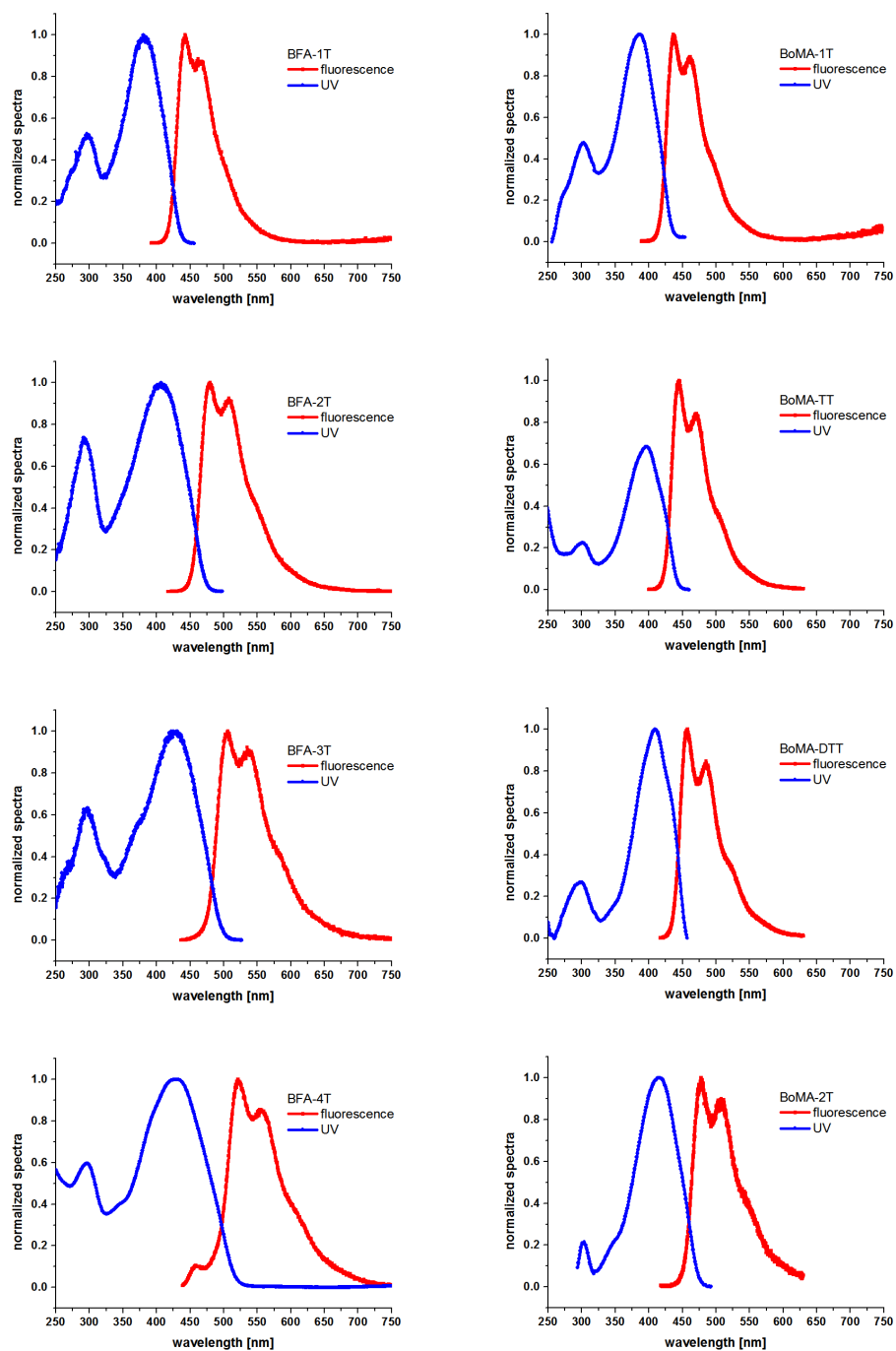


**Figure S51.** Absorption and emission spectra of BFA-1-4T and BoMA-1T, BoMA-TT, BoMA-DTT and BoMA-2T recorded from 1  $\mu$ M THF solution.

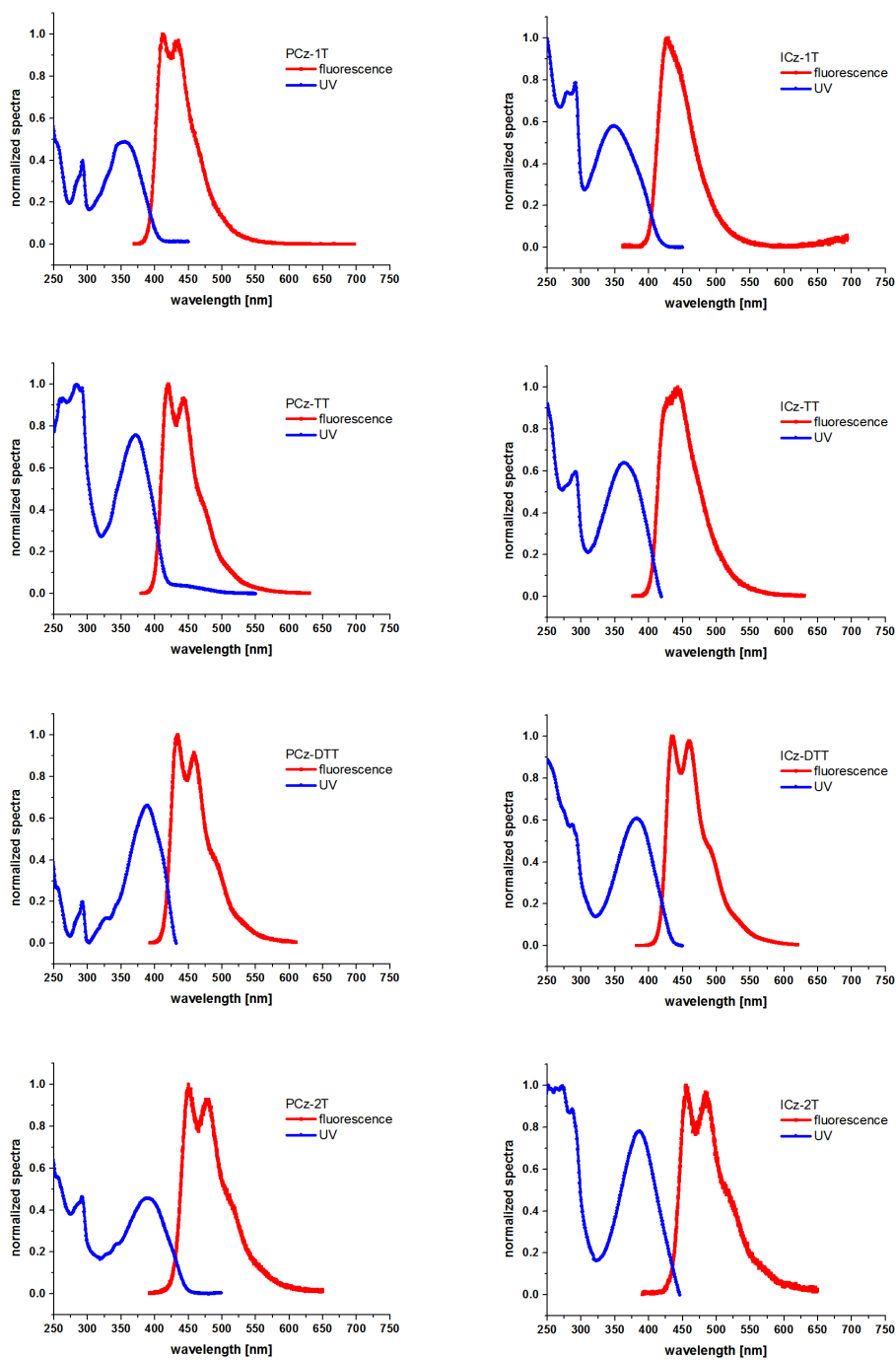


**Figure S52.** Absorption and emission spectra of PCz-1T, PCz-TT, PCz-DTT and PCz-2T and ICz-1T, ICz-TT, ICz-DTT and ICz-2T recorded from 1  $\mu$ M THF solution.

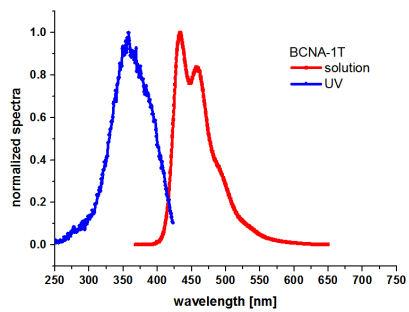
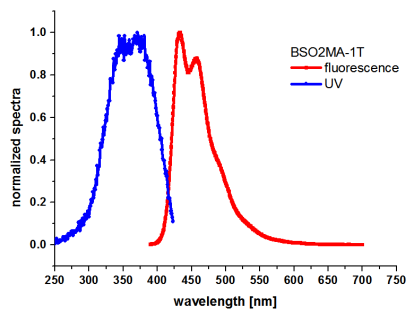


**Figure S53.** Absorption and emission spectra of BSO2MA-1T and BCNA-1T recorded from 1  $\mu$ M THF solution.



## C) OLED spectra

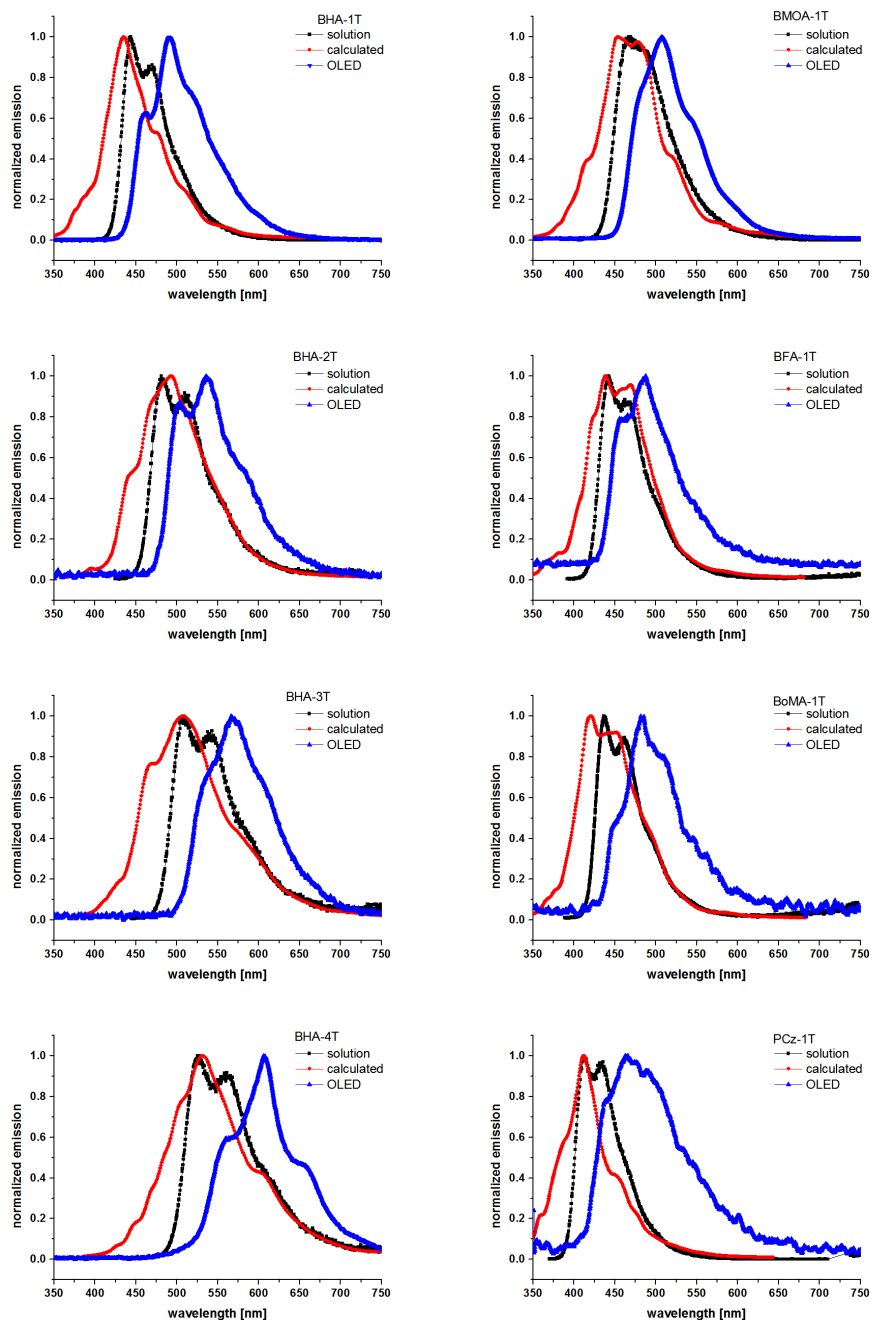


**Figure S54.** Comparison of experimental (solution and OLED) and simulated fluorescence spectra of BHA-1-4T, BMOA-1T, BFA-1T, BoMA-1T and PCz-1T. Solution refers to fluorescence measured from 1  $\mu\text{M}$  THF solution.

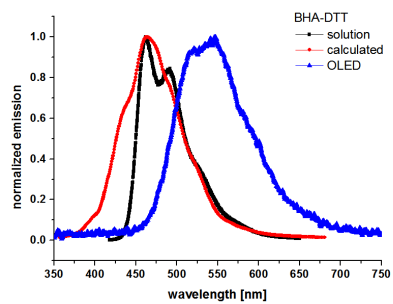
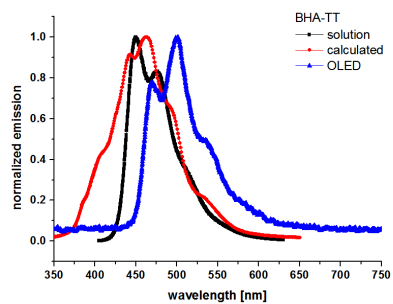
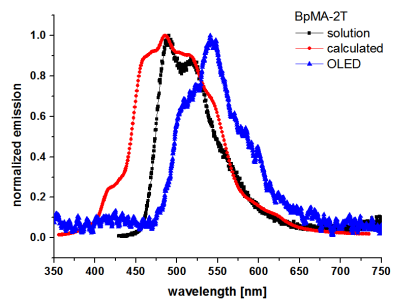
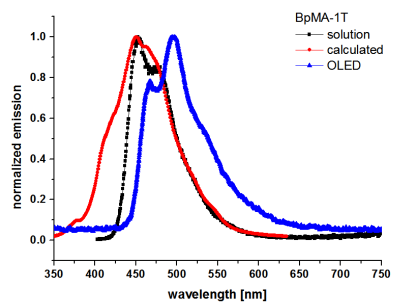


**Figure S55.** Comparison of experimental (solution and OLED) and simulated fluorescence spectra of BpMA-1T, BpMA-2T, BHA-TT and BHA-DTT. Solution refers to fluorescence measured from 1  $\mu\text{M}$  THF solution.

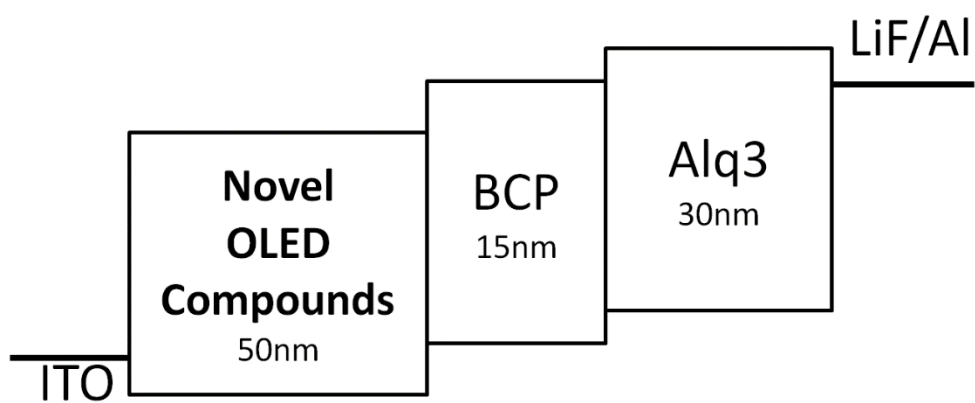


**Figure S56.** Schematic layout of bottom emitting OLEDs fabricated with selected novel OLED materials.

## D)computational part

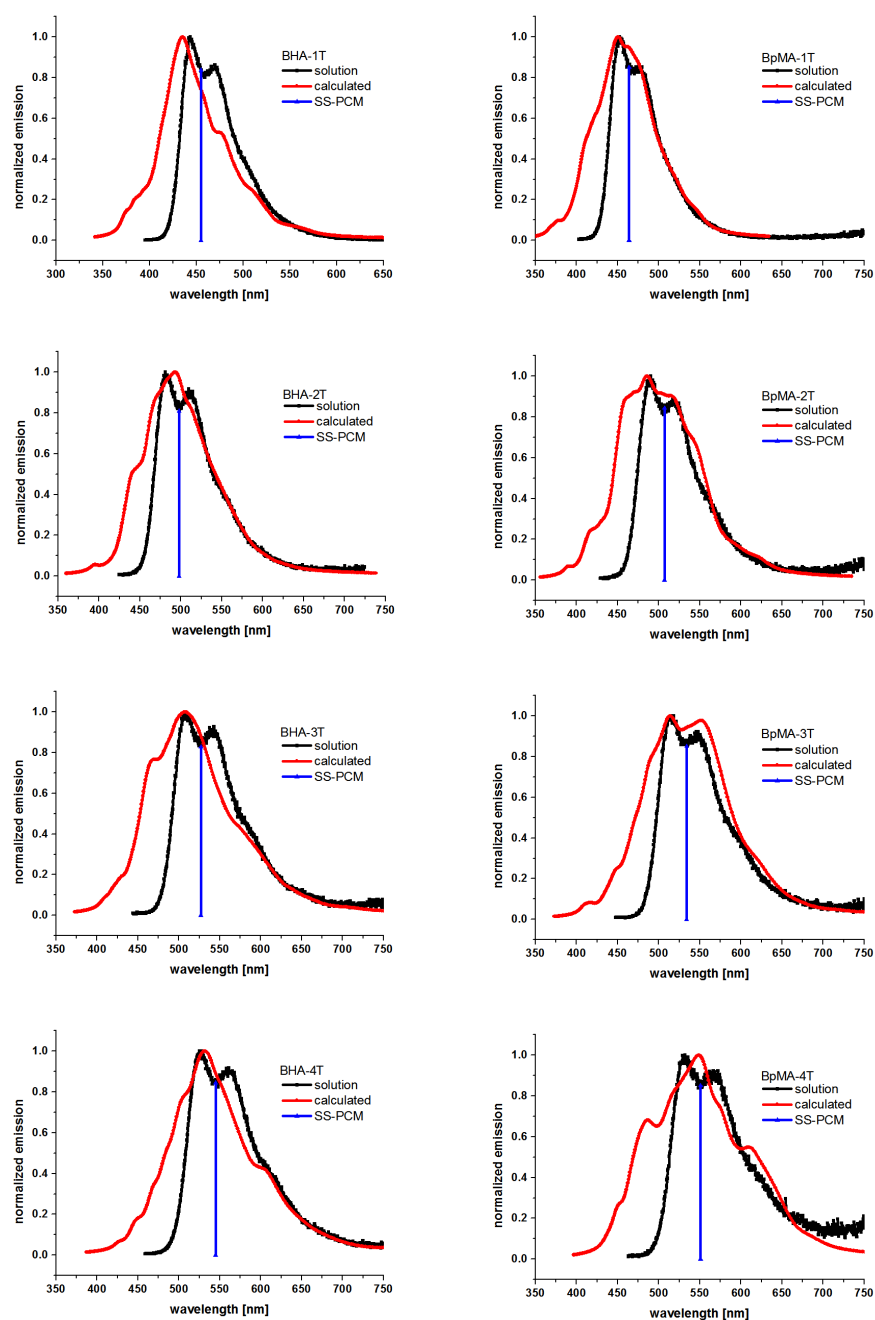


**Figure S57.** Comparison of experimental and computational results for BHA-1-4T and BpMA-1-4T; solution refers to fluorescence measured in 1  $\mu\text{M}$  THF solution, calculated refers to the spectra simulation and SS-PCM refers to the vertical emission.

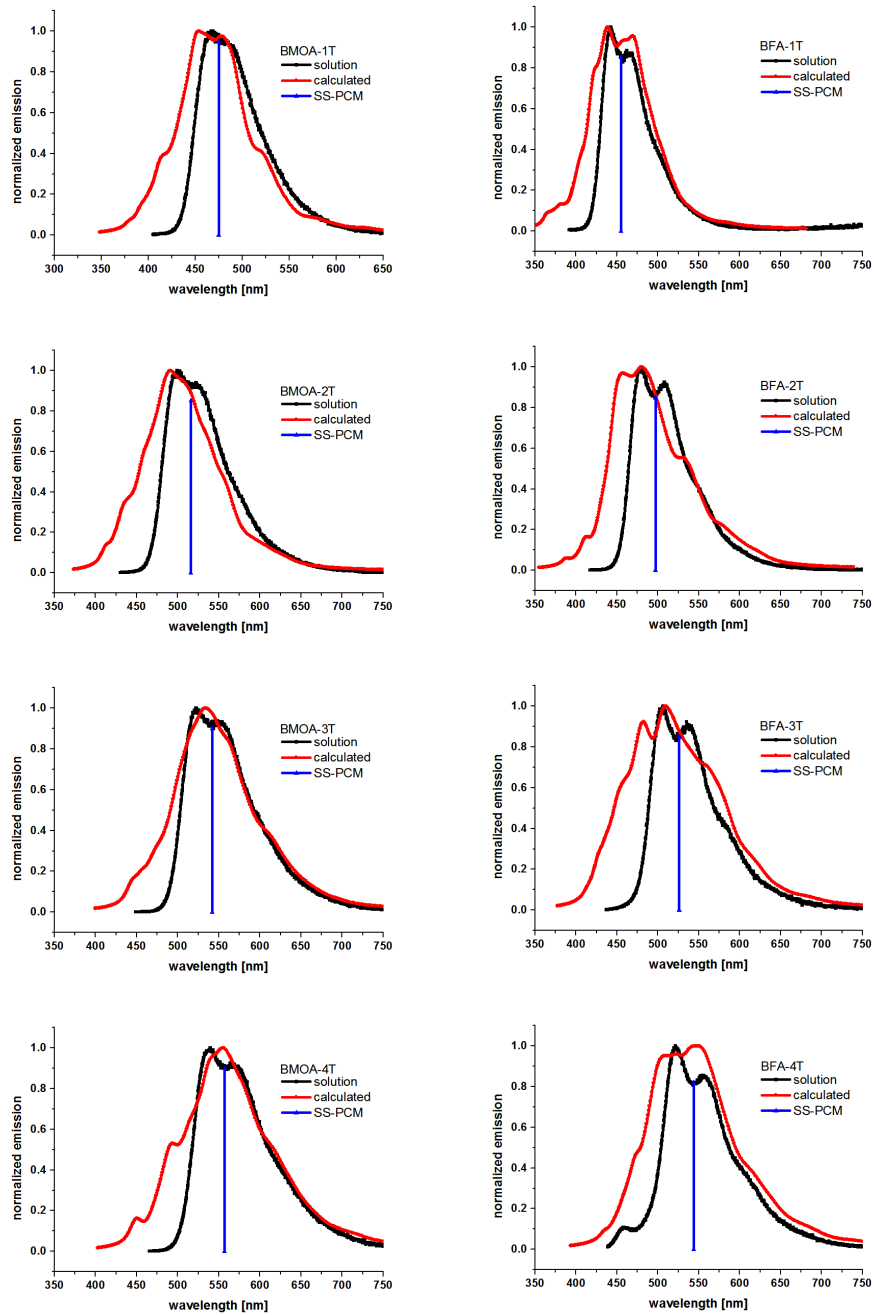


**Figure S58.** Comparison of experimental and computational results for BMOA-1-4T and BFA-1-4T; solution refers to fluorescence measured in 1  $\mu\text{M}$  THF solution, calculated refers to the spectra simulation and SS-PCM refers to the vertical emission.

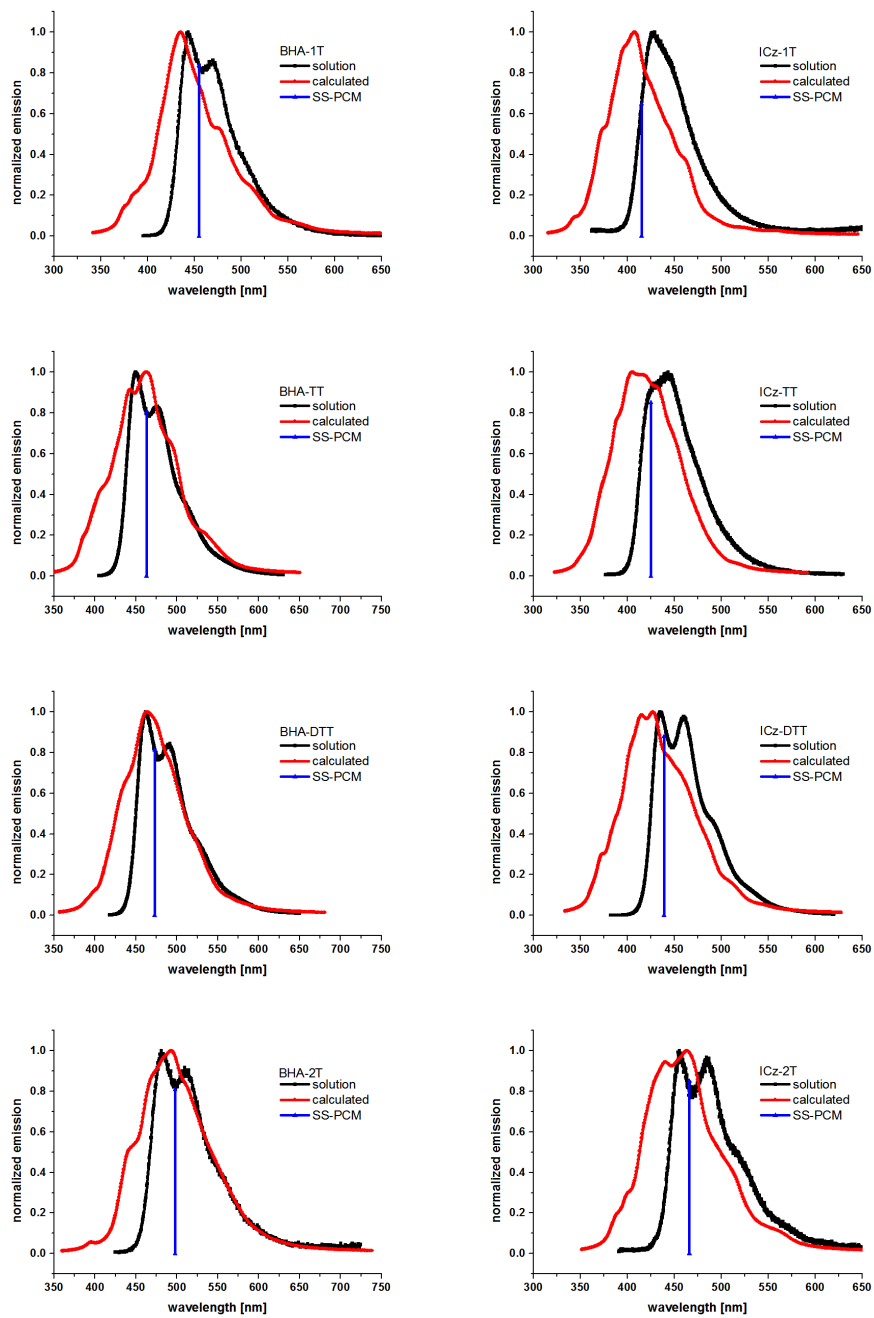


**Figure S59.** Comparison of experimental and computational results for BHA-1T, BHA-TT, BHA-DTT and BHA-2T and ICz-1T, ICz-TT, ICz-DTT and ICz-2T; solution refers to fluorescence measured in 1  $\mu\text{M}$  THF solution, calculated refers to the spectra simulation and SS-PCM refers to the vertical emission.

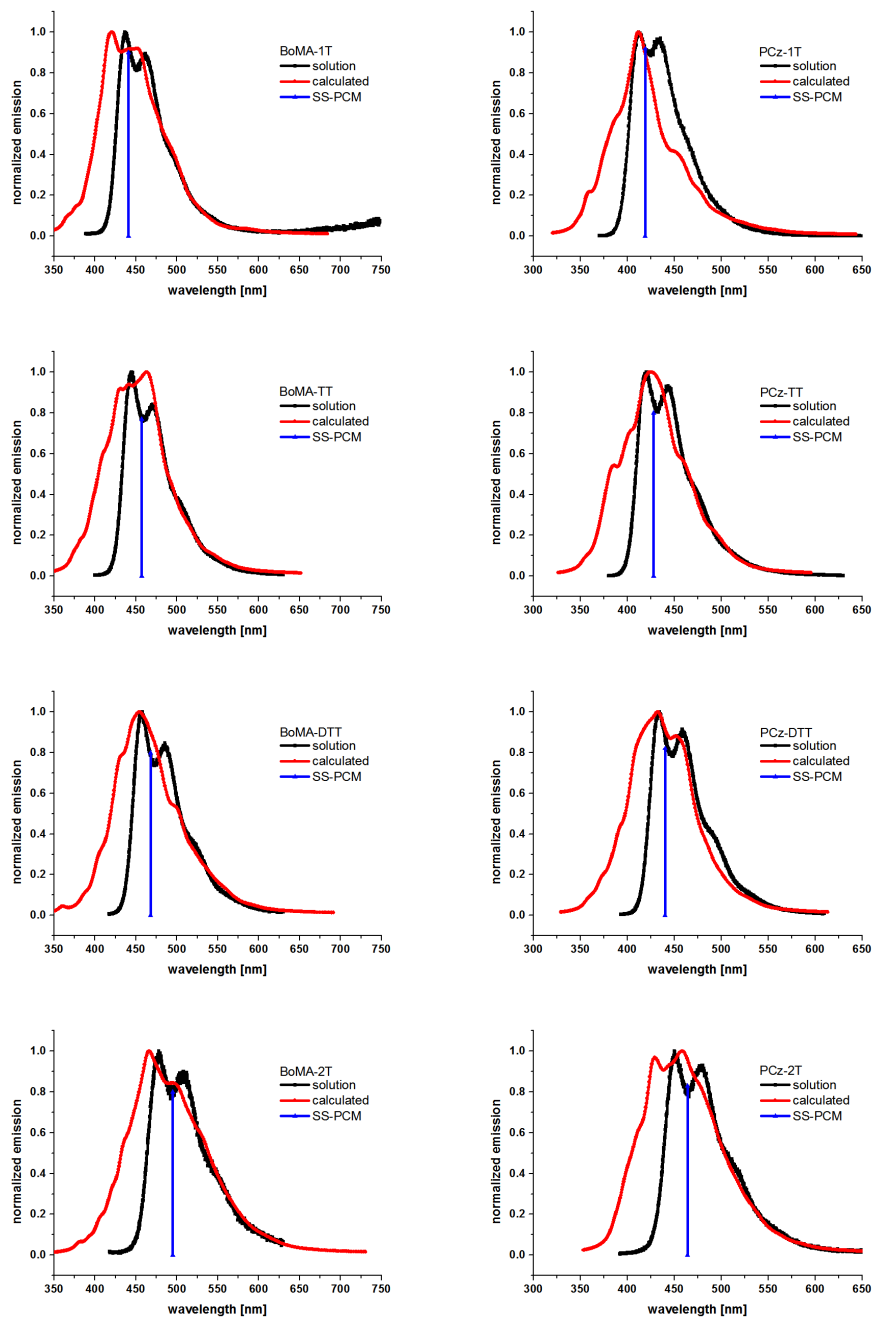


**Figure S60.** Comparison of experimental and computational results for BoMA-1T, BoMA-TT, BoMA-DTT and BoMA-2T and PCz-1T, PCz-TT, PCz-DTT and PCz-2T; solution refers to fluorescence measured in 1  $\mu\text{M}$  THF solution, calculated refers to the spectra simulation and SS-PCM refers to the vertical emission.

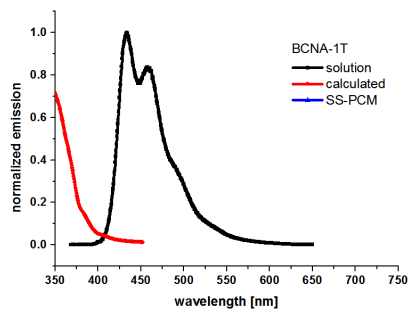
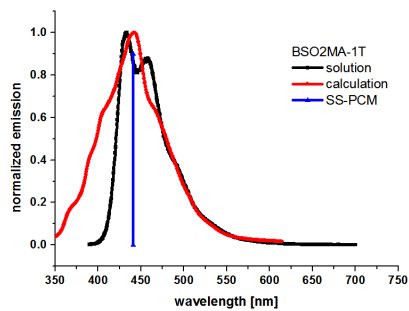


**Figure S61.** Comparison of experimental and computational results for BSO2MA-1T and BCNA-1T; solution refers to fluorescence measured in 1  $\mu\text{M}$  THF solution, calculated refers to the spectra simulation and SS-PCM refers to the vertical emission.



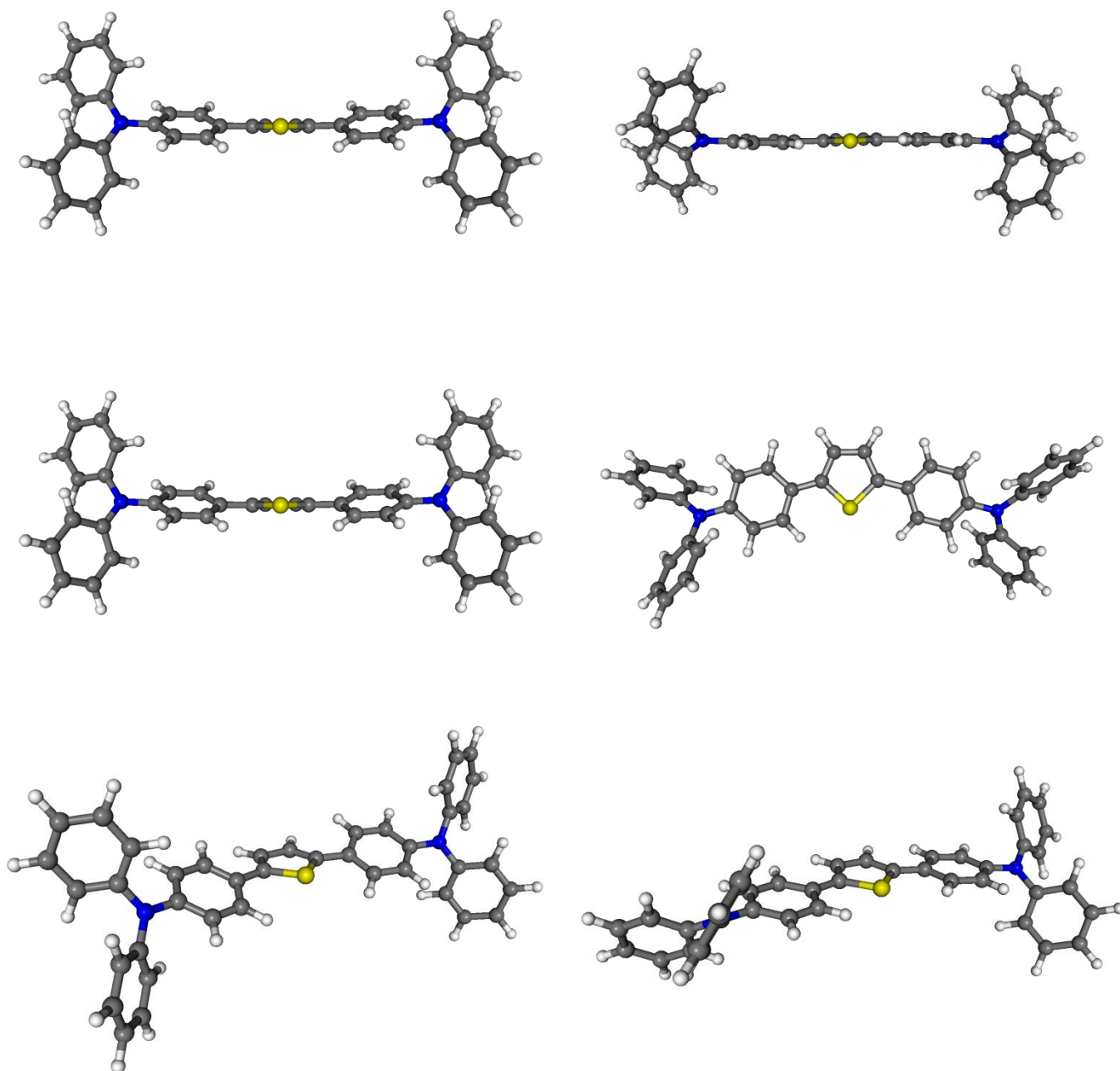


**Figure S62.** Molecular structures of BHA-1T (M06-2X/SVP/LR-PCM); left  $S_0$ , right  $S_1$ .

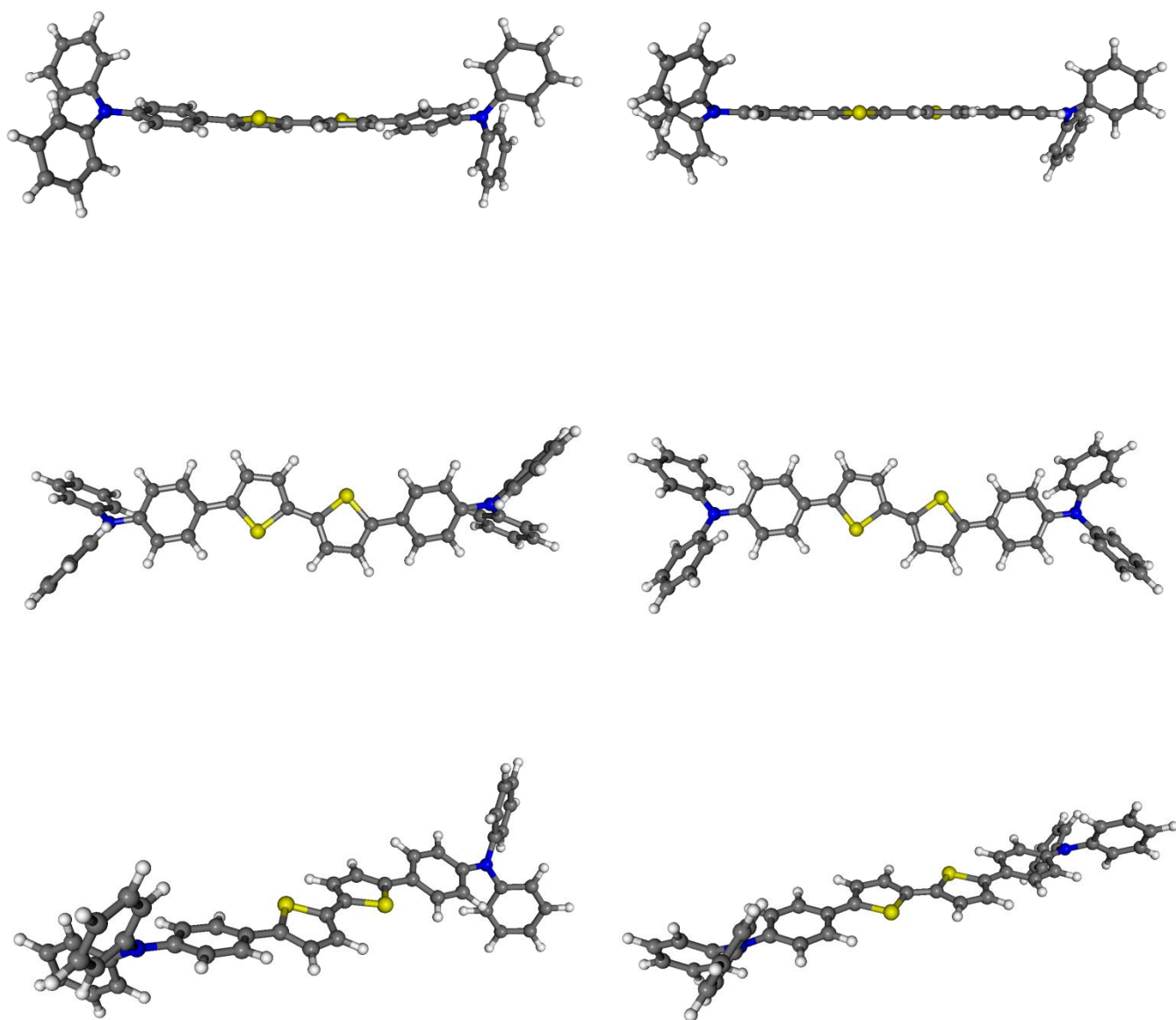


**Figure S63.** Molecular structures of BHA-2T (M06-2X/SVP/LR-PCM); left  $S_0$ , right  $S_1$ .

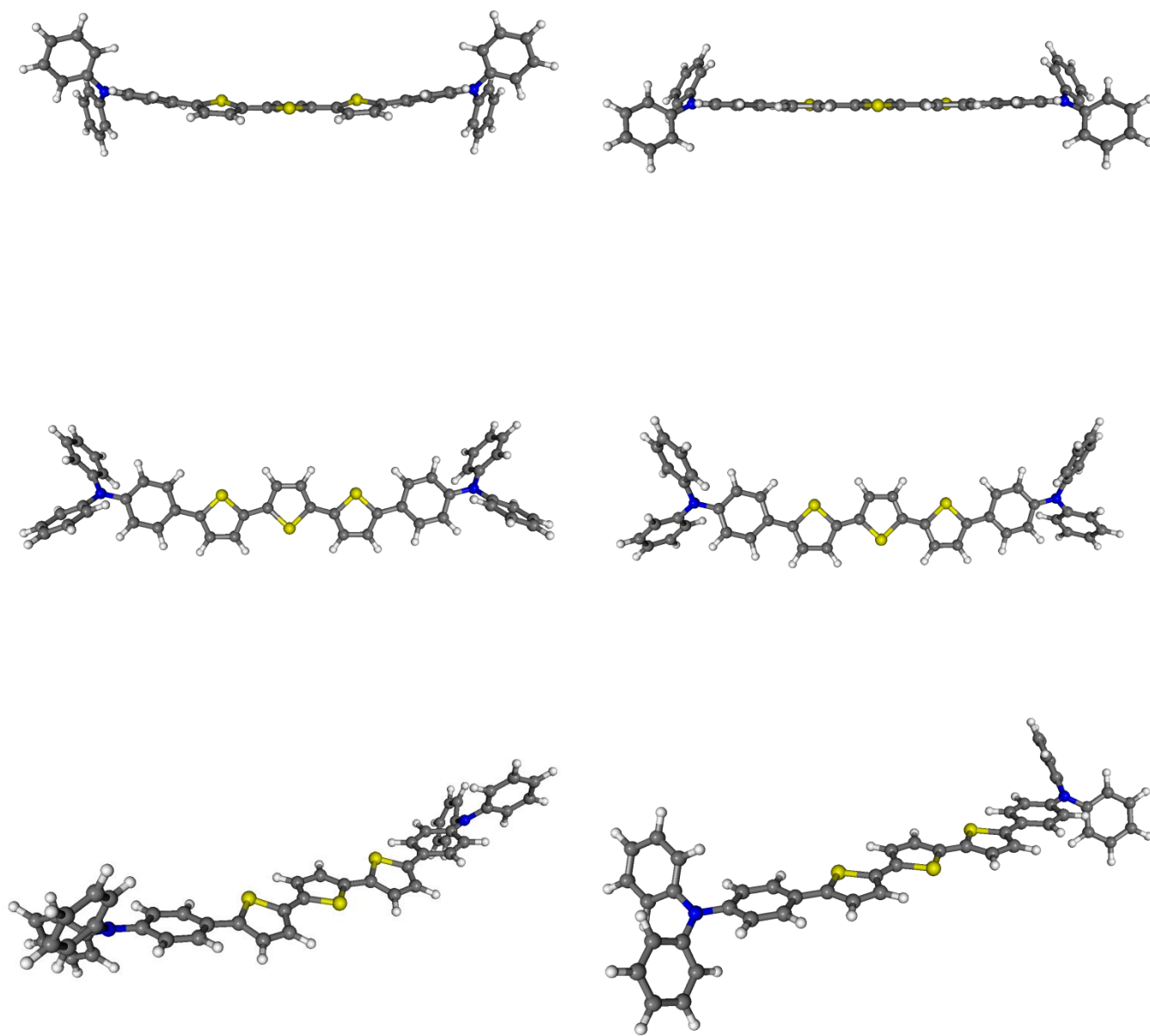


**Figure S64.** Molecular structures of BHA-3T (M06-2X/SVP/LR-PCM); left  $S_0$ , right  $S_1$ .

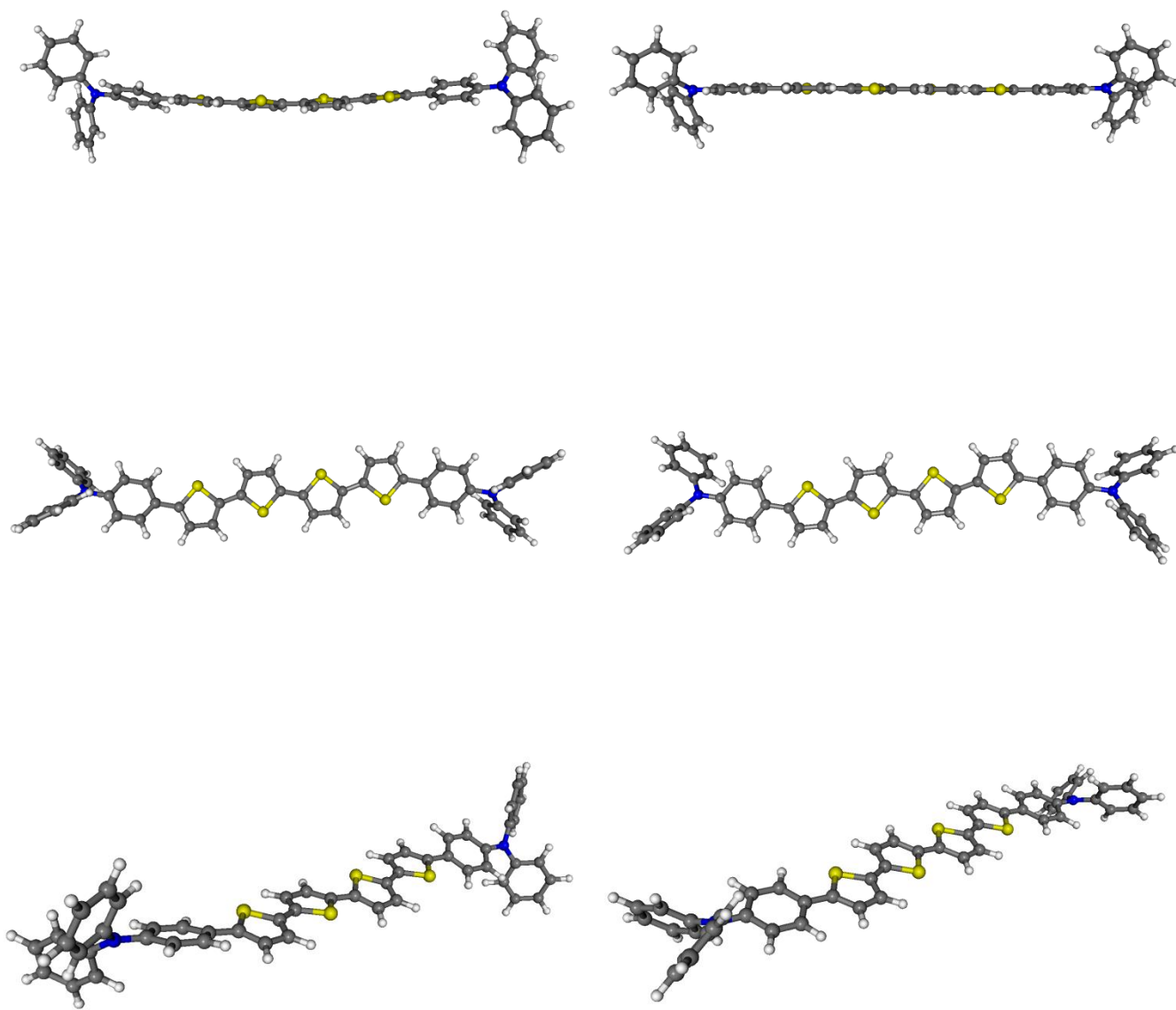


**Figure S65.** Molecular structures of BHA-4T (M06-2X/SVP/LR-PCM); left  $S_0$ , right  $S_1$ .

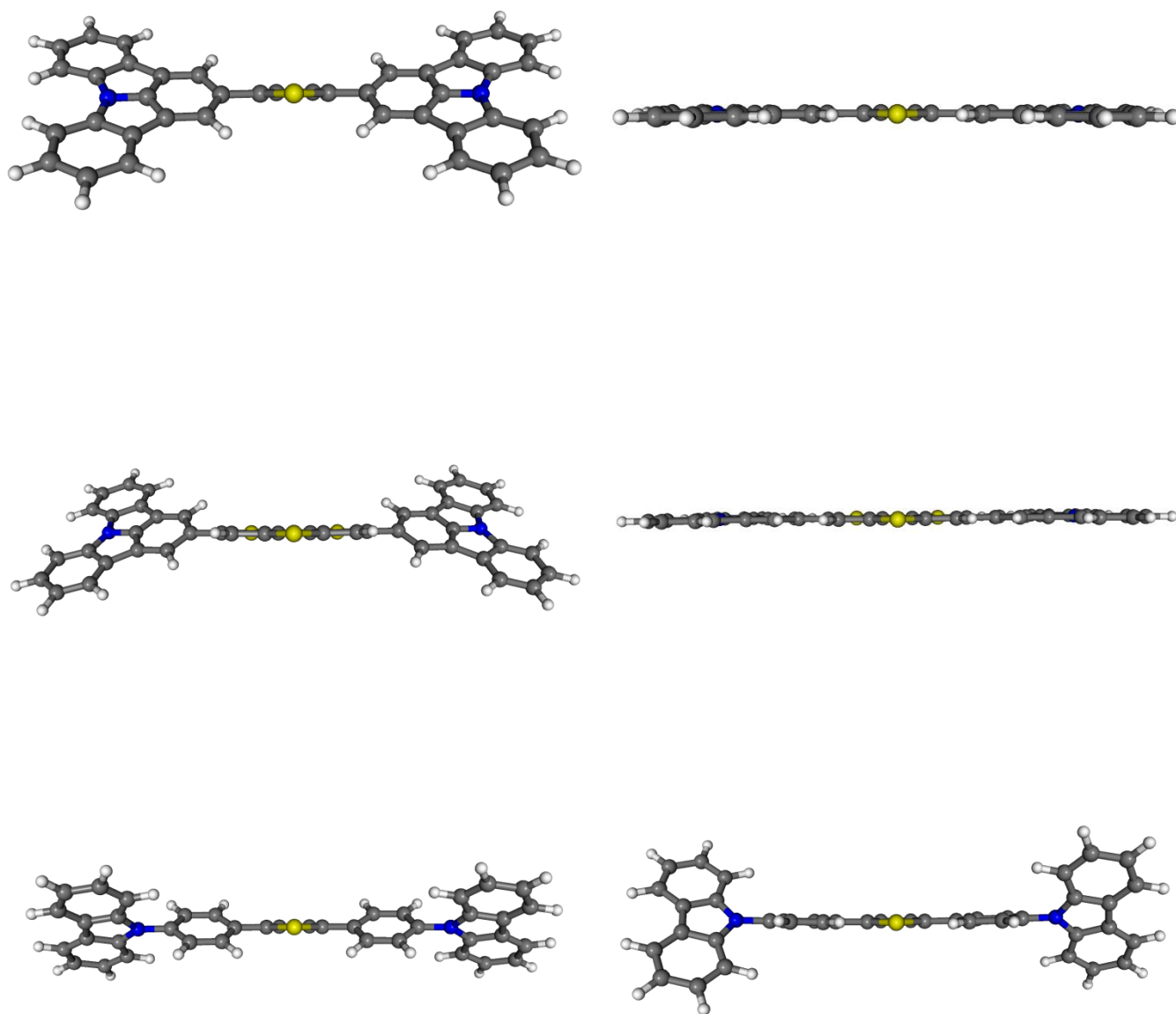


**Figure S66.** Molecular structures of ICz-1T (top), ICz-DTT (middle) and PCz-1T (bottom); (M06-2X/SVP/LR-PCM); left S<sub>0</sub>, right S<sub>1</sub>.



# Manuscript #6

Supporting Information

D. Lumpi\*, B. Holzer\*, **J. Binterger**, E. Horkel, S. Waid, H. D. Wanzenböck, M. Marchetti-Deschmann, C. Hametner, E. Bertagnolli, I. Kymissis, J. Fröhlich; *New J. Chem.* 2015

Reproduced from Ref.<sup>86</sup> with permission from the Centre National de la Recherche Scientifique (CNRS) and The Royal Society of Chemistry.





# Substituted Triphenylamines as Building Blocks for Star Shaped Organic Electronic Materials

## Supplementary Material

*Daniel Lumpi,<sup>a</sup> Brigitte Holzer,<sup>a</sup> Johannes Bintinger,<sup>a,b</sup> Ernst Horkel,<sup>a\*</sup> Simon Waid,<sup>c</sup> Heinz D. Wanzenböck,<sup>c</sup> Martina Marchetti-Deschmann,<sup>d</sup> Christian Hametner,<sup>a</sup> Emmerich Bertagnoli,<sup>c</sup> Ioannis Kymissis,<sup>b</sup> and Johannes Fröhlich<sup>a</sup>*

<sup>a</sup>Institute of Applied Synthetic Chemistry, Vienna University of Technology,

Getreidemarkt 9/163OC, A-1060 Vienna, Austria

<sup>b</sup>Department of Electrical Engineering, Columbia University,

520W 120<sup>th</sup> street, Suite 1300, 10027 New York, NY, United States

<sup>c</sup>Institute of Solid State Electronics, Vienna University of Technology,

Floragasse 7, A-1040 Vienna, Austria

<sup>d</sup>Institute of Chemical Technologies and Analytics, Vienna University of Technology,

Getreidemarkt 9/164IAC, A-1060 Vienna, Austria

[ernst.horkel@tuwien.ac.at](mailto:ernst.horkel@tuwien.ac.at)

## A) NMR Spectra

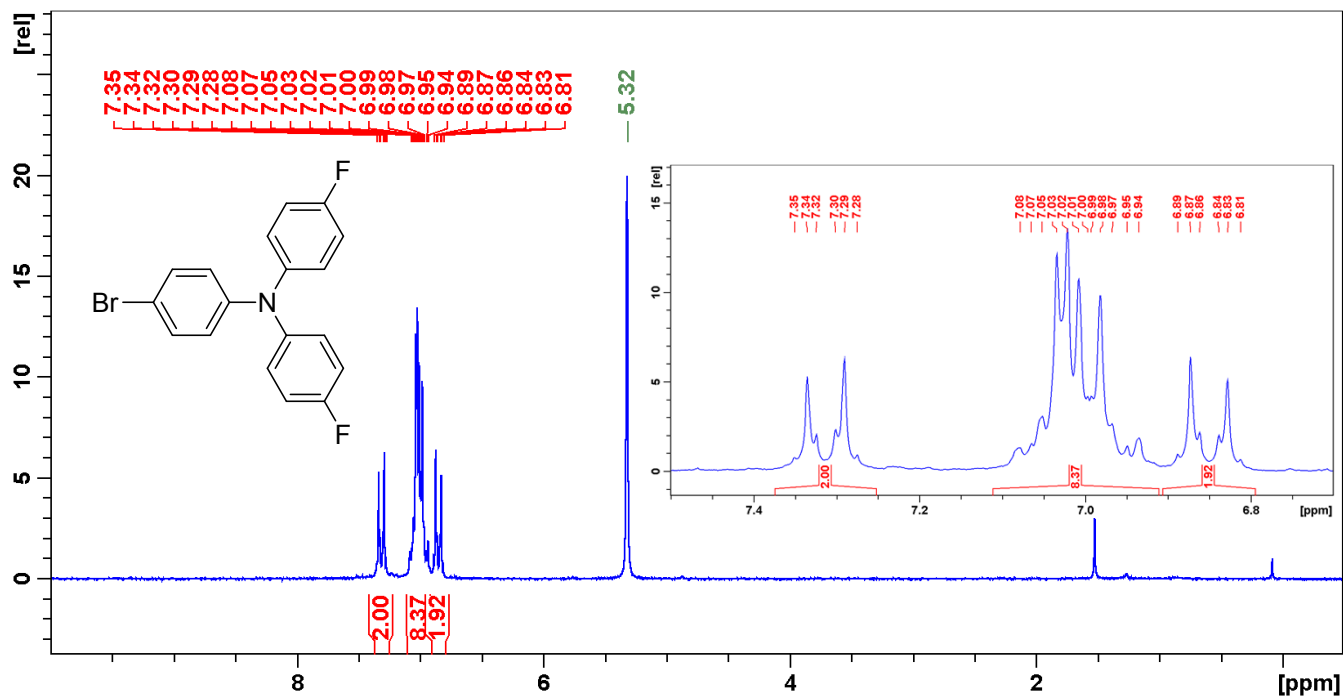


Figure S1. Proton NMR spectrum of compound **6c**.

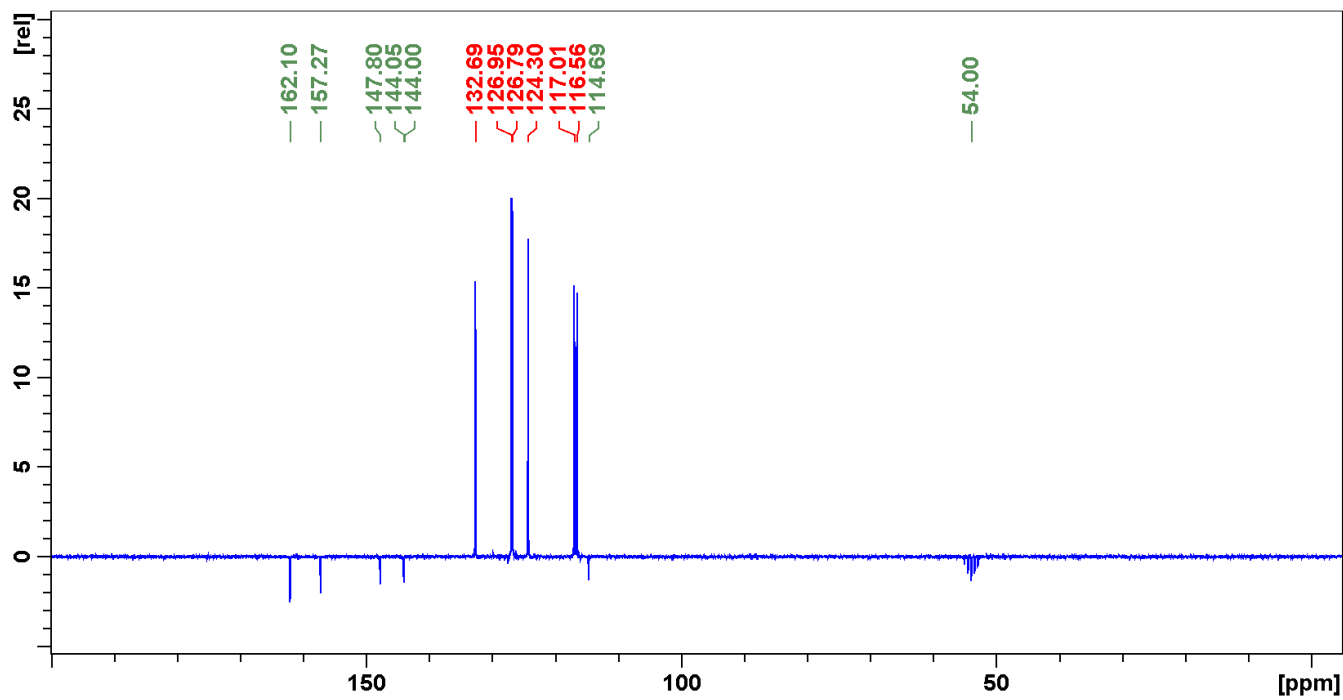


Figure S2. Carbon NMR spectrum of compound **6c**.

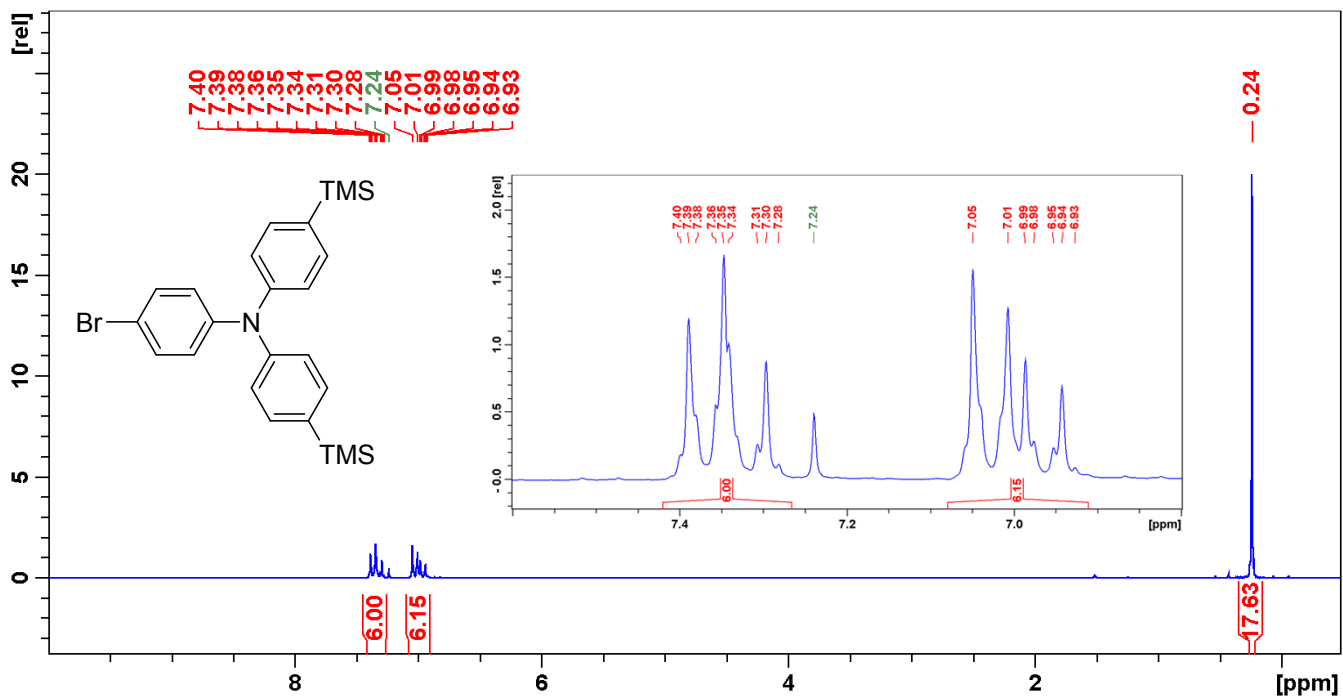


Figure S3. Proton NMR spectrum of compound 6e.

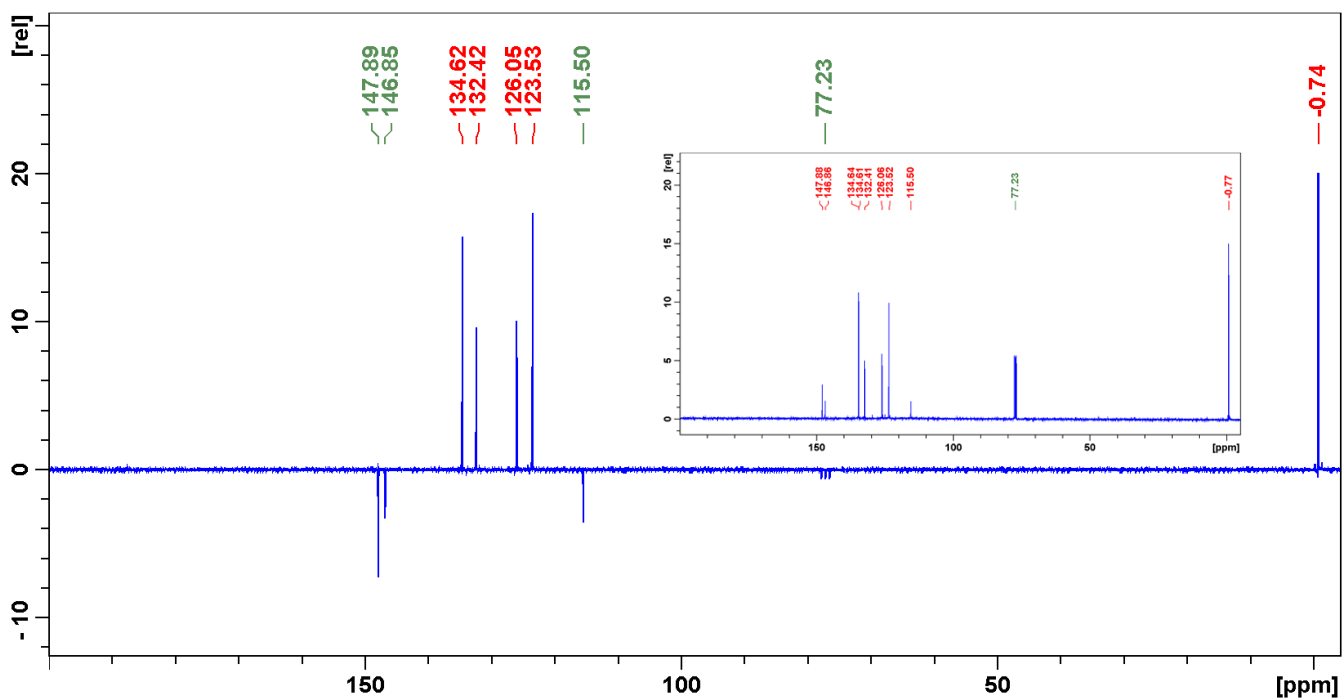


Figure S4. Carbon NMR spectrum of compound 6e.

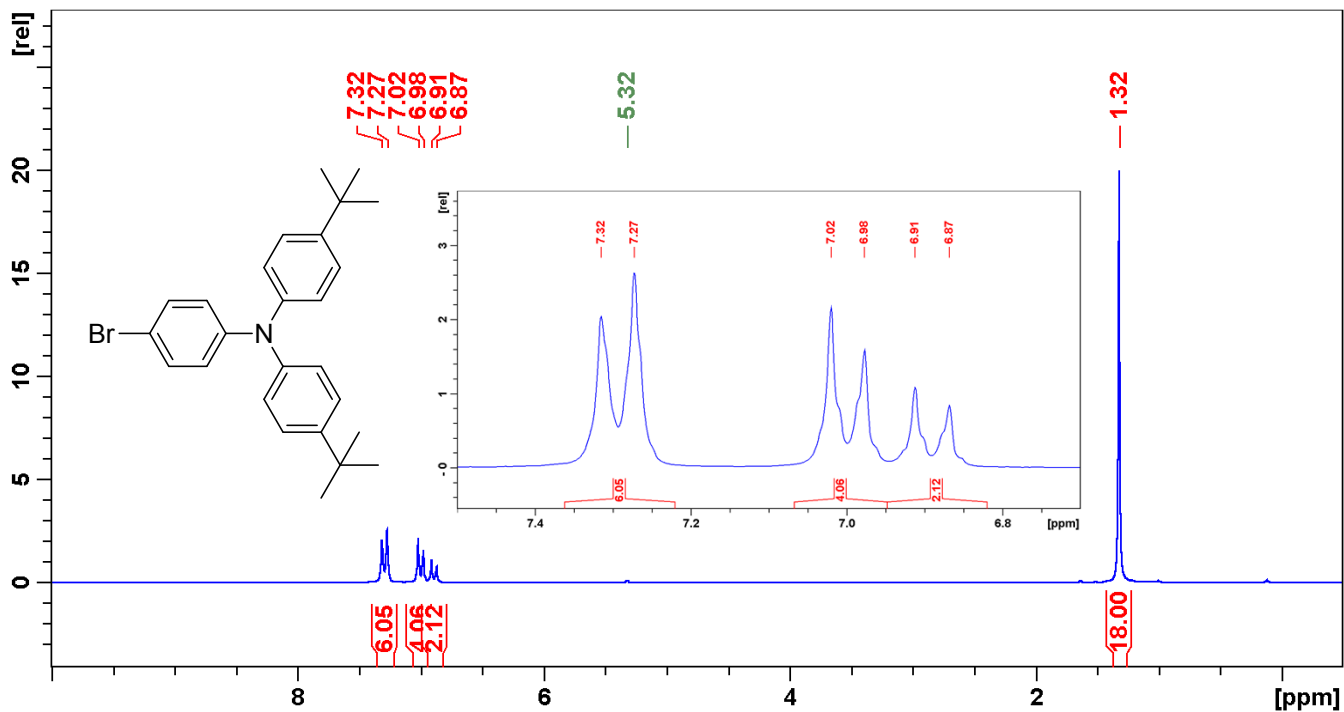


Figure S5. Proton NMR spectrum of compound **6f**.

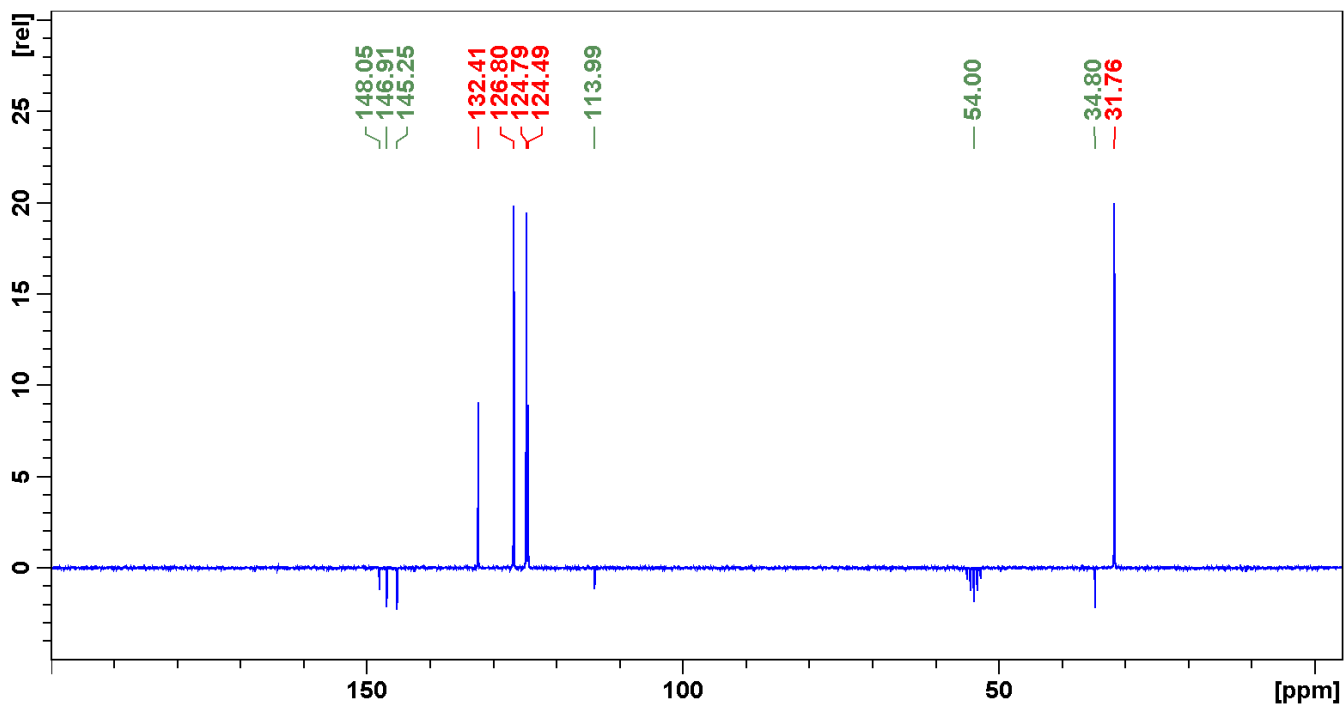


Figure S6. Carbon NMR spectrum of compound **6f**.

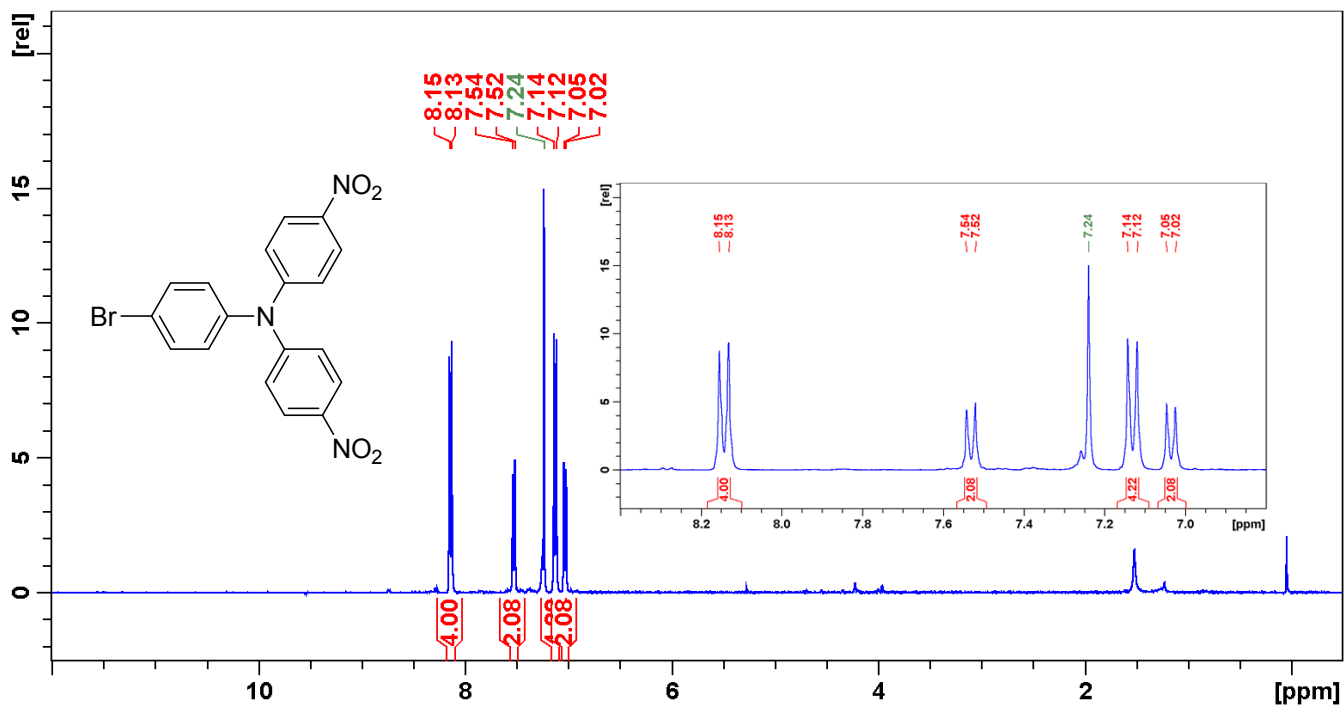


Figure S7. Proton NMR spectrum of compound **6g**.

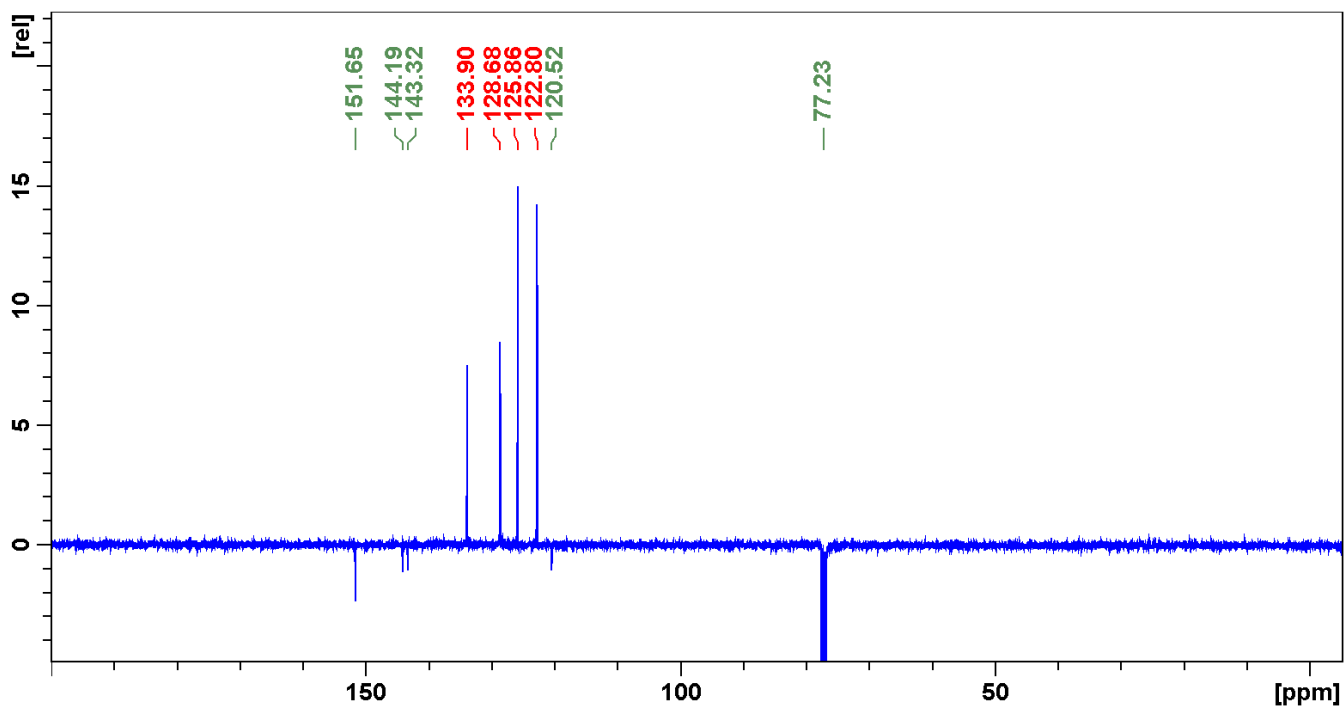


Figure S8. Carbon NMR spectrum of compound **6g**.

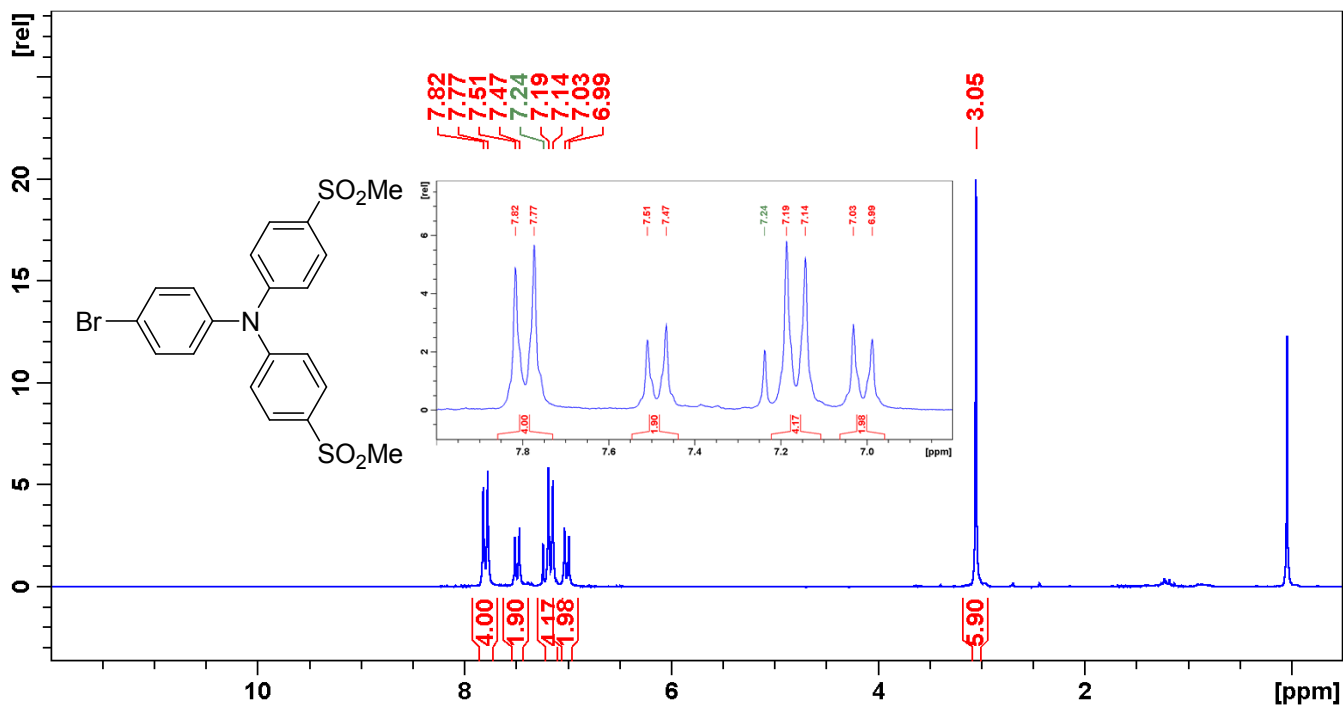


Figure S9. Proton NMR spectrum of compound **6h**.

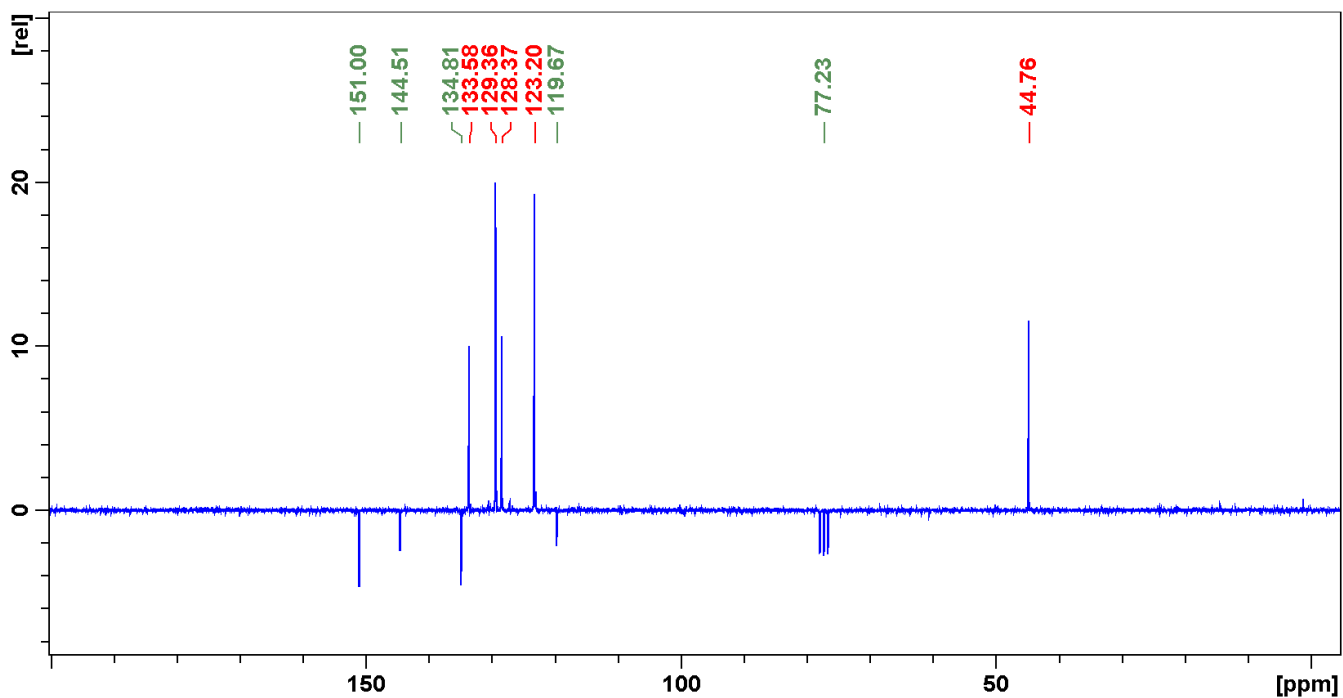


Figure S10. Carbon NMR spectrum of compound **6h**.

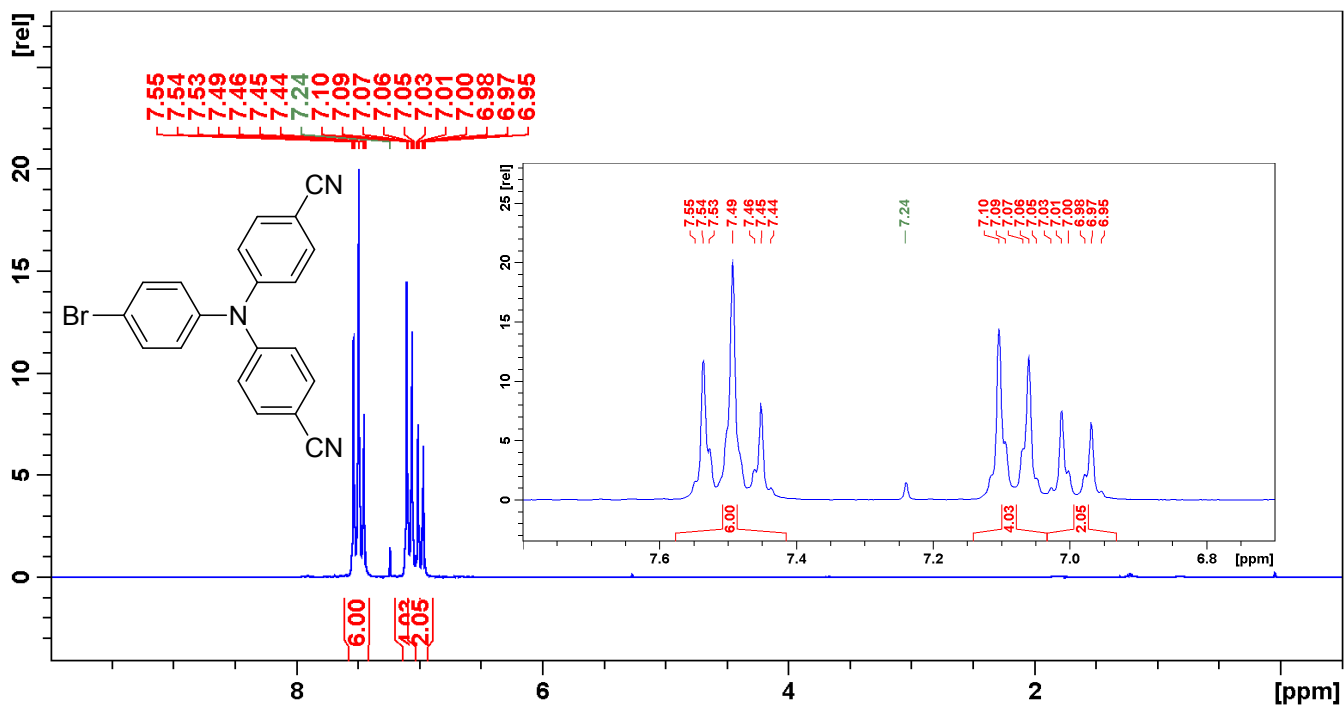


Figure S11. Proton NMR spectrum of compound **6i**.

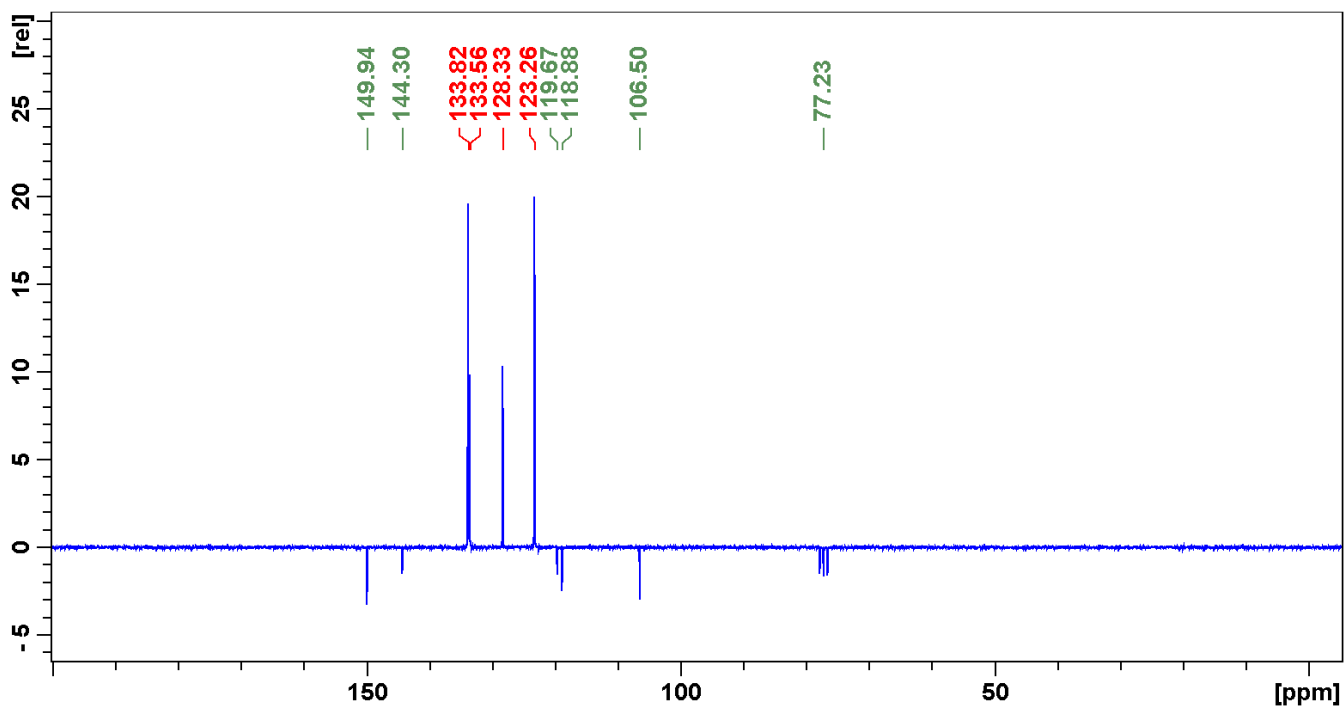


Figure S12. Carbon NMR spectrum of compound **6i**.

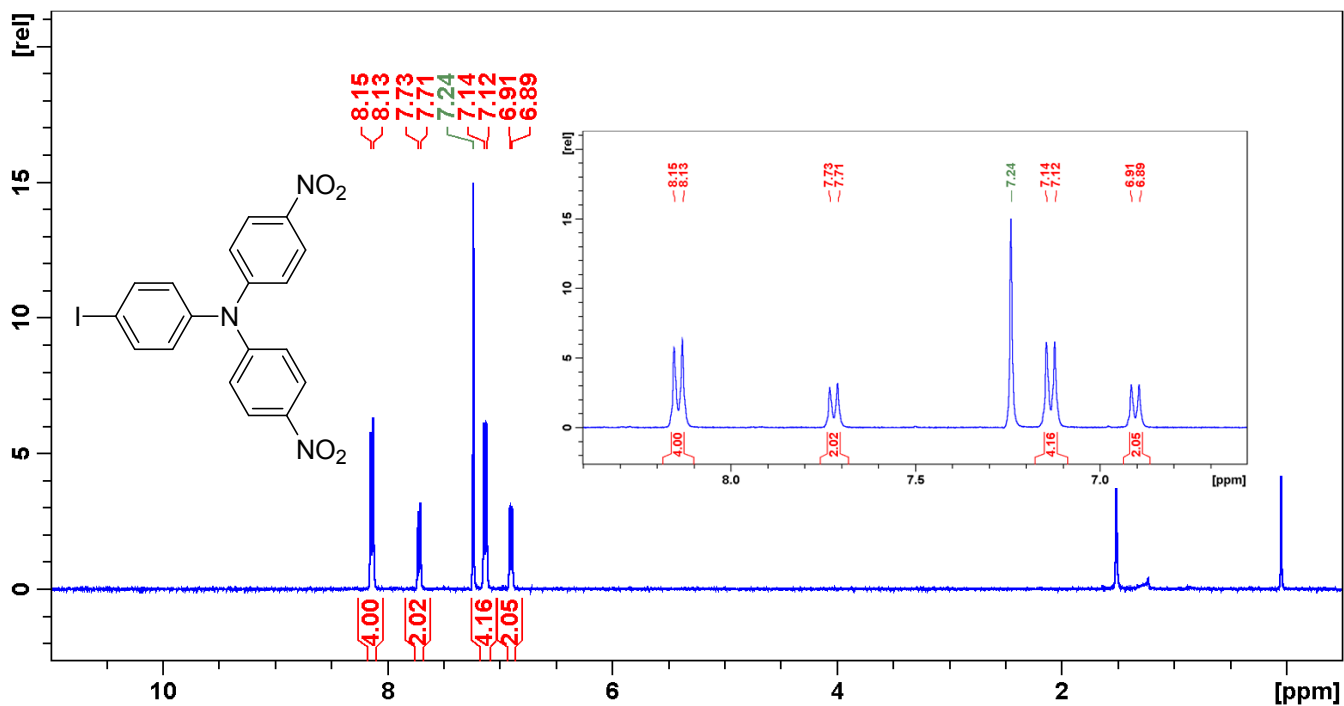


Figure S13. Proton NMR spectrum of compound **6j**.

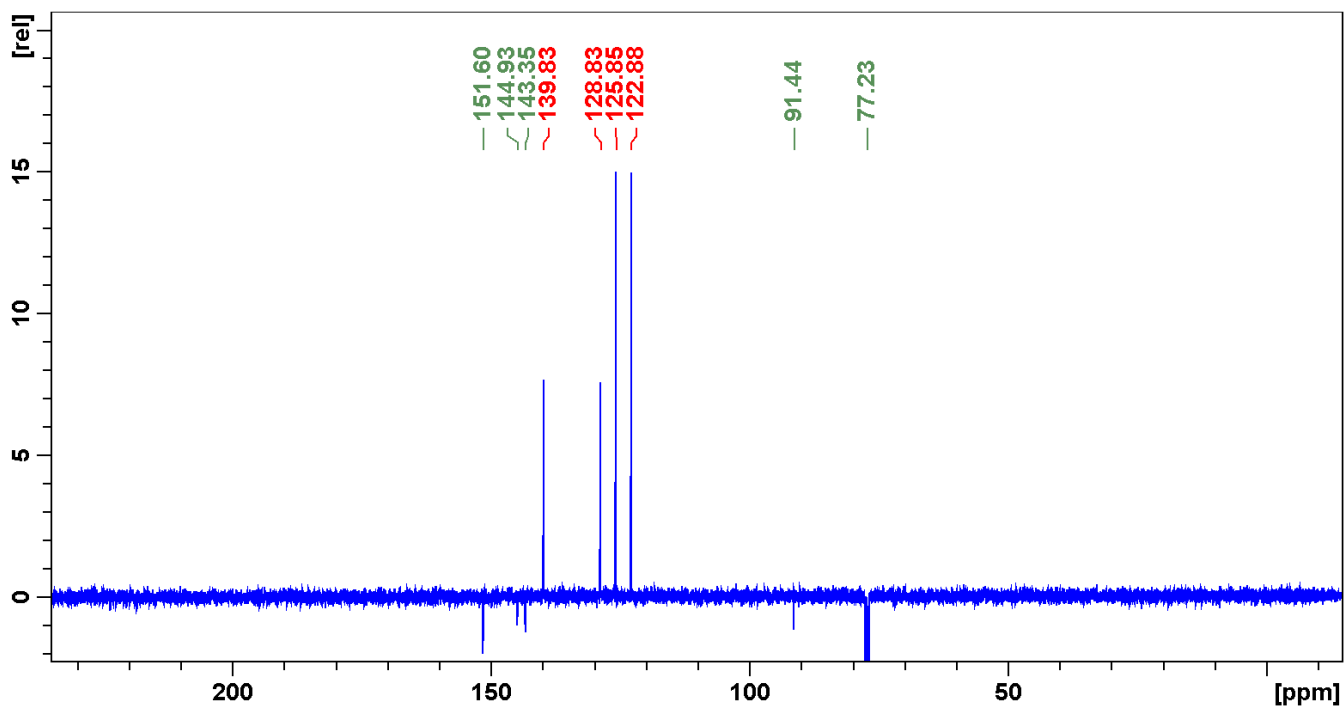


Figure S14. Carbon NMR spectrum of compound **6j**.



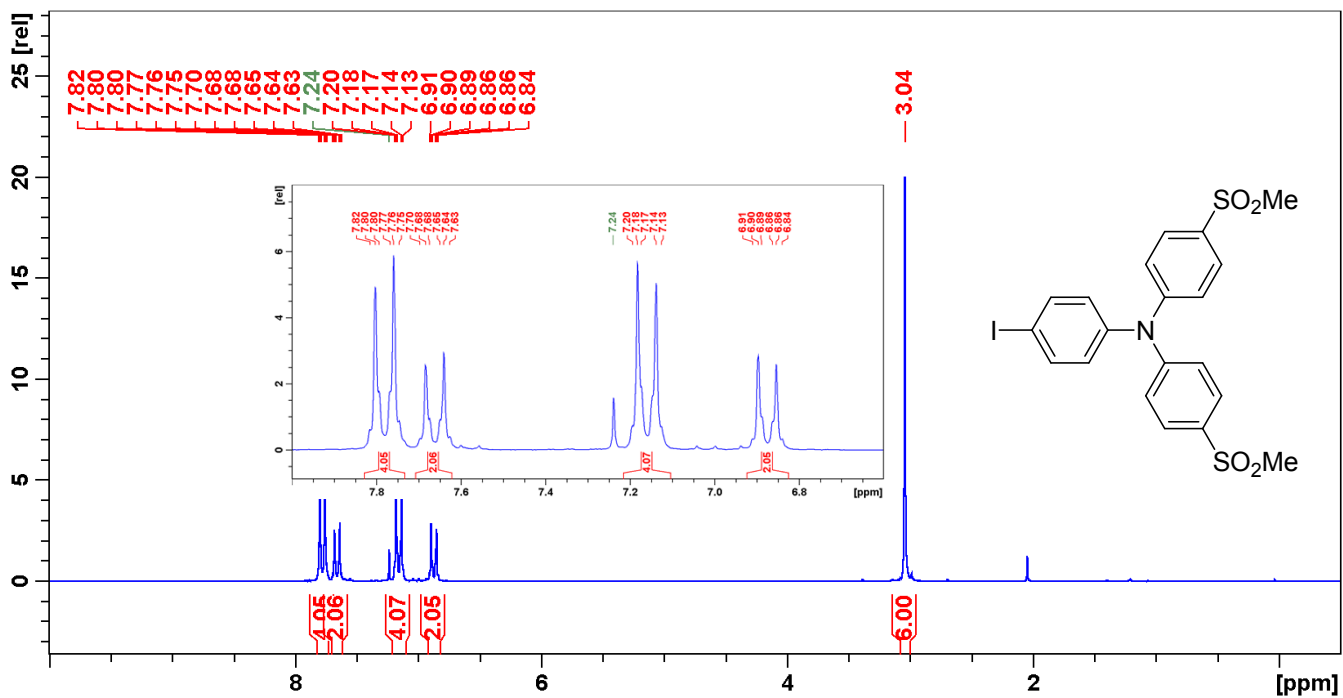


Figure S15. Proton NMR spectrum of compound **6k**.

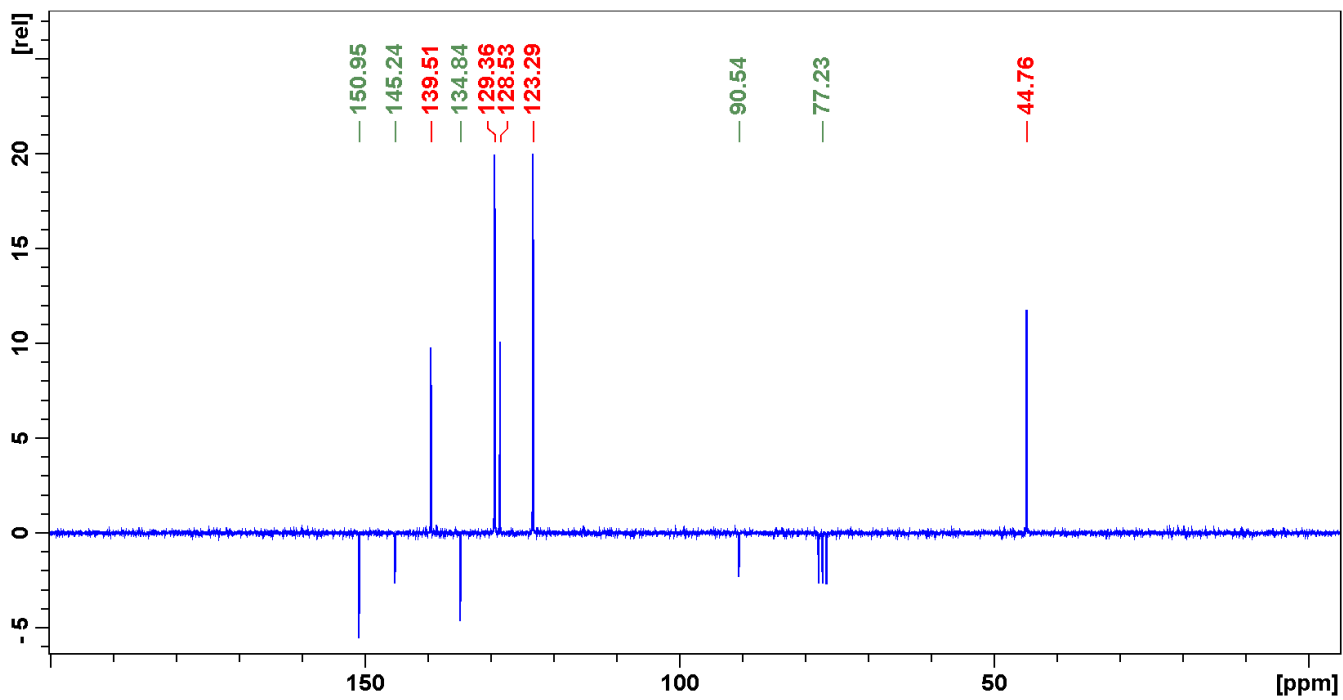


Figure S16. Carbon NMR spectrum of compound **6k**.

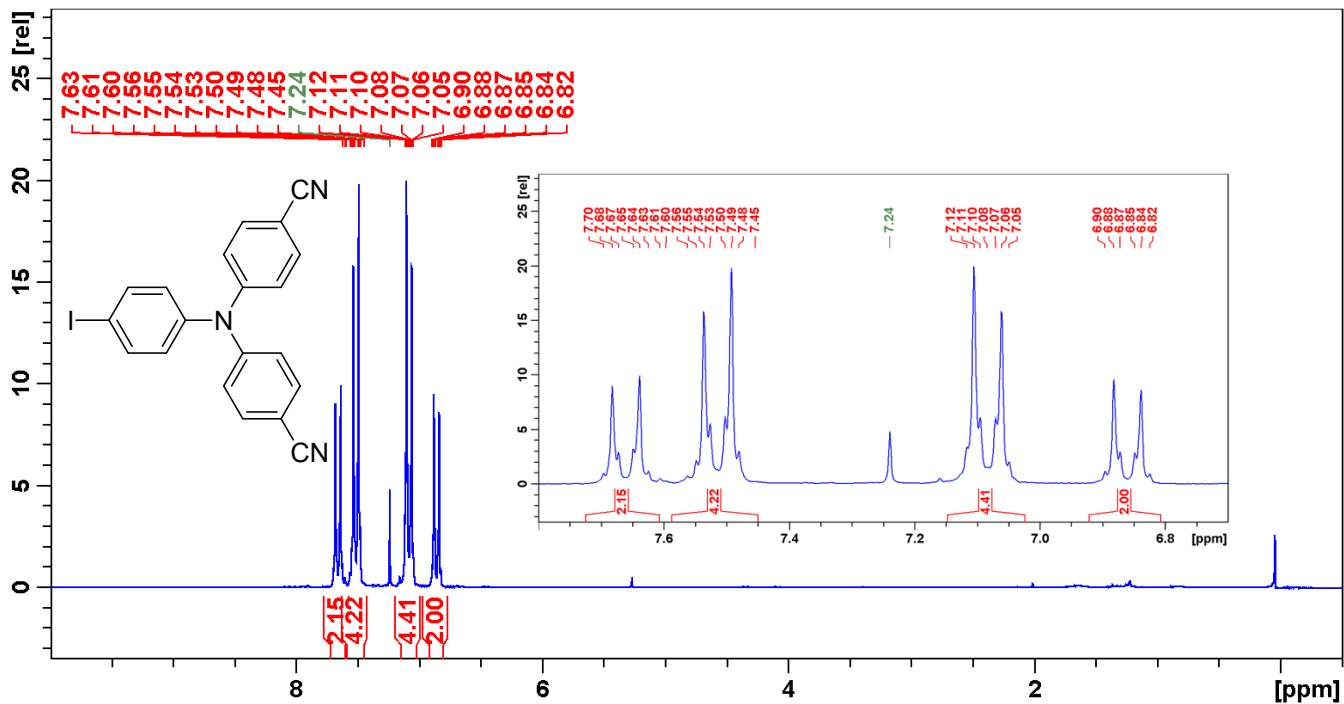


Figure S17. Proton NMR spectrum of compound **6l**.

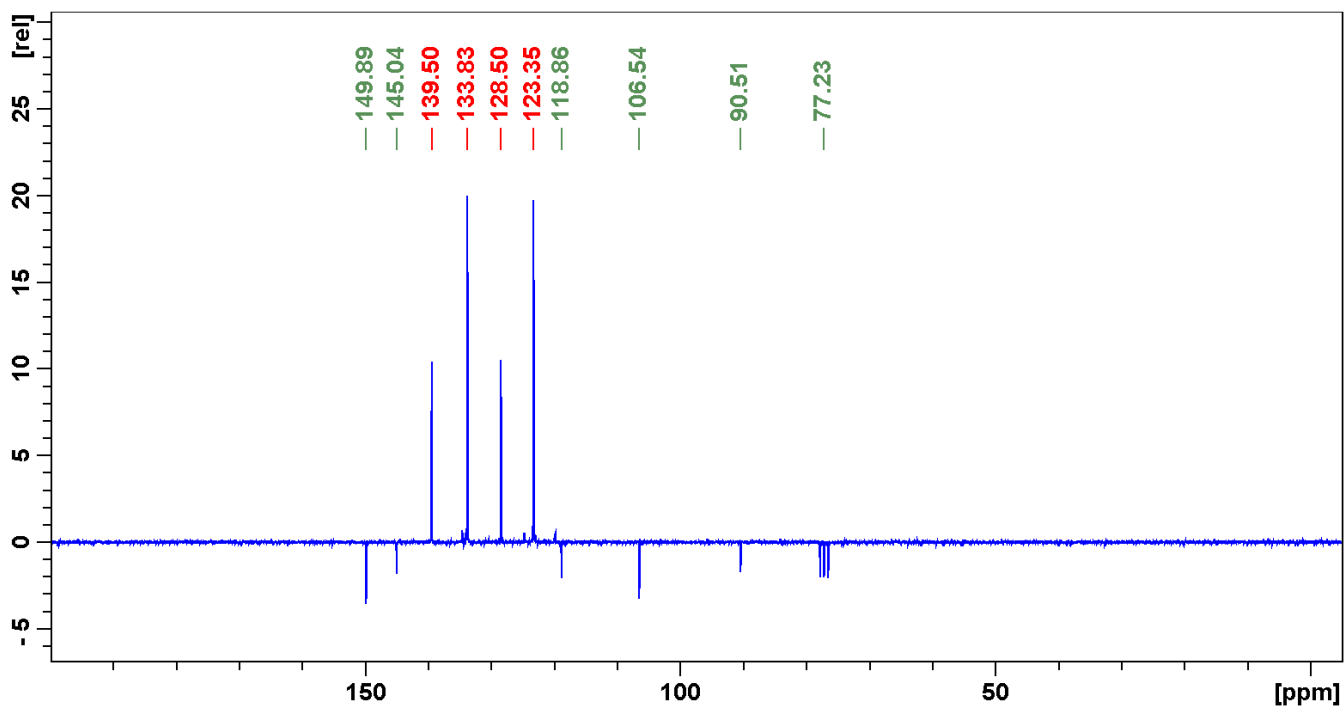


Figure S18. Carbon NMR spectrum of compound **6l**.

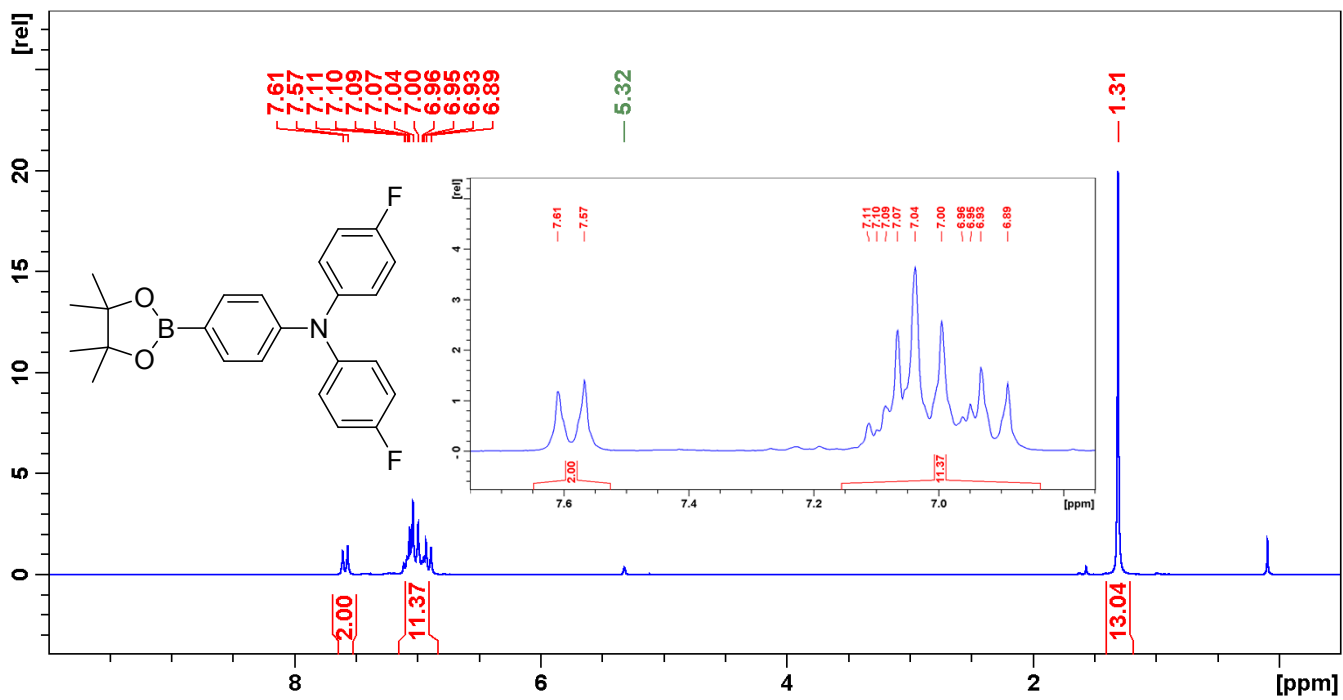


Figure S19. Proton NMR spectrum of compound **8c**.

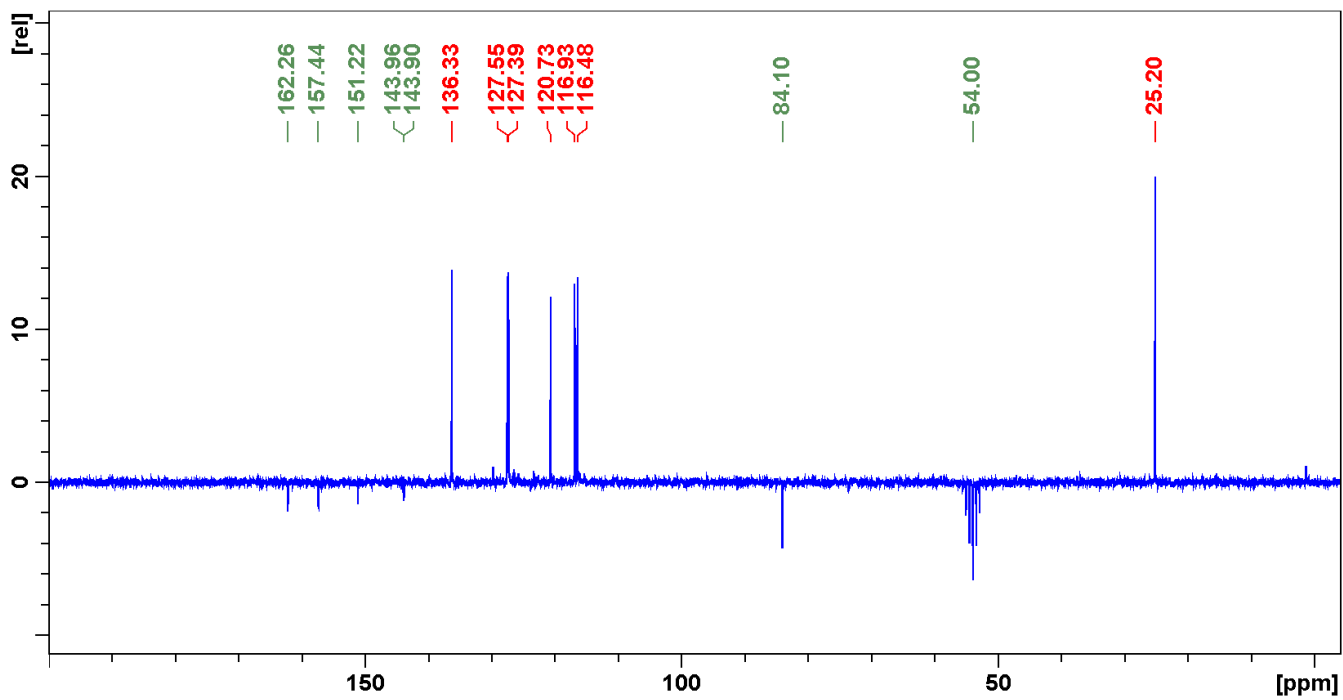


Figure S20. Carbon NMR spectrum of compound **8c**.

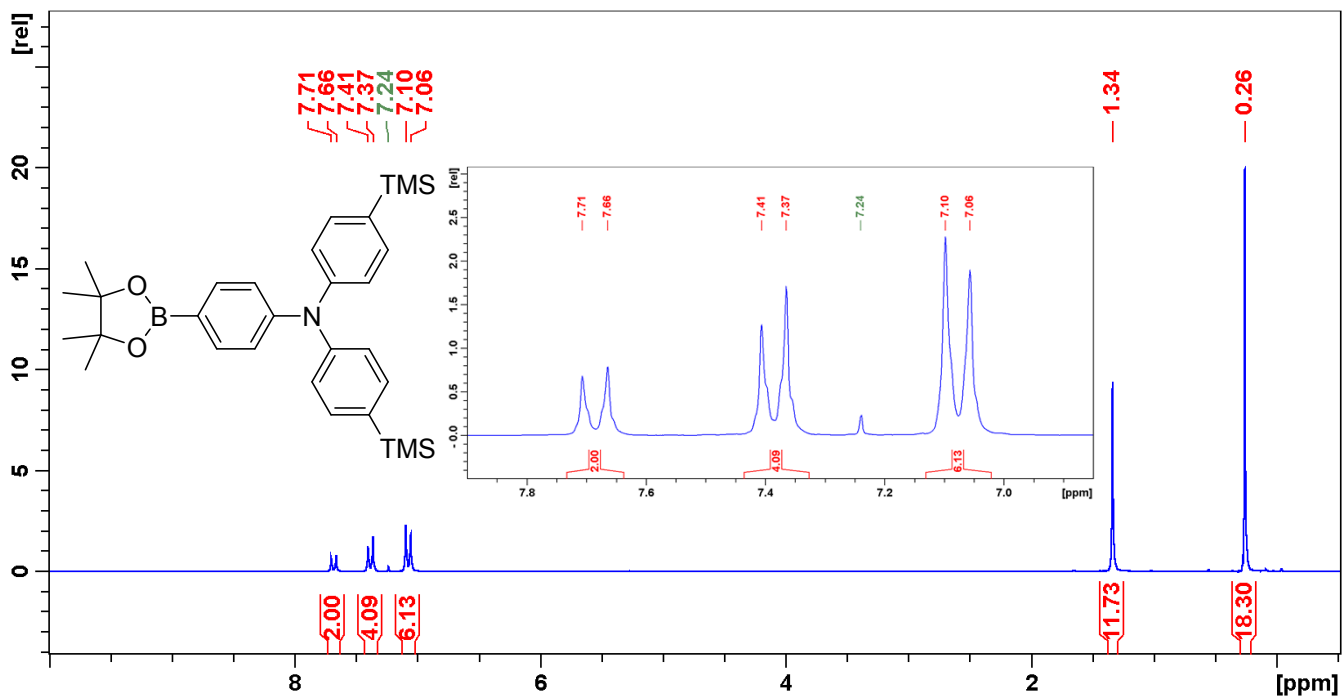


Figure S21. Proton NMR spectrum of compound **8e**.

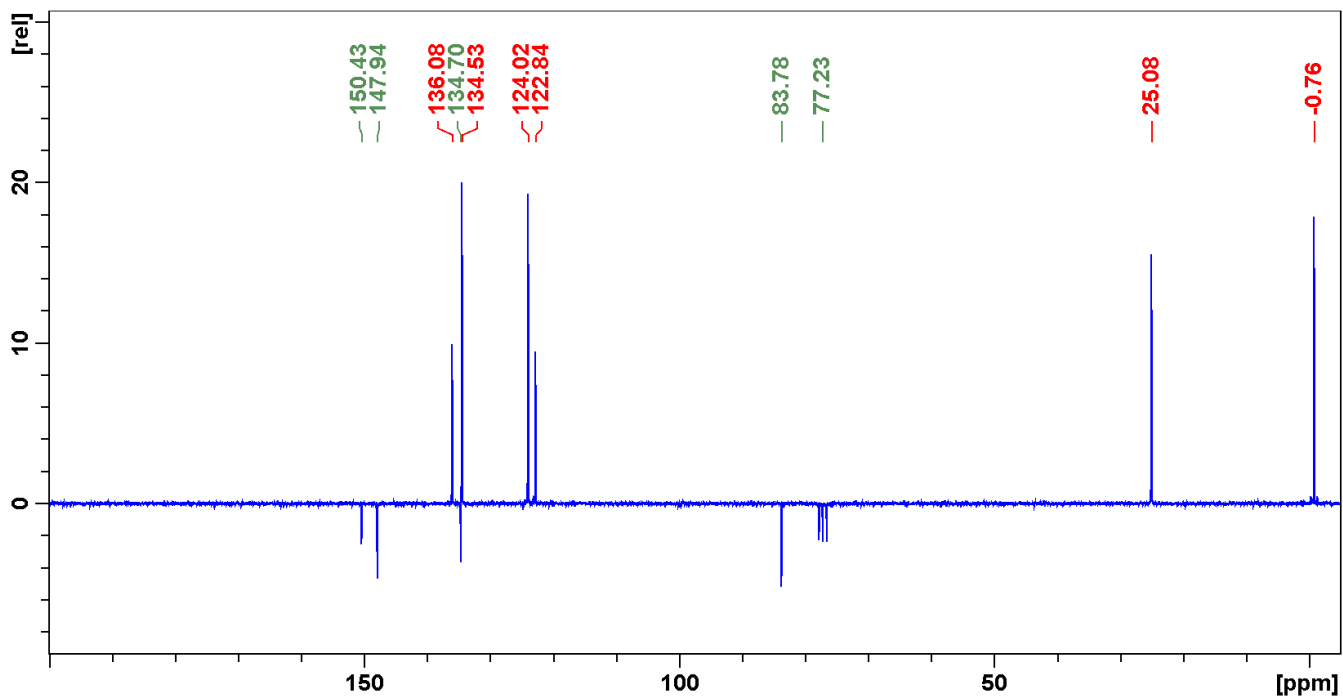


Figure S22. Carbon NMR spectrum of compound **8e**.

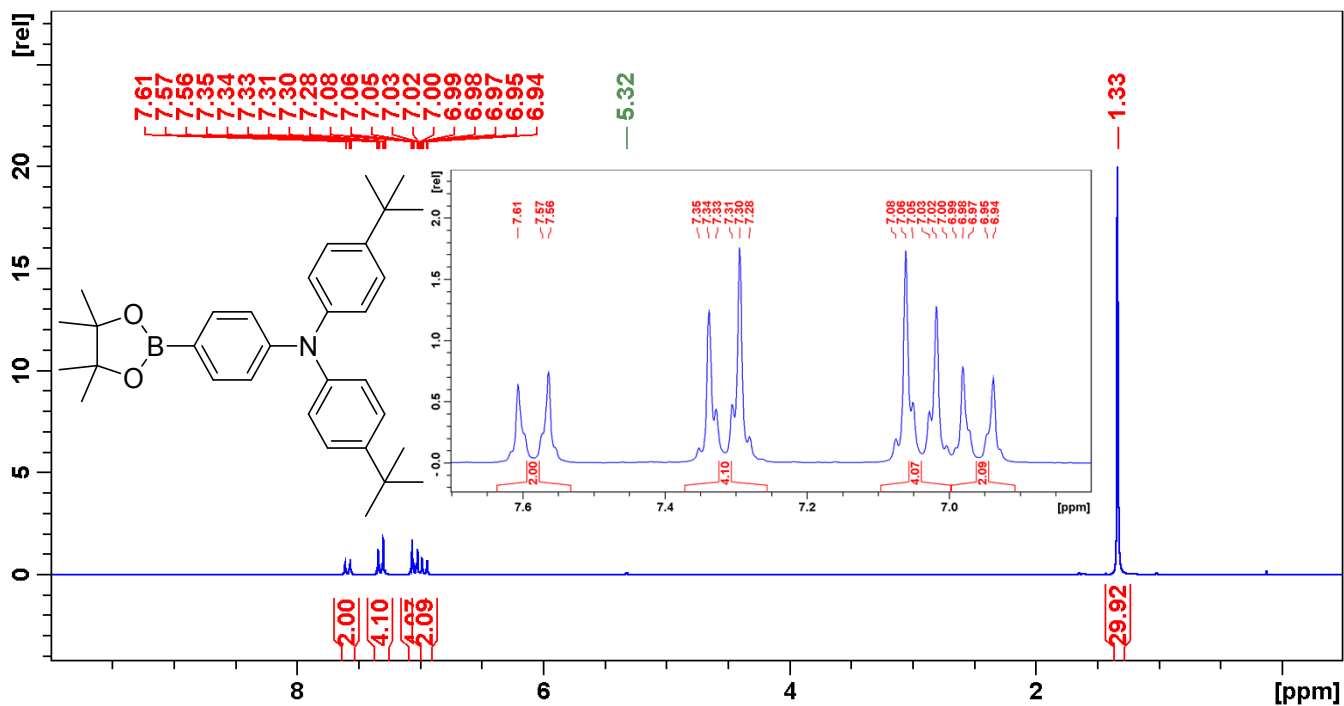


Figure S23. Proton NMR spectrum of compound **8f**.

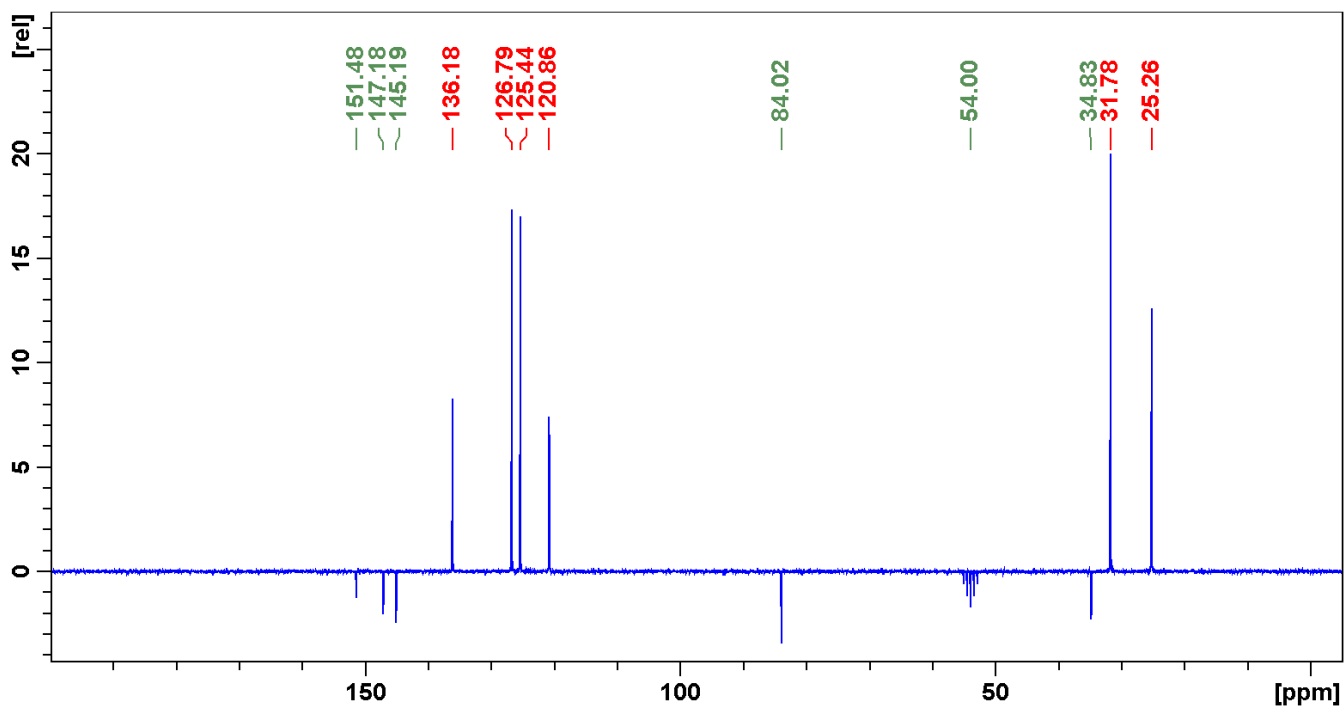


Figure S24. Carbon NMR spectrum of compound **8f**.

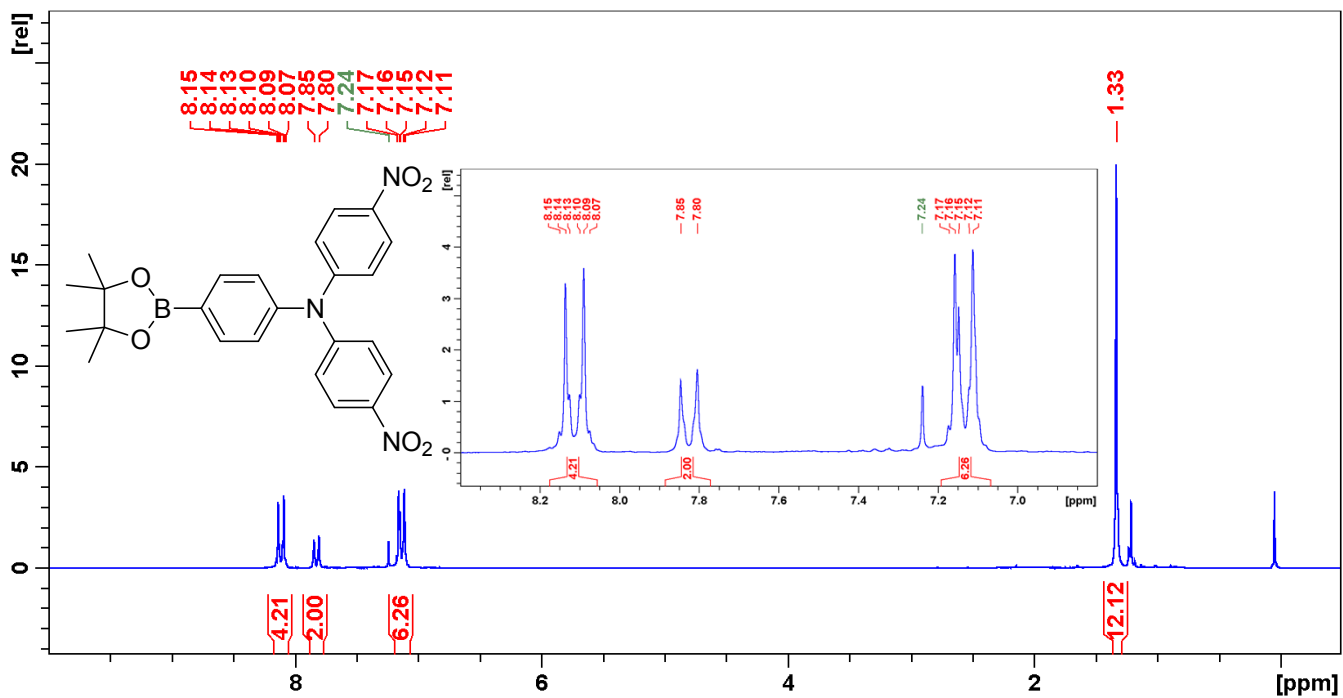


Figure S25. Proton NMR spectrum of compound **8g**.

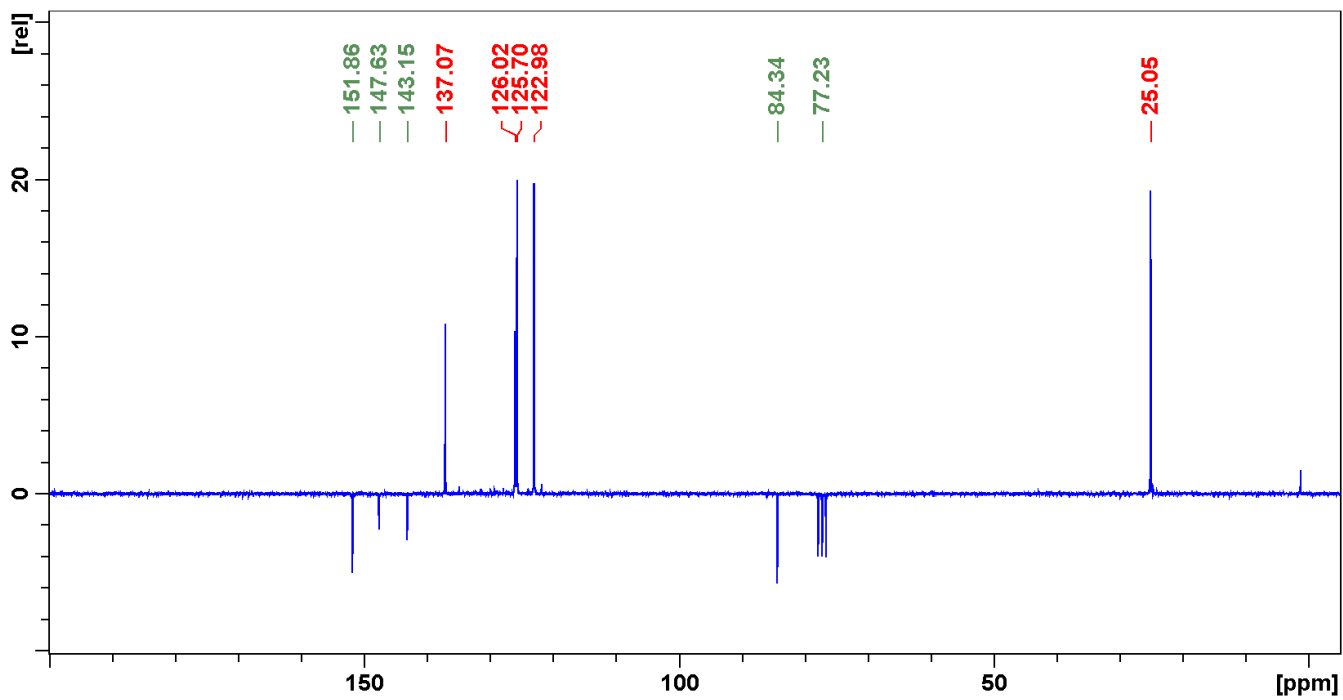


Figure S26. Carbon NMR spectrum of compound **8g**.

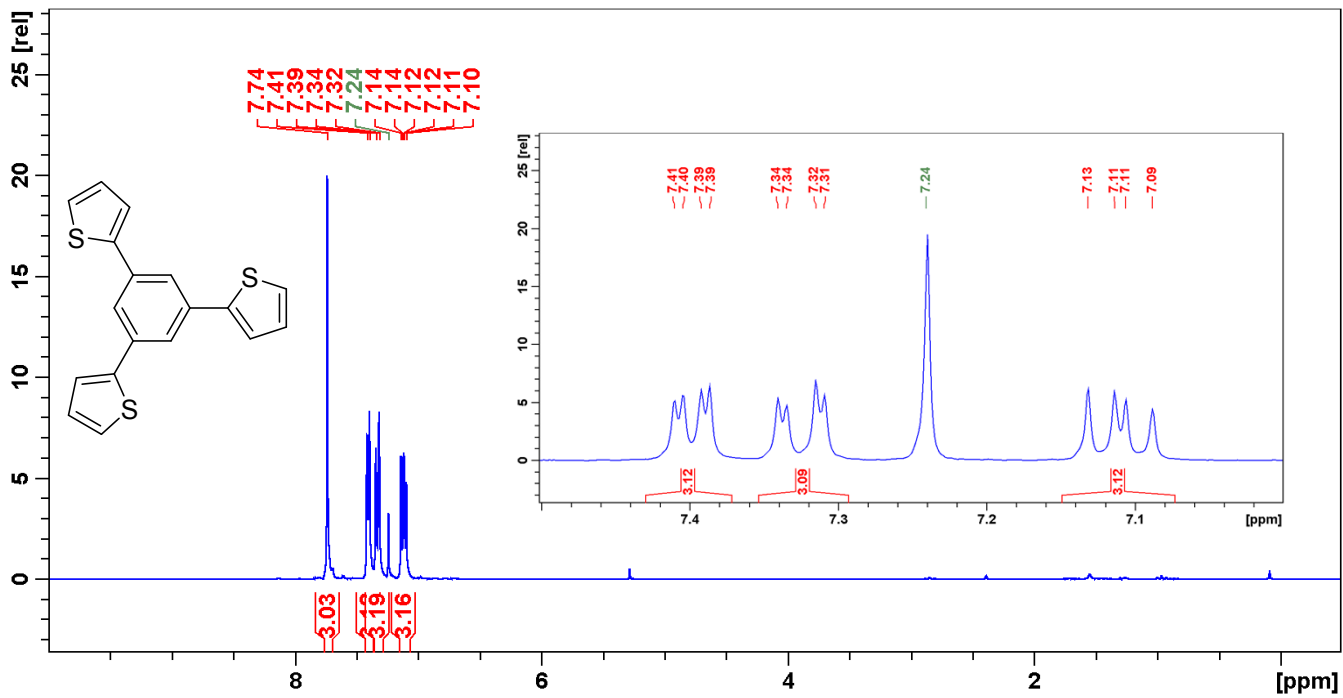


Figure S27. Proton NMR spectrum of compound 2.

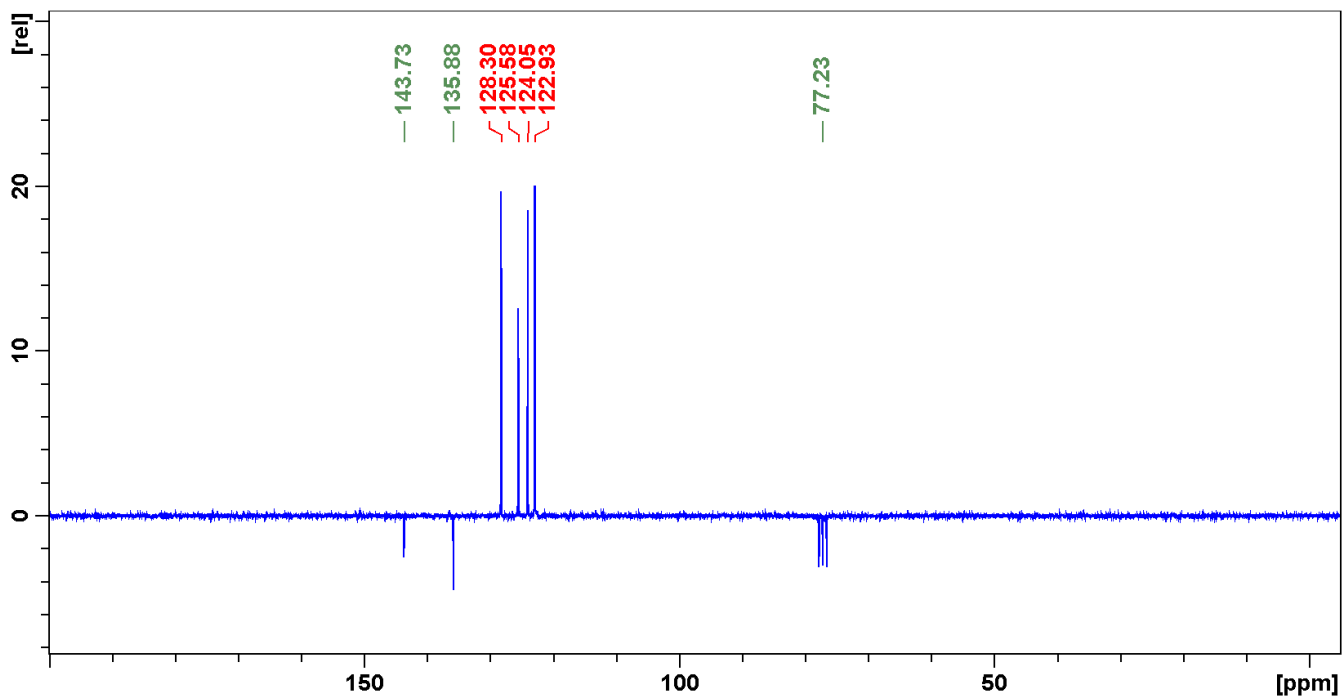


Figure S28. Carbon NMR spectrum of compound 2.

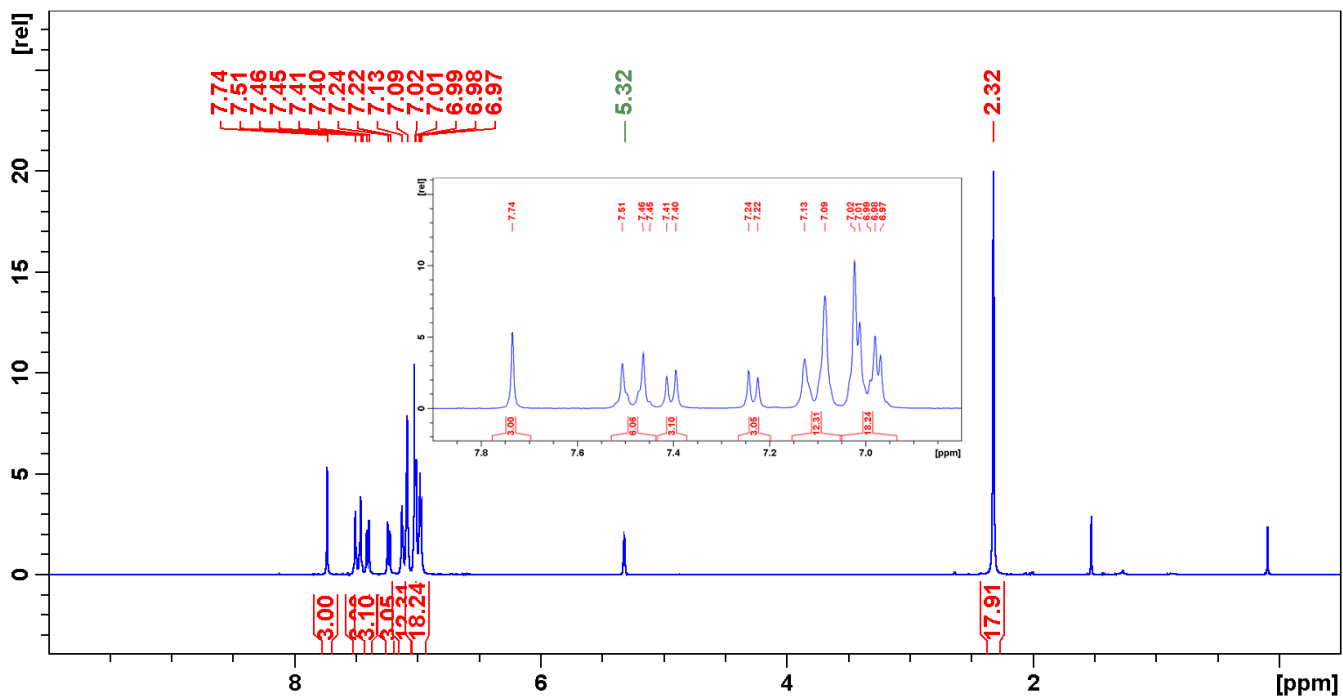


Figure S29. Proton NMR spectrum of compound S2.

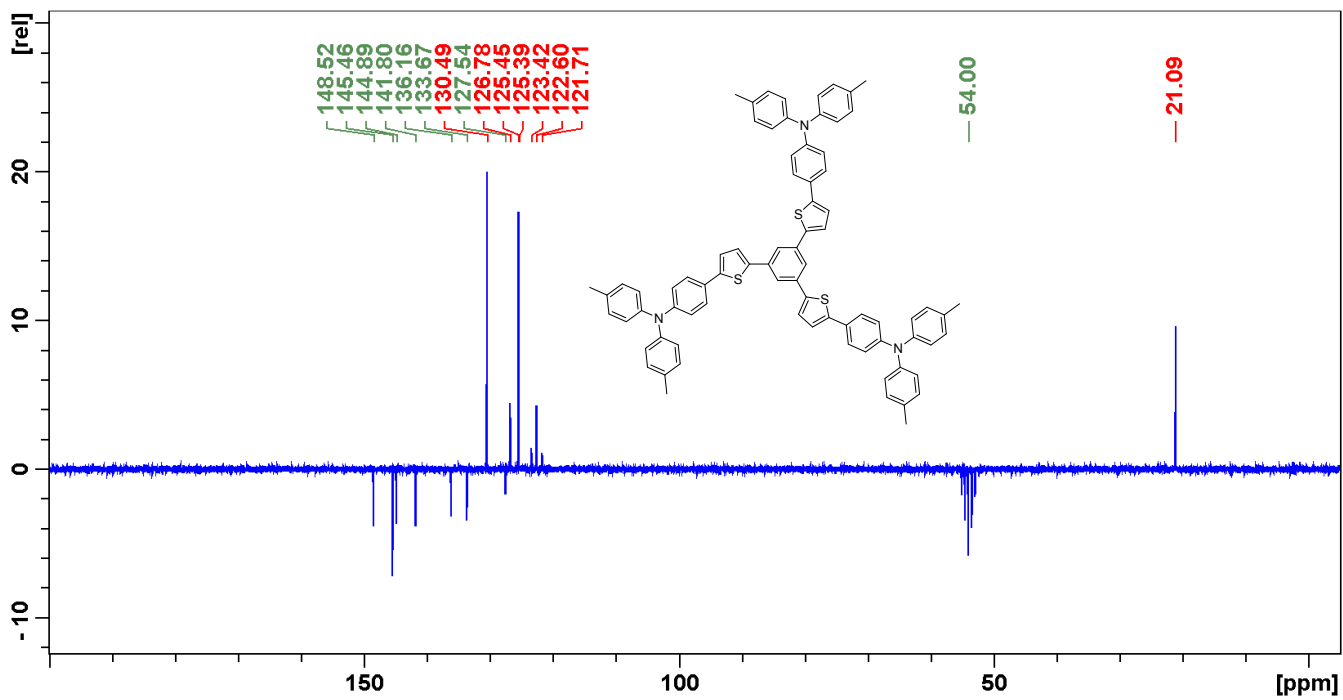


Figure S30. Carbon NMR spectrum of compound S2.



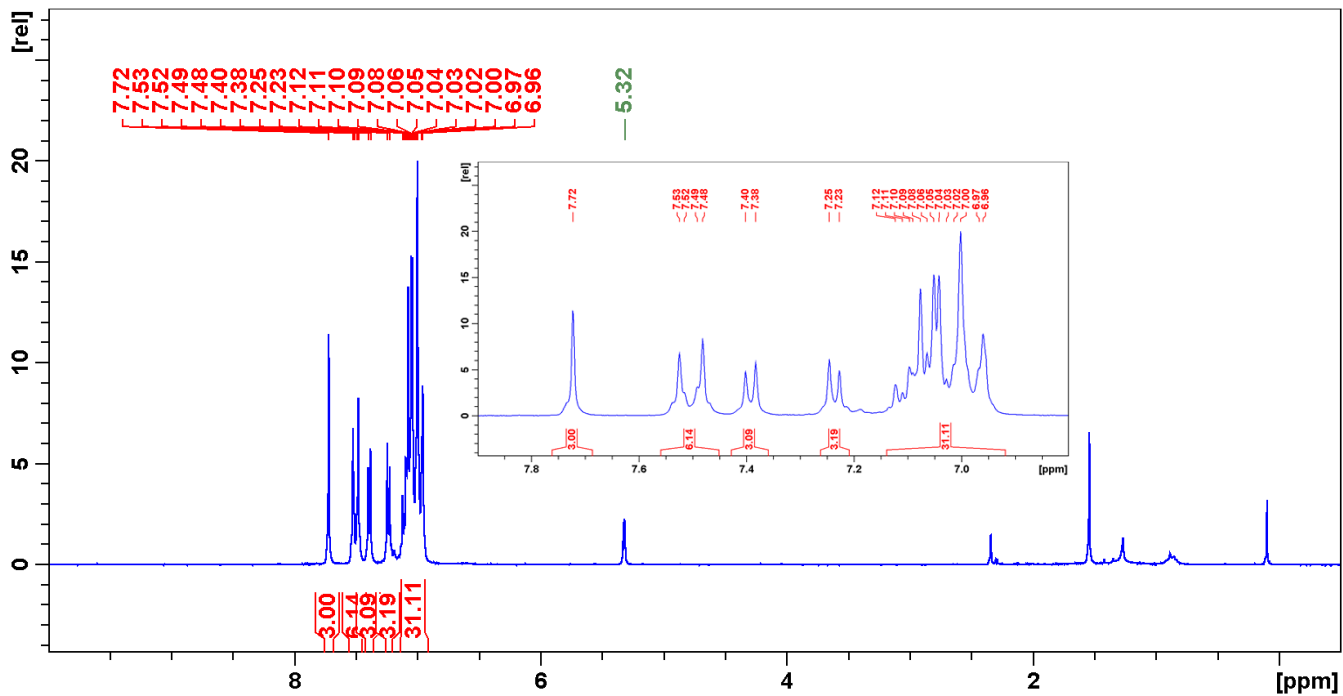


Figure S31. Proton NMR spectrum of compound S3.

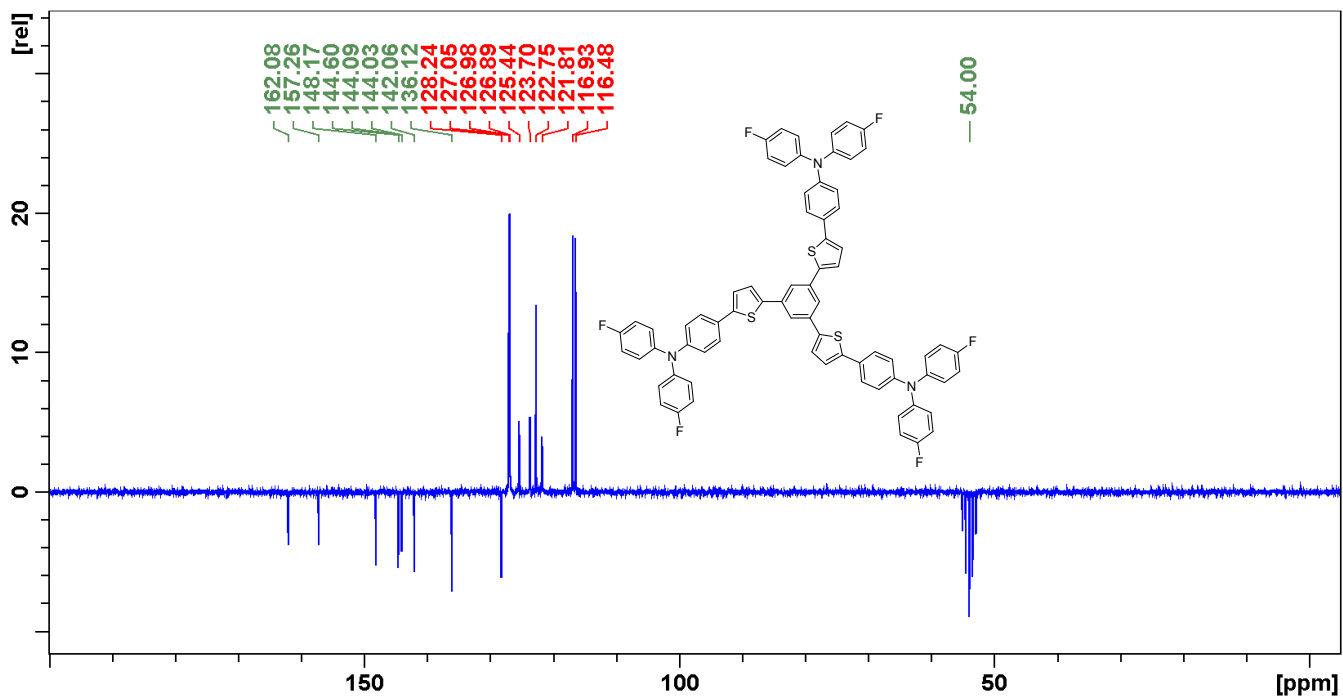


Figure S32. Carbon NMR spectrum of compound S3.

## B) Absorption and Emission Spectra

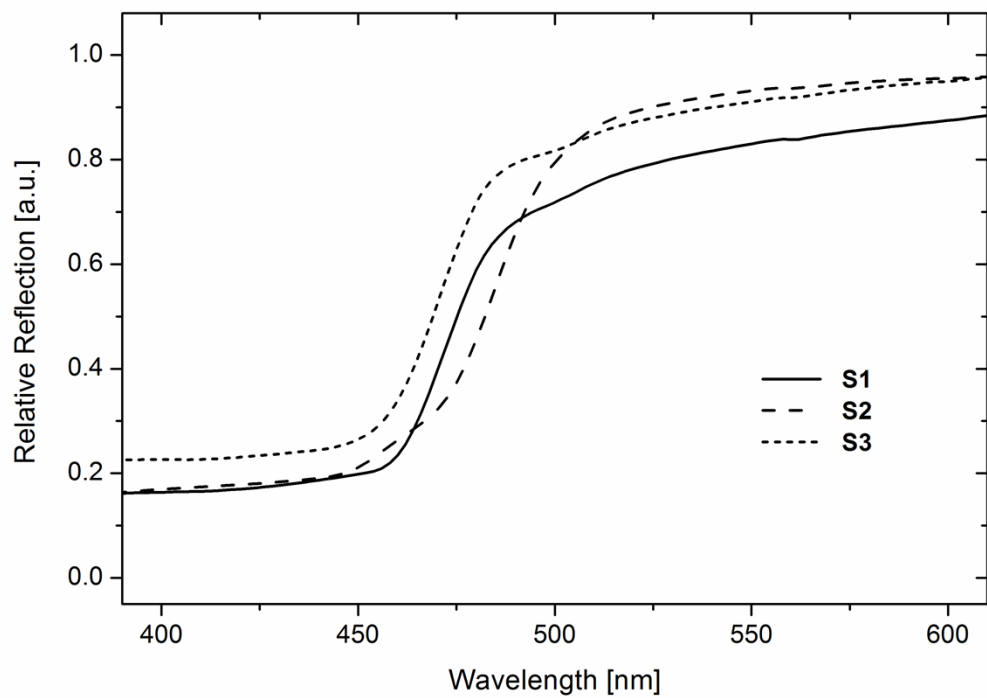


Figure S33. Absorption Spectra of Solid Samples

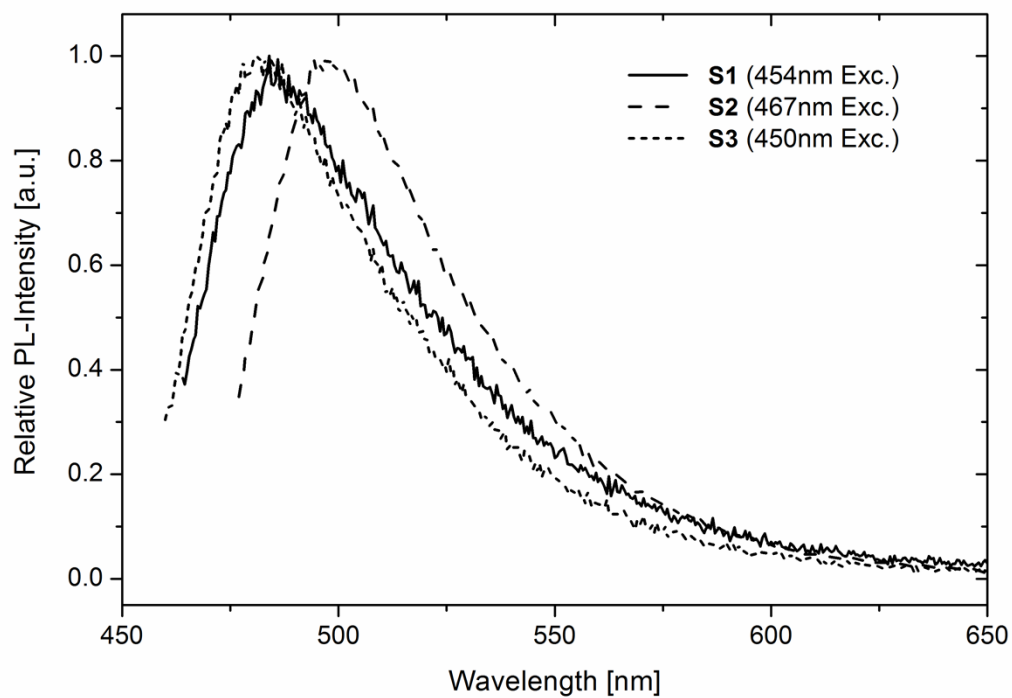


Figure S34. Emission Spectra of Solid Samples

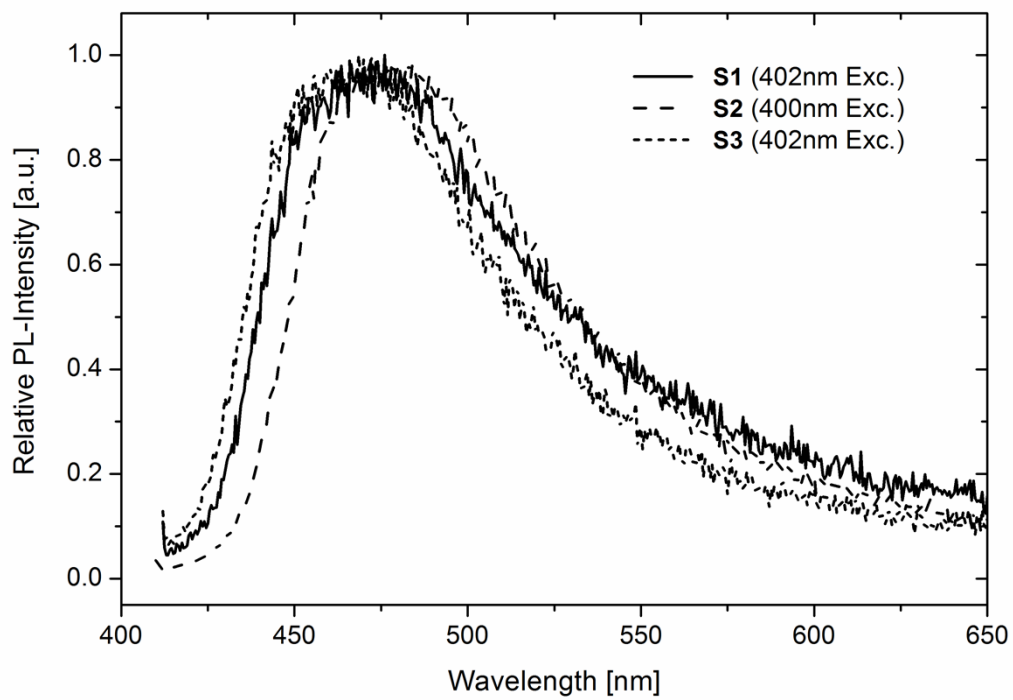


Figure S35. Emission Spectra of Film Samples

### C) HOMO/LUMO plots of S1-3

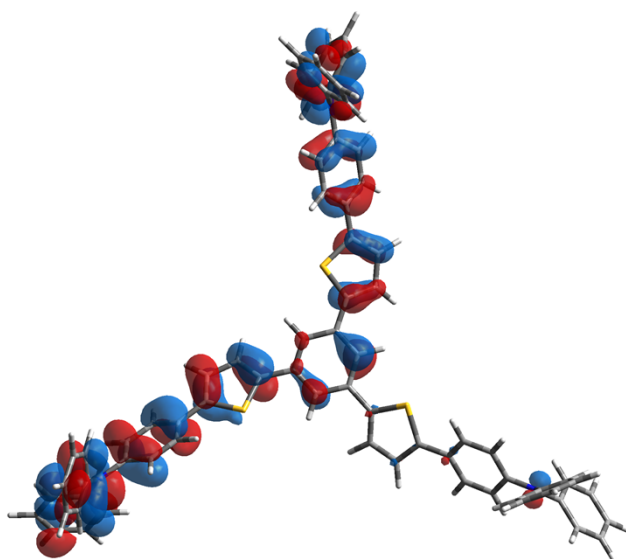
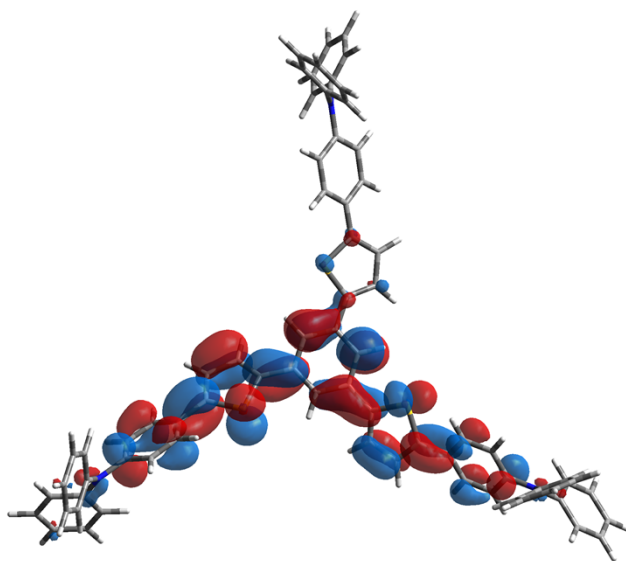


Figure S36. HOMO (bottom) and LUMO (top) of S1

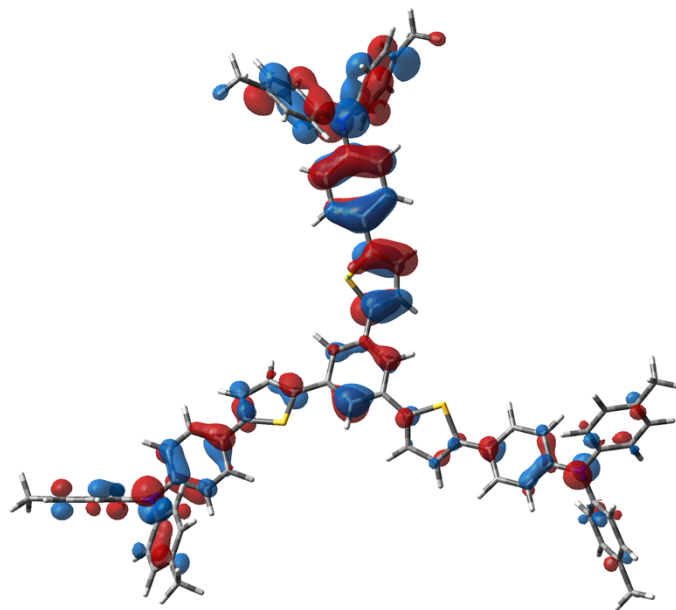
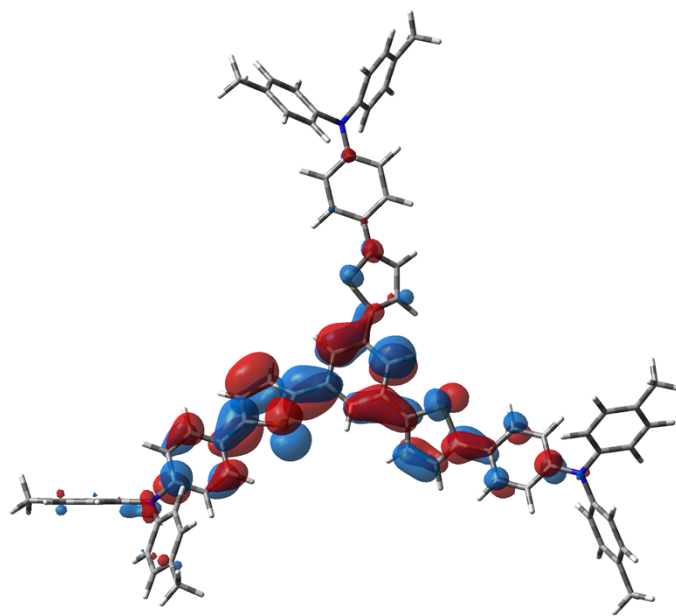


Figure S37. HOMO (bottom) and LUMO (top) of S2

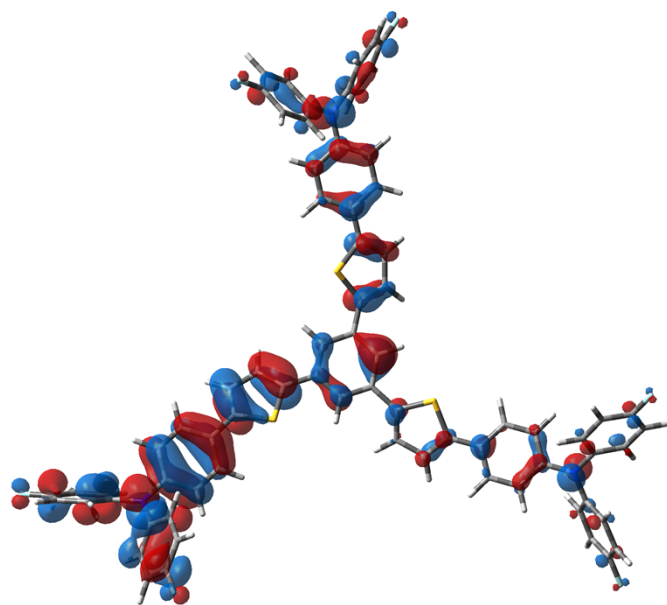
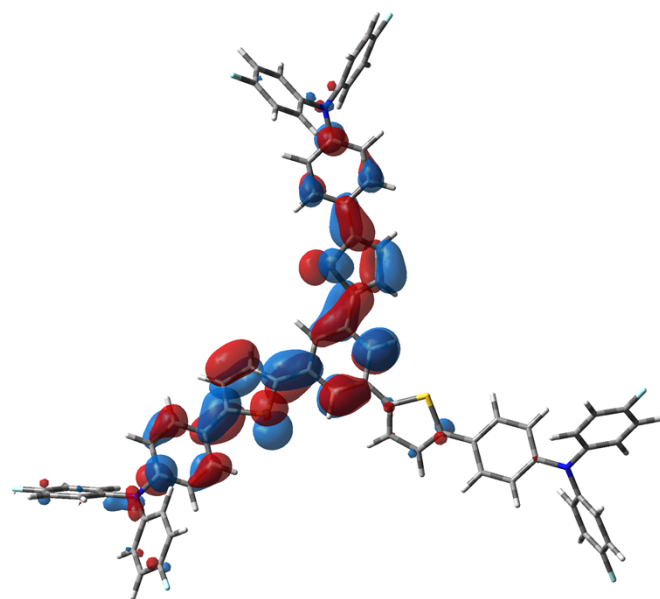


Figure S36. HOMO (bottom) and LUMO (top) of S3

# Manuscript #7

Supporting Information

P. Kautny, D. Lumpi\*, Y. Wang, A. Tissot, **J. Binterger**, E. Horkel, B. Stöger, C. Hametner, H. Hagemann, D. Ma, J. Fröhlich; *J. Mater. Chem. C*, 2014, 2 (11), 2069

Reproduced from Ref.<sup>87</sup> with permission from the Centre National de la Recherche Scientifique (CNRS) and The Royal Society of Chemistry.





# Electronic Supporting Information

## ESI

### **Oxadiazole based bipolar host materials employing planarized triarylamine donors for RGB PHOLEDs with low efficiency roll-off<sup>†</sup>**

Paul Kautny,<sup>a</sup> Daniel Lumpi,<sup>\*a</sup> Yanping Wang,<sup>b</sup> Antoine Tissot,<sup>c</sup>

Johannes Bintinger,<sup>a</sup> Ernst Horkel,<sup>a</sup> Berthold Stöger,<sup>d</sup> Christian Hametner,<sup>a</sup>

Hans Hagemann,<sup>c</sup> Dongge Ma,<sup>b</sup> and Johannes Fröhlich<sup>a</sup>

daniel.lumpi@tuwien.ac.at

<sup>a</sup> Institute of Applied Synthetic Chemistry, Vienna University of Technology, Getreidemarkt 9/163, A-1060 Vienna, Austria

<sup>b</sup> State Key Laboratory of Polymer Physics and Chemistry, Changchun Institute of Applied Chemistry, Chinese Academy of Sciences, Changchun, 130022, China

<sup>c</sup> Département de Chimie Physique, Université de Genève, 30, quai E. Ansermet, 1211 Geneva 4, Switzerland

<sup>d</sup> Institute of Chemical Technologies and Analytics, Vienna University of Technology, Getreidemarkt 9/164, A-1060 Vienna, Austria

## Content

**A. NMR Spectra**

**B. TGA/DSC**

**C. Cyclic Voltammetry**

**D. Phosphorescence Measurements**

**E. DFT Calculations**

**F. EL Spectra**

**G. Crystal Structure of Compound 3c**

## A) NMR Spectra

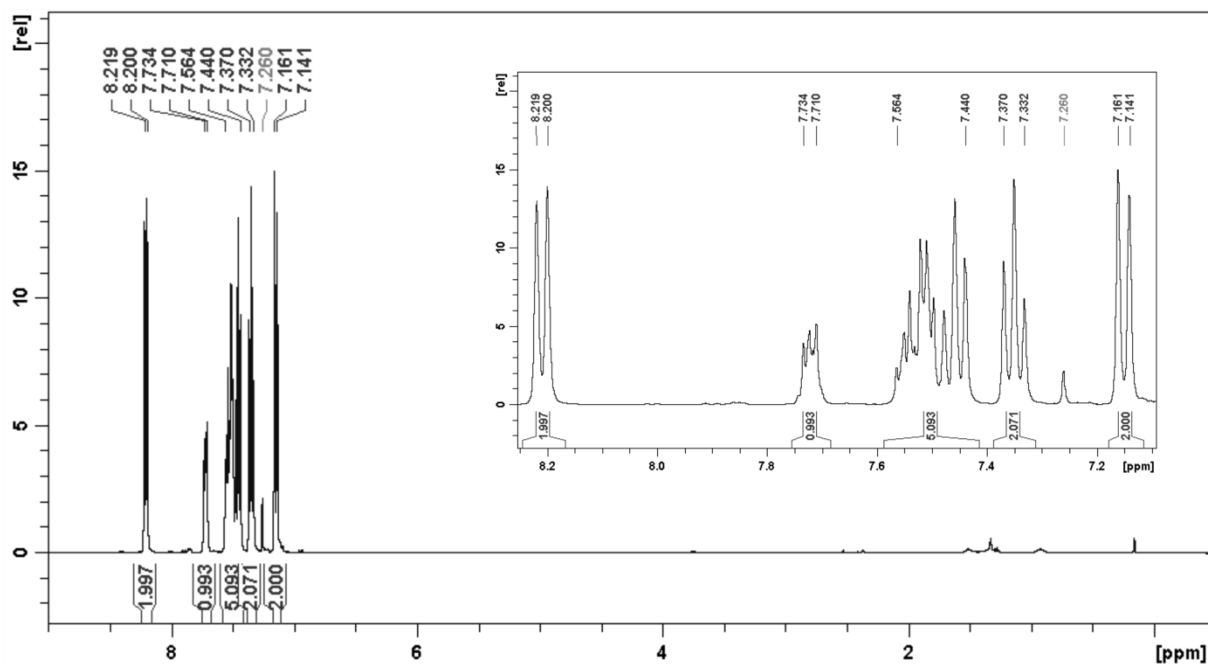


Figure S1. Proton NMR spectrum of compound **1ii**.

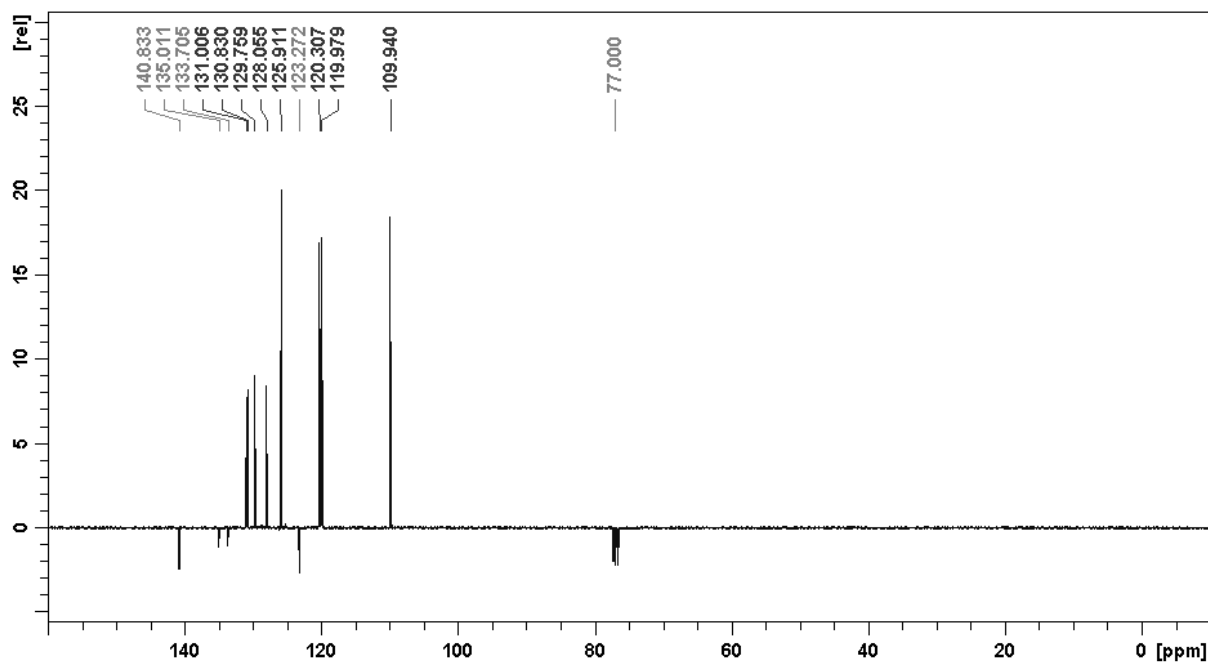


Figure S2. Carbon NMR spectrum of compound **1ii**.

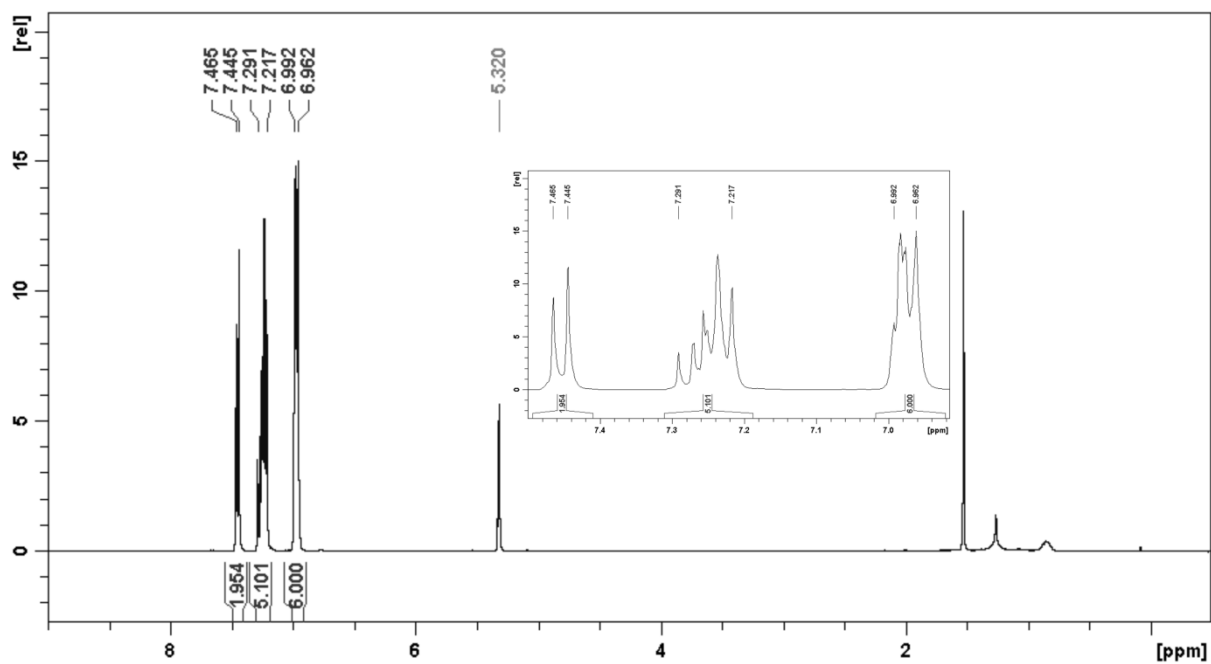


Figure S3. Proton NMR spectrum of compound **1iii**.

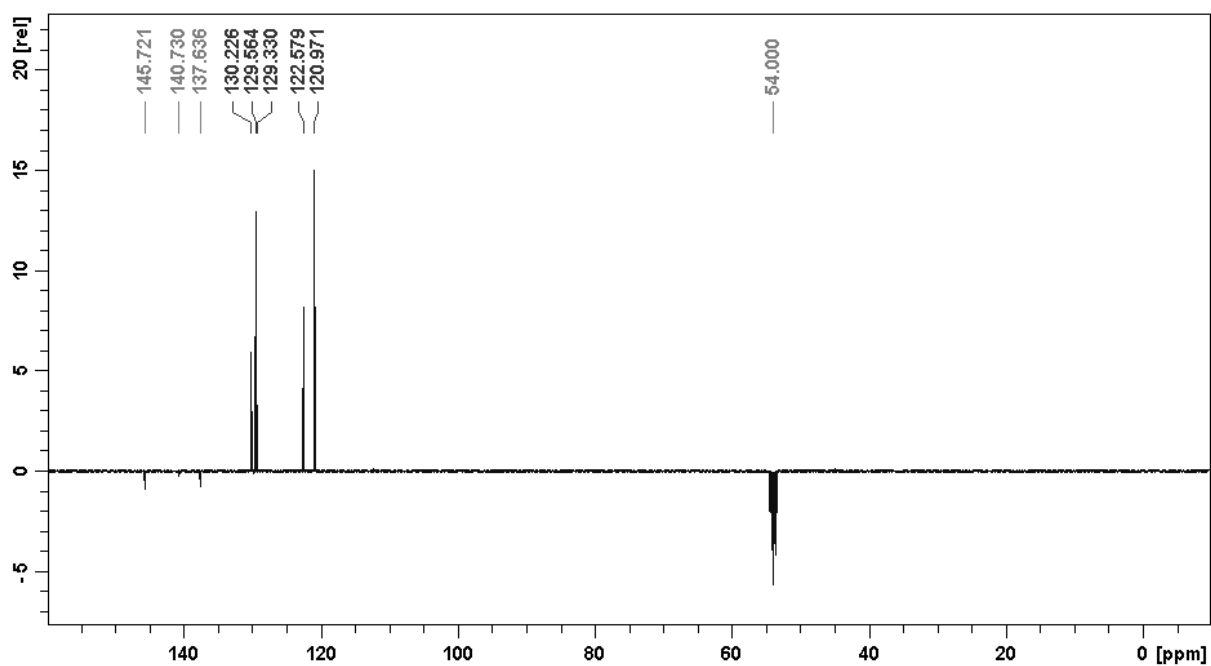


Figure S4. Carbon NMR spectrum of compound **1iii**.

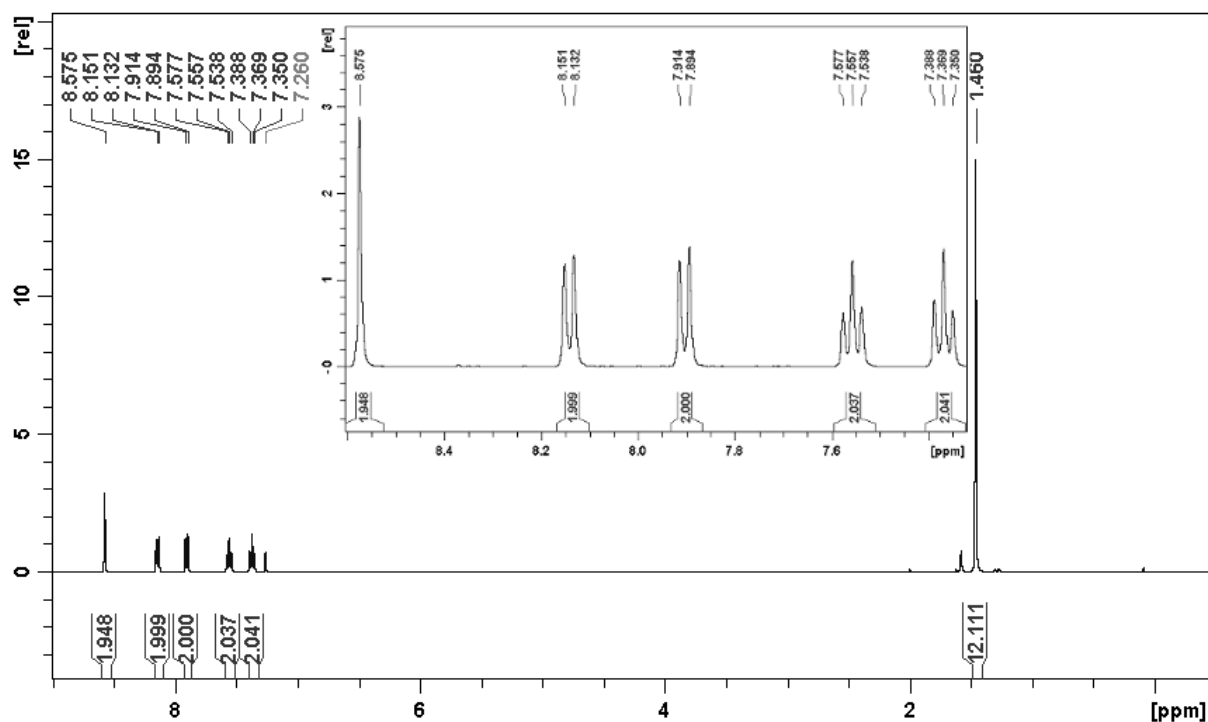


Figure S 5. Proton NMR spectrum of compound 3c.

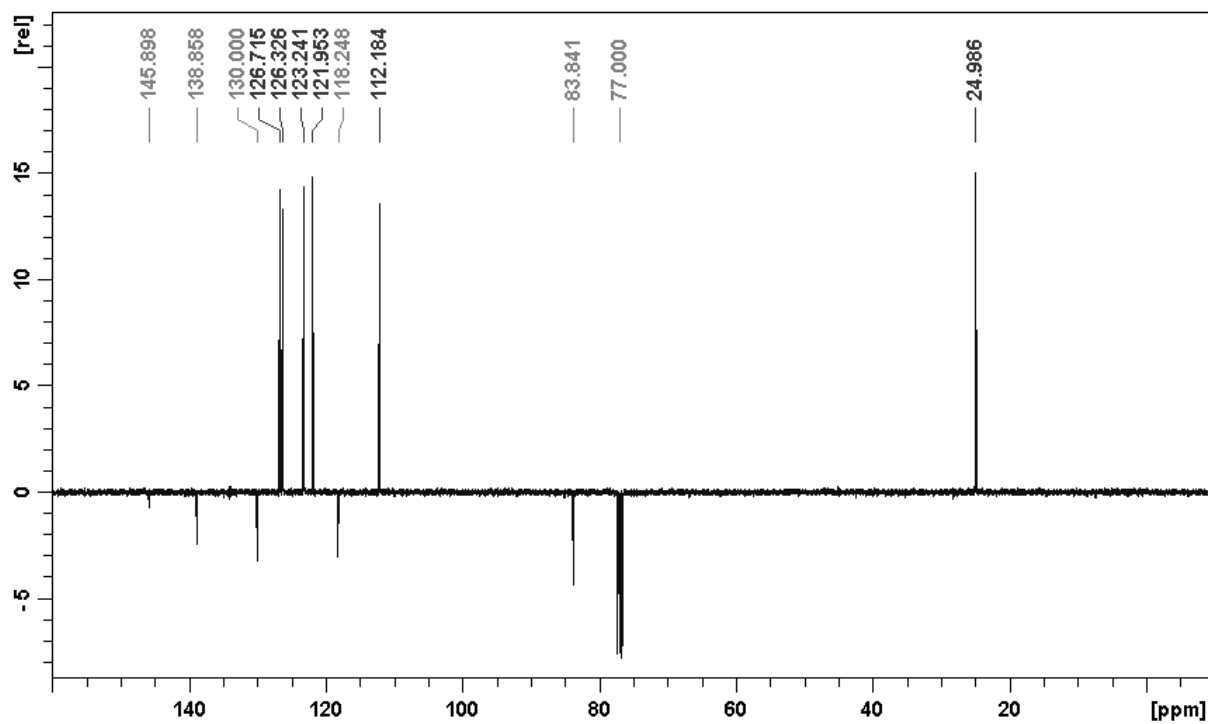


Figure S 6. Carbon NMR spectrum of compound 3c.

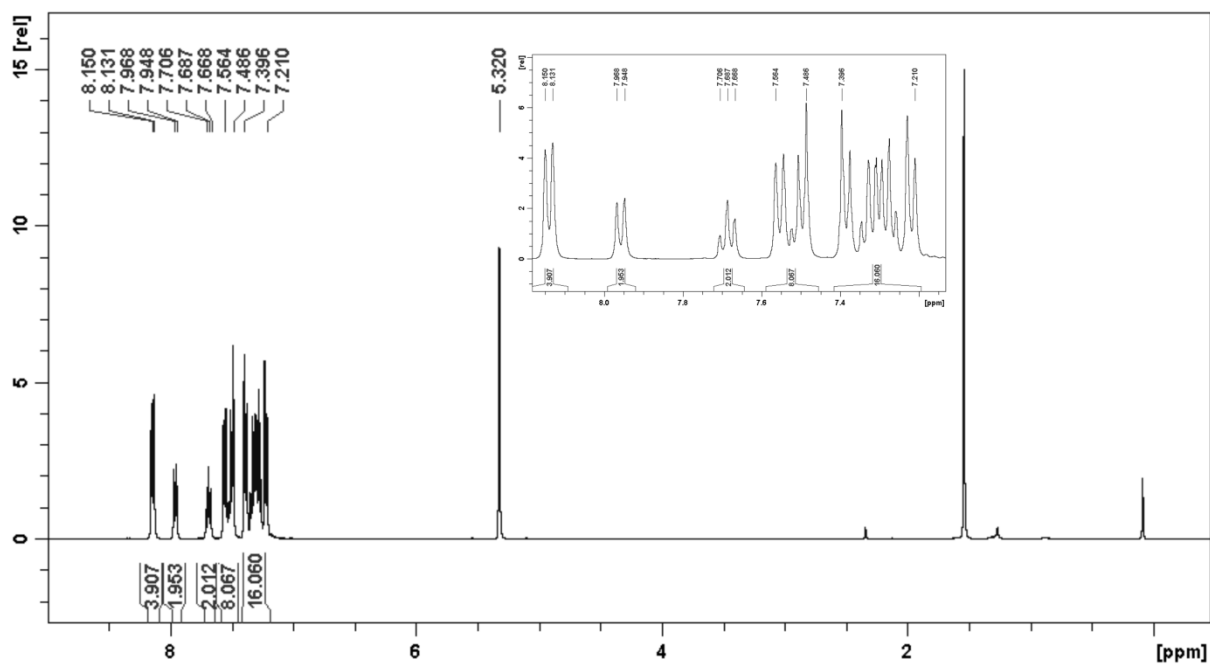


Figure S7. Proton NMR spectrum of compound o-PCzPOXD (5b).

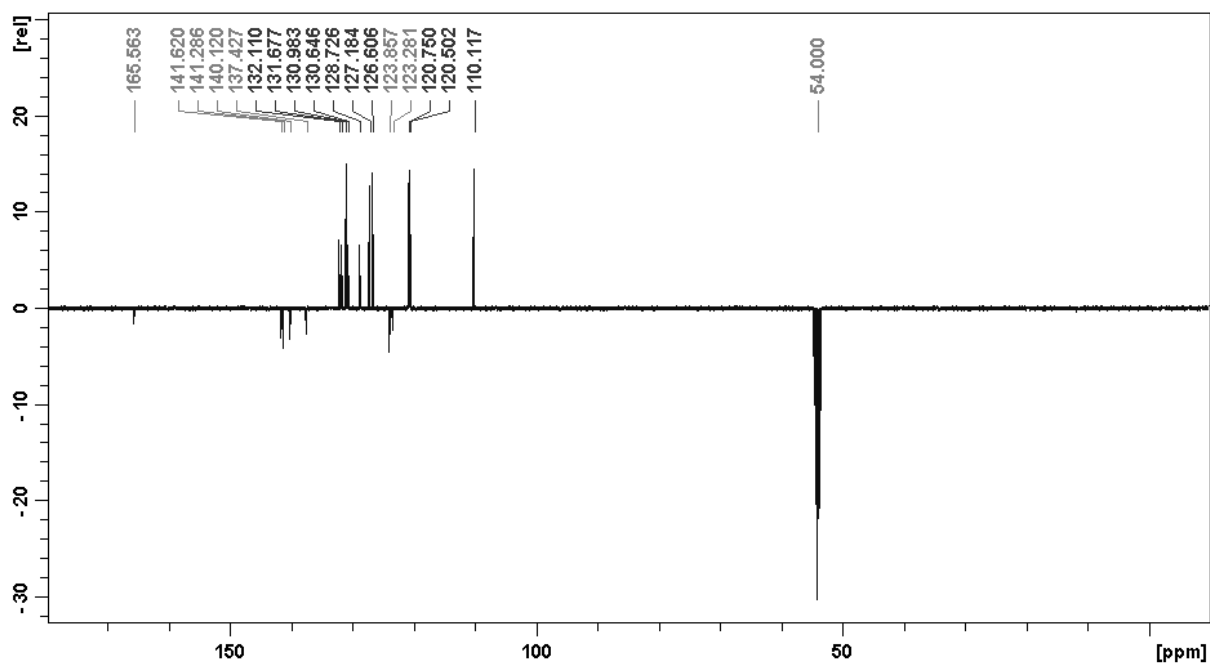


Figure S8. Carbon NMR spectrum of compound o-PCzPOXD (5b).

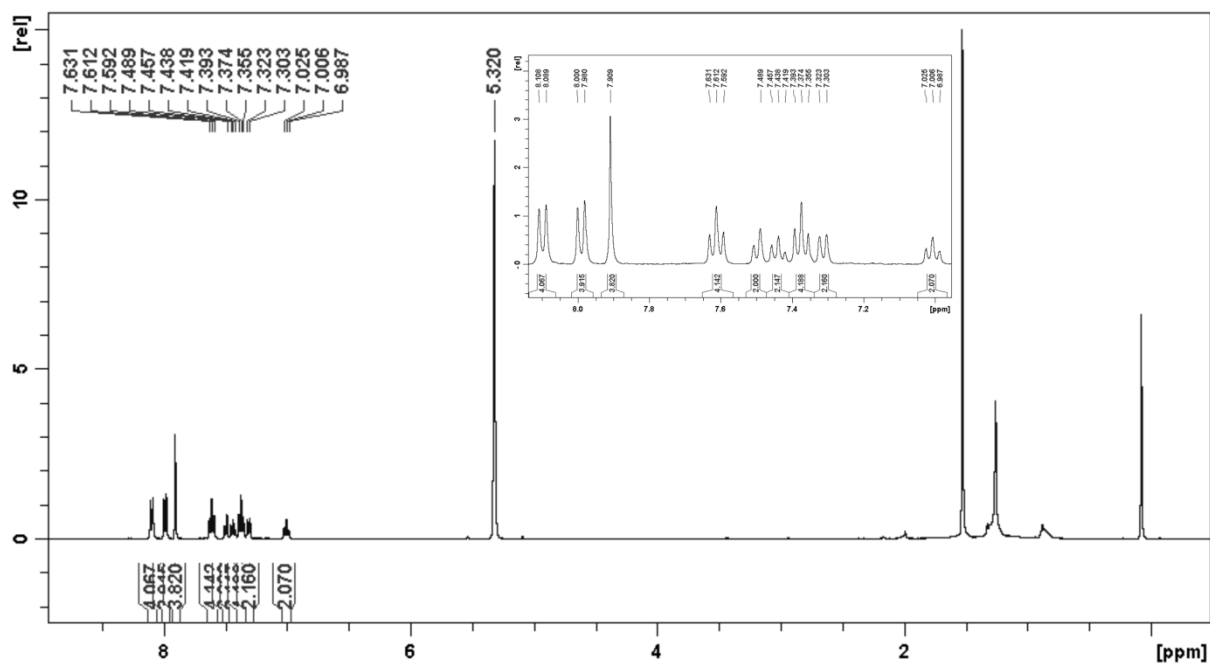


Figure S9. Proton NMR spectrum of compound o-ICzPOXD (**5c**).

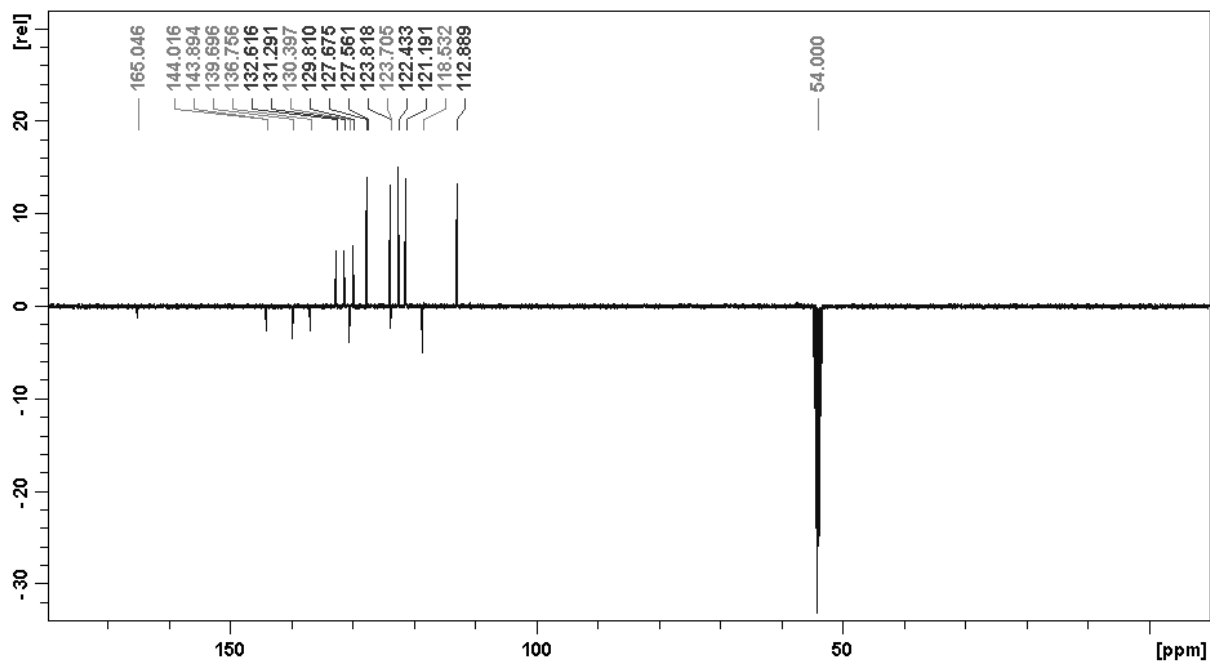


Figure S10. Carbon NMR spectrum of compound o-ICzPOXD (**5c**).

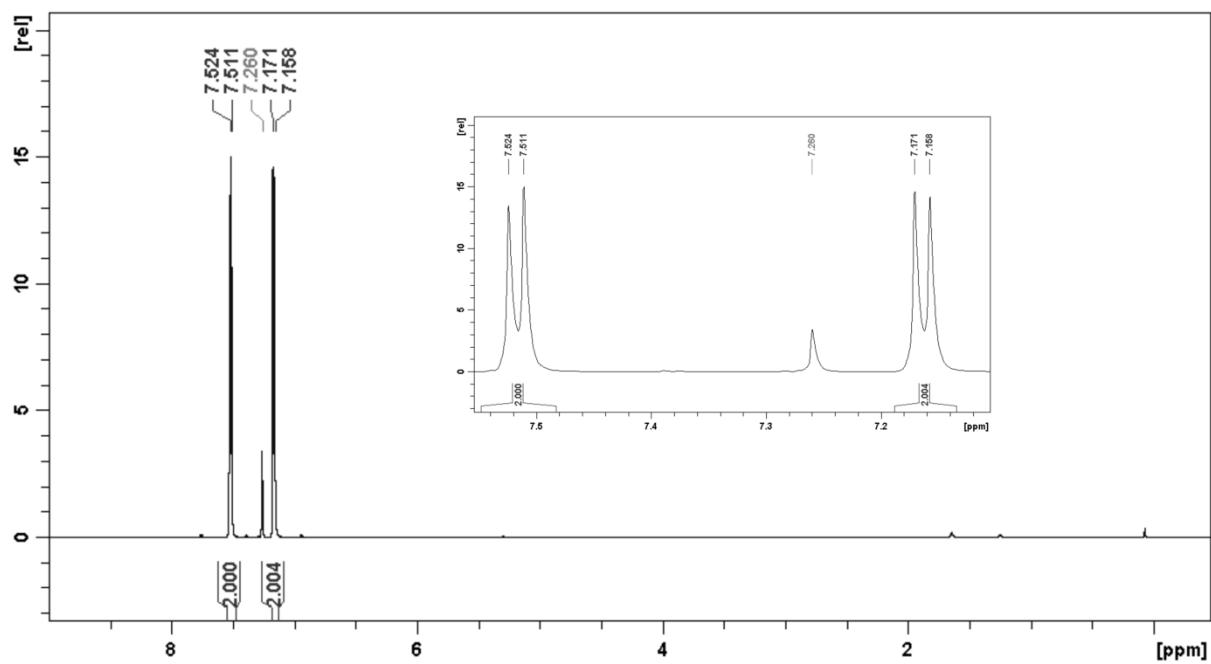


Figure S11. Proton NMR spectrum of compound 7i.

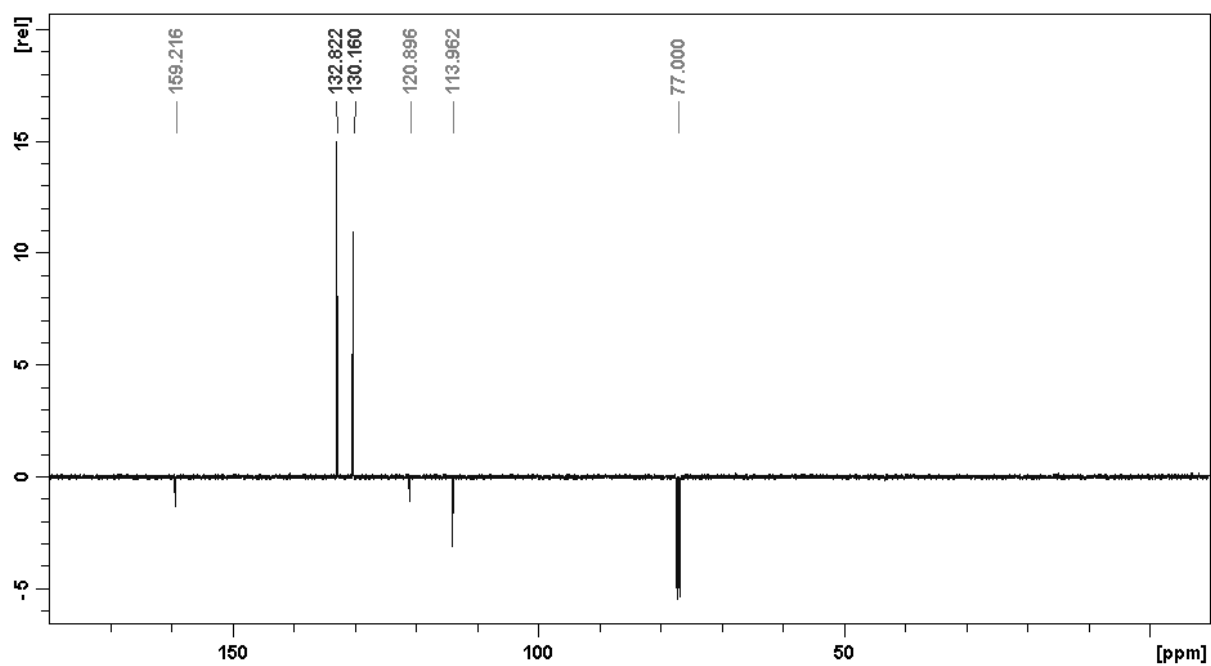


Figure S12. Carbon NMR spectrum of compound 7i.



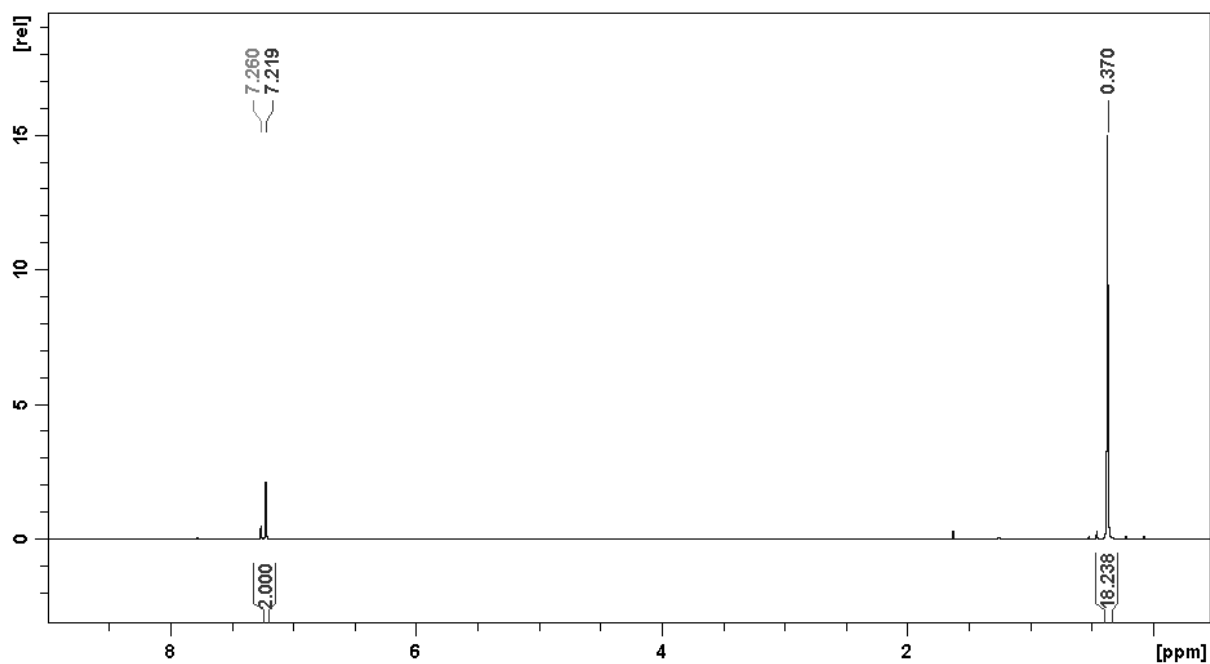


Figure S13. Proton NMR spectrum of compound 7ii.

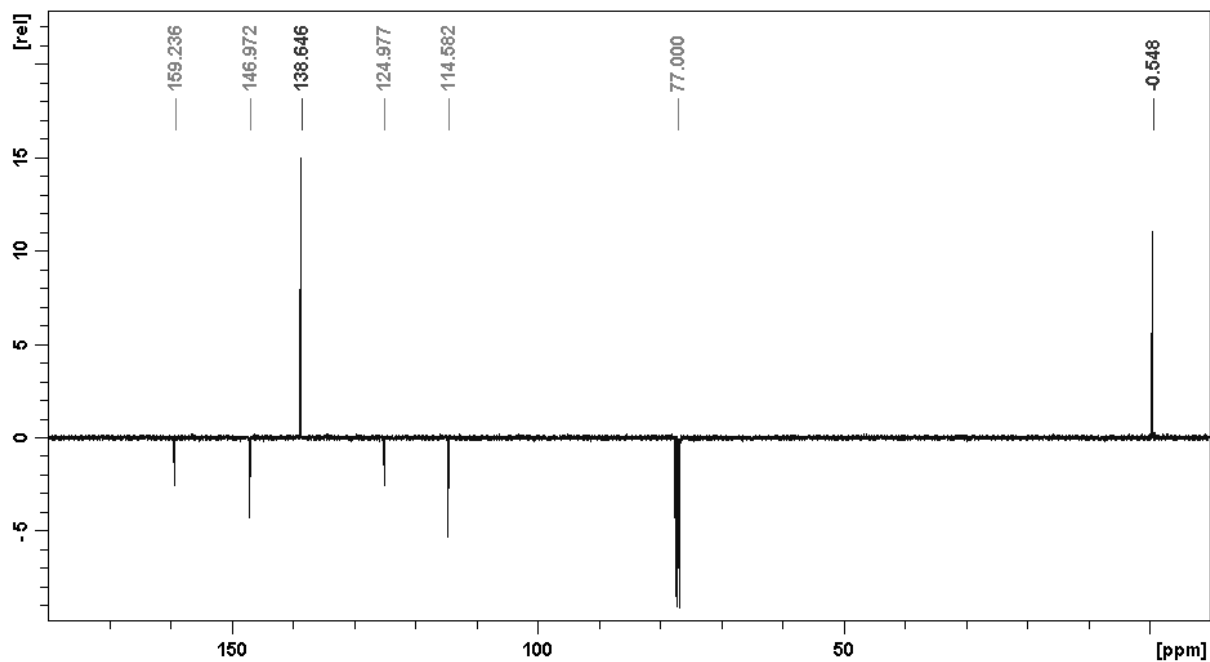


Figure S14. Carbon NMR spectrum of compound 7ii.

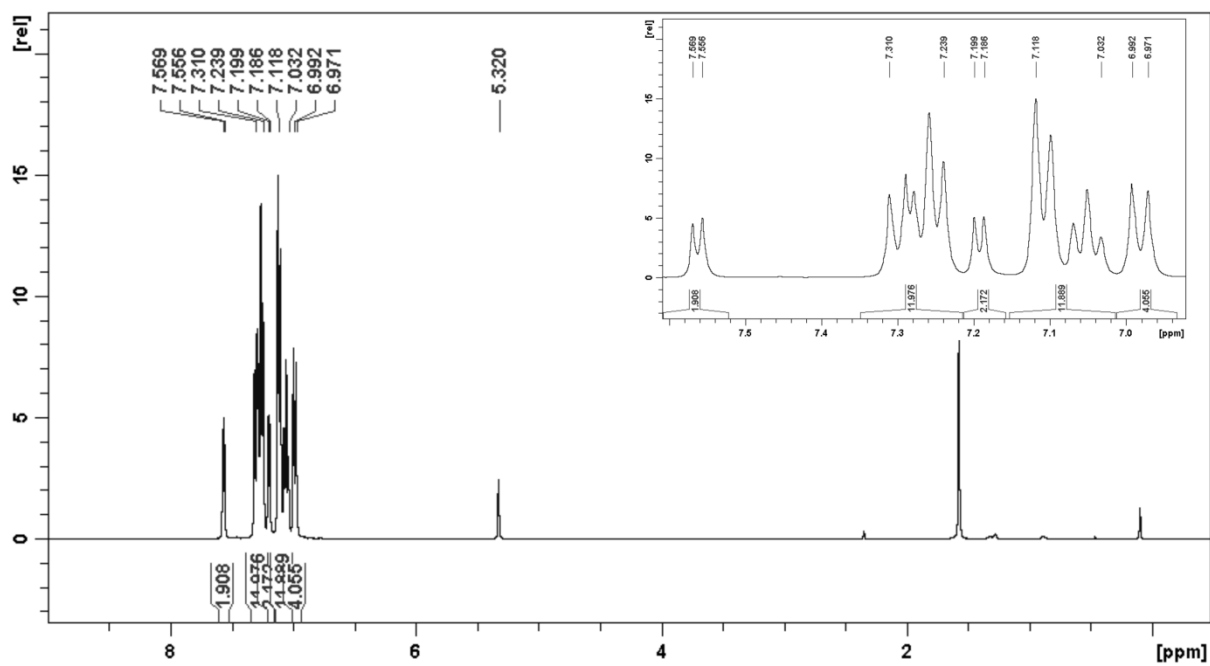


Figure S15. Proton NMR spectrum of compound o-TPATOXD (8a).

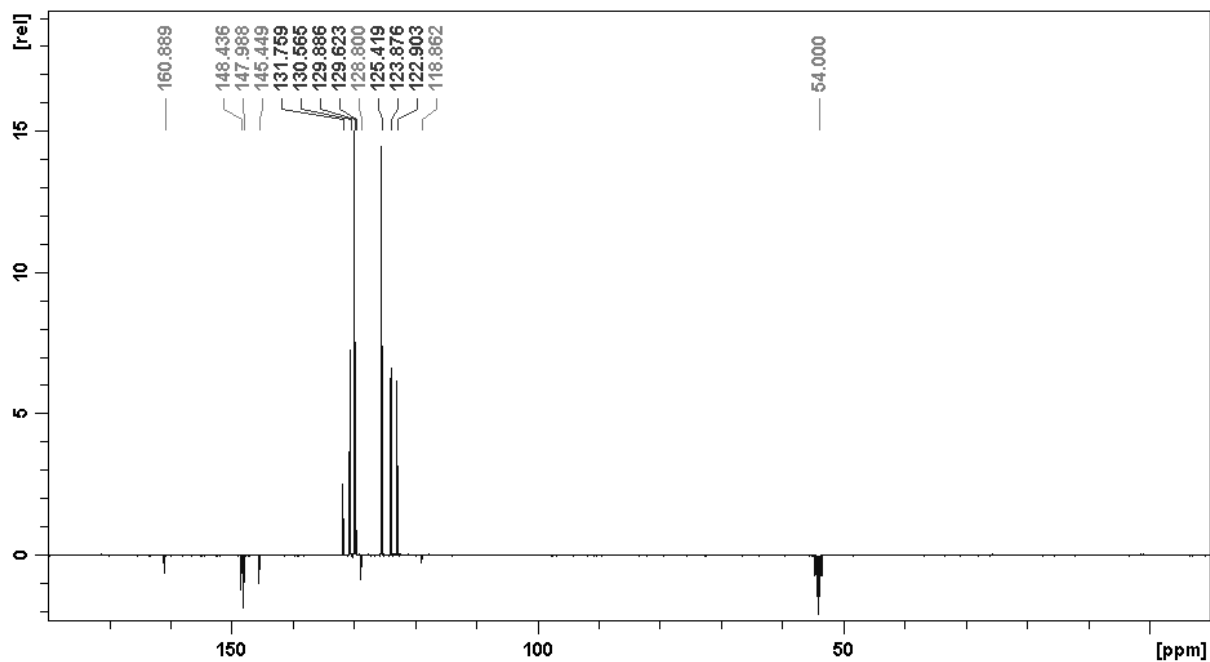


Figure S16. Carbon NMR spectrum of compound o-TPATOXD (8a).



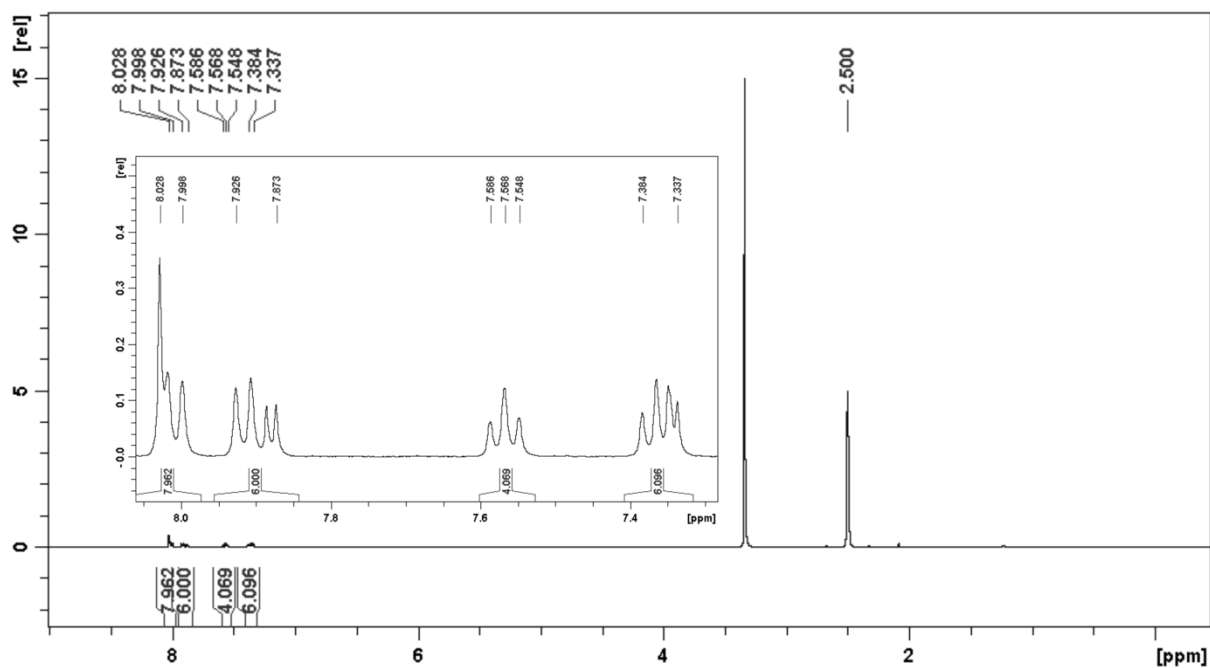


Figure S 19. Proton NMR spectrum of compound o-ICzTOXD (**8c**).

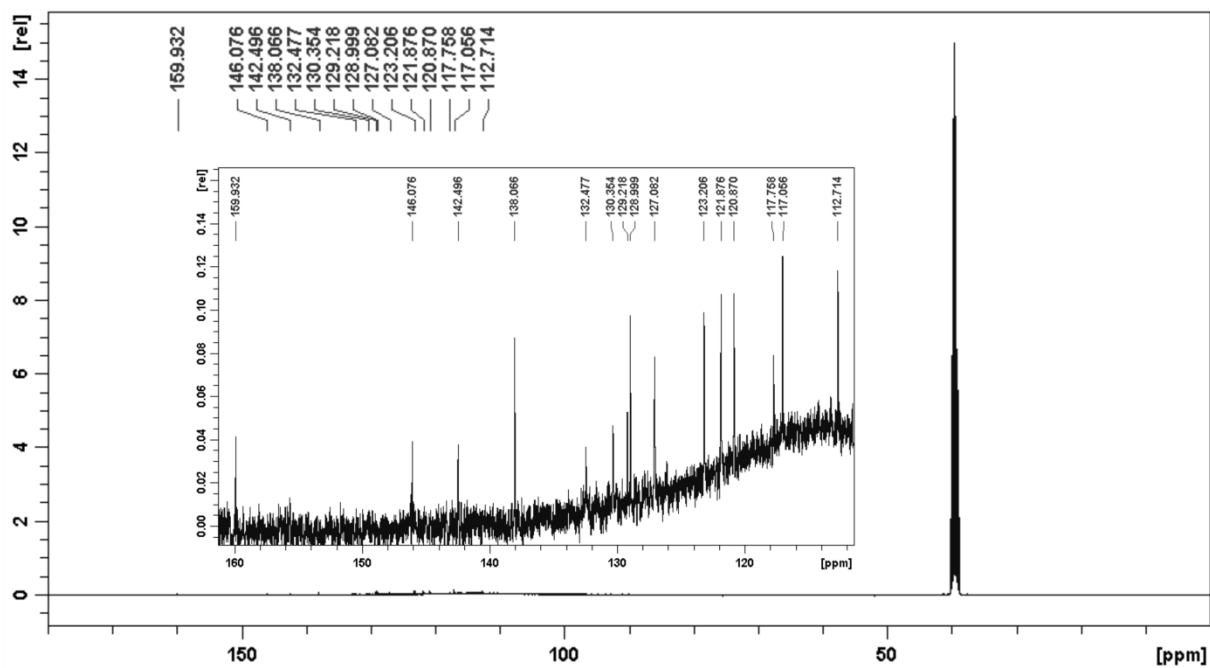


Figure S 20. Carbon NMR spectrum of compound o-ICzTOXD (**8c**).

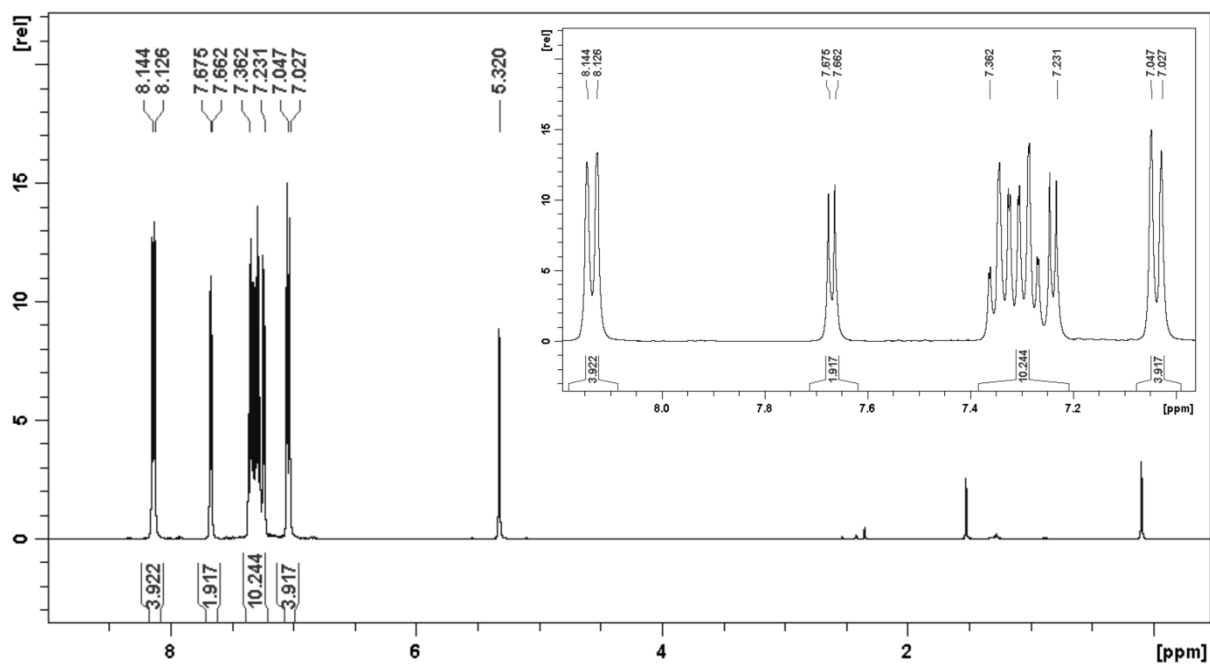


Figure S21. Proton NMR spectrum of compound o-CzTOXD (8d).

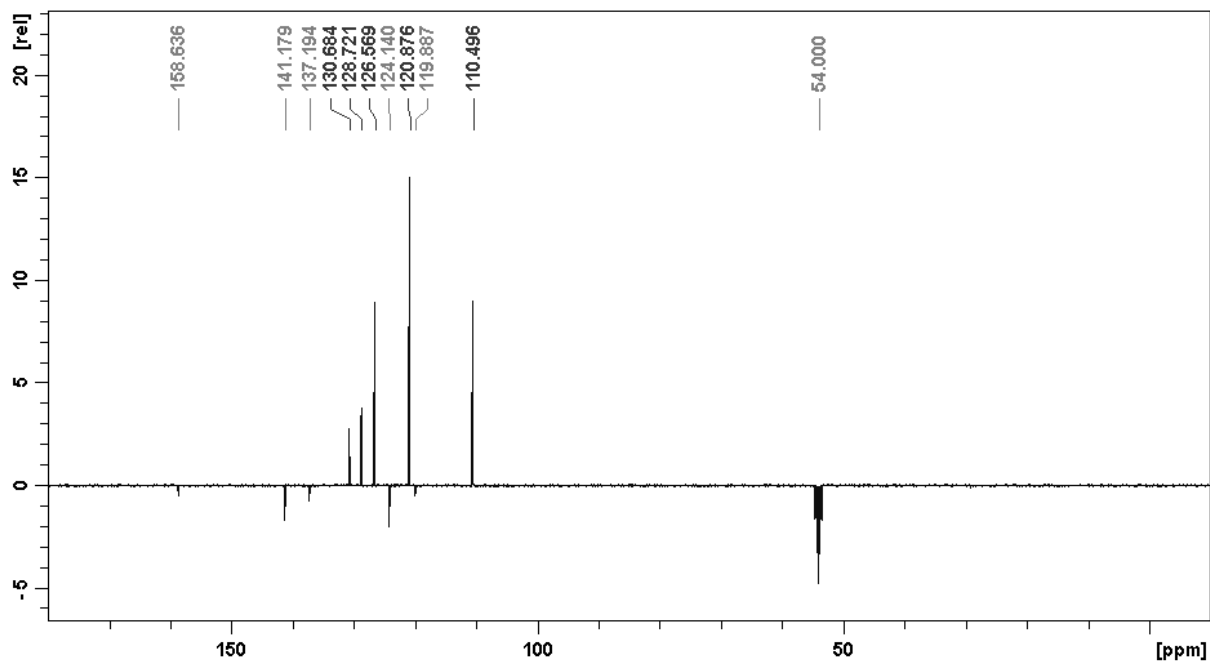


Figure S22. Carbon NMR spectrum of compound o-CzTOXD (8d).

## B) TGA/DSC

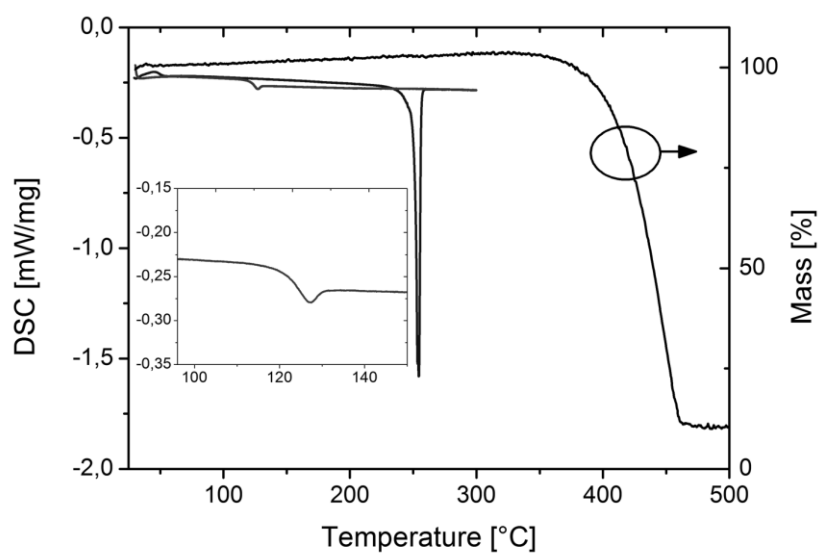


Figure S23. DSC and TG trace of o-PCzPOXD (**5b**) recorded at a heating rate of 5 °C min<sup>-1</sup>.

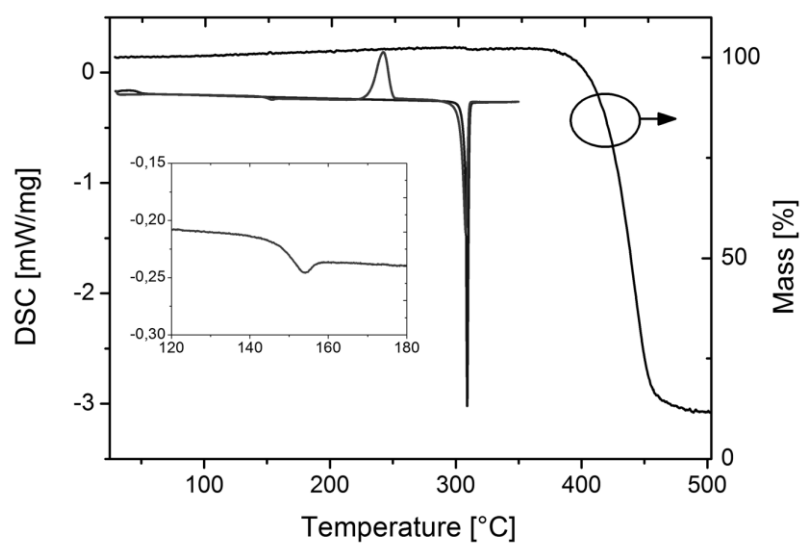


Figure S24. DSC and TG trace of o-ICzPOXD (**5c**) recorded at a heating rate of 5 °C min<sup>-1</sup>.

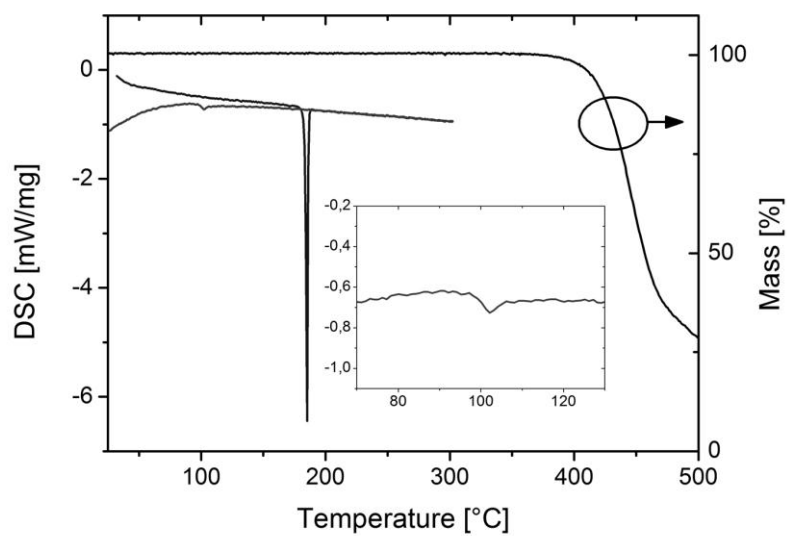


Figure S25. DSC and TG trace of o-TPATOXD (**8a**) recorded at a heating rate of 5 °C min<sup>-1</sup>.

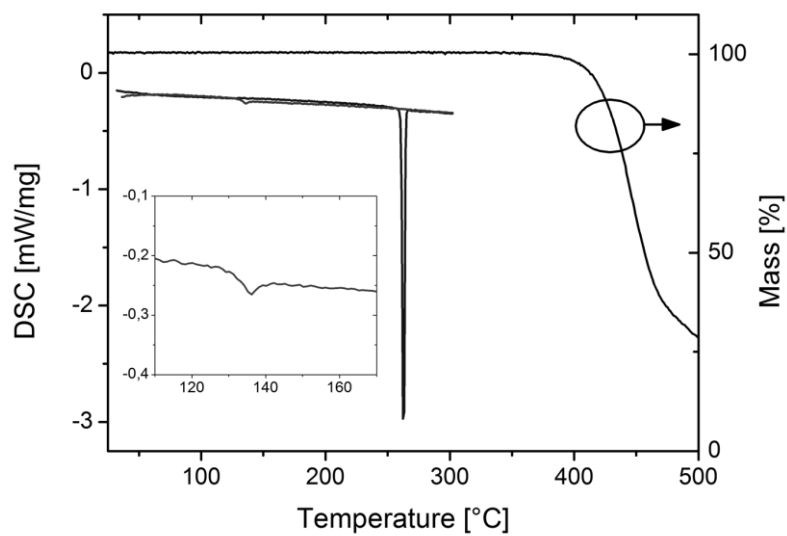


Figure S26. DSC and TG trace of o-PCzTOXD (**8b**) recorded at a heating rate of 5 °C min<sup>-1</sup>.

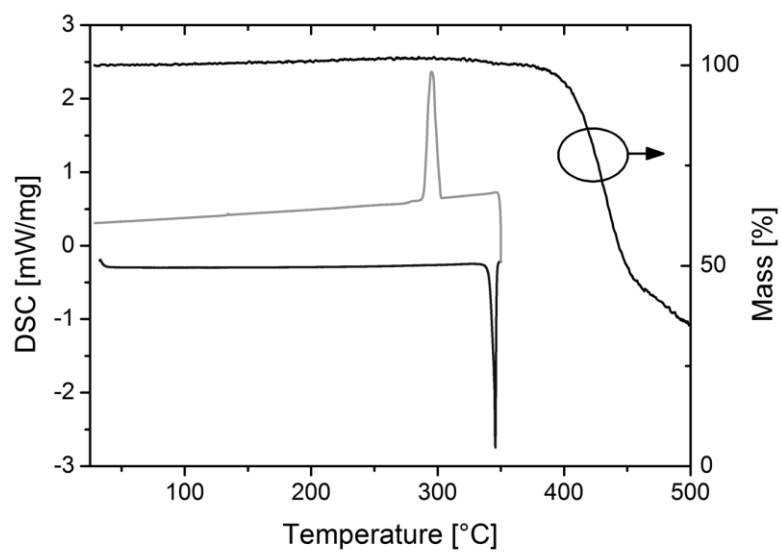


Figure S27. DSC and TG trace of *o*-ICzTOXD (**8c**) recorded at a heating rate of 5 °C min<sup>-1</sup>.

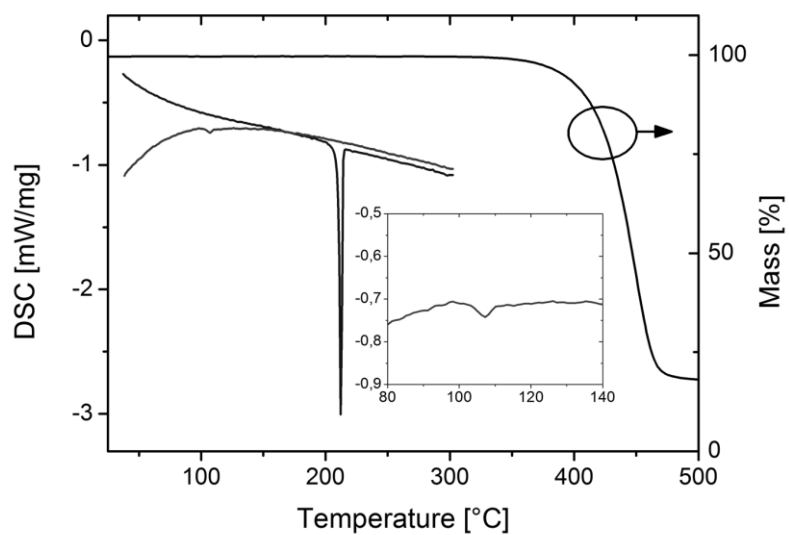


Figure S28. DSC and TG trace of *o*-CzTOXD (**8d**) recorded at a heating rate of 5 °C min<sup>-1</sup>.



### C)Cyclic Voltammetry

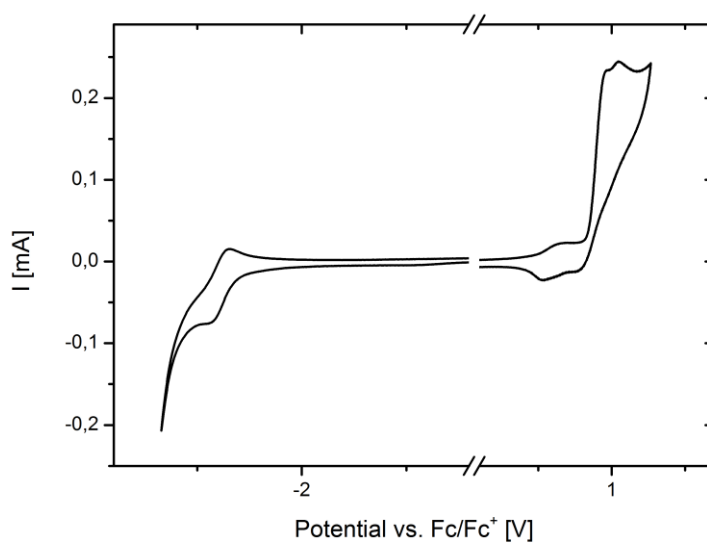


Figure S29. Cyclic voltammogram of o-PCzPOXD (**5b**).

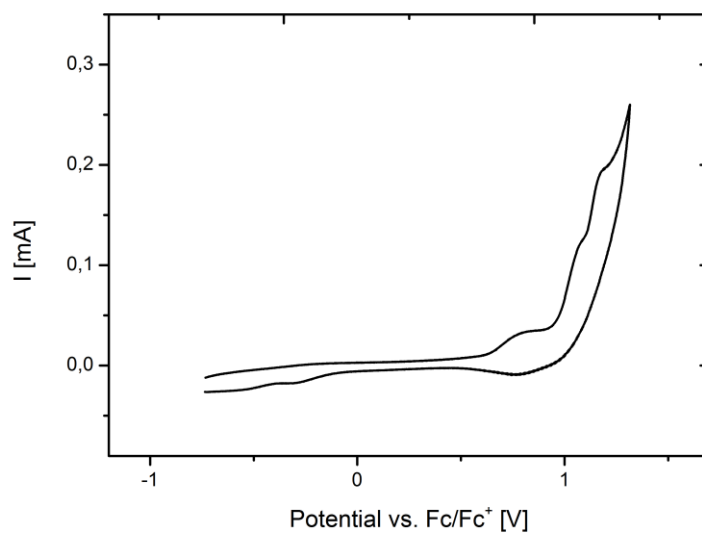


Figure S30. Cyclic voltammogram of o-ICzPOXD (**5c**).

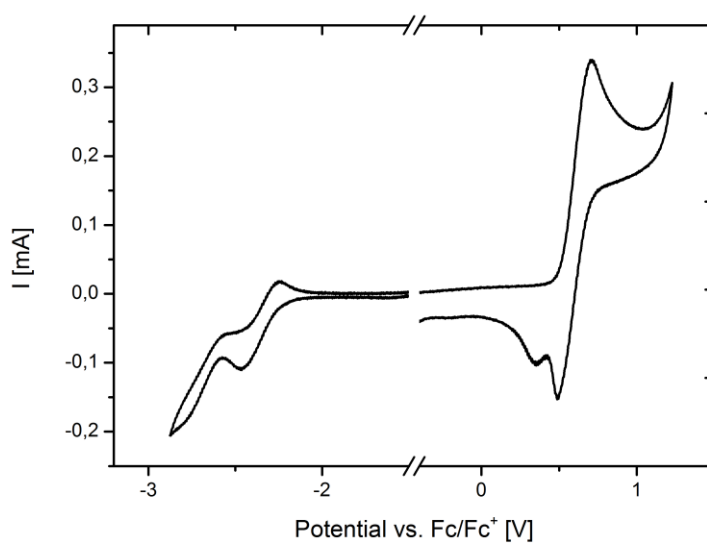


Figure S31. Cyclic voltammogram of o-TPATOXD (**8a**).

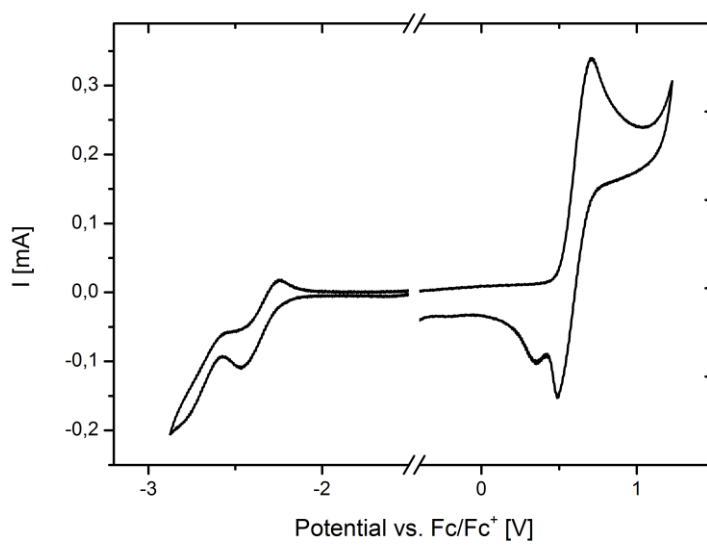


Figure S32. Cyclic voltammogram of o-PCzTOXD (**8b**).

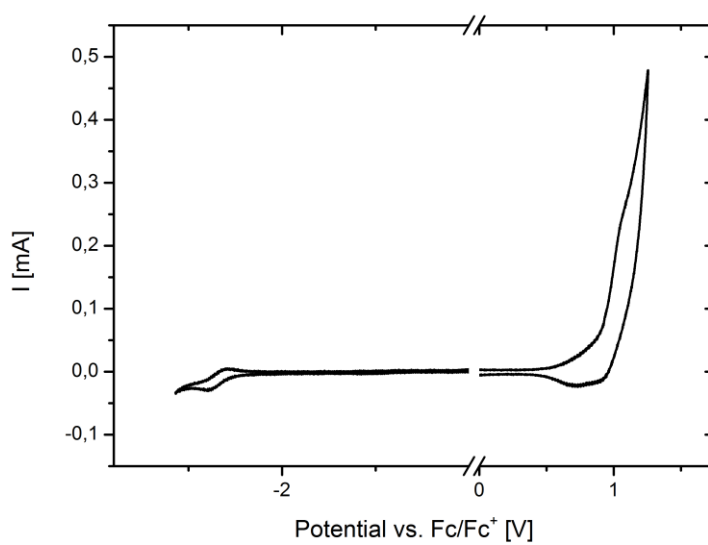


Figure S33. Cyclic voltammogram of o-ICzTOXD (**8c**).

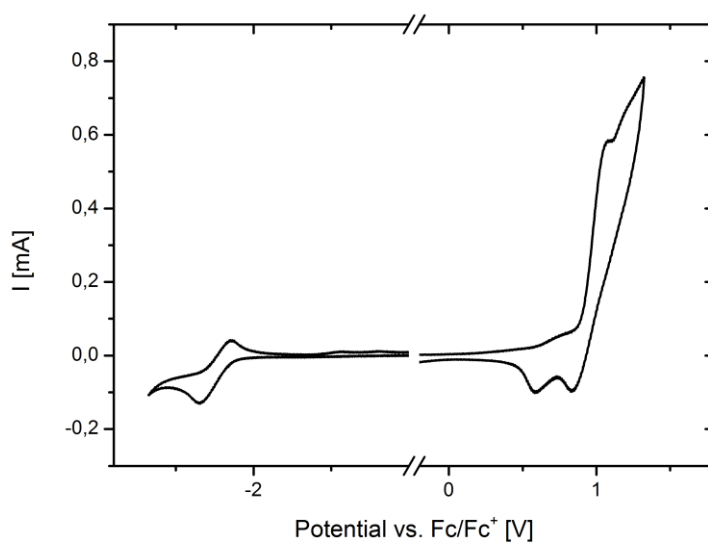


Figure S34. Cyclic voltammogram of o-CzTOXD (**8d**).

## D) Phosphorescence Measurements

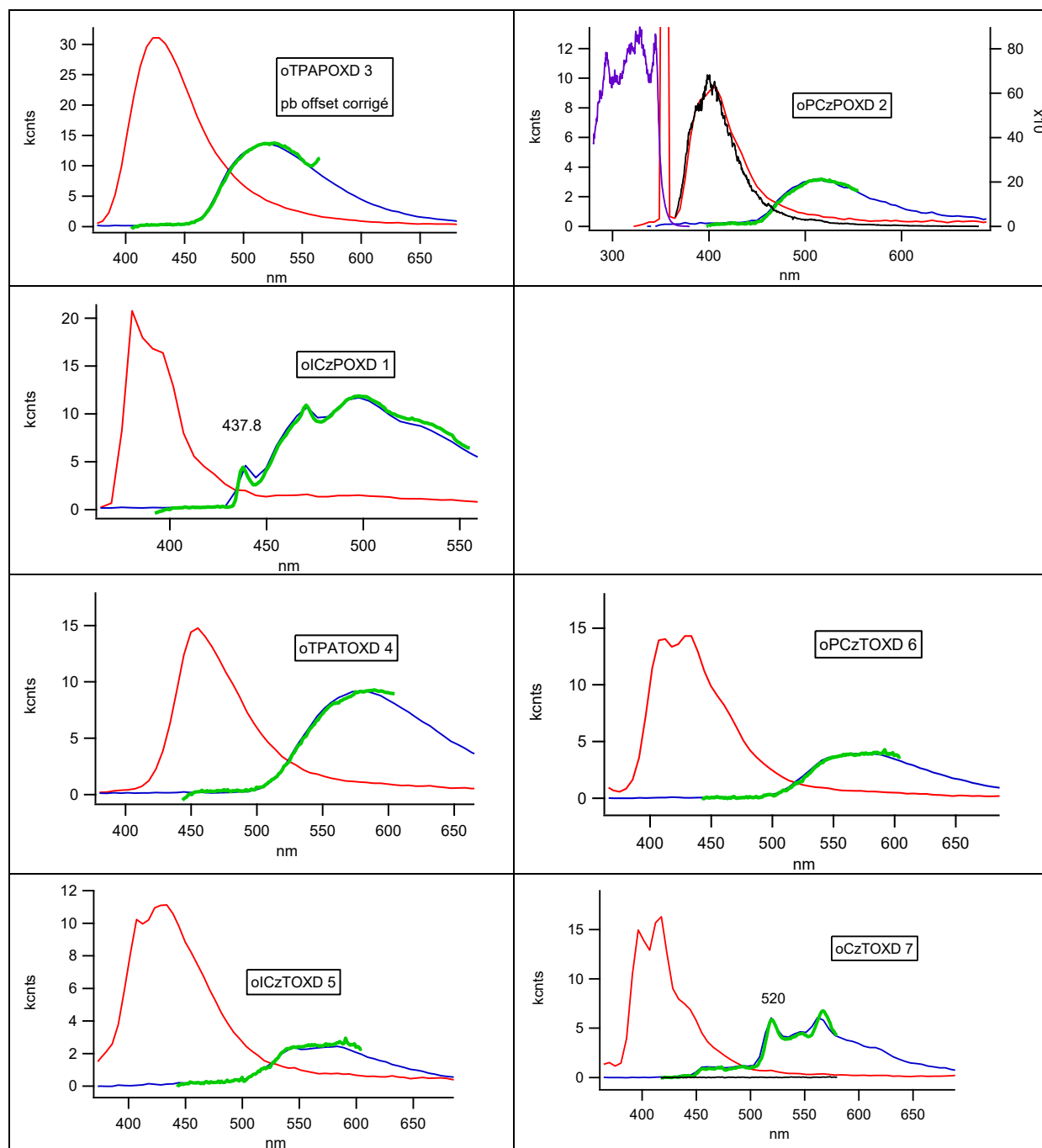


Figure S35. Singlet (red) and triplet (blue) emission spectra at 77 K with two different gratings to obtain higher resolution for the triplet emission (green).

## Lifetime Measurements

The singlet and triplet lifetimes of target materials are summarized in Table S2. Some samples present single exponential decay, others a more complex behavior; results are derived from single and double exponential fits of the data. Note that the errors for the double exponential fits are significant.

Table S2. Singlet and triplet lifetimes measured in toluene solutions at ambient temperature.

Sample	Singlet Lifetime		Triplet Lifetime
	$\tau_1$ [ns]	$\tau_2$ [ns]	$\tau$ [ms]
<b>o-TPAPOXD</b>	3.25(0.003)		~790
<b>o-PCzPOXD</b>	0.90(0.04)	2.0(45)	335(6)
<b>o-ICzPOXD</b>	0.66(0.017)	64.7(12)	349(2)
<b>o-TPATOXD</b>	1.57(0.002)		12.3
<b>o-PCzTOXD</b>	0.84(0.004)		8.3
<b>o-ICzTOXD</b>	0.53(0.009)		8.2
<b>o-CzTOXD</b>	1.28(0.004)	2.02(0.17)	11.0

## ***Experimental Parameter***

The determination of the emission lifetime at room temperature was done with Dr. François-Alexandre Mianney using a picosecond 375 nm laser source in conjunction with a detection set-up as described in (Muller, P. A., Högemann, C., Allonas, X., Jacques, P., Vauthey, E., Chem. Phys. Letters 326 (2000) 321.) Low temperature experiments were performed in frozen dilute toluene solutions using a Janis closed cycle cryostat (at 5 K) and a liquid nitrogen dewar fitted with quartz windows for measurements at ~80 K.

Time resolved experiments were obtained using a Quantel Brilliant tripled Nd-YAG laser (355 nm, 20 Hz repetition rate, pulse width ~5ns). Spectra were measured using a SPEX 270 monochromator equipped with both photomultiplier and CCD. This set-up is controlled using a home-built Labview-based program which allows using different instruments such as photon counting, oscilloscope, and additional mechanical shutters.

Additional absorption measurements were performed with a Cary 5000 instrument at room temperature, as well as emission and excitation spectra at room temperature and liquid nitrogen temperature using a Fluorolog FL3-22 instrument.

## E) DFT Calculations

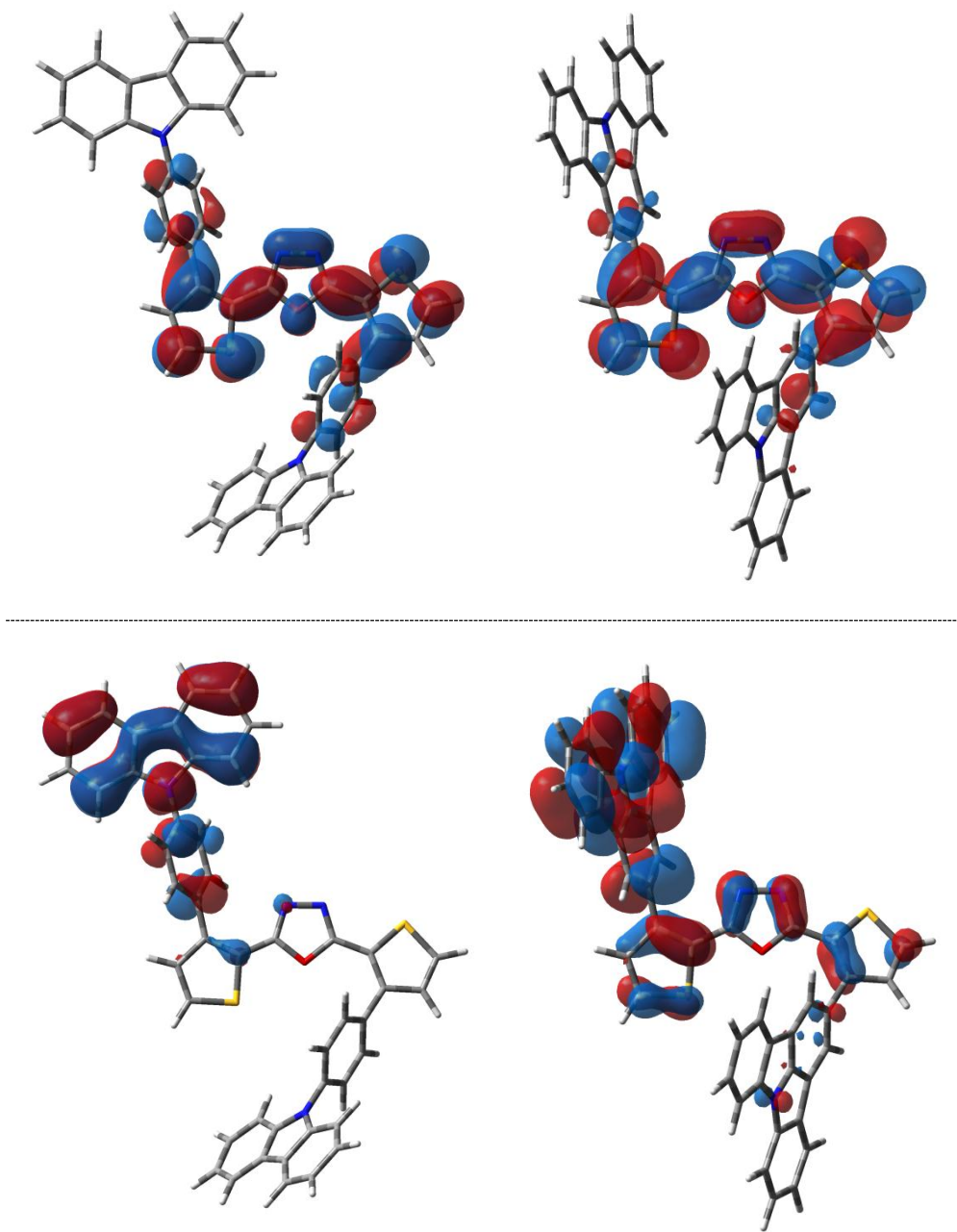


Figure S36. HOMO (bottom) and LUMO (top) of **o-PCzTOXD** (left) and **o-ICzTOXD** (right).

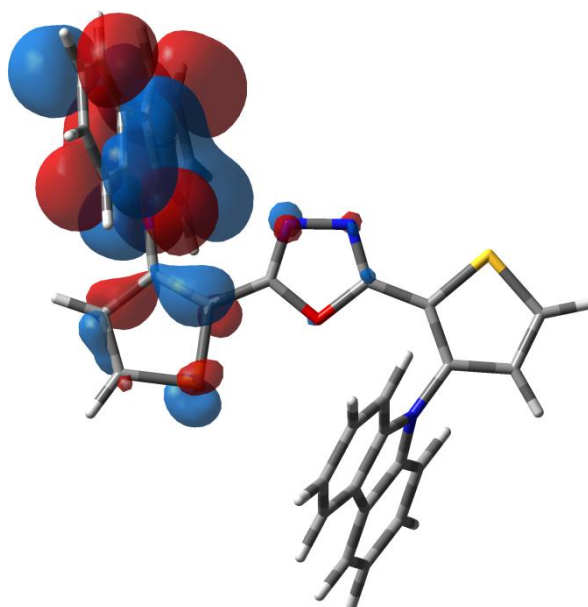
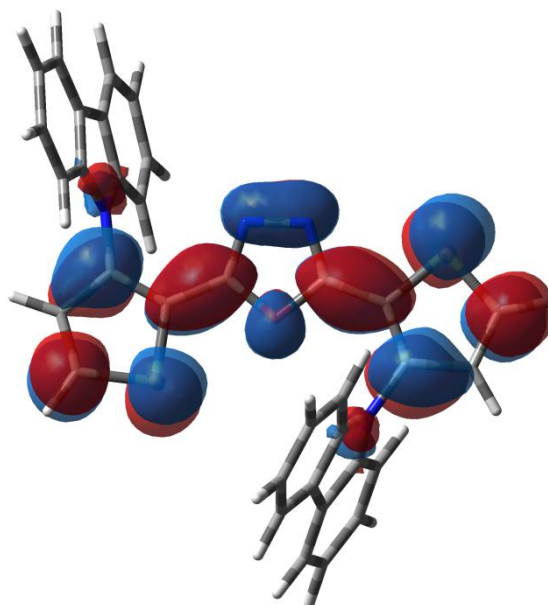
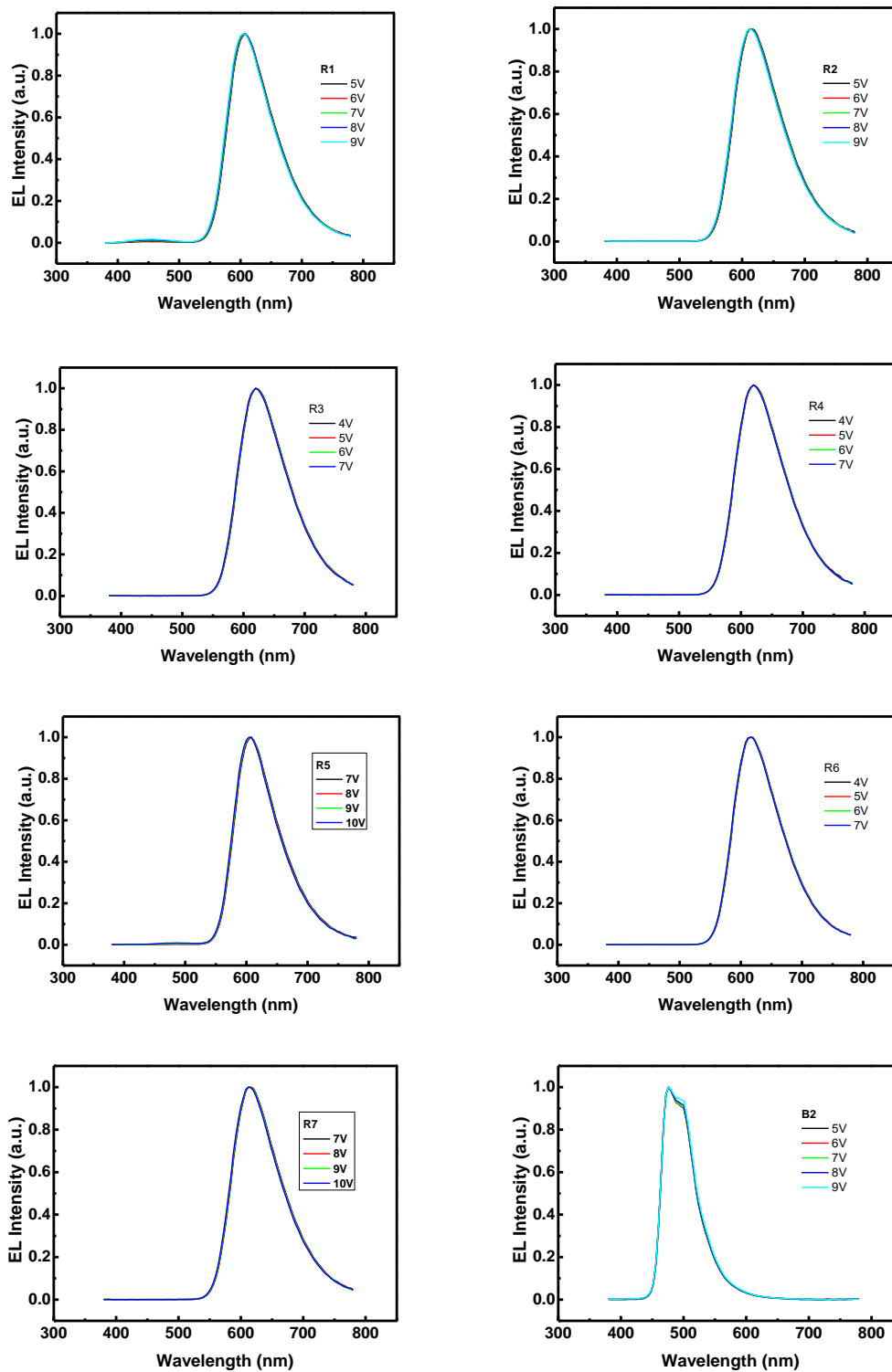


Figure S367. HOMO (bottom) and LUMO (top) of **o-CzTOXD**



## F) EL Spectra



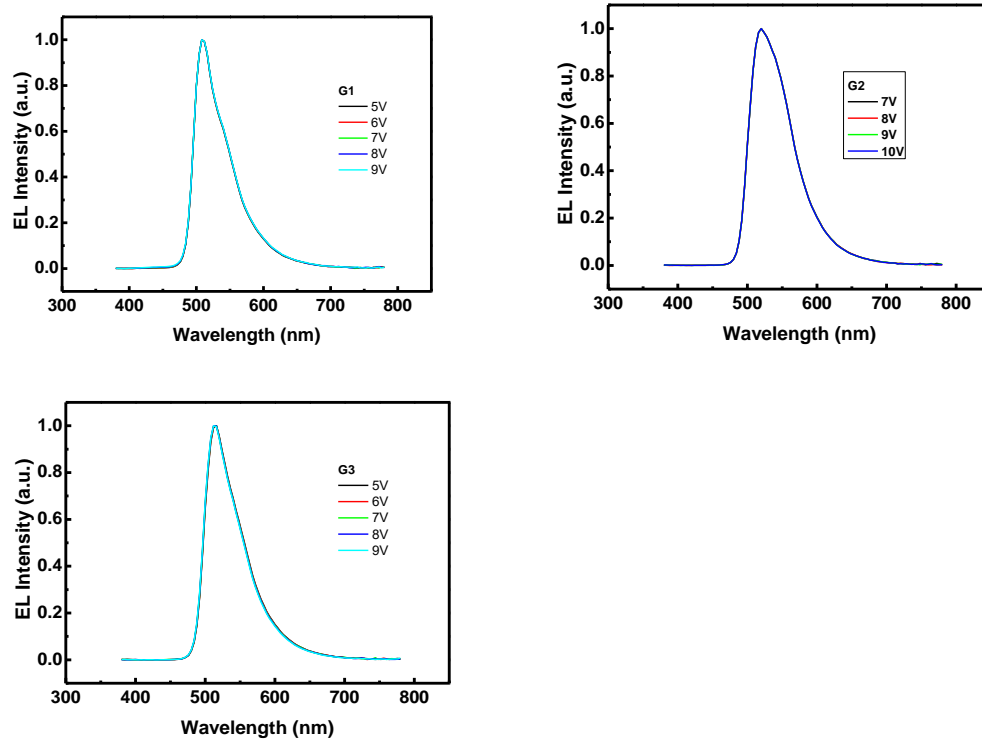


Figure S38. Electroluminescence (EL) spectra of all devices discussed in this study.

## G) Crystal Structure of Compound **3c**

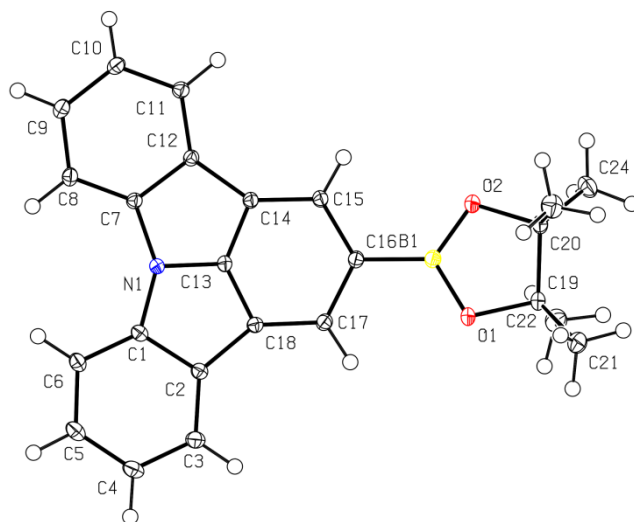


Figure S39. Molecular structure of **3c**; B, C, N, and O atoms are represented by yellow, white, blue and red ellipsoids drawn at 50% probability levels, H atoms by spheres of arbitrary radius.



## 6. Curriculum Vitae



# Johannes Binting

Hollitzergasse 2-6/55

1100 Vienna

phone: +43 660 54 99 735

e-Mail: [johannes.bintinger@gmail.com](mailto:johannes.bintinger@gmail.com)

May 2016



Date of birth: 08.03.1985      Nationality: Austrian  
Place of birth: Vienna      Status: married, one child (2014)

**Education:** **Vienna University of Technology (VUT), Vienna, Austria**  
Ph.D., Technical Chemistry – Synthesis      expected May **2016**  
MSc., Technical Chemistry – Synthesis      December **2011**  
passed with distinction  
BSc., Technical Chemistry – Synthesis      November **2009**

**Research Experience** **Vienna University of Technology (VUT), Vienna, Austria (01/2012 to present)**

*Institute of Applied Synthetic Chemistry* – Research group Prof. Johannes Fröhlich

- Using Click Chemistry for a Facile Approach Towards Self-Assembled Monolayer Field-Effect Transistors (SAMFETs): A New Versatile Approach for Sensing Applications
- Synthesis, Characterization and Printing Application of Alkylated Indolo[3,2-b]carbazoles
- Color Tuning of Oligothiophene Based Compounds – A Combined Experimental and Computational Approach
- Sterically tuned triarylaminines and oligothiophene derivatives as building blocks for novel organic electronic materials: synthesis and characterization

**Austrian Institute of Technology (AIT), Vienna, Austria (10/2015 to present)**

*BioSensor Technologies* – Research group: Prof. Wolfgang Knoll

- Synthesis and characterization of functionalized reduced-graphene oxide based gassensors for selective cyclohexanone detection

**Columbia University, New York, USA (11/2012-3/2013 and 4/2014-10/2014)**

*Department of Electrical Engineering* – Research group: Prof. Ioannis Kymissis

- Ultra-Cheap, Versatile and Robust USB-driven Sensor Platform
- Pneumatic Nozzle Printing as a Versatile Approach to Crystal Growth Management and Patterning of Printed Organic Thin Film Transistors
- Fabrication and Characterization of Organic Field Effect Transistors (OFET) Based on Dendritic Benzene Cored Triarylaminines

**Bowling Green State University, Ohio, USA (8/2012-11/2012)**

*Department of Chemistry* – Research group: Prof. Pavel Anzenbacher, Jr.

- Synthesis and Characterization of CBP Isomers as Host Materials and Their Implementation in Blue Phosphorescent PhOLED Devices

- Publications** 5 manuscripts based on the above mentioned projects are currently in preparation
- Published** Kautny, P.; Lumpi, D.; Wang, Y.; Tissot, A.; **Bintinger, J.**; Horkel, E.; Stoeger, B.; Hametner, C.; Hagemann, H.; Ma, D.; Fröhlich, J. *J. Mater. Chem. C*, **2014**, 2, 2069-2081
- Lumpi, D.; Holzer, B.; **Bintinger, J.**; Horkel, E.; Waid, S.; Marchetti-Deschmann, M.; Hametner, C.; Bertagnolli, E.; Kymissis, I.; Fröhlich, J. *New J. Chem.*, **2015**, 39, 1840-185
- Skills** **Synthesis and characterization of organic semiconductors:** purification and characterization of nitrogen and sulfur based organic electronic materials; 1D-2D NMR, GC-MS, TLC-MS, MPLC, gradient sublimation, fluorescence- and phosphorescence measurements, cyclic voltammetry
- Device fabrication and characterization:** SAMFETs, OFETs, OLEDs, PhOLEDs, Photolithography, (Co)-Evaporation, shadow masking, PE-CVD, contact profilometer, ToF-SIMS, XPS, AFM, FTIR, Keithley Semiconductor analyzer 4200
- reduced graphene oxide (rGO), CVD-graphene (wet and dry transfer process) and SWCNT-based devices for sensing applications; pneumatic nozzle printing technique for organic electronics
- Software** - Microsoft Office, Corel Draw, ChemOffice, Origin, Bruker-Thermo-PerkinElmer and Edinburgh software for data analysis - NMR, GC-MS, MPLC, UV, fluorescence
- Scholarships and Awards** Marietta Blau Scholarship **2014**  
 Marshall Plan Scholarship **2012**  
 Excellence scholarship from the Carinthian Industrialists Federation **2012**  
 Förderstipendium - Vienna University of Technology **2014**  
 Research scholarship – Vienna University of Technology **2015**  
 1<sup>st</sup> place at the International Forum-competition of Young Researchers: Nanotechnologies “IT”, St. Petersburg, April **2012**
- Conference Presentations** **Bintinger, J.**; *A chemist’s guide to electronics: from printable organic semiconductors to self-assembled monolayer field-effect transistors for sensing applications*; 31<sup>st</sup> workshop on novel Materials and superconductivity; oral presentation; Austria, February **2016**
- Bintinger, J.**; Bittner, R.; Yang, S.; , Bethge, O.; Hoffmann, H.; Kroeber, T.; Mikula, H.; Foelske-Schmitz, A.; Hradil, K.; Knoll, W.; Kymissis, I.; Fröhlich, J.; *Self-assembled monolayer field-effect transistors (SAMFETs): A new synthetic approach for sensing applications*; poster presentation; Fpi-12, Seattle USA; July **2015**
- Bintinger, J.**; Lumpi, D.; Horkel, E.; Hametner, C.; Fröhlich, J.; *A reliable synthetic route for planarized OLED compounds using condensed triarylamine and rigidified oligothiophenes*; 26<sup>th</sup> workshop Novel Materials and Superconductors, poster presentation, Austria, February **2011**
- Bintinger, J.**; Lumpi, D.; Horkel, E.; Hametner, C.; Fröhlich, J.; *A reliable synthetic route for planarized OLED compounds using condensed triarylamine and rigidified oligothiophenes*; XXIV<sup>th</sup> European Colloquium on Heterocyclic Chemistry; poster presentation, Austria, August **2010**
- Teaching Experience** **Vienna University of Technology (VUT)**, Vienna, Austria  
*Institute of Applied Synthetic Chemistry*
- University Assistant 11/2013-12/2014
  - Teaching Assistant 4/2010-1/2011
- Undergraduate level instructional laboratory course



**Occupation:** Vienna University of Technology, University Assistant, 11/2013-12/2014  
Vienna University of Technology, Teaching Assistant, 4/2010-1/2011  
promoter – advertising agency I-Punkt, 4/2009-7/2009 and 9/2009-10/2009  
civil service - MA 56 9/2003-9/2004  
youth coach (American Football, Vienna Vikings) 2003-2005

**Languages:** German (native), English (fluent in spoken and written), French (basic)

**Hobbies:** Rugby (Bowling Green State University 2012, RC Donau 2009-2013), American Football (Vienna Vikings 2000-2009, Austrian Junior National Team 2004, European All-Star Team 2004) hang gliding, snowboard tours, mountain biking (Austrian Top Six Marathon League 2001-2003) surfing, snorkeling, camping in our 1972 VW T2 camper van